MODERN BOREHOLE ANALYTICS

ANNULAR FLOW, HOLE CLEANING, AND PRESSURE CONTROL

WILSON C. CHIN

Modern Borehole Analytics

Modern Borehole Analytics

Annular Flow, Hole Cleaning, and Pressure Control

Wilson C. Chin

Wiley Global Headquarters
111 River Street, Hoboken, NJ 07030, USA

For details of our global editorial offices, customer services, and more information about Wiley products visit us at www.wiley.com.

Limit of Liability/Disclaimer of Warranty
While the publisher and authors have used their best efforts in preparing this work, they make no representations or warranties with respect to the accuracy or completeness of the contents of this work and specifically disclaim all warranties, including without limitation any implied warranties of merchantability or fitness for a particular purpose No warranty may be created or extended by sales representatives, written sales materials, or promotional statements for this work The fact that an organization, website, or product is referred to in this work as a citation and/or potential source of further information does not mean that the publisher and authors endorse the information or services the organization, website, or product may provide or recommendations it may make This work is sold with the understanding that the publisher is not engaged in rendering professional services The advice and strategies contained herein may not be suitable for your situation You should consult with a specialist where appropriate Neither the publisher nor authors shall be liable for any loss of profit or any other commercial damages, including but not limited to special, incidental, consequential, or other damages Further, readers should be aware that websites listed in this work may have changed or disappeared between when this work was written and when it is read.

Cover images: Wilson C. Chin
Cover design by: Kris Hackerott

Printed in USA

10 9 8 7 6 5 4 3 2 1

Contents

Preface

When I first joined the petroleum industry more than two decades ago, my exposure to field operations, or just about anything "oily," was minimal or next to nothing. My supervisor at Schlumberger, Larry Leising, would preach incessantly about the need for "hole cleaning," something that I, an M.I.T. Ph.D. firmly grounded in applied math, should focus on. Something important. Something that those new-fangled horizontal wells on the horizon died for. But no, that was impossible. My parents, who'd never made in past elementary school in China, I said, "paid good money" to send me to college. So explaining why I'm sitting next to a "rathole" or "dog house" on a drilling rig in the middle of nowhere cleaning holes would not go well with them. Or with my worthy ancestors. And so, annular flow and drilling safety would have to wait.

Some years later, I'd hear more "dirty stuff" about dirty stuff. Why mudcake was "bad" and responsible for differential sticking. Stuck drillstrings. Lost tools. Fishing jobs. Unimpressive things responsible for impressive hundreds of millions in damage each year. As for hole cleaning and cuttings transport, mudcake catastrophes were likewise "solved" by empirical "common sense" methods seemingly pulled from thin air. No one understood why they worked. Or why they probably didn't. War stories proliferated in trade journals and at conferences. And then there were well logging folks running "formation testers." Petrophysicists who curiously *wanted* good thick mudcakes. Cakes that would seal their pads well and enable the extraction of clean fluid samples. Thick ones that reduced invasion at the sandface so that pore pressure measurements actually measured formation (and not high borehole) values.

Like hole cleaning, what worked was anyone's guess. No one really knew why mudcakes grew "like $\sqrt{t}$." They just did, it seemed. But they really didn't. Many drillers believed that formation type didn't matter. But log analysts argued that formation permeabilities did. In fact, at really low mobilities, they could control the physics and dangerously reduce cake thickness. Along with pore pressure, of course. And pore pressure? In tight

zones, such as those encountered in today's unconventional applications, you couldn't even measure pore pressure without waiting hours! So, one might ask, now what? What are our alternatives? What can we really solve as a hard-pressed industry?

Those who have read the author's books over the years will appreciate that substantial personal efforts have been directed at annular flow modeling, cuttings transport, hole cleaning and pressure control. And that mudcake dynamics, and pore pressure and permeability prediction in tight formations, have also been the focus of extensive work in formation testing and real-time formation evaluation. And similarly with multiphase reservoir flow and mixing near to the wellbore. We've worked hard at many disciplines. A brief narrative of chronological developments appears in Chapter 1 in support of Chapters 2–8.

But it was not until the aftermath of the Deepwater Horizon incident that the underlying ideas for the present book developed. The author, at the time, served as Expert Witness in the Macondo litigation – an eye-opening event clearly highlighting the necessity for credible models of physical phenomena in support of operational safety. And it was during these activities that one key realization developed: that basic elements involving annular flow and pressure control, mudcake growth and dynamic coupling to the formation, and finally, permeability and pore pressure prediction in the reservoir, can be combined to provide an integrated software system for realistic well planning. One dictating how borehole flows are affected by mudcake and reservoir events, how annular flows can be manipulated, how mudcake growth can be controlled, and finally, how (once) elusive properties like permeability and pore pressure in tight reservoirs can be measured rapidly, economically and safely.

This objective forms the basis for the present book, appropriately entitled Modern Borehole Analytics for Annular Flow, Hole Cleaning and Pressure Control. But unlike the author's previous works which emphasized mathematics, algorithms and physical validations, this volume builds upon prior work and focuses on applications and software models that are available for immediate industry use. Very few equations this time, just the facts. And so, the journey comes full circle . . . from utter initial confusion to, hopefully, something practical, useful and significant.

Wilson C. Chin, Ph.D., M.I.T.
Houston, Texas and Beijing, China

Email: wilsonchin@aol.com
Phone: (832) 483-6899

Acknowledgements

This book is dedicated to Larry. Larry Leising, that is, fellow M.I.T. graduate and Schlumberger colleague who talked me into parting from a glamorous aerospace industry for petroleum endeavors unknown. His early insights on hole cleaning, horizontal wells and MWD telemetry, combined with practical experiences that he shared, made a significant difference in my research interests and modeling approaches over the years. Larry was forever helpful. At the time, I recall, "mud sirens" in MWD always jammed and downhole debris was blamed. I suggested simpler wind tunnel test methods to explore some "wild and crazy" ideas. Maybe jamming was a purely hydrodynamic effect. Maybe. Being the theoretician that I was then, I didn't know the difference between a squirrel cage blower and a ceiling fan. Larry was instrumental in building our wind tunnel, in developing our test methods, and in the important discovery of the "downstream rotor, stable open" mud sirens now in routine use – a game-changing invention he rightfully shares but never took credit for.

As usual, the author is indebted to Phil Carmical, Publisher at Scrivener Publishing, for his support and encouragement in disseminating his highly technical research monographs, together with equations, cryptic Greek symbols, formal algorithms and more. Our fruitful collaboration goes back some twenty years, first with annular flow modeling, then with reservoir engineering, horizontal drilling, formation testing, Measurement While Drilling and other disciplines. Phil and I share one common goal – we approach real world problems with the best scientific tools available and turn over each and every stone. In times of uncertainty, such as the economic turmoil now facing all of us, it is even more important to "solve problems right" and work more productively. What our industry needs is more math and not less, more questioning and less acceptance, and it is through this latest volume that we hope to stimulate thought and continuing research in engineering endeavors central to the modern exploration for oil and gas.

1
Fundamental Ideas and Background

As suggested in our title *Modern Borehole Analytics for Annular Flow, Hole Cleaning and Pressure Control* and in our Preface, this book deals generally with the subject of borehole flow modeling. We build upon original research efforts documented in the author's earlier monographs, (i) *Borehole Flow Modeling in Horizontal, Deviated and Vertical Wells* (Gulf Publishing, 1992), (ii) *Computational Rheology for Pipeline and Annular Flow* (Elsevier, 2001), and (iii) *Managed Pressure Drilling: Modeling, Strategy and Planning* (Elsevier, 2012).

The last book, which was translated into Chinese in 2016, presents major research results completed under Contract No. 08121-2502-01, sponsored by the United States Department of Energy – 2009 Research Partnership to Secure Energy for America (RPSEA), Ultra-Deepwater Exploration Program, for "Advanced Steady-State and Transient, Three-Dimensional, Single and Multi-phase, non-Newtonian Simulation System for Managed Pressure Drilling."

The foregoing "MPD book" supersedes the prior two and focuses on validated analytical and mathematical models. As such, it does not discuss experimental results in detail, such as those cited in its references. Nor does it address the subjects of mudcake characterization and growth, which are considered in (i) *Quantitative Methods in Reservoir Engineering, 2nd Edition – with New Topics in Formation Testing and Multilateral Well Flow Analysis* (Elsevier, 2017) for single-phase flows and (ii) *Formation Testing: Low Mobility Pressure Transient Analysis* (*with CNOOC*, John Wiley, 2015) for multiphase flows.

The subject of formation permeability and pore pressure prediction, which is very relevant to mudcake growth and coupling to the formation, especially tight formations, is also omitted from the MPD reference. It was largely developed in the context of formation tester pressure transient and contamination modeling, treated extensively in two books, (i) *Formation Testing Pressure Transient and Contamination Analysis* (*with CNOOC*, John Wiley, 2014) and (ii) *Formation Testing: Low Mobility Pressure Transient Analysis* (*with CNOOC*, John Wiley, 2015).

As explained in our Preface, the present volume focuses on practical applications, and not theory, whose inclusion would have made this work unwieldy and difficult to read. *The complete picture for borehole annulus, mudcake and formation is considered here.* It goes without saying that modern algorithms are sophisticated and output intensive. Gone are the days of simple engineering models and algebraic formulas designed for "back of the envelope" answers. Real solutions now require complicated partial differential equation formulations, whose field solutions demand computer menus offering different numerical options, outputs with three-dimensional color graphics, and varied post-processing utilities. With the exception of Chapter 6, which deals with mudcake growth in single-phase flow, together with formulas and source code, all of our models are hosted by advanced software. However, our software models, validated and in use at major service companies, are affordable, easy to use, and aimed at mainstream audiences.

In this first chapter, we will outline the basic problems solved – for details, the reader is referred to the foregoing cited book references. Our capabilities are described in terms of specific problems and their solutions. To ensure clarity, we described the formulations in terms of input menus and our results in terms of output data listings and color graphics. Users desiring further explanation or examples are encouraged to consult our references, or even better, replicate and extend our computed results. Our explanations below, while oriented to laymen and non-specialists, are nonetheless rigorous and scientifically correct.

1.1 Background, industry challenges and frustrations.

In the following sections, we introduce annular flow modeling (subject of Chapters 2, 3 and 4), mudcake dynamics (Chapters 5 and 6), and permeability and pore pressure prediction (Chapters 7 and 8). Only brief overviews of the problems are provided, as details are available in the referenced books. Applications are considered in specific chapters.

1.1.1 Annular flow modeling issues and problem definition.

The fundamental problem in downhole applications is borehole flow modeling in the annulus. Real annuli are typified by varied geometries, e.g., refer to those sketched in Figure 1-1.
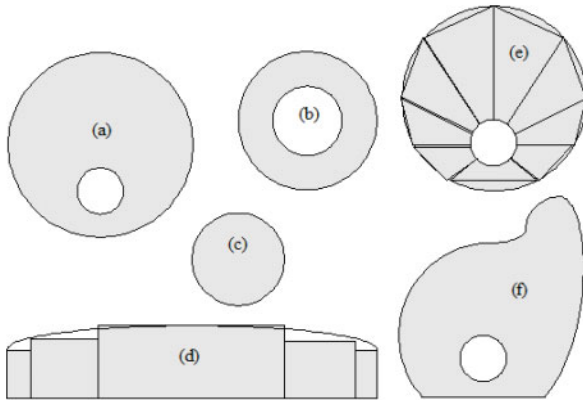
Figure 1-1. Real and idealized annular geometry models.

Figure 1-1c represents flow in a circular pipe. For many steady-state non-Newtonian flows, pipe solutions are available analytically, including closed form representations for the circular cross-section "plug flow" found at the center of the pipe in the case of yield stress fluids (plugs move as solid bodies and plug flows are convected downstream with constant speed). Some approaches to annular flow employ somewhat dubious notions related to "equivalent hydraulic radius," where flow rates for given pressure gradients are computed from an "equivalent" pipe flow – a somewhat questionable and ill-defined concept at best. For concentric annuli, e.g., Figure 1-1b, numerical solutions are available for Power law fluids only; in the case of Bingham plastics and Herschel-Bulkley fluids, a concentric "ring plug" wraps around the inner body – here. concentricity arises from symmetry considerations, but simple solutions do not appear to be available. Real annuli are highly eccentric, as in Figure 1-1a, and numerical solutions for non-yield cases are available in bipolar coordinates. Very often, simpler "pie-slice" models (see Figure 1-1e) are used, consisting of crude solution "slices" extracted from concentric solutions. When eccentricity is small, the annulus is often "unwrapped" as in Figure 1-1d, resulting in multiple "slot flows" solved by simpler rectangular flow formulas.

Of course, the general problem is represented by Figure 1-1f, where a highly eccentric annulus is shown, which may possess non-flat cuttings beds, irregularly shaped washouts, and so on. This general problem, and all of the simpler prior flows, have been solved by the author and are documented in his three annular flow books for Newtonian, Power law, Bingham plastic and Herschel-Bulkley fluids, for example, as schematically described by Figure 1-2 in terms of constitutive relations.
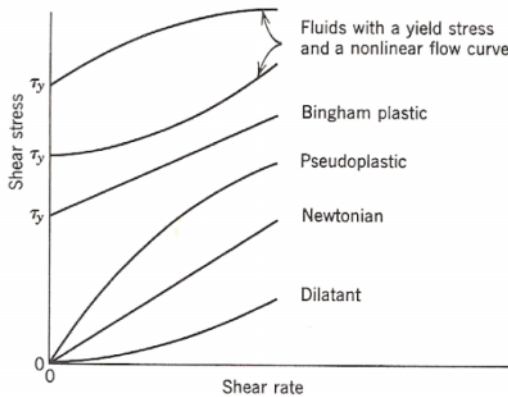
Figure 1-2. Constitutive relations for basic rheologies.

Plug flows, as we have noted, arise from yield stress effects; in a circular pipe, the plug is always circular and situated at the center of the pipe. For concentric annuli, by virtue of symmetry considerations, the plug is a *concentric ring* that wraps around the centerbody. Plug flows introduce nontrivial changes to velocity and stress patterns in the annular cross-section, and are associated with dynamic attributes important in hole cleaning and mud displacement in cementing applications.

For the general annulus in Figure 1-1f, the shape, size and location of the plug have long represented unresolved modeling challenges. Authors typically assume that a plug ring exists which wraps around the centerbody or drillpipe, although it will not form a perfect circle. A macroscopic "pie slice" view of the annulus is taken, and within each slice of the pie, a plug segment roughly parallel to the local outer annular contour is assumed. The cumulative effect of all such slices is a "wrap around plug ring" with variable azimuthal thickness. This seems to be reasonable, providing an implementable "recipe" or algorithm.

However, the logic is flawed. Consider a highly eccentric example where the inner pipe diameter is continuously reduced. At some point, one expects to find an oval or elliptical plug in the wide part of the annulus, as in the far right of Figure 1-3 – much like that of a circular pipe, although it will neither be circular in cross-section nor centered (however, the left two plug flows are reasonable). How its shape, size and location vary with geometric details, and in fact, with flow rate and non-Newtonian rheology, have been open questions until now.   The problem is solved numerically in *Managed Pressure Drilling* (2012) and we refer readers to the book for the detailed theory and applications.
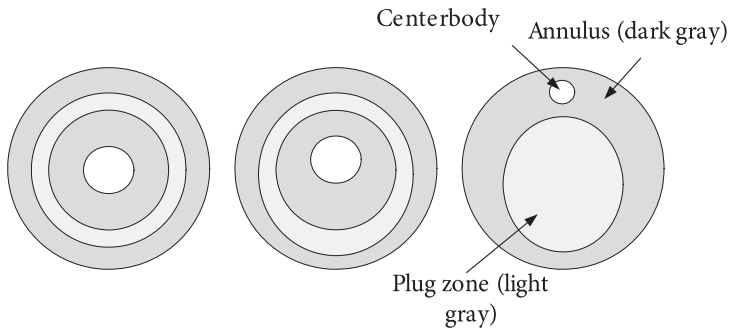
Figure 1-3. Different plug zone configurations.

The general borehole flow problem considered in the present book is defined in part by Figure 1-4. Here we have an arbitrary pumping schedule where different non-Newtonian fluids are pumped at different volume flow rates for different time durations down a circular drillpipe (or casing), through the drillbit, and finally, up the annulus. The annular geometry may be quite general, as noted earlier; in addition, the borehole axis may be curved (so that centrifugal forces enter the flow description). Furthermore, the pipe (or casing) may rotate and move axially as arbitrary functions of time, to be defined through computer menus to the user's discretion. Finally, the pump pressure gradient may be completely transient. In a typically eccentric annulus, plug flows are accurately calculated as noted above. This general annulus flow problem is treated in Chapters 2, 3 and 4 and in greater mathematical detail in the author's *Managed Pressure Drilling* (2012, 2016).   However, these chapters consider only those situations where the sandface is perfectly sealed, that is, fluid flow into and from the formation is disallowed – the mudcake, we emphasize, is impermeable to flow.
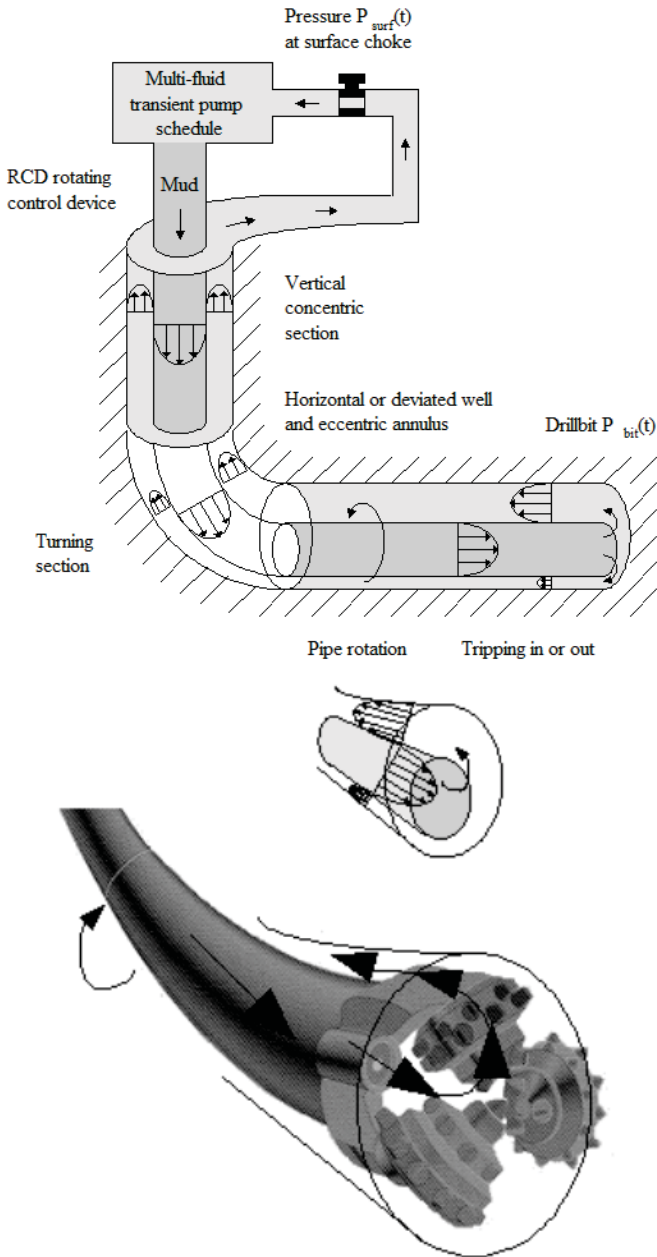
Figure 1-4. Eccentric flow model and general problem definition.

1.1.2 Mudcake growth, dynamic coupling and reservoir interaction.

Despite the apparent generality of our annular flow modeling algorithms, they have not included provision for flow into or out of the reservoir. Mudcake is assumed to exist, but in practice, its integrity may be degraded by excessive reservoir pressures. In this book, we consider weak-to-strong overbalanced flow into the formation. Solid particulates carried by drilling mud will leave a cake at the sandface that grows with time – the higher the filtration rate into the Darcy formation, the higher the cake growth rate and the stronger the mudcake barrier to flow.

It has long been assumed that mudcake grows in thickness like "$\sqrt{t}$" where t is time. However, when this result was first presented to the author as a fundamental result of fluid-dynamics, numerous questions arose. These are raised and addressed in Chin (1993, 2002, 2017), with the latest reference providing the most comprehensive treatment. In summary, the "$\sqrt{t}$ law" only applies when an incompressible mudcake grows on filter paper, that is, formation effects are negligible – and then, only in linear "top to bottom" or "left to right" flow. When formation effects are unimportant, but the "filter paper is curved" so that it is coincident with the circular trace of a well, the law does not apply. In fact, a more complicated time function applies, leading to a finite "time to plug" – a definite consideration when drilling slimholes. Furthermore, when the mobility (that is, permeability divided by viscosity) in the formation is comparable to that of the mudcake, a strong dynamical interaction and coupling is found. Cake growth will depend on mixing events in the reservoir while, of course, the dynamics of the reservoir are dependent on the volume of filtrate flow through the mudcake. For single-phase flows, relative simple analytical and numerical models are offered in Chapter 5, while for multiphase flows, the solution described in Chapter 6 requires the treatment of partial differential equations.

For many years, the above description was not useful for practical computations because the pore pressure on the downstream side of the flow was not available. To state that pore pressure was needed was to state the obvious, but without a number, no means of incorporating farfield reservoir effects were possible. Advances in formation testing, coupled with new pressure transient interpretation methods that use early time data in low mobility applications now provide permeability and pore pressure quickly and accurately. These are described in Chapters 7 and 8 where numerous examples are given. This book, in its totality, considers the borehole, the mudcake and the formation as a system.

1.2   Related prior work.

We emphasize that the work reported in this book, covering multiple petroleum disciplines, is the outgrowth of mature research conducted over more than two decades. Much of the subject matter has appeared in prior publications and patents, and many of our flow algorithms, which have been successfully commercialized, are offered by oil service companies to industry clients. Figures 1-5 to 1-10 provide a quick preview of our technical exposure – we wish only to show how our results are mature and well validated through field applications. Naturally, we've produced our share of mistakes, and should readers discover any glaring or subtle errors, we would welcome the findings.

Figure 1-5. Rheology book publications (1992-2016).
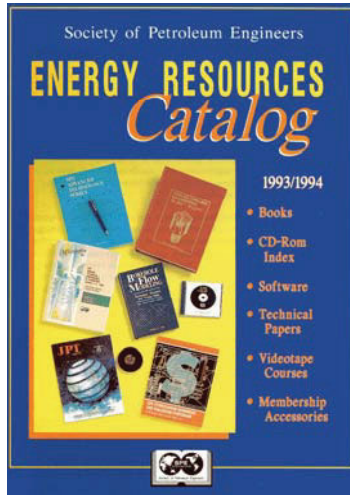
Figure 1-6. *Borehole Flow Modeling* (1992), our very first book related to petroleum engineering.
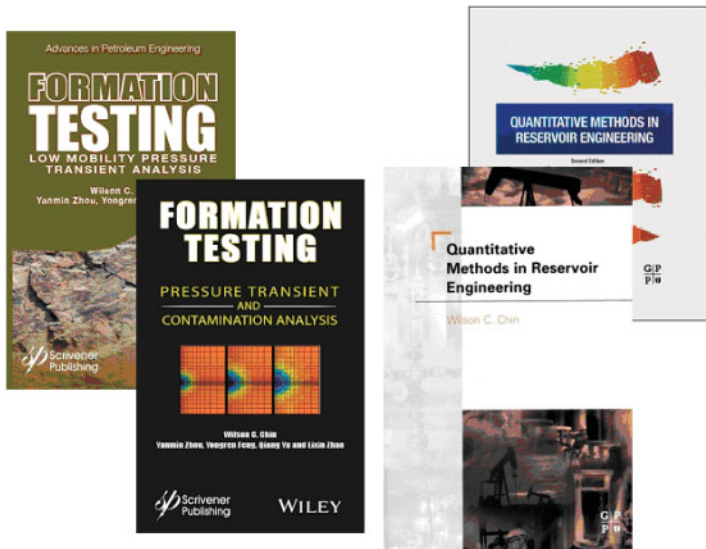
Figure 1-7. Formation testing and reservoir engineering monographs.

LAMINAR DISPLACEMENT OF VISCOPLASTIC FLUIDS IN ECCENTRIC ANNULI-
NUMERICAL SIMULATION AND EXPERIMENTAL VALIDATIONS

Mark Savery, Peng Tonnnukayakul and Wilson Chin [*]
Thana Deawwanich, Jeffery Liew and Q. Dzuy Nguyen [**]
Halliburton, Duncan, OK 73536

[**] School of Chemical Engineering, University of Adelaide, Adelaide, Australia, 5005

Summary: In the completion of oil and gas wells, zonal isolation requires proper cement placement with adequate bonding to the casing and formation. To achieve successful zonal isolation, the cement slurry must be properly designed to enable effective ... s. The rheological properties, pump rate, and interfacial mixing of these ... able computational modeling of these dynamic parameters is critical to

DISPLACEMENT OF VISCOPLASTIC FLUIDS IN ECCENTRIC
ANNULI: NUMERICAL SIMULATION AND EXPERIMENTAL
VALIDATION

Deawwanich[1], J.C. Liew[1], Q. D. Nguyen[1], M. Savery[2], N. Tonnukayakul[2] and W. Chin[2]
[1] School of Chemical Engineering, University of Adelaide, Adelaide, Australia
[2] Halliburton, Duncan, OK 73536, USA
tdeawwani@chemeng.adelaide.edu.au

STRACT

completion of oil and gas wells, zonal isolation requires proper cement placement with
uate bonding to the casing and formation. To achieve a successful cementing operation, the
ent slurry must be properly designed to enable effective displacement of the drilling fluid
n the annulus between the casing and wellbore. This is a complex process, involving time-
ndent displacement of non-Newtonian fluids in eccentric annuli. The rheology, flow rate,
...
...ement efficiency.
s is critical to pre-
ental data are also
development of a
rotation for flow-
ment experiments
metries and flow
alidate numerical

Flow Visualization and Numerical Simulation of Viscoplastic
Fluid Displacements in Eccentric Annuli

Q.D. Nguyen[a], T. Deawwanich[a], N. Tonnukayakul[b], M.R. Savery[b] and W. Chin[b]

AADE-08-DF-HO-08

Modeling Cement Placement Using a New 3-D Flow Simulator

Mark Savery, Wilson Chin, and Krishna Babu Yerubandi, Halliburton

Abstract
    The paper presents a new computational fluid dynamics
(CFD) simulator that models multiple aspects of mud
displacement during cementing. In 2001, Crook et al.
published an article[1] describing the "eight steps" to ensure
successful cement jobs. The top five steps relate directly to
the success of cement slurry placement, and never before has a
simulator been able to model all five together. The present
simulator dynamically models, in three dimensions (3-D), the
intermixing of wellbore fluids in both pipe and annuli with
casing movement during hole cleaning and cement slurry
placement.

displacement, especiall
one another.   Even a
operation can quickly
multiple variables. T
large-scale physical sti
empirically evaluate t
displacement efficiency
    More recently, bo
advantage of computatio
different aspects of the
geometries. Tehrani e
and experimental studies of laminar displacement in inclined

Figure 1-8. Related Halliburton work (1992-2009)
prior to *Managed Pressure Drilling* (2012, 2016).

RPSEA Selects Projects for the 2008 Ultra-Deepwater Program

Tue Sep 1, 2009 5:17pm EDT

New Research Will Help Meet U.S. Energy Demand and Lower Costs for Consumers

SUGAR LAND, Texas --(Business Wire)--

The Research Partnership to Secure Energy for America (RPSEA) announces twelve proposals have been selected for negotiations leading to an award under the 2008 Ultra-Deepwater Program focused on increasing the supply of ultra-deepwater and unconventional natural gas and other petroleum resources.

"These twelve projects continue to build the integrated research portfolio envisioned by the 2007 and 2008 approved Annual Plans for the Ultra-Deepwater and Unconventional Natural Gas and Other Petroleum Resources Research and Development Program to develop technologies and architectures for operations in ultra-deepwater," said RPSEA President C. Michael Ming.

"They add to the 17 projects selected for the 2007 Ultra-Deepwater Program to make an increasingly important contribution to the nation`s energy needs. This Program is designed to bring the resources of America`s leading universities, research institutions and technology innovators to bear on the development of domestic resources in water depths of 1,500 meters or greater by reducing costs, increasing efficiency, improving safety and minimizing environmental impacts."

While awards under the RPSEA Ultra-Deepwater Program are open to any U.S.-based organization, most projects involve a team consisting of researchers along with producers or service companies that are in a position to evaluate and apply new technology. Each proposal must provide a minimum of 20% cost share, with up to 50% for field demonstration projects.

The selected projects are as follows:

.

.

Advanced Steady-State and Transient, Three-Dimensional, Single and Multiphase, Non-Newtonian Simulation System for Managed Pressure Drilling

Project Leader: Stratamagnetic Software, LLC, Houston, Texas

.

Figure 1-9. Major United States Department of Energy award (2008).
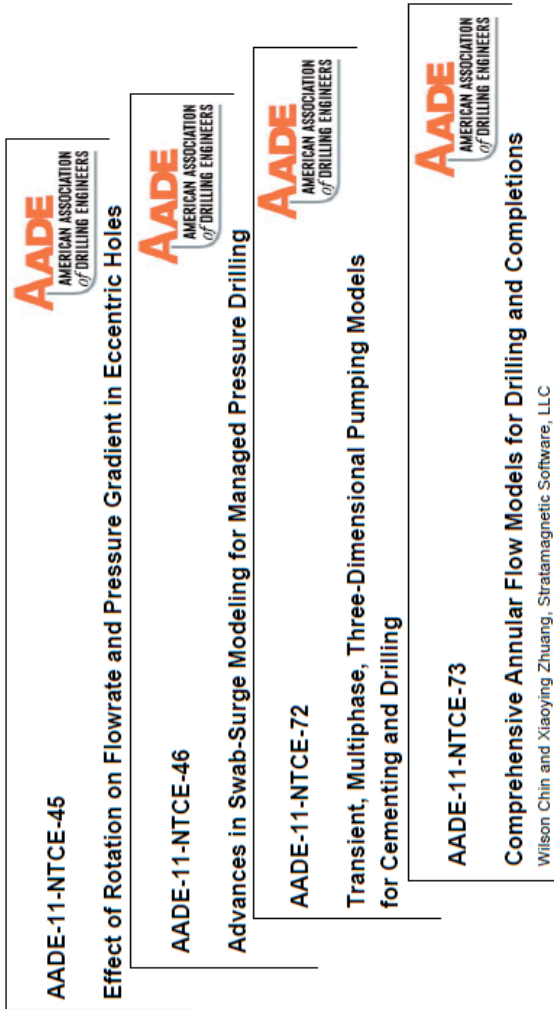
Figure 1-10. 2011 AADE National Technical Conference and Exhibition (Houston, Texas) – four annular flow papers.

Closing remarks. With these preliminaries concluded, we now describe numerous practical and important examples made possible by versatile math models that are now available to mainstream audiences. Reader feedback is encouraged and contact information appears in the final section "About the Author."

1.3 References.

- Chin, W.C., *Borehole Flow Modeling in Horizontal, Deviated and Vertical Wells*, Gulf Publishing, Houston, 1992.

- Chin, W.C., *Computational Rheology for Pipeline and Annular Flow*, Elsevier Science, London, 2001.

- Chin, W.C., *Quantitative Methods in Reservoir Engineering*, Elsevier Science, Amsterdam, 2002.

- Chin, W.C., *Managed Pressure Drilling: Modeling, Strategy and Planning, Elsevier*, Amsterdam, 2012.

- Chin, W.C., *Managed Pressure Drilling: Modeling, Strategy and Planning*, Chinese Edition, Elsevier, Singapore, 2016.

- Chin, W.C., *Quantitative Methods in Reservoir Engineering*, Second Edition, Elsevier Science, Amsterdam, 2017.

- Chin, W.C., Zhou, Y., Feng, Y., Yu, Q. and Zhao, L., *Formation Testing: Pressure Transient and Contamination Analysis*, John Wiley & Sons, Hoboken, New Jersey, 2014.

- Chin, W.C., Zhou, Y., Feng, Y. and Yu, Q., *Formation Testing: Low Mobility Pressure Transient Analysis*, John Wiley & Sons, Hoboken, New Jersey, 2015.

2
Steady Annular Flow

In this chapter, we will consider the subject of steady annular flows, and in doing so, additionally introduce issues and solutions related to a wide range of problem areas. First and foremost, we study flows through cross-sectional geometries that vary from concentric to highly eccentric; yield stress effects that may lead to "plug-like" zones having general size and shape; effects of washouts and cuttings beds on flow rate; Newtonian versus non-Newtonian fluid flow effects, particularly as they impact "pressure gradient versus volume flow rate" behavior; swab-surge in modern "managed pressure drilling" applications, where mud circulation may or may not co-exist with drillpipe movement; effects of drillpipe or casing rotation; and finally, effects of constant speed axial movement.

Moreover, we deal with interactions between different effects, and not academic specialties in isolation. In order to effectively convey the essential physics behind individual physical parameters, we have developed robust three-dimensional graphics that automatically load and execute within our software simulators – and, at the same time, we have kept the user interface as simple and intuitive as possible. In this book, we resist the temptation to "provide complete solutions to everything," recognizing that solutions to real-world problems are often more complicated than meets the eye. For example, cuttings transport efficiency will depend on velocity in vertical wells, surface viscous stress in horizontal and deviated well applications, not to mention gravity and rotation; and stuck pipe remediation will depend on fewer of these, but more so, on apparent viscosity. Toward these ends, we provided solutions for all key physical properties so that engineers can render their own judgements and develop custom solutions as required.

2.1 Graphical interface basics.

Here we introduce basic functions related to the graphical user interface design which hosts our annular flow simulation system. The interface is kept deliberately simple so that minimal "computerese" is required to operate the software. Geometric modifications to inputted concentric and (offset circular) eccentric annuli, e.g., nonuniform cuttings beds, washouts, fractures and so on, which are ideally drawn using mouse, pen, tablet or other visualization means, are defined using simple text queries posed with respect to displayed coordinate values. Development and user costs are reduced by adhering to these approaches. Once the borehole flow modeling software is installed, the simulator itself is launched by clicking on "MPD-Flow-Simulator.exe" as shown in Figure 2-1. Figures 2-1 to 2-4 are self-explanatory.
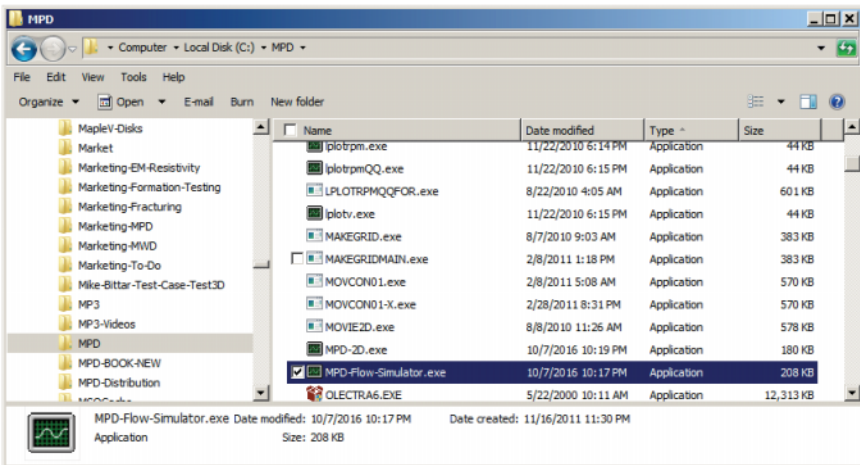
Figure 2-1. Launch menu.
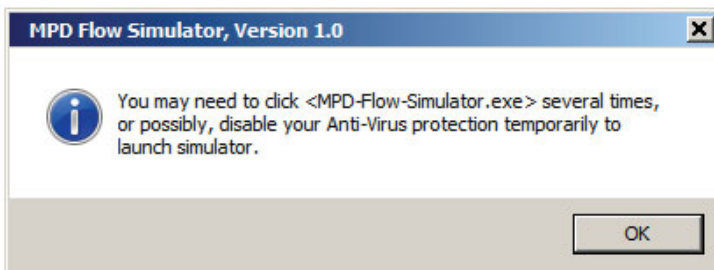
Figure 2-2. Running the application.
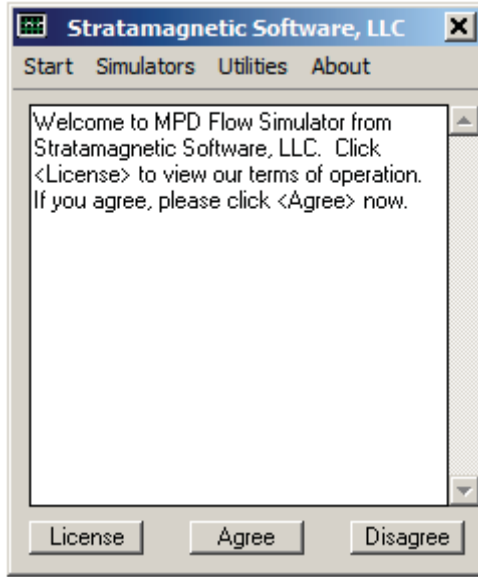
Figure 2-3. License agreement.
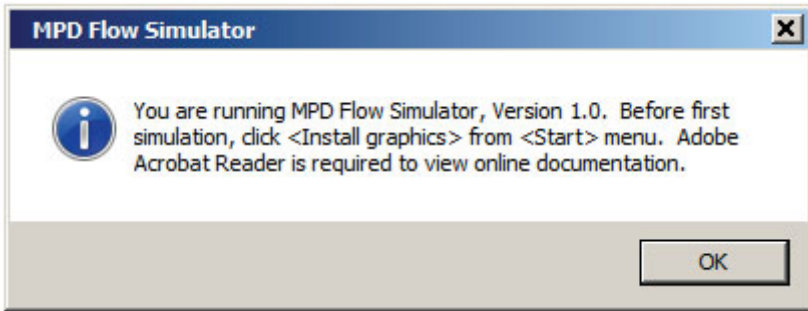
Figure 2-4. Viewing results and documentation.

The simulator main screen is shown in Figure 2-5. Content of an introductory nature is accessed from the left-most vertical "Start" menu appearing in Figure 2-6. The menu in Figure 2-7 hosts the three "high power" simulators developed in our research, while that in Figure 2-8 hosts "utility" programs which solve more limited mathematical and physical problems. We emphasize that, despite the "utilities" heading, the mini-simulators appearing in the menus are by no means simple. These represent solvers to special problem sets developed to independently validate the "high power" solvers already discussed.
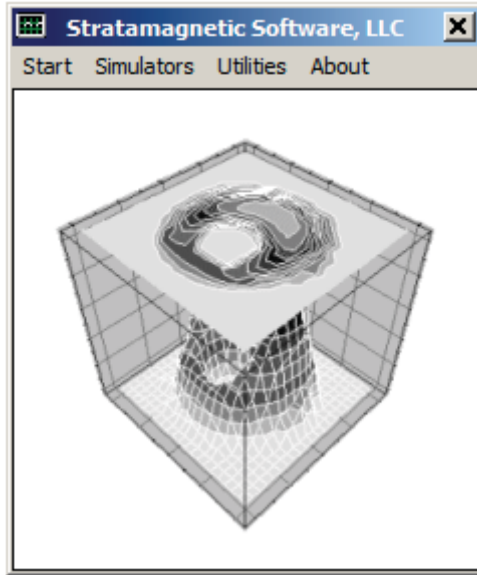
Figure 2-5. MPD flow simulator (main screen).
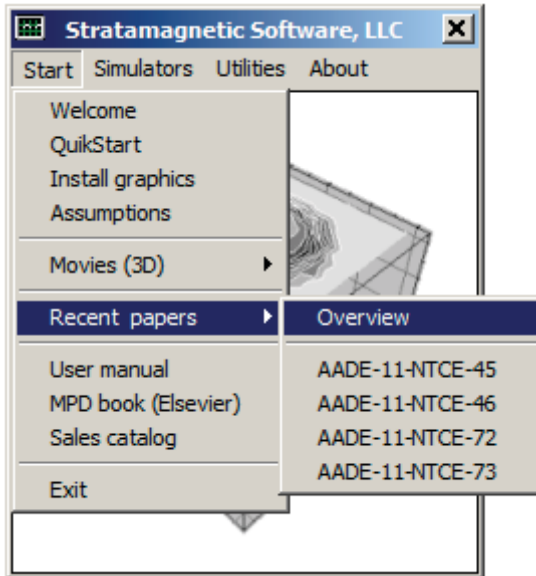
Figure 2-6. MPD flow simulator (start menu).
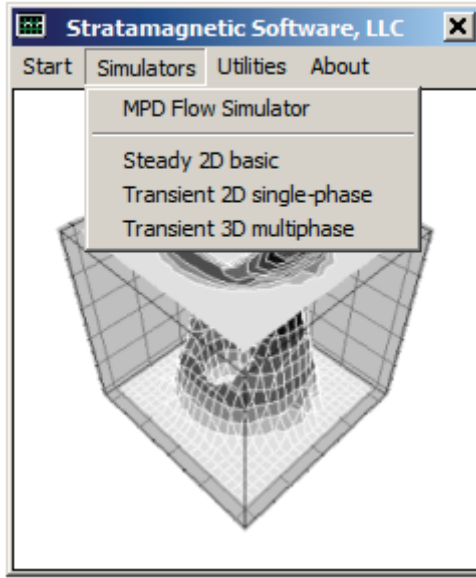
Figure 2-7. MPD flow simulator (simulator menu).
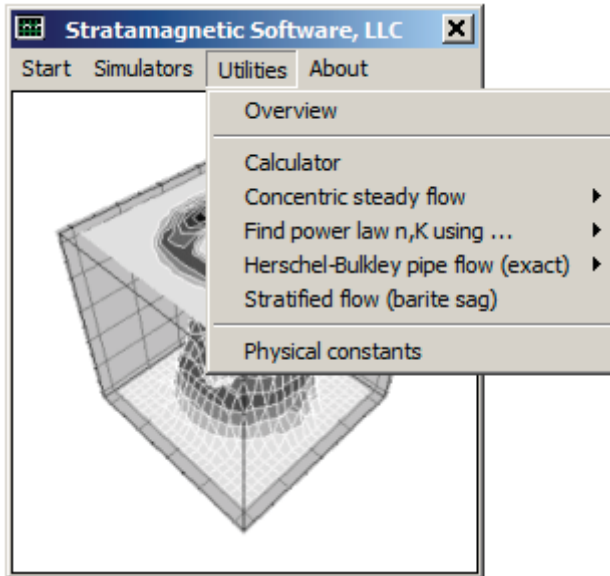
Figure 2-8. MPD flow simulator (utilities menu).
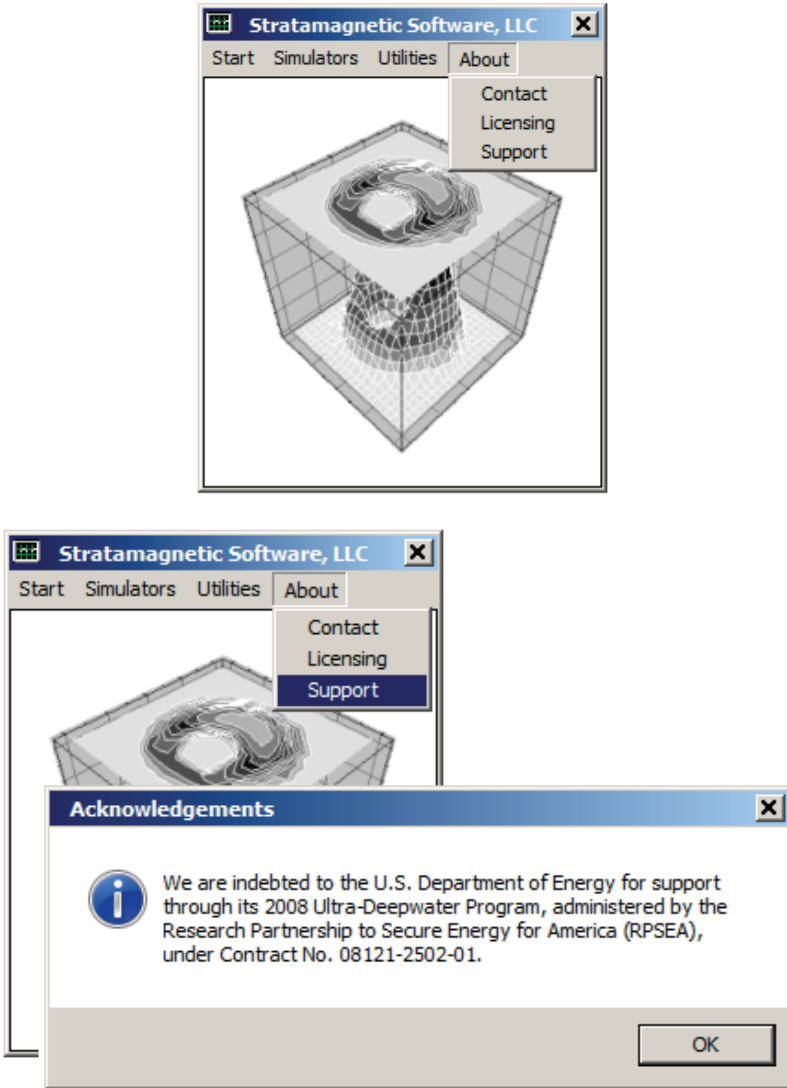
Figure 2-9. MPD flow simulator (contact menu).

Finally, Figure 2-9 contains information of an administrative nature that may be of use to organizations wishing to use our algorithms to host other drilling or cementing related applications, e.g., use of viscous stress fields to estimate borehole wall or cuttings bed erosion.

2.2   Steady flows – versatile capabilities.

The annular flow simulation system described in this book is as powerful and versatile as it is accurate. To introduce readers to its basic capabilities, we consider in the present Chapter 2 a set up problems designed to make learning both instructive and enjoyable.

2.2.1   Concentric Newtonian annular flow.

Several oil service companies market annular flow solvers that claim to solve problems in general annular domains, to include all-important fluids with yield stresses, which are responsible for zones which move in solid body or plug-like manner. In fact, as explained in Chapter 1, neither eccentricity nor yield stress dynamics is correctly handled, although calculated results are "deceptively realistic" because incorrect numbers are overlaid over a color image of the exact annular domain to give the illusion of correctness. In our approach, physical and mathematical correctness remain our highest priority.

And so, one might ask, "How can we demonstrate correctness of our algorithms?" To answer this question, we can turn to the utility program in Figure 2-10, which evaluates an exact, analytical solution for concentric Newtonian annular flow, for which the pipe or casing is non-rotating but which may move with constant (or zero) velocity. When this program is selected, the input screen (with nomenclature defined) shown in Figure 2-11 appears. For the parameters assumed, we click on "Find" to obtain the *exact* 947.1 gpm value in Figure 2-12.
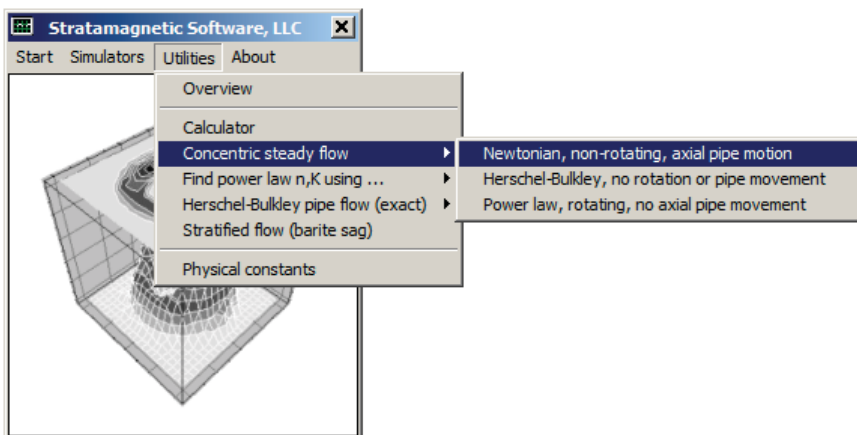
Figure 2-10. Concentric Newtonian annular flow.
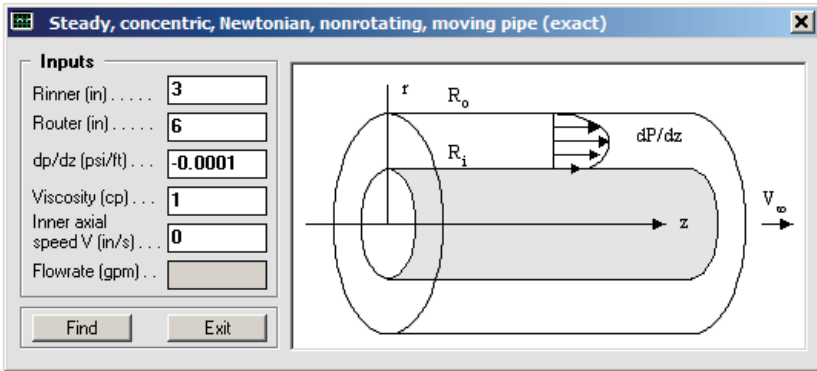
Figure 2-11. Calculating volume flow rate (note blank box).
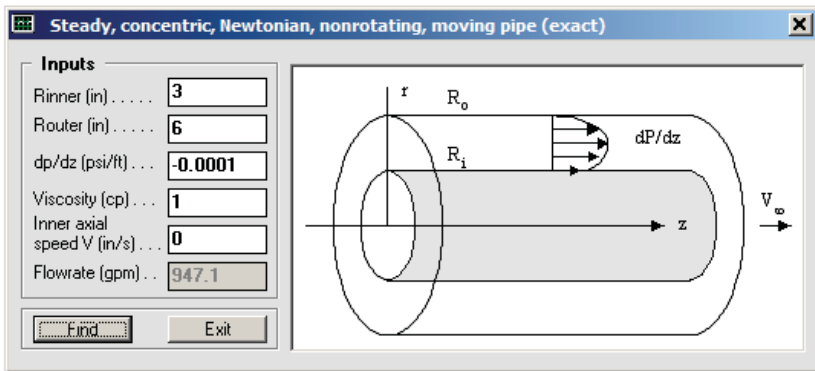
Figure 2-12. Volume flow rate calculated (blank box now populated).

We emphasize that the "947.1 gpm" is obtained from an exact solution of the Navier-Stokes equations, which utilizes a natural cylindrical, radial or polar coordinate system based formulation. By contrast, the "Steady 2D basic" solver in Figure 2-13 is based on a counter-intuitive *rectangular* system which is not cylindrical by any stretch of the imagination. However, as explained in our prior publications, the more powerful approach allows us to treat very general annular geometries as well as arbitrary Herschel-Bulkley fluids. In our presentation below, we demonstrate how a fine mesh numerical solution reproduces the foregoing flow rate. This is followed by a coarse mesh solution with high accuracy, and then, by a coarse mesh solution with a cuttings bed and a washout which modify an inputted concentric baseline geometry.
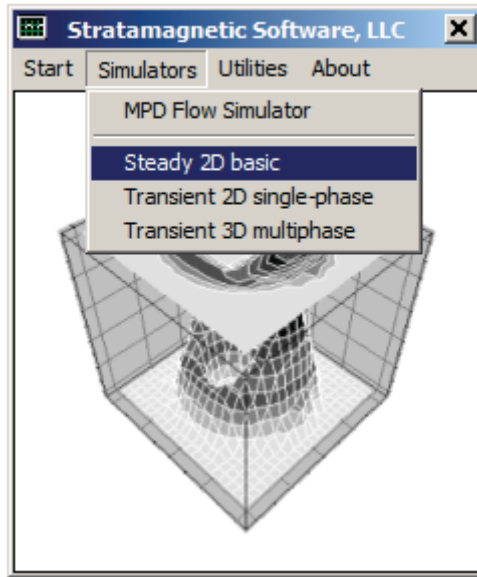
Figure 2-13. Steady 2D basic simulator.

As noted, we avoid "computerese" and specialized input routines to reduce development costs as well as software and hardware investments for users. The screen shots in Figure 2-14 request basic concentric or eccentric *circle* definition to the left of the illustration, which also defines our x-y coordinate system conventions. These simple inputs include circle center coordinates and radii. Some degree of error checking is provided to ensure that inner and outer contours are realistic and do not overlap. For example, the "Show Annulus" button in the Control Panel of Figure 2-14 leads to the display in Figure 2-15. Both diagrams are equivalent and are provided to assist in report generation.

At the bottom left (beneath those for geometric definition) are two additional input boxes. The numerical model allows borehole axis curvature. For example, a large value (such as the 10,000 ft shown) ensures that fluid flows straight without centrifugal effects. Also, constant speed axial movement is permitted, as is zero speed movement (no movement). The drill pipe or casing may move up or down, or left or right, in either direction depending on the algebraic sign assumed.
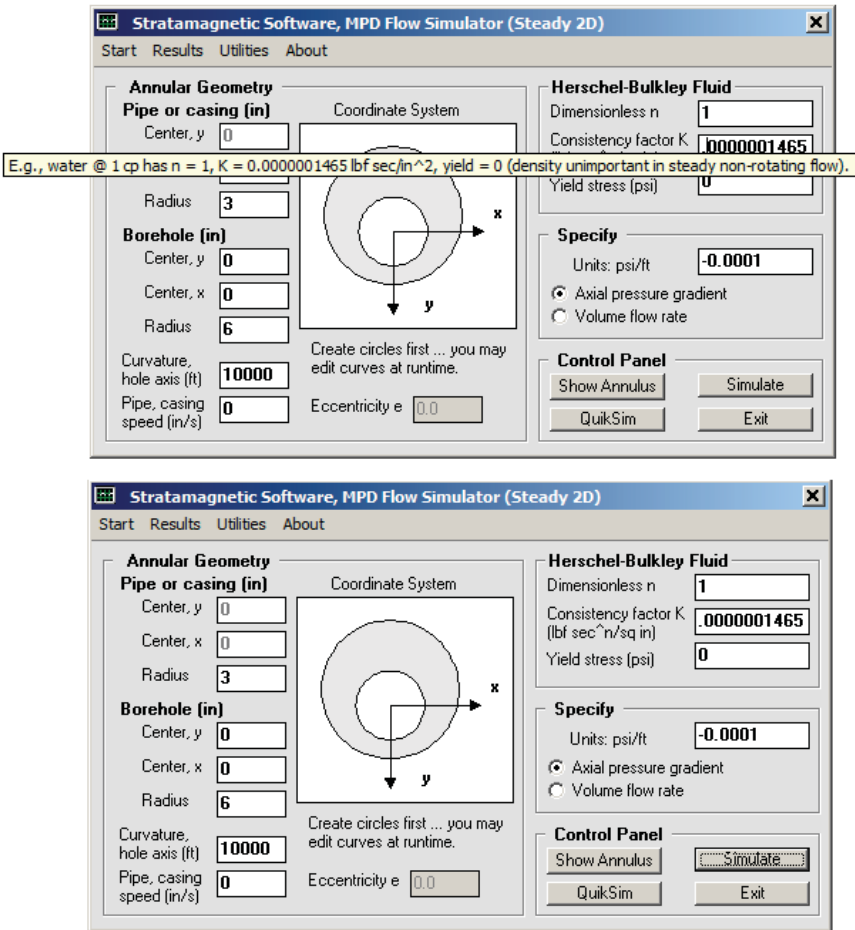
Figure 2-14. "Steady 2D basic" solver, input screen.

The upper right menu supports a general Herschel-Bulkley fluid, with arbitrary "n, K and yield stress" inputs. Note that these values can be obtained using a Fann viscometer – special calculation routines are offered by equipment suppliers or in reference books to estimate these values from measurements. The upper diagram shows a "tip box" that reminds users of example values for water. These three inputs are intrinsic properties of the drilling or completion fluid itself and are independent of the annular geometry and the flow rate (or equivalently, the axial pressure gradient).
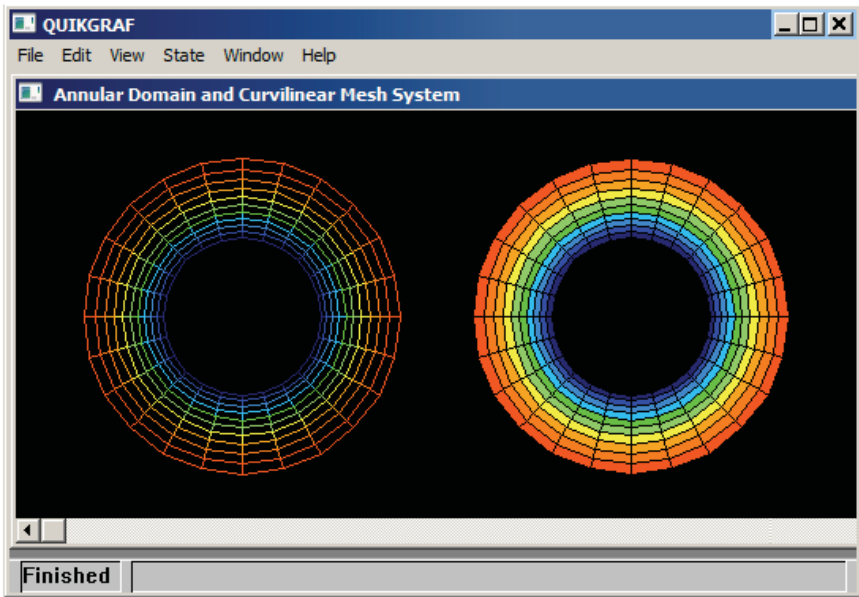
Figure 2-15. Display of concentric or eccentric circles.

Once "n, K and yield stress" are inputted, these, together with the annular geometry and the middle-right "environment menu," completely determine the solution. Here two options can be imposed. First, one can specify the axial pressure gradient – when its value is known, the solver iterates to determine the corresponding velocity field, and then, all related properties like apparent viscosity, strain rate, viscous stress, Stokes product and dissipation function are post-processed automatically. On the other hand, the pressure gradient is often unknown, since only the mud pump flow rate is given (in this chapter, steady single-phase flows are considered, while transient single-phase flows are treated in Chapter 3). When this is the case, the program intelligently guesses at the required pressure gradient – an example calculation is given later.

For the parameters in Figure 2-14, which are consistent with those in Figure 2-11, we click the "QuikSim" solver option. This provides the complete velocity field with minimal decision-making from the user, a process that requires at most 2-3 seconds on modern Windows computers. Internally selected is a fine 60 × 40 curvilinear grid (60 circumferentially and 40 radially) for offset circular annular of any eccentricity. The screens in Figures 2-16 and 2-17 automatically appear.
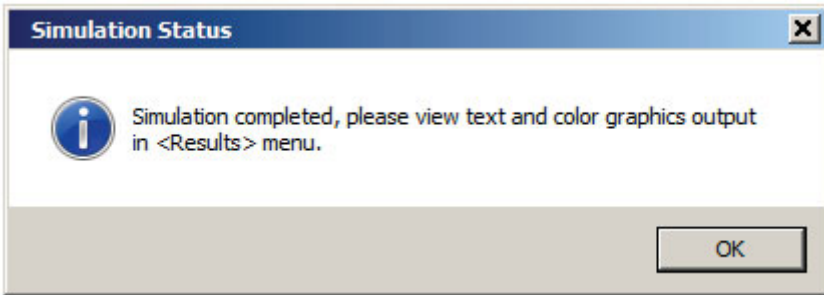
Figure 2-16. Results are always saved in the <Results> menu.
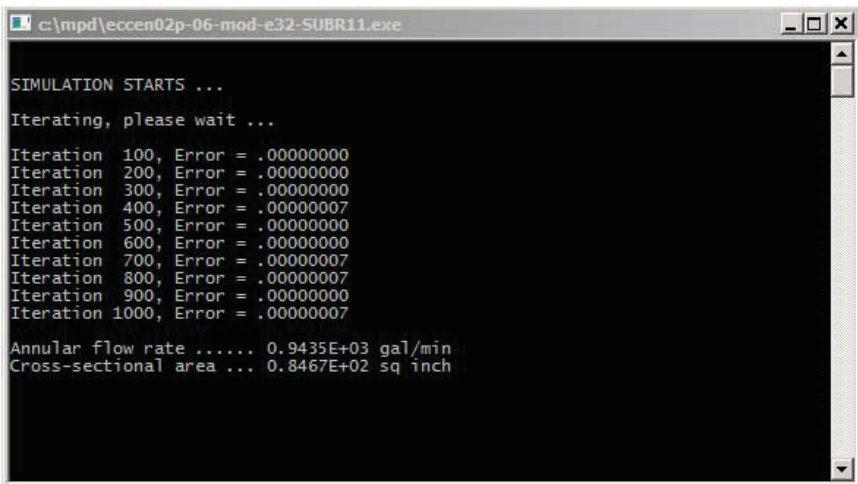
Figure 2-17. Iteration history with flow rate and annular area.

Figure 2-17 shows a converged flow rate of 943.5 gpm versus an exact value of 947.1 gpm. The ratio 947.1/943.5 or 1.004 indicates an error of less than ½%. The area of the annulus is also displayed. This is obtained from summing all the areas of all quadrilaterals on the curvilinear grid system (for example, see Figure 2-15 or Figure 2-30) based on internal geometric mappings used. In this case, the exact area of the annulus is π (6^2 - 3^2) = 84.82 versus the 84.67 above. The value of 84.82/84.67 is 1.002 and indicates almost no error in area. The corresponding velocity distribution is shown in the "planar plot" for velocity Figure 2-18, where the color red indicates that the highest speed is found near the center or widest part of the annulus.
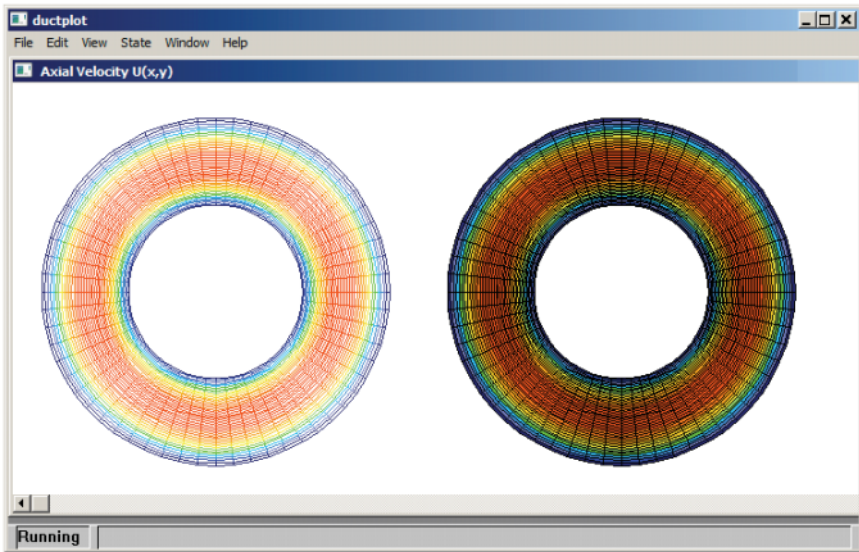
Figure 2-18. Computed "planar plot" for velocity distribution.
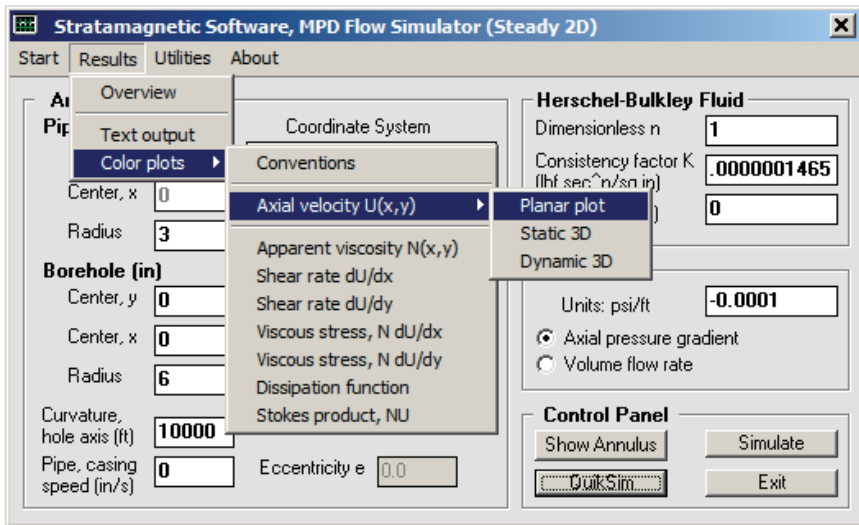
Figure 2-19. Other display options.

A "static view" option is also available for velocity, which supports contour plotting, whereas a "dynamic view" option allows rotations, translations and re-scaling, e.g., see Figures 2-20 and 2-11.
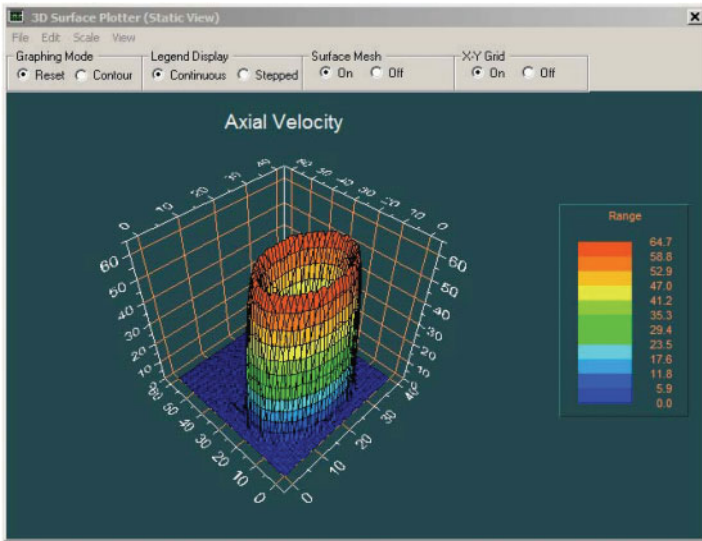
Figure 2-20. "Static view" velocity display option.
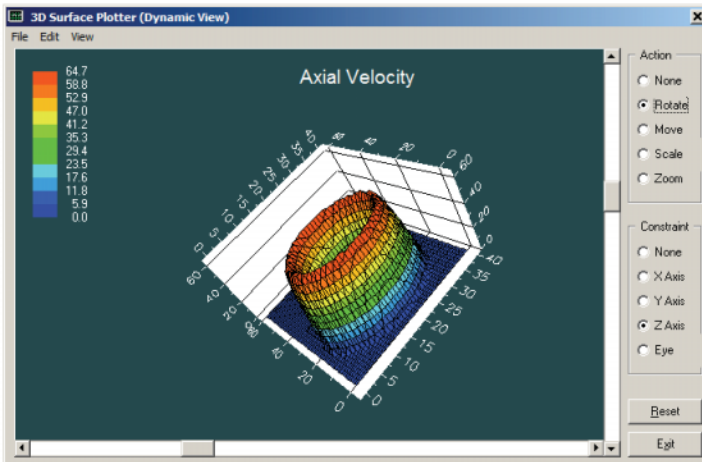
Figure 2-21. "Dynamic view" velocity display option.

As indicated in Figure 2-19, displays of other physical quantities are also supported. In this introductory Newtonian example, we omit many of these. For example, the "apparent viscosity" will be constant, and strains and viscous stresses will differ only by a multiplicative viscosity factor. The only two nontrivial results are x and y strains or stresses, which are rotated by 90 deg as expected in this concentric example.
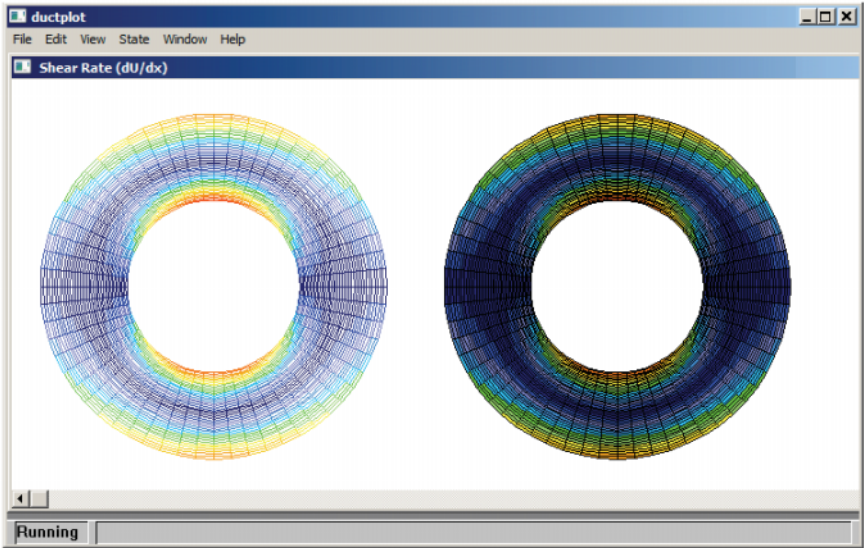
Figure 2-22. Strain field for $\partial U(x,y)/\partial x$.
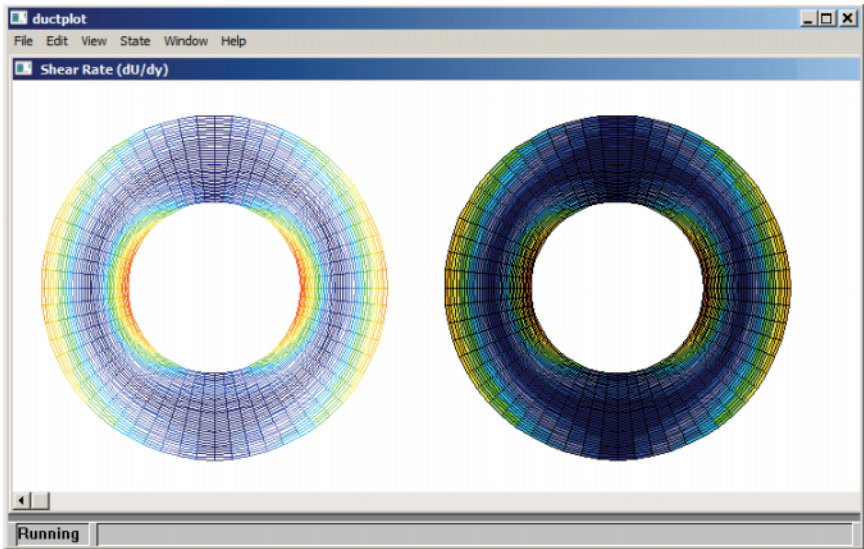
Figure 2-23. Strain field for $\partial U(x,y)/\partial y$.

Finally, text output is provided (see <Results> menu) and relevant results are given in Courier New font below.

```
QuikSim simulation mode assumed ...

Eccentric circles only, 61 x 41 hardcoded mesh.
Use full simulation mode for more runtime options.

Input coordinates are SHIFTED for on-screen
plotting and "8 1/2 x 11" output file printing: -

               SHIFTED PIPE/COLLAR COORDINATES:
          "Old X"      "Old Y"      "New X"      "New Y"
    1    0.3000E+01  0.0000E+00  0.1000E+02  0.7000E+01
    2    0.2984E+01 -0.3136E+00  0.9984E+01  0.6686E+01
    3    0.2934E+01 -0.6237E+00  0.9934E+01  0.6376E+01
    4    0.2853E+01 -0.9271E+00  0.9853E+01  0.6073E+01
    5    0.2741E+01 -0.1220E+01  0.9741E+01  0.5780E+01
    6    0.2598E+01 -0.1500E+01  0.9598E+01  0.5500E+01
    7    0.2427E+01 -0.1763E+01  0.9427E+01  0.5237E+01
    8    0.2229E+01 -0.2007E+01  0.9229E+01  0.4993E+01
    9    0.2007E+01 -0.2229E+01  0.9007E+01  0.4771E+01
   10    0.1763E+01 -0.2427E+01  0.8763E+01  0.4573E+01
   11    0.1500E+01 -0.2598E+01  0.8500E+01  0.4402E+01
   12    0.1220E+01 -0.2741E+01  0.8220E+01  0.4259E+01
   13    0.9271E+00 -0.2853E+01  0.7927E+01  0.4147E+01
   14    0.6237E+00 -0.2934E+01  0.7624E+01  0.4066E+01
   15    0.3136E+00 -0.2984E+01  0.7314E+01  0.4016E+01
   16    0.2265E-06 -0.3000E+01  0.7000E+01  0.4000E+01
   17   -0.3136E+00 -0.2984E+01  0.6686E+01  0.4016E+01
   18   -0.6237E+00 -0.2934E+01  0.6376E+01  0.4066E+01
   19   -0.9271E+00 -0.2853E+01  0.6073E+01  0.4147E+01
   20   -0.1220E+01 -0.2741E+01  0.5780E+01  0.4259E+01
   21   -0.1500E+01 -0.2598E+01  0.5500E+01  0.4402E+01
   22   -0.1763E+01 -0.2427E+01  0.5237E+01  0.4573E+01
   23   -0.2007E+01 -0.2229E+01  0.4993E+01  0.4771E+01
   24   -0.2229E+01 -0.2007E+01  0.4771E+01  0.4993E+01
   25   -0.2427E+01 -0.1763E+01  0.4573E+01  0.5237E+01
   26   -0.2598E+01 -0.1500E+01  0.4402E+01  0.5500E+01
   27   -0.2741E+01 -0.1220E+01  0.4259E+01  0.5780E+01
   28   -0.2853E+01 -0.9271E+00  0.4147E+01  0.6073E+01
   29   -0.2934E+01 -0.6237E+00  0.4066E+01  0.6376E+01
   30   -0.2984E+01 -0.3136E+00  0.4016E+01  0.6686E+01
   31   -0.3000E+01 -0.4530E-06  0.4000E+01  0.7000E+01
   32   -0.2984E+01  0.3136E+00  0.4016E+01  0.7314E+01
   33   -0.2934E+01  0.6237E+00  0.4066E+01  0.7624E+01
   34   -0.2853E+01  0.9271E+00  0.4147E+01  0.7927E+01
   35   -0.2741E+01  0.1220E+01  0.4259E+01  0.8220E+01
   36   -0.2598E+01  0.1500E+01  0.4402E+01  0.8500E+01
   37   -0.2427E+01  0.1763E+01  0.4573E+01  0.8763E+01
   38   -0.2229E+01  0.2007E+01  0.4771E+01  0.9007E+01
   39   -0.2007E+01  0.2229E+01  0.4993E+01  0.9229E+01
   40   -0.1763E+01  0.2427E+01  0.5237E+01  0.9427E+01
    .
    .
    .

   55    0.2427E+01  0.1763E+01  0.9427E+01  0.8763E+01
   56    0.2598E+01  0.1500E+01  0.9598E+01  0.8500E+01
   57    0.2741E+01  0.1220E+01  0.9741E+01  0.8220E+01
   58    0.2853E+01  0.9271E+00  0.9853E+01  0.7927E+01
   59    0.2934E+01  0.6237E+00  0.9934E+01  0.7624E+01
   60    0.2984E+01  0.3136E+00  0.9984E+01  0.7314E+01
```

Figure 2-24. Pipe or collar coordinates assumed.

```
            SHIFTED BOREHOLE ANNULUS COORDINATES:
          "Old X"      "Old Y"      "New X"      "New Y"
    1    0.6000E+01   0.0000E+00   0.1300E+02   0.7000E+01
    2    0.5967E+01  -0.6272E+00   0.1297E+02   0.6373E+01
    3    0.5869E+01  -0.1247E+01   0.1287E+02   0.5753E+01
    4    0.5706E+01  -0.1854E+01   0.1271E+02   0.5146E+01
    5    0.5481E+01  -0.2440E+01   0.1248E+02   0.4560E+01
    6    0.5196E+01  -0.3000E+01   0.1220E+02   0.4000E+01
    7    0.4854E+01  -0.3527E+01   0.1185E+02   0.3473E+01
    8    0.4459E+01  -0.4015E+01   0.1146E+02   0.2985E+01
    9    0.4015E+01  -0.4459E+01   0.1101E+02   0.2541E+01
   10    0.3527E+01  -0.4854E+01   0.1053E+02   0.2146E+01
   11    0.3000E+01  -0.5196E+01   0.1000E+02   0.1804E+01
   12    0.2440E+01  -0.5481E+01   0.9440E+01   0.1519E+01
   13    0.1854E+01  -0.5706E+01   0.8854E+01   0.1294E+01
   14    0.1247E+01  -0.5869E+01   0.8247E+01   0.1131E+01
   15    0.6272E+00  -0.5967E+01   0.7627E+01   0.1033E+01
   16    0.4530E-06  -0.6000E+01   0.7000E+01   0.1000E+01
   17   -0.6272E+00  -0.5967E+01   0.6373E+01   0.1033E+01
    .
    .
    .
   55    0.4854E+01   0.3527E+01   0.1185E+02   0.1053E+02
   56    0.5196E+01   0.3000E+01   0.1220E+02   0.1000E+02
   57    0.5481E+01   0.2440E+01   0.1248E+02   0.9440E+01
   58    0.5706E+01   0.1854E+01   0.1271E+02   0.8854E+01
   59    0.5869E+01   0.1247E+01   0.1287E+02   0.8247E+01
   60    0.5967E+01   0.6272E+00   0.1297E+02   0.7627E+01
```

Figure 2-25. Borehole contour coordinates assumed.
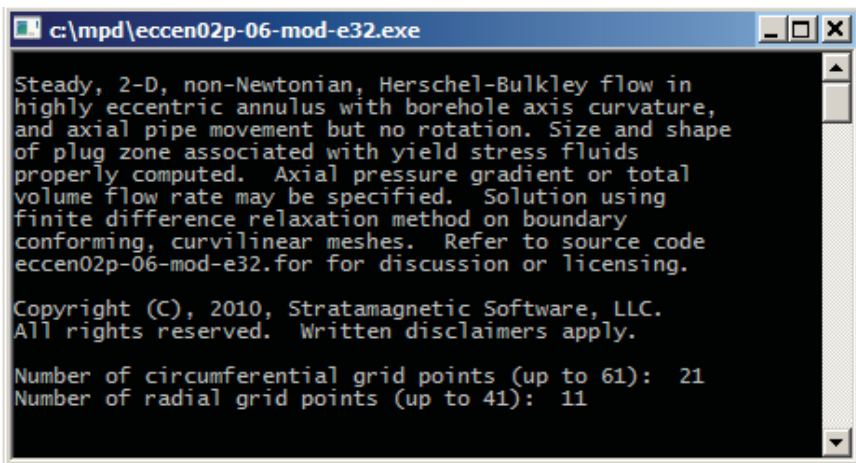
```
SIMULATION STARTS ...

Newtonian fluid assumed with exponent "n" equal
to 0.1000E+01 and consistency factor of 0.1465E-06
lbf sec^n/sq in.

A yield stress of 0.0000E+00 psi is taken.

Borehole axis radius of curvature is 0.1000E+05 ft.

Axial speed of inner pipe is 0.0000E+00 in/sec.

Axial pressure gradient assumed as -.1000E-03 psi/ft.

Iteration  100, Error = .00000000
Iteration  200, Error = .00000000
Iteration  300, Error = .00000000
Iteration  400, Error = .00000007
Iteration  500, Error = .00000000
Iteration  600, Error = .00000000
Iteration  700, Error = .00000007
Iteration  800, Error = .00000007
Iteration  900, Error = .00000000
Iteration 1000, Error = .00000007

Annular flow rate ...... 0.9435E+03 gal/min
Cross-sectional area ... 0.8467E+02 sq inch
```

Figure 2-26. Iteration error history and computed results.

2.2.2   Concentric Newtonian flow on coarse mesh.

In this short discussion, we do not use "QuikSim," but instead use "Simulate" to show all modeling features (see bottom right of Figure 2-19). We will demonstrate how using fewer grids is less accurate than greater, but the decrease in accuracy is not too large since the "boundary conforming" grid systems used all provide higher resolution near solid boundaries where flow gradients are largest. We will use coarse grids throughout this book for presentation purposes so that tables are shorter and diagrams are easier to comprehend. While QuikSim uses 60×40 grids by default (the screen below indicates "61" and "41" because the inputs count nodes as opposed to boxes), our coarse mesh in this example will be defined by 20 azimuthal (or circumferential) and 10 radial grids (or as explained, "21" and "11" as shown in Figure 2-27).


```
c:\mpd\eccen02p-06-mod-e32.exe                          _ □ ✕

Steady, 2-D, non-Newtonian, Herschel-Bulkley flow in
highly eccentric annulus with borehole axis curvature,
and axial pipe movement but no rotation. Size and shape
of plug zone associated with yield stress fluids
properly computed.  Axial pressure gradient or total
volume flow rate may be specified.  Solution using
finite difference relaxation method on boundary
conforming, curvilinear meshes.  Refer to source code
eccen02p-06-mod-e32.for for discussion or licensing.

Copyright (C), 2010, Stratamagnetic Software, LLC.
All rights reserved.  Written disclaimers apply.

Number of circumferential grid points (up to 61):  21
Number of radial grid points (up to 41):  11
```

Figure 2-27. Grid density definition.

We will omit for now all run-time queries related to geometric modification and end display options, since these will be considered in the following example in detail. For our purposes, we wish only to determine the consequences of coarse mesh assumptions. Figure 2-28 shows a computed flow rate of 921.4 gpm as opposed to an exact value of 947.1. The ratio 947.1/921.4 or 1.028 indicates less than a 3% error. The exact annular area of $\pi (6^2 - 3^2)$ or 84.82 compares with our approximate 83.57 for a 1.015 ratio or less than 2% error.
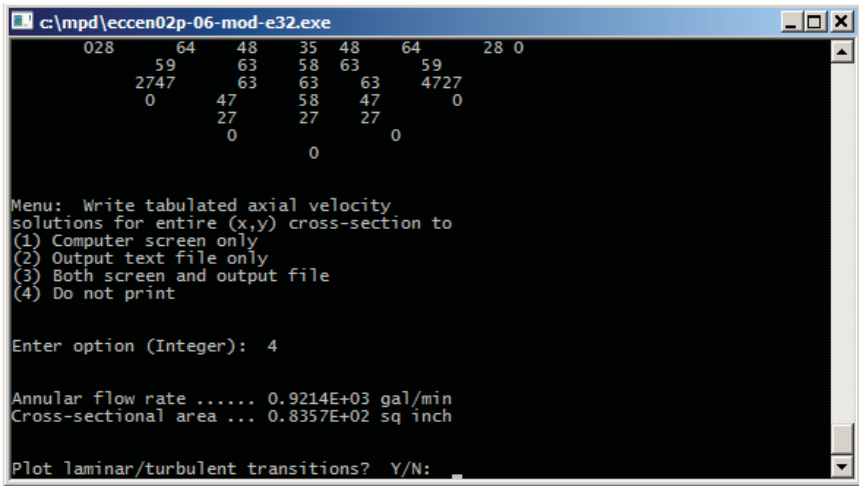
Figure 2-28. Computed coarse grid results.
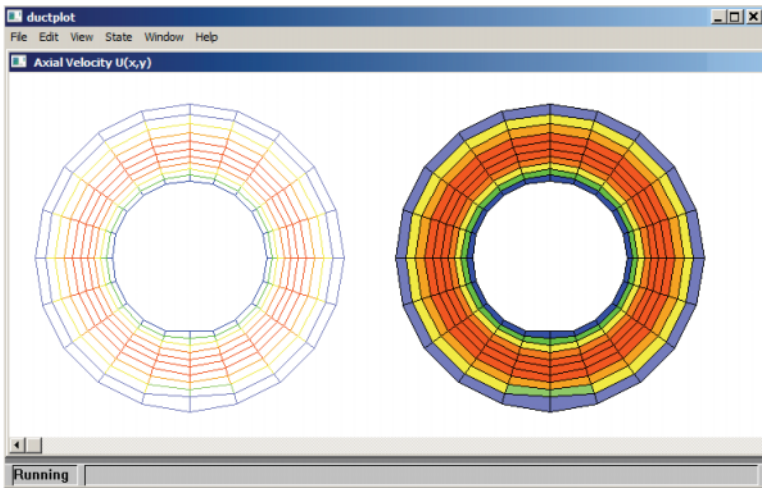
Figure 2-29. Coarse grid velocity distribution.

It is useful noting that our 60×40 fine mesh contains 2,400 grid blocks, while our coarse 20×10 mesh contains 200, which is only 10% of the larger number. This accuracy is attributed to a physically appealing "boundary conforming" curvilinear grid that preserves most of the details of the annular flow.

2.2.3 Coarse mesh Newtonian flow with cuttings bed and washout.

In Sections 2.2.1 and 2.2.2, we compared fine and coarse mesh solutions with that obtained from an exact analytical solution. We found that the coarse mesh result for flow rate was acceptable although, of course, fine grids are preferred. The latter are recommended since, for the curvilinear grid method developed in our research, computational times required for convergence are not substantially different.

In this section, we explain how cuttings beds and washouts can be modeled with relative ease. For presentation purposes, we use coarse meshes so that our ASCII diagrams and text printouts do not require excessive space. To model these non-ideal effects, the "Simulate" button must be used to access all editing and modeling options, and not the simple "QuikSim" option used previously. In the text appearing below, unformatted `Courier New font` denotes text appearing in an input screen window, while **`bold red Courier New font`** denotes responses entered by the user; text formatted in the present Times New Roman font represents our annotations and comments.

```
Steady, 2-D, non-Newtonian, Herschel-Bulkley flow in
highly eccentric annulus with borehole axis curvature,
and axial pipe movement but no rotation. Size and shape
of plug zone associated with yield stress fluids
properly computed.  Axial pressure gradient or total
volume flow rate may be specified.  Solution using
finite difference relaxation method on boundary
conforming, curvilinear meshes.  Refer to source code
eccen02p-06-mod-e32.for for discussion or licensing.

Copyright (C), 2010, Stratamagnetic Software, LLC.
All rights reserved.  Written disclaimers apply.

Number of circumferential grid points (up to 61):  21
Number of radial grid points (up to 41):  11

ASSUME (NON)CONCENTRIC CIRCLES INITIALLY ...

Now use "Print Screen" command to capture following
(x,y) coordinates for reference if any are to be modified ...

Please type <Return> to continue:

Pipe radius .3000E+01, centered at X = 0.000E+00, Y = 0.000E+00.
Hole radius .6000E+01, centered at X = 0.000E+00, Y = 0.000E+00.

All distances and coordinates in inches.
```

```
                  POSITIONS (INCHES):
Node:    Xinner      Yinner       Xouter      Youter
  1  0.3000E+01  0.0000E+00  0.6000E+01  0.0000E+00
  2  0.2853E+01 -0.9271E+00  0.5706E+01 -0.1854E+01
  3  0.2427E+01 -0.1763E+01  0.4854E+01 -0.3527E+01
  4  0.1763E+01 -0.2427E+01  0.3527E+01 -0.4854E+01
  5  0.9271E+00 -0.2853E+01  0.1854E+01 -0.5706E+01
  6  0.2265E-06 -0.3000E+01  0.4530E-06 -0.6000E+01
  7 -0.9271E+00 -0.2853E+01 -0.1854E+01 -0.5706E+01
  8 -0.1763E+01 -0.2427E+01 -0.3527E+01 -0.4854E+01
  9 -0.2427E+01 -0.1763E+01 -0.4854E+01 -0.3527E+01
 10 -0.2853E+01 -0.9271E+00 -0.5706E+01 -0.1854E+01
 11 -0.3000E+01 -0.4530E-06 -0.6000E+01 -0.9060E-06
 12 -0.2853E+01  0.9271E+00 -0.5706E+01  0.1854E+01
 13 -0.2427E+01  0.1763E+01 -0.4854E+01  0.3527E+01
 14 -0.1763E+01  0.2427E+01 -0.3527E+01  0.4854E+01
 15 -0.9271E+00  0.2853E+01 -0.1854E+01  0.5706E+01
 16  0.3577E-07  0.3000E+01  0.7155E-07  0.6000E+01
 17  0.9270E+00  0.2853E+01  0.1854E+01  0.5706E+01
 18  0.1763E+01  0.2427E+01  0.3527E+01  0.4854E+01
 19  0.2427E+01  0.1763E+01  0.4854E+01  0.3527E+01
 20  0.2853E+01  0.9271E+00  0.5706E+01  0.1854E+01


Display coordinates again?   Y/N:  n

You may modify (x,y) coordinates  point-by-point to
include cuttings bed, borehole swelling and erosion,
and also, noncircular drill collar effects ...

Points are individually queried in clockwise manner
starting from bottom of pipe/annulus at P .... again:

X/Y orientation:
o----> Y
|
|
P
|
V   X
```
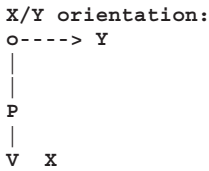
The table at the top of this page contains the internally generated (x,y) coordinates of concentric or eccentric circles defined by the upper left side of the menu in Figure 2-14.   If these numbers represent the desired concentric or offset circles, further use of this tabulation is not required. However, if it is desired to modify either the contour defining the annular wall or that describing the pipe or collar, then the table should be printed out (or "screen captured") for reference. Applications are varied. For example, one might modify the outer contour to evaluate the effects of cuttings bed height on bottom shear stress – if simulations show that stress levels reduce to the point that hole cleaning is no longer efficient, numerical tests can be conducted on required "n and K" values.

On the other hand, the inner contour may be modified in order to simulate the effects of square drill collars, or just as likely, elliptical or triangular cross-sections in non-petroleum applications.   In the screen capture results below, we demonstrate how the outer contour can be modified point-by-point so that the two concentric circles initially assumed are transformed into an annular cross-section with a flat bottom cuttings bed and a washout to the upper right.   The reader should separately plot, study the responses below and compare the redefined numbers with those with the table at the top of the previous page.

```
Modify borehole wall shape?  Y/N:  y

Point  1:   X =   6.0000, Y =   0.0000
Modify above coordinates?  Y/N:  y
O  Enter new X value:  4
O  Enter new Y value:  0

Point  2:   X =   5.7063, Y =  -1.8541
Modify above coordinates?  Y/N:  y
O  Enter new X value:  4
O  Enter new Y value:  -1.8541

Point  3:   X =   4.8541, Y =  -3.5267
Modify above coordinates?  Y/N:  y
O  Enter new X value:  4
O  Enter new Y value:  -3.5267

Point  4:   X =   3.5267, Y =  -4.8541
Modify above coordinates?  Y/N:  y
O  Enter new X value:  4
O  Enter new Y value:  -4.8541

Point  5:   X =   1.8541, Y =  -5.7063
Modify above coordinates?  Y/N:  n

Point  6:   X =   0.0000, Y =  -6.0000
Modify above coordinates?  Y/N:  n

Point  7:   X =  -1.8541, Y =  -5.7063
Modify above coordinates?  Y/N:  n

Point  8:   X =  -3.5267, Y =  -4.8541
Modify above coordinates?  Y/N:  n

Point  9:   X =  -4.8541, Y =  -3.5267
Modify above coordinates?  Y/N:  n

Point 10:   X =  -5.7063, Y =  -1.8541
Modify above coordinates?  Y/N:  n

Point 11:   X =  -6.0000, Y =   0.0000
Modify above coordinates?  Y/N:  n
```

```
Point 12:    X =  -5.7063, Y =    1.8541
Modify above coordinates?  Y/N:  n

Point 13:    X =  -4.8541, Y =    3.5267
Modify above coordinates?  Y/N:  y
O  Enter new X value:  -7
O  Enter new Y value:  3.5267

Point 14:    X =  -3.5267, Y =    4.8541
Modify above coordinates?  Y/N:  y
O  Enter new X value:  -7.5
O  Enter new Y value:  4.8541

Point 15:    X =  -1.8541, Y =    5.7063
Modify above coordinates?  Y/N:  n

Point 16:    X =   0.0000, Y =    6.0000
Modify above coordinates?  Y/N:  n

Point 17:    X =   1.8541, Y =    5.7063
Modify above coordinates?  Y/N:  n

Point 18:    X =   3.5267, Y =    4.8541
Modify above coordinates?  Y/N:  y
O  Enter new X value:  4
O  Enter new Y value:  4.8541

Point 19:    X =   4.8541, Y =    3.5267
Modify above coordinates?  Y/N:  y
O  Enter new X value:  4
O  Enter new Y value:  3.5267

Point 20:    X =   5.7063, Y =    1.8541
Modify above coordinates?  Y/N:  y
O  Enter new X value:  4
O  Enter new Y value:  1.8541
```

This completes the process required for modifying the outer annular contour. The software next asks if the inner contour is to be modified, and in this example, we respond negatively. Following this response, a revised listing of outer and inner (x,y) points is given. Again, we emphasize that the smaller number of points used is chosen for presentation purposes only. In actual use, a greater number of grid points will lead to smoother geometries and computed velocities.

```
Modify inner pipe shape? Y/N:  n
```

```
FINAL (POSSIBLY MODIFIED) PIPE/HOLE COORDINATES:


                    POSITIONS (INCHES):
Node:   Xinner      Yinner       Xouter      Youter
  1  0.3000E+01  0.0000E+00   0.4000E+01  0.0000E+00
  2  0.2853E+01 -0.9271E+00   0.4000E+01 -0.1854E+01
  3  0.2427E+01 -0.1763E+01   0.4000E+01 -0.3527E+01
  4  0.1763E+01 -0.2427E+01   0.4000E+01 -0.4854E+01
  5  0.9271E+00 -0.2853E+01   0.1854E+01 -0.5706E+01
  6  0.2265E-06 -0.3000E+01   0.4530E-06 -0.6000E+01
  7 -0.9271E+00 -0.2853E+01  -0.1854E+01 -0.5706E+01
  8 -0.1763E+01 -0.2427E+01  -0.3527E+01 -0.4854E+01
  9 -0.2427E+01 -0.1763E+01  -0.4854E+01 -0.3527E+01
 10 -0.2853E+01 -0.9271E+00  -0.5706E+01 -0.1854E+01
 11 -0.3000E+01 -0.4530E-06  -0.6000E+01 -0.9060E-06
 12 -0.2853E+01  0.9271E+00  -0.5706E+01  0.1854E+01
 13 -0.2427E+01  0.1763E+01  -0.7000E+01  0.3527E+01
 14 -0.1763E+01  0.2427E+01  -0.7500E+01  0.4854E+01
 15 -0.9271E+00  0.2853E+01  -0.1854E+01  0.5706E+01
 16  0.3577E-07  0.3000E+01   0.7155E-07  0.6000E+01
 17  0.9270E+00  0.2853E+01   0.1854E+01  0.5706E+01
 18  0.1763E+01  0.2427E+01   0.4000E+01  0.4854E+01
 19  0.2427E+01  0.1763E+01   0.4000E+01  0.3527E+01
 20  0.2853E+01  0.9271E+00   0.4000E+01  0.1854E+01

COMPLETE ANNULAR CONFIGURATION:

X/Y orientation:

o----> Y
|
|
V
  X
                                             11
                                          11

                         11
                11              11
          11


      11
                        1
                 1        1
                 1          1
  11              1                  1              11

          1                          1

  11          1                      1          11

          1                          1

  11          1                 1          11
               1               1
                  1   1   1


      11    11      11      11      11   11   11
```

```
Is pipe outside of annulus?  Y/N: n
```

Note that the "1" and "11" in the diagram of the previous page refer to "radial" grid lines "1" (at the pipe) and "11" (at the annular wall). Cuttings bed and washout "x" coordinates are shown in red in the prior table. The grid generation equations are next solved internally, using a numerically stable method that is automated and transparent to the user. This process requires 2-3 seconds on typical Windows computers.

```
Grid generation initiated,
please wait ...

Iteration  1
Iteration  2
.
.
Iteration 15
Iteration 16
Iteration 17
Iteration 18
Iteration 19
Iteration 20
Iteration 21
Iteration 22, Tolerance = .7304E-02

COMPUTED MESH SYSTEM:

X/Y orientation:

o----> Y
|
|
V
  X
                                                 11
                                            11

                        11
                11     10      1011  10
          11       9       9      9      9
          10       8       7   7 8   8       10
            9        7     6   6      7     9
    11           7     5     4   5     6      8
      10        5    3     2   3    5      7
         8 7      3 2   1      1   3    5 6
          5 3    1            1      4
   1110 9      2                 2            91011
      8 6 4                          4 6 7
         3                          2

   1110 8 7 5 4 2               2 3 5 7 8 91011

          5 3                      2 4 5
       9 8 6                          6 8 9
   1110          4 3                 2 4          1011
         7 5    3 2           1 3   5 7
        9      6 5   3 1    3   3   5 6      9
      10       9 8     7    7   7    7 9    10
    11     1110    11       11    1011    11    11
```
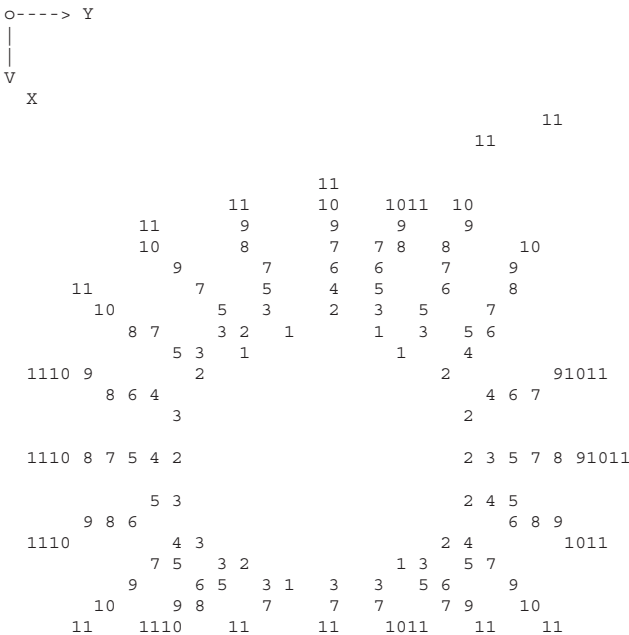
The numerical solution for the velocity field now begins.

```
Grid generated.  Now solve for annular flow ...

SIMULATION STARTS ...

Iterating, please wait ...
Iteration  100, Error = .00000006
Iteration  200, Error = .00000006
.
Iteration  900, Error = .00000006
Iteration 1000, Error = .00000006

Note:  In contour plots, absolute value of velocity
is displayed to two significant digits (in/sec).
See tabulated answers for exact magnitudes.

Enter <Return> to continue:
COMPUTED AXIAL VELOCITY:

X/Y orientation:

o----> Y
|
|
V
  X
                                                   0
                                                 0

                             0
                   0         2      3 0   7
              0         4     4      5      9
              2         5     6   7 6  10        7
            4       6     6   7    10     9
       0          6     5   5   6     9    10
        2           5   3   2   4   8    10
         5 6      3 1   0       0   5   8 9
           5 3   0               0     6
   0 2 4           1                 2         5 3 0
      5 6 4                              5 7 7
          3                          2

   0 2 5 6 5 4 1                      1 3 6 6 6 4 2 0

          5 3                         1 4 5
       4 5 6                              6 5 4
   0 2         3 2                   1 3        2 0
          5 4   1 0            0 1   4 5
         4       3 2   0 0   0   0   2 3      4
          3       2 3     1     1   1    3 2     3
          0       0 1     0         0   0 0    0      0

Menu:  Write tabulated axial velocity
solutions for entire (x,y) cross-section to
(1) Computer screen only
(2) Output text file only
(3) Both screen and output file
(4) Do not print

Enter option (Integer):  2
```
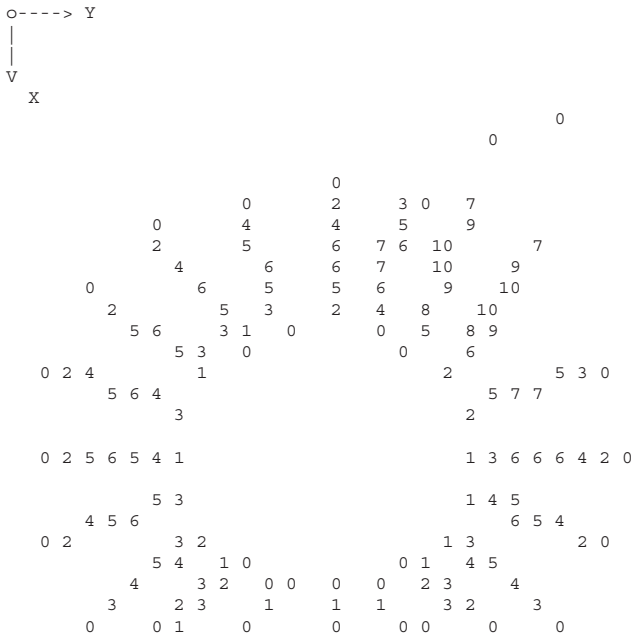
```
Annular flow rate ...... 0.9079E+03 gal/min
Cross-sectional area ... 0.7986E+02 sq inch
```

The computed velocity field in the annular cross-section is now available and displayed in ASCII character form on the previous page. The complete iterative solution requires 2-3 seconds on typical Windows computers. Due to spacing considerations, only the first two significant digits (for in/sec units) are displayed. The "0" values shown indicate that the no-slip condition at solid surfaces is satisfied. When the inner pipe or casing moves, that "0" would be replaced by the axial translation speed. Immediately beneath the ASCII plot (and analogous plots for other physical quantities to be discussed) is a simple menu allowing the user to review tabulated values of point-by-point in the flow cross-section. The user may view these solutions on-screen, print to file only, print to both screen and file, or not at all.

A more attractive color velocity plot (automatically generated) appears in Figure 2-30 where a high (red) velocity at the washout is observed that may encourage further erosion. The flow rate at the bottom of the annulus is extremely slow, as is known to be the case in narrow crevices. Figure 2-31 presents velocity plots in a "static view" mode that supports contour plotting, while Figure 2-31 supports a "dynamic view" that supports rotations, translations and rescalings.
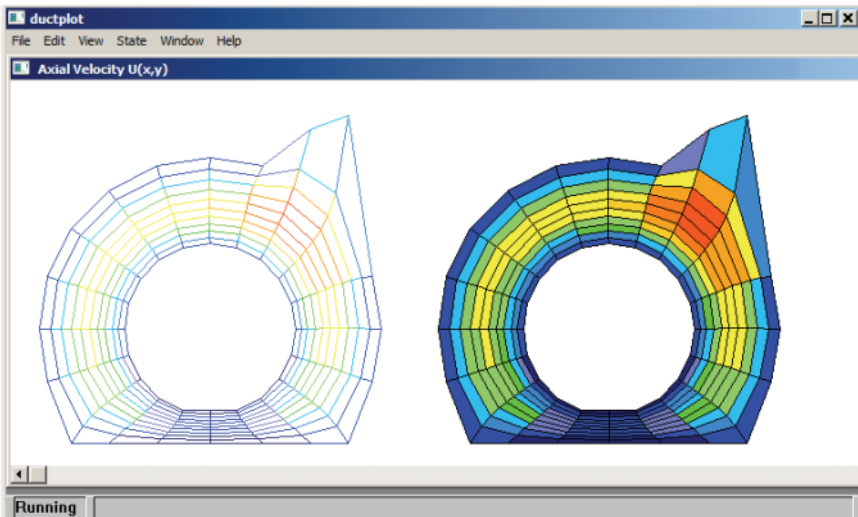
Figure 2-30. Planar velocity plot (hole with cuttings bed and washout).
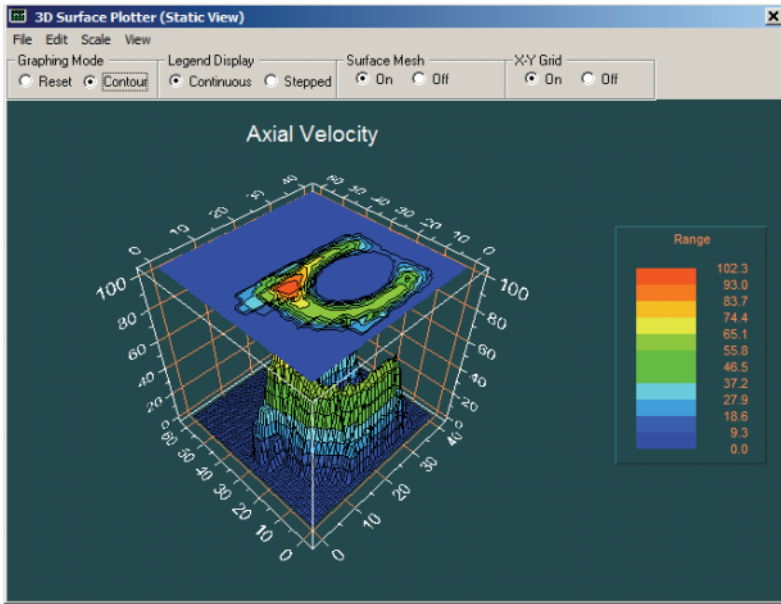
Figure 2-31. Static velocity plot (hole with cuttings bed and washout).
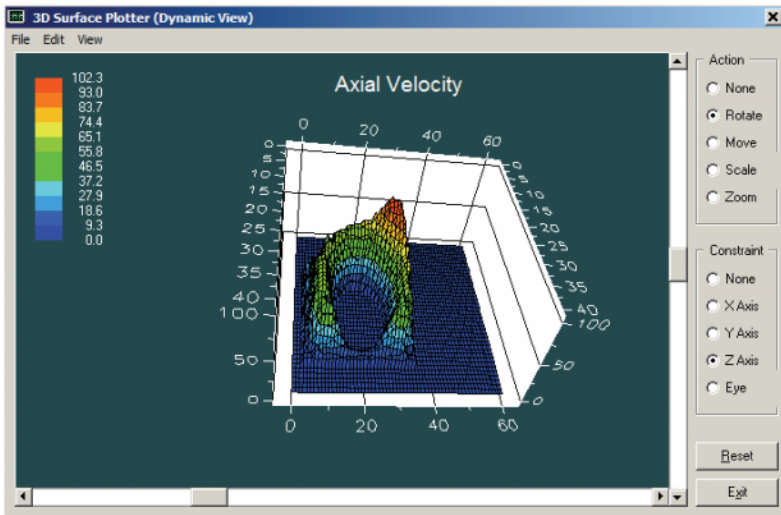
Figure 2-32. Dynamic velocity plot (annulus with
bottom cuttings bed and washout).

As noted earlier, displays such as that in Figure 2-30 can be rendered more attractive by increasing mesh density – our use of coarse meshes is only motivated by presentation objectives. Additional run-time display options are available to users, e.g., apparent viscosity, x and y shear rates, x and y viscous stresses, Stokes product and dissipation function. For instance, "laminar versus turbulent flow maps" are also created if desired –

```
Plot laminar/turbulent transitions?  Y/N:  y
```

If this selection is selected, the user first inputs the "critical Reynolds number," typically 2,100 for idealized Newtonian flows on smooth flat plates. Then, in a diagram similar to the foregoing ASCII velocity plot, "L" appears at laminar points while "T" appears at those turbulent. Such flow stability plots are repeatable as often as are necessary. Examples are given later. We note that, for all flow properties cited, the tabulation menu discussed earlier appears, providing users with multiple options to document numerical values. In what follows below, we have listed portions of the text output file automatically created by the software and available from the <Results> menu. These results appear in Courier New font. Most details are shown for the velocity field, but for all other flow properties, fewer are retained due to space limitations.

```
Full option simulation mode assumed ...

Steady, 2-D, non-Newtonian, Herschel-Bulkley flow in
highly eccentric annulus with borehole axis curvature,
and axial pipe movement but no rotation. Size and shape
of plug zone associated with yield stress fluids
properly computed.  Axial pressure gradient or total
volume flow rate may be specified.  Solution using
finite difference relaxation method on boundary
conforming, curvilinear meshes.  Refer to source code
eccen02p-06-mod-e32.for for discussion or licensing.

Copyright (C), 2010, Stratamagnetic Software, LLC.
All rights reserved.  Written disclaimers apply.

Borehole axis radius of curvature (ft):  0.1000E+05

ASSUME (NON)CONCENTRIC CIRCLES INITIALLY ...

Pipe radius .3000E+01, centered at X = 0.000E+00, Y = 0.000E+00.
Hole radius .6000E+01, centered at X = 0.000E+00, Y = 0.000E+00.
All distances and coordinates in inches.
```

```
                        POSITIONS (INCHES):
Node:    Xinner       Yinner       Xouter       Youter
  1   0.3000E+01   0.0000E+00   0.6000E+01   0.0000E+00
  2   0.2853E+01  -0.9271E+00   0.5706E+01  -0.1854E+01
  3   0.2427E+01  -0.1763E+01   0.4854E+01  -0.3527E+01
  4   0.1763E+01  -0.2427E+01   0.3527E+01  -0.4854E+01
  5   0.9271E+00  -0.2853E+01   0.1854E+01  -0.5706E+01
  6   0.2265E-06  -0.3000E+01   0.4530E-06  -0.6000E+01
  7  -0.9271E+00  -0.2853E+01  -0.1854E+01  -0.5706E+01
  8  -0.1763E+01  -0.2427E+01  -0.3527E+01  -0.4854E+01
  9  -0.2427E+01  -0.1763E+01  -0.4854E+01  -0.3527E+01
 10  -0.2853E+01  -0.9271E+00  -0.5706E+01  -0.1854E+01
 11  -0.3000E+01  -0.4530E-06  -0.6000E+01  -0.9060E-06
 12  -0.2853E+01   0.9271E+00  -0.5706E+01   0.1854E+01
 13  -0.2427E+01   0.1763E+01  -0.4854E+01   0.3527E+01
 14  -0.1763E+01   0.2427E+01  -0.3527E+01   0.4854E+01
 15  -0.9271E+00   0.2853E+01  -0.1854E+01   0.5706E+01
 16   0.3577E-07   0.3000E+01   0.7155E-07   0.6000E+01
 17   0.9270E+00   0.2853E+01   0.1854E+01   0.5706E+01
 18   0.1763E+01   0.2427E+01   0.3527E+01   0.4854E+01
 19   0.2427E+01   0.1763E+01   0.4854E+01   0.3527E+01
 20   0.2853E+01   0.9271E+00   0.5706E+01   0.1854E+01


FINAL (POSSIBLY MODIFIED) PIPE/HOLE COORDINATES:

                        POSITIONS (INCHES):
Node:    Xinner       Yinner       Xouter       Youter
  1   0.3000E+01   0.0000E+00   0.4000E+01   0.0000E+00
  2   0.2853E+01  -0.9271E+00   0.4000E+01  -0.1854E+01
  3   0.2427E+01  -0.1763E+01   0.4000E+01  -0.3527E+01
  4   0.1763E+01  -0.2427E+01   0.4000E+01  -0.4854E+01
  5   0.9271E+00  -0.2853E+01   0.1854E+01  -0.5706E+01
  6   0.2265E-06  -0.3000E+01   0.4530E-06  -0.6000E+01
  7  -0.9271E+00  -0.2853E+01  -0.1854E+01  -0.5706E+01
  8  -0.1763E+01  -0.2427E+01  -0.3527E+01  -0.4854E+01
  9  -0.2427E+01  -0.1763E+01  -0.4854E+01  -0.3527E+01
 10  -0.2853E+01  -0.9271E+00  -0.5706E+01  -0.1854E+01
 11  -0.3000E+01  -0.4530E-06  -0.6000E+01  -0.9060E-06
 12  -0.2853E+01   0.9271E+00  -0.5706E+01   0.1854E+01
 13  -0.2427E+01   0.1763E+01  -0.7000E+01   0.3527E+01
 14  -0.1763E+01   0.2427E+01  -0.7500E+01   0.4854E+01
 15  -0.9271E+00   0.2853E+01  -0.1854E+01   0.5706E+01
 16   0.3577E-07   0.3000E+01   0.7155E-07   0.6000E+01
 17   0.9270E+00   0.2853E+01   0.1854E+01   0.5706E+01
 18   0.1763E+01   0.2427E+01   0.4000E+01   0.4854E+01
 19   0.2427E+01   0.1763E+01   0.4000E+01   0.3527E+01
 20   0.2853E+01   0.9271E+00   0.4000E+01   0.1854E+01


Input coordinates are SHIFTED for on-screen
plotting and "8 1/2 x 11" output file printing: -
```
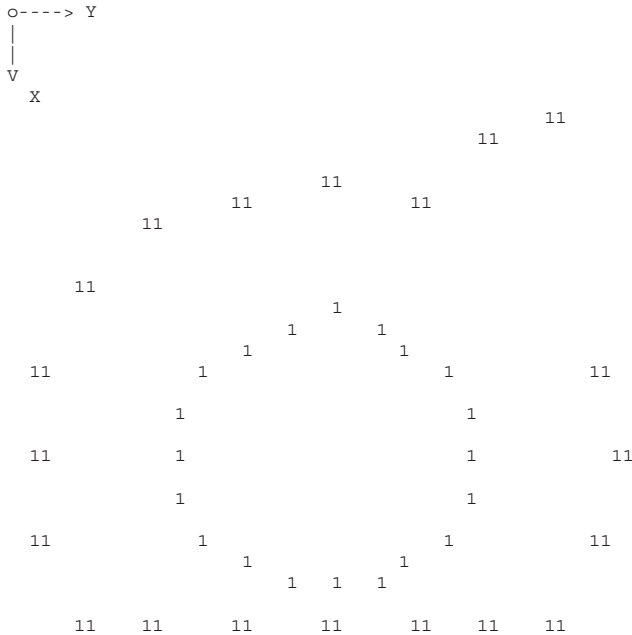
```
              SHIFTED PIPE/COLLAR COORDINATES:
          "Old X"      "Old Y"       "New X"       "New Y"
   1     0.3000E+01   0.0000E+00   0.1150E+02   0.7000E+01
   2     0.2853E+01  -0.9271E+00   0.1135E+02   0.6073E+01
   3     0.2427E+01  -0.1763E+01   0.1093E+02   0.5237E+01
   4     0.1763E+01  -0.2427E+01   0.1026E+02   0.4573E+01
   5     0.9271E+00  -0.2853E+01   0.9427E+01   0.4147E+01
   6     0.2265E-06  -0.3000E+01   0.8500E+01   0.4000E+01
   7    -0.9271E+00  -0.2853E+01   0.7573E+01   0.4147E+01
   8    -0.1763E+01  -0.2427E+01   0.6737E+01   0.4573E+01
   9    -0.2427E+01  -0.1763E+01   0.6073E+01   0.5237E+01
  10    -0.2853E+01  -0.9271E+00   0.5647E+01   0.6073E+01
  11    -0.3000E+01  -0.4530E-06   0.5500E+01   0.7000E+01
  12    -0.2853E+01   0.9271E+00   0.5647E+01   0.7927E+01
  13    -0.2427E+01   0.1763E+01   0.6073E+01   0.8763E+01
  14    -0.1763E+01   0.2427E+01   0.6737E+01   0.9427E+01
  15    -0.9271E+00   0.2853E+01   0.7573E+01   0.9853E+01
  16     0.3577E-07   0.3000E+01   0.8500E+01   0.1000E+02
  17     0.9270E+00   0.2853E+01   0.9427E+01   0.9853E+01
  18     0.1763E+01   0.2427E+01   0.1026E+02   0.9427E+01
  19     0.2427E+01   0.1763E+01   0.1093E+02   0.8763E+01
  20     0.2853E+01   0.9271E+00   0.1135E+02   0.7927E+01

              SHIFTED BOREHOLE ANNULUS COORDINATES:
          "Old X"      "Old Y"       "New X"       "New Y"
   1     0.4000E+01   0.0000E+00   0.1250E+02   0.7000E+01
   2     0.4000E+01  -0.1854E+01   0.1250E+02   0.5146E+01
   3     0.4000E+01  -0.3527E+01   0.1250E+02   0.3473E+01
   4     0.4000E+01  -0.4854E+01   0.1250E+02   0.2146E+01
   5     0.1854E+01  -0.5706E+01   0.1035E+02   0.1294E+01
   6     0.4530E-06  -0.6000E+01   0.8500E+01   0.1000E+01
   7    -0.1854E+01  -0.5706E+01   0.6646E+01   0.1294E+01
   8    -0.3527E+01  -0.4854E+01   0.4973E+01   0.2146E+01
   9    -0.4854E+01  -0.3527E+01   0.3646E+01   0.3473E+01
  10    -0.5706E+01  -0.1854E+01   0.2794E+01   0.5146E+01
  11    -0.6000E+01  -0.9060E-06   0.2500E+01   0.7000E+01
  12    -0.5706E+01   0.1854E+01   0.2794E+01   0.8854E+01
  13    -0.7000E+01   0.3527E+01   0.1500E+01   0.1053E+02
  14    -0.7500E+01   0.4854E+01   0.1000E+01   0.1185E+02
  15    -0.1854E+01   0.5706E+01   0.6646E+01   0.1271E+02
  16     0.7155E-07   0.6000E+01   0.8500E+01   0.1300E+02
  17     0.1854E+01   0.5706E+01   0.1035E+02   0.1271E+02
  18     0.4000E+01   0.4854E+01   0.1250E+02   0.1185E+02
  19     0.4000E+01   0.3527E+01   0.1250E+02   0.1053E+02
  20     0.4000E+01   0.1854E+01   0.1250E+02   0.8854E+01

Axial speed of inner pipe (inches/sec):  0.0000E+00
```

```
COMPLETE ANNULAR CONFIGURATION:

X/Y orientation:

o----> Y
|
|
V
  X


                                                        11
                                                  11

                              11
                   11                  11
           11


     11
                               1
                       1           1
                     1                 1
   11                1                      1                 11
                 1                           1

   11                1                       1             11

                 1                           1

   11                    1                 1             11
                   1               1
                         1   1   1

        11     11       11        11        11     11    11
```
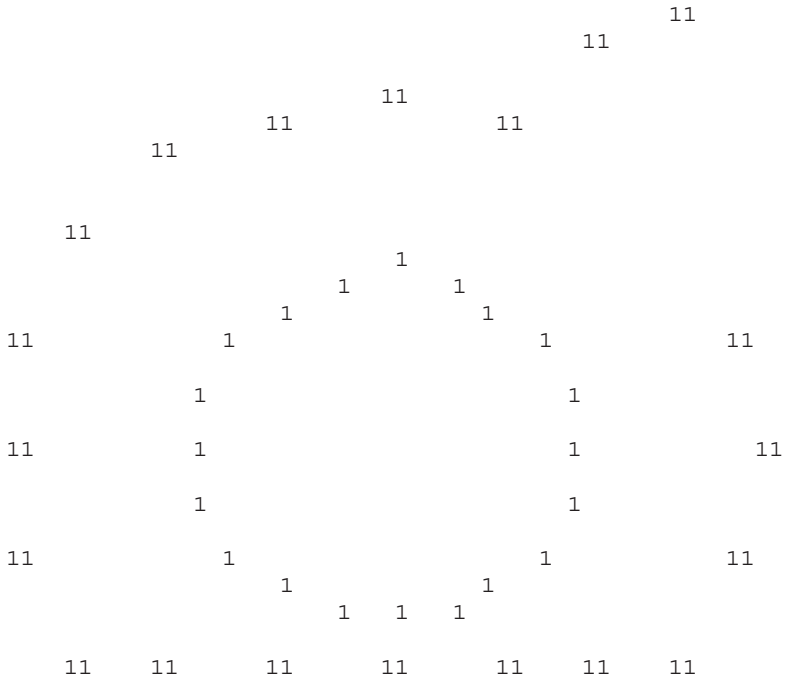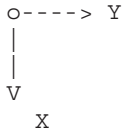
COMPUTED MESH SYSTEM:

X/Y orientation:

o----> Y
|
|
V
  X

```
                                                              11
                                                          11

                                    11
                        11          10     1011   10
             11              9          9       9        9
             10              8          7    7 8    8         10
                  9              7      6    6          7      9
        11              7       5     4    5       6       8
          10              5    3     2    3    5        7
             8 7       3 2    1          1    3     5 6
                5 3    1                   1       4
     1110 9          2                          2            91011
          8 6 4                                    4 6 7
                3                                  2

     1110 8 7 5 4 2                          2 3 5 7 8 91011

                5 3                            2 4 5
          9 8 6                                  6 8 9
     1110              4 3                    2 4         1011
             7 5    3 2              1 3    5 7
                9       6 5    3 1    3    3    5 6       9
          10         9 8       7      7    7      7 9    10
             11    1110      11       11    1011    11     11
```
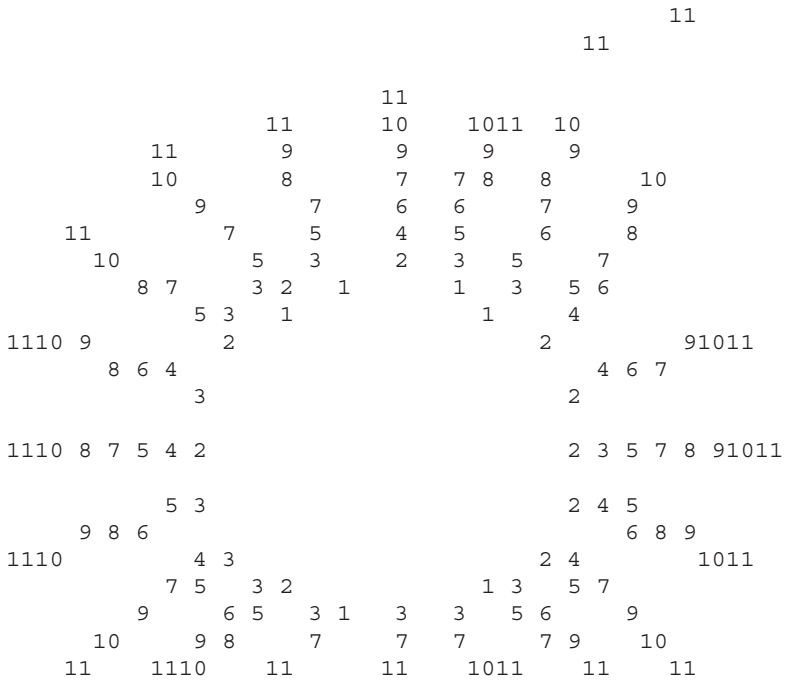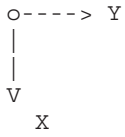
```
SIMULATION STARTS ...

Newtonian fluid assumed with exponent "n" equal
to .1000E+01 and consistency factor of .1465E-06
lbf sec^n/sq in.

A yield stress of .0000E+00 psi, is taken.

Axial pressure gradient assumed as -.1000E-03 psi/ft.

Iteration  100, Error = .00000006
Iteration  200, Error = .00000006
Iteration  300, Error = .00000006
Iteration  400, Error = .00000006
Iteration  500, Error = .00000006
Iteration  600, Error = .00000006
Iteration  700, Error = .00000006
Iteration  800, Error = .00000006
Iteration  900, Error = .00000006
Iteration 1000, Error = .00000006


COMPUTED AXIAL VELOCITY:

X/Y orientation:

o----> Y
|
|
V
  X
                                                      0
                                                   0

                             0
                        0       2     3 0   7
                0       4       4     5     9
                2       5       6   7 6  10       7
                   4       6    6   7    10    9
          0          6     5    5   6     9   10
            2          5   3    2   4   8    10
             5 6     3 1   0        0   5   8 9
                5 3   0              0     6
       0 2 4       1                 2           5 3 0
          5 6 4                         5 7 7
                3                     2

       0 2 5 6 5 4 1                 1 3 6 6 6 4 2 0

             5 3                     1 4 5
          4 5 6                        6 5 4
       0 2       3 2                1 3        2 0
             5 4   1 0         0 1   4 5
            4     3 2   0 0   0   0   2 3     4
            3     2 3     1     1   1     3 2     3
          0     0 1     0       0     0 0     0       0
```
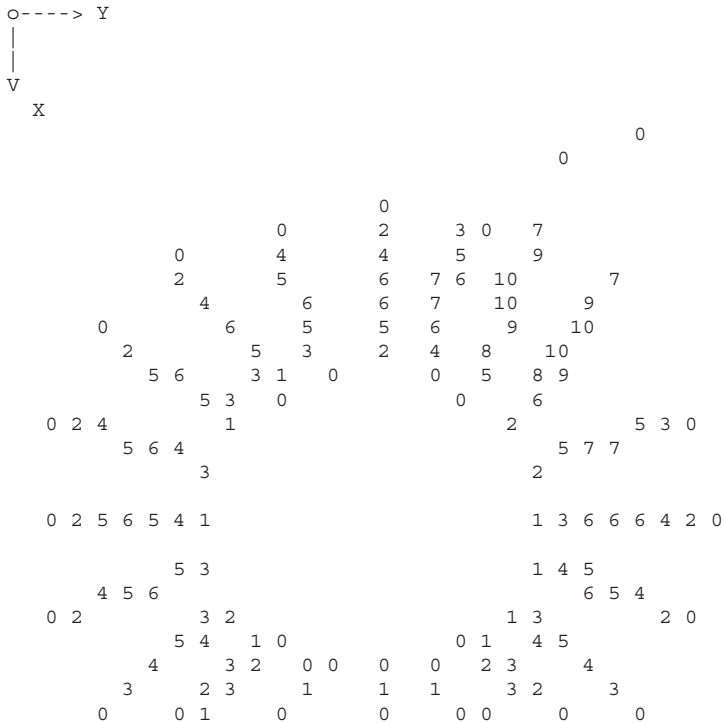
```
EXACT AXIAL VELOCITIES (IN/SEC):

Results for inner boundary, Contour No. 1:
#  1  X=0.1135E+02  Y=0.7000E+01  Answer = 0.0000E+00
#  2  X=0.1135E+02  Y=0.6073E+01  Answer = 0.0000E+00
#  3  X=0.1093E+02  Y=0.5237E+01  Answer = 0.0000E+00
#  4  X=0.1026E+02  Y=0.4573E+01  Answer = 0.0000E+00
#  5  X=0.9427E+01  Y=0.4147E+01  Answer = 0.0000E+00
#  6  X=0.8500E+01  Y=0.4000E+01  Answer = 0.0000E+00
#  7  X=0.7573E+01  Y=0.4147E+01  Answer = 0.0000E+00
#  8  X=0.6737E+01  Y=0.4573E+01  Answer = 0.0000E+00
#  9  X=0.6073E+01  Y=0.5237E+01  Answer = 0.0000E+00
# 10  X=0.5647E+01  Y=0.6073E+01  Answer = 0.0000E+00
# 11  X=0.5500E+01  Y=0.7000E+01  Answer = 0.0000E+00
# 12  X=0.5647E+01  Y=0.7927E+01  Answer = 0.0000E+00
# 13  X=0.6073E+01  Y=0.8763E+01  Answer = 0.0000E+00
# 14  X=0.6737E+01  Y=0.9427E+01  Answer = 0.0000E+00
# 15  X=0.7573E+01  Y=0.9853E+01  Answer = 0.0000E+00
# 16  X=0.8500E+01  Y=0.1000E+02  Answer = 0.0000E+00
# 17  X=0.9427E+01  Y=0.9853E+01  Answer = 0.0000E+00
# 18  X=0.1026E+02  Y=0.9427E+01  Answer = 0.0000E+00
# 19  X=0.1093E+02  Y=0.8763E+01  Answer = 0.0000E+00
# 20  X=0.1135E+02  Y=0.7927E+01  Answer = 0.0000E+00

Results for Contour No.  2:
#  1  X=0.1147E+02  Y=0.7000E+01  Answer = 0.4005E+01
#  2  X=0.1144E+02  Y=0.6019E+01  Answer = 0.4005E+01
#  3  X=0.1103E+02  Y=0.5130E+01  Answer = 0.8502E+01
#  4  X=0.1036E+02  Y=0.4415E+01  Answer = 0.1509E+02
#  5  X=0.9488E+01  Y=0.3951E+01  Answer = 0.1802E+02
#  6  X=0.8499E+01  Y=0.3789E+01  Answer = 0.1893E+02
#  7  X=0.7507E+01  Y=0.3944E+01  Answer = 0.1919E+02
#  8  X=0.6611E+01  Y=0.4400E+01  Answer = 0.1928E+02
#  9  X=0.5900E+01  Y=0.5111E+01  Answer = 0.1936E+02
# 10  X=0.5443E+01  Y=0.6005E+01  Answer = 0.1961E+02
# 11  X=0.5283E+01  Y=0.6996E+01  Answer = 0.2041E+02
# 12  X=0.5430E+01  Y=0.7983E+01  Answer = 0.2273E+02
# 13  X=0.5865E+01  Y=0.8878E+01  Answer = 0.2697E+02
# 14  X=0.6575E+01  Y=0.9597E+01  Answer = 0.2612E+02
# 15  X=0.7492E+01  Y=0.1006E+02  Answer = 0.2195E+02
# 16  X=0.8495E+01  Y=0.1021E+02  Answer = 0.1982E+02
# 17  X=0.9487E+01  Y=0.1005E+02  Answer = 0.1828E+02
# 18  X=0.1036E+02  Y=0.9585E+01  Answer = 0.1516E+02
# 19  X=0.1103E+02  Y=0.8871E+01  Answer = 0.8514E+01
# 20  X=0.1144E+02  Y=0.7981E+01  Answer = 0.4006E+01

Results for Contour No.  3:
#  1  X=0.1158E+02  Y=0.7000E+01  Answer = 0.7489E+01
#  2  X=0.1154E+02  Y=0.5961E+01  Answer = 0.7488E+01
#  3  X=0.1113E+02  Y=0.5014E+01  Answer = 0.1610E+02
#  4  X=0.1047E+02  Y=0.4246E+01  Answer = 0.2835E+02
#  5  X=0.9553E+01  Y=0.3740E+01  Answer = 0.3357E+02
#  6  X=0.8498E+01  Y=0.3562E+01  Answer = 0.3516E+02
#  7  X=0.7436E+01  Y=0.3727E+01  Answer = 0.3561E+02
#  8  X=0.6477E+01  Y=0.4215E+01  Answer = 0.3577E+02
#  9  X=0.5715E+01  Y=0.4976E+01  Answer = 0.3593E+02
# 10  X=0.5225E+01  Y=0.5933E+01  Answer = 0.3638E+02
# 11  X=0.5051E+01  Y=0.6991E+01  Answer = 0.3786E+02
# 12  X=0.5198E+01  Y=0.8044E+01  Answer = 0.4223E+02
# 13  X=0.5639E+01  Y=0.9001E+01  Answer = 0.5072E+02
# 14  X=0.6396E+01  Y=0.9779E+01  Answer = 0.4927E+02
# 15  X=0.7404E+01  Y=0.1028E+02  Answer = 0.4089E+02
# 16  X=0.8489E+01  Y=0.1044E+02  Answer = 0.3684E+02
```

```
# 17  X=0.9551E+01  Y=0.1026E+02  Answer = 0.3407E+02
# 18  X=0.1047E+02  Y=0.9754E+01  Answer = 0.2849E+02
# 19  X=0.1113E+02  Y=0.8986E+01  Answer = 0.1612E+02
# 20  X=0.1154E+02  Y=0.8039E+01  Answer = 0.7490E+01

Results for Contour No.   4:
#  1  X=0.1170E+02  Y=0.7000E+01  Answer = 0.1033E+02
#  2  X=0.1164E+02  Y=0.5897E+01  Answer = 0.1033E+02
#  3  X=0.1125E+02  Y=0.4889E+01  Answer = 0.2260E+02
#  4  X=0.1059E+02  Y=0.4064E+01  Answer = 0.3959E+02
#  5  X=0.9624E+01  Y=0.3514E+01  Answer = 0.4634E+02
#  6  X=0.8498E+01  Y=0.3319E+01  Answer = 0.4831E+02
#  7  X=0.7360E+01  Y=0.3494E+01  Answer = 0.4887E+02
#  8  X=0.6332E+01  Y=0.4016E+01  Answer = 0.4906E+02
#  9  X=0.5516E+01  Y=0.4831E+01  Answer = 0.4926E+02
# 10  X=0.4991E+01  Y=0.5855E+01  Answer = 0.4986E+02
# 11  X=0.4802E+01  Y=0.6986E+01  Answer = 0.5186E+02
# 12  X=0.4949E+01  Y=0.8108E+01  Answer = 0.5795E+02
# 13  X=0.5390E+01  Y=0.9131E+01  Answer = 0.7093E+02
# 14  X=0.6197E+01  Y=0.9973E+01  Answer = 0.6909E+02
# 15  X=0.7309E+01  Y=0.1052E+02  Answer = 0.5624E+02
# 16  X=0.8483E+01  Y=0.1069E+02  Answer = 0.5059E+02
# 17  X=0.9620E+01  Y=0.1049E+02  Answer = 0.4701E+02
# 18  X=0.1059E+02  Y=0.9937E+01  Answer = 0.3979E+02
# 19  X=0.1125E+02  Y=0.9111E+01  Answer = 0.2264E+02
# 20  X=0.1164E+02  Y=0.8103E+01  Answer = 0.1033E+02

Results for Contour No.   5:
#  1  X=0.1181E+02  Y=0.7000E+01  Answer = 0.1241E+02
#  2  X=0.1174E+02  Y=0.5826E+01  Answer = 0.1241E+02
#  3  X=0.1137E+02  Y=0.4753E+01  Answer = 0.2779E+02
#  4  X=0.1072E+02  Y=0.3867E+01  Answer = 0.4854E+02
#  5  X=0.9701E+01  Y=0.3269E+01  Answer = 0.5589E+02
#  6  X=0.8497E+01  Y=0.3057E+01  Answer = 0.5790E+02
#  7  X=0.7279E+01  Y=0.3244E+01  Answer = 0.5845E+02
#  8  X=0.6177E+01  Y=0.3803E+01  Answer = 0.5865E+02
#  9  X=0.5303E+01  Y=0.4675E+01  Answer = 0.5888E+02
# 10  X=0.4739E+01  Y=0.5773E+01  Answer = 0.5955E+02
# 11  X=0.4535E+01  Y=0.6982E+01  Answer = 0.6186E+02
# 12  X=0.4684E+01  Y=0.8179E+01  Answer = 0.6923E+02
# 13  X=0.5115E+01  Y=0.9270E+01  Answer = 0.8717E+02
# 14  X=0.5972E+01  Y=0.1018E+02  Answer = 0.8513E+02
# 15  X=0.7208E+01  Y=0.1077E+02  Answer = 0.6735E+02
# 16  X=0.8478E+01  Y=0.1096E+02  Answer = 0.6052E+02
# 17  X=0.9697E+01  Y=0.1074E+02  Answer = 0.5665E+02
# 18  X=0.1072E+02  Y=0.1013E+02  Answer = 0.4878E+02
# 19  X=0.1137E+02  Y=0.9247E+01  Answer = 0.2784E+02
# 20  X=0.1174E+02  Y=0.8174E+01  Answer = 0.1241E+02

Results for Contour No.   6:
#  1  X=0.1193E+02  Y=0.7000E+01  Answer = 0.1361E+02
#  2  X=0.1185E+02  Y=0.5747E+01  Answer = 0.1360E+02
#  3  X=0.1150E+02  Y=0.4603E+01  Answer = 0.3138E+02
#  4  X=0.1087E+02  Y=0.3652E+01  Answer = 0.5476E+02
#  5  X=0.9787E+01  Y=0.3004E+01  Answer = 0.6164E+02
#  6  X=0.8497E+01  Y=0.2775E+01  Answer = 0.6335E+02
#  7  X=0.7191E+01  Y=0.2974E+01  Answer = 0.6381E+02
#  8  X=0.6011E+01  Y=0.3573E+01  Answer = 0.6398E+02
#  9  X=0.5073E+01  Y=0.4508E+01  Answer = 0.6420E+02
# 10  X=0.4469E+01  Y=0.5684E+01  Answer = 0.6487E+02
# 11  X=0.4250E+01  Y=0.6979E+01  Answer = 0.6726E+02
# 12  X=0.4402E+01  Y=0.8255E+01  Answer = 0.7535E+02
# 13  X=0.4806E+01  Y=0.9418E+01  Answer = 0.9880E+02
```

```
# 14  X=0.5712E+01  Y=0.1040E+02  Answer = 0.9682E+02
# 15  X=0.7101E+01  Y=0.1105E+02  Answer = 0.7345E+02
# 16  X=0.8475E+01  Y=0.1124E+02  Answer = 0.6603E+02
# 17  X=0.9782E+01  Y=0.1100E+02  Answer = 0.6241E+02
# 18  X=0.1087E+02  Y=0.1035E+02  Answer = 0.5502E+02
# 19  X=0.1150E+02  Y=0.9398E+01  Answer = 0.3144E+02
# 20  X=0.1185E+02  Y=0.8253E+01  Answer = 0.1361E+02

Results for Contour No.   7:
#  1  X=0.1204E+02  Y=0.7000E+01  Answer = 0.1378E+02
#  2  X=0.1197E+02  Y=0.5659E+01  Answer = 0.1378E+02
#  3  X=0.1164E+02  Y=0.4436E+01  Answer = 0.3297E+02
#  4  X=0.1105E+02  Y=0.3416E+01  Answer = 0.5762E+02
#  5  X=0.9881E+01  Y=0.2716E+01  Answer = 0.6284E+02
#  6  X=0.8497E+01  Y=0.2471E+01  Answer = 0.6398E+02
#  7  X=0.7097E+01  Y=0.2685E+01  Answer = 0.6428E+02
#  8  X=0.5832E+01  Y=0.3327E+01  Answer = 0.6440E+02
#  9  X=0.4827E+01  Y=0.4329E+01  Answer = 0.6459E+02
# 10  X=0.4180E+01  Y=0.5590E+01  Answer = 0.6519E+02
# 11  X=0.3945E+01  Y=0.6977E+01  Answer = 0.6741E+02
# 12  X=0.4104E+01  Y=0.8340E+01  Answer = 0.7552E+02
# 13  X=0.4456E+01  Y=0.9576E+01  Answer = 0.1050E+03
# 14  X=0.5405E+01  Y=0.1063E+02  Answer = 0.1034E+03
# 15  X=0.6991E+01  Y=0.1134E+02  Answer = 0.7372E+02
# 16  X=0.8473E+01  Y=0.1155E+02  Answer = 0.6641E+02
# 17  X=0.9877E+01  Y=0.1129E+02  Answer = 0.6353E+02
# 18  X=0.1105E+02  Y=0.1059E+02  Answer = 0.5786E+02
# 19  X=0.1164E+02  Y=0.9565E+01  Answer = 0.3304E+02
# 20  X=0.1197E+02  Y=0.8341E+01  Answer = 0.1378E+02

Results for Contour No.   8:
#  1  X=0.1216E+02  Y=0.7000E+01  Answer = 0.1278E+02
#  2  X=0.1209E+02  Y=0.5558E+01  Answer = 0.1277E+02
#  3  X=0.1180E+02  Y=0.4248E+01  Answer = 0.3199E+02
#  4  X=0.1126E+02  Y=0.3156E+01  Answer = 0.5616E+02
#  5  X=0.9987E+01  Y=0.2403E+01  Answer = 0.5855E+02
#  6  X=0.8498E+01  Y=0.2143E+01  Answer = 0.5897E+02
#  7  X=0.6996E+01  Y=0.2374E+01  Answer = 0.5909E+02
#  8  X=0.5640E+01  Y=0.3063E+01  Answer = 0.5916E+02
#  9  X=0.4563E+01  Y=0.4137E+01  Answer = 0.5929E+02
# 10  X=0.3869E+01  Y=0.5489E+01  Answer = 0.5976E+02
# 11  X=0.3619E+01  Y=0.6978E+01  Answer = 0.6159E+02
# 12  X=0.3795E+01  Y=0.8437E+01  Answer = 0.6896E+02
# 13  X=0.4048E+01  Y=0.9747E+01  Answer = 0.1043E+03
# 14  X=0.5026E+01  Y=0.1088E+02  Answer = 0.1039E+03
# 15  X=0.6881E+01  Y=0.1166E+02  Answer = 0.6725E+02
# 16  X=0.8474E+01  Y=0.1187E+02  Answer = 0.6088E+02
# 17  X=0.9982E+01  Y=0.1160E+02  Answer = 0.5907E+02
# 18  X=0.1126E+02  Y=0.1085E+02  Answer = 0.5636E+02
# 19  X=0.1180E+02  Y=0.9753E+01  Answer = 0.3205E+02
# 20  X=0.1209E+02  Y=0.8442E+01  Answer = 0.1278E+02

Results for Contour No.   9:
#  1  X=0.1227E+02  Y=0.7000E+01  Answer = 0.1039E+02
#  2  X=0.1221E+02  Y=0.5443E+01  Answer = 0.1039E+02
#  3  X=0.1199E+02  Y=0.4033E+01  Answer = 0.2753E+02
#  4  X=0.1152E+02  Y=0.2867E+01  Answer = 0.4885E+02
#  5  X=0.1010E+02  Y=0.2062E+01  Answer = 0.4758E+02
#  6  X=0.8498E+01  Y=0.1790E+01  Answer = 0.4738E+02
#  7  X=0.6888E+01  Y=0.2040E+01  Answer = 0.4736E+02
#  8  X=0.5433E+01  Y=0.2779E+01  Answer = 0.4737E+02
#  9  X=0.4279E+01  Y=0.3932E+01  Answer = 0.4745E+02
# 10  X=0.3536E+01  Y=0.5382E+01  Answer = 0.4776E+02
```

```
# 11  X=0.3271E+01  Y=0.6982E+01  Answer = 0.4903E+02
# 12  X=0.3477E+01  Y=0.8548E+01  Answer = 0.5495E+02
# 13  X=0.3553E+01  Y=0.9936E+01  Answer = 0.9469E+02
# 14  X=0.4523E+01  Y=0.1113E+02  Answer = 0.9650E+02
# 15  X=0.6778E+01  Y=0.1199E+02  Answer = 0.5316E+02
# 16  X=0.8479E+01  Y=0.1222E+02  Answer = 0.4860E+02
# 17  X=0.1010E+02  Y=0.1194E+02  Answer = 0.4789E+02
# 18  X=0.1152E+02  Y=0.1114E+02  Answer = 0.4897E+02
# 19  X=0.1199E+02  Y=0.9968E+01  Answer = 0.2757E+02
# 20  X=0.1221E+02  Y=0.8557E+01  Answer = 0.1039E+02

Results for Contour No. 10:
#  1  X=0.1239E+02  Y=0.7000E+01  Answer = 0.6310E+01
#  2  X=0.1235E+02  Y=0.5308E+01  Answer = 0.6308E+01
#  3  X=0.1221E+02  Y=0.3781E+01  Answer = 0.1802E+02
#  4  X=0.1189E+02  Y=0.2539E+01  Answer = 0.3279E+02
#  5  X=0.1023E+02  Y=0.1692E+01  Answer = 0.2854E+02
#  6  X=0.8499E+01  Y=0.1409E+01  Answer = 0.2813E+02
#  7  X=0.6771E+01  Y=0.1680E+01  Answer = 0.2805E+02
#  8  X=0.5212E+01  Y=0.2474E+01  Answer = 0.2804E+02
#  9  X=0.3974E+01  Y=0.3711E+01  Answer = 0.2807E+02
# 10  X=0.3178E+01  Y=0.5268E+01  Answer = 0.2821E+02
# 11  X=0.2899E+01  Y=0.6989E+01  Answer = 0.2884E+02
# 12  X=0.3152E+01  Y=0.8681E+01  Answer = 0.3284E+02
# 13  X=0.2890E+01  Y=0.1016E+02  Answer = 0.7087E+02
# 14  X=0.3755E+01  Y=0.1141E+02  Answer = 0.7713E+02
# 15  X=0.6691E+01  Y=0.1234E+02  Answer = 0.3073E+02
# 16  X=0.8487E+01  Y=0.1260E+02  Answer = 0.2864E+02
# 17  X=0.1022E+02  Y=0.1231E+02  Answer = 0.2866E+02
# 18  X=0.1189E+02  Y=0.1146E+02  Answer = 0.3283E+02
# 19  X=0.1221E+02  Y=0.1022E+02  Answer = 0.1804E+02
# 20  X=0.1235E+02  Y=0.8692E+01  Answer = 0.6312E+01

Results for borehole annulus boundary, Contour No. 11:
#  1  X=0.1250E+02  Y=0.7000E+01  Answer = 0.0000E+00
#  2  X=0.1250E+02  Y=0.5146E+01  Answer = 0.0000E+00
#  3  X=0.1250E+02  Y=0.3473E+01  Answer = 0.0000E+00
#  4  X=0.1250E+02  Y=0.2146E+01  Answer = 0.0000E+00
#  5  X=0.1035E+02  Y=0.1294E+01  Answer = 0.0000E+00
#  6  X=0.8500E+01  Y=0.1000E+01  Answer = 0.0000E+00
#  7  X=0.6646E+01  Y=0.1294E+01  Answer = 0.0000E+00
#  8  X=0.4973E+01  Y=0.2146E+01  Answer = 0.0000E+00
#  9  X=0.3646E+01  Y=0.3473E+01  Answer = 0.0000E+00
# 10  X=0.2794E+01  Y=0.5146E+01  Answer = 0.0000E+00
# 11  X=0.2500E+01  Y=0.7000E+01  Answer = 0.0000E+00
# 12  X=0.2794E+01  Y=0.8854E+01  Answer = 0.0000E+00
# 13  X=0.1500E+01  Y=0.1053E+02  Answer = 0.0000E+00
# 14  X=0.1000E+01  Y=0.1185E+02  Answer = 0.0000E+00
# 15  X=0.6646E+01  Y=0.1271E+02  Answer = 0.0000E+00
# 16  X=0.8500E+01  Y=0.1300E+02  Answer = 0.0000E+00
# 17  X=0.1035E+02  Y=0.1271E+02  Answer = 0.0000E+00
# 18  X=0.1250E+02  Y=0.1185E+02  Answer = 0.0000E+00
# 19  X=0.1250E+02  Y=0.1053E+02  Answer = 0.0000E+00
# 20  X=0.1250E+02  Y=0.8854E+01  Answer = 0.0000E+00

Annular flow rate ...... 0.9079E+03 gal/min
Cross-sectional area ... 0.7986E+02 sq inch
```

```
NEW STABILITY CALCULATION:

Mud assumed to be .1000E+01 times as dense as water,
with critical Reynolds number of .2000E+04 in annulus.

LAMINAR/TURBULENT STABILITY ZONES:


X/Y orientation:

o----> Y
|
|
V
  X


                                                    L
                                                 L

                               L
                    L          T       T L     T
             L          T      T          T       T
             T          T      T    T T    T            T
                T           T     T  T       T      T
         L          T       T     T  T       T       T
          T             T  T      T  T   T      T
           T T      T T    L        L    T    T T
             T T    L            L        T
    L T T        T                    T            T T L
       T T T                              T T T
          T                               T

    L T T T T T T                  T T T T T T T L

          T T                          T T T
       T T T                              T T T
    L T          T T                  T T          T L
          T T    T T            L T    T T
       T        T T   T L   T    T    T T      T
        T         T T     T     T    T     T T     T
       L      L T     L        L     T L    L      L


Avg Reynolds number, bottom half annulus: .1665E+06
Average Reynolds  number, entire annulus: .2235E+06
```
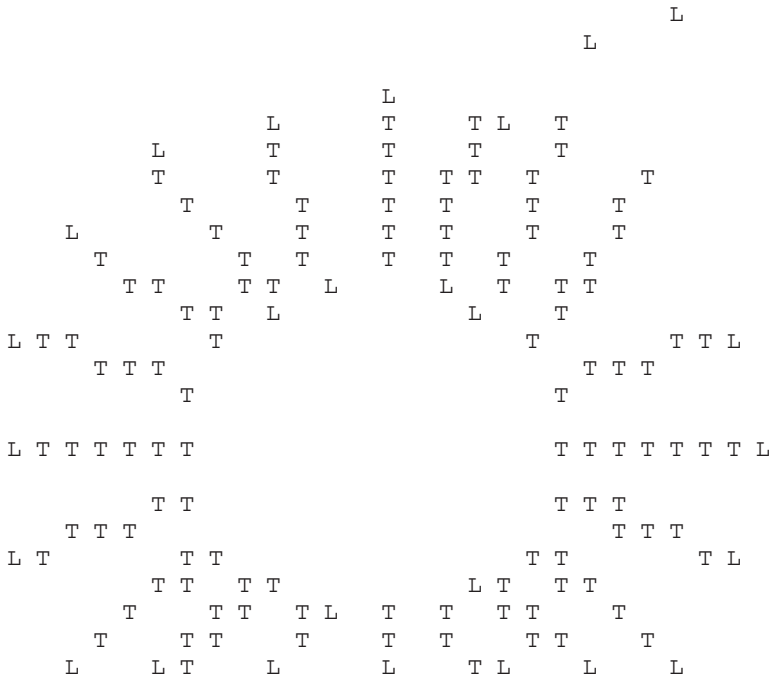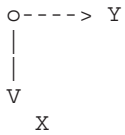
```
PLOT OF "APPARENT VISCOSITY" VS (X,Y):

COMPUTED APPARENT VISCOSITY:

X/Y orientation:

o----> Y
|
|
V
  X
                                                    14
                                                  14

                              14
                    14        14    1414  14
              14          14        14    14    14
              14          14        14  1414  14        14
                14        14      14  14    14      14
          14          14      14    14  14      14      14
           14            14  14      14  14  14      14
              1414      1414  14        14  14  1414
                1414  14              14    14
         141414          14                      14          141414
             141414                                141414
                14                                  14

        14141414141414                        1414141414141414

                1414                              141414
             141414                                  141414
        1414          1414                    1414          1414
                1414  1414                    1414  1414
              14      1414  1414  14  14  1414      14
            14      1414      14    14  14    1414      14
            14      1414      14      14    1414    14    14


EXACT APPARENT VISCOSITIES (LBF SEC/SQ IN):

Results for inner boundary, Contour No. 1:
#  1  X=0.1135E+02  Y=0.7000E+01  Answer = 0.1465E-06
#  2  X=0.1135E+02  Y=0.6073E+01  Answer = 0.1465E-06
#  3  X=0.1093E+02  Y=0.5237E+01  Answer = 0.1465E-06
#  4  X=0.1026E+02  Y=0.4573E+01  Answer = 0.1465E-06
.
.
.
```
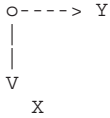
Apparent viscosity tabulations are similar to those for velocity. In the present simulation, a Newtonian fluid is assumed so that all "apparent viscosity" values are identical and equal to the Newtonian viscosity. Tabulations for apparent viscosity are therefore omitted. For non-Newtonian applications, values will vary throughout space and also with flow rate or pressure gradient.

```
PLOT OF STRESS "AppVisc x dU(x,y)/dx" VS (X,Y):

COMPUTED (ABSOLUTE VALUE OF) VISCOUS STRESSES:

X/Y orientation:
o----> Y
|
|
V
  X
                                                    3
                                                  9

                              11
                      11      9    1215   6
                9        6       6     8     4
                7        3       1   2 5   2          2
                   5        1     1   0     0      1
         6           0      3     6   3     2      0
           5         3   8    12   9   4     1
              2 0      7 9 13      15   9   4 3
                 2 5  11              14      6
      3 2 1         6                    9              0 1 1
          1 0 2                            3 1 1
                 2                          4


      0 0 0 0 0 0 0                         0 0 0 0 0 0 0 0

               0 2                         3 1 0
         1 1 0                               0 1 1
      3 2           2 4                5 2              2 3
              1 1    4 6             7 4   1 1
            3      0 1    3 6    3    3   1 0       3
          4      5 3     1     0   1     2 5     4
          5     10 7    7       4     5 7     10      5


EXACT VISCOUS STRESSES (PSI):

Results for inner boundary, Contour No. 1:
#  1  X=0.1135E+02  Y=0.7000E+01  Answer = 0.4688E-05
#  2  X=0.1135E+02  Y=0.6073E+01  Answer = 0.6129E-05
#  3  X=0.1093E+02  Y=0.5237E+01  Answer = 0.7569E-05
#  4  X=0.1026E+02  Y=0.4573E+01  Answer = 0.7503E-05
#  5  X=0.9427E+01  Y=0.4147E+01  Answer = 0.4306E-05
#  6  X=0.8500E+01  Y=0.4000E+01  Answer = -.1303E-07
#  7  X=0.7573E+01  Y=0.4147E+01  Answer = -.4475E-05
#  8  X=0.6737E+01  Y=0.4573E+01  Answer = -.8526E-05
#  9  X=0.6073E+01  Y=0.5237E+01  Answer = -.1177E-04
# 10  X=0.5647E+01  Y=0.6073E+01  Answer = -.1397E-04
# 11  X=0.5500E+01  Y=0.7000E+01  Answer = -.1514E-04
# 12  X=0.5647E+01  Y=0.7927E+01  Answer = -.1554E-04
# 13  X=0.6073E+01  Y=0.8763E+01  Answer = -.1474E-04
# 14  X=0.6737E+01  Y=0.9427E+01  Answer = -.1055E-04
# 15  X=0.7573E+01  Y=0.9853E+01  Answer = -.4982E-05
# 16  X=0.8500E+01  Y=0.1000E+02  Answer = -.4651E-07
# 17  X=0.9427E+01  Y=0.9853E+01  Answer = 0.4339E-05
# 18  X=0.1026E+02  Y=0.9427E+01  Answer = 0.7526E-05
# 19  X=0.1093E+02  Y=0.8763E+01  Answer = 0.7576E-05
# 20  X=0.1135E+02  Y=0.7927E+01  Answer = 0.6129E-05
```

Additional results are omitted due to space limitations.

```
PLOT OF STRESS "AppVisc x dU(x,y)/dy" VS (X,Y):

COMPUTED (ABSOLUTE VALUE OF) VISCOUS STRESSES:

X/Y orientation:
o----> Y
|
|
V
  X
                                                      9
                                                  1

                            0
                     3      0     1 2    0
              6          2      0     1      0
              5          1      0   1 1   1        7
                   3        0    0  2     1      4
          9          0     1    0  2     3      2
           7          2    2    0  3   4      0
             2 0      5 6   4        5   7   4 2
                3 7   8            10     6
       10 8 5         9                  11              71013
            3 1 6                          6 0 1
                 8                         12

       11 8 3 1 4 611                      12 9 4 1 3 6 911

              4 8                          11 6 4
         5 2 1                              1 3 5
       10 8          5 7                  8 5              811
              1 4    4 5            5 4    4 1
            1      2 3    1 1    1   1   3 2      1
          3      0 1    0      0   0     2 0      3
          5      0 0      0        0   0 0      0     5


EXACT VISCOUS STRESSES (PSI):

Results for inner boundary, Contour No. 1:
#  1  X=0.1135E+02  Y=0.7000E+01  Answer = 0.2465E-05
#  2  X=0.1135E+02  Y=0.6073E+01  Answer = -.1551E-05
#  3  X=0.1093E+02  Y=0.5237E+01  Answer = -.5566E-05
#  4  X=0.1026E+02  Y=0.4573E+01  Answer = -.1044E-04
#  5  X=0.9427E+01  Y=0.4147E+01  Answer = -.1338E-04
#  6  X=0.8500E+01  Y=0.4000E+01  Answer = -.1438E-04
#  7  X=0.7573E+01  Y=0.4147E+01  Answer = -.1376E-04
#  8  X=0.6737E+01  Y=0.4573E+01  Answer = -.1173E-04
#  9  X=0.6073E+01  Y=0.5237E+01  Answer = -.8549E-05
# 10  X=0.5647E+01  Y=0.6073E+01  Answer = -.4531E-05
# 11  X=0.5500E+01  Y=0.7000E+01  Answer = 0.1706E-07
# 12  X=0.5647E+01  Y=0.7927E+01  Answer = 0.5049E-05
# 13  X=0.6073E+01  Y=0.8763E+01  Answer = 0.1066E-04
# 14  X=0.6737E+01  Y=0.9427E+01  Answer = 0.1439E-04
# 15  X=0.7573E+01  Y=0.9853E+01  Answer = 0.1511E-04
# 16  X=0.8500E+01  Y=0.1000E+02  Answer = 0.1487E-04
# 17  X=0.9427E+01  Y=0.9853E+01  Answer = 0.1352E-04
# 18  X=0.1026E+02  Y=0.9427E+01  Answer = 0.1047E-04
# 19  X=0.1093E+02  Y=0.8763E+01  Answer = 0.5572E-05
# 20  X=0.1135E+02  Y=0.7927E+01  Answer = 0.1551E-05
```
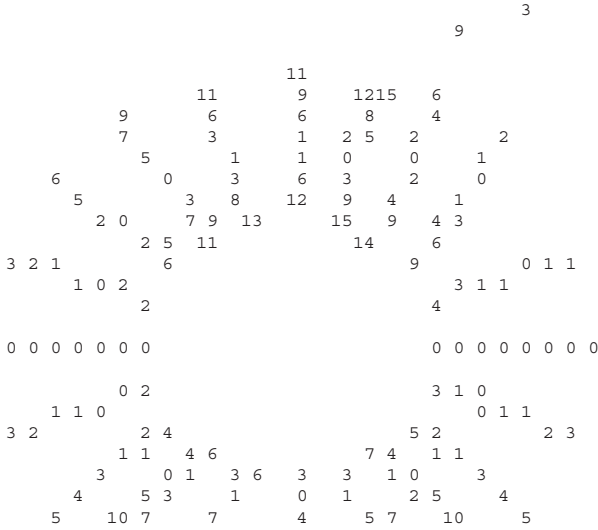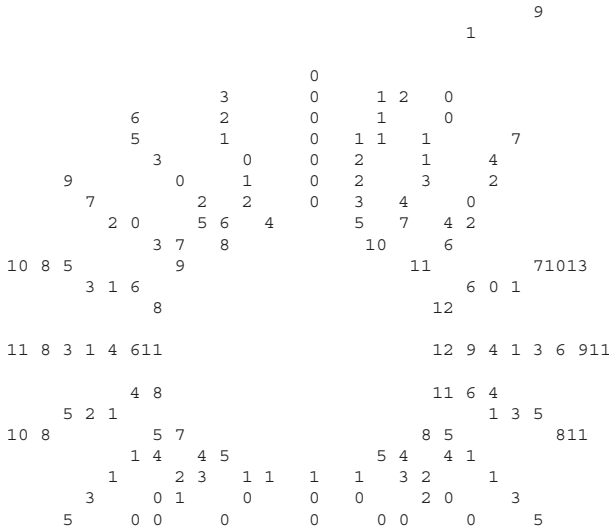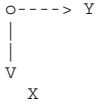
Additional results are omitted due to space limitations.

```
PLOT OF DISSIPATION FUNCTION VS (X,Y):

COMPUTED DISSIPATION FUNCTION:

X/Y orientation:
o----> Y
|
|
V
  X
                                                      7
                                              6

                            9
                      9       5    1119   3
              9           2       3     5     1
              5           0       0   0 2   0         3
                2           0     0   0     0       1
        8           0     1     3   1     1       0
          5             1   5    10   7   2       0
            0 0       5 9  14       18  10   2 0
              1 5   14                22     5
      8 5 2         9                     15          4 712
          0 0 2                               3 0 0
                5                             11

      8 5 0 0 1 2 9                       10 6 1 0 1 2 5 9

            1 5                           9 3 1
        2 0 0                               0 0 2
      8 5           2 5                 7 2           5 8
            0 1   2 4             6 2   1 0
          1       0 0   1 2   0   1   0 0       1
          2       2 1     0     0   0     0 2     2
          4         6 4     3     1     2 3     7     4


EXACT DISSIPATION FUNCTION (LBF/(SEC X SQ IN)):

Results for inner boundary, Contour No. 1:
#  1  X=0.1135E+02  Y=0.7000E+01  Answer = 0.1915E-03
#  2  X=0.1135E+02  Y=0.6073E+01  Answer = 0.2728E-03
#  3  X=0.1093E+02  Y=0.5237E+01  Answer = 0.6025E-03
#  4  X=0.1026E+02  Y=0.4573E+01  Answer = 0.1128E-02
#  5  X=0.9427E+01  Y=0.4147E+01  Answer = 0.1348E-02
#  6  X=0.8500E+01  Y=0.4000E+01  Answer = 0.1412E-02
#  7  X=0.7573E+01  Y=0.4147E+01  Answer = 0.1429E-02
#  8  X=0.6737E+01  Y=0.4573E+01  Answer = 0.1436E-02
#  9  X=0.6073E+01  Y=0.5237E+01  Answer = 0.1445E-02
# 10  X=0.5647E+01  Y=0.6073E+01  Answer = 0.1472E-02
# 11  X=0.5500E+01  Y=0.7000E+01  Answer = 0.1564E-02
# 12  X=0.5647E+01  Y=0.7927E+01  Answer = 0.1823E-02
# 13  X=0.6073E+01  Y=0.8763E+01  Answer = 0.2258E-02
# 14  X=0.6737E+01  Y=0.9427E+01  Answer = 0.2172E-02
# 15  X=0.7573E+01  Y=0.9853E+01  Answer = 0.1728E-02
# 16  X=0.8500E+01  Y=0.1000E+02  Answer = 0.1509E-02
# 17  X=0.9427E+01  Y=0.9853E+01  Answer = 0.1377E-02
# 18  X=0.1026E+02  Y=0.9427E+01  Answer = 0.1135E-02
# 19  X=0.1093E+02  Y=0.8763E+01  Answer = 0.6037E-03
# 20  X=0.1135E+02  Y=0.7927E+01  Answer = 0.2729E-03
```
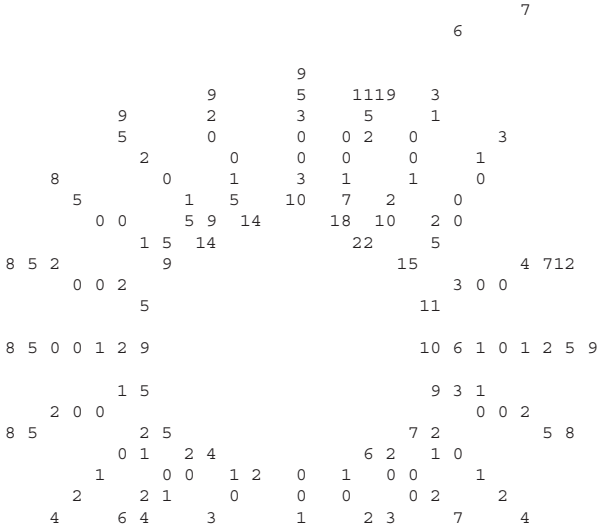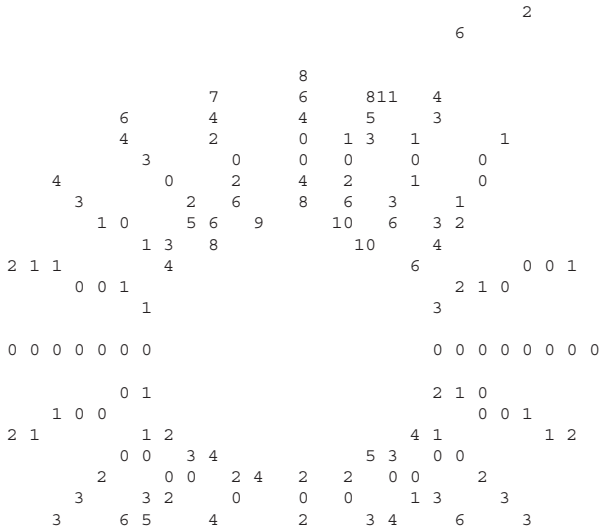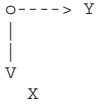
Additional results are omitted due to space limitations.

```
PLOT OF SHEAR RATE "dU(x,y)/dx" VS (X,Y):

COMPUTED (ABSOLUTE VALUE OF) SHEAR RATES:

X/Y orientation:
o----> Y
|
|
V
  X
                                                         2
                                                    6

                                     8
                         7           6       811    4
                 6           4       4        5      3
                 4           2       0    1 3   1         1
                    3           0        0   0     0      0
            4           0       2        4   2     1      0
              3           2   6      8    6   3      1
                1 0       5 6     9        10   6    3 2
                   1 3    8              10       4
       2 1 1           4                    6              0 0 1
           0 0 1                                   2 1 0
               1                                  3

         0 0 0 0 0 0 0                          0 0 0 0 0 0 0 0

                 0 1                              2 1 0
            1 0 0                                      0 0 1
       2 1           1 2                    4 1              1 2
               0 0    3 4                 5 3    0 0
           2        0 0    2 4    2    2    0 0       2
         3        3 2       0       0    0     1 3       3
         3        6 5       4       2      3 4    6       3


EXACT SHEAR RATES (1/SEC):

Results for inner boundary, Contour No. 1:
#  1  X=0.1135E+02  Y=0.7000E+01  Answer =  0.3200E+02
#  2  X=0.1135E+02  Y=0.6073E+01  Answer =  0.4183E+02
#  3  X=0.1093E+02  Y=0.5237E+01  Answer =  0.5166E+02
#  4  X=0.1026E+02  Y=0.4573E+01  Answer =  0.5121E+02
#  5  X=0.9427E+01  Y=0.4147E+01  Answer =  0.2939E+02
#  6  X=0.8500E+01  Y=0.4000E+01  Answer = -.8894E-01
#  7  X=0.7573E+01  Y=0.4147E+01  Answer = -.3055E+02
#  8  X=0.6737E+01  Y=0.4573E+01  Answer = -.5820E+02
#  9  X=0.6073E+01  Y=0.5237E+01  Answer = -.8035E+02
# 10  X=0.5647E+01  Y=0.6073E+01  Answer = -.9536E+02
# 11  X=0.5500E+01  Y=0.7000E+01  Answer = -.1033E+03
# 12  X=0.5647E+01  Y=0.7927E+01  Answer = -.1061E+03
# 13  X=0.6073E+01  Y=0.8763E+01  Answer = -.1006E+03
# 14  X=0.6737E+01  Y=0.9427E+01  Answer = -.7198E+02
# 15  X=0.7573E+01  Y=0.9853E+01  Answer = -.3401E+02
# 16  X=0.8500E+01  Y=0.1000E+02  Answer = -.3175E+00
# 17  X=0.9427E+01  Y=0.9853E+01  Answer =  0.2962E+02
# 18  X=0.1026E+02  Y=0.9427E+01  Answer =  0.5137E+02
# 19  X=0.1093E+02  Y=0.8763E+01  Answer =  0.5171E+02
# 20  X=0.1135E+02  Y=0.7927E+01  Answer =  0.4184E+02
```
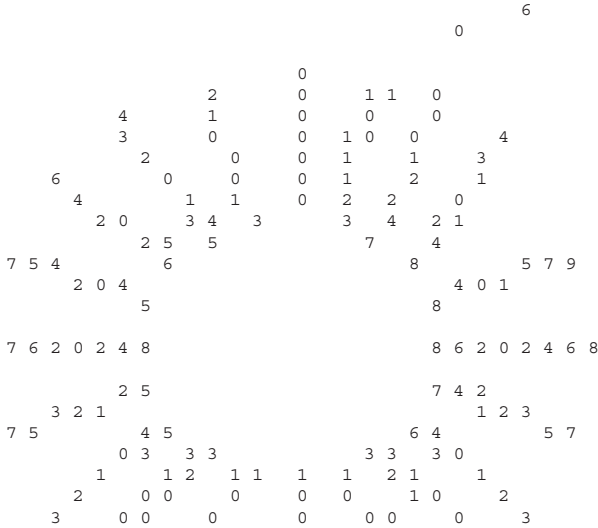
Additional results are omitted due to space limitations.

```
PLOT OF SHEAR RATE "dU(x,y)/dy" VS (X,Y):

COMPUTED (ABSOLUTE VALUE OF) SHEAR RATES:

X/Y orientation:
o----> Y
|
|
V
  X

                                                    6
                                                 0

                                     0
                            2        0      1 1    0
                     4          1     0        0      0
                     3          0        0  1 0    0          4
                        2         0       0  1       1       3
                6          0      0      0  1       2       1
                 4           1   1      0  2    2        0
                  2 0        3 4    3        3    4    2 1
                     2 5    5                7      4
           7 5 4          6                        8              5 7 9
              2 0 4                              4 0 1
                    5                              8

           7 6 2 0 2 4 8                      8 6 2 0 2 4 6 8

              2 5                                  7 4 2
           3 2 1                                 1 2 3
        7 5            4 5                    6 4            5 7
              0 3    3 3              3 3    3 0
                 1      1 2    1 1    1    1    2 1        1
              2      0 0        0      0    0      1 0      2
           3      0 0        0        0      0 0      0      3


EXACT SHEAR RATES (1/SEC):

Results for inner boundary, Contour No. 1:
#  1  X=0.1135E+02  Y=0.7000E+01  Answer = 0.1682E+02
#  2  X=0.1135E+02  Y=0.6073E+01  Answer = -.1058E+02
#  3  X=0.1093E+02  Y=0.5237E+01  Answer = -.3799E+02
#  4  X=0.1026E+02  Y=0.4573E+01  Answer = -.7124E+02
#  5  X=0.9427E+01  Y=0.4147E+01  Answer = -.9132E+02
#  6  X=0.8500E+01  Y=0.4000E+01  Answer = -.9817E+02
#  7  X=0.7573E+01  Y=0.4147E+01  Answer = -.9393E+02
#  8  X=0.6737E+01  Y=0.4573E+01  Answer = -.8008E+02
#  9  X=0.6073E+01  Y=0.5237E+01  Answer = -.5835E+02
# 10  X=0.5647E+01  Y=0.6073E+01  Answer = -.3093E+02
# 11  X=0.5500E+01  Y=0.7000E+01  Answer = 0.1165E+00
# 12  X=0.5647E+01  Y=0.7927E+01  Answer = 0.3447E+02
# 13  X=0.6073E+01  Y=0.8763E+01  Answer = 0.7275E+02
# 14  X=0.6737E+01  Y=0.9427E+01  Answer = 0.9822E+02
# 15  X=0.7573E+01  Y=0.9853E+01  Answer = 0.1032E+03
# 16  X=0.8500E+01  Y=0.1000E+02  Answer = 0.1015E+03
# 17  X=0.9427E+01  Y=0.9853E+01  Answer = 0.9230E+02
# 18  X=0.1026E+02  Y=0.9427E+01  Answer = 0.7149E+02
# 19  X=0.1093E+02  Y=0.8763E+01  Answer = 0.3803E+02
# 20  X=0.1135E+02  Y=0.7927E+01  Answer = 0.1059E+02
```
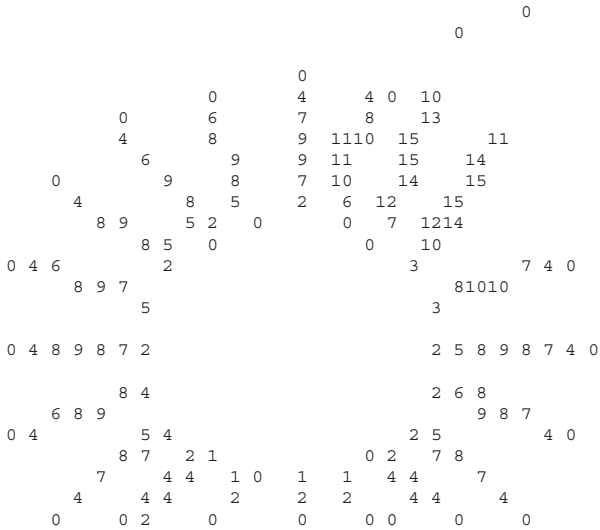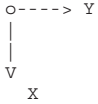
Additional results are omitted due to space limitations.

```
PLOT OF "STOKES PRODUCT" VS (X,Y):

COMPUTED STOKES PRODUCT:

X/Y orientation:
o----> Y
|
|
V
  X
                                                        0
                                                    0

                                    0
                        0           4       4 0  10
               0               6         7       8     13
               4               8        9  1110  15        11
                  6                9     9  11     15      14
          0              9         8     7  10     14      15
             4              8    5      2    6  12     15
               8 9        5 2    0         0   7  1214
                 8 5      0                  0   10
       0 4 6          2                   3            7 4 0
           8 9 7                               81010
               5                              3

       0 4 8 9 8 7 2                        2 5 8 9 8 7 4 0

           8 4                              2 6 8
         6 8 9                                9 8 7
       0 4           5 4                  2 5           4 0
             8 7   2 1            0 2   7 8
          7       4 4   1 0    1   1   4 4       7
        4       4 4       2      2   2       4 4      4
          0       0 2       0         0   0 0       0       0


EXACT STOKES PRODUCT (LBF/IN):

Results for inner boundary, Contour No. 1:
#  1  X=0.1135E+02  Y=0.7000E+01  Answer = 0.0000E+00
#  2  X=0.1135E+02  Y=0.6073E+01  Answer = 0.0000E+00
#  3  X=0.1093E+02  Y=0.5237E+01  Answer = 0.0000E+00
#  4  X=0.1026E+02  Y=0.4573E+01  Answer = 0.0000E+00
#  5  X=0.9427E+01  Y=0.4147E+01  Answer = 0.0000E+00
#  6  X=0.8500E+01  Y=0.4000E+01  Answer = 0.0000E+00
#  7  X=0.7573E+01  Y=0.4147E+01  Answer = 0.0000E+00
#  8  X=0.6737E+01  Y=0.4573E+01  Answer = 0.0000E+00
#  9  X=0.6073E+01  Y=0.5237E+01  Answer = 0.0000E+00
# 10  X=0.5647E+01  Y=0.6073E+01  Answer = 0.0000E+00
# 11  X=0.5500E+01  Y=0.7000E+01  Answer = 0.0000E+00
# 12  X=0.5647E+01  Y=0.7927E+01  Answer = 0.0000E+00
# 13  X=0.6073E+01  Y=0.8763E+01  Answer = 0.0000E+00
# 14  X=0.6737E+01  Y=0.9427E+01  Answer = 0.0000E+00
# 15  X=0.7573E+01  Y=0.9853E+01  Answer = 0.0000E+00
# 16  X=0.8500E+01  Y=0.1000E+02  Answer = 0.0000E+00
# 17  X=0.9427E+01  Y=0.9853E+01  Answer = 0.0000E+00
# 18  X=0.1026E+02  Y=0.9427E+01  Answer = 0.0000E+00
# 19  X=0.1093E+02  Y=0.8763E+01  Answer = 0.0000E+00
# 20  X=0.1135E+02  Y=0.7927E+01  Answer = 0.0000E+00
```

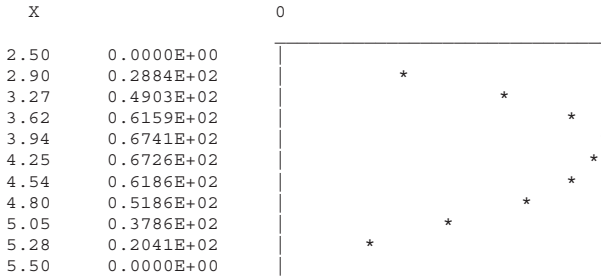Additional results are omitted due to space limitations.

```
TABULATION OF CALCULATED AVERAGE QUANTITIES, I:
Area weighted means of absolute values taken over
BOTTOM HALF of annular cross-section ...
O  Axial annular velocity  (inches/sec):  .2614E+02
O  Apparent viscosity (lbf sec / sq in):  .1465E-06
O  Viscous stress, AppVis x dU/dx (psi):  .2806E-05
O  Viscous stress, AppVis x dU/dy (psi):  .4162E-05
O  Dissipation fnction (lbf/(sec sqin)):  .3138E-03
O  Shear rate dU/dx (Recip sec, 1 /sec):  .1915E+02
O  Shear rate dU/dy (Recip sec, 1 /sec):  .2841E+02
O  Stokes product Vel x AppVis (lbf/in):  .3830E-05

TABULATION OF CALCULATED AVERAGE QUANTITIES, II:
Area weighted means of absolute values taken over
ENTIRE annular (x,y) cross-section ...
O  Axial annular velocity  (inches/sec):  .3509E+02
O  Apparent viscosity (lbf sec / sq in):  .1465E-06
O  Viscous stress, AppVis x dU/dx (psi):  .3997E-05
O  Viscous stress, AppVis x dU/dy (psi):  .4329E-05
O  Dissipation fnction (lbf/(sec sqin)):  .4247E-03
O  Shear rate dU/dx (Recip sec, 1 /sec):  .2728E+02
O  Shear rate dU/dy (Recip sec, 1 /sec):  .2955E+02
O  Stokes product Vel x AppVis (lbf/in):  .5140E-05

VERTICAL SYMMETRY PLANE ABOVE DRILL PIPE
Axial velocity distribution (in/sec):
     X                    0
                           _____
    2.50    0.0000E+00    |
    2.90    0.2884E+02    |              *
    3.27    0.4903E+02    |                     *
    3.62    0.6159E+02    |                          *
    3.94    0.6741E+02    |                             *
    4.25    0.6726E+02    |                             *
    4.54    0.6186E+02    |                          *
    4.80    0.5186E+02    |                     *
    5.05    0.3786E+02    |               *
    5.28    0.2041E+02    |          *
    5.50    0.0000E+00    |

VERTICAL SYMMETRY PLANE BELOW DRILL PIPE
Axial velocity distribution (in/sec):
     X                    0
                           _____
   11.35    0.0000E+00    |
   11.47    0.4005E+01    |        *
   11.58    0.7489E+01    |             *
   11.70    0.1033E+02    |                 *
   11.81    0.1241E+02    |                    *
   11.93    0.1361E+02    |                      *
   12.04    0.1378E+02    |                       *
   12.16    0.1278E+02    |                    *
   12.27    0.1039E+02    |                 *
   12.39    0.6310E+01    |            *
   12.50    0.0000E+00    |
```
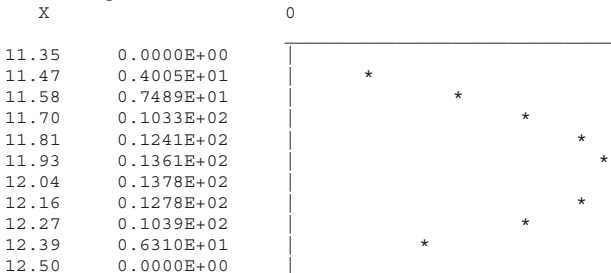
```
VERTICAL SYMMETRY PLANE ABOVE DRILL PIPE
Apparent viscosity distribution (lbf sec/sq in):
        X                         0
                         _____
    2.50     0.1465E-06   |                                      *
    2.90     0.1465E-06   |                                      *
    3.27     0.1465E-06   |                                      *
    3.62     0.1465E-06   |                                      *
    3.94     0.1465E-06   |                                      *
    4.25     0.1465E-06   |                                      *
    4.54     0.1465E-06   |                                      *
    4.80     0.1465E-06   |                                      *
    5.05     0.1465E-06   |                                      *
    5.28     0.1465E-06   |                                      *
    5.50     0.1465E-06   |                                      *

VERTICAL SYMMETRY PLANE BELOW DRILL PIPE
Apparent viscosity distribution (lbf sec/sq in):
        X                         0
                         _____
   11.35     0.1465E-06   |                                      *
   11.47     0.1465E-06   |                                      *
   11.58     0.1465E-06   |                                      *
   11.70     0.1465E-06   |                                      *
   11.81     0.1465E-06   |                                      *
   11.93     0.1465E-06   |                                      *
   12.04     0.1465E-06   |                                      *
   12.16     0.1465E-06   |                                      *
   12.27     0.1465E-06   |                                      *
   12.39     0.1465E-06   |                                      *
   12.50     0.1465E-06   |                                      *

VERTICAL SYMMETRY PLANE ABOVE DRILL PIPE
Viscous stress, AppVis x dU/dx  (psi):
        X                                    0
                         _____
    2.50     0.1197E-04                      |              *
    2.90     0.9321E-05                      |            *
    3.27     0.6672E-05                      |         *
    3.62     0.4002E-05                      |     *
    3.94     0.1316E-05                      |*
    4.25    -0.1382E-05                  *   |
    4.54    -0.4093E-05              *       |
    4.80    -0.6822E-05           *          |
    5.05    -0.9574E-05        *             |
    5.28    -0.1235E-04     *                |
    5.50    -0.1514E-04                      |

VERTICAL SYMMETRY PLANE BELOW DRILL PIPE
Viscous stress, AppVis x dU/dx  (psi):
        X                                    0
                         _____
   11.35     0.4688E-05                      |                  *
   11.47     0.3916E-05                      |               *
   11.58     0.3143E-05                      |             *
   11.70     0.2312E-05                      |          *
   11.81     0.1431E-05                      |      *
   11.93     0.5102E-06                      |*
   12.04    -0.4364E-06                   *  |
   12.16    -0.1389E-05               *      |
   12.27    -0.2317E-05            *         |
   12.39    -0.3178E-05         *            |
   12.50    -0.4039E-05      *               |
```

```
VERTICAL SYMMETRY PLANE ABOVE DRILL PIPE
Dissipation function (lbf/(sec x sq in)):
       X                            0
                        _____
    2.50     0.9781E-03  |                          *
    2.90     0.5935E-03  |                 *
    3.27     0.3053E-03  |        *
    3.62     0.1114E-03  |*
    3.94     0.1417E-04  |
    4.25     0.1518E-04  |
    4.54     0.1160E-03  |*
    4.80     0.3188E-03  |      *
    5.05     0.6262E-03  |             *
    5.28     0.1042E-02  |                    *
    5.50     0.1564E-02  |                                *

VERTICAL SYMMETRY PLANE BELOW DRILL PIPE
Dissipation function (lbf/(sec x sq in)):
       X                            0
                        _____
   11.35     0.1915E-03  |                                *
   11.47     0.1323E-03  |                       *
   11.58     0.8401E-04  |              *
   11.70     0.4583E-04  |       *
   11.81     0.1862E-04  |*
   11.93     0.3546E-05  |
   12.04     0.1612E-05  |
   12.16     0.1319E-04  |*
   12.27     0.3719E-04  |      *
   12.39     0.6991E-04  |          *
   12.50     0.1123E-03  |                 *

VERTICAL SYMMETRY PLANE ABOVE DRILL PIPE
Shear rate dU/dx  (1/sec):
       X                                   0
                        _____
    2.50     0.8171E+02              |                     *
    2.90     0.6362E+02              |                  *
    3.27     0.4554E+02              |               *
    3.62     0.2732E+02              |            *
    3.94     0.8984E+01              |*
    4.25    -0.9432E+01         *    |
    4.54    -0.2794E+02             *|
    4.80    -0.4657E+02          *   |
    5.05    -0.6535E+02       *      |
    5.28    -0.8433E+02    *         |
    5.50    -0.1033E+03              |

VERTICAL SYMMETRY PLANE BELOW DRILL PIPE
Shear rate dU/dx  (1/sec):
       X                                   0
                        _____
   11.35     0.3200E+02              |                        *
   11.47     0.2673E+02              |                     *
   11.58     0.2145E+02              |                  *
   11.70     0.1578E+02              |               *
   11.81     0.9769E+01              |          *
   11.93     0.3482E+01              |*
   12.04    -0.2979E+01           *  |
   12.16    -0.9478E+01         *    |
   12.27    -0.1581E+02        *     |
   12.39    -0.2169E+02      *       |
   12.50    -0.2757E+02    *         |
```
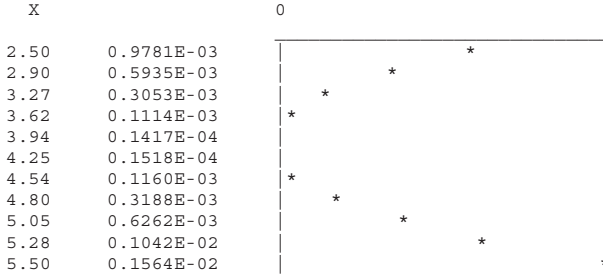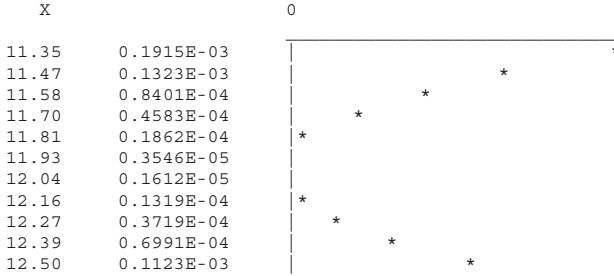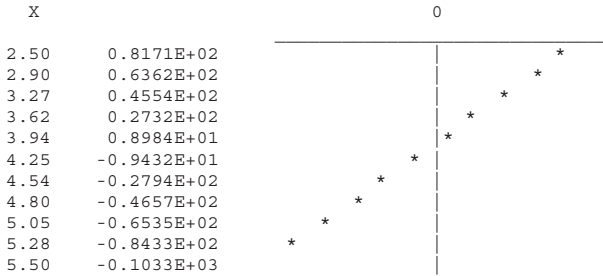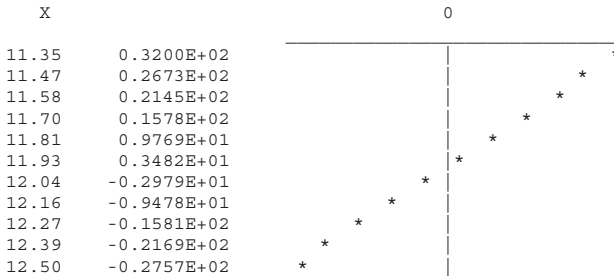
```
VERTICAL SYMMETRY PLANE ABOVE DRILL PIPE
Stokes product (lbf/in):
       X                        0
                               _____
    2.50     0.0000E+00        |
    2.90     0.4225E-05        |              *
    3.27     0.7182E-05        |                   *
    3.62     0.9023E-05        |                        *
    3.94     0.9876E-05        |                           *
    4.25     0.9854E-05        |                           *
    4.54     0.9063E-05        |                        *
    4.80     0.7598E-05        |                   *
    5.05     0.5547E-05        |              *
    5.28     0.2990E-05        |        *
    5.50     0.0000E+00        |


VERTICAL SYMMETRY PLANE BELOW DRILL PIPE
Stokes product (lbf/in):
       X                        0
                               _____
   11.35     0.0000E+00        |
   11.47     0.5868E-06        |        *
   11.58     0.1097E-05        |             *
   11.70     0.1513E-05        |                 *
   11.81     0.1818E-05        |                   *
   11.93     0.1993E-05        |                     *
   12.04     0.2019E-05        |                      *
   12.16     0.1872E-05        |                   *
   12.27     0.1522E-05        |                *
   12.39     0.9244E-06        |           *
   12.50     0.0000E+00        |
```
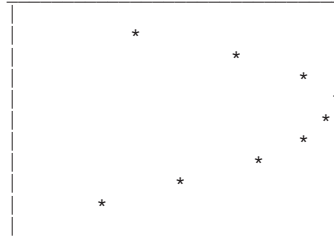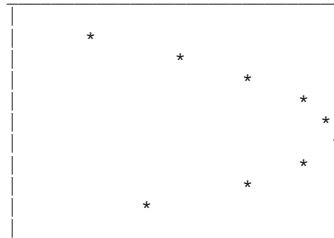
2.2.4 Eccentricity effects, pressure gradient fixed.

We consider the "R_{outer} = 6 in, R_{inner} = 3 in" geometry previously studied.   A Newtonian fluid (water) is assumed with the pressure gradient specified.   We vary borehole eccentricity and determine its effect on volume flow rate (the eccentricity is available from coordinate inputs and found in the shaded box at the bottom of the user interface). Calculated results for eccentricities of 0.000, 0.333, 0.500, 0.667 and 0.833 are given in the "planar velocity plots" in Figures 2-33 to 2-37. It is instructive to note how increasing eccentricity increases volume flow rate when the applied pressure gradient is fixed. The trend seems to hold for many non-Newtonian applications, but general conclusions cannot be offered. It is important to emphasize that our curvilinear grid method provides an almost exact numerical solution to the problem, and further, that solutions are available in 2-3 seconds on most Windows computers. Figures 2-38 and 2-39 provide additional velocity display options. Figure 2-40 displays viscous stresses in the two orthogonal directions – their shapes are similar to those for shear rates since the two are proportional to viscosity which is constant here for Newtonian flows.

2.2.4.1 Eccentricity = 0.000 for annulus.
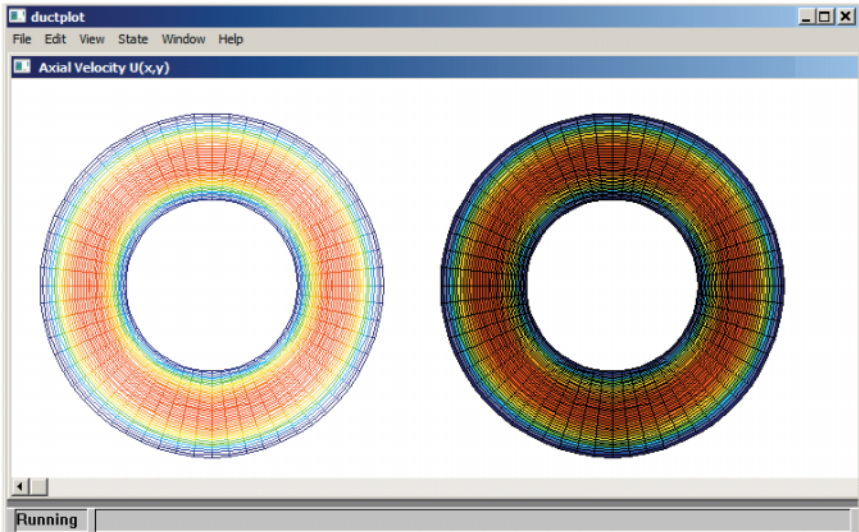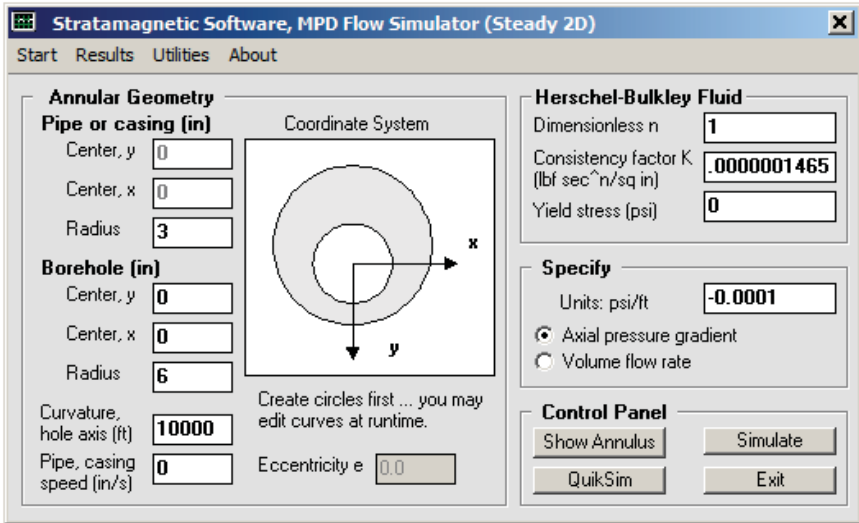

```
Annular flow rate ...... 0.9435E+03 gal/min
Cross-sectional area ... 0.8467E+02 sq inch
```

Figure 2-33. Eccentricity = 0.000 for annulus
(note, the 943.5 gpm flow rate was obtained earlier).

2.2.4.2 Eccentricity = 0.333 for annulus.
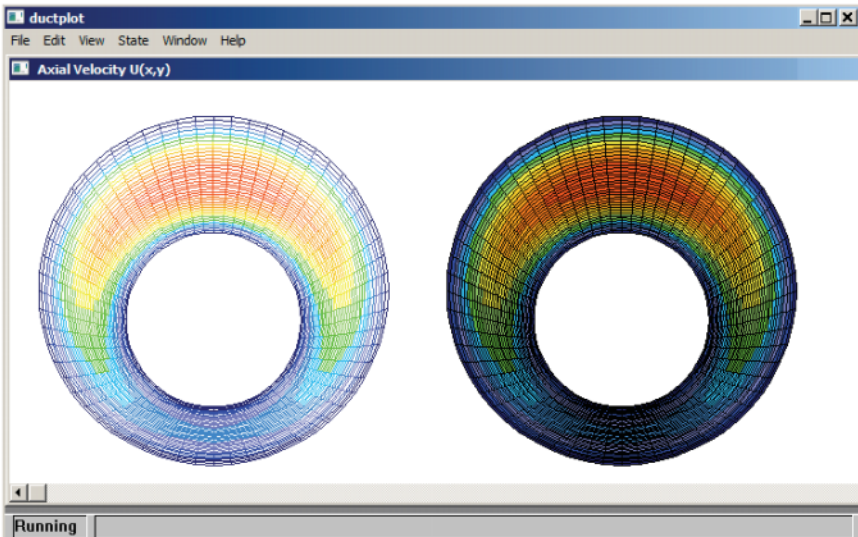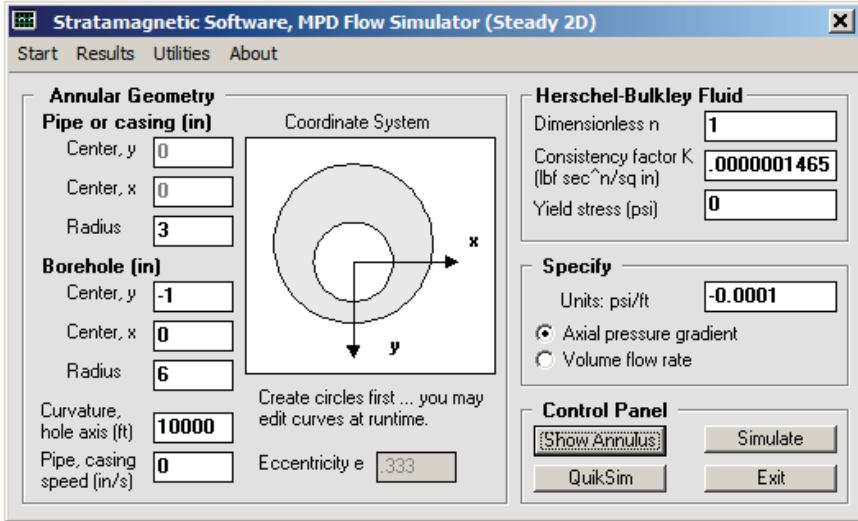

```
Annular flow rate ...... 0.1092E+04 gal/min
Cross-sectional area ... 0.8467E+02 sq inch
```

Figure 2-34. Eccentricity = 0.333 for annulus.

2.2.4.3 Eccentricity = 0.500 for annulus.
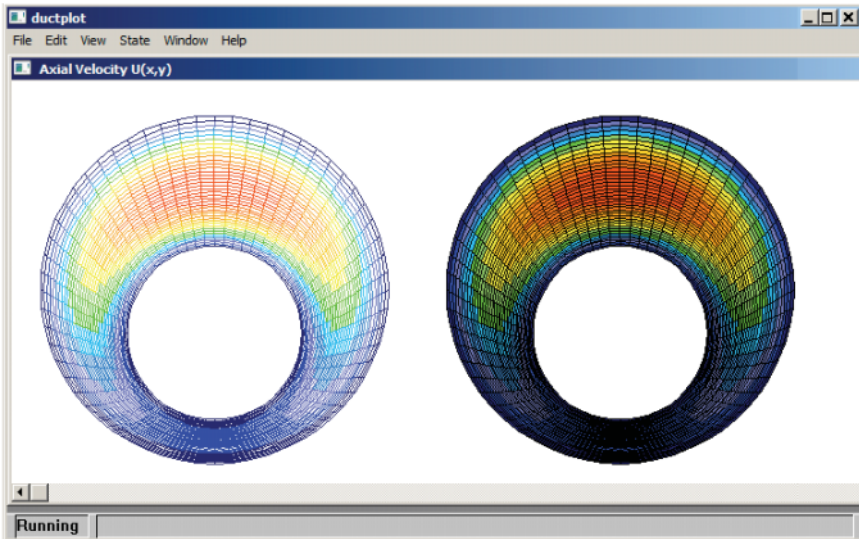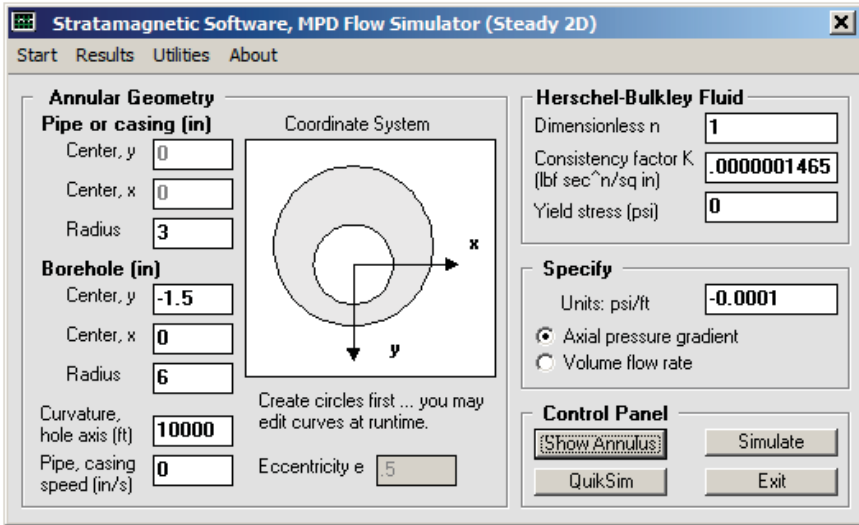

```
Annular flow rate ...... 0.1273E+04 gal/min
Cross-sectional area ... 0.8467E+02 sq inch
```

Figure 2-35. Eccentricity = 0.500 for annulus.

2.2.4.4 Eccentricity = 0.667 for annulus.
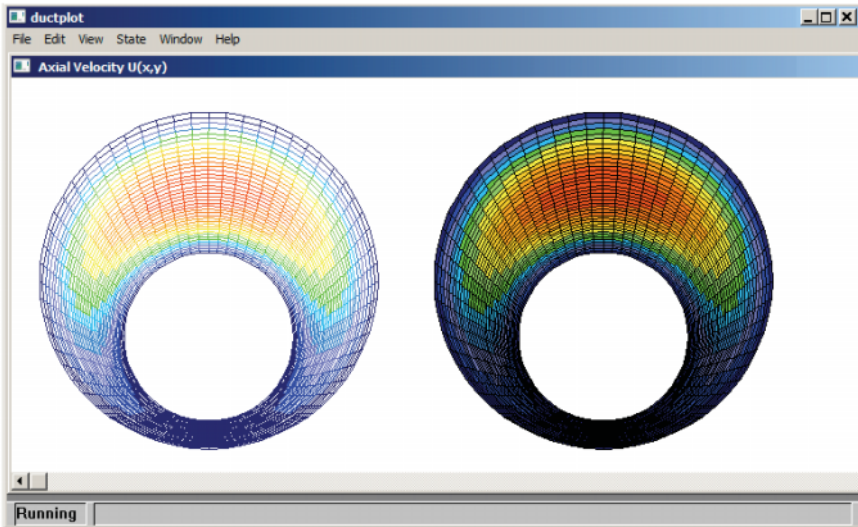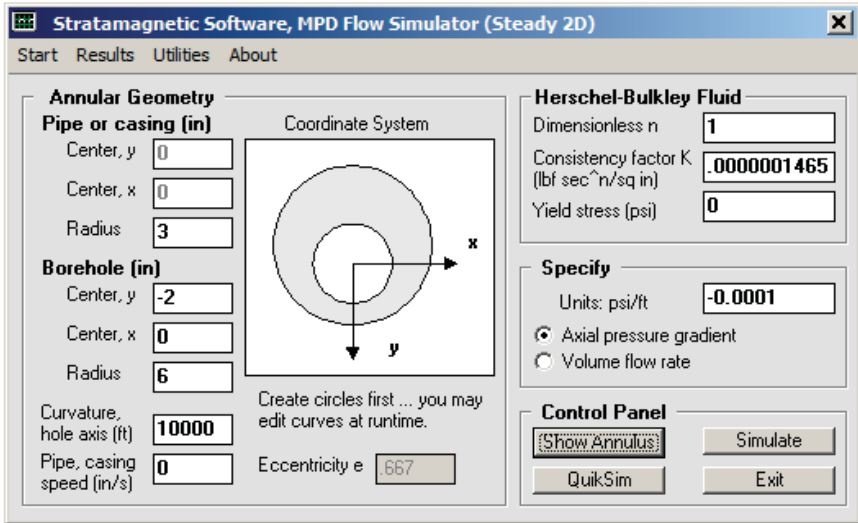

```
Annular flow rate ...... 0.1521E+04 gal/min
Cross-sectional area ... 0.8467E+02 sq inch
```

Figure 2-36. Eccentricity = 0.667 for annulus.

2.2.4.5 Eccentricity = 0.833 for annulus.
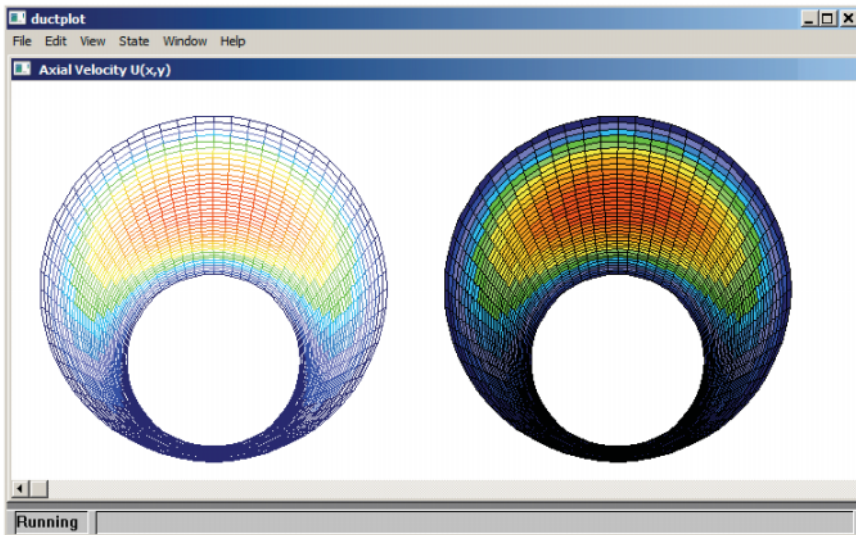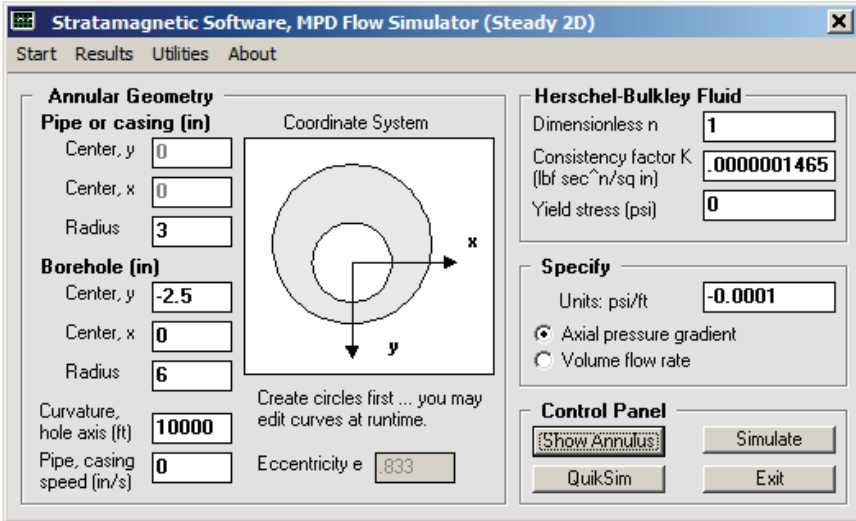

```
Annular flow rate ...... 0.1830E+04 gal/min

Cross-sectional area ... 0.8467E+02 sq inch
```

Figure 2-37. Eccentricity = 0.883 for annulus (planar plot).
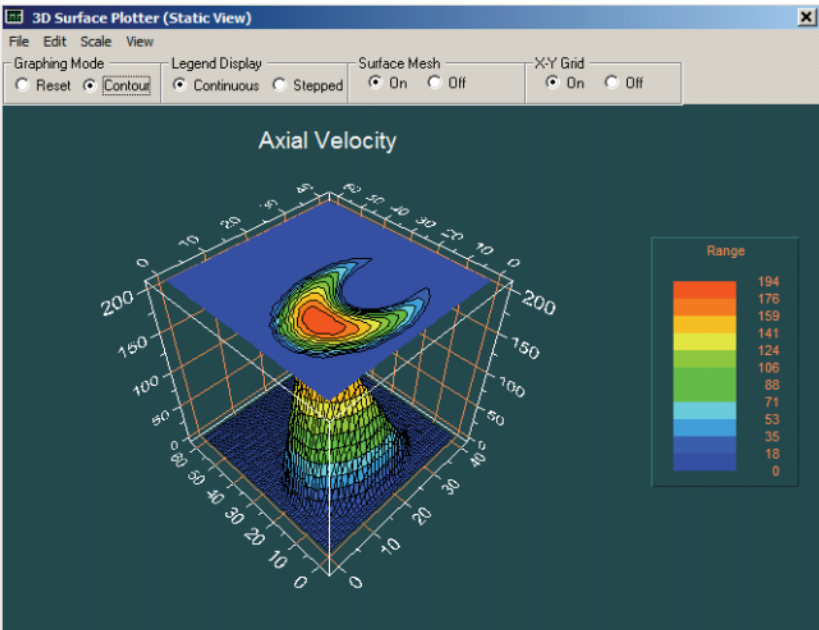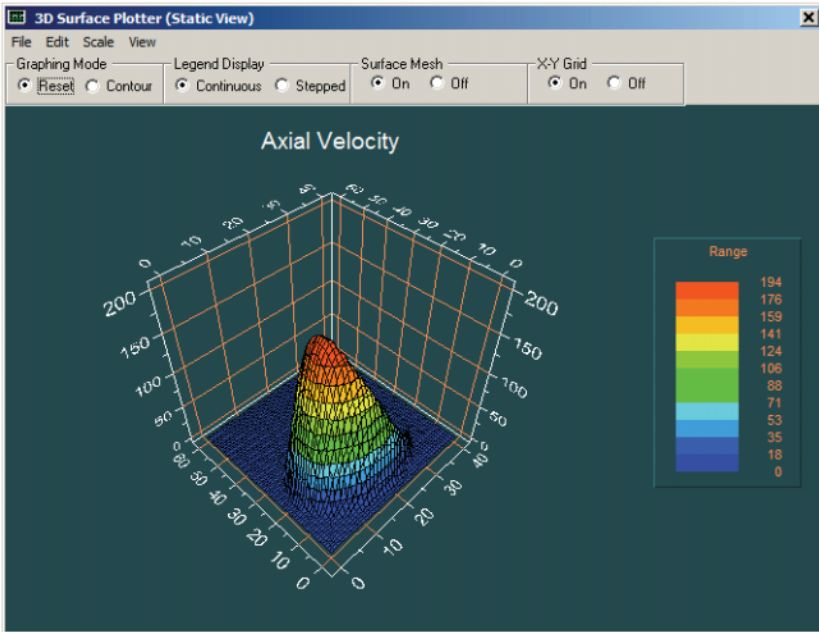
Figure 2-38. Eccentricity = 0.883 for annulus (static views).
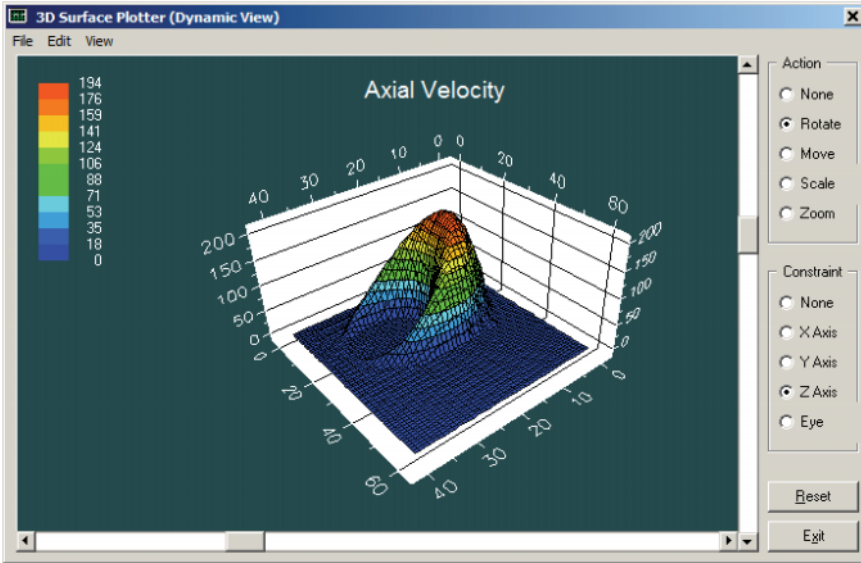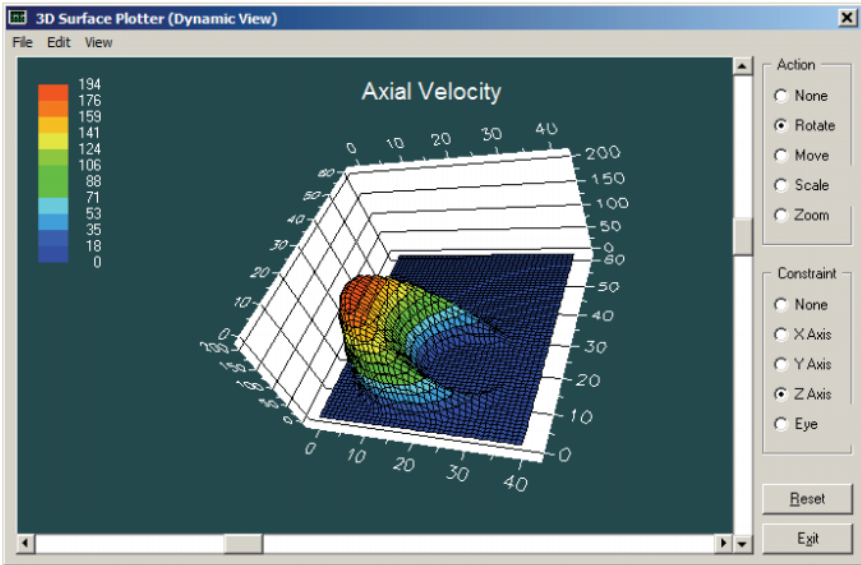
Figure 2-39. Eccentricity = 0.883 for annulus (dynamic views).
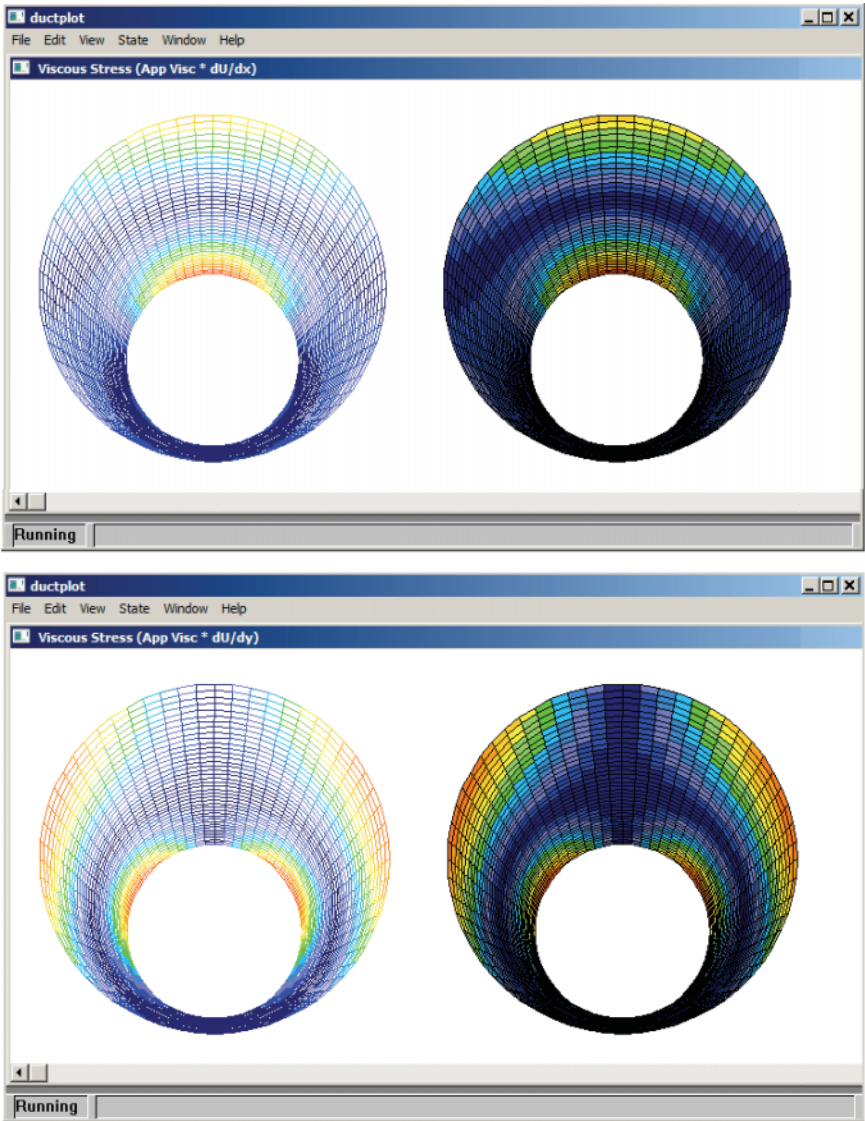
Figure 2-40. Eccentricity = 0.883 for annulus, viscous shear stress plots.

2.2.5 Eccentricity = 0.833 for annulus, volume flow rate specified.

In the foregoing examples, the axial pressure gradient is specified at – 0.0001 psi/ft. Computations were fast because the pressure gradient itself appears in the governing differential equations. Very often, it is the volume flow rate that is prescribed and the pressure gradient is not known. In this case, the software intelligently assumes a target gradient and successively refines it until computed results provide the required flow rate to fourth place decimal place accuracy. The iteration history is displayed on-screen in a process taking approximately one minute – it is also available in text output obtained from the <Results> menu. As an example, we use results from Figure 2-37 where the flow rate of 1,830 gpm corresponds to an 0.833 eccentricity. The iteration history (using the automatically selected QuikSim mode) is duplicated immediately beneath Figure 2-41.
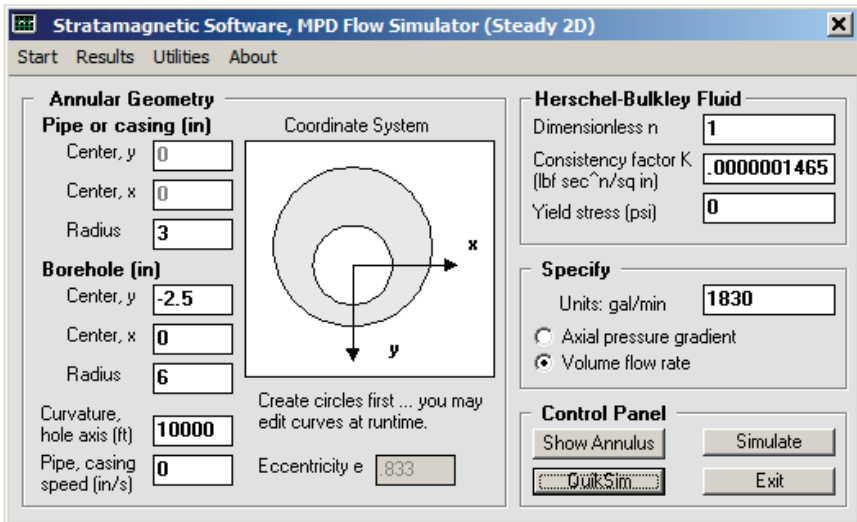
Figure 2-41. Formulation with volume flow rate specified.

```
QuikSim simulation mode assumed ...
Eccentric circles only, 61 x 41 hardcoded mesh.
Use full simulation mode for more runtime options.
 .
 .
 .
```

```
SIMULATION STARTS ...

Newtonian fluid assumed with exponent "n" equal
to 0.1000E+01 and consistency factor of 0.1465E-06
lbf sec^n/sq in.

A yield stress of 0.0000E+00 psi is taken.
Borehole axis radius of curvature is 0.1000E+05 ft.
Axial speed of inner pipe is 0.0000E+00 in/sec.
Target flow rate of 0.1830E+04 gal/min specified.

Iterating on pressure gradient to match flow rate ...

Iteration  100, Error = .00000012
Iteration  200, Error = .00000006
Iteration  300, Error = .00000006
Iteration  400, Error = .00000000
Iteration  500, Error = .00000012
Iteration  600, Error = .00000006
Iteration  700, Error = .00000024
Iteration  800, Error = .00000018
Iteration  900, Error = .00000012
Iteration 1000, Error = .00000012

O  Axial pressure gradient of -.1000E+00 psi/ft
   yields volume flow rate of 0.1830E+07 gal/min.

Flow rate target error is 0.9988E+05 %

Iteration  100, Error = .00000012
Iteration  200, Error = .00000006
Iteration  300, Error = .00000006
Iteration  400, Error = .00000000
Iteration  500, Error = .00000012
Iteration  600, Error = .00000006
Iteration  700, Error = .00000024
Iteration  800, Error = .00000018
Iteration  900, Error = .00000012
Iteration 1000, Error = .00000012

O  Axial pressure gradient of -.5000E-01 psi/ft
   yields volume flow rate of 0.9149E+06 gal/min.

Flow rate target error is 0.4989E+05 %

Iteration  100, Error = .00000012
Iteration  200, Error = .00000006
Iteration  300, Error = .00000006
Iteration  400, Error = .00000000
Iteration  500, Error = .00000012
Iteration  600, Error = .00000006
Iteration  700, Error = .00000024
Iteration  800, Error = .00000018
Iteration  900, Error = .00000012
Iteration 1000, Error = .00000012
```

```
O  Axial pressure gradient of -.2500E-01 psi/ft
   yields volume flow rate of 0.4574E+06 gal/min.

Flow rate target error is 0.2490E+05 %

Iteration  100, Error = .00000012
Iteration  200, Error = .00000006
Iteration  300, Error = .00000006
Iteration  400, Error = .00000000
Iteration  500, Error = .00000012
Iteration  600, Error = .00000006
Iteration  700, Error = .00000024
Iteration  800, Error = .00000018
Iteration  900, Error = .00000012
Iteration 1000, Error = .00000012

O  Axial pressure gradient of -.1250E-01 psi/ft
   yields volume flow rate of 0.2287E+06 gal/min.

Flow rate target error is 0.1240E+05 %

Iteration  100, Error = .00000012
Iteration  200, Error = .00000006
Iteration  300, Error = .00000006
Iteration  400, Error = .00000000
Iteration  500, Error = .00000012
Iteration  600, Error = .00000006
Iteration  700, Error = .00000024
Iteration  800, Error = .00000018
Iteration  900, Error = .00000012
Iteration 1000, Error = .00000012

O  Axial pressure gradient of -.6250E-02 psi/ft
   yields volume flow rate of 0.1144E+06 gal/min.

Flow rate target error is 0.6149E+04 %

Iteration  100, Error = .00000012
Iteration  200, Error = .00000006
Iteration  300, Error = .00000006
Iteration  400, Error = .00000000
Iteration  500, Error = .00000012
Iteration  600, Error = .00000006
Iteration  700, Error = .00000024
Iteration  800, Error = .00000018
Iteration  900, Error = .00000012
Iteration 1000, Error = .00000012
```

```
O  Axial pressure gradient of -.3125E-02 psi/ft
   yields volume flow rate of 0.5718E+05 gal/min.

Flow rate target error is 0.3025E+04 %

Iteration  100, Error = .00000012
Iteration  200, Error = .00000006
Iteration  300, Error = .00000006
Iteration  400, Error = .00000000
Iteration  500, Error = .00000012
Iteration  600, Error = .00000006
Iteration  700, Error = .00000024
Iteration  800, Error = .00000018
Iteration  900, Error = .00000012
Iteration 1000, Error = .00000012

O  Axial pressure gradient of -.1563E-02 psi/ft
   yields volume flow rate of 0.2859E+05 gal/min.

Flow rate target error is 0.1462E+04 %

Iteration  100, Error = .00000012
Iteration  200, Error = .00000006
Iteration  300, Error = .00000006
Iteration  400, Error = .00000000
Iteration  500, Error = .00000012
Iteration  600, Error = .00000006
Iteration  700, Error = .00000024
Iteration  800, Error = .00000018
Iteration  900, Error = .00000012
Iteration 1000, Error = .00000012

O  Axial pressure gradient of -.7813E-03 psi/ft
   yields volume flow rate of 0.1429E+05 gal/min.

Flow rate target error is 0.6811E+03 %

Iteration  100, Error = .00000012
Iteration  200, Error = .00000006
Iteration  300, Error = .00000006
Iteration  400, Error = .00000000
Iteration  500, Error = .00000012
Iteration  600, Error = .00000006
Iteration  700, Error = .00000024
Iteration  800, Error = .00000018
Iteration  900, Error = .00000012
Iteration 1000, Error = .00000012
```

```
O  Axial pressure gradient of -.3906E-03 psi/ft
   yields volume flow rate of 0.7147E+04 gal/min.

Flow rate target error is 0.2906E+03 %

Iteration  100, Error = .00000012
Iteration  200, Error = .00000006
Iteration  300, Error = .00000006
Iteration  400, Error = .00000000
Iteration  500, Error = .00000012
Iteration  600, Error = .00000006
Iteration  700, Error = .00000024
Iteration  800, Error = .00000018
Iteration  900, Error = .00000012
Iteration 1000, Error = .00000012

O  Axial pressure gradient of -.1953E-03 psi/ft
   yields volume flow rate of 0.3574E+04 gal/min.

Flow rate target error is 0.9528E+02 %

Iteration  100, Error = .00000012
Iteration  200, Error = .00000006
Iteration  300, Error = .00000006
Iteration  400, Error = .00000000
Iteration  500, Error = .00000012
Iteration  600, Error = .00000006
Iteration  700, Error = .00000024
Iteration  800, Error = .00000018
Iteration  900, Error = .00000012
Iteration 1000, Error = .00000012

O  Axial pressure gradient of -.9766E-04 psi/ft
   yields volume flow rate of 0.1787E+04 gal/min.

Flow rate target error is 0.2359E+01 %

Iteration  100, Error = .00000012
Iteration  200, Error = .00000006
Iteration  300, Error = .00000006
Iteration  400, Error = .00000000
Iteration  500, Error = .00000012
Iteration  600, Error = .00000006
Iteration  700, Error = .00000024
Iteration  800, Error = .00000018
Iteration  900, Error = .00000012
Iteration 1000, Error = .00000012
```

```
O  Axial pressure gradient of -.1953E-03 psi/ft
   yields volume flow rate of 0.3574E+04 gal/min.

Flow rate target error is 0.9528E+02 %

Iteration  100, Error = .00000016
Iteration  200, Error = .00000016
Iteration  300, Error = .00000016
Iteration  400, Error = .00000000
Iteration  500, Error = .00000000
Iteration  600, Error = .00000000
Iteration  700, Error = .00000008
Iteration  800, Error = .00000000
Iteration  900, Error = .00000000
Iteration 1000, Error = .00000008

O  Axial pressure gradient of -.1465E-03 psi/ft
   yields volume flow rate of 0.2680E+04 gal/min.

Flow rate target error is 0.4646E+02 %

Iteration  100, Error = .00000000
Iteration  200, Error = .00000010
Iteration  300, Error = .00000000
Iteration  400, Error = .00000000
Iteration  500, Error = .00000000
Iteration  600, Error = .00000010
Iteration  700, Error = .00000000
Iteration  800, Error = .00000000
Iteration  900, Error = .00000020
Iteration 1000, Error = .00000010

O  Axial pressure gradient of -.1221E-03 psi/ft
   yields volume flow rate of 0.2234E+04 gal/min.

Flow rate target error is 0.2205E+02 %

Iteration  100, Error = .00000011
Iteration  200, Error = .00000000
Iteration  300, Error = .00000011
Iteration  400, Error = .00000011
Iteration  500, Error = .00000022
Iteration  600, Error = .00000011
Iteration  700, Error = .00000000
Iteration  800, Error = .00000000
Iteration  900, Error = .00000000
Iteration 1000, Error = .00000000
```

```
O   Axial pressure gradient of -.1099E-03 psi/ft
    yields volume flow rate of 0.2010E+04 gal/min.

Flow rate target error is 0.9846E+01 %

Iteration  100, Error = .00000012
Iteration  200, Error = .00000012
Iteration  300, Error = .00000000
Iteration  400, Error = .00000000
Iteration  500, Error = .00000012
Iteration  600, Error = .00000012
Iteration  700, Error = .00000000
Iteration  800, Error = .00000000
Iteration  900, Error = .00000000
Iteration 1000, Error = .00000000

O   Axial pressure gradient of -.1038E-03 psi/ft
    yields volume flow rate of 0.1899E+04 gal/min.

Flow rate target error is 0.3743E+01 %

Iteration  100, Error = .00000024
Iteration  200, Error = .00000024
Iteration  300, Error = .00000000
Iteration  400, Error = .00000000
Iteration  500, Error = .00000012
Iteration  600, Error = .00000036
Iteration  700, Error = .00000000
Iteration  800, Error = .00000000
Iteration  900, Error = .00000000
Iteration 1000, Error = .00000012

O   Axial pressure gradient of -.1007E-03 psi/ft
    yields volume flow rate of 0.1843E+04 gal/min.

Pressure gradient found iteratively, -.1007E-03 psi/ft,
to yield 0.1843E+04 gal/min vs target 0.1830E+04 gal/min.

Note:  Iterations terminate within 1% of target rate.
Refine result by manually changing pressure gradient.

Annular flow rate ...... 0.1843E+04 gal/min
Cross-sectional area ... 0.8467E+02 sq inch
```

This shows how a – 0.0001007 psi/ft is (almost) identical to the value – 0.0001 psi/ft assumed earlier. Each iteration cycle furnishes a pressure gradient value with a complementary flow rate. If "gpm" were plotted against "dp/dz" for each of the iteration cycles, one would have a straight line relationship for Newtonian flows. However, when non-Newtonian fluids are considered, the relationship will generally be nonlinear. General conclusions cannot be offered in the non-Newtonian case and results must be determined computationally case-by-case.

2.2.6   Eccentricity = 0.833 for annulus, pressure gradient specified, yield stress allowed.

In this section, we consider the effects of yield stress. First let us reconsider the example of Figure 2-37, in which the eccentricity was 0.833 and the flow rate was 1,830 gpm. A Newtonian fluid (water) was assumed. The results immediately below are identical to those in Figure 2-37 and are repeated here so that the subsequent (yield stress) results can be easily understood visually.
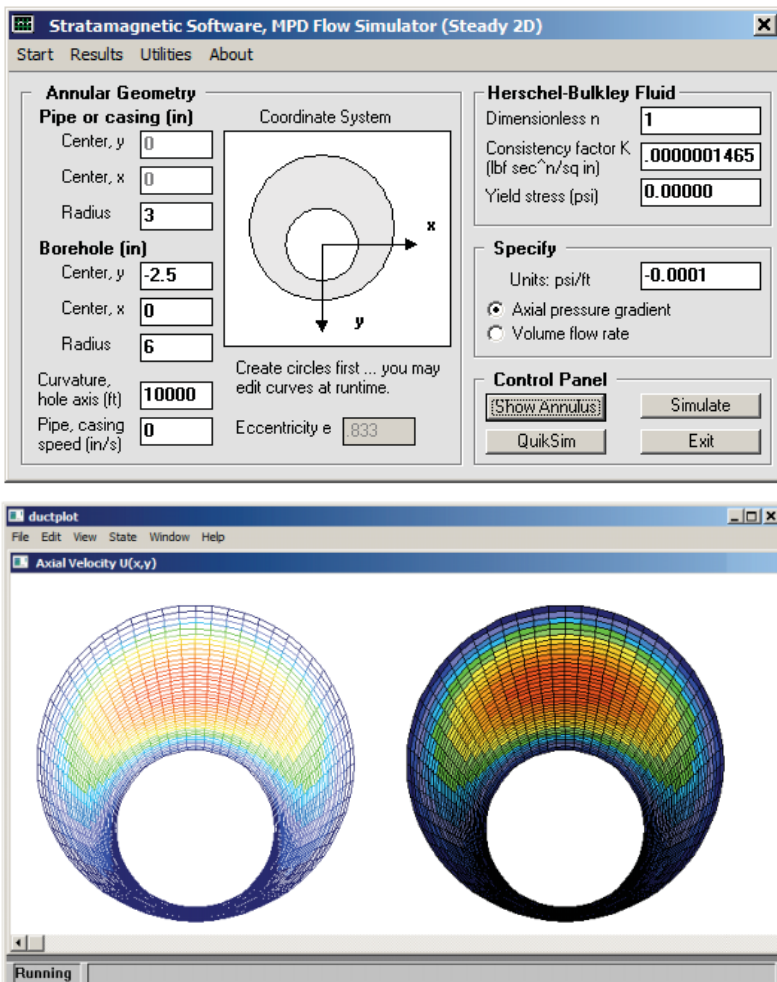
Figure 2-42. Eccentricity = 0.833, Newtonian fluid (water), 1,830 gpm.

The prior calculation assumed a Newtonian fluid (water) with 1 cp viscosity (a very low value by drilling or cementing standards, but useful for prior validation purposes). We now wish to study the effects of yield stress. In our hypothetical Bingham plastic (where n = 1), we assume a yield stress of 0.00001 psi and the same pressure gradient. The calculated flow rate is 541.0 gpm, or about 30% of the 1,830 gpm obtained previously. Whereas the red zone in Figure 2-42 is a paraboloid, the reds in Figures 2-43 and 2-44 are wider, taking "plug-like" forms that do *not* wrap around the inner pipe.
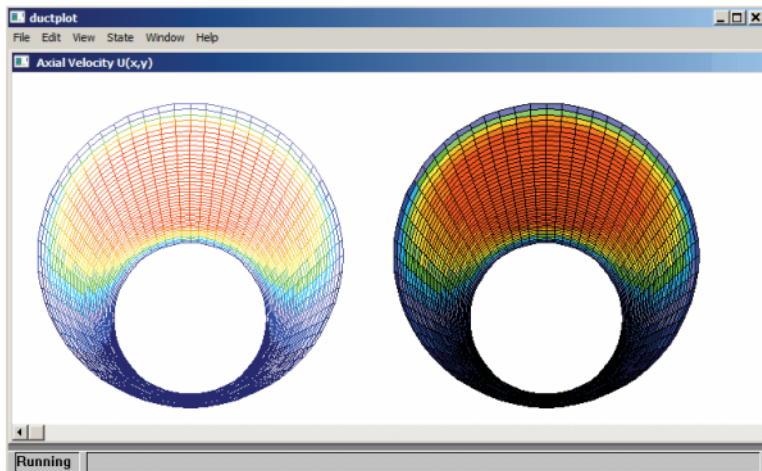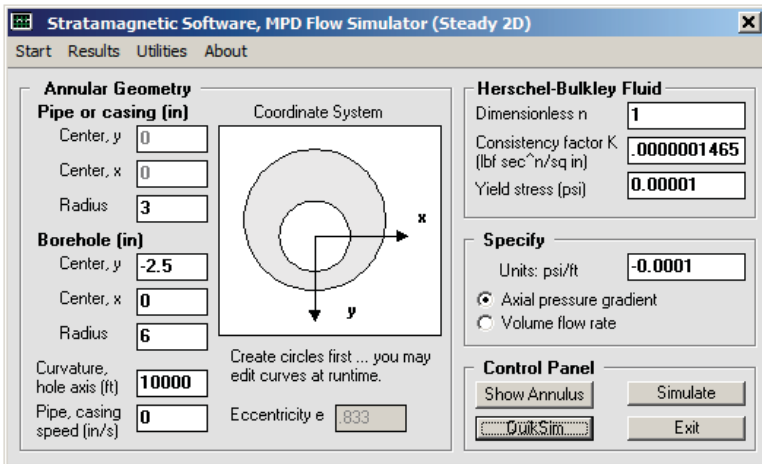
Figure 2-43. Eccentricity = 0.833, Bingham plastic, 541 gpm.
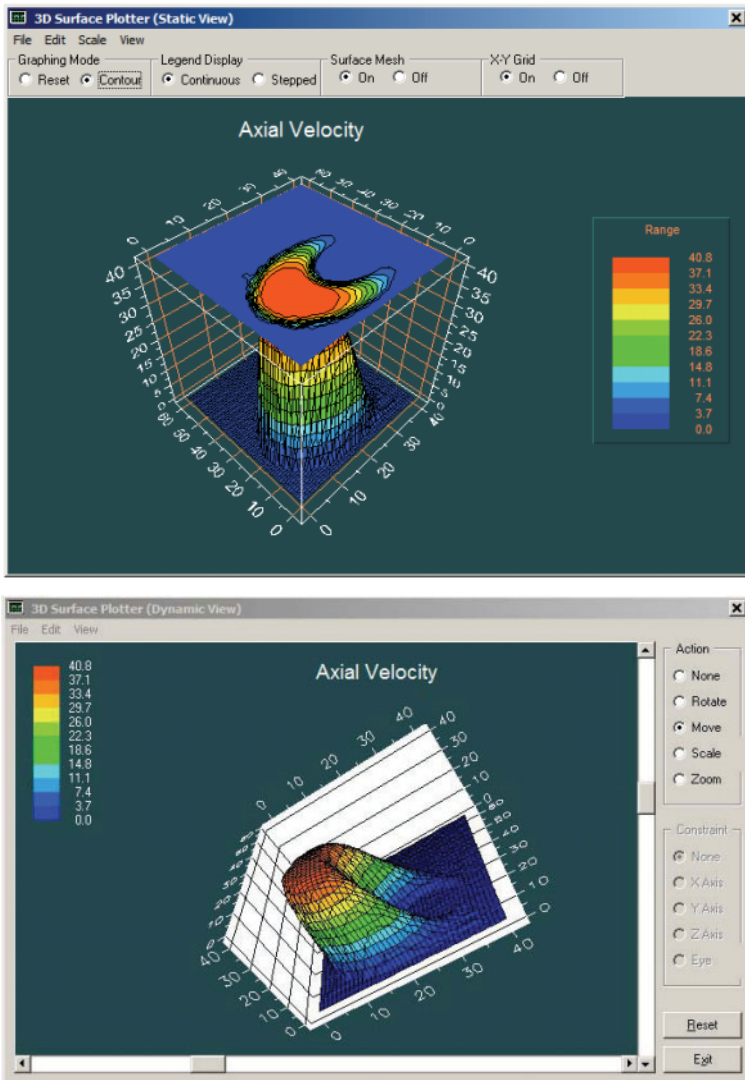
Figure 2-44. Eccentricity = 0.833, Bingham plastic, 541 gpm.

The static and dynamic velocity plots above, obtained from the <Results> menu, clearly illustrate the "flat top" nature of flows with yield stress – these should be compared with Figures 2-38 and 2-39 for simple water. Yield and non-yield fluids have different hole cleaning properties, a fact evident from our contrasting velocity and shear profiles.

In our introductory calculations with water, which is Newtonian and does not possess yield stress, the viscosity is constant. A result of the formulation is that apparent viscosity is likewise constant and equal to the input viscosity. Because "viscous stress = apparent viscosity *times* shear rate," it was not necessary to plot both shear rate and viscous stress – nor was it necessary to plot apparent viscosity at all. This changes with the addition of yield stress, no matter how slight. From the <Results> menu, we can plot the apparent viscosity for the present calculation. Even though n = 1 appears "almost Newtonian," Figure 2-45 indicates that apparent viscosity varies substantially and is largest in the widest part of the annulus. Because this varies, it is necessary to recognize the physical differences between shear rates and viscous shear stresses, and within each category, the two very different orthogonal components. In any new engineering data interpretation application, all of these quantities (and their averages over different portions of the annulus) must be considered as possible curve-fitting candidates. Shear rates and viscous shear stresses are given in Figures 2-46 and 2-47.
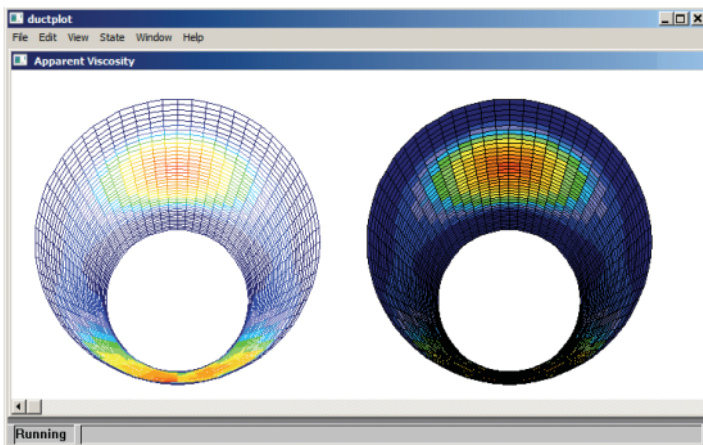
Figure 2-45. Apparent viscosity.

In Chapter 1, we noted that several commercial solvers *assume* that a ring-like plug zone wraps around the pipe in eccentric applications, in much the same manner as it would in concentric flows. Figure 2-48 repeats the formulation of Figure 2-14 but with a yield stress, showing that a thick ring does indeed wrap around the pipe. However, Figures 2-43 and 2-44 clearly show a stand-alone plug occupying the widest part of the annulus that does *not* wrap around the pipe in ring-like manner.
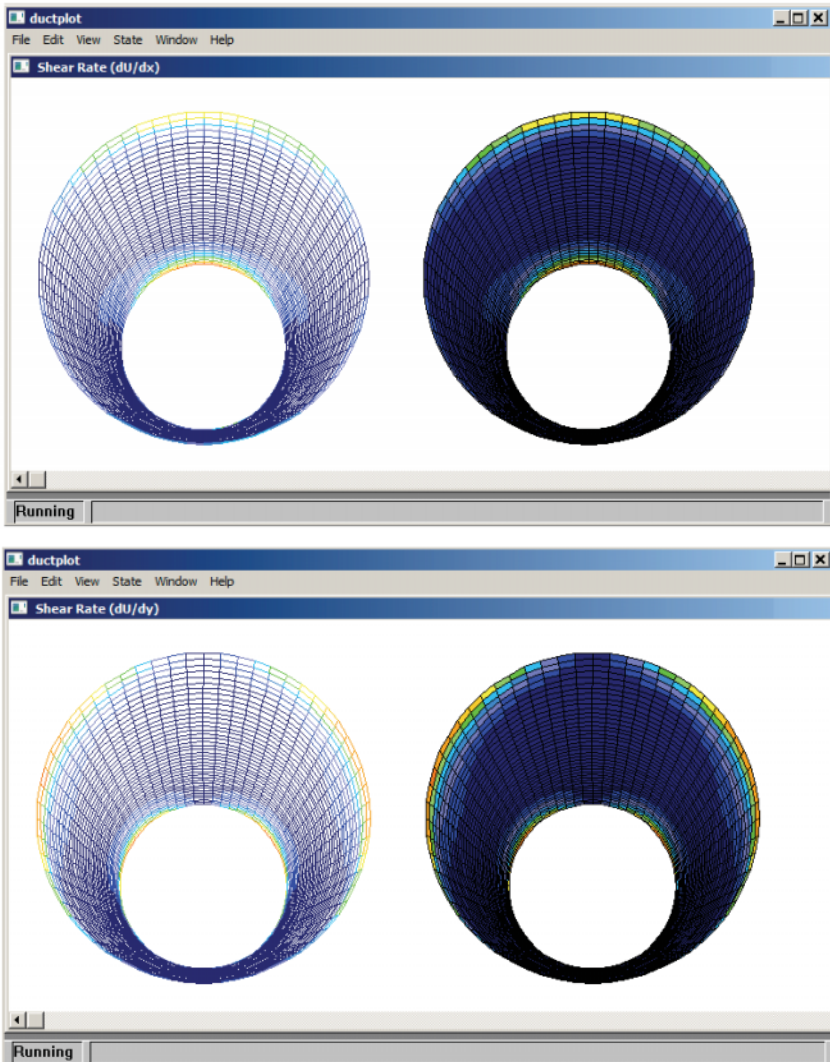
Figure 2-46. Shear rates.

In fact, our iterative scheme does *not* make any a priori assumption on plug zone size or shape, but allows the algorithm to intelligently "find" the correct geometric form and location, whether it be ring or plug-like. Where hole cleaning and pressure control are concerned, operational decisions must not be left to common-sense since intuition is unreliable.
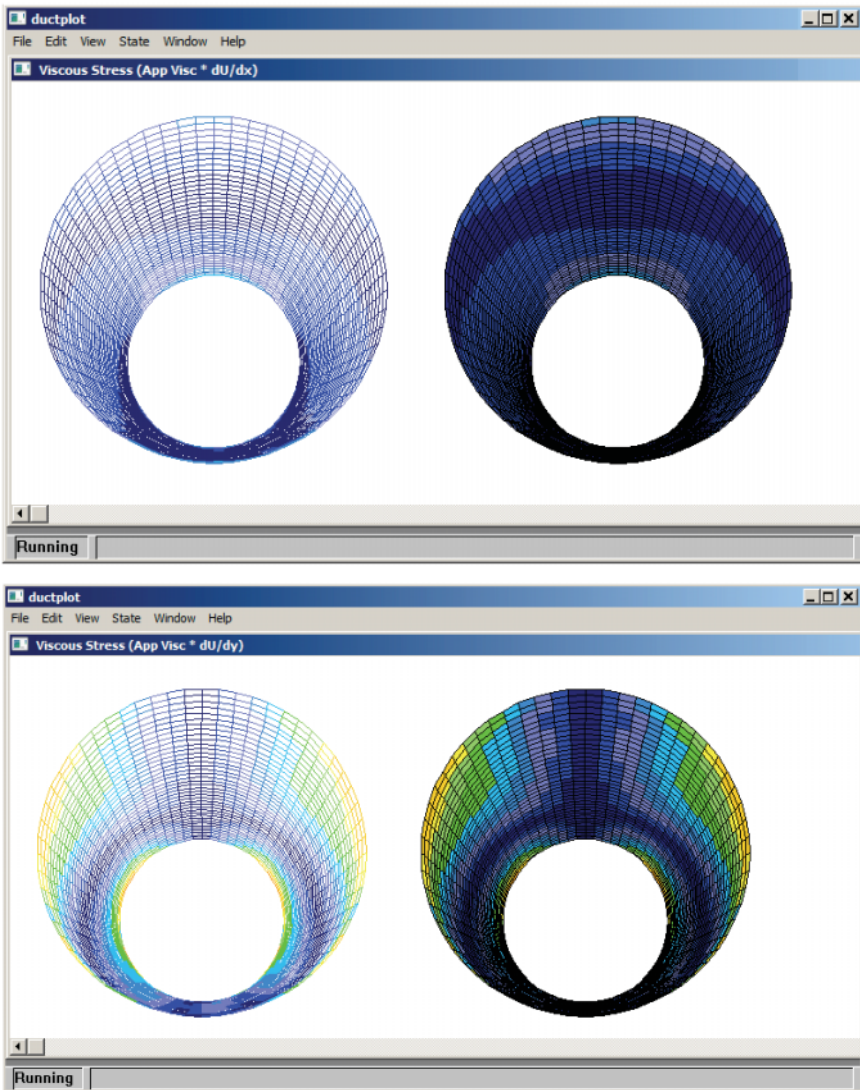
Figure 2-47. Viscous shear stresses.

Finally, we note that the plug flow in Figure 2-48 possesses a flow rate of 179.1 gpm compared to the results for Figures 2-14 and 2-17 (without yield stress) where 943.5 was obtained. Both examples assumed identical pressure gradients. In order to increase flow rate, yield stress fluids would require much larger pressure gradients.
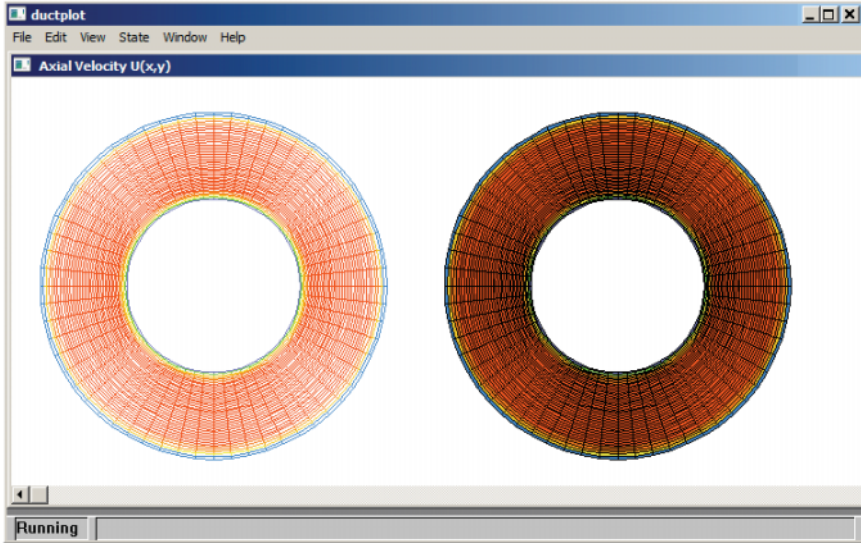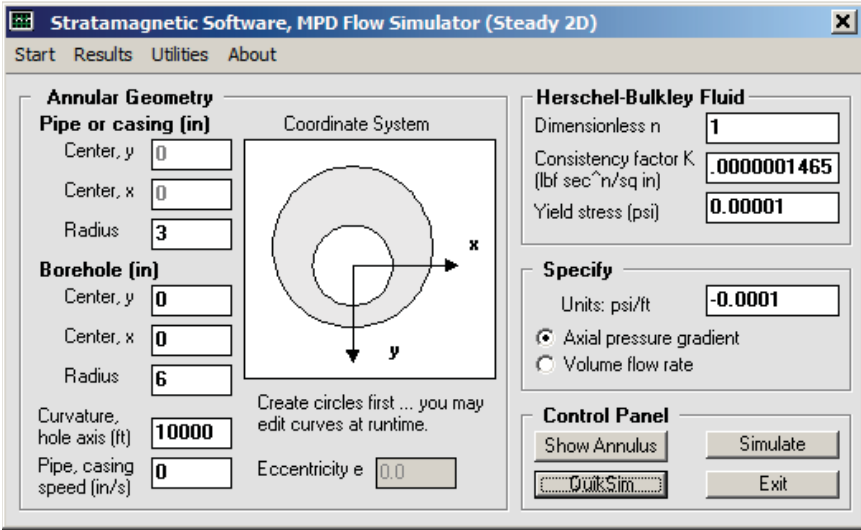
Annular flow rate ...... 0.1791E+03 gal/min
Cross-sectional area ... 0.8467E+02 sq inch

Figure 2-48. Concentric annulus with yield stress
and expected "wrap-around" plug ring.

2.2.7   Non-Newtonian effects, pressure gradient versus flow rate curve, no yield stress.

For Power law fluids, our simulator provides "Find n, K" utilities as shown in Figure 2-49. When yield stress is present, so that stress is offset from zero, the reader should consult utilities found in the literature.
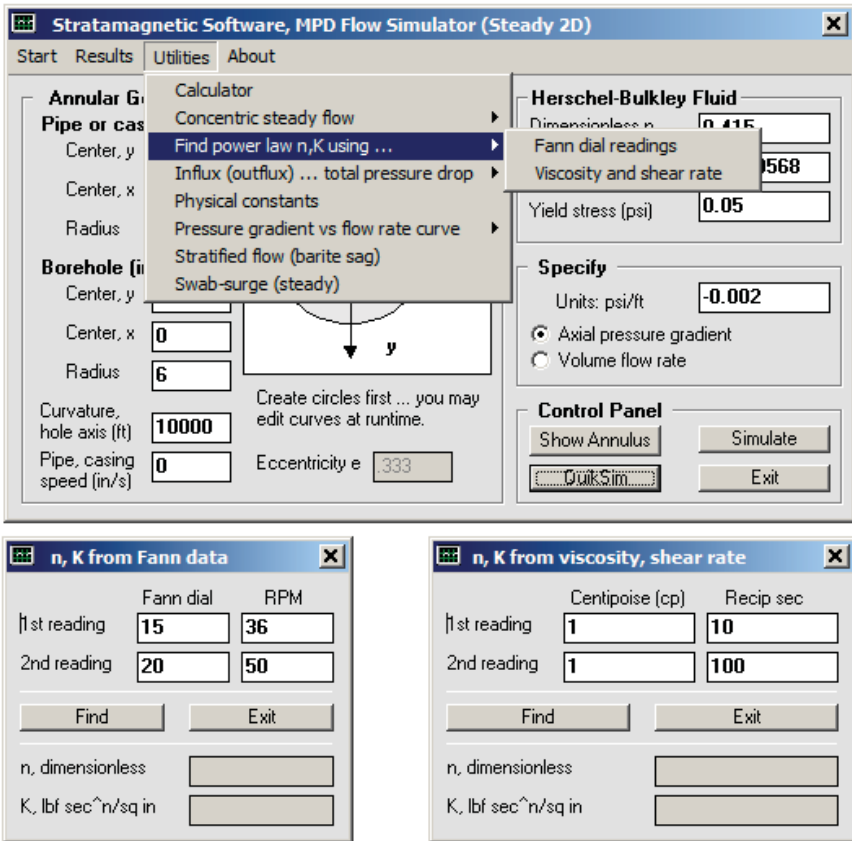
Figure 2-49. Finding n and K for Power law fluids.

In the present "small n" application (with n = 0.415), higher pressure resistance is expected. *In this example, we will illustrate a "bad" simulation.* Note that the very small pressure gradient assumed on the following page is not likely to support flow – this is borne out by calculated results as we will show.
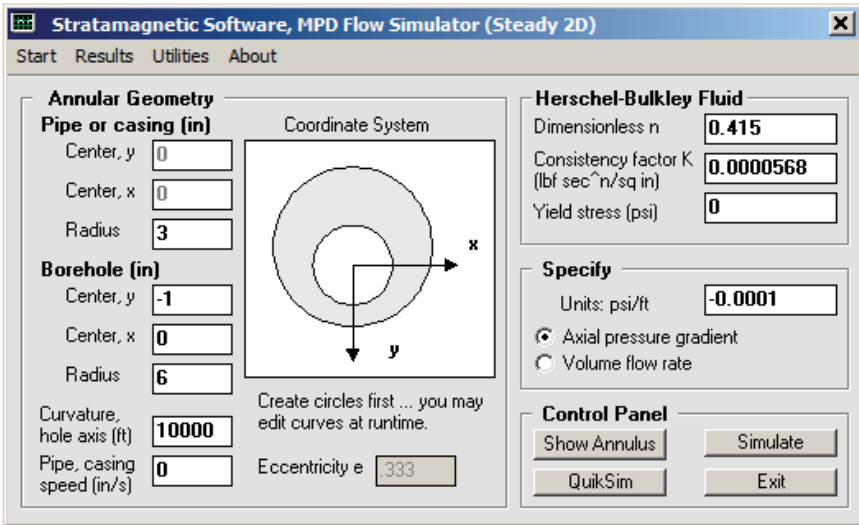
For the parameters above, we run QuikSim, which immediately leads to the following screen.
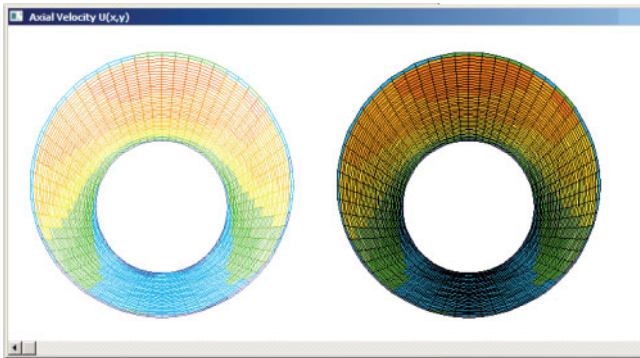
Figure 2-50. A bad simulation result (highest velocity ad edges) associated with very small pressure gradients.

The above result is free of unstable "wiggles," so that the numerics has converged *mathematically*. But this does not guarantee that the flow physically exists. To determine a realistic flow, we increase the pressure gradient next. The result in Figure 2-51 correctly shows maximum velocity in the widest part of the annulus and is thus acceptable. In Figure 2-50, the red zone extends almost to the top, a non-physical result – there is presently no automatic checking or correction for this.
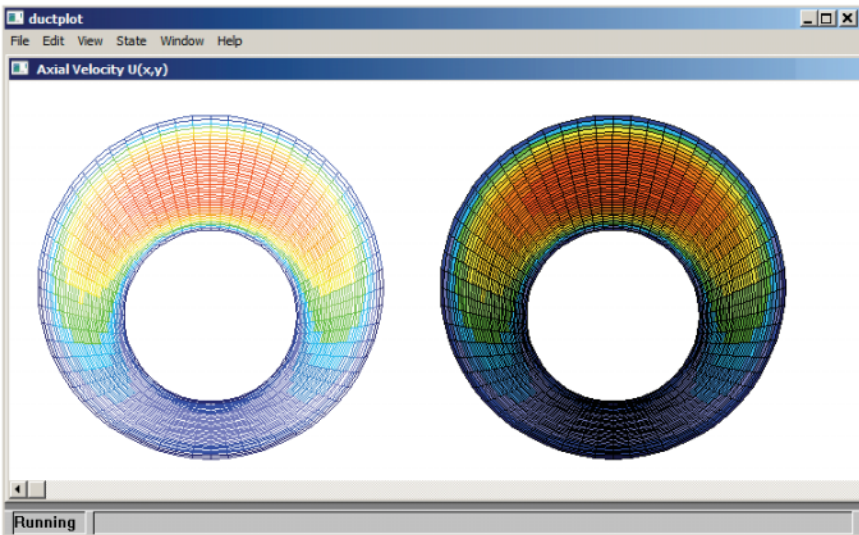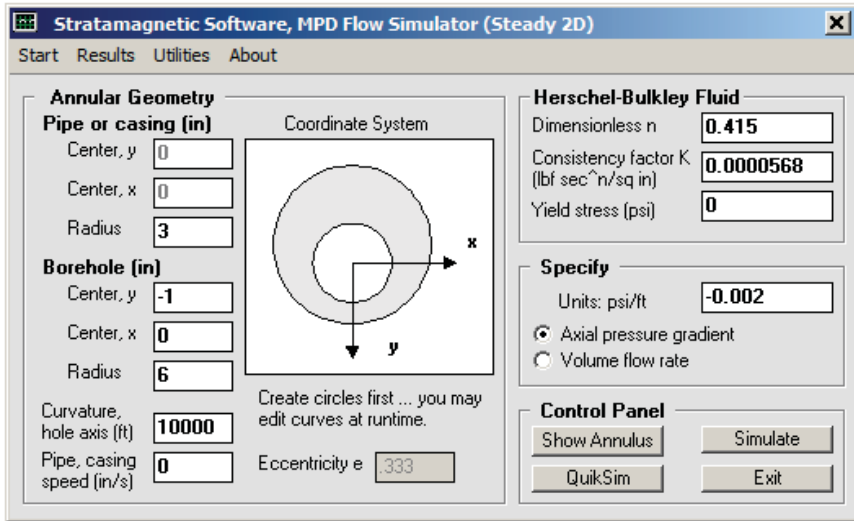
Figure 2-51.   Increased (absolute value of) pressure gradient gives correct "highest velocity in widest part of annulus" result – a correct computational check point.

The corresponding iteration history appears on-screen as follows.

```
SIMULATION STARTS ...

Power law fluid assumed with exponent "n" equal
to 0.4150E+00 and consistency factor of 0.5680E-04
lbf sec^n/sq in.

A yield stress of 0.0000E+00 psi is taken.

Borehole axis radius of curvature is 0.1000E+05 ft.

Axial speed of inner pipe is 0.0000E+00 in/sec.

Axial pressure gradient assumed as -.2000E-02 psi/ft.
Iteration  100, Error = .00004658
Iteration  200, Error = .00000357
Iteration  300, Error = .00001419
Iteration  400, Error = .00002193
Iteration  500, Error = .00002035
Iteration  600, Error = .00001082
Iteration  700, Error = .00000159
Iteration  800, Error = .00002819
Iteration  900, Error = .00002729
Iteration 1000, Error = .00001568

Annular flow rate ...... 0.4060E+03 gal/min
Cross-sectional area ... 0.8467E+02 sq inch
```

We next introduce a "pressure gradient vs flow rate curve" feature as shown in Figure 2-52a. This automatically provides field-usable results important to pumping without the need for interactive work.
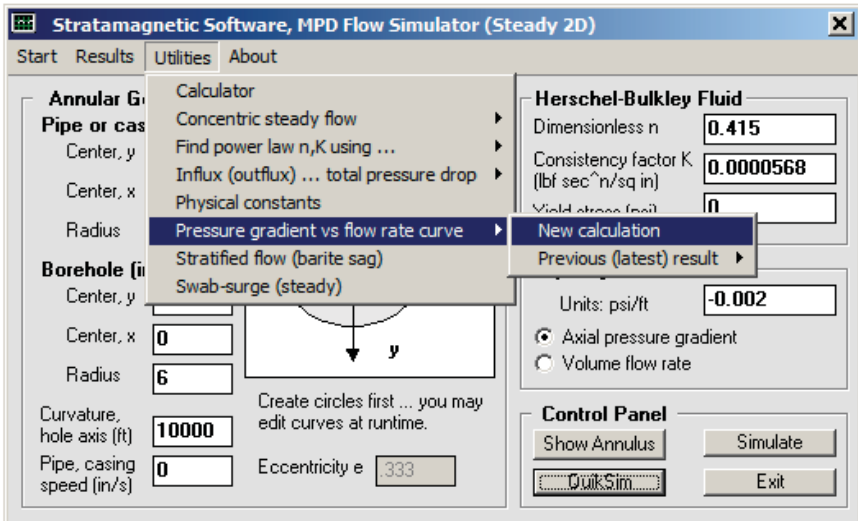
Figure 2-52a. "Pressure gradient vs flow rate curve" menu.
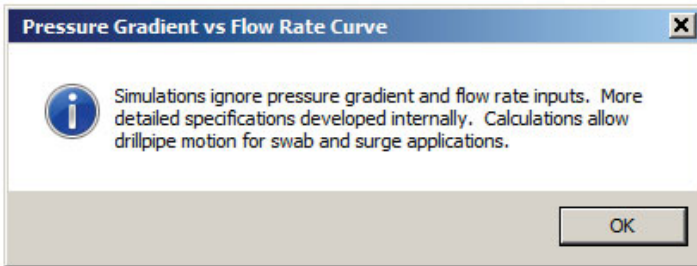
Figure 2-52b. "Pressure gradient vs flow rate curve" menu.

In this computational mode, pressure gradients are internally selected and calculated flow rates are obtained. Internally, a maximal 1,500 gpm is first chosen and the pressure gradient is iteratively determined. Then, flow rate is reduced and the procedure is repeated, until finally, the flow rate vanishes. Had we randomly assumed pressure gradient values, calculated flow rates would have been "anywhere" and computations would be indefinitely lengthy.

```
.
.
.
   Iteration  700, Error = .00001248
   Iteration  800, Error = .00002060
   Iteration  900, Error = .00001153
   Iteration 1000, Error = .00003072

O  Axial pressure gradient of -.3516E-02 psi/ft
   yields volume flow rate of 0.1369E+04 gal/min.
   Iterations continuing ...

Flow rate target error is, .8764E+01 %

   Iteration  100, Error = .00094903
   Iteration  200, Error = .00001371
   Iteration  300, Error = .00002183
   Iteration  400, Error = .00000709
   Iteration  500, Error = .00001222
   Iteration  600, Error = .00000270
   Iteration  700, Error = .00002910
   Iteration  800, Error = .00003013
   Iteration  900, Error = .00000354
   Iteration 1000, Error = .00003124

O  Axial pressure gradient of -.3906E-02 psi/ft
   yields volume flow rate of 0.1727E+04 gal/min.
   Iterations continuing ...

Flow rate target error is, .1512E+02 %
```

```
Iteration  100, Error = .00083349
Iteration  200, Error = .00000324
Iteration  300, Error = .00003260
Iteration  400, Error = .00001421
Iteration  500, Error = .00004461
Iteration  600, Error = .00001087
Iteration  700, Error = .00002278
Iteration  800, Error = .00001055
Iteration  900, Error = .00001212
Iteration 1000, Error = .00001870

O  Axial pressure gradient of -.3711E-02 psi/ft
   yields volume flow rate of 0.1542E+04 gal/min.
   Iterations continuing ...

Flow rate target error is, .2775E+01 %

Iteration  100, Error = .00077861
Iteration  200, Error = .00000598
Iteration  300, Error = .00000443
Iteration  400, Error = .00000078
Iteration  500, Error = .00001706
Iteration  600, Error = .00001729
Iteration  700, Error = .00002194
Iteration  800, Error = .00000886
Iteration  900, Error = .00000166
Iteration 1000, Error = .00001274

O  Axial pressure gradient of -.3613E-02 psi/ft
   yields volume flow rate of 0.1454E+04 gal/min.
   Iterations continuing ...

Flow rate target error is, .3100E+01 %

Iteration  100, Error = .00083349
Iteration  200, Error = .00000324
Iteration  300, Error = .00003260
Iteration  400, Error = .00001421
Iteration  500, Error = .00004461
Iteration  600, Error = .00001087
Iteration  700, Error = .00002278
Iteration  800, Error = .00001055
Iteration  900, Error = .00001212
Iteration 1000, Error = .00001870

O  Axial pressure gradient of -.3711E-02 psi/ft
   yields volume flow rate of 0.1542E+04 gal/min.
   Iterations continuing ...

Flow rate target error is, .2775E+01 %

Iteration  100, Error = .00083123
Iteration  200, Error = .00000645
Iteration  300, Error = .00000818
Iteration  400, Error = .00000678
```

```
Iteration  500, Error = .00001947
Iteration  600, Error = .00003442
Iteration  700, Error = .00000893
Iteration  800, Error = .00001764
Iteration  900, Error = .00001269
Iteration 1000, Error = .00001334

O  Axial pressure gradient of -.3662E-02 psi/ft
   yields volume flow rate of 0.1497E+04 gal/min.
   Iterations continuing ...

Pressure gradient found iteratively, -.3662E-02 psi/ft,
to yield 0.1497E+04 gal/min vs target 0.1500E+04 gal/min.
Note:  Iterations terminate within 1% of target rate.
Refine result by manually changing pressure gradient.
Annular flow rate ...... 0.1497E+04 gal/min
Cross-sectional area ... 0.8467E+02 sq inch


SIMULATION STARTS ...

Iterating, please wait ...

Iteration  100, Error = .00083123
Iteration  200, Error = .00000645
Iteration  300, Error = .00000818
Iteration  400, Error = .00000678
Iteration  500, Error = .00001947
Iteration  600, Error = .00003442
Iteration  700, Error = .00000893
Iteration  800, Error = .00001764
Iteration  900, Error = .00001269
Iteration 1000, Error = .00001334
Pressure gradient ........-.3662E-02 psi/ft
Annular flow rate ...... 0.1497E+04 gal/min

.
.
.
```

The following plots in Figure 2-53 are automatically generated.
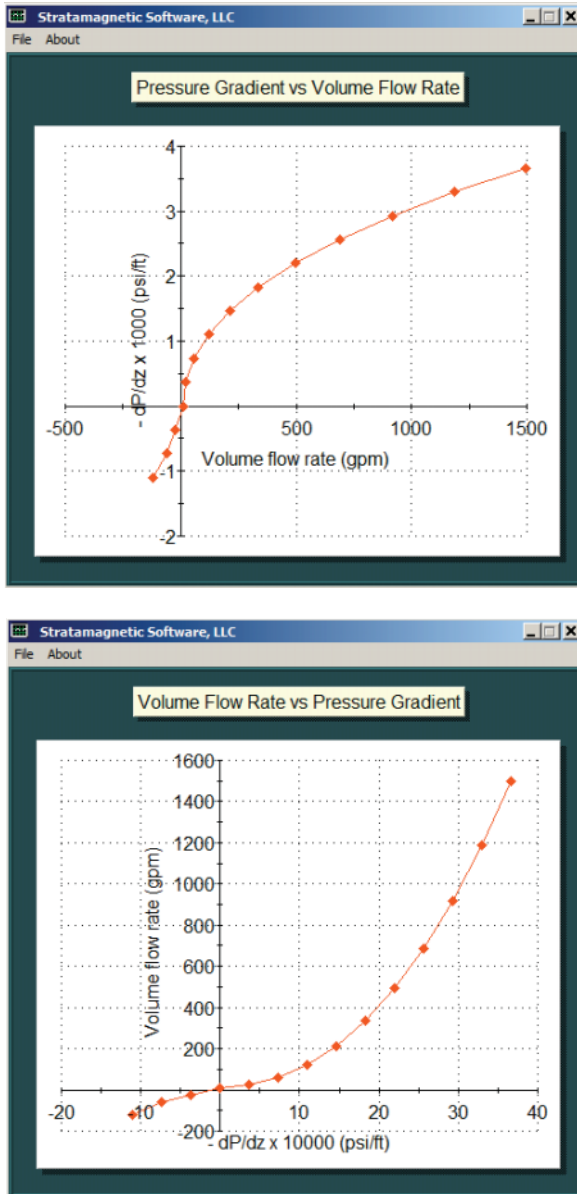
Figure 2-53. Calculated nonlinear pressure gradient vs flow rate curves.
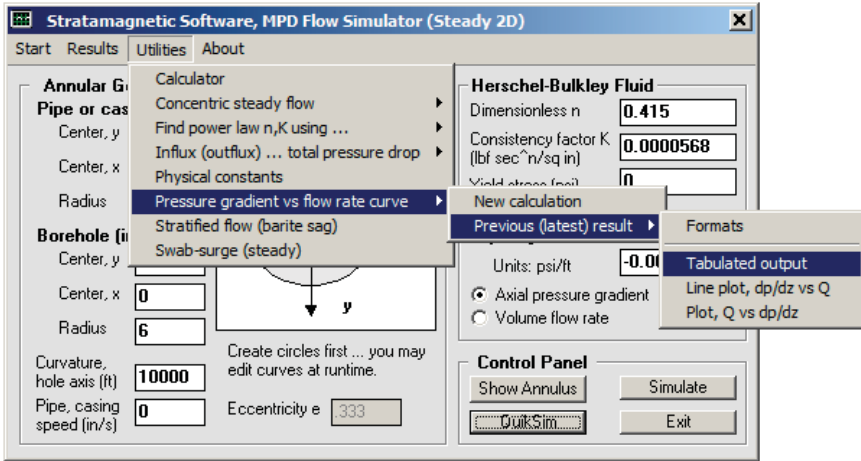
Figure 2-54. Tabulated results.

```
INPUT PARAMETER SUMMARY
Borehole axis radius of curvature (ft):   0.1000E+05
Inner circle center coordinate, x (in):   0.0000E+00
            center coordinate ,y (in):    0.0000E+00
                        radius (in):      0.3000E+01
Outer circle center coordinate, x (in):   -.1000E+01
            center coordinate, y (in):    0.0000E+00
                        radius (in):      0.6000E+01
High density 61 x 41 grid assumed here.
Herschel-Bulkley, power law exponent n:   0.4150E+00
     Consistency K (lbf sec^n/sq in):     0.5680E-04
                Yield stress (psi):       0.0000E+00
Drillpipe or casing speed ... (in/sec):   0.0000E+00


        dp/dx (in/sec)          GPM
        -0.0036621          1497.1901855
        -0.0032959          1187.6020508
        -0.0029297           918.5358887
        -0.0025635           688.2970581
        -0.0021973           495.0298767
        -0.0018311           337.4926758
        -0.0014648           213.5508575
        -0.0010986           121.1940842
        -0.0007324            58.1657524
        -0.0003662            23.5422707
         0.0000000            10.7184649
         0.0003662           -23.3589420
         0.0007324           -58.1738434
         0.0010986          -121.1780090
```

It is of interest to examine the last several entries, that is,

```
 -0.0010986              121.1940842
 -0.0007324               58.1657524
 -0.0003662               23.5422707
  0.0000000               10.7184649
  0.0003662              -23.3589420
  0.0007324              -58.1738434
  0.0010986             -121.1780090
```

Note the antisymmetry about the "0" solution (highlighted above in red). This antisymmetry just means if the pressure gradient were reversed in sign, the flow would reverse in direction. This calculated result also lends credibility to the numerical algorithm and solution.

2.2.8 Non-Newtonian effects, pressure gradient versus flow rate curve, non-zero yield stress.

In this example, we consider a *nonlinear* non-zero yield stress problem with an unexpected solution.
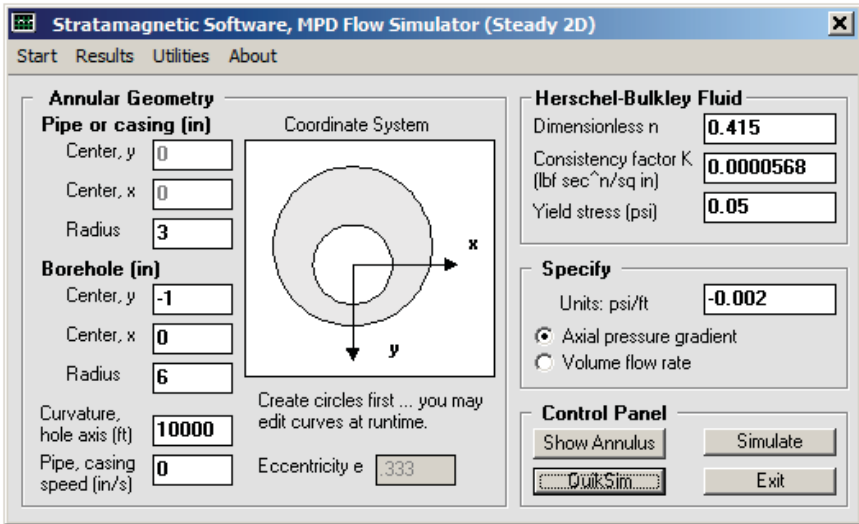
Figure 2-55a. Nonzero yield stress (Herschel-Bulkley fluid).

As usual, we always perform a QuikSim analysis to obtain a computational check point – in this case, the calculated result in Figure 2-55b is very good, with the red zone at the center of the widest area. The on-screen iteration history is provided immediately below the figure.
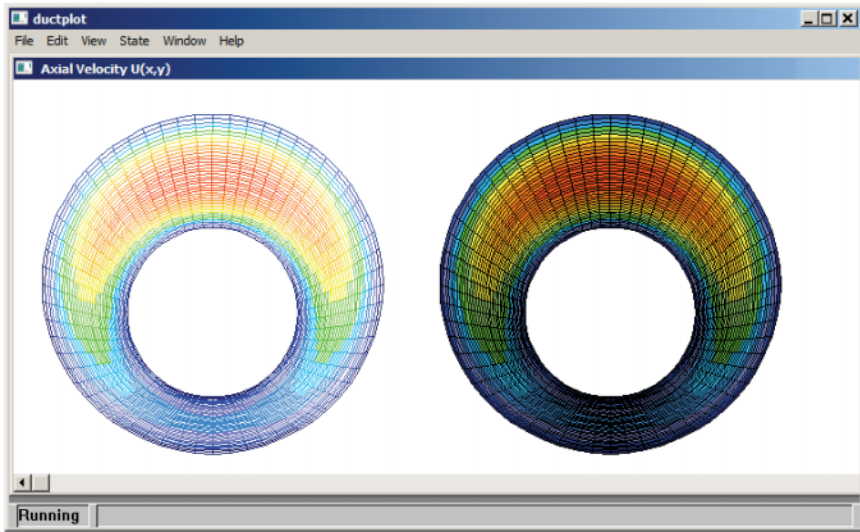
Figure 2-55b. Physically reasonable results achieved for computational test point.

```
SIMULATION STARTS ...

Iterating, please wait ...

Iteration  100, Error = .00000015
Iteration  200, Error = .00000008
Iteration  300, Error = .00000008
Iteration  400, Error = .00000000
Iteration  500, Error = .00000000
Iteration  600, Error = .00000000
Iteration  700, Error = .00000000
Iteration  800, Error = .00000015
Iteration  900, Error = .00000000
Iteration 1000, Error = .00000008

Annular flow rate ...... 0.2596E+03 gal/min
Cross-sectional area ... 0.8467E+02 sq inch
```

Now, we apply the pressure gradient versus flow rate curve generator utility. The straight lines obtained in Figure 2-56 were completely unexpected, and demonstrate that in non-Newtonian flow, almost any result is likely! Tabulated results are also given.
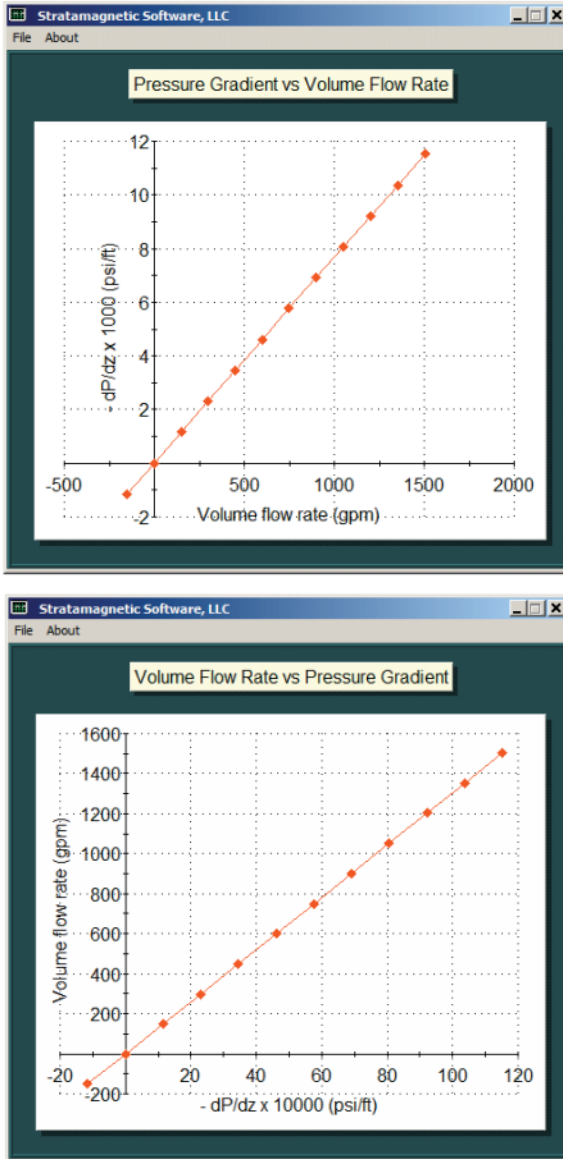
Figure 2-56. Unexpected straight-line behavior for nonlinear fluid.

```
INPUT PARAMETER SUMMARY
Borehole axis radius of curvature (ft):  0.1000E+05
Inner circle center coordinate, x (in):  0.0000E+00
            center coordinate ,y (in):  0.0000E+00
                        radius (in):  0.3000E+01
Outer circle center coordinate, x (in):  -.1000E+01
            center coordinate, y (in):  0.0000E+00
                        radius (in):  0.6000E+01
High density 61 x 41 grid assumed here.
Herschel-Bulkley, power law exponent n:  0.4150E+00
     Consistency K (lbf sec^n/sq in):  0.5680E-04
                Yield stress (psi):  0.5000E-01
Drillpipe or casing speed ... (in/sec):  0.0000E+00

         dp/dx (in/sec)          GPM
         -0.0115234        1505.7982178
         -0.0103711        1353.9306641
         -0.0092187        1202.3701172
         -0.0080664        1051.1138916
         -0.0069141         900.1593628
         -0.0057617         749.4988403
         -0.0046094         599.1206055
         -0.0034570         449.0112000
         -0.0023047         299.1535645
         -0.0011523         149.5151672
          0.0000000          -0.0002420
          0.0011523        -149.5156555
```

Let us compare these results with previous "no yield stress results" below.

```
         dp/dx (in/sec)          GPM
         -0.0036621        1497.1901855
         -0.0032959        1187.6020508
         -0.0029297         918.5358887
         -0.0025635         688.2970581
         -0.0021973         495.0298767
         -0.0018311         337.4926758
         -0.0014648         213.5508575
         -0.0010986         121.1940842
         -0.0007324          58.1657524
         -0.0003662          23.5422707
          0.0000000          10.7184649
          0.0003662         -23.3589420
          0.0007324         -58.1738434
          0.0010986        -121.1780090
```

The pressure gradient found is much higher to obtain same flow rate. Miraculously, the pressure gradient vs flow rate graph is linear, an unexpected result usually generally true of Newtonian fluids only.

2.2.9 Power law fluid in eccentric annulus, effect of pipe or casing speed.

Here we consider the effect of casing speed on "pressure gradient versus flow rate" behavior. The stationary "zero speed" limit was considered previously and selected results are replicated below. As noted earlier, the portion of the curve near the origin is correctly antisymmetric about it and provides a computational check point. The right side indicates that the more negative the pressure gradient, the higher (more positive) the flow rate is (the "100 ft/s assumed corresponds to a typical rapid walking speed).
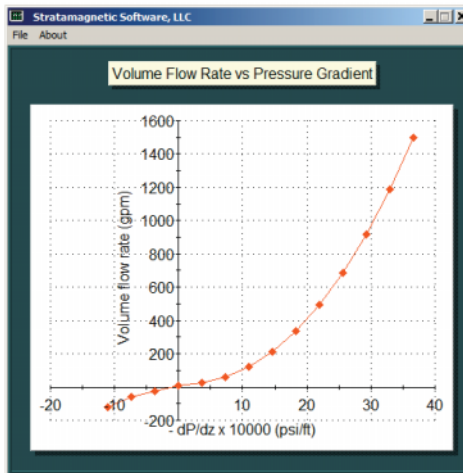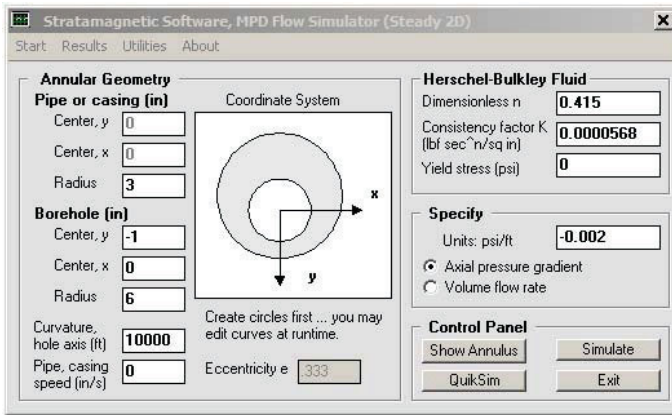
Figure 2-57a. Stationary drillpipe or casing speed.
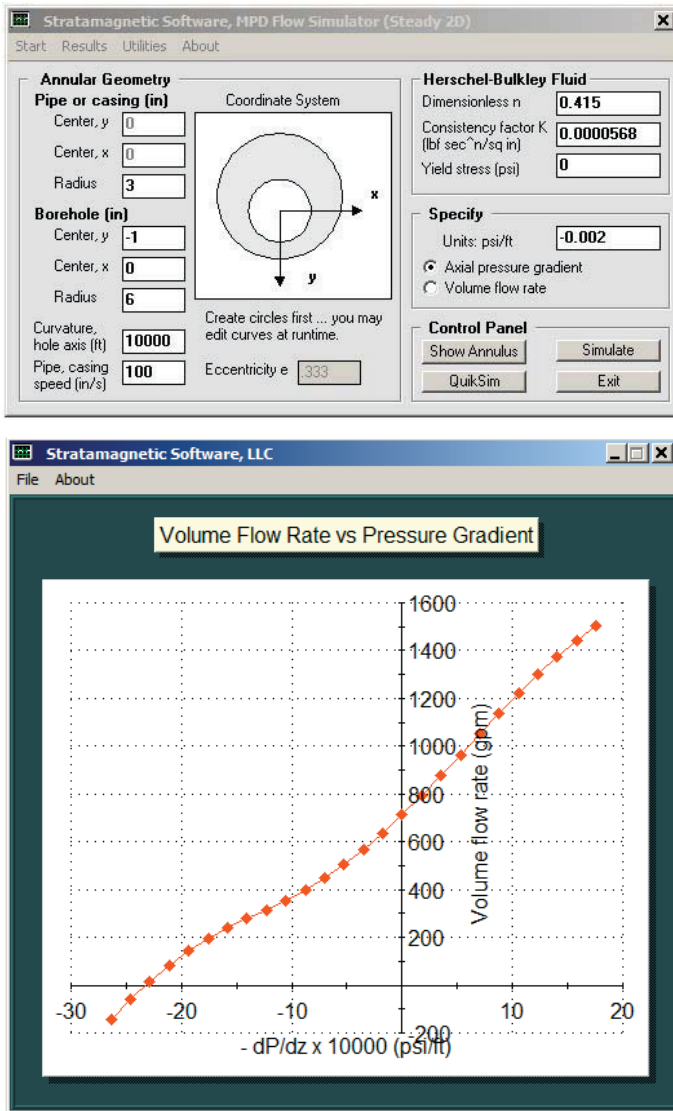
Figure 2-57b. Positive drillpipe or casing speed.

The above curve for "100 in/s" shows that, even without a pressure gradient, a flow rate near 700 gpm is obtained because the pipe is dragging fluid forward in the direction of the pumped flow.
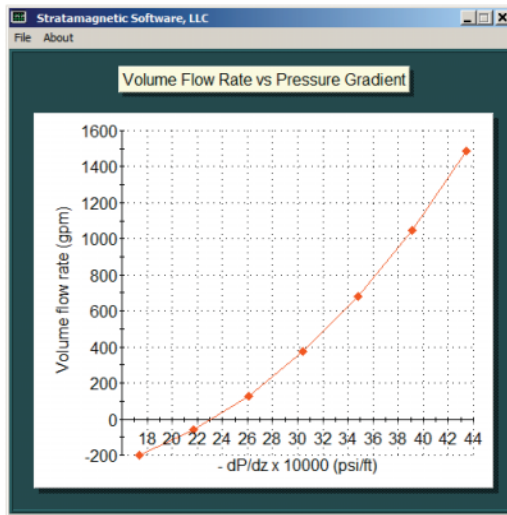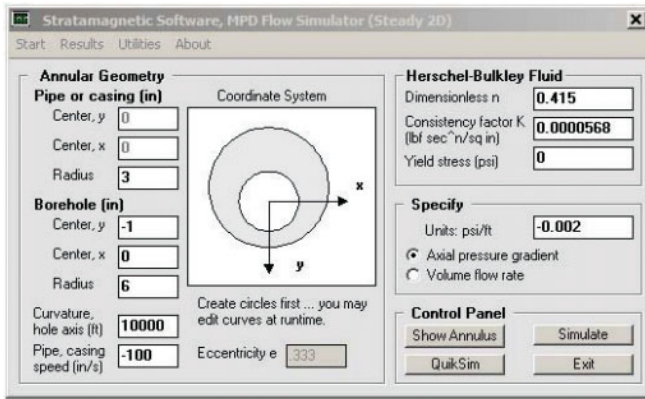
Figure 2-57c. Negative drillpipe or casing speed.

On the other hand, when pipe is pulled in a direction opposite to the flow, it requires more pressure gradient to move fluid – for a flow rate of 1,500 gpm, the above shows that "44" is required whereas for the two prior simulations, we had "37" and "18." The results in this section are useful in "slow swab-surge" applications without sudden pipe movements. When pipes are quickly jerked, the drillbit acts as a piston that rapidly "bangs" the fluid to produce "water hammer" pressures that are much stronger and follow different physical laws. Such problems are encountered in Measurement While Drilling "mud pulse" telemetry applications (e.g., see Chin (2014) and Chin et al (2014)).

2.2.10 Steady-state swab-surge in eccentric annuli for Power law fluids with and without circulation (no rotation).

Here we apply our steady-state, non-Newtonian flow simulator to swab-surge analysis for eccentric annuli with and without mud circulation. This problem is important to new hardware capabilities in managed pressure drilling that allow continuous mud circulation while tripping in and out of the hole. We focus on long deviated and horizontal wells for which hole eccentricity is important. Conventional models are either concentric, which are inapplicable, or one-dimensional, in which case details of the annular cross-section are impossible to model. Our work describes completely new methods that support accurate prediction of pressure distributions in the hole.
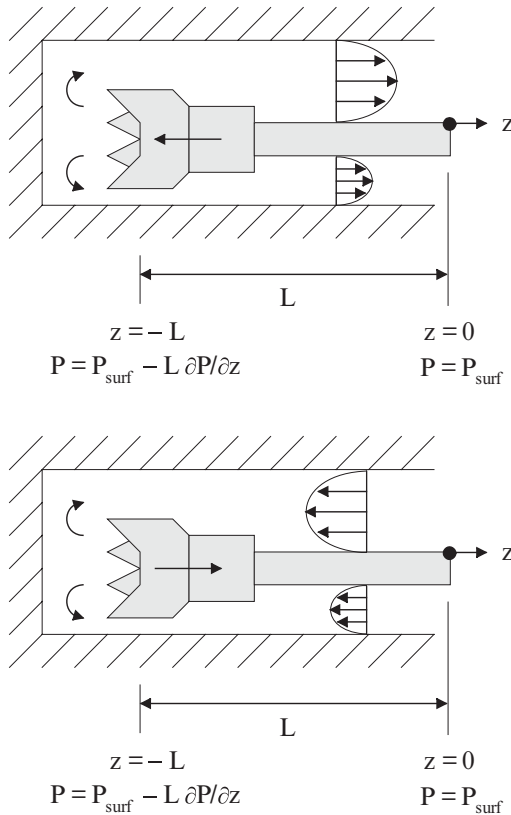
Figure 2-58a. Coordinate system and conventions.

Basic concepts.   Our simulator predicts the constant pressure gradient $\partial P/\partial z$ needed to induce a specified volumetric flow rate Q for any Herschel-Bulkley fluid in an eccentric annulus.   By convention, when Q is positive or "flowing to the right," the pressure P falls in the direction of increasing z.   Analogously, when Q is negative or "flowing to the left," P increases with increasing z.

Let us first consider flows *without* mud circulation.   In the <u>top</u> diagram of Figure 2-58a, the drillpipe and bit are shown moving toward the bottom of the hole and displacing fluid as it moves to the left.   This fluid must then flow to the right as shown and will produce a positive Q.   Now, the equation for pressure is simply $P = z\ \partial P/\partial z$ + constant.   If $z = 0$ represents the surface where $P = P_{surf}$ is fixed by the driller and $z = -L$ is the bit location with L being the borehole length, then the pressure at the bit is just $P_{bit} = -L\ \partial P/\partial z + P_{surf}$.   Since $\partial P/\partial z < 0$, we have $P_{bit} >> P_{surf}$, which formally shows that in a "surge" situation the bottomhole pressure greatly exceeds that at the surface.

Next, consider the <u>bottom</u> diagram in Figure 2-58a.   Here we "swab" the drillstring, pulling it out of the hole.   To fill the void left by the drillbit, the flow, Q, must travel towards the left, for which we have $\partial P/\partial z > 0$.   Then, $P_{bit} = -L\ \partial P/\partial z + P_{surf}$ implies that $P_{bit} << P_{surf}$ which formally shows that pressure is greatly reduced at the bit.   Increased pressures at the bit are associated with formation invasion and the possibility of fracturing the rock, while decreased pressures may increase the likelihood of blowouts.

The main simulation objective is accurate prediction of P_{bit} as a function of annular geometry, fluid rheology and (positive or negative) tripping speed in the presence of mud circulation at any pump rate.   In order to produce meaningful results, the simulator must be able to model general eccentricities, arbitrary Herschel-Bulkley parameters, plus non-zero drillpipe speeds for any pump rate, as the steady-state flow simulator described here will in an *exact* manner.

There are several scenarios that must be considered in addressing this problem which are outlined in Figure 2-58b.   Surge situations, as shown in diagrams (a) and (b), are straightforward to model.   In (a) without mud flow, the net flow $Q > 0$ simply flows to the right.   When mud is pumped down the drillstring, as shown in (b), the flow rate Q is simply increased, as shown by the exaggerated velocity profile.
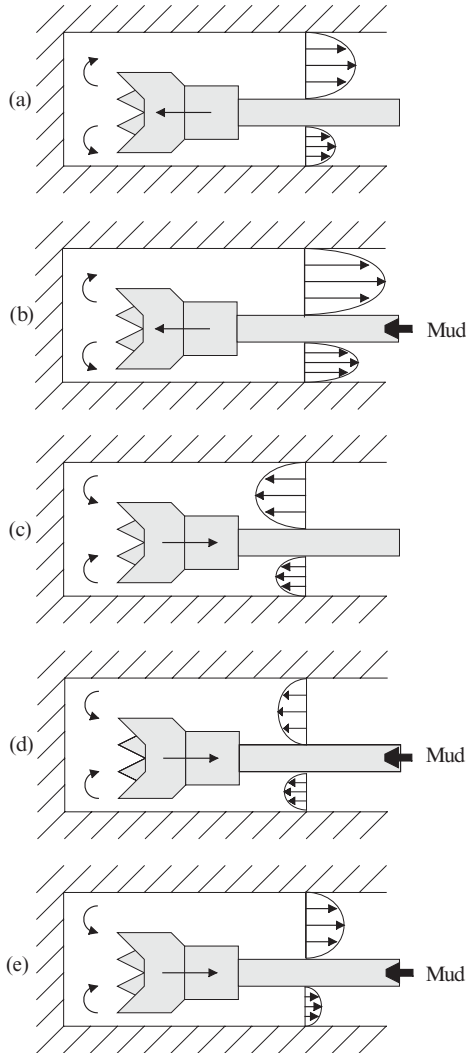
Figure 2-58b. Five flow scenarios in continuous flow managed
pressure drilling operations.

Swab scenarios are slightly more subtle. In (c) without mud flow,
pulling the drillstring out of the hole induces a negative flow $Q < 0$ to the
left. In (d), mud is pumped down the drillstring at a low pump rate. If
the rate is low enough, Q will still be negative. On the other hand, if the
pump rate is high, as suggested in (e), the net flow will come out of the

hole, with Q > 0 now being positive. In this limit, pulling the drillstring out of the hole is consistent with pressures at the bit that exceed those at the surface.

The foregoing five scenarios are obvious in retrospect, and we have summarized them only because they do not arise in more conventional studies where mud does not circulate. Note that the equation "$P_{bit} = -L \, \partial P/\partial z + P_{surf}$" is all that is necessary to calculate pressure at the bit. Again, L is the hole or drillstring length, P_{surf} is the known pressure at the surface choke, and $\partial P/\partial z$ represents output produced by the simulator.

Macroscopic rheological properties. Unlike Newtonian flows where the viscosity is a constant once and for all (assuming no pressure or temperature dependencies), the apparent viscosity in a non-Newtonian flow varies throughout the cross-section, and depends on geometrical details plus flow rate or pressure gradient. Despite the "confusion," it is nonetheless a useful correlator for cuttings transport and hole cleaning efficiency and may be significant in stuck pipe assessment.

Apparent viscosity, we emphasize, is not a property intrinsic to the fluid; however, for Herschel-Bulkley fluids, "n," "K" and "τ_{yield}" are. These "microscopic" properties are inputted into the simulator to create an all-important "pressure gradient versus flow rate curve" that describes "macroscopic" properties for the overall flow. This curve is important to swab-surge analysis: once the combined flow rate due to surface pumping plus tripping is known, it gives the pressure gradient required for use in the equation "$P_{bit} = -L \, \partial P/\partial z + P_{surf}$." We will give examples of different curves obtained for different fluid types and annular geometries next. We will introduce the basic analysis concepts by way of software modules that have been developed to host our calculations.

Newtonian fluids. The three Herschel-Bulkley parameters noted above can be determined from viscometer measurements using any number of regression techniques available in the literature (for zero-yield flows of Newtonian and Power law fluids, n, and K can be determined using the built-in utilities shown in Figure 2-49.). Once these are available, they are entered into the top right text boxes of the simulator interface in Figure 2-58c-1 where, for the present example, we have assumed the properties of water at 1 cp.   For the concentric geometry indicated, clicking on "QuikSim" leads to a flow rate of 943.5 gpm. Next, in Figure 2-58c-2, we increase the eccentricity, ε, from 0.0 to 0.667 for the same input parameters, and obtain the greatly increased flow rate of 1,521 gpm (it is well known that increases in eccentricity generally

lead to increases in flow rate under the same assumed pressure gradient.). Figures 2-58c-1 and 2-58c-2 represent the results of "single analysis mode" simulations when detailed results for a single calculation are required.

Much quicker results are obtained when the option in Figure 2-58c-3 is selected. This option ignores the "pressure gradient specified" or "flow rate specified" prescriptions, and leads, within a minute or two, to the results in Figure 2-58c-4, here for our eccentric annulus. It is important to observe two general features characteristic of Newtonian flows. First, the "pressure gradient versus flow rate curve" passes through the origin; second, the curve is a straight line whose slope depends only on the geometry of the annulus and the viscosity of the fluid. Once this slope is determined for a specific eccentric annulus at any given pressure gradient, either computationally or experimentally, the same applies to all pressure gradients. In this sense, Newtonian flows represent an exception to general nonlinear fluid rheologies, where every case must be treated on an individual basis. The straight line nature of the curve means that changes in flow rate lead to proportional changes in pressure gradient.
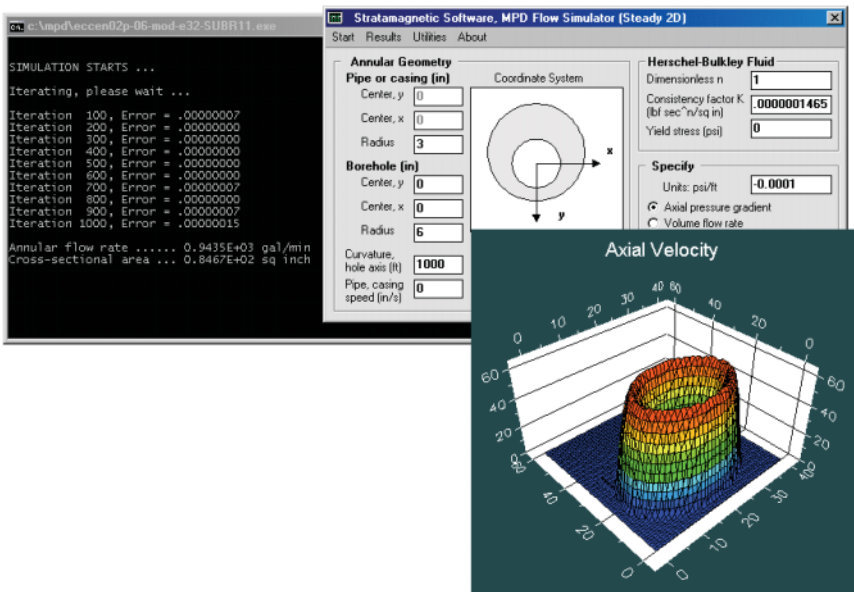
Figure 2-58c-1. Newtonian concentric ($\varepsilon = 0.0$) flow.
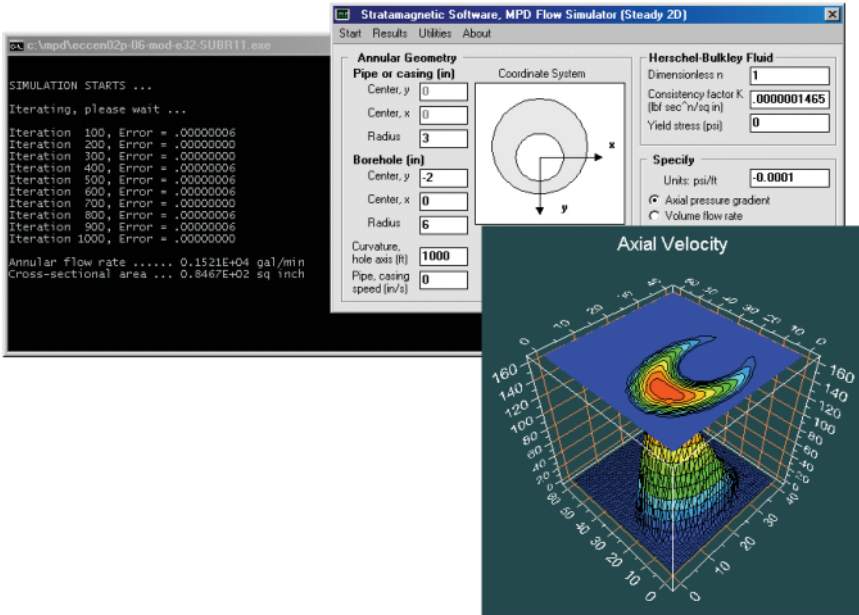
Figure 2-58c-2. Newtonian eccentric ($\varepsilon = 0.667$) flow.
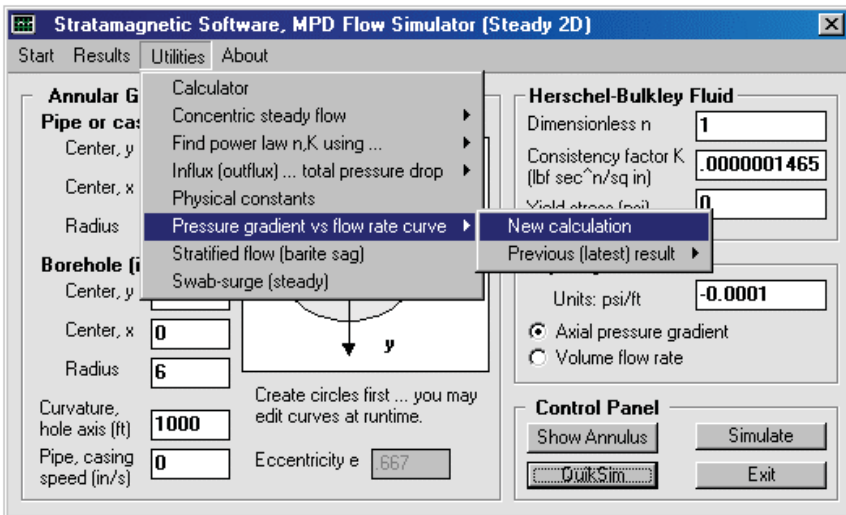
Figure 2-58c-3. Newtonian dp/dz versus flow rate calculation
($\varepsilon = 0.667$).
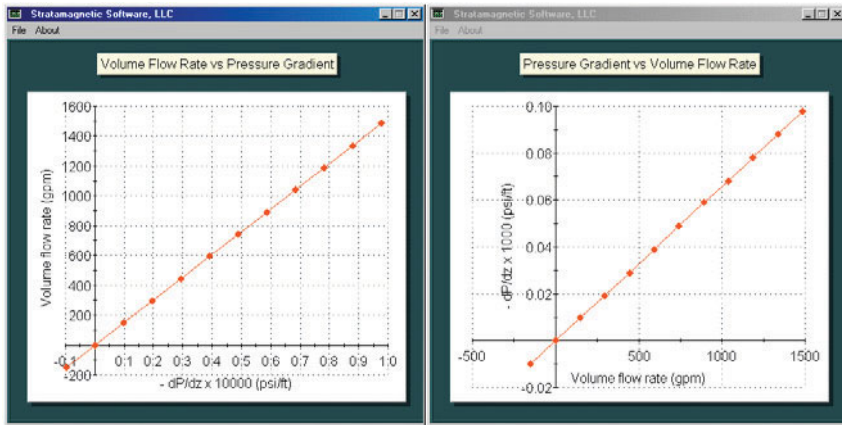
Figure 2-58c-4. Newtonian dp/dz versus flow rate behavior ($\varepsilon = 0.667$).

Finally, we note that for the "pressure gradient versus flow rate curve" option in Figure 2-58c-3, we had fixed the pipe or casing speed to zero for our calculations. In general, this can be a positive or negative constant, making the resulting curve useful in swab-surge applications when tripping at rapid speeds (compared to a nominal speed in the annulus). We will give example calculations later.

Power law fluids. Next we reconsider the above concentric and eccentric geometries for zero-yield power fluids, now with $n = 0.415$ and $K = 0.0000944$ lbf sec^n/in.^{2} (this unweighted mud was used in a recent laboratory study). The significant departure of 'n' from unity implies large nonlinearities. This is reflected in the highly curved lines in Figures 2-58d-1 and 2-58d-2, showing that incremental changes in flow rate to not lead to proportional changes to pressure gradient – the exact changes are rate dependent. Also note the significant differences going from concentric (vertical well) to eccentric (deviated or horizontal well) applications. These results serve as a warning that models based on over-simplified geometric assumptions can lead to operational hazards.
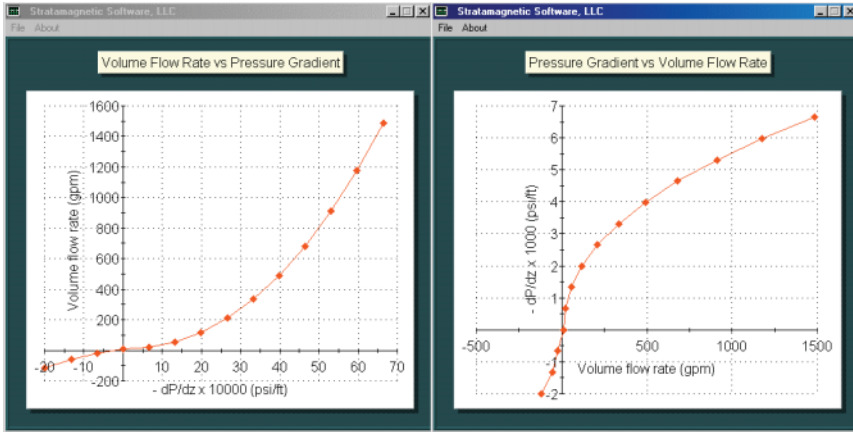
Figure 2-58d-1. Power law concentric flow ($\varepsilon = 0.0$).
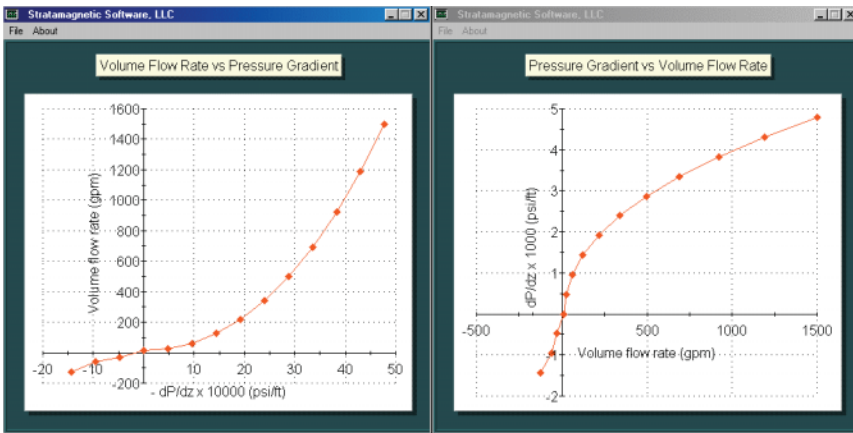
Figure 2-58d-2. Power law eccentric flow ($\varepsilon = 0.667$).

Swab-surge examples. Now we consider an application for "tripping with pumps off" and also "with continuous circulation" which demonstrates the subtleties of flow nonlinearity. If we invoke the "Swab-surge (steady)" option from the main interface in Figure 2-49, we obtain the Swab-Surge Worksheet in Figure 2-58e-1 (The embedded calculations conservatively assume that the drillbit completely blocks the annulus and that fluid does not pass through the nozzles.) We at first turn off the mud pump while assuming a hole radius of 4 in and a "tripping in" speed of 5,000 ft./hr.

The Worksheet indicates that, following the convention of Figure 2-58a, we have a positive induced flow rate of +217.6 gpm while the drillpipe speed is negative with a value of –16.67 in./sec. (The drillbit is assumed to completely block the hole.) The Worksheet instructs the user to enter "217.6" and "–16.67" as we have in Figure 2-58e-2 for the eccentric annulus and Power law fluid assumed. Clicking on "Show Annulus" produces the display in Figure 2-58e-3. The required pressure gradient dp/dz is – 0.006494 psi/ft (minus values indicate high surge pressures at the bit).
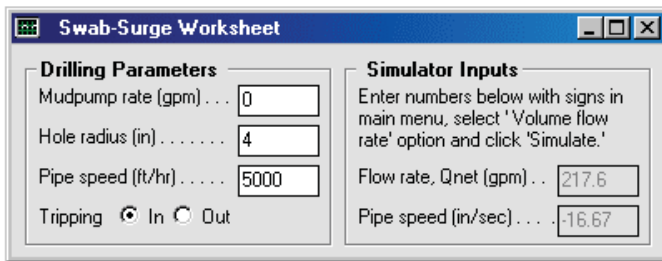
Figure 2-58e-1. Assumptions for surge run with pumps off.
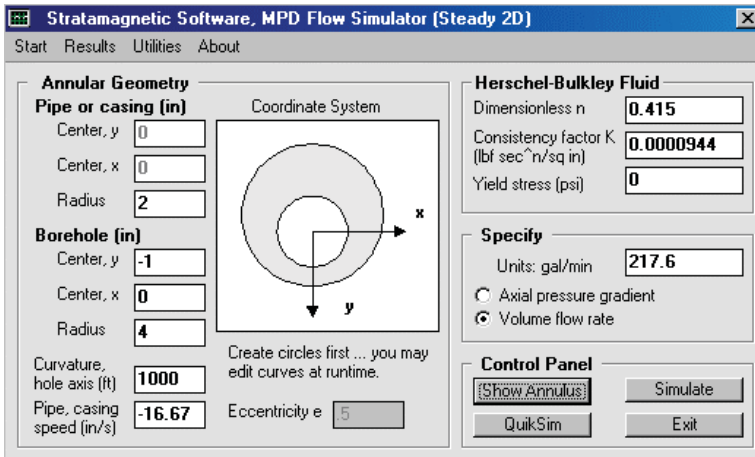
Figure 2-58e-2. Additional assumptions for surge run with pumps off.
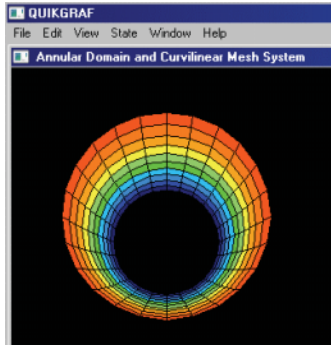
Figure 2-58e-3. Eccentric annulus and curvilinear grid assumed (internal grid used in computations is finer).
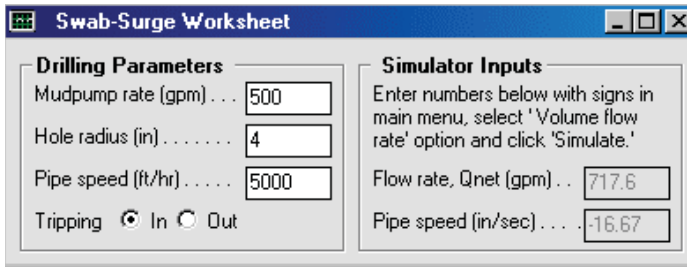
Figure 2-58e-4. Assumptions for surge run with pumps on.
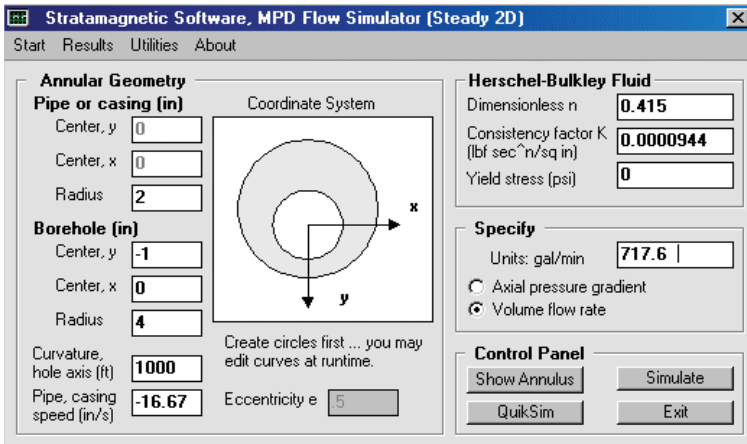
Figure 2-58e-5. Additional assumptions for surge run with pumps on.

Now, consider an identical situation except that the pump is circulating at 500 gpm.   The screens analogous to Figures 2-58e-1 and 2-58e-2 are given above. Clicking on "QuikSim" (as before) shows that the required pressure gradient now becomes – 0.01045 psi/ft.   This pressure drop is steeper than before, as expected, because the flow rate is higher.   It is interesting that the flow rate ratio between the two runs above is 717.6/217.6 or 3.30. The ratio of pressure gradients, however, is 0.01045/0.006494 or 1.61.   In a Newtonian flow, the "3.30" and "1.61" numbers would have been identical. For non-Newtonian flows, they typically are not, and general conclusions cannot be given – results must be found by case-by-case computations. This example points to the danger of using Newtonian models even for crude estimates.

In the next calculation, we consider "tripping out" in a swab application with pumps off. Instead of "+217.6" and "-16.67" as we had before, Figure 2-58e-6 shows that the relevant numbers are reversed, with "-217.6" and "+16.67." When these replace their counterparts in Figure 2-58e-2, "QuikSim" analysis correctly shows that the axial pressure gradient is now + 0.006494 psi/ft. instead of – 0.006494 psi/ft. This positive sign, as discussed earlier, indicates lower pressures relative to those at the surface.   Now let us recall the equation "$P_{bit} = -L \, \partial P/\partial z + P_{surf}$ " for pressure at the drillbit. Suppose that $P_{surf} = 14.7$ psi is open to the atmosphere. Then, we can express bit pressure in psi if L is given in feet via $P_{bit} = 14.7 - 0.006494 \, L$. In this example, P_{bit} vanishes if L = 2,264 feet, at which point the possibility of a blowout increases significantly.

Figure 2-58e-6. Assumptions for swab run with pumps off.

What would be the effect if, as in Figure 2-58e-4, we ran the mud pump at 500 gpm? The corresponding Swab-Surge Worksheet would appear as it does in Figure 2-58e-7, showing a net flow rate of 282.4 gpm. The calculation suggested by Figure 2-58e-8 gives a negative pressure gradient of – 0.005811 psi/ft. This shows that our 500 gpm pump rate is enough to prevent overly low pressures when tripping out at 5,000 ft./hr. While we have focused on low pressures that may allow blowouts, it is obvious that a similar analysis allows us to select pump rates that will not fracture the formation when the frac gradient is known.

Figure 2-58e-7. Assumptions for swab run with pumps on.

Figure 2-58e-8. Additional assumptions for swab run with pumps on.

Neutral pressure gradient operation. Our simulator allows us to pose and solve still another problem of interest in swabbing operations. Suppose, as in the above, we wish to trip out at 5,000 ft./hr or 16.67 in./sec. We found from a prior analysis that this action is responsible for a negative flow rate of – 217.6 gpm, with the left-bound annular fluid flow arising from the need to fill the borehole void left by the retreating drillstring. We ask ourselves which net flow rate would allow us to maintain a "neutral pressure gradient" of 0.00 psi/ft, that is, one that allows us to have a constant pressure along the annulus equal to the surface choke pressure. If we run the simulator with +16.67 in./sec. and 0.00 psi/ft. in "specify axial pressure gradient" mode, we obtain a net flow rate of 53.52 gpm. This 53.52 gpm is, of course, the flow rate obtained by simply dragging the drillstring along without an imposed pressure gradient. In other words, the pump must be operated at 217.6 + 53.52 or 271.1 gpm to create a simple dragging flow and to produce the required zero pressure gradient.

This "reverse thinking" can be verified directly. It is easily validated by the forward calculation in Figure 2-58e-9. This calls for us to enter 53.52 in the volumetric flow rate screen of Figure 2-58e-10. Clicking "QuikSim" leads to an extremely small – 0.00001221 psi/ft. which allows us to impress surface choke pressure directly on the drillbit. Pressure is constant along the borehole. This predictive capability is a direct result of our ability to model drillpipe movement in a rigorous computational manner in very complicated borehole environments. We again note that the simulator was applied to a highly nonlinear Power law fluid with pipe movement in a very eccentric annulus.

Figure 2-58e-9. Surface mud pump rate needed for vanishing axial pressure gradient while tripping out.
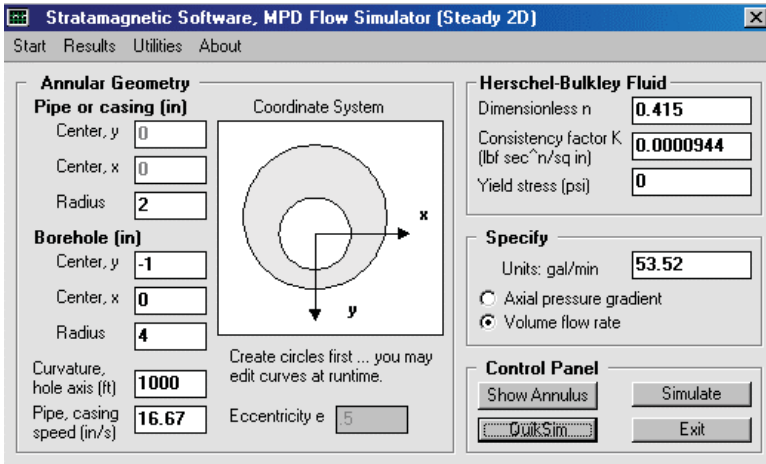
Figure 2-58e-10. Calculation providing zero axial pressure gradient.

2.2.11 Steady-state swab-surge in concentric annuli for Power law fluids with drillpipe rotation but small pipe movement.

The approach taken to model swab-surge effects in Example 2.2.10 is straightforward. Basically, the Swab-Surge Worksheet is used to compute a kinematic volumetric flow rate correction to the mud pump flow rate that accounts for changes in void space near the drillbit due to tripping out or in. The new flow rate is then used in the annular flow analysis together with the correctly signed drillpipe speed. We employ this approach throughout for swab-surge applications. When the drillpipe rotates, a closed form analytical solution for the complete flow field is developed in Chin (2012) that allows general steady rotation at any rpm provided the annulus is concentric and stationary in the axial direction. This latter assumption is satisfactory for slow tripping speeds, as they invariably should be in operations, given safety considerations. The simpler simulator is accessed as shown in Figure 2-59a.
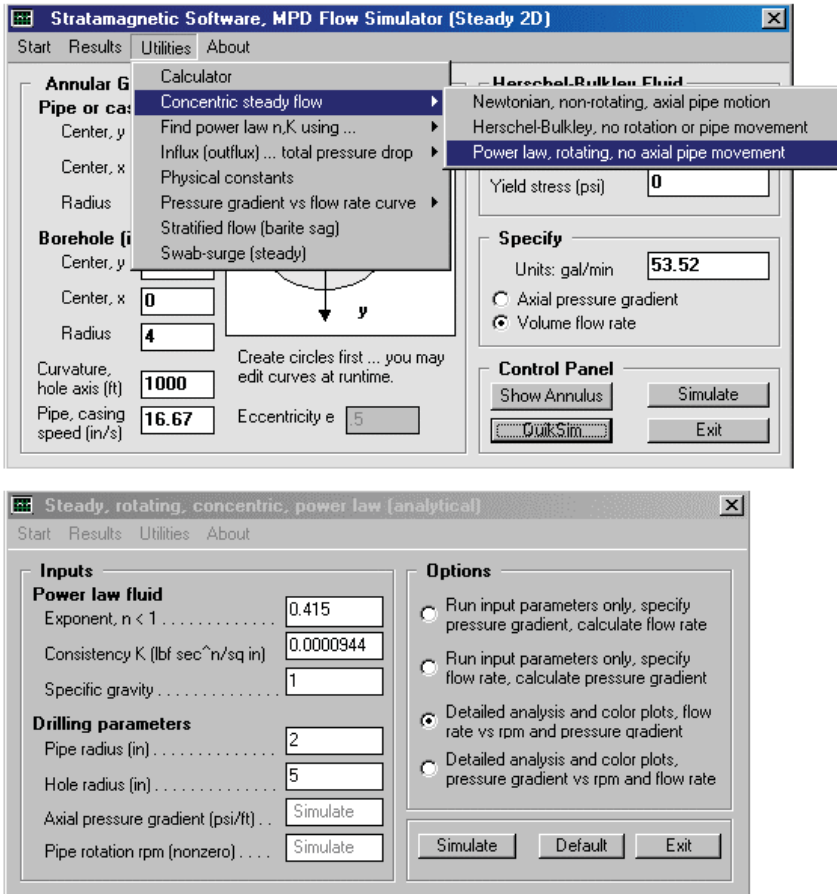
Figure 2-59a. Concentric, rotating, Power law flow.

Four run-time options are shown in the above screen at the right. The first two provide detailed results for single run-sets (detailed examples are developed in Chapter 5). The third and fourth options provide fast calculations for "GPM vs RPM and dP/dz" and "dP/dz vs RPM and GPM," typically requiring about fifteen seconds of computing time, with automated three-dimensional color plots that allow zooming and mouse rotation. Results shown in Figures 2-59b,c clearly illustrate the roles of rotation and pressure gradient that must be understood in managed pressure drilling applications.
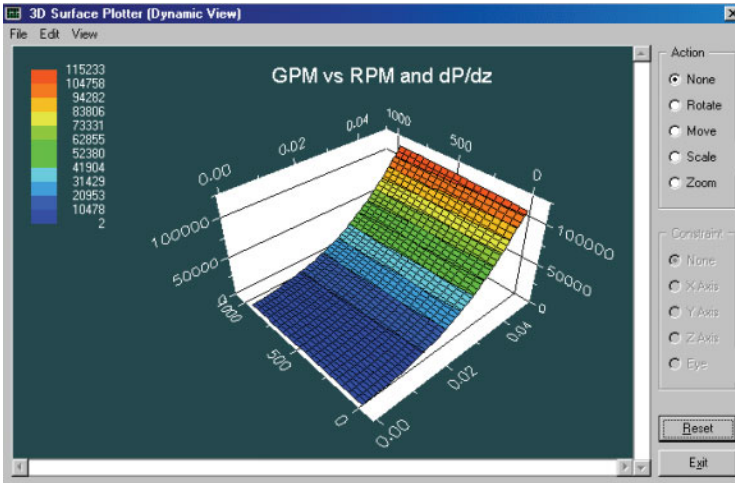
Figure 2-59b. GPM versus RPM and dP/dz.
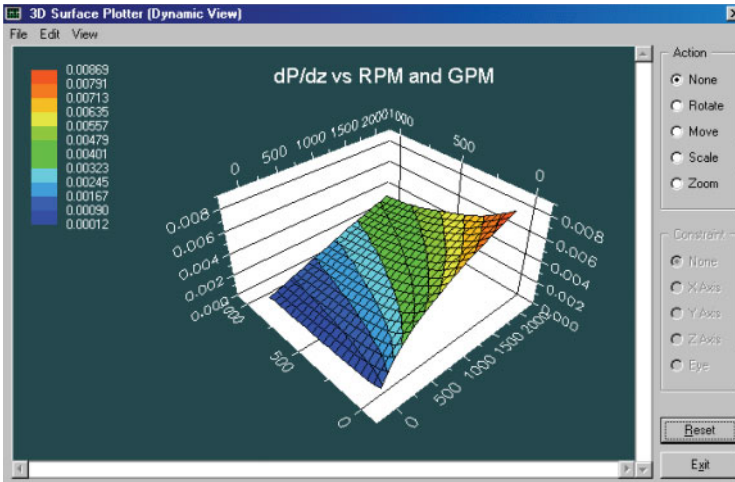
Figure 2-59c. dP/dz versus RPM and GPM.

2.2.12   Steady-state swab-surge in eccentric annuli for Herschel-Bulkley fluids with drillpipe rotation and axial movement.

In Example 2.2.11, we addressed pressure gradient computations for general flow rates and rotational speeds for Power law fluids in a concentric annulus under steady conditions without axial pipe movement.   For such flows, the convective terms in the momentum

equations vanish identically. The effect of rotation is restricted to shear-thinning so that, for a given pressure gradient, increases in rotation rate will reduce apparent viscosity and increase volumetric flow. These effects, well known in the older literature, apply mainly to vertical wells.

Run A. In deviated and horizontal wells, annular eccentricity is the rule. While shear-thinning remains important, a nonlinear convective term (whose magnitude is proportional to density and rotational speed and which is variable throughout the cross-section) appears and modifies the local axial pressure gradient. For most practical geometries, this will reduce the flow relative to that found for the eccentric non-rotating problem for the same applied pressure gradient. Equivalently, for the same flow rate, the pressure drop increases significantly. These properties are important in managed pressure drilling.
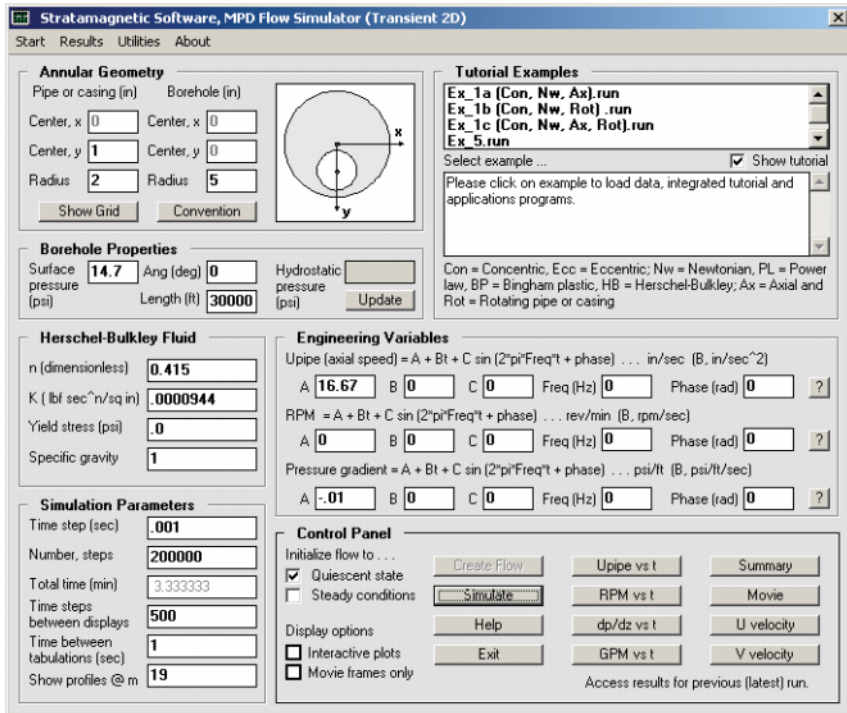
Figure 2-60a-1. Transient 2D flow menu (no rotation).

The direct computation of steady rotating flow in an eccentric annulus is often an unstable numerical process. Solutions have been published by various authors who have all given few computational details related to convergence properties and computing times. Such schemes tend to destabilize at higher specific gravities and rotational speeds, and unfortunately, in the ranges typical of most drilling applications. Fortunately, steady rotating flow solutions can be computed by solving the transient formulation asymptotically for large times. In Figure 2-60a-1, we have set up flow simulations for a Power law fluid in an eccentric annulus with axial pipe movement but no rotation. The problem is integrated in time starting with quiescent conditions. Figure 2-60a-2 shows computed volumetric flow rates reaching constant levels at 941.0 gpm after about one minute of computing time (this is interestingly, but fortuitously, also the physical time scale) with convergence to steady-state achieved very stably. The maximum axial flow is found, as expected, at the wide side of the annulus.
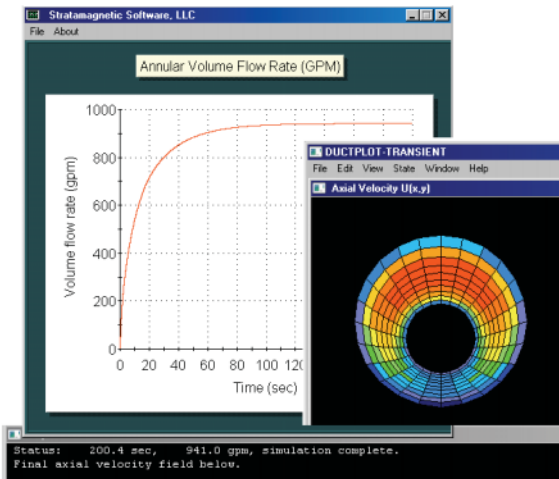
Figure 2-60a-2. Eccentric Power law results without pipe rotation.

Run B.   Repeating the foregoing simulation to allow drillstring rotation is straightforward. For example, we simply change the "0" in the RPM box to "100" (as seen from Figure 2-60b-1) , and completely automated calculations lead to a reduced flow rate of 562.2 gpm as shown in Figure 2-60b-2. As is well known, the location of maximum axial velocity moves azimuthally, and our results are consistent with this observation, a fact that may be useful in cuttings transport and hole cleaning applications. Computed results also indicate that the time to reach equilibrium decreases with rotation. The results presented here, for pipe moving both axially and azimuthally, show that pressure gradient calculations are doable and straightforwardly performed for general Power law fluids in highly eccentric annuli.
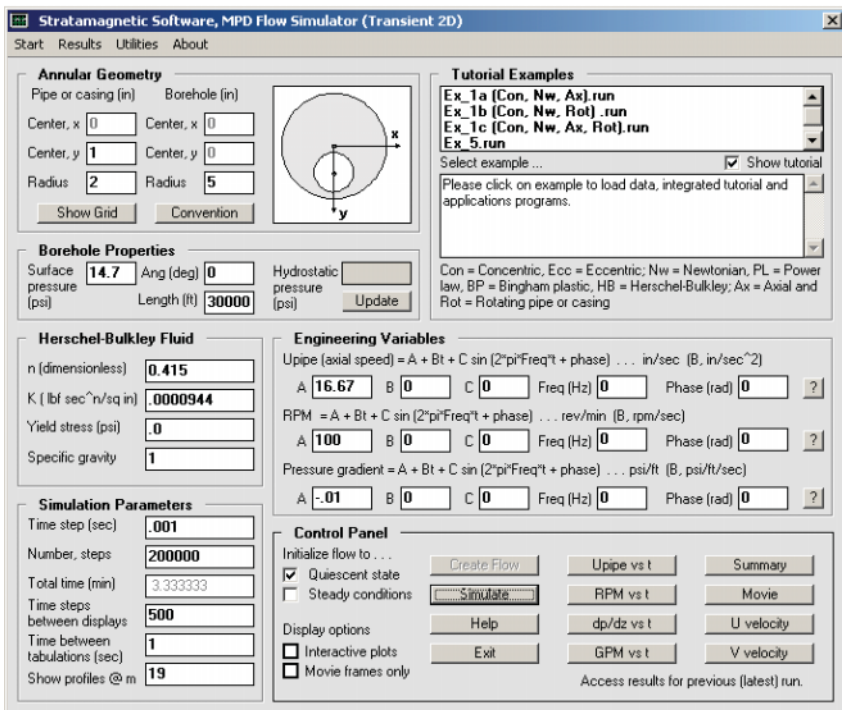
Figure 2-60b-1. Modified flow with 100 rpm drillstring rotation.
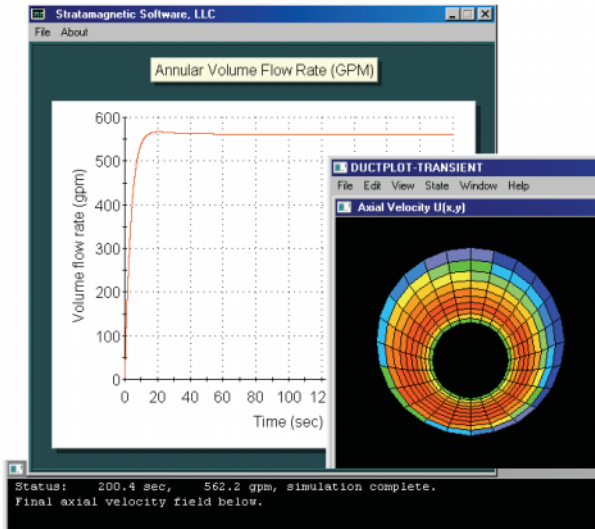
Figure 2-60b-2. Reduced flow rate achieved in shorter time.

Run C. In the next calculation, we repeat that in Figure 2-60b-1, which included axial pipe movement and nonzero rotational speed in addition to borehole eccentricity and non-Newtonian Power law flow, but now consider the additive effects of Herschel-Bulkley yield stress. In Figure 2-60c-1, we modify the previous "0" to "0.002 psi" and leave all other parameters unchanged. As before, the calculations require about 30 seconds and are performed stably.

Figure 2-60c-2 shows that the volumetric flow rate is reduced from 562.2 gpm to 516.9 gpm, for a 9 percent reduction. One might have asked what the required pressure gradient would be for our yield stress fluid if we needed to maintain a 562 gpm flow rate. For our steady flow solver, direct "pressure gradient specified" and inverse "flow rate specified" calculation modes were available. For mathematical reasons, this is not practical for transient simulations. A simple procedure requires us to manually attempt reasonable pressure gradient guesses. This procedure can be very efficient. For this example, the author determined that – 0.011 psi/ft. would yield 562 gpm after three tries or about two minutes of desk time. In other words, the presence of yield stress steepened the pressure gradient by a substantial 10 percent.
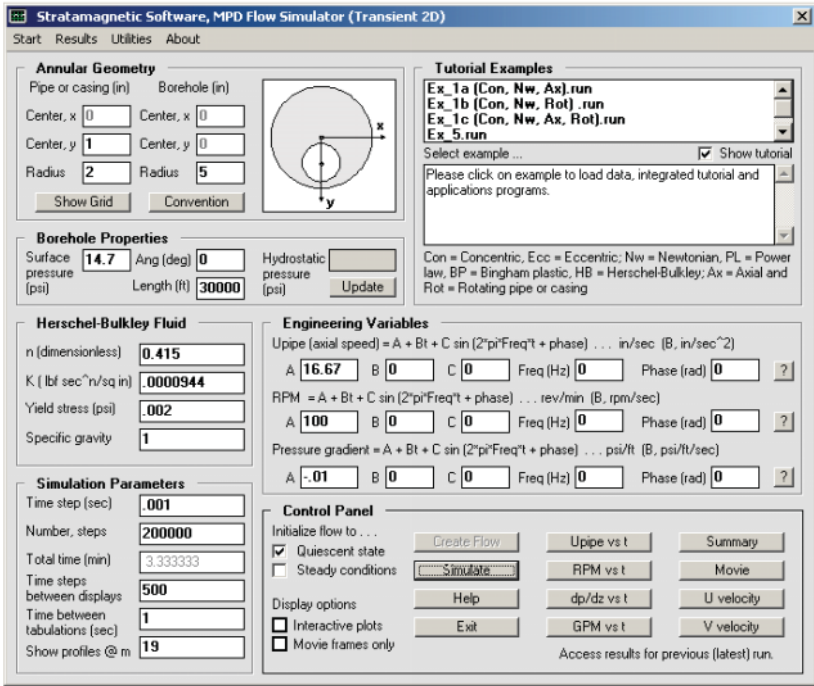
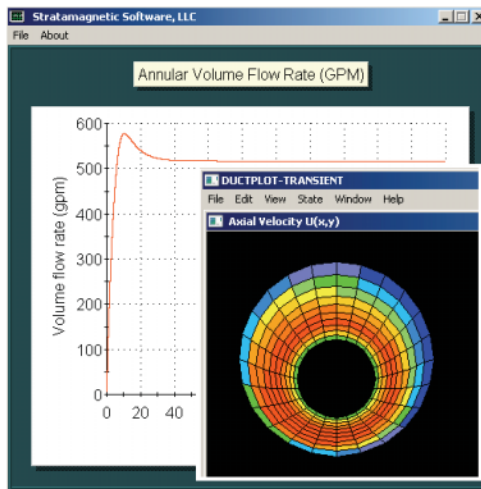**Figure 2-60c-1.** Flow at 100 rpm now with 0.002 psi yield stress.

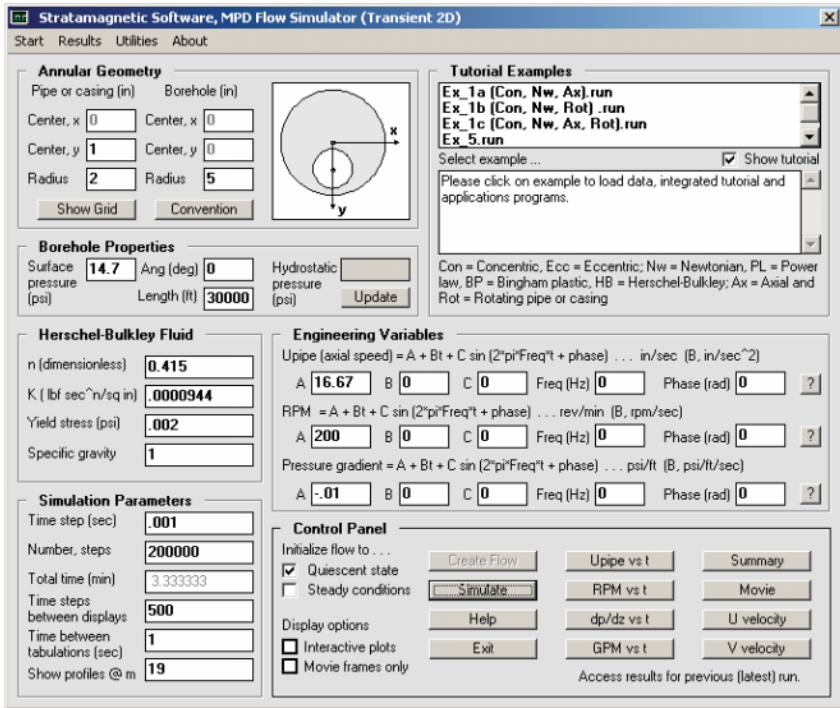**Figure 2-60c-2.** Flow at 100 rpm now with 0.002 psi yield stress.

Figure 2-60d-1. Flow at 200 rpm with 0.002 psi yield stress.

Run D. Next, we re-consider the yield stress problem, in Figure 2-60c-1 and determine the consequences of increasing rotation rate from 100 to 200 rpm. The input screen is shown in Figure 2-60d-1. The effect of doubling rotational speed is a decreased flow rate for the same – 0.01 psi/ft, in this case a much smaller 443.3 gpm, as shown in Figure 2-60d-2. And what if we had insisted on 562 gpm? Then, some simple manual "cut and try" calculations with different pressure gradient guesses lead to a substantially steepened – 0.0131 psi/ft, a value that was obtained within two minutes with four different guesses.

Favorable effect of rotation on hole cleaning. The detailed effects of rotation and yield stress have been discussed in the context of eccentric borehole annuli with coupled axial drillstring movement. These calculations represent completely new industry capabilities. It is interesting to note that, from Figure 2-60a-2 for non-rotating flow, the location of maximum axial flow speed lies symmetrically at the top at the wide side of the eccentric annulus. When rotation exists, as shown in

Figures 2-60b-2, 2-60c-2 and 2-60d-2, the location of the maximum moves azimuthally as shown, consistently with other known investigations (note that "red" in these three diagrams denote different speeds.). That increased relative speeds are achieved at the bottom of the annulus is consistent with the improved hole cleaning ability of drillstrings under rotation observed under many field conditions. Of course, this improvement comes at the expense of steepened pressure gradients, a crucial trade-off whose value must be assessed by the drilling engineer. The end decision made at the rig site will depend on "the numbers" which can only be obtained computationally.
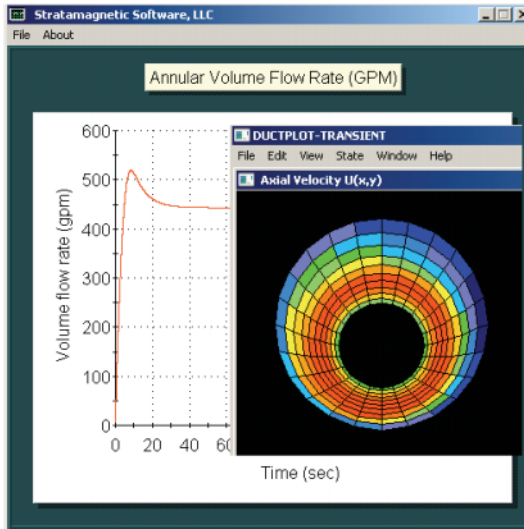

Figure 2-60d-2. Flow at 200 rpm with 0.002 psi yield stress.

Run E. Here we study the effect of slow-down in drillstring rotational rate. Acceleration and deceleration are always encountered in start-up and shut-down. We repeat the calculation of Figure 2-60d-1, starting with 200 rpm for our nonzero yield stress fluid. But as shown in Figure 2-60e-1, we allow our 200 rpm to slow down to 0, as seen from the "- 0.5" deceleration rate selected under the RPM menu. Clicking on "?" to the right produces a plot of the assumed RPM versus time curve in Figure 2-60e-2 (note that numerous time functions for axial pipe speed, rotational rate, and pressure gradient are permissible with the simulator).

The calculated flow rate versus time response is shown in Figure 2-60e-3. This flow rate increases as expected, with drillstring rotation rate decreasing.   In this transient simulation, the location of maximum axial velocity is not stationary, but instead propagates azimuthally about the eccentric annulus. A "snapshot" at one instant in time is shown in Figure 2-60e-4. Although this example is purely transient, we have included it in our steady eccentric annular flow chapter to highlight the importance (or, perhaps, unpredictability) of transient effects.   The shape of the transient rate curve in Figure 2-60e-3, we emphasize, is obtained for a simple Herschel-Bulkley fluid and not one with "memory" effects.
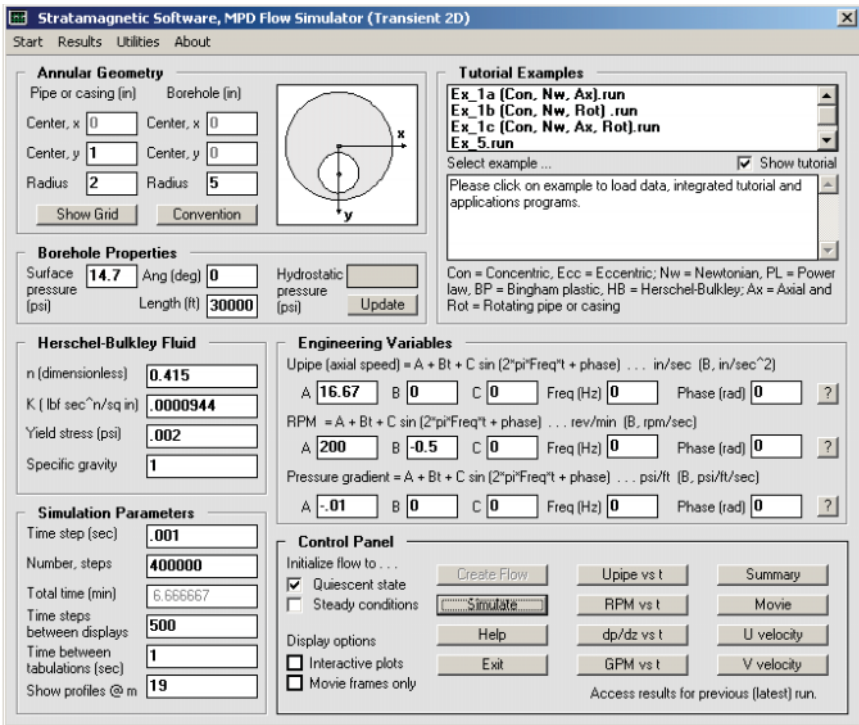

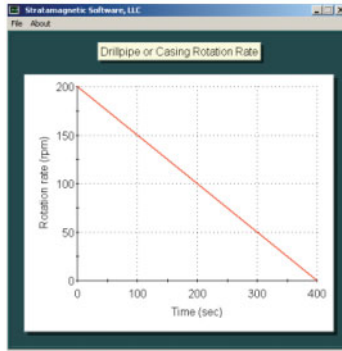**Figure 2-60e-1**. Decreasing rotational rate, from 200 to 0 rpm.

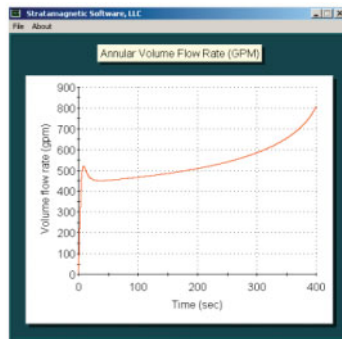**Figure 2-60e-2**. Linearly decreasing rpm, from 200 to 0.

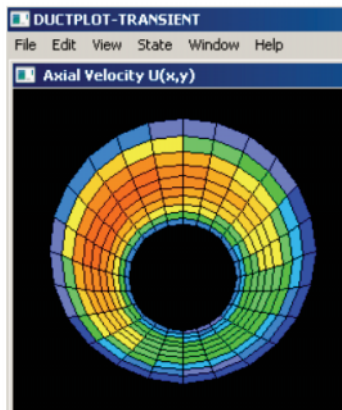**Figure 2-60e-3**. Transient increasing flow rate with decreasing rpm.

Figure 2-60e-4. Transient movement of maximum point
as rpm rotation rate decreases.

Run F. In this example, we consider a complete steady swab-surge application with high annular eccentricity, a nonlinear yield stress fluid, and allow the drillpipe to move axially while simultaneously rotating. This demonstrates our math capabilities and provides a full summary of the menu sequences needed to perform similar calculations. To proceed, the "Swab-Surge Worksheet" is invoked from the main "MPD Flow Simulator (Steady 2D)" in Figure 2-60f-1. In the Worksheet, we consider a five-inch radius hole and a pipe trip-out speed of 5,000 ft./hr. During this operation, we wish to pump continuously, with the surface mud pump rate set at 856.9 gpm. Now, as the drillpipe withdraws from the hole, fluid rushes in to fill the bottom void. The Worksheet shows an effective annular flowrate of 516.9 gpm and a pipe speed of 16.67 in/sec.
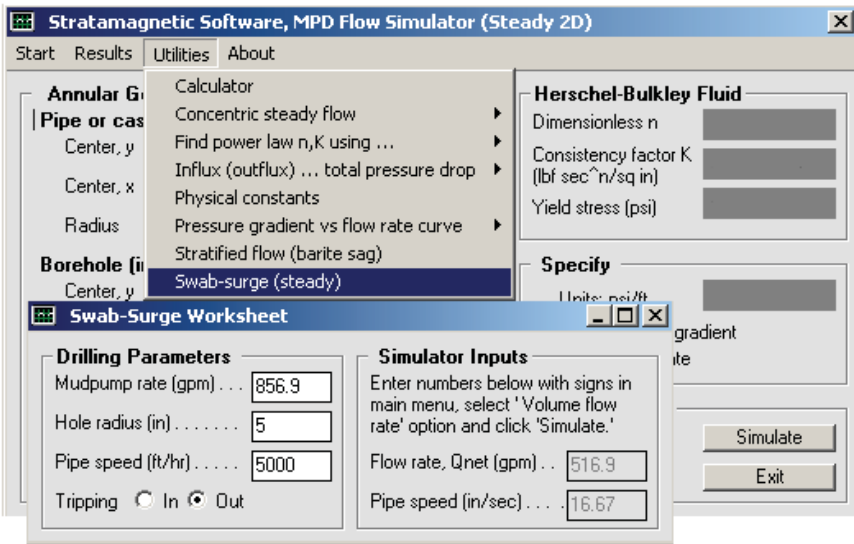

Figure 2-60f-1. Running the "Swab-Surge Worksheet" (areas that do not affect Worksheet calculator are shown shaded)

Now, we study the non-Newtonian flow of a Herschel-Bulkley fluid with $n = 0.415$, $K = 0.0000944$ lbf $\sec^n$/in.^{2} and $\tau_{yield} = 0.002$ psi, in an annulus formed by a 4-inch diameter pipe in a 10-inch diameter hole, with an eccentricity of 0.3333. We demonstrate the solution process for flows without and with rotation. If we wish to consider axial movement only but *without* rotation, we can   run the steady flow calculation in Figure 2-60f-2 in "volumetric flow rate specified" mode. Clicking on "QuikSim" produces the screen output iteration history shown next.

```
SIMULATION STARTS ...
Herschel-Bulkley model, with exponent "n" equal
to 0.4150E+00 and consistency factor of 0.9440E-04
lbf sec^n/sq in.
A yield stress of 0.2000E-02 psi is taken.
Borehole axis radius of curvature is 0.1000E+04 ft.
Axial speed of inner pipe is 0.1667E+02 in/sec.
Target flow rate of 0.5169E+03 gal/min specified.

Iterating on pressure gradient to match flow rate ...

Iteration  100, Error = .00672962
Iteration  200, Error = .00248959
Iteration  300, Error = .00119476
Iteration  400, Error = .00052236
Iteration  500, Error = .00019270
Iteration  600, Error = .00005923
Iteration  700, Error = .00001814
Iteration  800, Error = .00000521
Iteration  900, Error = .00000171
Iteration 1000, Error = .00000047

O  Axial pressure gradient of -.1000E+00 psi/ft
   yields volume flow rate of 0.4076E+06 gal/min.

Flow rate target error is 0.7876E+05 %

Iteration  100, Error = .00371665
Iteration  200, Error = .00067117
Iteration  300, Error = .00014123
Iteration  400, Error = .00002945
Iteration  500, Error = .00000702
Iteration  600, Error = .00000192
Iteration  700, Error = .00000038
Iteration  800, Error = .00000010
Iteration  900, Error = .00000010
Iteration 1000, Error = .00000010

O  Axial pressure gradient of -.5000E-01 psi/ft
   yields volume flow rate of 0.4141E+05 gal/min.

Flow rate target error is 0.7911E+04 %
.
.
.
.

O  Axial pressure gradient of -.6250E-02 psi/ft
   yields volume flow rate of 0.6708E+03 gal/min.

Flow rate target error is 0.2977E+02 %

Iteration  100, Error = .00000000
Iteration  200, Error = .00000011
Iteration  300, Error = .00000000
Iteration  400, Error = .00000011
Iteration  500, Error = .00000011
Iteration  600, Error = .00000011
Iteration  700, Error = .00000000
Iteration  800, Error = .00000021
Iteration  900, Error = .00000011
Iteration 1000, Error = .00000000

O  Axial pressure gradient of -.4688E-02 psi/ft
   yields volume flow rate of 0.5217E+03 gal/min.

Pressure gradient found iteratively, -.4688E-02 psi/ft,
to yield 0.5217E+03 gal/min vs target 0.5169E+03 gal/min.

Note:  Iterations terminate within 1% of target rate.
Refine result by manually changing pressure gradient.
```
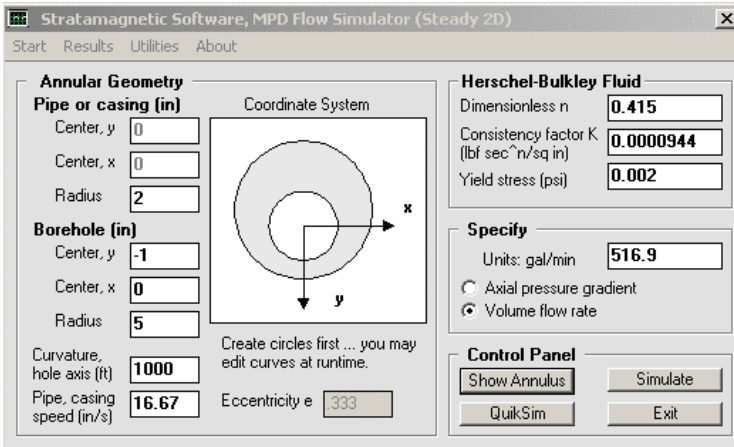
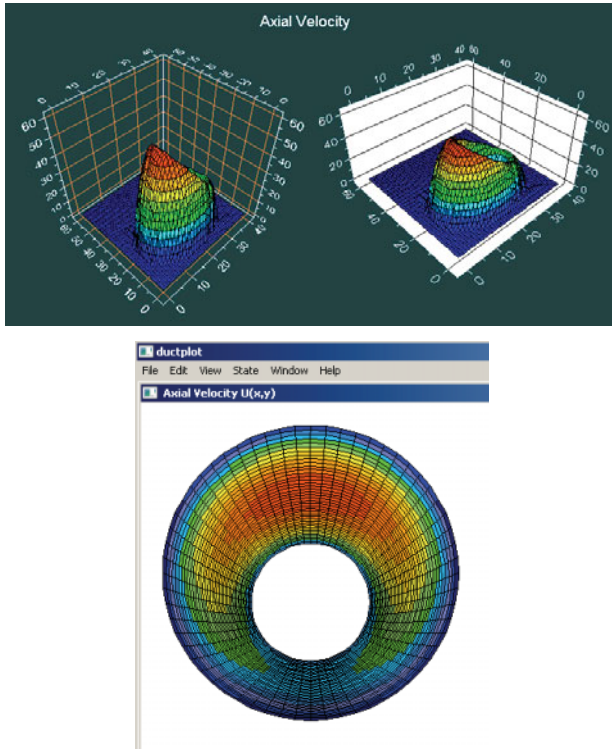**Figure 2-60f-2.** Steady 2D solver.

Figure 2-60f-3. Computed axial velocity (non-rotating).

In other words, the pressure gradient associated with the *non-rotating* flow is – .004688 psi/ft. The corresponding axial velocity field is shown in Figure 2-60f-3 in a variety of available plots. Note that for non-rotating flows, our "Steady 2D" solver automatically computes the required pressure gradient using an internal inverse procedure. It has not been possible to develop a steady solver that allows rotation which is also unconditionally numerically stable. This does not, fortunately, mean that steady rotating flows cannot be computed.
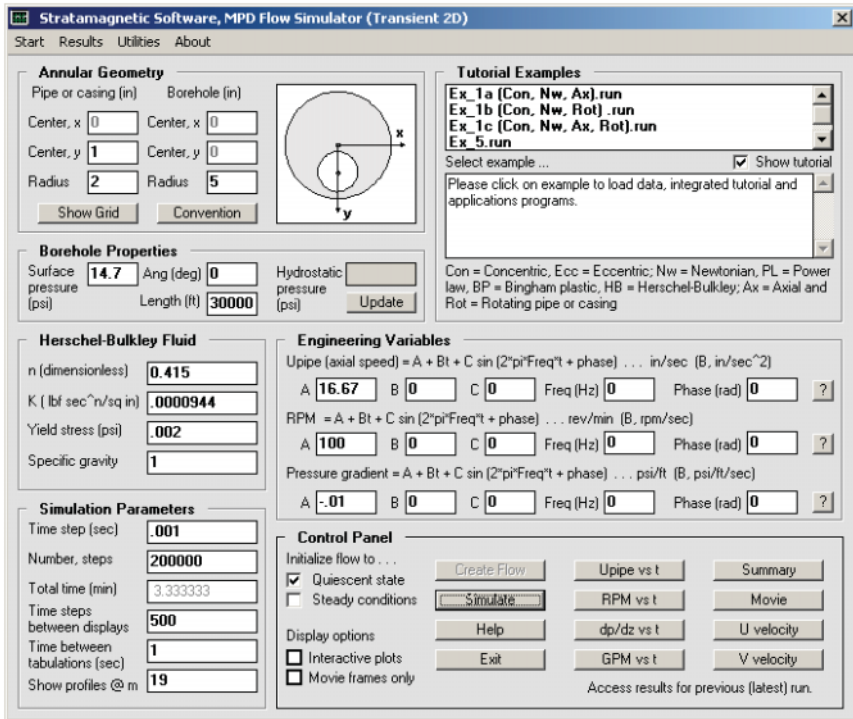

Figure 2-60f-4. Transient 2D solver.

We demonstrate how by considering the effect of a 100 rpm rotational rate. We use the "Transient 2D" solver in Figure 2-60f-4, with input boxes completed for the same simulation parameters. Our strategy is to solve a fully transient problem until steady-state behavior is obtained.

Because a "flow rate specified" mode is not available for transient calculations, one must resort to repeated guesses for pressure gradient, but we have found that three or four will usually lead to a flow rate within 1 to 2 percent of the target value. Since each trial calculation equilibrates quite rapidly, as shown in Figure 2-60f-5, the total "desk time" required is often two minutes or less.

For this rotating flow run, a pressure gradient of – 0.01 psi/ft. is required, as compared to the – .004688 psi/ft. obtained in the non-rotating case. In other words, pressure gradients are twice as severe because of rotation. The "Results" menu in Figure 2-60f-4 provides numerous post-processed results in addition to those of Figure 2-60f-5. For example, axial and azimuthal velocity distributions are available, as given in Figure 2-60f-6, as are detailed color plots of different physical properties like apparent viscosity, shear rate and viscous stress.
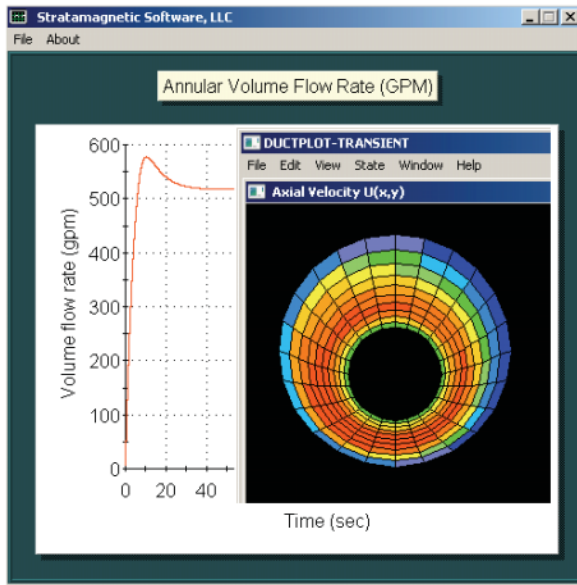

Figure 2-60f-5. Flow rate history and velocity distribution (note, maximum axial velocities appear at annular bottom).
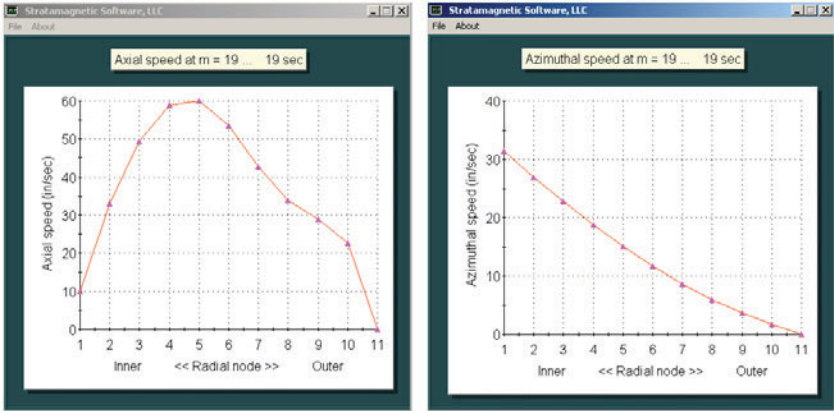
Figure 2-60f-6. Axial and azimuthal velocities at m = 19 cross-section.

2.2.13 Transient swab-surge on a steady-state basis.

Let us recall that the axial momentum equation takes the general form "$\rho\ (\partial u/\partial t + v\ \partial u/\partial y + w\ \partial u/\partial x)\ = -\ \partial p/\partial z + \partial S_{zy}/\partial y + \partial S_{zx}/\partial x$" when body forces and variations in the "z" direction are ignored. The resulting two-dimensional equation applies to transient flows with rotation and axial movement as well as to all rheological models. Techniques are developed in Chin (2012) to integrate this in time and applications are also given. If true transient effects, i.e., those modeled by the "$\partial u/\partial t$" term, can be ignored, the resulting $\rho\ (v\ \partial u/\partial y + w\ \partial u/\partial x)$ $\approx -\ \partial p/\partial z + \partial S_{zy}/\partial y + \partial S_{zx}/\partial x$ underlies the prior work. If continuous but transient flow rate pumping is allowed during tripping, but under quasi-steady conditions, one might ask how the downhole "pressure response versus time" response is constructed. The answer is available in the illustrative procedures developed earlier. We recapitulate the basic ideas, which may or may not be obvious. First, the "flow rate versus pressure gradient curve" is constructed using, possibly, a combination of the steady-state models described, e.g., one that might take the forms in Figure 2-58d-1 or 2-58d-2. At any time $t = t_n$, we have an assumed volumetric flow rate Q_n for which a pressure gradient $(\partial P/\partial z)_n$ is now known. Then, the downhole pressure at the drillbit is simply $P_n = (\partial P/\partial z)_n\ L + P_{surf}\ (t_n)$ where L is the borehole length and $P_{surf}\ (t_n)$ is the surface choke pressure. This $P_n(t_n)$ can be plotted against t_n for display.

2.2.14 Equivalent circulating density (ECD) calculations.

A formula is available for equivalent circulating density (ECD) calculation whose derivation is very straightforward. Again, we start from first principles with $\rho \, (\partial u/\partial t + v \, \partial u/\partial y + w \, \partial u/\partial x) \ = - \, \rho g - \partial p/\partial z + \partial S_{zy}/\partial y + \partial S_{zx}/\partial x$ where we have now included the body force $- \, \rho g$ (where g is the acceleration due to gravity) and assumed "z" to be vertical. The left-side is "ma" while the right is "F" in "F = ma." The first two terms on the right can be factored as $- \, g \, (\rho + 1/g \; \partial p/\partial z)$, from which it is clear that the combination $1/g \; \partial p/\partial z$ has the dimensions of the density, ρ. This is the "equivalent circulating density" because it provides an additive correction to ρ for hydrostatic applications.

When the pressure gradient $\partial p/\partial z$ is available from flow calculations, the formula ECD = $1/g \; \partial p/\partial z$ applies. If the pressure gradient is expressed as N psi/ft, where N is dimensionless, then ECD = 19.25 N lbm/gal. For example, if a viscous non-Newtonian pipe or annular flow is associated with a pressure gradient of - 0.01 psi/ft, then we have ECD = 19.25 (0.01) lbm/gal or 0.1925 lbm/gal (This might be compared to the density of water, with a value of approximately 8.33 lbm/gal.). ECDs provide a useful way for appreciatingpressure gradient magnitudes, but are, in themselves, not fundamentally important in fluid-dynamics. However, they are useful in MPD job planning.

2.3 References.

- Chin, W.C., *Borehole Flow Modeling in Horizontal, Deviated and Vertical Wells*, Gulf Publishing, Houston, 1992.

- Chin, W.C., *Computational Rheology for Pipeline and Annular Flow*, Elsevier Science, London, 2001.

- Chin, W.C., "Modeling and Simulation of Managed Pressure Drilling for Improved Design, Risk Assessment, Training and Operations," *RPSEA Ultra-Deepwater Technology Conference*, Houston, Tx, June 22-23, 2010.

- Chin, W.C., "Flow Simulation Methods for Managed Pressure Drilling and Cementing," *Drilling and Completing Trouble Zones Conference*, Galveston, Tx, Oct. 19-21, 2010.

- Chin, W.C., *Managed Pressure Drilling: Modeling, Strategy and Planning*, Elsevier, Amsterdam, 2012.

- Chin, W.C., *Managed Pressure Drilling: Modeling, Strategy and Planning*, Chinese Edition, Elsevier, Singapore, 2017.

- Chin, W.C., and Zhuang, X., "Exact Non-Newtonian Flow Analysis of Yield Stress Fluids in Highly Eccentric Borehole Annuli with Pipe or Casing Translation and Rotation," Paper 131234-PP, *CPS/SPE International Oil & Gas Conference and Exhibition*, Beijing, China, June 8-10, 2010.

- Chin, W.C., and Zhuang, X., "Effect of Rotation on Flowrate and Pressure Gradient in Eccentric Holes," Paper AADE-11-NTCE-45, *AADE 2011 National Technical Conference and Exhibition*, Houston, TX, April 12-14, 2011 (a).

- Chin, W.C., and Zhuang, X., "Advances in Swab-Surge Modeling for Managed Pressure Drilling," Paper AADE-11-NTCE-46, *AADE 2011 National Technical Conference and Exhibition*, Houston, TX, April 12-14, 2011 (b).

- Chin, W.C., and Zhuang, X., "Transient, Multiphase, Three-Dimensional Pumping Models for Cementing and Drilling," Paper AADE-11-NTCE-72, *AADE 2011 National Technical Conference and Exhibition*, Houston, TX, April 12-14, 2011 (c).

- Chin, W.C., and Zhuang, X., "Comprehensive Annular Flow Models for Drilling and Completions," Paper AADE-11-NTCE-73, *AADE 2011 National Technical Conference and Exhibition*, Houston, TX, April 12-14, 2011 (d).

- Chin, W.C. and Zhuang, X., "Advances in Swab-Surge Modeling for Managed Pressure Drilling," Paper OTC-21115-PP, *2011 Offshore Technology Conference*, Houston, TX, May 2-5, 2011 (e).

3
Transient Single-Phase Flows

We will show how non-Newtonian flows in highly eccentric annuli can be computed under general transient conditions with the drillstring or casing undergoing arbitrary coupled reciprocation and rotation in the presence of pressure changes in the mud pump. Thus, the drillpipe may rest near the formation, risking economic losses due to cuttings transport inefficiencies and stuck pipe. Aside from its role in pressure loss and velocity field calculations, our simulator capabilities are also important in jarring applications, with the effects of flow rate ramp-up and ramp-down accounted for.

An important use of the transient algorithm introduced here does not include truly unsteady flow at all. In steady flow problems with non-zero constant rotation rate, an unconditionally stable numerical solution is not presently available in the literature; in fact, purely steady methods destabilize as specific gravity and rpm values approach those used in field practice. In this chapter, we show how steady-state flows with constant rotation rates can be computed as steady asymptotic limits of highly transient problems. An application in Chapter 2 had applied this transient method to steady-state swab-surge where pipe rotation was significant. Because rotation significantly affects pressure fields, the algorithm described here is extremely important and represents the only available method dealing with rotation issues.

We will first design examples to validate the integration method by seeking agreement with known analytical solutions.   The effects of rotation are studied for Newtonian flows (which, because of constant viscosities, never exhibit shear-thinning) as well as non-Newtonian fluids. Foams as well as heavy muds are considered. Then, the separate effects of transient pipe reciprocation, unsteady pipe rotation and general mud pump flow variation are considered, and finally, all three simulation modes are permitted.   Importantly, the analytical and numerical formulations are constructed in such a manner that the least and most complicated applications require almost identical rapid computing times. More general transient capabilities can be developed by simply modifying modularized Fortran subroutines.

3.1   Validation runs, three different approaches to steady, Power law, non-rotating, concentric annular flow.

Before studying transient effects in detail, we explore the accuracy of three different methods we have developed in the limit of steady, non-rotating, concentric, non-Newtonian Power law flow. Specifically, we consider an inner radius of 2 in, an outer radius of 4 in, $n = 0.8$, $K = 0.00001375$ lbf sec^n/sq in. and a pressure gradient of $– 0.02388$ psi/ft. In the first case, we run the finite-difference-based simulator based on curvilinear meshes in QuikSim fine-mesh mode to find a flow rate of 1,494 gpm, as shown in Figure 3-1a (this simulator *does* allow for pipe or casing axial movement and yield stress modeling).

Next, we consider the simulator used for rotating, Power law flow, noting that it does not allow axial pipe movement. Approximations were employed to facilitate closed form analytical solutions in Chin (2012); the nature of the math used does not allow "0 rpm" to be entered directly, so a value of "1" is used instead (this simulator also will not model Newtonian flows with $n = 1$). The software produces a solution of 1,491 gpm, as shown in Figure 3-1b. Finally, we use the *exact* Herschel-Bulkley solver, which assumes a completely immobile inner pipe, running it in the limit of vanishing yield stress; this gives a solution of 1,523 gpm, as shown in Figure 3-1c. The difference between the largest and smallest predictions is about 2 percent, which is reassuring given that the three models are derived from completely different assumptions and methods.
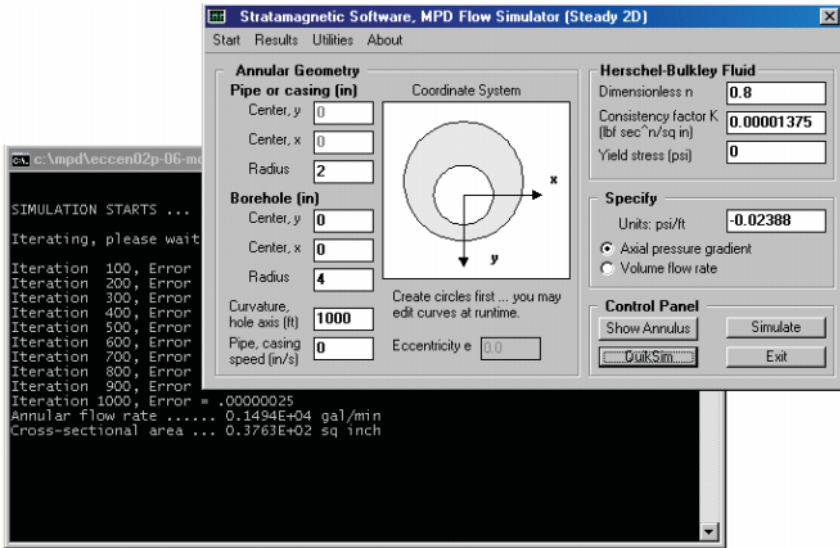
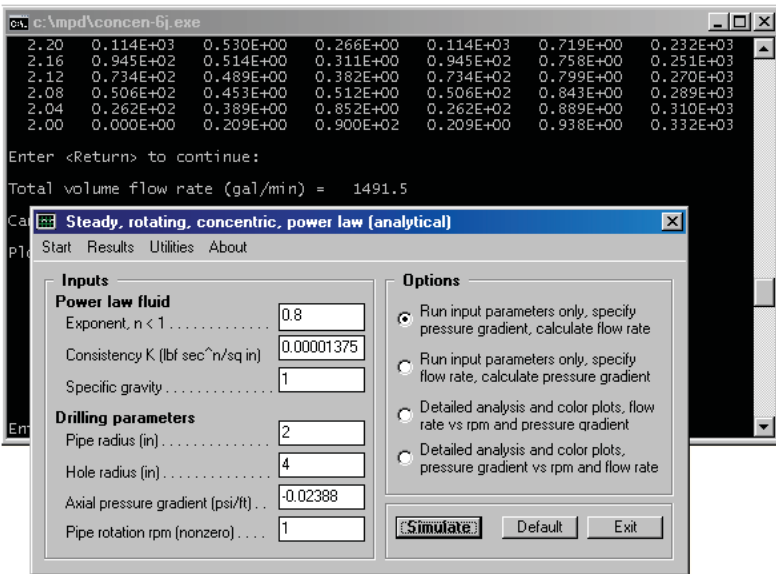**Figure 3-1a.** Finite-difference curvilinear grid simulator result.

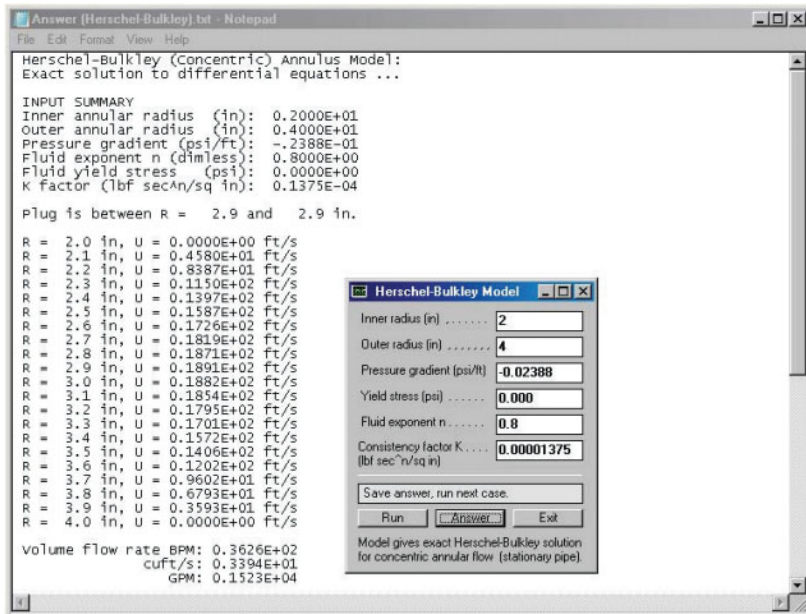**Figure 3-1b.** Rotating, Power law approximate flow result.

Figure 3-1c. Herschel-Bulkley simulator, *exact* results.

3.2 Validation run for transient, Newtonian, non-rotating, concentric annular flow.

The excellent agreement obtained in Example 3.1 between three completely different steady flow models should provide a strong degree of user confidence. In the present validation example, we consider Newtonian, non-rotating, concentric annular flow, for which an exact, closed form, steady solution of the Navier-Stokes equation is available using the simulator in Figure 3-2a. Here, inner and outer radii are 3 and 6 inches, respectively, and a viscosity of 1 cp and a pressure gradient of - 0.0001 psi/ft. are assumed. This simulator also allows axial pipe movement, but we disallow it in the validation below. Figure 3-2a shows that the flow rate is 947.1 gpm.

Now we use the finite-difference-based, curvilinear grid, transient simulator in Figure 3-2b to show how the large-time solution of a transient problem is consistent with the steady-state solution obtained above from an analytical method. We have assumed a very small specific gravity of 0.01. As will be seen, this allows finite difference numerical solutions to achieve steady-state rapidly, since in the non-

rotating case, the dependence on density vanishes – small densities, in fact, imply small mechanical inertias for fast equilibration. The asymptotic flow rate is 928.4 gpm, for a small 2 percent error. Importantly, the unsteady model shows that the physical time scale required to achieve this steady condition, starting from a quiescent state, is about 30 sec. (the computation requires about fifteen seconds). The reader should note the inputs used. Also, the "engineering variables" hidden by the graph are identically zero.
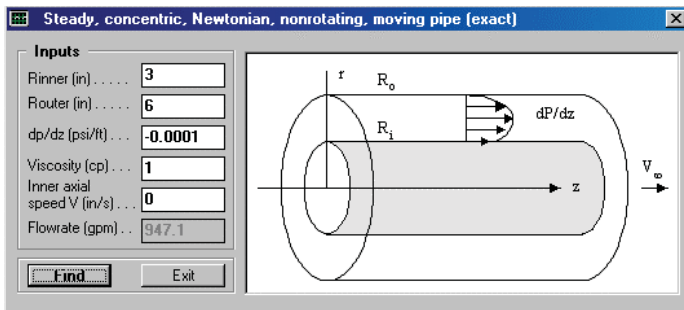
Figure 3-2a. Exact, steady, Newtonian flow solution.

In Figure 3-2c, we re-run the foregoing simulation with all inputs unchanged except that the specific gravity is increased to 2.0, corresponding to a heavy 16.7 lbm/gal mud, and the time step is increased to 0.005 sec. The same asymptotic flow rate of 928.4 gpm is achieved and the time scale to attain steady-state from quiescent conditions is about one hour (the simulation itself, for 1,200,000 time steps, requires about four minutes of computing). The transient simulator illustrates the role of inertia in establishing steady conditions.

We have demonstrated that our transient finite difference results are consistent with the exact analytical steady solution (We used our curvilinear grid approach and considered both low and high specific gravity runs.). Importantly, if transient analysis is used to find steady flows, at least in non-rotating problems, then low specific gravity fluids should be assumed because low mechanical inertias lead to very rapid physical equilibration.

Figure 3-2b. Low specific gravity transient solution.
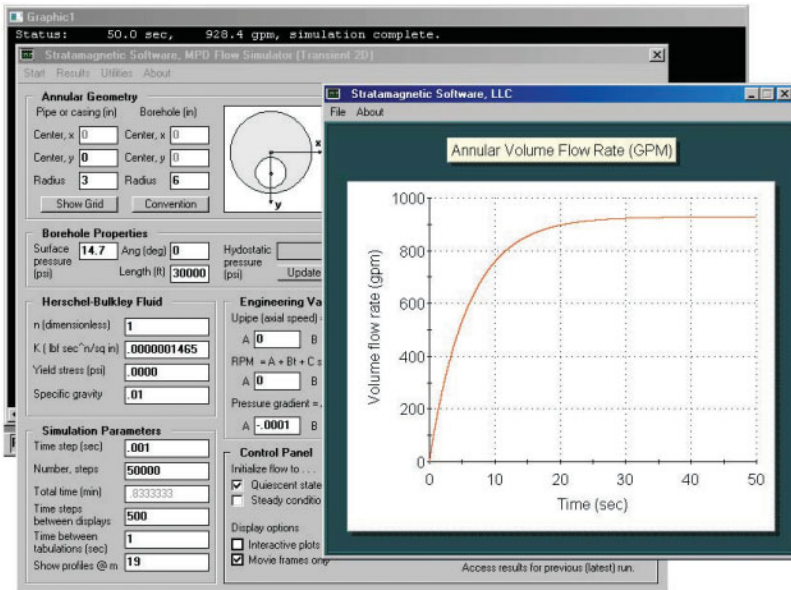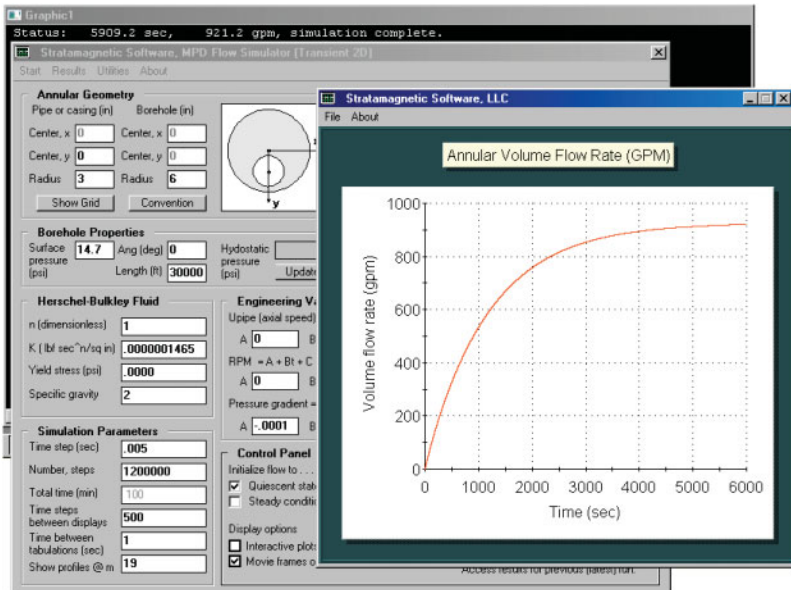

Figure 3-2c. High specific gravity transient solution.

3.3 Validation run for transient, Newtonian, non-rotating, eccentric annular flow.

In this consistency check, we examine *eccentric* annular flows, for which no analytical or exact solutions are available. We assume a Newtonian fluid with a viscosity of 10 cp, and also, that the pipe is not rotating or moving axially. The transient solution in Figure 3-3a requires about five seconds of computing time, and yields an asymptotic steady-state flow rate of 107.2 gpm.
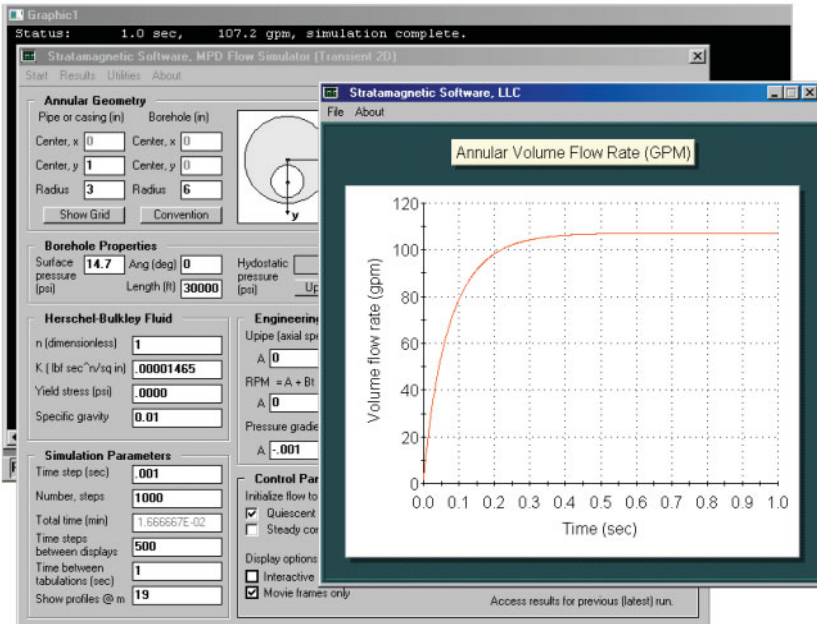
Figure 3-3a. Transient, Newtonian, non-rotating flow solution.

The complementary steady flow computation in Figure 3-3b, using the same 25 × 11 mesh, yields an identical 107.2 gpm, much better than this author had anticipated. This is all the more remarkable because the steady solver uses an iterative, implicit, successive line over-relaxation (SLOR) method whereas the transient method uses an explicit time integration procedure. Note that the QuikSim fine mesh solution yields 109.2 gpm, for less than a 2 percent difference. That the two final results for unsteady and steady flow are consistent bodes well for our transient and steady solvers.

Again, we emphasize that the steady flow solver handles constant axial pipe speed motion without rotation, while the unsteady solver handles coupled axial and rotary movement, both under general transient conditions.
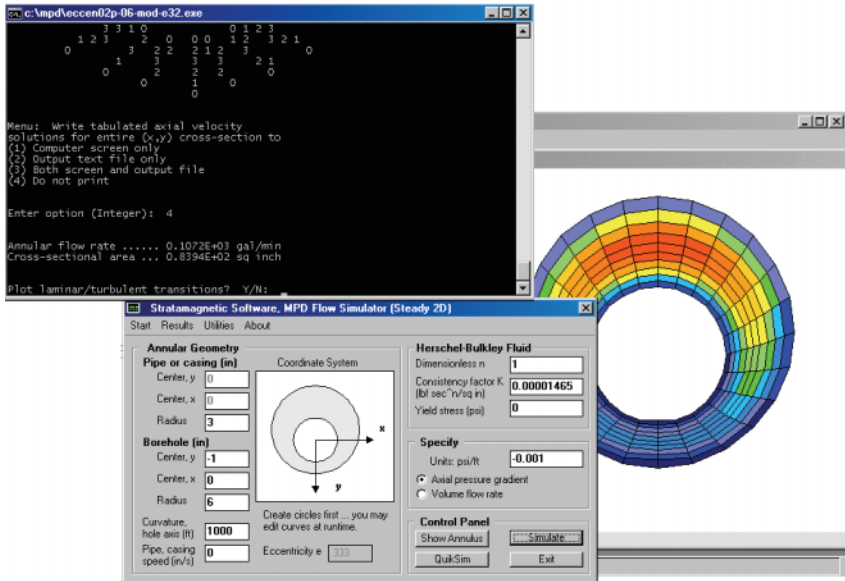
Figure 3-3b. Steady flow computation on identical mesh.

3.4 Effect of steady rotation for laminar Power law flows in concentric annuli.

In this example, we use our closed form analytical solution developed for steady, rotating, Power law fluids in *concentric annuli* to explore pressure gradient and flow rate relationships in a non-Newtonian application. The user interface is shown in Figure 3-4a where the third option is selected. Using automatically defined internal parameters, this simulation plots flow rate (gpm) on the vertical axis and pressure gradient (dp/dz) and rotational rate (rpm) on the two horizontal axes, as shown in Figure 3-4b. It is clear from this figure that as the (absolute value of) pressure gradient increases for fixed rpm, flow rate increases, as would be expected. Interestingly, as the rotational rate increases at fixed dp/dz, the flow rate also increases. This is explained by the reduction in apparent viscosity induced by rotation due to shear-thinning.

This result also appears in several related and well known investigations external to the petroleum industry. It is, importantly, consistent with the results of classical studies reported in the well-regarded book *Dynamics of Polymeric Liquids* by Bird, Armstrong and Hassager (1987). Their Example 4.2-5 conclusion "shows that the flow in the axial direction is enhanced because of the imposed shearing in the tangential direction, since this additional shearing causes the viscosity to be lowered." The numerical analysis by the respected authors Savins and Wallick (1966) also supports our findings. From their Abstract, "the most interesting consequence of the coupling effect is that the axial flow resistance is lowered in a helical flow with the result, for example, that for a given applied axial pressure gradient, the axial discharge rate in a helical flow field is higher than in a purely annular flow field." In the analysis, the authors observe that "it is seen that the effect of a helical flow produced by impressing a relative rotation on the z directed annular flow is to increase the axial discharge rate. This result is not unexpected. The preceding viscosity profile analyses showed that the shear-dependent viscosity is lowered, hence the axial flow resistance is lowered." Finally, from their Summary, "in contrast, if the fluid were Newtonian the superimposed laminar flows would be non-interfering in that there would be no coupling among the discharge rate, axial pressure gradient, relative rotation, and torque through the viscosity coefficient." Recall that we have proven this latter observation directly from the governing Navier-Stokes equations. Several subsequent theoretical and experimental petroleum publications also support the foregoing results.

It is important to emphasize that, in all of the above works and in the present Example 3.4, laminar, *concentric* annular flows are considered. For concentric flows, the nonlinear inertia (or convective) terms in the governing momentum equations vanish identically and velocity coupling is possible only through changes to apparent viscosity or shear-thinning. Early publications focused, fortuitously, on this limit – from the mathematical perspective, for simplicity, and from the drilling perspective, by the vertical well applications prior to 1990. In the past two decades, with deviated and horizontal wells becoming predominant in exploration, conflicting relationships between pressure gradient and flow rate have been reported. These conflicts arise because of annular eccentricity. In general non-Newtonian flows, shear-thinning is always present; however, when eccentricity exists, the applied pressure gradient is effectively modified by a spatially-dependent convective term that is

proportional to fluid density and rotational rate.   The complicated interplay between flow rate, applied pressure gradient, fluid rheology, rotational rate and annular geometry cannot be described by casual "rules of thumb;" however, it can be obtained as the solution of coupled nonlinear partial differential equations as described in this book and particularly in this chapter.

Let us return for now to concentric annular flow analysis. Figure 3-4c provides a different view of the results from that provided by Figure 3-4b. It is obtained by selecting the last option in Figure 3-4a. Note that each figure uses hundreds of solution points, and both are produced, because analytical solutions are used, in less than one second of computing time. Again, the increase in flow rate (for a fixed pressure gradient) obtained when rotational rate increases is well accepted in the older literature, but confusion and inconsistencies have arisen in recent studies, a point we address in several examples next.
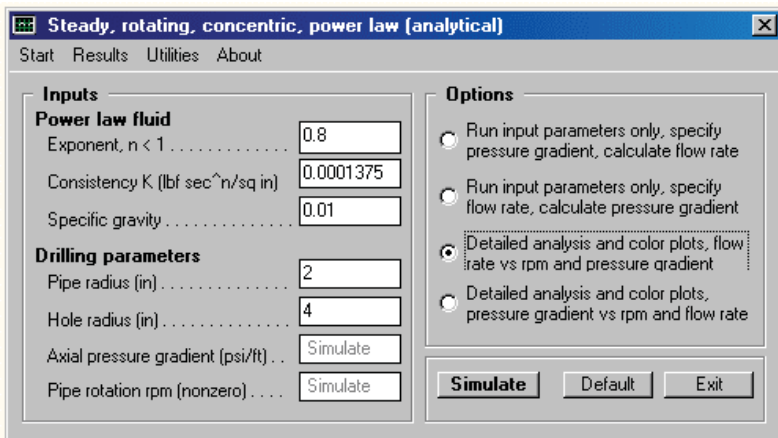

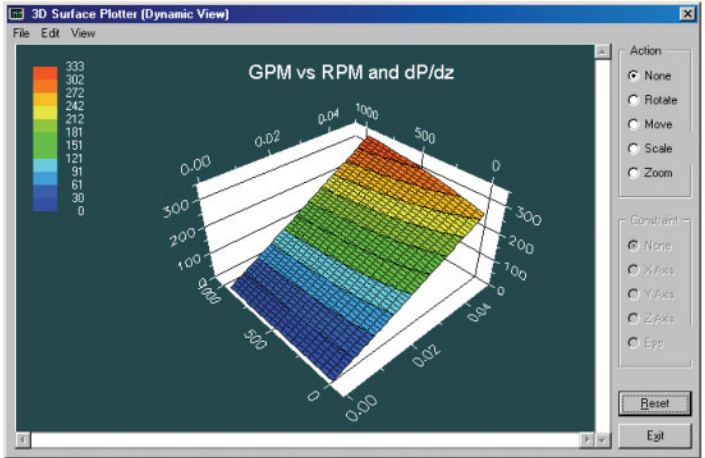**Figure 3-4a.** Steady, rotating, Power law simulator.

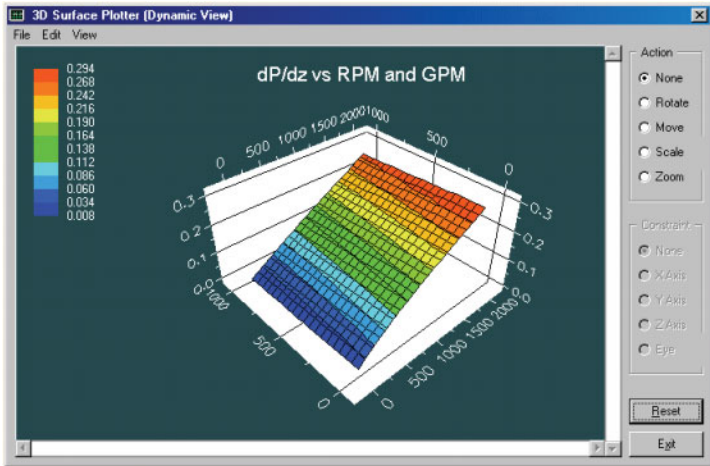**Figure 3-4b.** GPM versus RPM and dp/dz.

Figure 3-4c. dp/dz versus RPM and GPM.

3.5   Effect of steady-state rotation for Newtonian fluid flow in eccentric annuli.

Here we consider the effects of annular eccentricity. To isolate rheological effects, we assume a Newtonian fluid with constant viscosity so shear-thinning is impossible. The eccentricity is 0.333. As a validation point, we first obtain the flow rate under non-rotating conditions using the steady-state, curvilinear grid flow solver in Figure 3-5a. For the assumptions shown, the flow rate is 109.2 gpm (the parameters corresponding to the "engineering variables" not shown are identically zero). Next, we run the transient simulator for the same non-rotating flow conditions, as shown in Figure 3-5b, to obtain a nearly identical flow rate of 107.2 (the difference is less than 2 percent). The agreement is excellent.

Now, we importantly ask, "What if the drillpipe or casing were rotated? Does the flow rate increase or decrease, assuming the same pressure gradient?" In Figure 3-5c, we assume a somewhat high 400 rpm to demonstrate numerical stability, but also the fact that the asymptotic steady flow rate *decreases* to 99.4 gpm, a flow rate reduction of about 8 percent. Thus, in the complementary problem where flow rate is specified and pressure gradient is to be determined, we can expect to see similar order-of-magnitude increases to pressure drop.   These changes are significant to drilling safety in managed pressure drilling.

The exact decrease or increase depends on rheological and geometric parameters, and will vary from run to run. Differences as high as 50 percent have been observed. But why did flow rate increase in Example 3-4 but decrease here? The explanation is simple. In the previous example, the gpm increase was due to a decrease in non-Newtonian apparent viscosity arising from rotation; also, for concentric annuli, the inertia terms in the axial momentum equations vanish identically.   In this example, the viscosity is constant and does not change.   A non-vanishing "$\rho v/r \; \partial U/\partial \theta$" inertia term is new.   The azimuthal velocity v is proportional to rpm, while $\partial U/\partial \theta$" is related to eccentricity.   The term acts as a spatially variable pressure gradient modifier.   These reasons are subtle but clear when we examine the governing partial differential equations. We chose Newtonian fluids in this example to isolate rheological effects in order to ascertain the importance of the rotating flow inertia terms alone.
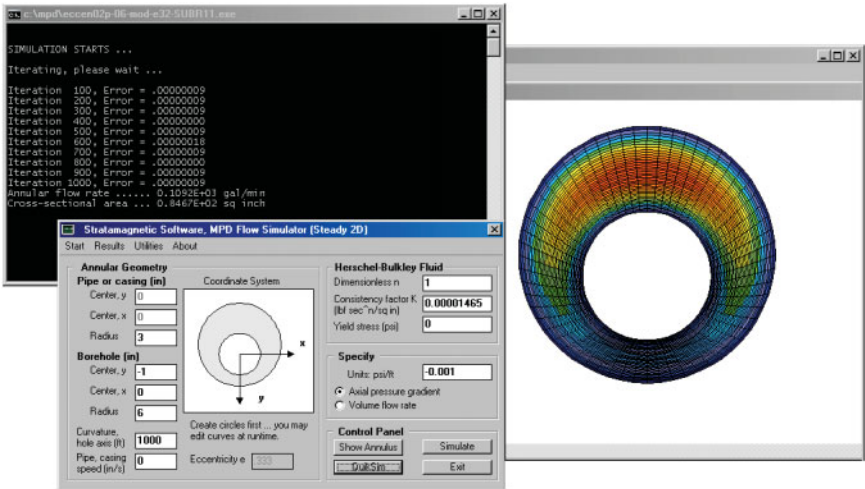
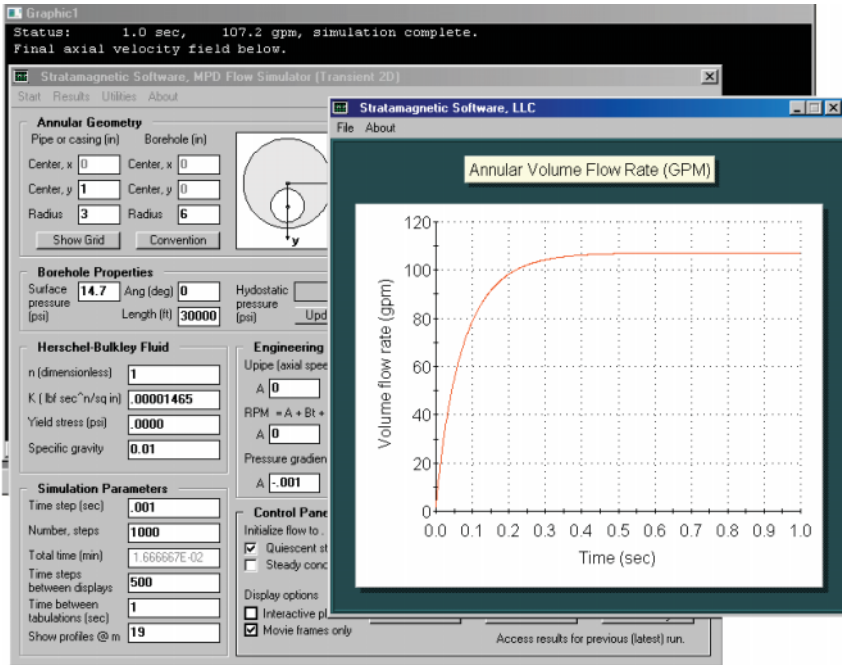**Figure 3-5a.** Steady-state solution without rotation.

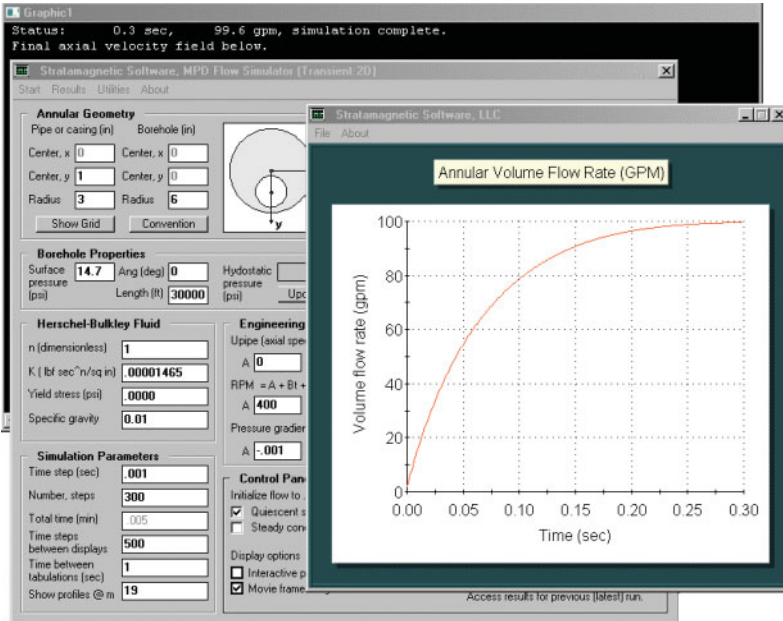**Figure 3-5b.** Transient Newtonian solution without rotation.

Figure 3-5c. Transient rotating solution from quiescent state (the curve actually peaks at 100 and then asymptotes to 99.4 gpm).
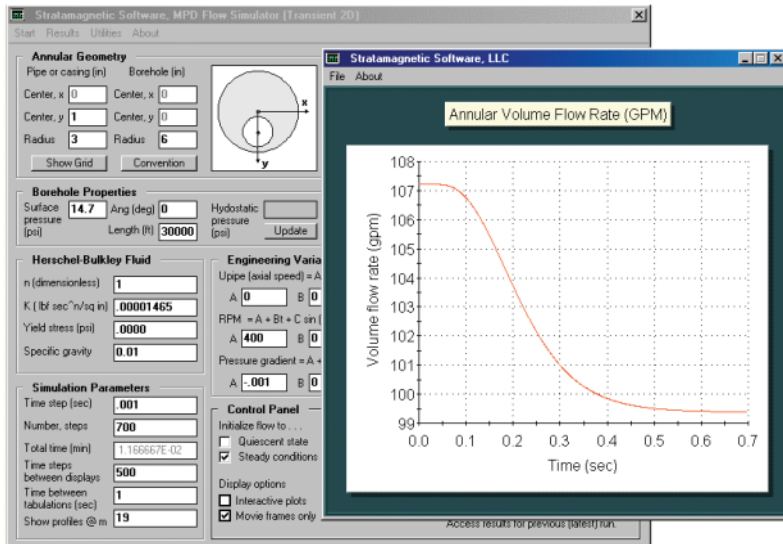
Figure 3-5d. Transient rotating solution from flowing state.

In the Control Panel of Figure 3-5b, we checked "Initialize flow to quiescent state." This assumes vanishing initial flow. We now check "steady conditions" for our starting point. The simulator first calculates a steady non-rotating flow, and then at t = 0, uses this flow to initialize time integrations. This corresponds to a non-rotating pipe with flow that is suddenly rotated. Figure 3-5d shows how the flow rate decreases suddenly from 107.2 gpm to 99.4 gpm, highlighting the effects of rotation (computing time is about one second). Even for this high rotational rate, the transient algorithm for coupled axial and azimuthal movement is fast and stable. Our results demonstrate the usefulness of numerical simulation in drilling safety and operations.

3.6 Effect of steady rotation for Power law flows in highly eccentric annuli at low densities (foams).

The annulus in Figure 3-5a, while not concentric, is not highly eccentric. In this example, we examine a cross-section with high eccentricity and also allow for nonlinear Power law fluid motion. Here, the eccentricity is 0.5. Results for a non-rotating pipe are given in Figure 3-6a, where a steady flow rate of 1,052 gpm is indicated. The time required to achieve steady-state is approximately one second. What happens if we rotate the drillpipe at 300 rpm? Figure 3-6b shows that with rotation, the time to reach steady conditions is reduced; also, the flow rate decreases to 905.8 gpm. This suggests that in the complementary problem when volumetric flow rate is fixed, the effect of rotation is to increase (the absolute value of) pressure gradient. Consistent with the previous example, the decrease in flow rate occurs because of inertia effects. We emphasize that the flow rate reduction due to rotation seen here is a sizeable 16 percent. Finally, in Figure 3-6c, we re-run the simulation with the initial fluid assumed to be non-rotating and flowing. The results show an equilibration time of one second between steady-states so that flow changes are sudden and dangerous. The steady-state flow rate is again about 900 gpm. There is a "bump" in the gpm versus time curve, one seen repeatedly in many such simulations. Whether or not this effect is real will require laboratory observation. All of the calculations for this example were performed stably, as our line graphs show, and required only 2 to 3 seconds of computing time.
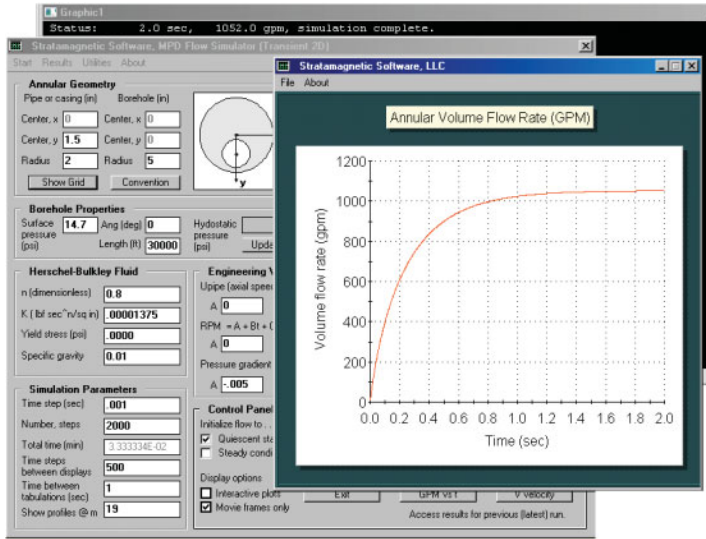
Figure 3-6a. Power law flow with non-rotating pipe.
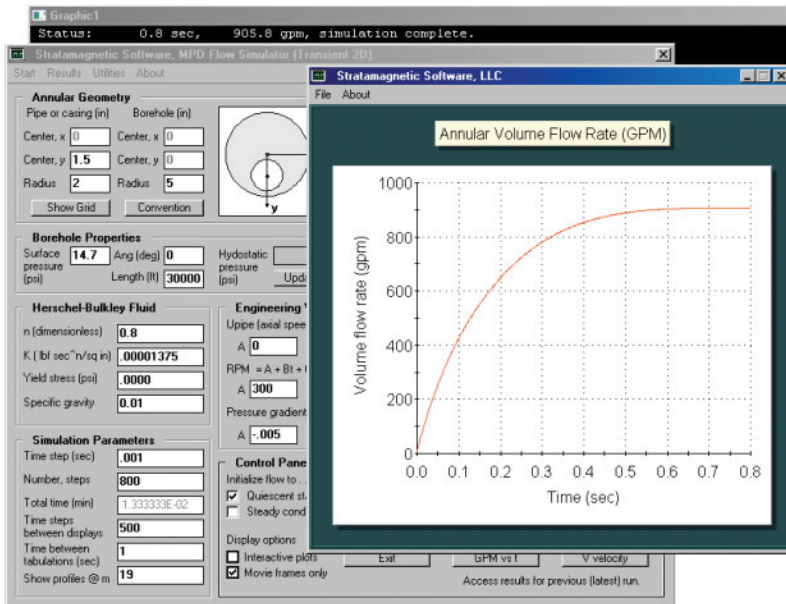
Figure 3-6b. Power law flow with rotating pipe (zero starting conditions).
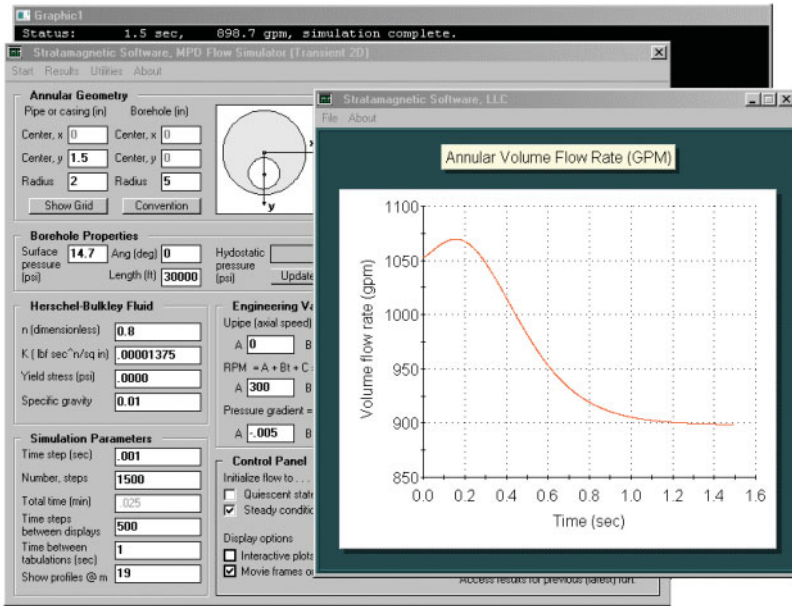
Figure 3-6c. Power law flow with rotating pipe (from flowing conditions).

It is important to point out some important software details associated with flow initialization. For steady flow formulations, the initial state of the flow does not appear as a parameter because there is no variation in time (Actually, it does in a numerically sense, since initial solution guesses are taken, although internally to the software.). For transient formulations, the initial state must be specified. If quiescent stagnant-flow conditions are selected, the box shown in Figure 3-6d is checked and "Simulate" can be clicked immediately.
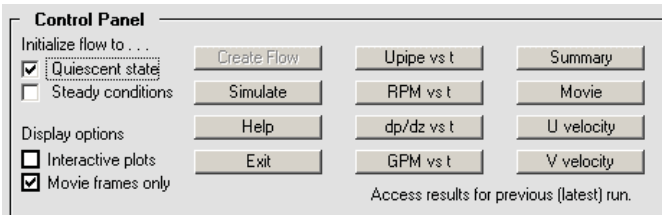
Figure 3-6d. Assuming quiescent, stagnant-flow initial conditions.

On the other hand, the fluid may be moving initially at t = 0, and *then*, the transient flow specifications shown in the user interface is applied. If the initial flow is not rotating, we know that its solution does not depend on density; we can therefore calculate it assuming a very small value of ρ together with large time steps. If we wish to initialize to a non-rotating steady flow, the message box in Figure 3-6e appears, reminding the user to click "Create Flow" to start this process. Once this is completed, the "Simulate" button can be clicked to perform the required transient analysis.
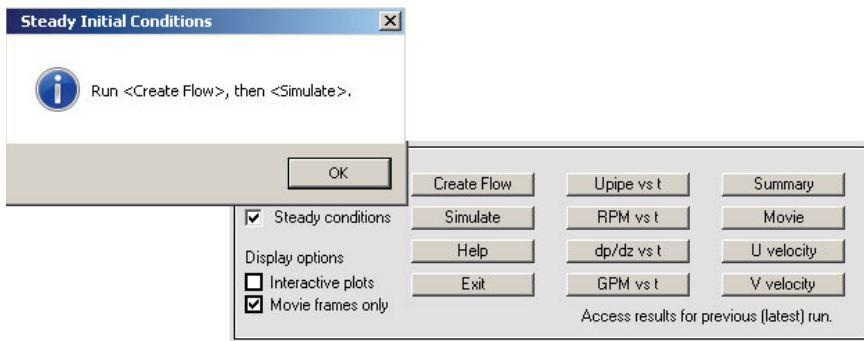
Figure 3-6e. Creating a non-rotating, steady initial flow.

If the starting flow is rotating, its solution does depend on density and time steps will need to be very small to ensure convergence. This initialization is not supported at the present time because the solution procedure cannot be made as robust or automatic as desired by the author, but continuing research is being pursued in this area.

3.7 Effect of steady rotation for Power law flows in highly eccentric annuli at high densities (heavy muds).

We emphasized earlier that for non-rotating flows, the effects of density vanish at large times. Thus, in computing non-rotating steady-state flows with the transient algorithm, it is advantageous to use as small a fluid density as possible in order to quickly converge the calculations. Here we wish to evaluate the effects of mud weight under rotating conditions. For the non-Newtonian eccentric flow in Figure 3-7a, a very low specific gravity of 0.01 leads to a flow rate of 898.5 gpm. Next we wish to consider the opposite extreme, e.g., a heavy mud or cement with a specific gravity of two.

Because the unstable convective term never vanishes when the pipe rotates (Its magnitude is proportional to fluid density and pipe rpm.), we decrease the time step to 0.0001 sec. and increase the number of time steps simulated. The resulting flow rate is a much lower 135.1 gpm. Computation times for the two runs are five seconds and two minutes, approximately. Finally, we reduce the specific gravity to 1.0, i.e., an unweighted mud. Will the flow rate vary linearly with density, that is, fall midway between 135.1 and 898.5 gpm? Figure 3-7c shows that the flow rate is, in fact, 160.1 gpm. This unpredictability shows why computer models are important to real-world field job planning.
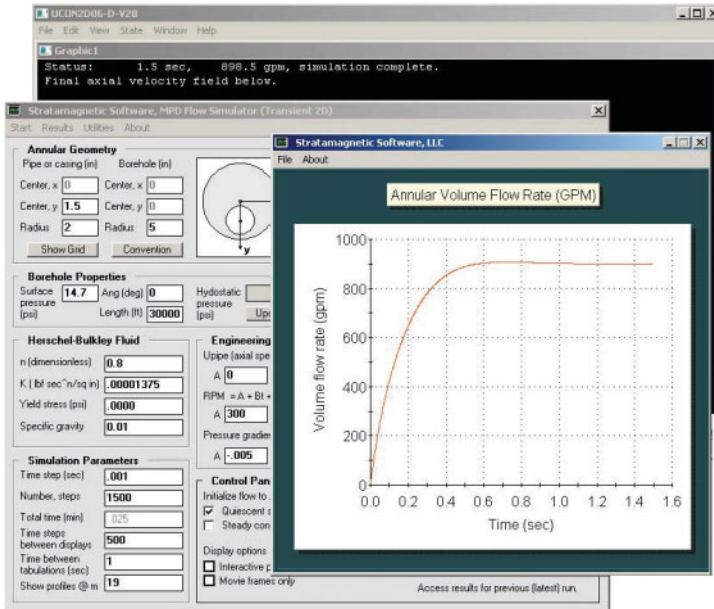
Figure 3-7a. Very low density fluid (e.g., foam) at high rpm.
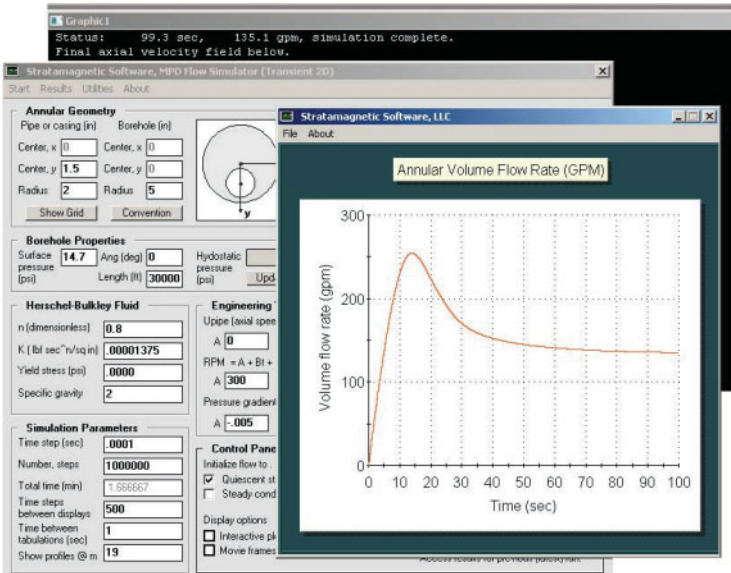
Figure 3-7b. Very high density fluid (e.g., heavy mud or cement) at high rpm.
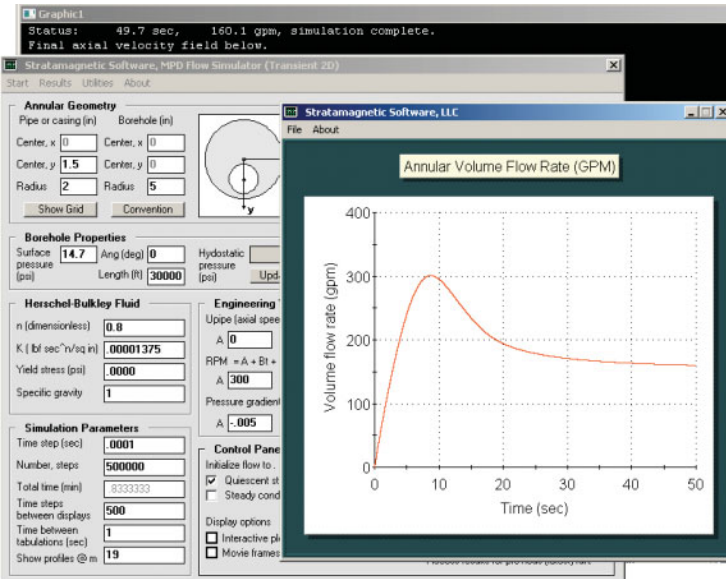
Figure 3-7c. Unweighted fluid (e.g., water or brine) at high rpm.

3.8   Effect of mud pump ramp-up and ramp-down flow rate under non-rotating and rotating conditions.

In Figure 3-8a, we consider a Power law fluid in an eccentric annulus under a constant imposed pressure gradient of – 0.005 psi/ft. with the drillpipe completely stationary.   This is seen to produce a steady-state flow rate of 1,051.8 gpm as shown.   In practice, the mud pump starts and stops, and transient effects are associated with ramp-up and ramp-down.   We ask, "How are pressure gradient and flow rate transient properties related?"
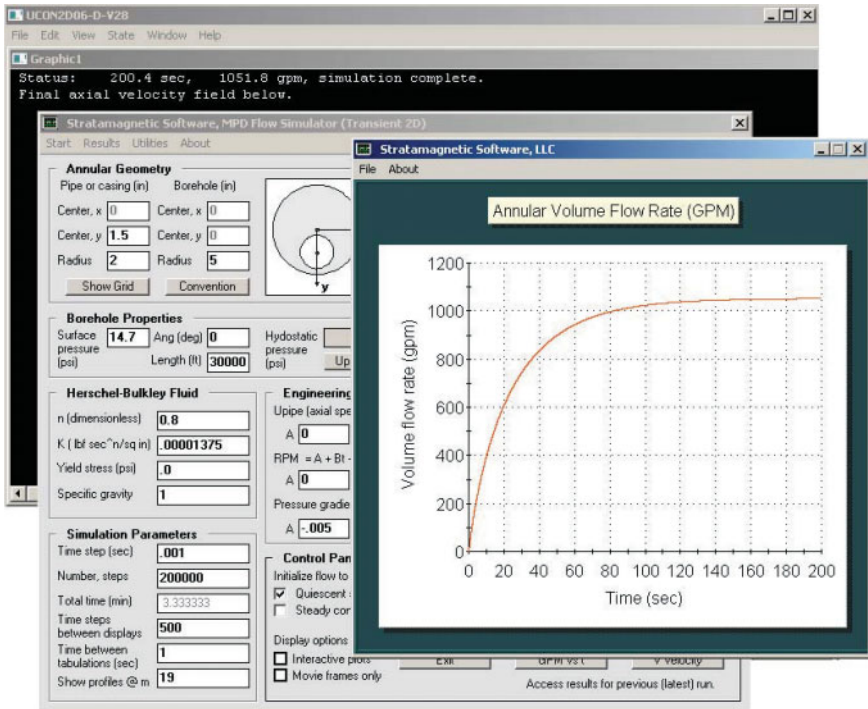
Figure 3-8a. Constant pressure gradient calculation.

To answer this question, we modify several menu entries of Figure 3-8a so that the pressure gradient is no longer constant.   The assumption shown in Figure 3-8b allows a sinusoidal ramp-up from quiet conditions to our previous value of – 0.005 psi/ft, followed by a full ramp-down. This is accompanied by time mesh refinement plus the use of additional time steps.

Clicking on the "?" to the far right of the pressure gradient menu produces the left-side diagram of Figure 3-8c showing pressure assumptions. The right-side diagram gives the computed volumetric flow rate as a function of time.

Next, we determine the effect of drillstring rotation. We simply change the zero rotation input in Figure 3-8b to allow for a 100 rpm rotational rate as shown in Figure 3-8d. For the same pressure gradient variation as above, the flow rate is now substantially reduced as shown in Figure 3-8e.
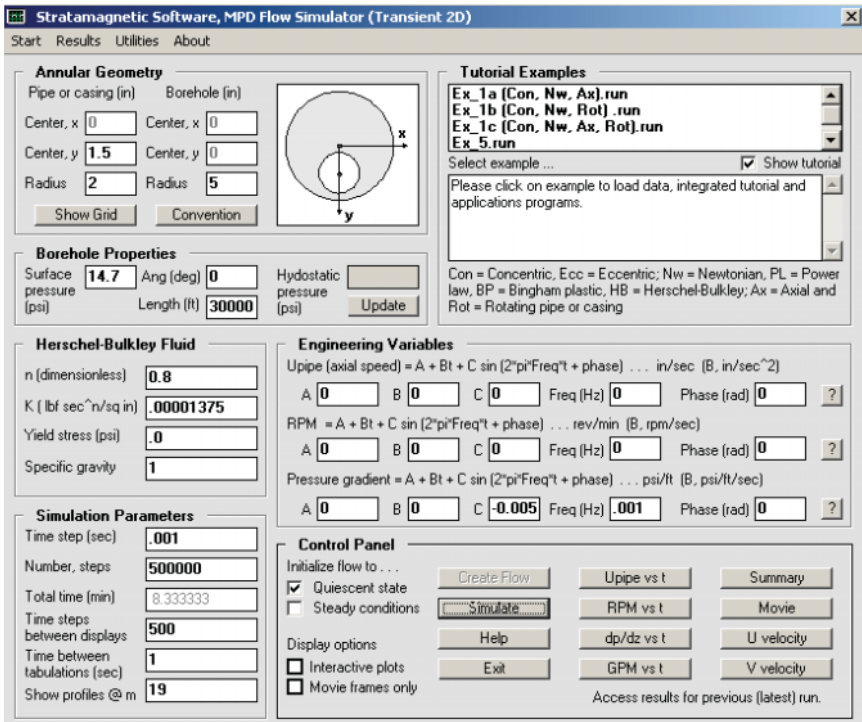
Figure 3-8b. Mud pump ramp-up and ramp-down.
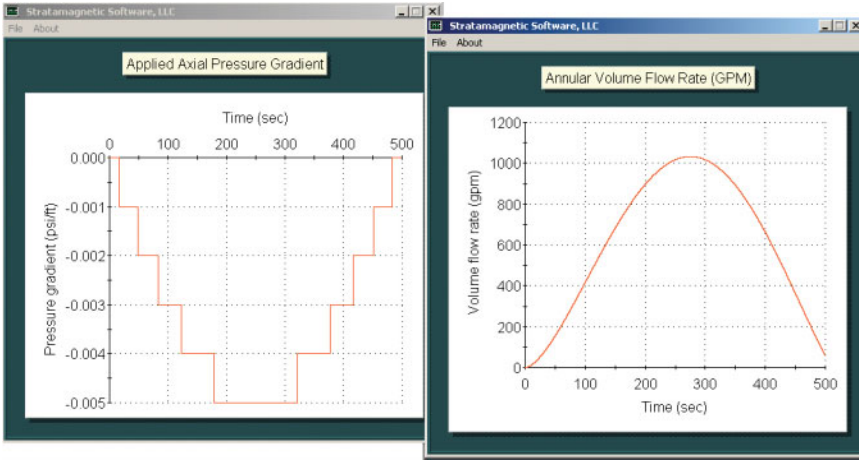
Figure 3-8c. Assumed pressure gradient and calculated flow rate.
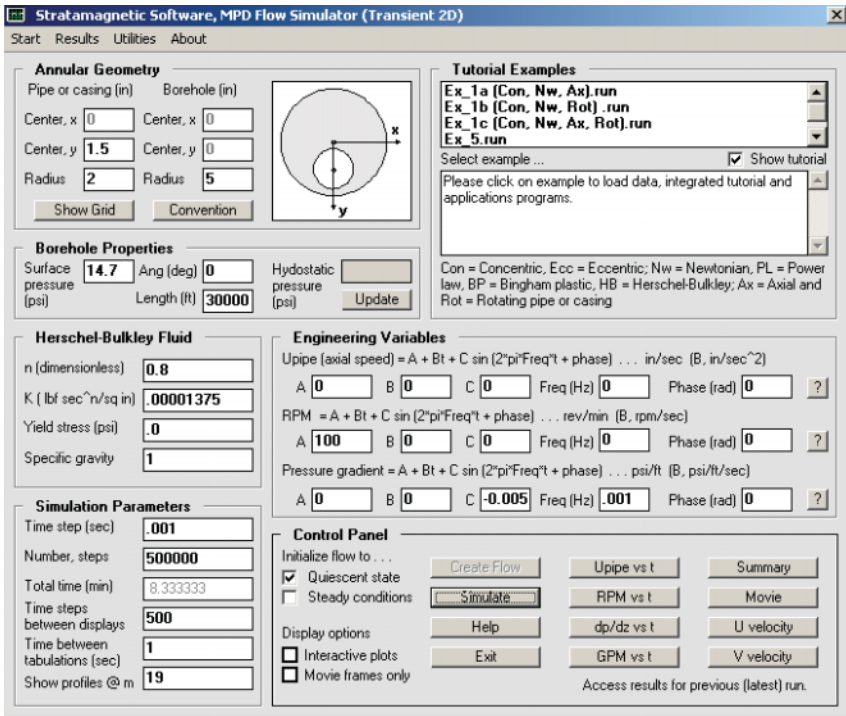
Figure 3-8d. Increasing rotational rate to 100 rpm.
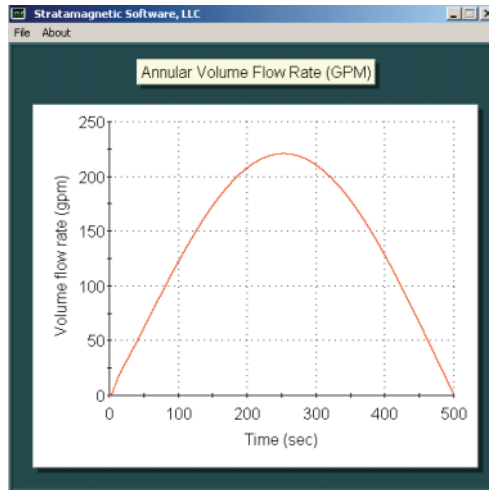
Figure 3-8e. Significantly reduced volumetric flow rate with rotation.

3.9   Effect of rotational and azimuthal start-up.

In this example, we study the effects of drillstring rotational start-up on the baseline non-rotating problem defined in Figure 3-9a for a Power law fluid in an eccentric annulus. Figure 3-9b shows that after 100 sec, the (almost) steady flow rate is 1,024.0 gpm. What happens when the drillstring is rotating at a fixed constant 100 rpm for the duration of the start-up process? This new flow is easily obtained by changing the constant rpm input in Figure 3-9a to that in Figure 3-9c, to produce the flow rate history shown in Figure 3-9d. After 100 sec, the flow has fully equilibrated at the reduced rate 221.1 gpm. There is a flow rate "overshoot" near 350 gpm early on that we have observed on all rotational flow calculations. We next determine the effects of rotational start-up. In Figure 3-9e, we now choose the "Bt" input option for RPM definition, typing "1" into that box for the time step information assumed. In Figure 3-9f, we show at the left how the same 100 rpm is achieved as before, but at the end of the 100 sec. period. The right-side diagram shows a flow rate returning to the 200 gpm range; however, the flow rate overshoot is now near 600 gpm.
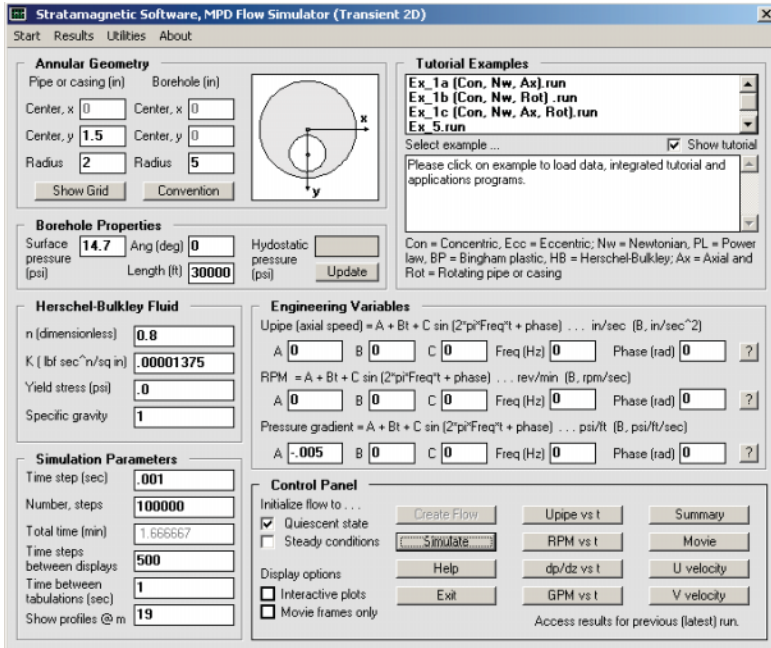
Figure 3-9a. Non-rotating flow.
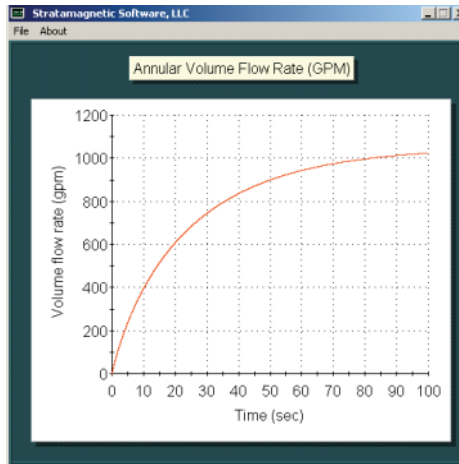
Figure 3-9b. Non-rotating flow.
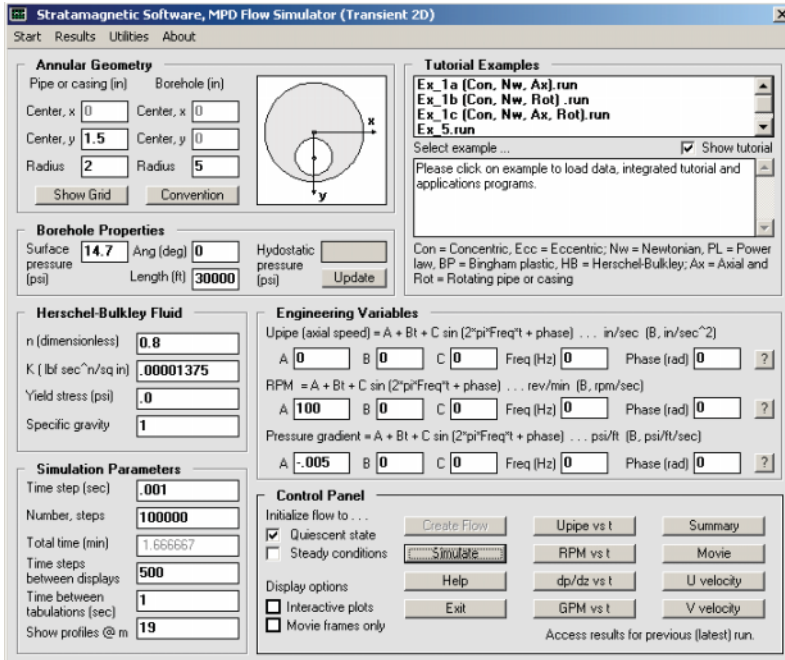
Figure 3-9c. Constant 100 rpm throughout.
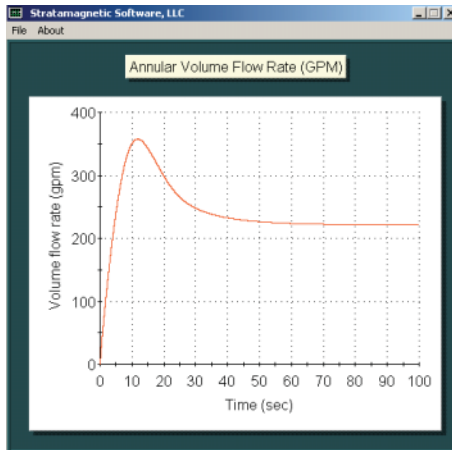
Figure 3-9d. Constant 100 rpm throughout.
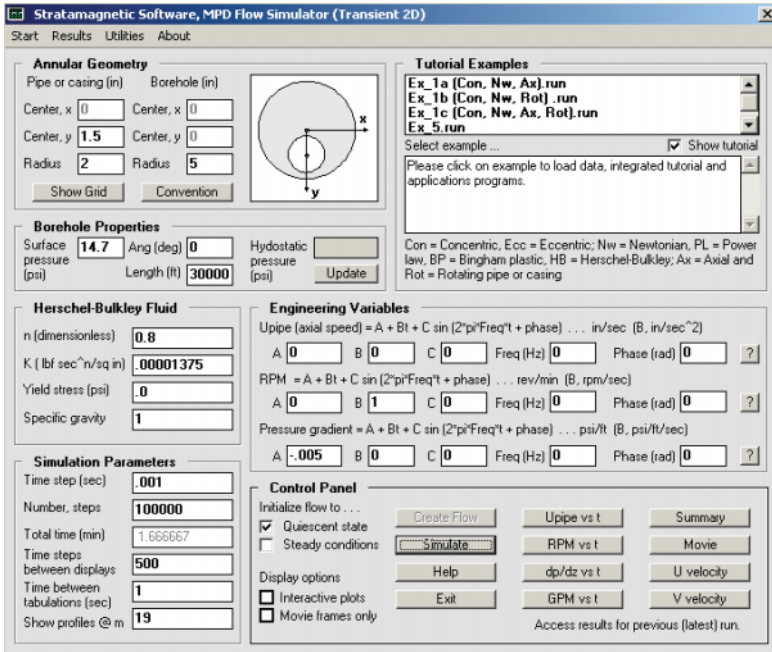
Figure 3-9e. Linearly increasing rpm with time.
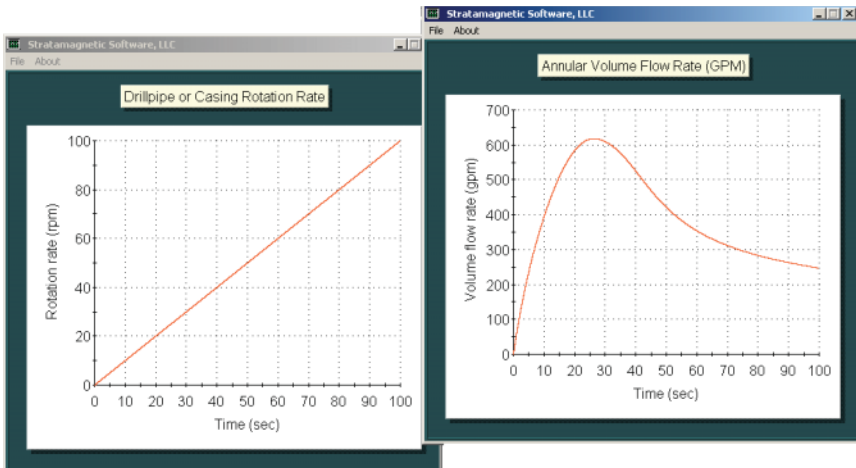
Figure 3-9f. Linearly increasing rpm with time.

3.10 Effect of axial drillstring movement.

In this *non-rotating* drillstring example, we study the effects of axial movement on the baseline problem defined previously in Figure 3-9a for a Power law fluid in an eccentric annulus. Again, Figure 3-9b shows that after 100 sec, the (almost) steady flow rate is 1,024.0 gpm assuming stationary pipe. If a constant +20 in./sec. is modeled instead, we have an increased 1,132.6 gpm, whereas if –20 in./sec. is taken, we find a reduced 912.6 gpm. Computer screens for these simple constant-speed dragging calculations are not shown.

In field applications, the drillstring is often reciprocated axially to facilitate jarring operations or cuttings removal while the mud pump acts under an almost constant pressure gradient condition. One might ask what the effects on flow rate, apparent viscosity, shear rate and viscous stress are, with the answers sure to assist the engineer in interpreting the physical consequences of his actions.   For example, increases in bottomhole stress may improve hole cleaning while reductions in apparent viscosity may lubricate the drillstring. In Figure 3-10a, we alter the "U_{pipe}" input to allow sinusoidal drillstring reciprocation with a peak-to-peak amplitude of 20 in./sec. and a frequency of 0.1 Hz. Clicking on the "?" at the far right will produce the pipe displacement speed history at the left of Figure 3-10b. At the right is the stably computed oscillatory flow rate.

The "Results" menu in Figure 3-10c provides additional post-processed results useful for correlation purposes. For instance, "Color plots" provides displays of the physical quantities appearing in the list, several of which are shown in Figure 3-10d. Notice in Figure 3-10a that we had elected to save "movie frames" showing the axial velocity distribution evolving in time (The "interactive plot" option would produce line graph results during simulation.).   Playing the "Axial velocity – Movie" option produces a movie, which can be viewed continuously or frame-by-frame.   Typical movie frames (with time increasing to the right) are shown in Figure 3-10e. All of the post-processing options described here are also available for rotating flow problems.
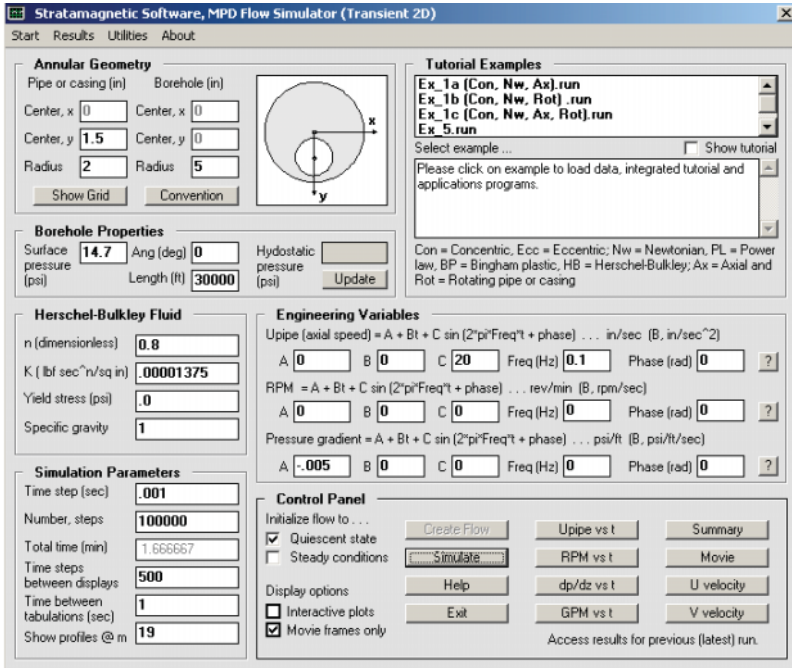
Figure 3-10a. Sinusoidal drillstring reciprocation.
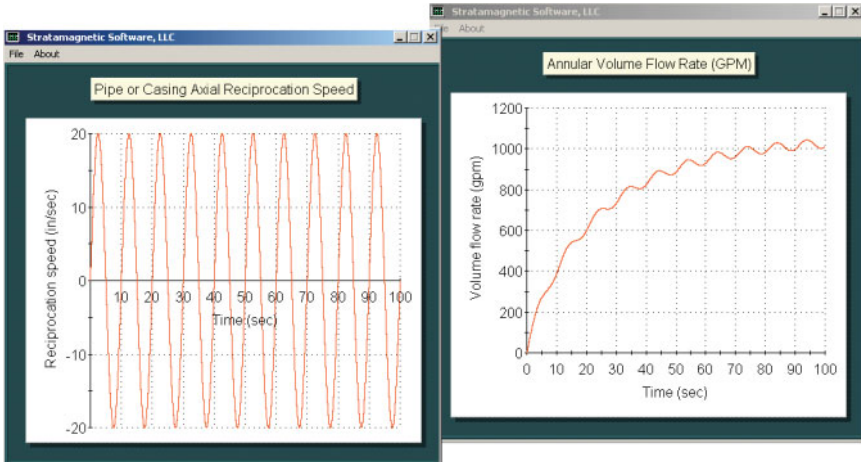
Figure 3-10b. Pipe displacement history and computed flow rate.
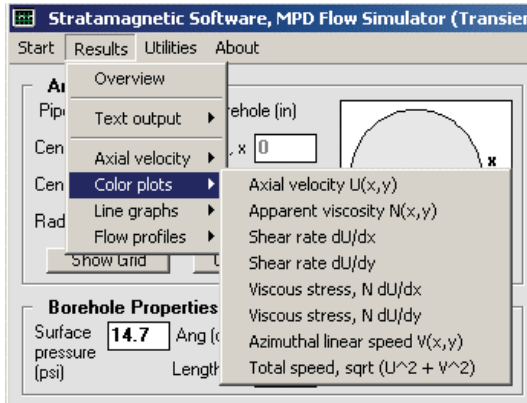
Figure 3-10c. Example color output.
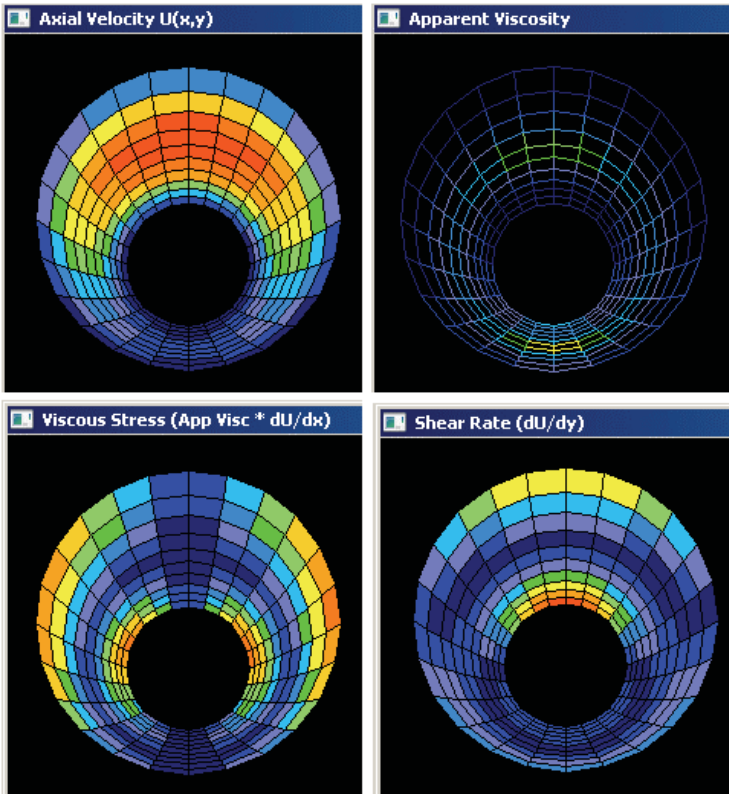
Figure 3-10d. Example color output for several physical quantities.
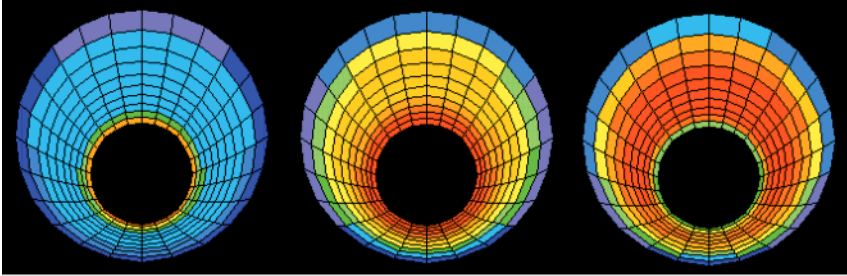
Figure 3-10e. Frames from axial velocity movie (time increasing).

3.11 Combined rotation and sinusoidal reciprocation.

In this example, again for transient, nonlinear, non-Newtonian Power law flow in an eccentric annulus, we combine two previous calculations and demonstrate the ease with which combined sinusoidal axially reciprocating pipe motion and drillstring rotation can be modeled, literally by filling in input boxes and clicking. The assumptions are given in Figure 3-11a, assumed pipe displacement histories are displayed in Figure 3-11b, and the computed volumetric flow rate is provided in Figure 3-11c. Note from this curve the pronounced overshoots and flow rate fluctuations. We have modeled the mud pump as a constant pressure gradient source in our work that leads to variable flow rate. In reality, the pump may act more as a constant rate source that leads to time-dependent pressure gradients.   This latter model is much more complicated mathematically and cannot be solved within a reasonable time. However, the percent fluctuations seen from flow rate curves such as that in Figure 3-11c represent those for pressure gradient and can be used meaningfully for managed pressure job planning.
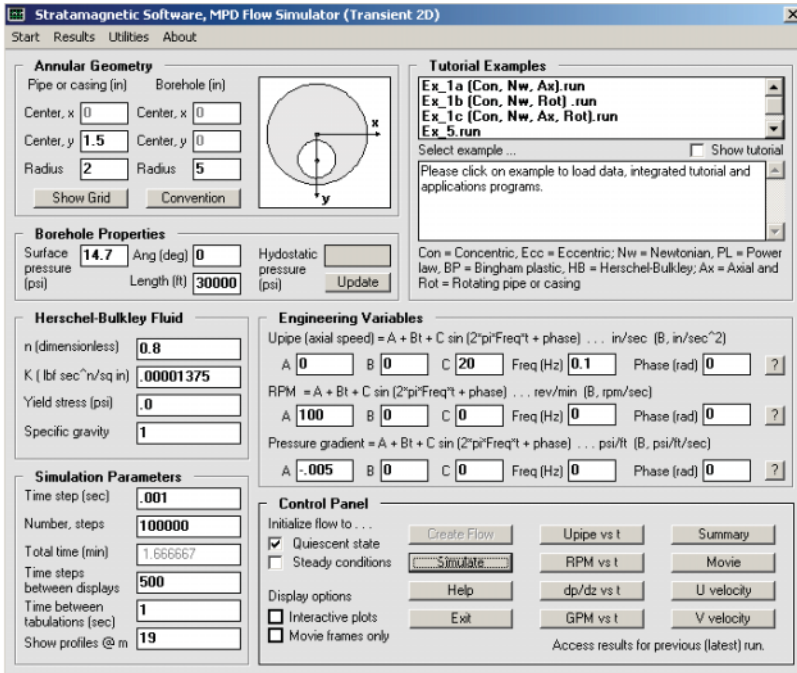
Figure 3-11a. Combined transient reciprocation and rotation.
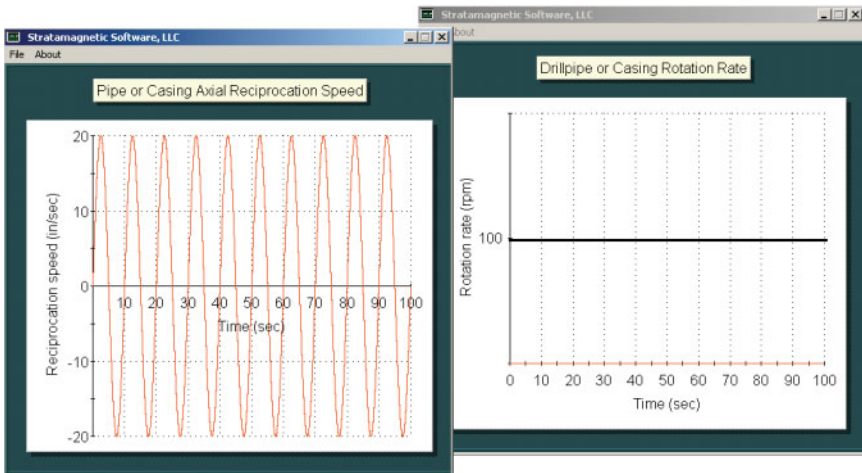
Figure 3-11b. Pipe displacement history display.
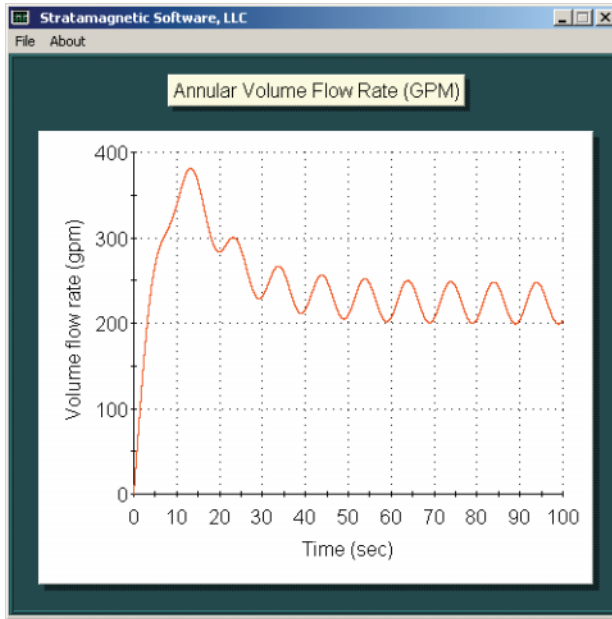
Figure 3-11c. Computed volumetric flow rate.

3.12 Combined rotation and sinusoidal reciprocation in presence of mud pump flow rate ramp-up for yield stress fluid.

This comprehensive example illustrates the high level of simulation complexity offered by our math model.   Here we again consider an eccentric annulus, however, now containing a Herschel-Bulkley yield stress fluid. The drillpipe is allowed to axially reciprocate sinusoidally in time, while rotational rate increases linearly with time. The mud pump pressure gradient is allowed to steepen with time from start-up to describe increased pumping action.   All of these effects are coupled nonlinearly. They can be computed quickly and stably, and if numerical instabilities are encountered, they can be remedied by decreasing time step size. To accommodate this possibility, the algorithm is efficiently coded to make optimal use of memory resources and will allow up to 10,000,000 time steps, for which calculations may require fifteen minutes or more. The assumptions are shown in Figure 3-12a, while detailed pipe displacement histories, applied pressure gradients and computed volumetric flow rate are given in Figure 3-12b.
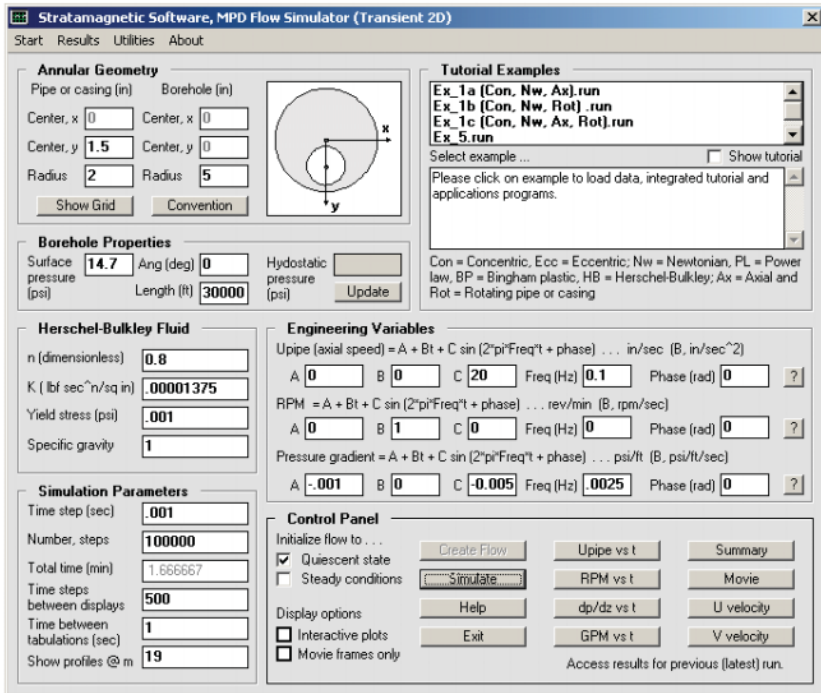
Figure 3-12a. Basic assumptions, comprehensive example.

In this chapter, we have demonstrated how the most general transient single-phase, constant density, non-Newtonian Hershel-Bulkley fluid with yield stress can be studied as it flows through an eccentric annulus in the presence of coupled and arbitrary drillpipe axial reciprocation, unsteady rotation and time-varying axial pressure gradient. The algorithm and its strengths and limitations have been explained previously.   Because the physical problem is nonlinear, general conclusions are not available and each problem must be treated on a case-by-case basis. To support this endeavor, all efforts have been made to render the method simple to use, with all text output, report generation and color graphics completely automated. There is no requirement on the part of the user for any special skills in fluid dynamics, advanced mathematics or computer modeling. The model is new, and certainly, as more becomes known about its properties and the consequences of general borehole flows, we will update our exposition accordingly.
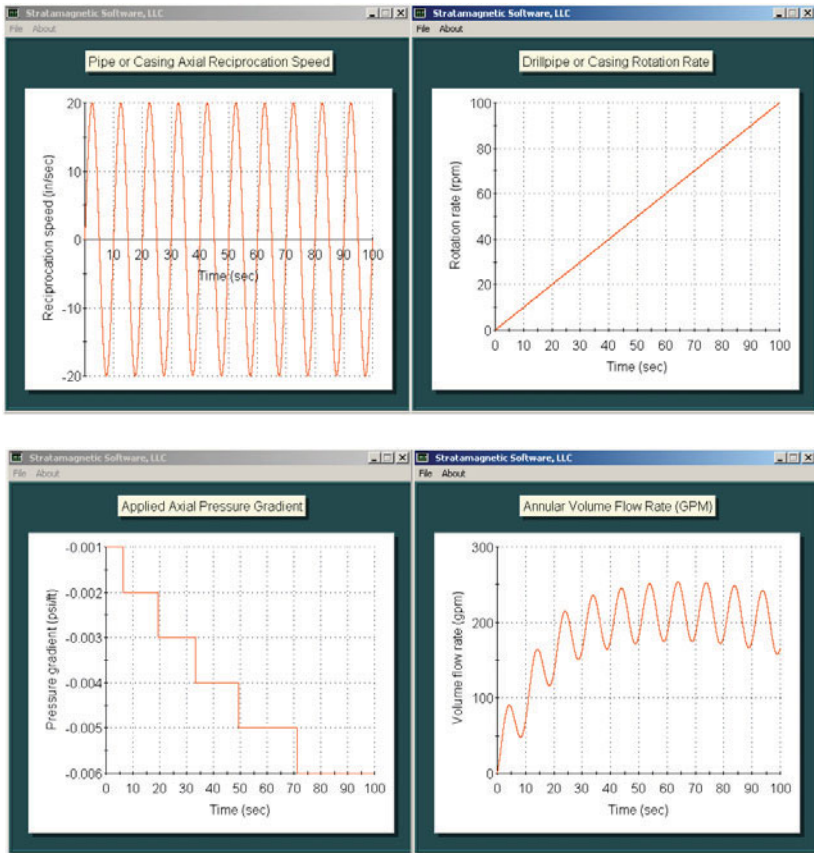
Figure 3-12b. More assumptions and computed flow rate with time.

3.13 References.

- Chin, W.C., *Borehole Flow Modeling in Horizontal, Deviated and Vertical Wells*, Gulf Publishing, Houston, 1992.

- Chin, W.C., *Computational Rheology for Pipeline and Annular Flow*, Elsevier Science, London, 2001.

- Chin, W.C., "Modeling and Simulation of Managed Pressure Drilling for Improved Design, Risk Assessment, Training and Operations," *RPSEA Ultra-Deepwater Technology Conference*, Houston, Tx, June 22-23, 2010.

- Chin, W.C., "Flow Simulation Methods for Managed Pressure Drilling and Cementing," *Drilling and Completing Trouble Zones Conference*, Galveston, Tx, Oct. 19-21, 2010.

- Chin, W.C., *Managed Pressure Drilling: Modeling, Strategy and Planning*, Elsevier, Amsterdam, 2012.

- Chin, W.C., *Managed Pressure Drilling: Modeling, Strategy and Planning*, Chinese Edition, Elsevier, Singapore, 2017.

- Chin, W.C., and Zhuang, X., "Exact Non-Newtonian Flow Analysis of Yield Stress Fluids in Highly Eccentric Borehole Annuli with Pipe or Casing Translation and Rotation," Paper 131234-PP, *CPS/SPE International Oil & Gas Conference and Exhibition*, Beijing, China, June 8-10, 2010.

- Chin, W.C., and Zhuang, X., "Effect of Rotation on Flowrate and Pressure Gradient in Eccentric Holes," Paper AADE-11-NTCE-45, *AADE 2011 National Technical Conference and Exhibition*, Houston, TX, April 12-14, 2011 (a).

- Chin, W.C., and Zhuang, X., "Advances in Swab-Surge Modeling for Managed Pressure Drilling," Paper AADE-11-NTCE-46, *AADE 2011 National Technical Conference and Exhibition*, Houston, TX, April 12-14, 2011 (b).

- Chin, W.C., and Zhuang, X., "Transient, Multiphase, Three-Dimensional Pumping Models for Cementing and Drilling," Paper AADE-11-NTCE-72, *AADE 2011 National Technical Conference and Exhibition*, Houston, TX, April 12-14, 2011 (c).

- Chin, W.C., and Zhuang, X., "Comprehensive Annular Flow Models for Drilling and Completions," Paper AADE-11-NTCE-73, *AADE 2011 National Technical Conference and Exhibition*, Houston, TX, April 12-14, 2011 (d).

- Chin, W.C. and Zhuang, X., "Advances in Swab-Surge Modeling for Managed Pressure Drilling," Paper OTC-21115-PP, *2011 Offshore Technology Conference*, Houston, TX, May 2-5, 2011 (e).

4

Transient Multiphase Flows

In this chapter, we consider general problems for managed pressure drilling and cementing flow simulation. All of the "building block" tools solved in the "Steady 2D" and "Transient 2D" simulators are brought to bear in the transient, three-dimensional, multiphase applications treated here. Subtle modeling issues and mathematical formulations presented in Chin (2012, 2016) are not duplicated here – in this book, we focus only on practical calculations. Again, we address the computation of pressure profiles along the borehole and particularly at the drillbit for all times when a general pumping schedule is allowed at the mud pump. Diffusion effects at fluid interfaces are discussed as the needs arise.

The general formulation models the complete system, encompassing (1) surface pumping of general fluids with user-defined time and rate schedules, (2) non-Newtonian flows down the drillpipe, (3) capture of pressure losses through the drillbit, and (4) flows up the borehole annulus. For both pipe and annulus, fluid mixing is permitted via the introduction of coupled momentum and concentration equations. For the borehole, general annular eccentricity is allowed. Once the basic setup work is undertaken, that is, defining fluid interface positions (a simple process to be discussed shortly) and completing the pressure gradient entries in Figure 4-1 using pressure solvers provided through the check boxes shown, the calculation of borehole pressure profiles (that is, pressure versus axial position) at any instant in time requires just minutes of hand calculation (this process will be automated in the future).
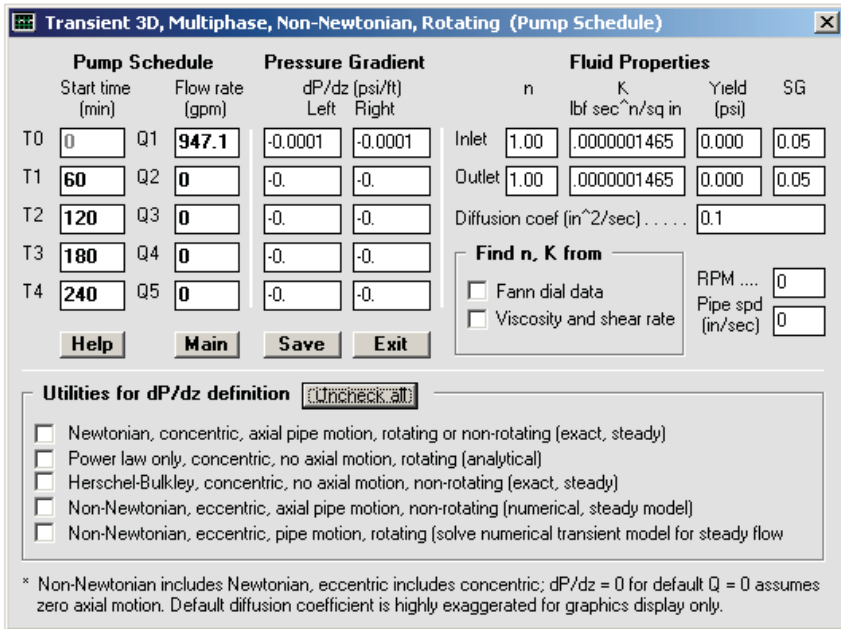
Figure 4-1. Non-Newtonian mixtures, rotating (pump schedule) –
This menu and application will be discussed in detail later.

For cementing applications, the degree to which contiguous fluids mix or do not mix is important to zonal isolation. Here, detailed calculations for interfacial mixing yield details related to diffusion zone geometry and time scales for mixing. These calculations, which are not required for managed pressure drilling applications, may require anywhere from minutes to an hour, depending on numerical stability requirements dictated by fluid density, apparent viscosity and rotational rate parameters (the controlling variable is $\rho\omega/\mu$, where ρ is density, ω is rotational rate, and μ represents an average apparent viscosity). With these preliminaries said, we now present detailed calculated validations and results.

4.1   Single fluid in pipe and borehole system – calculating total pressure drops for general non-Newtonian fluids.

The general problem considered is shown in Figure 4-2 (Our analysis applies to open and closed systems.).   A positive displacement mud pump forces drilling fluid or cement into a drillpipe centralized in a concentric annulus. This vertical hole turns into a deviated or horizontal borehole with an eccentric annulus through an intermediate (possibly, eccentric) section with radius of curvature, R.   Note that Figure 4-2 is used to establish conventions and a frame of reference for discussion only.   In fact, our "vertical concentric section" may represent another deviated or horizontal one with an eccentric cross-section, and the turning section (however unlikely) may be concentric, if desired.   Length scales may be assigned arbitrarily and out-of-plane sections are permissible. Thus, the geometry considered here is quite general.
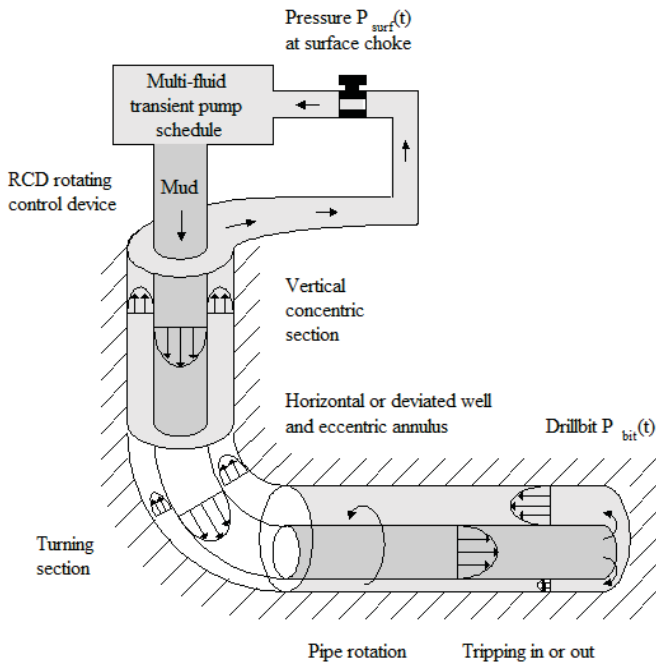
Figure 4-2. Managed pressure system simulation.

We emphasize here "single" in the section title. When only a single fluid is considered, the problems are two-dimensional because the flows in the pipe and annulus are unchanged with time in the axial direction. Only the flow rate changes. For any given flow rate, a single calculation determines what happens in the drillpipe entirely and similarly for the annulus. When multiple fluids are introduced at the inlet with different slug lengths, a three-dimensional transient model is obviously required that supports moving interfaces. Net pressure drops will vary with time since the fluid system is constantly changing. Significant complications arise which are studied in the remainder of this chapter.

4.2   Interface tracking and total pressure drop for multiple fluids pumped in drillpipe and eccentric borehole system.

In this example, we will consider a centered or eccentered drillpipe (with cross-sectional area A_{pipe}) located in a borehole annulus whose geometry is unchanged along its length. The annular area is $A_{annulus}$. Note that while pipe area is simply available from "πR_{pipe}^2," the same is not true for the annulus if the cross-sectional contours from two initially eccentered circles have been edited to incorporate washouts, cuttings beds or fractures. If so, the "Steady 2D" simulator automatically computes and displays total cross-sectional area by summing incremental trapezoidal areas constructed from the curvilinear grid.

Now, mud progresses down the drillpipe, then out through the drillbit, and finally, flows upward in the return annulus. At the outset $t = 0$, a single initial fluid with Herschel-Bulkley properties (n_0, K_0, $\tau_{0,0}$) is assumed to exist in the pipe and annular system (n is the fluid exponent, K is the consistency factor, and τ_0 is the yield stress). The initial fluid may be flowing or quiescent. At $t = 0+$, the mud pump starts to act according to a user-defined schedule with piecewise constant rates. At $t = t_0 = 0+$, Fluid "1" with properties (n_1, K_1, $\tau_{0,1}$) is pumped into the pipe at the volumetric flow rate of Q_1, while at $t = t_1$, a second Fluid, "2," with properties (n_2, K_2, $\tau_{0,2}$) is pumped at rate Q_2, and so on. In fact –

- Fluid "1" pumped at rate Q_1: $t_0 \le t < t_1$
- Fluid "2" pumped at rate Q_2: $t_1 \le t < t_2$
- Fluid "3" pumped at rate Q_3: $t_2 \le t < t_3$
- Fluid "4" pumped at rate Q_4: $t_3 \le t < t_4$
- Fluid "5" pumped at rate Q_5: $t \ge t_4$

The overall pumping process is illustrated from the top of Figure 4-2-1. Here, fluid introduced at the far right into the drillpipe travels to the left, then turns at the drillbit (not shown), and finally progresses to the very far right. The middle diagram shows five interfaces (starting at t_0, t_1, t_2, t_3 and t_4) associated with the onset of each pump action. The location "z_1" (using the "little z" left-pointing coordinate system shown) describes the interface separating the initial fluid ahead of it with Fluid "1" just behind it. Similarly, "z_2" separates Fluid "1" ahead of it and Fluid "2" behind it. The last Fluid "5" is a single fluid that is pumped continuously without stoppage with flow rate Q_5 for t $\geq t_4$. While more interfaces are easily handled programming-wise, a limit of five (which models six fluid slugs) to enable rapid modeling and job prototyping, was assumed, since this number suffices for most rig site planning purposes. Once the first interface reaches the end of the drillpipe, shown with length L, that is, $z_1 = L$, it turns into the borehole annulus and travels to the right.   Similar descriptions apply to the remaining interfaces. Annular interfaces are described by the "big (as in capital) Z" right-pointing coordinate system at the bottom in Figure 4-2-1. When Z_1 = L, the first fluid pumped will have reached the surface.

Figure 4-2-1 provides a "snapshot" obtained for a given instant in time. At different times, the locations of the interfaces will be different, and pressure profiles along the borehole (and hence, at the drillbit) will likewise be different. Also, while our discussion focuses on drilling applications with distinct mud interfaces, it is clear that all of our results apply to cement-spacer-mud systems.

Now, we wish to determine the locations of $z_{1,2,3,4,5}$ and $Z_{1,2,3,4,5}$ as functions of time. In general, this is a difficult problem if the fluids are compressible, or if significant mixing is found at fluid interfaces, or both. However, if the lengths of the fluid slugs are long compared to the annular diameter (so that mixing zones are not dynamically significant), and further, if the pump acts instantaneously and transient fluid effects reach equilibrium quickly, interface tracking can be accomplished kinematically. Once the locations of all interfaces are known for any instant in time, pressure drop calculations (for each fluid slug) proceed using the non-Newtonian flow models developed previously.
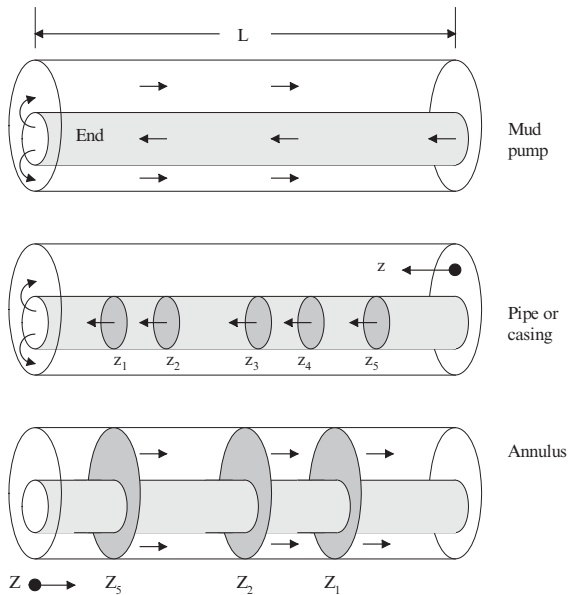
Figure 4-2-1. General pumping schedule.

Two output tables are provided by our "interface tracker." The calculations are performed almost instantaneously by the software model. The two are, respectively, "Drillpipe Fluid Interfaces vs Time" and "Annular Fluid Interfaces vs Time," as shown in Figures 4-2-2 and 4-2-3. The numbers assumed for these tables are obviously not realistic, and for this reason, the units shown in the headings should be ignored for now. They were chosen so that all results fit on the printed page, with all values allowing convenient visual checking and understanding of the computer output.

Note that 0's at early times along a z column indicate absence of the particular fluid in the drillpipe. Also, once the interface has reached the position "100," the end of the borehole in this illustration, the subsequent 0's are no longer meaningful and are used only to populate the table. Note that the very small annular area of $A_{annulus}$ selected later was designed only so that we can "watch the fluid move" in the table of Figure 4-2-3.

ELAPSED TIME		FLOW	Drillpipe Fluid Interface (feet)				
Minutes	Hours	GPMs	z(1)	z(2)	z(3)	z(4)	z(5)
0	0.	1	0	0	0	0	0
1	0.	1	1	0	0	0	0
2	0.	1	2	0	0	0	0
3	0.	1	3	0	0	0	0
4	0.	1	4	0	0	0	0
5	0.	2	5	0	0	0	0
6	0.	2	7	2	0	0	0
7	0.	2	9	4	0	0	0
8	0.	2	11	6	0	0	0
9	0.	2	13	8	0	0	0
10	0.	3	15	10	0	0	0
11	0.	3	18	13	3	0	0
12	0.	3	21	16	6	0	0
13	0.	3	24	19	9	0	0
14	0.	3	27	22	12	0	0
15	0.	4	30	25	15	0	0
16	0.	4	34	29	19	4	0
17	0.	4	38	33	23	8	0
18	0.	4	42	37	27	12	0
19	0.	4	46	41	31	16	0
20	0.	5	50	45	35	20	0
21	0.	5	55	50	40	25	5
22	0.	5	60	55	45	30	10
23	0.	5	65	60	50	35	15
24	0.	5	70	65	55	40	20
25	0.	5	75	70	60	45	25
26	**0.**	**5**	**80**	**75**	**65**	**50**	**30**
27	0.	5	85	80	70	55	35
28	0.	5	90	85	75	60	40
29	0.	5	95	90	80	65	45
30	0.	5	100	95	85	70	50
31	1.	5	0	100	90	75	55
32	1.	5	0	0	95	80	60
33	1.	5	0	0	100	85	65
34	1.	5	0	0	0	90	70
35	1.	5	0	0	0	95	75
36	1.	5	0	0	0	100	80
37	1.	5	0	0	0	0	85
38	1.	5	0	0	0	0	90
39	1.	5	0	0	0	0	95
40	1.	5	0	0	0	0	100
41	1.	5	0	0	0	0	0

Figure 4-2-2. "Drillpipe Fluid Interfaces vs Time."

ELAPSED TIME		FLOW	Annular Fluid Interface (feet)				
Minutes	Hours	GPMs	Z(5)	Z(4)	Z(3)	Z(2)	Z(1)
0	0.	1	0	0	0	0	0
1	0.	1	0	0	0	0	0
2	0.	1	0	0	0	0	0
3	0.	1	0	0	0	0	0
4	0.	1	0	0	0	0	0
5	0.	2	0	0	0	0	0
6	0.	2	0	0	0	0	0
7	0.	2	0	0	0	0	0
8	0.	2	0	0	0	0	0
9	0.	2	0	0	0	0	0
10	0.	3	0	0	0	0	0
11	0.	3	0	0	0	0	0
12	0.	3	0	0	0	0	0
13	0.	3	0	0	0	0	0
14	0.	3	0	0	0	0	0
15	0.	4	0	0	0	0	0
16	0.	4	0	0	0	0	0
17	0.	4	0	0	0	0	0
18	0.	4	0	0	0	0	0
19	0.	4	0	0	0	0	0
20	0.	5	0	0	0	0	0
21	0.	5	0	0	0	0	0
22	0.	5	0	0	0	0	0
23	0.	5	0	0	0	0	0
24	0.	5	0	0	0	0	0
25	0.	5	0	0	0	0	0
26	**0.**	**5**	**0**	**0**	**0**	**0**	**0**
27	0.	5	0	0	0	0	0
28	0.	5	0	0	0	0	0
29	0.	5	0	0	0	0	0
30	0.	5	0	0	0	0	0
31	1.	5	0	0	0	0	10
32	1.	5	0	0	0	10	20
33	1.	5	0	0	0	20	30
34	1.	5	0	0	10	30	40
35	1.	5	0	0	20	40	50
36	**1.**	**5**	**0**	**0**	**30**	**50**	**60**
37	1.	5	0	10	40	60	70
38	1.	5	0	20	50	70	80
39	1.	5	0	30	60	80	90
40	1.	5	0	40	70	90	100
41	1.	5	10	50	80	100	0
42	1.	5	20	60	90	0	0
43	1.	5	30	70	100	0	0
44	1.	5	40	80	0	0	0
45	1.	5	50	90	0	0	0
46	1.	5	60	100	0	0	0
47	1.	5	70	0	0	0	0
48	1.	5	80	0	0	0	0
49	1.	5	90	0	0	0	0
50	1.	5	100	0	0	0	0
51	1.	5	0	0	0	0	0

Figure 4-2-3. "Annular Fluid Interfaces vs Time."

To facilitate visual interpretation, we have assumed that $A_{pipe} = 1$ and $A_{annulus} = 0.5$, so that the nominal linear displacement speeds in the pipe and annulus are $U_{pipe} = Q/A_{pipe}$ and $U_{annulus} = Q/A_{annulus}$. The borehole length is assumed for clarity to be 100. At the same time, we pump according to the schedule

- Fluid "1" at a rate of $Q_1 = 1$: $0 = t_0 \leq t < t_1 = 5$
- Fluid "2" at a rate of $Q_2 = 2$: $5 = t_1 \leq t < t_2 = 10$
- Fluid "3" at a rate of $Q_3 = 3$: $10 = t_2 \leq t < t_3 = 15$
- Fluid "4" at a rate of $Q_4 = 4$: $15 = t_3 \leq t < t_4 = 20$
- Fluid "5" at a rate of $Q_5 = 5$: $t \geq t_4 = 20$

where our five interfaces originate at t_0, t_1, t_2, t_3 and t_4. We next explain Figure 4-2-2. The left column provides elapsed minutes, while the second provides elapsed hours. The volumetric flow rate is given in the third column. The corresponding drillpipe fluid interfaces $z_{1,2,3,4,5}$ are given in the five remaining columns. Also, each change in flow rate (associated with a new interface) is separated by a single horizontal line spacing to enhance clarity. Consider the result for z_1. In the first time block with $U_{pipe} = 1/1 = 1$, the interface advances at a rate of "1." In the second block with $U_{pipe} = 2/1$, the interfaces advances at the rate "2." As time increases, the easily recognized rate increments are 3, 4, and 5 following the above pump schedule.

The z_1 interface starts moving at $t = 0$. Now we turn to the second interface and study the column for z_2 results. At $t = 5$, the second interface starts moving. Because we are already in the second time block, the interface moves at the rate "2." Subsequent speeds are 3, 4 and 5. Similarly, z_3 starts at $t = 10$ and rate increments with 3, followed by 4 and 5, and so on. We have described Figure 4-2-2 from the perspective of tracking individual fronts. However, the table is important for pressure calculations. Let us consider the results obtained at $t = 26$ (These are shown in bold font for emphasis.). In particular, we have

ELAPSED TIME		FLOW	Drillpipe Fluid Interface (feet)				
Minutes	Hours	GPMs	z(1)	z(2)	z(3)	z(4)	z(5)
26	**0.**	**5**	**80**	**75**	**65**	**50**	**30**

This printout indicates that, at $t = 26$, the front z_1 is located at $z = 80$, while the last front z_5 is located at $z = 30$. The drillpipe thus contains six distinct fluid slugs at $100 > z > 80$, $80 > z > 75$, $75 > z > 65$, $65 > z > 50$, $50 > z > 30$, and $30 > z > 0$ where "100" refers to the assumed borehole length. In fact –

100 > z > 80 contains "initial fluid" with properties (n_0, K_0, $\tau_{0,0}$)

80 > z > 75 contains Fluid "1" with properties (n_1, K_1, $\tau_{0,1}$)

75 > z > 65 contains Fluid "2" with properties (n_2, K_2, $\tau_{0,2}$)

65 > z > 50 contains Fluid "3" with properties (n_3, K_3, $\tau_{0,3}$)

50 > z > 30 contains Fluid "4" with properties (n_4, K_4, $\tau_{0,4}$)

30 > z > 0 contains Fluid "5" with properties (n_5, K_5, $\tau_{0,5}$)

If a non-Newtonian 2D flow model for a Herschel-Bulkley fluid in a circular pipe were available that gave the pressure gradient $(\partial P/\partial z)_{pipe,n}$ for any of the given fluid slugs "n" flowing at rate Q with a pipe radius $(A_{pipe}/\pi)^{1/2}$, then the total drillpipe pressure drop is simply calculated from $(100 - 80)$ $(\partial P/\partial z)_{pipe,0}$ + $(80 - 75)$ $(\partial P/\partial z)_{pipe,1}$ + $(75 - 65)$ $(\partial P/\partial z)_{pipe,2}$ + $(65\text{-}50)$ $(\partial P/\partial z)_{pipe,3}$ + $(50 - 30)$ $(\partial P/\partial z)_{pipe,4}$ + $(30 - 0)$ $(\partial P/\partial z)_{pipe,5}$. The flow rate, Q, used would be the one applicable at the time the snapshot was taken, in this case, Q = 5 at t = 26 (A single rate applies to all slugs at any instant in time.). Now, at time t = 26, Figure 4-2-3 shows, as indicated by "0's," that none of the pumped fluids have arrived in the annulus, that is –

ELAPSED TIME		FLOW	Annular Fluid Interface (feet)				
Minutes	Hours	GPMs	Z(5)	Z(4)	Z(3)	Z(2)	Z(1)
26	0.	5	0	0	0	0	0

Thus, the only fluid residing in the annulus is the initial fluid. If the pressure gradient obtained from a 2D eccentric flow analysis is $(\partial P/\partial z)_{annulus,0}$, then the pressure drop in the annulus is just $(100 - 0)$ $(\partial P/\partial z)_{annulus,0}$. If we further denote by Δ the pressure drop through the drillbit, then the total pressure drop through the entire pipe-bit-annulus system is obtained by summing the prior three results, that is, $(100 - 80)$ $(\partial P/\partial z)_{pipe,0}$ + $(80 - 75)$ $(\partial P/\partial z)_{pipe,1}$ + $(75 - 65)$ $(\partial P/\partial z)_{pipe,2}$ + $(65\text{-}50)$ $(\partial P/\partial z)_{pipe,3}$ + $(50 - 30)$ $(\partial P/\partial z)_{pipe,4}$ + $(30 - 0)$ $(\partial P/\partial z)_{pipe,5}$ + Δ + $(100 - 0)$ $(\partial P/\partial z)_{annulus,0}$, which is the pressure (additive to the surface choke pressure, P_{SURF}) required at the mud pump to support this multi-slug flow.

The software that creates Figure 4-2-2 also provides the times at which fluid interfaces in the drillpipe enter the borehole annulus. These are obtained from the table in Figure 4-2-2 by noting the "100" marker. In this case, we have

```
Borehole total length L, is:      100 ft.
Fluid "1" enters annulus at:       30 min.
Fluid "2" enters annulus at:       31 min.
Fluid "3" enters annulus at:       33 min.
Fluid "4" enters annulus at:       36 min.
Fluid "5" enters annulus at:       40 min.
```

We next consider another time frame, say t = 36, for which our drillpipe interfaces have entered the annulus, and explain how annular pressure drops are determined, e.g., see Figure 4-2-4.   For this time frame, Figure 4-2-3 gives

ELAPSED TIME		FLOW	Annular Fluid Interface (feet)				
Minutes	Hours	GPMs	Z(5)	Z(4)	Z(3)	Z(2)	Z(1)
36	1.	5	0	0	30	50	60

This indicates that three interfaces exist in the annulus, with Z_1 located at the far right $Z = 60$, followed by Z_2 at $Z = 50$ and Z_3 at $Z = 30$. Since the fluid ahead of Z_1 is the "initial fluid," the total annular pressure drop is calculated from the sum $(100 - 60) (\partial P/\partial z)_{annulus,0} + (60 - 50) (\partial P/\partial z)_{annulus,1} + (50 - 30) (\partial P/\partial z)_{annulus,2} + (30 - 0) (\partial P/\partial z)_{annulus,3}$ where subscripts denote fluid type for the annular model.
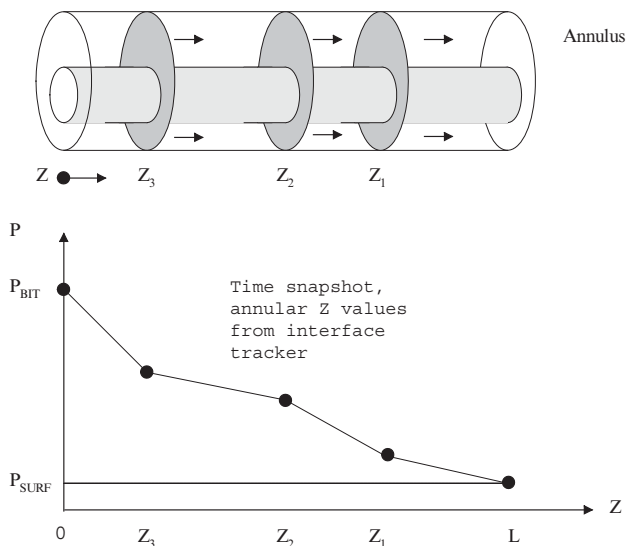
Figure 4-2-4. Example annular interface distribution.

We note that the actual pressure P_{BIT} at the drillbit *in the formation* is obtained by adding the total annular pressure drop to the pressure P_{SURF} obtained at the surface choke.   The value of P_{SURF} is in itself a "boundary condition," and, importantly, the pressure, P_{BIT}, at the bottom of the annulus *in the formation* does not depend on the pressure drop Δ through the drillbit.   On the other hand, the pressure required at the pump to move the system includes pipe, bit and annular losses, as shown in Figure 4-2-5 for one interface configuration.
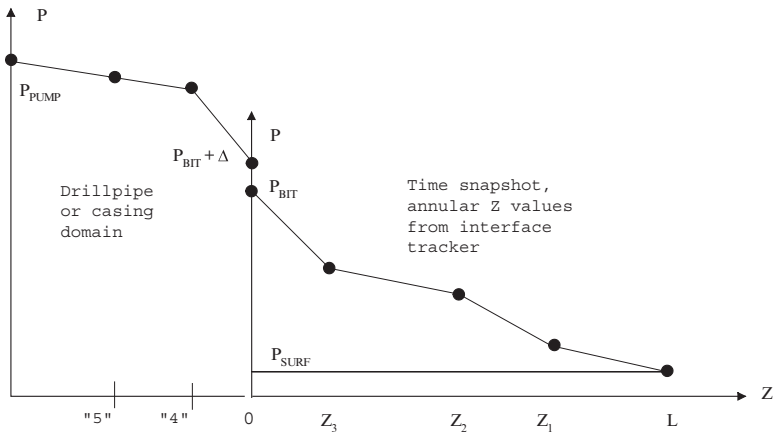
Figure 4-2-5. Complete drillpipe-drillbit-annulus system.

Interface tracking and example. Here we describe the software module that has been implemented to track multiple fluid interfaces, leading to results such as those in Figures 4-2-2 and 4-2-3. For clarity, we previously did not work in physical units, choosing (unrealistic) numerical inputs whose results were simple to visualize and understand and parameters that allowed complete tables to fit on single printed pages. Here we return to physical units and work with a more realistic example. Our "Interface Tracker" is executed from the user screen in Figure 4-2-6, which shows default run parameters.   Actual run parameters span many ranges and combinations of different numbers. For instance, pump rates will typically vary over 100 – 1,500 gpm and time schedules will vary up to days. Borehole lengths may vary from 5,000 to 30,000 feet. Pipe and annular areas are very different from run to run. In order to provide meaningful tabulations that are reasonable in file size, time increments are therefore expressed in minutes.

To execute this program, click "Run." When a blue status screen appears and instructs the user the click "Answer," results analogous to Figures 4-2-2 and 4-2-3 are provided. For completeness, we perform our calculations now and explain the outputs at selected instants in time. These calculations require approximately five seconds.

Figure 4-2-6. "Interface Tracker" with default inputs.

The output file reproduced below contains a summary of all input parameters. Again note that for interface tracking, provided that our fluid slugs are long compared to the annular diameter and interfacial mixing is confined to a small axial extent, the tracking process can be performed kinematically (using the pumping schedule and overall geometric parameters alone) and does not depend on the dynamics or rheologies of the fluids (These are used after-the-fact for pressure calculations as explained previously.). We now explain selected entries at various times. At the present writing, interface positions must be inferred from tabular results; however, this process (together with integrated color graphics) will be automated in the near future.

```
Pump Schedule, Interface Tracking ...

 100 gpm:     0 min < T <    60 min
 200 gpm:    60 min < T <   120 min
 300 gpm:   120 min < T <   180 min
 400 gpm:   180 min < T <   240 min
 500 gpm:             T >   240 min


Drillpipe area (ft^2):  0.250E+00
Annular area   (ft^2):  0.500E+00
Borehole length (ft):  0.500E+04
Time simulation (min):      600
```

ELAPSED TIME		FLOW	Drillpipe Fluid Interface (feet)				
Minutes	Hours	GPMs	z(1)	z(2)	z(3)	z(4)	z(5)
0	0.0	100	0	0	0	0	0
1	0.0	100	53	0	0	0	0
2	0.0	100	106	0	0	0	0
3	0.1	100	160	0	0	0	0
4	0.1	100	213	0	0	0	0
5	0.1	100	267	0	0	0	0
6	0.1	100	320	0	0	0	0
7	0.1	100	374	0	0	0	0
8	0.1	100	427	0	0	0	0
9	0.2	100	481	0	0	0	0
10	0.2	100	534	0	0	0	0
11	0.2	100	588	0	0	0	0
12	0.2	100	641	0	0	0	0
13	0.2	100	695	0	0	0	0
14	0.2	100	748	0	0	0	0
15	0.2	100	802	0	0	0	0
16	0.3	100	855	0	0	0	0
17	0.3	100	909	0	0	0	0
18	0.3	100	962	0	0	0	0
19	0.3	100	1015	0	0	0	0

This first table tracks fluid interfaces in the drillpipe or casing. At t = 20 min, the first interface is located at 1,069 ft (Refer to coordinate system in the middle diagram of Figure 4-2-1.). By t = 25 min, it has traveled to 1,336 ft. No other fluid has entered the pipe. This means that the initial fluid is located in the range $5,000 > z > 1,336$ while the first fluid pumped is found in $1,336 > z > 0$.

20	**0.3**	**100**	**1069**	**0**	**0**	**0**	**0**
21	0.3	100	1122	0	0	0	0
22	0.4	100	1176	0	0	0	0
23	0.4	100	1229	0	0	0	0
24	0.4	100	1283	0	0	0	0
25	**0.4**	**100**	**1336**	**0**	**0**	**0**	**0**
26	0.4	100	1390	0	0	0	0
27	0.4	100	1443	0	0	0	0
28	0.5	100	1497	0	0	0	0
29	0.5	100	1550	0	0	0	0
30	0.5	100	1604	0	0	0	0
31	0.5	100	1657	0	0	0	0
32	0.5	100	1711	0	0	0	0
33	0.6	100	1764	0	0	0	0
34	0.6	100	1818	0	0	0	0
35	0.6	100	1871	0	0	0	0
36	0.6	100	1925	0	0	0	0
37	0.6	100	1978	0	0	0	0
38	0.6	100	2031	0	0	0	0
39	0.6	100	2085	0	0	0	0
40	0.7	100	2138	0	0	0	0
41	0.7	100	2192	0	0	0	0
42	0.7	100	2245	0	0	0	0
43	0.7	100	2299	0	0	0	0
44	0.7	100	2352	0	0	0	0
45	0.8	100	2406	0	0	0	0
46	0.8	100	2459	0	0	0	0
47	0.8	100	2513	0	0	0	0
48	0.8	100	2566	0	0	0	0
49	0.8	100	2620	0	0	0	0
50	0.8	100	2673	0	0	0	0
51	0.9	100	2727	0	0	0	0
52	0.9	100	2780	0	0	0	0
53	0.9	100	2834	0	0	0	0
54	0.9	100	2887	0	0	0	0
55	0.9	100	2940	0	0	0	0
56	0.9	100	2994	0	0	0	0
57	0.9	100	3047	0	0	0	0
58	1.0	100	3101	0	0	0	0
59	1.0	100	3154	0	0	0	0
60	1.0	200	3208	0	0	0	0
61	1.0	200	3315	106	0	0	0
62	1.0	200	3422	213	0	0	0
63	1.0	200	3529	320	0	0	0
64	1.1	200	3636	427	0	0	0
65	1.1	200	3743	534	0	0	0
66	1.1	200	3850	641	0	0	0
67	1.1	200	3956	748	0	0	0
68	1.1	200	4063	855	0	0	0
69	1.1	200	4170	962	0	0	0

At t = 70 min, the first interface has reached 4,277 ft, while the second interface is located at 1,069 ft. This means that the initial fluid is located in the region 5,000 > z > 4,277. The first fluid is found in 4,277 > z > 1,069, while the second appears in 1,069 > z > 0.

70	1.2	200	4277	1069	0	0	0
71	1.2	200	4384	1176	0	0	0
72	1.2	200	4491	1283	0	0	0
73	1.2	200	4598	1390	0	0	0
74	1.2	200	4705	1497	0	0	0
75	1.2	200	4812	1604	0	0	0

At approximately t = 76 min the first interface is located at 4,919 ft, while the second is found at 1,711 ft. Recall that the borehole length is assumed to be 5,000 ft. At t = 77 min, the first interface has been flushed out of the pipe and it has flowed into the annulus. This is noted in remarks at the end of this table, i.e., "Fluid "1" enters annulus at: 77 min." From the t = 77 line, the second interface is located at 1,818 ft. Thus, the first fluid is to be found in the region 5,000 > z > 1,818 while the second fluid is located in the range 1,818 > z > 0.

76	1.3	200	4919	1711	0	0	0
77	1.3	200	0	1818	0	0	0
78	1.3	200	0	1925	0	0	0
79	1.3	200	0	2031	0	0	0
80	1.3	200	0	2138	0	0	0
81	1.4	200	0	2245	0	0	0
82	1.4	200	0	2352	0	0	0
83	1.4	200	0	2459	0	0	0
84	1.4	200	0	2566	0	0	0
85	1.4	200	0	2673	0	0	0
86	1.4	200	0	2780	0	0	0
87	1.5	200	0	2887	0	0	0
88	1.5	200	0	2994	0	0	0
89	1.5	200	0	3101	0	0	0
90	1.5	200	0	3208	0	0	0
91	1.5	200	0	3315	0	0	0
92	1.5	200	0	3422	0	0	0
93	1.5	200	0	3529	0	0	0
94	1.6	200	0	3636	0	0	0
95	1.6	200	0	3743	0	0	0
96	1.6	200	0	3850	0	0	0
97	1.6	200	0	3956	0	0	0
98	1.6	200	0	4063	0	0	0
99	1.6	200	0	4170	0	0	0

At t = 100 min the second interface is located at 4,277 ft. This means that the first fluid is found in 5,000 > z > 4,277 and the second is in 4,277 > z > 0.

100	1.7	200	0	4277	0	0	0
101	1.7	200	0	4384	0	0	0
102	1.7	200	0	4491	0	0	0
103	1.7	200	0	4598	0	0	0
104	1.7	200	0	4705	0	0	0
105	1.8	200	0	4812	0	0	0
106	1.8	200	0	4919	0	0	0
107	1.8	200	0	0	0	0	0
108	1.8	200	0	0	0	0	0
109	1.8	200	0	0	0	0	0
110	1.8	200	0	0	0	0	0
111	1.9	200	0	0	0	0	0
112	1.9	200	0	0	0	0	0
113	1.9	200	0	0	0	0	0
114	1.9	200	0	0	0	0	0
115	1.9	200	0	0	0	0	0
116	1.9	200	0	0	0	0	0
117	2.0	200	0	0	0	0	0
118	2.0	200	0	0	0	0	0
119	2.0	200	0	0	0	0	0
120	2.0	300	0	0	0	0	0
121	2.0	300	0	0	160	0	0
122	2.0	300	0	0	320	0	0
123	2.0	300	0	0	481	0	0
124	2.1	300	0	0	641	0	0
125	2.1	300	0	0	802	0	0
126	2.1	300	0	0	962	0	0
127	2.1	300	0	0	1122	0	0
128	2.1	300	0	0	1283	0	0
129	2.2	300	0	0	1443	0	0

At t = 130 min the third interface is located at 1,604 ft. This means that the second fluid is located in 5,000 > z > 1,604, while the third fluid is found in 1,604 > z > 0.

130	2.2	300	0	0	1604	0	0
131	2.2	300	0	0	1764	0	0
132	2.2	300	0	0	1925	0	0
133	2.2	300	0	0	2085	0	0
134	2.2	300	0	0	2245	0	0
135	2.2	300	0	0	2406	0	0
136	2.3	300	0	0	2566	0	0
137	2.3	300	0	0	2727	0	0
138	2.3	300	0	0	2887	0	0
139	2.3	300	0	0	3047	0	0

```
140     2.3    300      0      0     3208      0      0
141     2.3    300      0      0     3368      0      0
142     2.4    300      0      0     3529      0      0
143     2.4    300      0      0     3689      0      0
144     2.4    300      0      0     3850      0      0
145     2.4    300      0      0     4010      0      0
146     2.4    300      0      0     4170      0      0
147     2.5    300      0      0     4331      0      0
148     2.5    300      0      0     4491      0      0
149     2.5    300      0      0     4652      0      0
```

At t = 150 min the third interface is located at 4,812 ft. Since the pipe length is 5,000 ft, it is about to be flushed out of the end of the pipe. In the next thirty minutes, approximately, there are no interfaces in the pipe. The "all 0" printout indicates that the only fluid in the pipe is the third fluid.

```
150     2.5    300      0      0     4812      0      0
151     2.5    300      0      0     4972      0      0
152     2.5    300      0      0        0      0      0
153     2.5    300      0      0        0      0      0
154     2.6    300      0      0        0      0      0
155     2.6    300      0      0        0      0      0
156     2.6    300      0      0        0      0      0
157     2.6    300      0      0        0      0      0
158     2.6    300      0      0        0      0      0
159     2.7    300      0      0        0      0      0
160     2.7    300      0      0        0      0      0
161     2.7    300      0      0        0      0      0
162     2.7    300      0      0        0      0      0
163     2.7    300      0      0        0      0      0
164     2.7    300      0      0        0      0      0
165     2.8    300      0      0        0      0      0
166     2.8    300      0      0        0      0      0
167     2.8    300      0      0        0      0      0
168     2.8    300      0      0        0      0      0
169     2.8    300      0      0        0      0      0
170     2.8    300      0      0        0      0      0
171     2.8    300      0      0        0      0      0
172     2.9    300      0      0        0      0      0
173     2.9    300      0      0        0      0      0
174     2.9    300      0      0        0      0      0
175     2.9    300      0      0        0      0      0
176     2.9    300      0      0        0      0      0
177     3.0    300      0      0        0      0      0
178     3.0    300      0      0        0      0      0
179     3.0    300      0      0        0      0      0
180     3.0    400      0      0        0      0      0
```

Now, the fourth interface has entered the pipe. The third fluid is located in the range 5,000 > z > 213 while the fourth fluid is found in 213 > z > 0.

181	3.0	400	0	0	0	213	0
182	3.0	400	0	0	0	427	0
183	3.0	400	0	0	0	641	0
184	3.1	400	0	0	0	855	0
185	3.1	400	0	0	0	1069	0
186	3.1	400	0	0	0	1283	0
187	3.1	400	0	0	0	1497	0
188	3.1	400	0	0	0	1711	0
189	3.2	400	0	0	0	1925	0
190	3.2	400	0	0	0	2138	0
191	3.2	400	0	0	0	2352	0
192	3.2	400	0	0	0	2566	0
193	3.2	400	0	0	0	2780	0
194	3.2	400	0	0	0	2994	0
195	3.2	400	0	0	0	3208	0
196	3.3	400	0	0	0	3422	0
197	3.3	400	0	0	0	3636	0
198	3.3	400	0	0	0	3850	0
199	3.3	400	0	0	0	4063	0
200	3.3	400	0	0	0	4277	0

At t = 201 min the fourth interface has migrated to 4,491 ft. The third fluid is located in the region 5,000 > z > 4,491, while the fourth fluid occupies almost the entire length of the pipe in 4,491 > z > 0. By t = 204 min the fourth interface will have left the pipe and turned into the annulus. Then the fourth fluid completely occupies the pipe.

201	3.3	400	0	0	0	4491	0
202	3.4	400	0	0	0	4705	0
203	3.4	400	0	0	0	4919	0
204	3.4	400	0	0	0	0	0
205	3.4	400	0	0	0	0	0
206	3.4	400	0	0	0	0	0
207	3.5	400	0	0	0	0	0
208	3.5	400	0	0	0	0	0
209	3.5	400	0	0	0	0	0
210	3.5	400	0	0	0	0	0
211	3.5	400	0	0	0	0	0
212	3.5	400	0	0	0	0	0
213	3.5	400	0	0	0	0	0
214	3.6	400	0	0	0	0	0
215	3.6	400	0	0	0	0	0
216	3.6	400	0	0	0	0	0
217	3.6	400	0	0	0	0	0
218	3.6	400	0	0	0	0	0

219	3.7	400	0	0	0	0	0
220	3.7	400	0	0	0	0	0
221	3.7	400	0	0	0	0	0
222	3.7	400	0	0	0	0	0
223	3.7	400	0	0	0	0	0
224	3.7	400	0	0	0	0	0
225	3.8	400	0	0	0	0	0
226	3.8	400	0	0	0	0	0
227	3.8	400	0	0	0	0	0
228	3.8	400	0	0	0	0	0
229	3.8	400	0	0	0	0	0
230	3.8	400	0	0	0	0	0
231	3.8	400	0	0	0	0	0
232	3.9	400	0	0	0	0	0
233	3.9	400	0	0	0	0	0
234	3.9	400	0	0	0	0	0
235	3.9	400	0	0	0	0	0
236	3.9	400	0	0	0	0	0
237	4.0	400	0	0	0	0	0
238	4.0	400	0	0	0	0	0
239	4.0	400	0	0	0	0	0
240	4.0	500	0	0	0	0	0
241	4.0	500	0	0	0	0	267
242	4.0	500	0	0	0	0	534
243	4.1	500	0	0	0	0	802
244	4.1	500	0	0	0	0	1069
245	4.1	500	0	0	0	0	1336
246	4.1	500	0	0	0	0	1604
247	4.1	500	0	0	0	0	1871
248	4.1	500	0	0	0	0	2138
249	4.2	500	0	0	0	0	2406

At t = 250 min the fifth interface is located at 2,673 ft. This means that the fourth fluid is found in 5,000 > z > 2,673, while the fifth fluid is found in the region 2,673 > z > 0.

250	4.2	500	0	0	0	0	2673
251	4.2	500	0	0	0	0	2940
252	4.2	500	0	0	0	0	3208
253	4.2	500	0	0	0	0	3475
254	4.2	500	0	0	0	0	3743
255	4.2	500	0	0	0	0	4010
256	4.3	500	0	0	0	0	4277
257	4.3	500	0	0	0	0	4545
258	4.3	500	0	0	0	0	4812

At t = 259 min the fifth interface has left the pipe, and the fifth fluid now completely occupies the pipe as indicated by the "all 0" data below. Note that while, in Figure 4-2-6, we have allowed for a total of 600 minutes of simulation, the printout here terminates at t = 259 min because nothing of dynamical significance occurs beyond this time (The only fluid in the pipe will be the fifth fluid, and this printout is eliminated for convenience.). The Fortran simulator used to calculate interfaces permits up to 10,000 minutes of rig-time modeling, or, approximately one week, of continuous pumping with six different fluids.

```
  259      4.3    500      0       0       0       0       0

  Borehole total length L, is:    5000 ft.
  Fluid "1" enters annulus at:      77 min.
  Fluid "2" enters annulus at:     107 min.
  Fluid "3" enters annulus at:     152 min.
  Fluid "4" enters annulus at:     204 min.
  Fluid "5" enters annulus at:     259 min.
```

The summary above is printed for convenience and is obtained by interrogating the tabular pipe data. Now that we have completed the tracking of all five interfaces in the pipe, the software algorithm turns to interface tracking in the annulus. The middle diagram in Figure 4-2-1 used a "left-pointing, little z" coordinate system for pipe flow with the origin at the far right, but now, as shown in the bottom diagram of Figure 4-2-1, we use a "right-pointing, big Z" convention for annular flow with an origin at the far left. Also note that the tabular interface headings for pipe flow took the form $z(1)$, $z(2)$, …, $z(5)$. However, for annular flow, we reverse the order of the tabulation to $Z(5)$, $Z(4)$, …, $Z(1)$ as shown below. The reason for this will be obvious. From the above summary, the first interface does not enter the annulus until t = 77 min. Thus, prior to t = 77 min only the initial fluid exists in the annulus. For this reason, the annular table below contains 0's everywhere until approximately t = 78 min. We will continue our discussion at the t = 78 min time entry.

ELAPSED	TIME	FLOW	Annular Fluid Interface (feet)				
Minutes	Hours	GPMs	Z(5)	Z(4)	Z(3)	Z(2)	Z(1)
0	0.0	100	0	0	0	0	0
1	0.0	100	0	0	0	0	0
2	0.0	100	0	0	0	0	0
3	0.1	100	0	0	0	0	0
4	0.1	100	0	0	0	0	0
5	0.1	100	0	0	0	0	0
6	0.1	100	0	0	0	0	0

7	0.1	100	0	0	0	0	0
8	0.1	100	0	0	0	0	0
9	0.2	100	0	0	0	0	0
10	0.2	100	0	0	0	0	0
11	0.2	100	0	0	0	0	0
12	0.2	100	0	0	0	0	0
13	0.2	100	0	0	0	0	0
14	0.2	100	0	0	0	0	0
15	0.2	100	0	0	0	0	0
16	0.3	100	0	0	0	0	0
17	0.3	100	0	0	0	0	0
18	0.3	100	0	0	0	0	0
19	0.3	100	0	0	0	0	0
20	0.3	100	0	0	0	0	0
21	0.3	100	0	0	0	0	0
22	0.4	100	0	0	0	0	0
23	0.4	100	0	0	0	0	0
24	0.4	100	0	0	0	0	0
25	0.4	100	0	0	0	0	0
26	0.4	100	0	0	0	0	0
27	0.4	100	0	0	0	0	0
28	0.5	100	0	0	0	0	0
29	0.5	100	0	0	0	0	0
30	0.5	100	0	0	0	0	0
31	0.5	100	0	0	0	0	0
32	0.5	100	0	0	0	0	0
33	0.6	100	0	0	0	0	0
34	0.6	100	0	0	0	0	0
35	0.6	100	0	0	0	0	0
36	0.6	100	0	0	0	0	0
37	0.6	100	0	0	0	0	0
38	0.6	100	0	0	0	0	0
39	0.6	100	0	0	0	0	0
40	0.7	100	0	0	0	0	0
41	0.7	100	0	0	0	0	0
42	0.7	100	0	0	0	0	0
43	0.7	100	0	0	0	0	0
44	0.7	100	0	0	0	0	0
45	0.8	100	0	0	0	0	0
46	0.8	100	0	0	0	0	0
47	0.8	100	0	0	0	0	0
48	0.8	100	0	0	0	0	0
49	0.8	100	0	0	0	0	0
50	0.8	100	0	0	0	0	0
51	0.9	100	0	0	0	0	0
52	0.9	100	0	0	0	0	0
53	0.9	100	0	0	0	0	0
54	0.9	100	0	0	0	0	0
55	0.9	100	0	0	0	0	0
56	0.9	100	0	0	0	0	0

57	0.9	100	0	0	0	0	0
58	1.0	100	0	0	0	0	0
59	1.0	100	0	0	0	0	0
60	1.0	200	0	0	0	0	0
61	1.0	200	0	0	0	0	0
62	1.0	200	0	0	0	0	0
63	1.0	200	0	0	0	0	0
64	1.1	200	0	0	0	0	0
65	1.1	200	0	0	0	0	0
66	1.1	200	0	0	0	0	0
67	1.1	200	0	0	0	0	0
68	1.1	200	0	0	0	0	0
69	1.1	200	0	0	0	0	0
70	1.2	200	0	0	0	0	0
71	1.2	200	0	0	0	0	0
72	1.2	200	0	0	0	0	0
73	1.2	200	0	0	0	0	0
74	1.2	200	0	0	0	0	0
75	1.2	200	0	0	0	0	0
76	1.3	200	0	0	0	0	0
77	1.3	200	0	0	0	0	0

At t = 78 min we find that the first interface (under the Z(1) heading) is located at Z = 53 ft. Thus, the first fluid is found in 0 < Z < 53, while the initial fluid is found in 53 < Z < 5,000 (again, "5,000" represents the surface).

78	1.3	200	0	0	0	0	53
79	1.3	200	0	0	0	0	106
80	1.3	200	0	0	0	0	160
81	1.4	200	0	0	0	0	213
82	1.4	200	0	0	0	0	267
83	1.4	200	0	0	0	0	320
84	1.4	200	0	0	0	0	374
85	1.4	200	0	0	0	0	427
86	1.4	200	0	0	0	0	481
87	1.5	200	0	0	0	0	534
88	1.5	200	0	0	0	0	588
89	1.5	200	0	0	0	0	641
90	1.5	200	0	0	0	0	695
91	1.5	200	0	0	0	0	748
92	1.5	200	0	0	0	0	802
93	1.5	200	0	0	0	0	855
94	1.6	200	0	0	0	0	909
95	1.6	200	0	0	0	0	962
96	1.6	200	0	0	0	0	1015
97	1.6	200	0	0	0	0	1069
98	1.6	200	0	0	0	0	1122
99	1.6	200	0	0	0	0	1176
100	1.7	200	0	0	0	0	1229

101	1.7	200	0	0	0	0	1283
102	1.7	200	0	0	0	0	1336
103	1.7	200	0	0	0	0	1390
104	1.7	200	0	0	0	0	1443
105	1.8	200	0	0	0	0	1497
106	1.8	200	0	0	0	0	1550
107	1.8	200	0	0	0	0	1604
108	1.8	200	0	0	0	53	1657
109	1.8	200	0	0	0	106	1711
110	1.8	200	0	0	0	160	1764
111	1.9	200	0	0	0	213	1818
112	1.9	200	0	0	0	267	1871
113	1.9	200	0	0	0	320	1925
114	1.9	200	0	0	0	374	1978
115	1.9	200	0	0	0	427	2031
116	1.9	200	0	0	0	481	2085
117	2.0	200	0	0	0	534	2138
118	2.0	200	0	0	0	588	2192
119	2.0	200	0	0	0	641	2245
120	2.0	300	0	0	0	695	2299
121	2.0	300	0	0	0	775	2379
122	2.0	300	0	0	0	855	2459
123	2.0	300	0	0	0	935	2539
124	2.1	300	0	0	0	1015	2620
125	2.1	300	0	0	0	1096	2700
126	2.1	300	0	0	0	1176	2780
127	2.1	300	0	0	0	1256	2860
128	2.1	300	0	0	0	1336	2940
129	2.2	300	0	0	0	1417	3021
130	2.2	300	0	0	0	1497	3101
131	2.2	300	0	0	0	1577	3181
132	2.2	300	0	0	0	1657	3261
133	2.2	300	0	0	0	1737	3342
134	2.2	300	0	0	0	1818	3422
135	2.2	300	0	0	0	1898	3502
136	2.3	300	0	0	0	1978	3582
137	2.3	300	0	0	0	2058	3662
138	2.3	300	0	0	0	2138	3743
139	2.3	300	0	0	0	2219	3823
140	2.3	300	0	0	0	2299	3903
141	2.3	300	0	0	0	2379	3983
142	2.4	300	0	0	0	2459	4063
143	2.4	300	0	0	0	2539	4144
144	2.4	300	0	0	0	2620	4224
145	2.4	300	0	0	0	2700	4304
146	2.4	300	0	0	0	2780	4384
147	2.5	300	0	0	0	2860	4464
148	2.5	300	0	0	0	2940	4545
149	2.5	300	0	0	0	3021	4625

At t = 150 min the first interface is approaching the surface, since it is located at 4,705 ft. (the surface location is 5,000 ft). The second Z(2) interface is found at 3,101 ft. Thus, the initial fluid is found in 4,705 < Z < 5,000, while the first fluid is in 3,101 < Z < 4,705. The second fluid is located in 0 < Z < 3,101.

150	2.5	300	0	0	0	3101	4705
151	2.5	300	0	0	0	3181	4785
152	2.5	300	0	0	0	3261	4865
153	2.5	300	0	0	80	3342	4946

Now, the first interface has left the annulus and entered the mud tank at the surface. The second interface is located at 3,422 ft. while the third interface is found at 160 ft. Thus, the first fluid is found in 3,422 < Z < 5,000, while the second is found in 160 < Z < 3,422. The third fluid is located in 0 < Z < 160.

154	2.6	300	0	0	160	3422	0
155	2.6	300	0	0	240	3502	0
156	2.6	300	0	0	320	3582	0
157	2.6	300	0	0	401	3662	0
158	2.6	300	0	0	481	3743	0
159	2.7	300	0	0	561	3823	0
160	2.7	300	0	0	641	3903	0
161	2.7	300	0	0	721	3983	0
162	2.7	300	0	0	802	4063	0
163	2.7	300	0	0	882	4144	0
164	2.7	300	0	0	962	4224	0
165	2.8	300	0	0	1042	4304	0
166	2.8	300	0	0	1122	4384	0
167	2.8	300	0	0	1203	4464	0
168	2.8	300	0	0	1283	4545	0
169	2.8	300	0	0	1363	4625	0

At t = 170 min the second interface is located at 4,705 ft. while the third is found at 1,443 ft. Thus, the first fluid is located in 4,705 < Z < 5,000, while the second is found in 1,443 < Z < 4,705. The third fluid is found in 0 < Z < 1,443. At approximately t = 173 min the second interface leaves the annulus and completely disappears from the system. Then, the second fluid is found in the region 1,684 < Z < 5,000, while the third is located in 0 < Z < 1,684.

170	2.8	300	0	0	1443	4705	0
171	2.8	300	0	0	1523	4785	0
172	2.9	300	0	0	1604	4865	0
173	2.9	300	0	0	1684	4946	0
174	2.9	300	0	0	1764	0	0

175	2.9	300	0	0	1844	0	0
176	2.9	300	0	0	1925	0	0
177	3.0	300	0	0	2005	0	0
178	3.0	300	0	0	2085	0	0
179	3.0	300	0	0	2165	0	0
180	3.0	400	0	0	2245	0	0
181	3.0	400	0	0	2352	0	0
182	3.0	400	0	0	2459	0	0
183	3.0	400	0	0	2566	0	0
184	3.1	400	0	0	2673	0	0
185	3.1	400	0	0	2780	0	0
186	3.1	400	0	0	2887	0	0
187	3.1	400	0	0	2994	0	0
188	3.1	400	0	0	3101	0	0
189	3.2	400	0	0	3208	0	0
190	3.2	400	0	0	3315	0	0
191	3.2	400	0	0	3422	0	0
192	3.2	400	0	0	3529	0	0
193	3.2	400	0	0	3636	0	0
194	3.2	400	0	0	3743	0	0
195	3.2	400	0	0	3850	0	0
196	3.3	400	0	0	3956	0	0
197	3.3	400	0	0	4063	0	0
198	3.3	400	0	0	4170	0	0
199	3.3	400	0	0	4277	0	0

At t = 200 min, the third interface is located at 4,384 ft. Thus, the second fluid is found in 4,384 < Z < 5,000 while the first appears in 0 < Z < 4,384 (Recall that, at t = 173 min, the second interface has left the annulus.). By now, the interpretation process for both pipe and annulus should be apparent. We turn finally to t = 296 min.

200	**3.3**	**400**	**0**	**0**	**4384**	**0**	**0**
201	3.3	400	0	0	4491	0	0
202	3.4	400	0	0	4598	0	0
203	3.4	400	0	0	4705	0	0
204	3.4	400	0	0	4812	0	0
205	3.4	400	0	106	4919	0	0
206	3.4	400	0	213	0	0	0
207	3.5	400	0	320	0	0	0
208	3.5	400	0	427	0	0	0
209	3.5	400	0	534	0	0	0
210	3.5	400	0	641	0	0	0
211	3.5	400	0	748	0	0	0
212	3.5	400	0	855	0	0	0
213	3.5	400	0	962	0	0	0
214	3.6	400	0	1069	0	0	0
215	3.6	400	0	1176	0	0	0
216	3.6	400	0	1283	0	0	0

217	3.6	400	0	1390	0	0	0
218	3.6	400	0	1497	0	0	0
219	3.7	400	0	1604	0	0	0
220	3.7	400	0	1711	0	0	0
221	3.7	400	0	1818	0	0	0
222	3.7	400	0	1925	0	0	0
223	3.7	400	0	2031	0	0	0
224	3.7	400	0	2138	0	0	0
225	3.8	400	0	2245	0	0	0
226	3.8	400	0	2352	0	0	0
227	3.8	400	0	2459	0	0	0
228	3.8	400	0	2566	0	0	0
229	3.8	400	0	2673	0	0	0
230	3.8	400	0	2780	0	0	0
231	3.8	400	0	2887	0	0	0
232	3.9	400	0	2994	0	0	0
233	3.9	400	0	3101	0	0	0
234	3.9	400	0	3208	0	0	0
235	3.9	400	0	3315	0	0	0
236	3.9	400	0	3422	0	0	0
237	4.0	400	0	3529	0	0	0
238	4.0	400	0	3636	0	0	0
239	4.0	400	0	3743	0	0	0
240	4.0	500	0	3850	0	0	0
241	4.0	500	0	3983	0	0	0
242	4.0	500	0	4117	0	0	0
243	4.1	500	0	4251	0	0	0
244	4.1	500	0	4384	0	0	0
245	4.1	500	0	4518	0	0	0
246	4.1	500	0	4652	0	0	0
247	4.1	500	0	4785	0	0	0
248	4.1	500	0	4919	0	0	0
249	4.2	500	0	0	0	0	0
250	4.2	500	0	0	0	0	0
251	4.2	500	0	0	0	0	0
252	4.2	500	0	0	0	0	0
253	4.2	500	0	0	0	0	0
254	4.2	500	0	0	0	0	0
255	4.2	500	0	0	0	0	0
256	4.3	500	0	0	0	0	0
257	4.3	500	0	0	0	0	0
258	4.3	500	0	0	0	0	0
259	4.3	500	0	0	0	0	0
260	4.3	500	133	0	0	0	0
261	4.3	500	267	0	0	0	0
262	4.4	500	401	0	0	0	0
263	4.4	500	534	0	0	0	0
264	4.4	500	668	0	0	0	0
265	4.4	500	802	0	0	0	0
266	4.4	500	935	0	0	0	0

267	4.4	500	1069	0	0	0	0
268	4.5	500	1203	0	0	0	0
269	4.5	500	1336	0	0	0	0
270	4.5	500	1470	0	0	0	0
271	4.5	500	1604	0	0	0	0
272	4.5	500	1737	0	0	0	0
273	4.6	500	1871	0	0	0	0
274	4.6	500	2005	0	0	0	0
275	4.6	500	2138	0	0	0	0
276	4.6	500	2272	0	0	0	0
277	4.6	500	2406	0	0	0	0
278	4.6	500	2539	0	0	0	0
279	4.7	500	2673	0	0	0	0
280	4.7	500	2807	0	0	0	0
281	4.7	500	2940	0	0	0	0
282	4.7	500	3074	0	0	0	0
283	4.7	500	3208	0	0	0	0
284	4.7	500	3342	0	0	0	0
285	4.8	500	3475	0	0	0	0
286	4.8	500	3609	0	0	0	0
287	4.8	500	3743	0	0	0	0
288	4.8	500	3876	0	0	0	0
289	4.8	500	4010	0	0	0	0
290	4.8	500	4144	0	0	0	0
291	4.8	500	4277	0	0	0	0
292	4.9	500	4411	0	0	0	0
293	4.9	500	4545	0	0	0	0
294	4.9	500	4678	0	0	0	0
295	4.9	500	4812	0	0	0	0

At t = 296 min the Z(5) interface is located at 4,946 ft, very close to the surface, located at 5,000 ft. Thus, the fifth fluid is found in 0 < Z < 4,946, while the fourth fluid is found in 4,946 < Z < 5,000. The computation of pressures in the annulus and in the pipe follow the general discussions given previously. For documentation purposes, we refer to both tables and their included explanations as "Figure 4-2-7."

296	**4.9**	**500**	**4946**	**0**	**0**	**0**	**0**
297	4.9	500	0	0	0	0	0

Figure 4-2-7. Pipe and annular interface position table.

On real interfaces.   In the above calculations, we speak of interfaces as being located at "z = …" or "Z = …," that is, "interfaces are flat." This description suffices from the macroscopic perspective. If we require details about the narrower mixing zone between two contiguous fluids, we then "zoom" in to perform boundary-layer type calculations using pressure gradient information obtained as discussed above. Calculation procedures of the "boundary layer" type are explained and provided later. Typical mixing zones, shown in Figure 4-2-8, are clearly not planar in the detailed description.
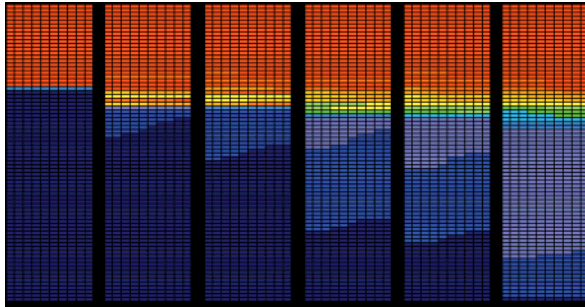
Figure 4-2-8. Propagating and diffusing front in time, constructed from movie frames for viscosity history using exaggerated diffusion.

4.3 Calculating annular and drillpipe pressure loss.

Discussion 4-2 describes our "interface tracker," an important modeling tool that determines where our six fluids are at any instant in time. Once the length of a particular "fluid slug" is available, the volumetric pump rate Q at that instant is used to determine the pressure gradient applicable to the non-Newtonian fluid in question. The pressure loss associated with this slug is simply the product of length and pressure gradient. This idea was illustrated using both drillpipe and annular examples in the previous discussion. For the sake of completeness, we now summarize key analytical results available for non-Newtonian pipe flows and also recapitulate our new simulation capabilities for eccentric annular flows. Note that our pump schedule is transient, with Q's that vary in time; however, within a defined time interval, the Q in question is constant. In mathematics, this is known as a "piecewise constant" specification. This approach makes it is possible to use steady-state models within the framework of transient pumping.

Newtonian pipe flow model. Several exact, closed form, analytical solutions are available in the literature for different types of rheologies in flow in circular pipe. We will review these results and offer key formulas without proof. Figure 4-3-1 illustrates straight, axisymmetric, pipe flow, where the axial velocity, $u(r) > 0$, depends on the radial coordinate $r > 0$. With these conventions, the "shear rate," $du/dr < 0$, is negative, that is, $u(r)$ decreases as r increases. Very often, the notation $d\gamma/dt = - du/dr > 0$ is used. If the viscous shear stress, τ, and the shear rate are linearly related by

$$\tau = - \mu \, du/dr > 0 \qquad (4\text{-}3\text{-}1a)$$

where μ is the viscosity, a constant or temperature dependent quantity, then two simple relationships can be derived for pipe flow.
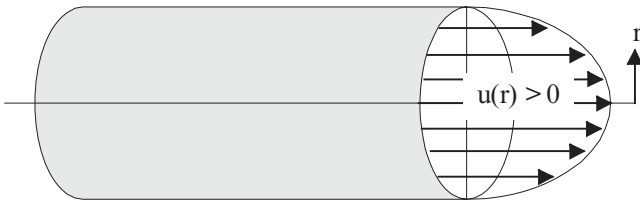
Note, $du/dr < 0$

Figure 4-3-1. Axisymmetric pipe flow.

Let $\Delta p > 0$ be the (positive) pressure drop over a pipe of length L, and R be the inner radius of the pipe. Then, the radial velocity distribution satisfies

$$u(r) = [\Delta p /(4\mu \, L)] \, (R^2 - r^2) > 0 \qquad (4\text{-}3\text{-}1b)$$

Note that u is constrained by a "no-slip" velocity condition at $r = R$. If the product of "$u(r)$" and the infinitesimal ring area "$2\pi r \, dr$" is integrated over (0,R), we obtain the volumetric flow rate expressed by

$$Q = \pi R^4 \Delta p /(8\mu \, L) > 0 \qquad (4\text{-}3\text{-}1c)$$

Equation 4-3-1c is the well-known Hagen-Poiseuille formula for flow in a pipe. These solutions do not include unsteadiness or compressibility. These results are exact relationships derived from the Navier-Stokes equations, which govern viscous flows when the stress-strain relationships take the linear form in Equation 4-3-1a. We

emphasize that the Navier-Stokes equations apply to Newtonian flows only, and not to more general rheological models.

Note that viscous stress (and the wall value τ_w) can be calculated from Equation 4-3-1a, but the following formulas can also be used,

$$\tau(r) = r \, \Delta p / 2L > 0 \qquad\qquad (4\text{-}3\text{-}2a)$$

$$\tau_w = R \, \Delta p / 2L > 0 \qquad\qquad (4\text{-}3\text{-}2b)$$

Equations 4-3-2a,b apply generally to steady laminar flows in circular pipes, and importantly, whether the rheology is Newtonian or not. But they do not apply to ducts with other cross-sections, nor to annular flows, even concentric ones, whatever the fluid.

Bingham plastic pipe flow. Bingham plastics satisfy a slightly modified constitutive relationship, usually written in the form,

$$\tau = \tau_0 - \mu \, du/dr \qquad\qquad (4\text{-}3\text{-}3a)$$

where τ_0 represents the yield stress of the fluid. In other words, fluid motion will not initiate until stresses exceed yield; in a moving fluid, a "plug flow" moving as a solid body is always found below a "plug radius" defined by

$$R_p = 2\tau_0 \, L / \Delta p \qquad\qquad (4\text{-}3\text{-}3b)$$

The "if-then" nature of this model renders it nonlinear, despite the (misleading) linear appearance in Equation 4-3-3a. Fortunately, simple solutions are known,

$$u(r) = (1/\mu) \, [\{\Delta p /(4L)\} \, (R^2 - r^2) - \tau_0 \, (R - r)], \; R_p \leq r \leq R \qquad (4\text{-}3\text{-}3c)$$

$$u(r) = (1/\mu) \, [\{\Delta p /(4L)\} \, (R^2 - R_p^2) - \tau_0 \, (R - R_p)], \; 0 \leq r \leq R_p \qquad (4\text{-}3\text{-}3d)$$

$$Q/(\pi R^3) = [\, \tau_w /(4\mu)] \, [1 - 4/3 \, (\tau_0 /\tau_w) + 1/3 \, (\tau_0 /\tau_w)^4 \,] \qquad (4\text{-}3\text{-}3e)$$

Power law fluids in pipe flow. Power law fluids without yield stress satisfy Equation 4-3-4a, and the rate solutions in Equations 4-3-4b,c.

$$\tau = K \, (\, \text{-} \, du/dr)^n \qquad\qquad (4\text{-}3\text{-}4a)$$

$$u(r) = (\Delta p/2KL)^{1/n} \, [n/(n+1)] \, (\, R^{(n+1)/n} - r^{(n+1)/n} \,) \qquad (4\text{-}3\text{-}4b)$$

$$Q/(\pi R^3) = [R\Delta p/(2KL)]^{1/n} \, n/(3n+1) \qquad\qquad (4\text{-}3\text{-}4c)$$
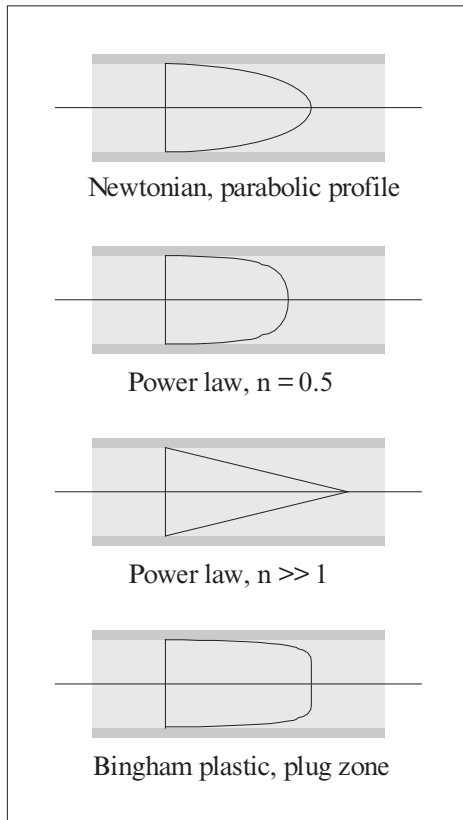
Figure 4-3-2. Typical non-Newtonian velocity profiles.

Herschel-Bulkley pipe flow model. This model combines Power law with yield stress characteristics, with the result that,

$$\tau = \tau_0 + K\,(\,-du/dr)^n \tag{4-3-5a}$$

$$u(r) = K^{-1/n}\,(\Delta p/2L)^{-1}\,\{n/(n+1)\} \tag{4-3-5b}$$
$$\times\,[(R\Delta p/2L\, -\tau_0)^{(n+1)/n} - (r\Delta p/2L\, -\tau_0)^{(n+1)/n}],\ R_p \leq r \leq R$$

$$u(r) = K^{-1/n}\,(\Delta p/2L)^{-1}\,\{n/(n+1)\} \tag{4-3-5c}$$
$$\times\,[(R\Delta p/2L\, -\tau_0)^{(n+1)/n} - (R_p\,\Delta p/2L\, -\tau_0)^{(n+1)/n}],\ 0 \leq r \leq R_p$$

$$Q/(\pi R^3) = K^{-1/n}\,(R\Delta p/2L)^{-3}\,(R\Delta p/2L\, -\tau_0)^{(n+1)/n} \tag{4-3-5d}$$
$$\times\,[(R\Delta p/2L\, -\tau_0)^2\,n\,/(3n+1) + 2\,\tau_0\,(R\Delta p/2L\, -\tau_0)\,n\,/(2n+1) + \tau_0^2\,n/(n+1)]$$

where the plug radius R_p is again defined by Equation 4-3-3b.

Ellis fluids in pipe flow.   Ellis fluids satisfy a more complicated constitutive relationship, with the following known results,

$$\tau = - du/dr /(A + B \tau^{\alpha-1}) \qquad\qquad (4\text{-}3\text{-}6a)$$

$$u(r) = A \Delta p (R^2 - r^2)/(4L) + B(\Delta p/2L)^{\alpha} (R^{\alpha+1} - r^{\alpha+1})/(\alpha + 1) \qquad\qquad (4\text{-}3\text{-}6b)$$

$$Q/(\pi R^3) = A\tau_w/4 + B \tau_w^{\alpha}/(\alpha+3) \qquad\qquad (4\text{-}3\text{-}6c)$$

$$= A(R\Delta p/2L) /4 + B (R\Delta p/2L)^{\alpha}/(\alpha+3)$$

Dozens of additional rheological models appear in the literature, but the most common ones used in petroleum engineering are those given here. Typical qualitative features of the associated velocity profiles are shown in Figure 4-3-2.

Annular flow solutions.   We next discuss annular flow solutions. As noted earlier in this book, annular flow solutions that are useful in petroleum engineering are lacking.   The only known exact, closed form, analytical solution is a classic one describing Newtonian flow in a concentric annulus.   Let R be the outer radius, and κR be the inner radius, so that $0 < \kappa < 1$.   Then, it can be shown that,

$$u(r) = [R^2 \Delta p /(4\mu L)]$$
$$\times [1 - (r/R)^2 + (1- \kappa^2) \log_e (r/R) / \log_e (1/\kappa)] \qquad (4\text{-}3\text{-}7a)$$

$$Q = [\pi R^4 \Delta p /(8\mu L)] [1 - \kappa^4 - (1- \kappa^2)^2 / \log_e (1/\kappa)] \qquad (4\text{-}3\text{-}7b)$$

For non-Newtonian flows, even for concentric geometries, numerical procedures are required, e.g., see Fredrickson and Bird (1958), Bird, Stewart, and Lightfoot (1960), or Skelland (1967).

Analytically based   treatments for eccentric annuli formed from circles are available through bipolar coordinate formulations.   These are ultimately numerical in nature and require significant amounts of algebra in their development.   Because the methods are limited to circles, and not generalizable to practical geometries with cuttings beds, washouts, and other borehole anomalies, they are not discussed in this book.

The mappings we have developed, we emphasize, can and have been extended to three-dimensional applications that allow changes of cross-sectional geometry along the borehole.   Moreover, the effects of multiphase flow with diffusive mixing have been incorporated in the author's models.   Recent publications describing these specialized efforts appear in Savery, Darby, and Chin (2007); Deawwanich, Liew, Nguyen, Savery, Tonmukayakul, and Chin (2008); Nguyen, Deawwanich,

Tonmukayakul, Savery, and Chin (2008); Savery, Chin, and Babu Yerubandi (2008); and Savery, Tonmukayakul, Chin, Deawwanich, Liew, and Nguyen (2008). We note that the algorithms developed in this book are faster and more stable than the models just referenced, particularly in handling spatial derivatives of apparent viscosity and the coupling of rotating flows to axial effects. We next review the eccentric annular flow capabilities with respect to their use in total pressure drop in Discussion 4-2.

Review of steady eccentric flow models. As noted, models do not presently exist for non-Newtonian yield stress fluids in arbitrary eccentric annuli, either for steady or transient flow, with or without pipe rotation, except for those developed in this book. Only those software models that are fast and numerically stable are discussed and offered for general dissemination. We take this opportunity to summarize these methods now because Discussion 4-2 importantly describes the roles played by our steady-state "building block" modules. From that discussion, we noted how the pressure profile in the drillpipe and borehole system (as a function of time) requires computations that look something like "$(100 - 80) (\partial P/\partial z)_{pipe,0} + (80 - 75) (\partial P/\partial z)_{pipe,1} + (75 - 65) (\partial P/\partial z)_{pipe,2} + (65-50) (\partial P/\partial z)_{pipe,3} + (50 - 30) (\partial P/\partial z)_{pipe,4} + (30 - 0) (\partial P/\partial z)_{pipe,5} + \Delta + (100 - 0) (\partial P/\partial z)_{annulus,0}$," where pipe flow equations are succinctly given above and the annular pressure drops require our sophisticated computational modeling tools.
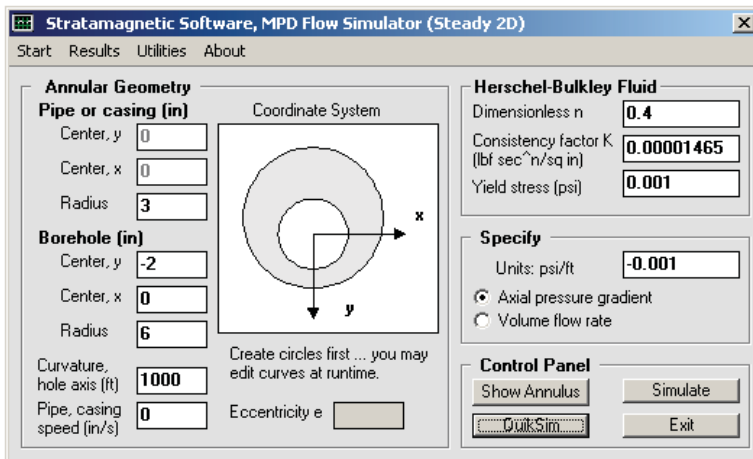
Figure 4-3-3. MPD Flow Simulator, "Steady 2D."

First, we emphasize the importance of our steady flow simulator, whose user interface is shown in Figure 4-3-3. This computes all flow properties for eccentric non-rotating annular flows (allowing washouts, cuttings beds and other geometric anomalies), assuming general Herschel-Bulkley fluids, importantly in the "volumetric flow rate specified" mode in which the required pressure gradients are automatically calculated without user intervention. Here, the size and shape of all plug zones are calculated naturally using an extended Herschel-Bulkley model. The model includes borehole radius of curvature effects, should Figure 4-2-1 incorporate turns from vertical to horizontal.
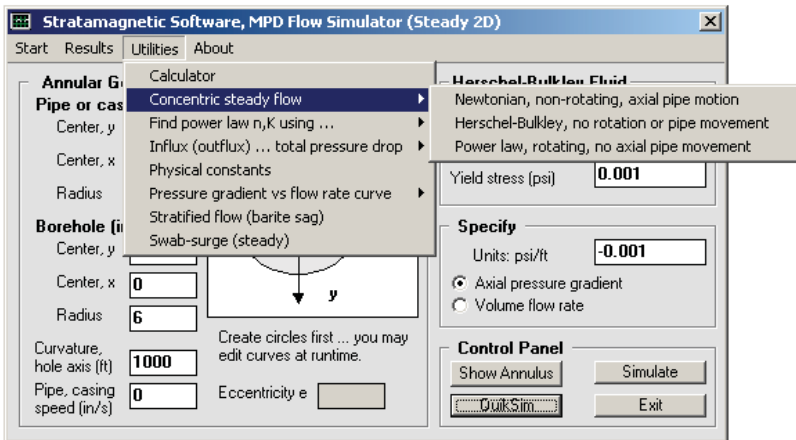
Figure 4-3-4. MPD Flow Simulator, "Steady 2D" utilities.

Our steady two-dimensional simulator also includes analytical solutions for concentric annuli, as shown in Figure 4-3-4. These are "Newtonian, non-rotating, axial pipe motion," "Herschel-Bulkley, no rotation or pipe movement," and "Power law, rotating, no axial pipe movement." For eccentric flows, when detailed spatial plots for physical properties are not required, the fast mode shown in Figure 4-3-5 gives numerous pressure gradient results in one or two minutes of computing time. Our steady 2D eccentric solver assumes zero pipe rotation.
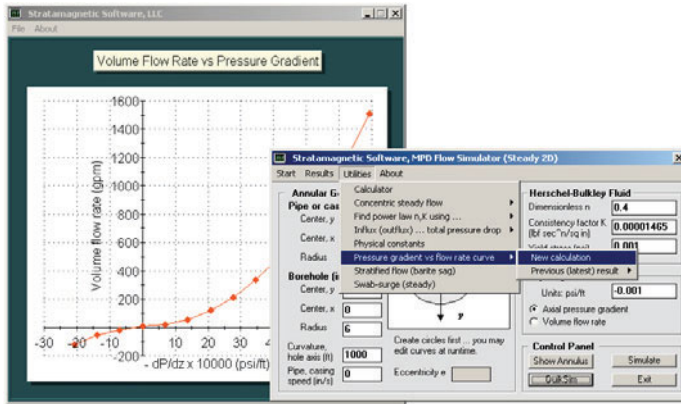
Figure 4-3-5. Rapid calculation of multiple flow solutions.
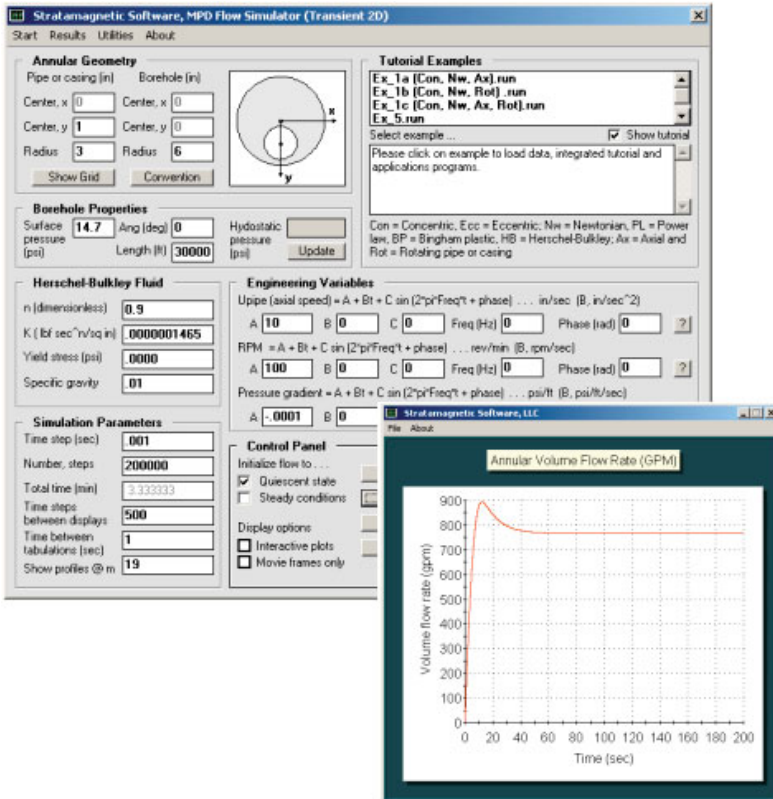
Figure 4-3-6. "Transient 2D" solver.

As indicated elsewhere in this book, the computation of steady flows with pipe rotation within the framework of a purely steady formulation is an unstable numerical process at present. This is not to say that steady flows with rotation cannot be computed. They can, as noted in Figure 4-3-6, provided we treat the unsteady problem and carry out our computations for large times until steady conditions are reached. This often requires one minute or less for fluids with low specific gravity, and sometimes, as many as three minutes for heavy weight muds or cements. Figure 4-3-6 shows how steady-state pressure gradients can be obtained for given flow rates. Once the target flow rate is given, the search for the required pressure gradient may take several intelligent guesses. In closing, we have summarized all of the methods we have devised to obtain pressure gradients when target flow rates are specified.

4.4 Herschel-Bulkley pipe flow analysis.

As noted, the calculation of pressure at the drillbit (in the formation) and pressure along the borehole is completely determined by the distribution of pressure gradient in the hole and the value of pressure at the surface choke. If, however, the pressure needed at the mud pump to support the flow is required, also needed are the pressure loss through the drillbit as well as the pressure drop in the drillpipe. For non-rotating pipe flow, exact, closed form, circular pipe flow solutions for radial velocity distribution and total volumetric flow rate are available for Herschel-Bulkley fluids from Equations 4-3-5a,b,c,d. Thus, the same properties for the subsets including Newtonian, Power law and Bingham plastic fluids are also available.

The general mathematical solution has been incorporated into two software programs for convenience. The first, shown in Figure 4-4-1a, solves Equation 4-3-5d for pressure gradient when the flow rate is given. This represents a nonlinear algebraic equation for the unknown. The example here applies to a 10 cp Newtonian fluid. For the parameters shown, the required pressure gradient is about – 0.001 psi/ft. In Figure 4-4-1b, we introduce yield stress to this fluid, so that it now acts as a Bingham plastic. We expect that the pressure gradient should steepen because there is greater difficulty in moving the fluid. In fact, the pressure gradient is now about – 0.015 psi/ft. Finally, in Figure 4-4-1c, we change the fluid exponent from 1.0 to 0.8, so that the fluid is now of a Herschel-Bulkley type.

In this case, the pressure gradient is obtained as – 0.014 psi/ft. It is interesting how the presence of yield stress introduces large changes to pressure gradient over Newtonian flows.
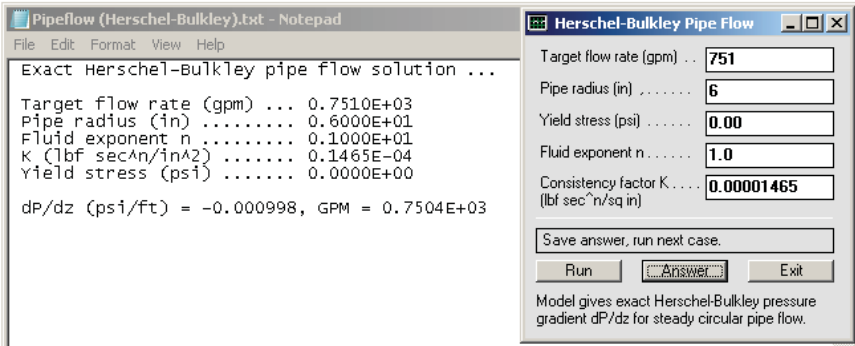
Figure 4-4-1a. Newtonian fluid, flow rate given.
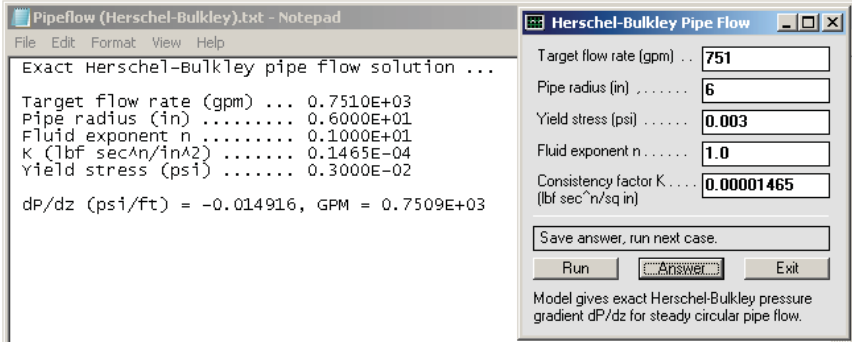
Figure 4-4-1b. Bingham plastic, flow rate given.
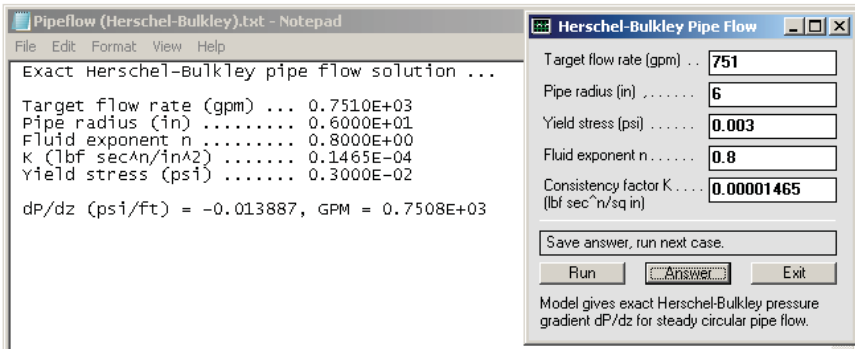
Figure 4-4-1c. Herschel-Bulkley fluid, flow rate given.

In Figure 4-4-2a, we demonstrate our second use of Equations 4-3-5a,b,c,d, namely, computing total flow rate and radial velocity distribution for any Herschel-Bulkley fluid. Here, a Newtonian fluid is assumed, and the classic paraboloidal velocity profile is obtained. In Figure 4-4-2b, we illustrate this capability with a Herschel-Bulkley fluid. The graph clearly indicates the presence of a plug zone. The plug radius is also given in the output.
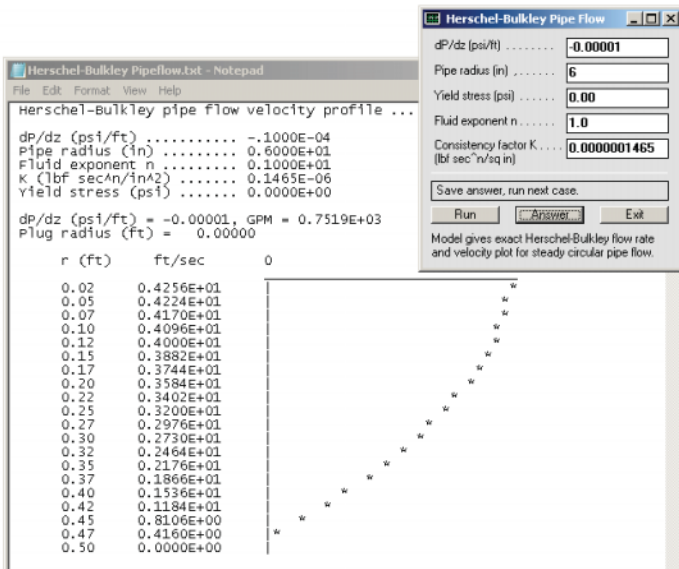
Figure 4-4-2a. Newtonian fluid, pressure gradient given.
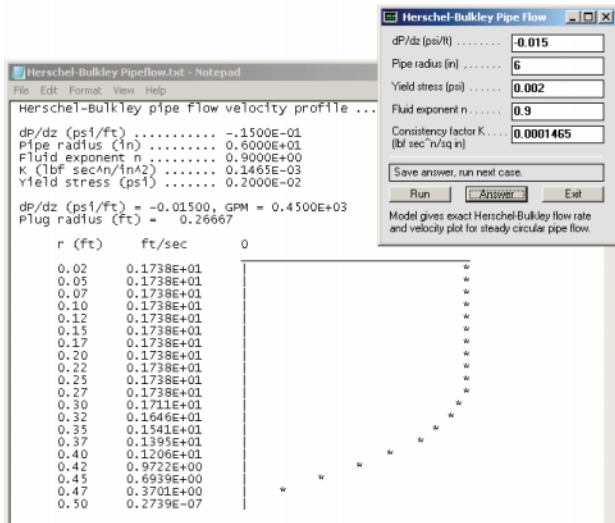
Figure 4-4-2b. Herschel-Bulkley fluid, pressure gradient given.

4.5 Transient, three-dimensional, eccentric multiphase flow analysis for non-rotating Newtonian fluids.

Here we introduce multiphase flow computations for a special limit of the general problem, one assuming Newtonian mixtures in concentric or eccentric annuli (with possible cross-sectional changes in the axial direction), however, without pipe or casing rotation. Later, we remove our Newtonian, non-rotating flow restrictions and consider general non-Newtonian fluids in eccentric annuli with steady pipe rotation. Software for the present limit was developed because the solution process could be automated and Newtonian applications do exist. But our purposes are two-fold: first, to illustrate basic flow concepts, and second, to demonstrate that our formulation, solution and software foundation for subsequent development are sound and correct.

Example 1. We first show that our exact, steady, concentric Newtonian flow solution and the transient numerical model under consideration are consistent in the concentric single-phase flow limit. This is intended to validate the software architecture, which is complicated and which forms the basis for other models. The simulator for our exact solution is launched from the earlier "Steady 2D" menu in Figure 4-5-1, leading to the applications program in Figure 4-5-2. Note how the assumed parameters yield a flow rate of 947.1 gpm.
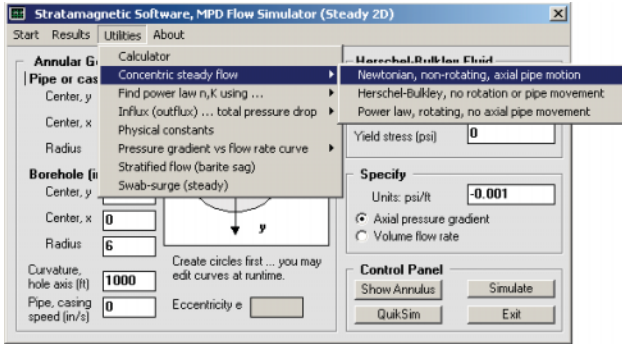
Figure 4-5-1. General "Steady 2D" menu.
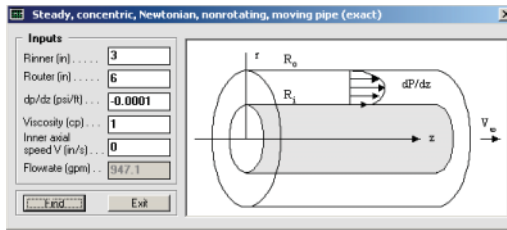
Figure 4-5-2. Exact two-dimensional Newtonian flow solution.

Next, we launch the "Transient 3D, Multiphase, Newtonian, Non-Rotating" flow simulator in Figure 4-5-3. For multiphase problems, it is not meaningful to specify pressure gradients as in single-phase calculations; these gradients vary with space and time as local fluids mix and it is impossible to state clearly what they are. One is therefore forced to specify total flow rate, at least approximately, and this specification must be used when dealing with multiphase applications. Our simulator operates in a "specify flow rate" mode.

In order to be completely consistent with Figure 4-5-2, we assume a 1 cp viscosity for both "left" and "right" fluids, zero pipe speed, plus identical geometries. We also assume identical small specific gravities; low mechanical inertias allow larger time steps and reduce integration times needed for convergence. Internal to the software, $C = 0$ means left properties, i.e., μ_{left} and ρ_{left}, while $C = 1$ means right; since left and right properties are identical, the choice $C_{left} = C_{right} = 1$ ensures that $C = 1$ continuously throughout and the fluid is homogeneous. Note that, in Figure 4-5-3, we have entered 947.1 as the target flow rate.

Once numerical integrations begin, the imposed motion must overcome "nonuniformities" associated with the uniform (unsheared) flow used to initialize the calculation, plus, of course, the effects of inertia. After some time, the calculations converge, e.g., Figure 4-5-4 gives a flow rate of 949.1 gpm for an error of 0.2 percent. For the 10,000 time steps shown, the computing time is about five minutes for this three-dimensional run. We have used the transient, three-dimensional, two-phase flow solver to reproduce an exact steady, two-dimensional, single-phase flow result. In general, single-phase flows can be calculated this way, although this is obviously sub-optimal. However, the example was designed to show that the numerical model is basically correct.
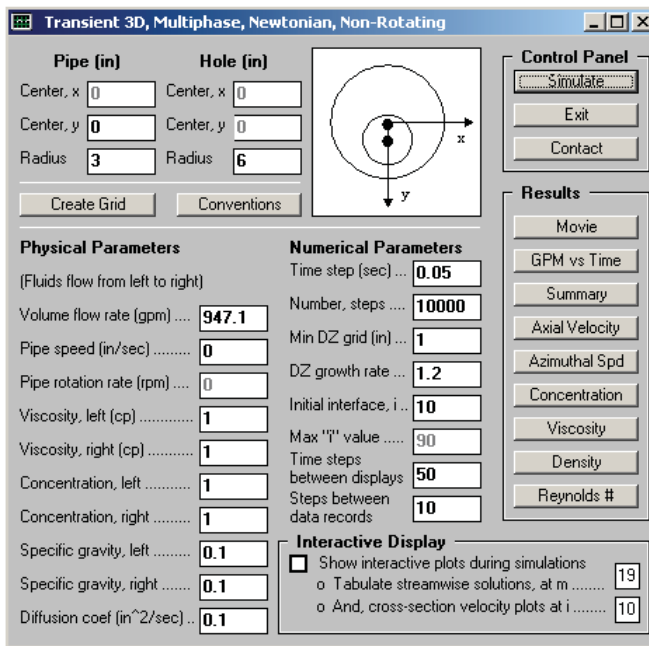
Figure 4-5-3. Consistent transient simulation parameters.
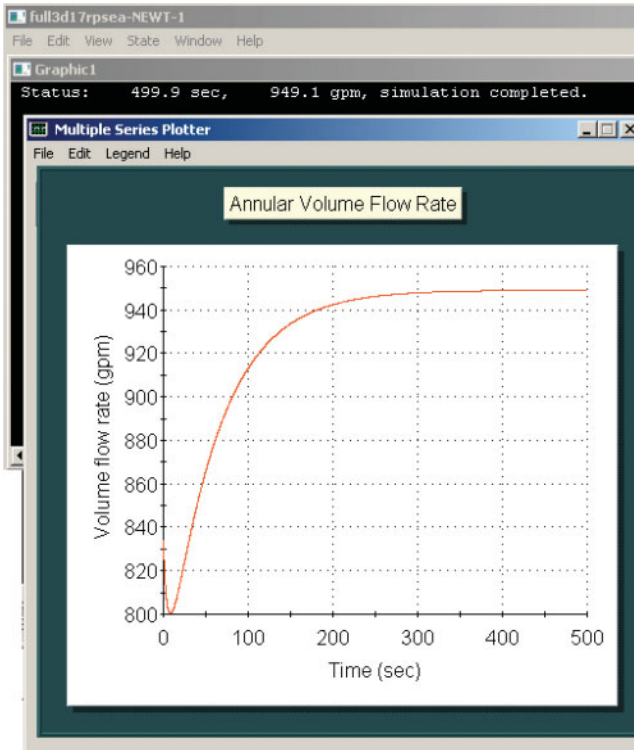
Figure 4-5-4. Example 1, smoothly convergent flow rate history.

Transient flow subtleties. Again, we remind the reader of certain difficulties encountered in transient flow modeling. In steady flow analysis, whether concentric or eccentric, computations for flow rate (when pressure gradients are given) are very rapid and vice-versa. For linear Newtonian flows, these are especially fast. If $(\partial P/\partial z)_1$ corresponding to Q_1 is known from just one eccentric or concentric calculation or experiment, then the identity $(\partial P/\partial z)_2/Q_2 = (\partial P/\partial z)_1/Q_1$ allows us to immediately obtain $(\partial P/\partial z)_2$ when Q_2 is given or Q_2 when $(\partial P/\partial z)_2$ is given. For non-Newtonian flows, the nonlinearity of the pressure gradient and flow rate relationship disallows this simple rescaling. However, the "Specify volumetric flow rate" option in Figure 4-5-1 does use a rapidly convergent half-step method to guess the pressure gradient corresponding to a target flow rate to within 1 percent accuracy.

In transient calculations, one can *in principle* specify total volumetric flow rate at each instant in time. However, to achieve the required solution, numerous trial and error attempts using different pressure gradients will have to be made at each time step. When this is repeated for the entire range of time integration, the computations needed are voluminous and require hours or overnight runs. This is particularly unacceptable if, say during the calculations, instabilities are encountered – then, all of the numerical effort expended will be wasted. Thus, we ask if there is an acceptable compromise, that is, "Is there an approximate pressure gradient we can use in a constant flow rate process?"

For Newtonian, non-rotating flows, the answer is "Yes." We recall from our theoretical discussion for steady single-phase flow that volumetric flow rate is directly proportional to the pressure gradient $\partial P/\partial z$ and inversely related to the viscosity μ. If "1" and "2" now denote two positions along the three-dimensional channel (at a fixed instant in time) without area changes, then constancy of flow rate implies that $(\partial P/\partial z)_1/\mu_1 = (\partial P/\partial z)_2/\mu_2$. Suppose that the volumetric flow rate at the (left) inlet and the starting viscosity are specified. Then, the pressure gradient required for the eccentric Newtonian flow can be obtained from the "Steady 2D" solver in Figure 4-5-1. As the fluid at the inlet flows downstream, it mixes with "right" fluid and local concentrations will change. The underlying viscosity will consequently change, in a manner consistent with an assumed mixing relationship (taken, again, as the Todd-Longstaff law). If the local viscosity is now μ_2, then the corresponding pressure gradient is $(\partial P/\partial z)_2 = (\partial P/\partial z)_1 \, \mu_2 \, /\mu_1$, showing correctly, for instance, that an increase in viscosity will require an increase in pressure gradient.

This procedure has been programmed into the solver of Figure 4-5-3 – there is no need to operate the simulator in Figure 4-5-1 because the procedure has been completely automated. Again, starting pressure gradients are obtained from inlet conditions and local values are obtained by concentration-dependent rescaling. This automation is only convenient for Newtonian mixtures where there is no pipe rotation – the "$(\partial P/\partial z)_1/\mu_1 = (\partial P/\partial z)_2/\mu_2$" law does not apply to eccentric problems with rotation, although it remains valid for concentric rotating flow because axial and azimuthal modes decouple. For more complicated problems, a more complete approach applies, with different degrees of complexity depending on the nature of the underlying flow. The general problem will be considered in a separate discussion.
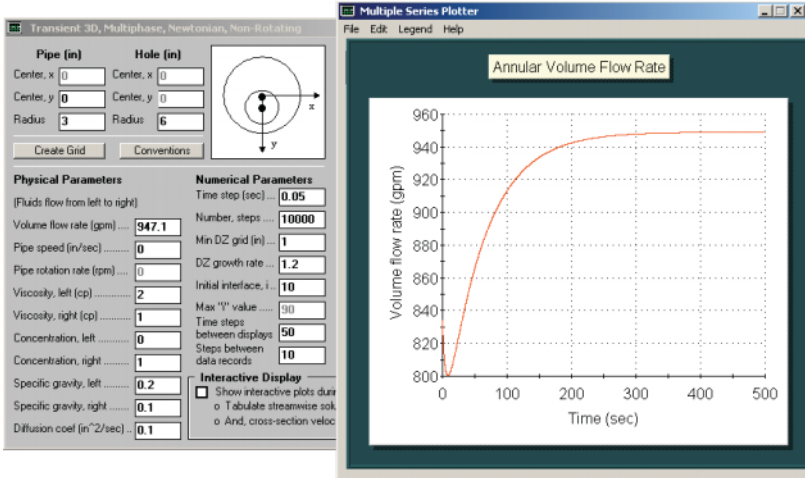
Figure 4-5-5. Example 2 calculation.
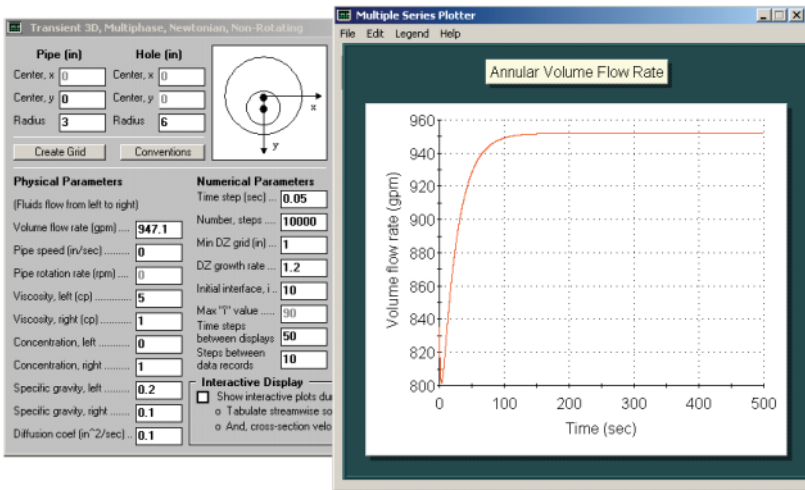
Figure 4-5-6. Example 3 calculation.

Examples 2 and 3.   For our second calculation, we repeat the above simulation except that we double the inlet-outlet viscosity and density ratios as shown in Figure 4-5-5. Note that, in order to track two different phases, the concentrations at the inlet and outlet are set to 0 and 1, respectively. The calculation yields almost identical flow rates and flow rate history curves. Why? This occurs because, in Newtonian

mixtures, the ratio of density to viscosity controls the dynamics and not either parameter alone; there is, however, an effect associated with the ratio of density to diffusion coefficient, which need not always be small. Thus, the effects of the doubling almost cancel. In our third simulation, we set our inlet-outlet viscosity and density ratios to 5 and 2, respectively. Figure 4-5-6 shows that the volumetric flow rate history changes somewhat, with the predominant effect being the time required to reach equilibrium.

Detailed description of the simulator appears in Discussion 4-6. The reader should study the description since many of its software features are shared by the more general solver introduced in Discussion 4-7. This discussion, "Transient, 3D, eccentric multiphase analysis for general rotating non-Newtonian fluids – simulator description," deals with real two-phase flows in which the mixing of non-Newtonian fluids, in the presence of rotation, is addressed. Mixing is controlled by numerous factors: convection, diffusion, annular geometry, rheology, flow rate, and initial conditions. This complexity means that general conclusions are difficult to formulate and that each flow solution must be interpreted on a case-by-case basis. Predictions should be substantiated by laboratory experiment and field data whenever possible.

4.6   Transient, 3D, eccentric multiphase analysis for non-rotating Newtonian fluids – simulator description.

Here we describe in detail the operation of our "Transient 3D, Multiphase, Newtonian, Non-Rotating" flow simulator in Figure 4-6-1. Again, this stand-alone module was developed because the model could be rigorously formulated and fully automated – it is also, of course, useful as a planning tool in itself. We emphasize that the module applies to highly eccentric annuli and does allow limited cross-sectional geometric modification along borehole axis. Many of the user features described here are also incorporated in our more general multiphase solver for non-Newtonian rotating flow. The upper left text boxes of Figure 4-6-1 host the annulus definition function common to all of our simulators, with "Create Grid" displaying the curvilinear grid chosen to host the eccentric annulus at run time – this feature provides needed error checking to ensure that circles do not cross over. Clicking "Create Grid," in this case, leads to Figure 4-6-2. The "Conventions" button provides explanations on azimuthal grid numbering conventions needed to select cross-section plots for run-time interactive displays and movies.
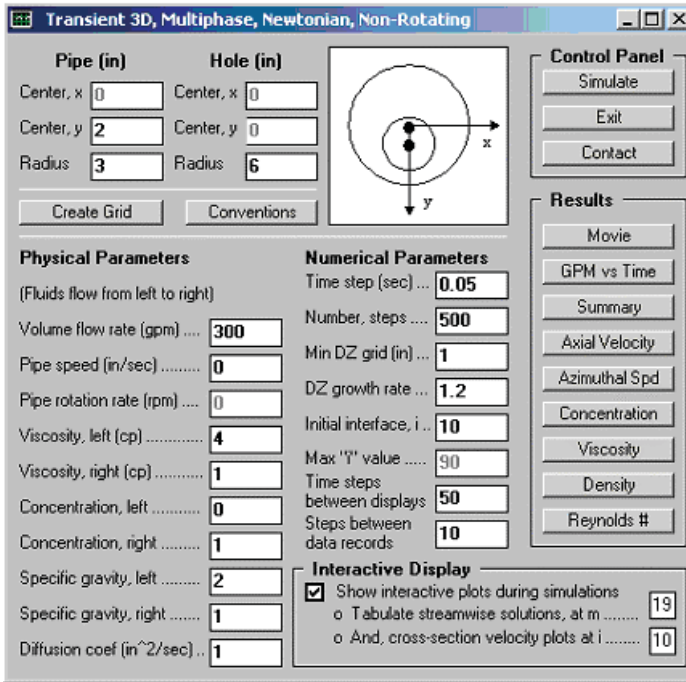
Figure 4-6-1. Basic user interface with default parameters.
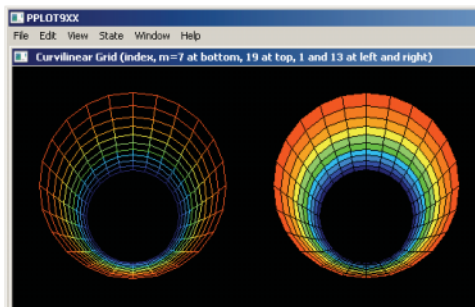
Figure 4-6-2. Curvilinear grid used in present example.

Our annular fluid flows from left to right, with the inlet at the left and the outlet at the right. Fluid properties are inputted in the lower left menu. We have selected default run inputs that will provide a good "fast start" user experience – simply uncheck the "Interactive Display" box, click "Simulate," and allow the simulation to run to completion (This process that requires less than one minute.), and finally, click "Movie."

A movie showing computed results, e.g., see Figure 4-6-12, automatically launches, showing the evolution of the convection and mixing process. The inputs in Figure 4-6-1 show a heavier, more viscous fluid as the displacing fluid. The diffusion coefficient used is unusually large, only to provide viewable results (such as those in Figure 4-6-12), because the graphical displays used at the present time are capable of providing twelve colors only.   For actual use, diffusion coefficients available in the environmental or chemical engineering literature should be entered, or those obtained in laboratory studies. Detailed numbers are outputted for plotting using commercial software, and the manner in which these are accessed is described later.
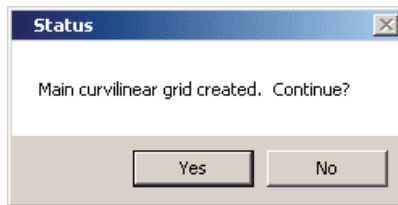
Figure 4-6-3. Curvilinear grid for main eccentric annulus created.
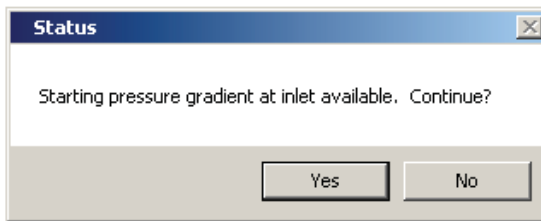
Figure 4-6-4. Starting pressure gradient computed using "Steady 2D."

Once the annular geometry and run-time inputs are entered, clicking "Simulate" leads to the status box shown in Figure 4-6-3, indicating that the main curvilinear grid for the eccentric annulus just inputted has been computed. Clicking "Yes" prompts the simulator to solve (using the grid just created) a steady, two-dimensional "Specify volumetric flow rate" problem for the inlet conditions and target low rate prescribed, a process that requires up to 2-3 seconds. When this is completed, the status box in Figure 4-6-4 appears. Clicking "Yes" leads to the query in Figure 4-6-5. If this query is answered affirmatively, the sub-menu and message box in Figure 4-6-6 appears. This allows the user to redefine a portion of the main annulus, whose axial index "i" for the spatial coordinate z_i varies

from 1 to 90. For the example shown, the main grid parameters repeated in Figure 4-6-5 are altered so that they are replaced by the concentric annulus in Figure 4-6-7. Clicking "Apply" leads to the display in Figure 4-6-8. For the present example, we repeat our steps but do not alter the main annulus – while the numerical engine is presently set up the correctly calculate the effects of this change, the graphical displays are still being developed at this time (The annulus modification feature *is* usable except for this graphical limitation.).
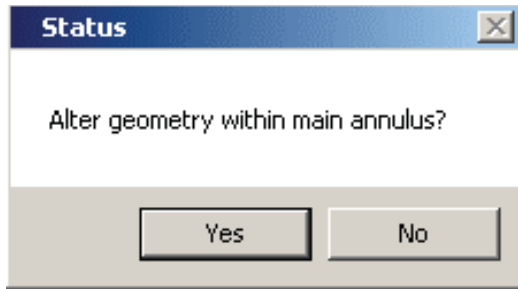
Figure 4-6-5. Option to alter annulus for limited axial extent.
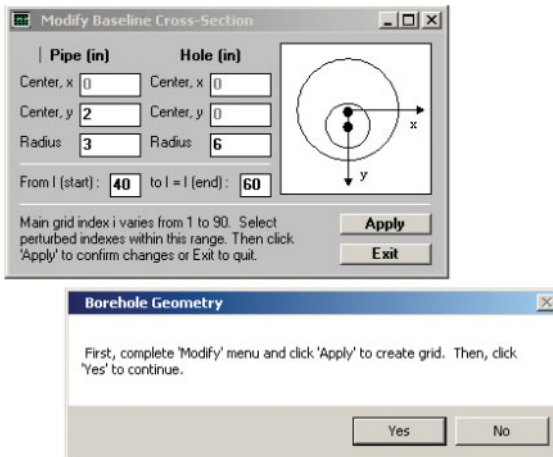
Figure 4-6-6. Perturbation annulus definition.
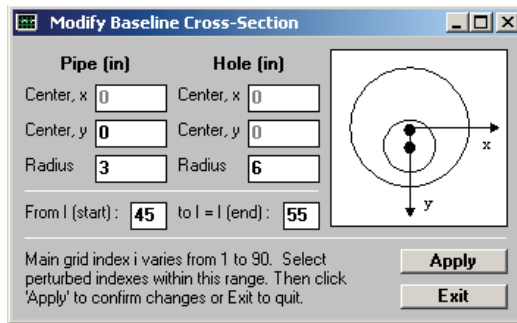
Figure 4-6-7. Concentric annulus defined in 45 < I < 55.
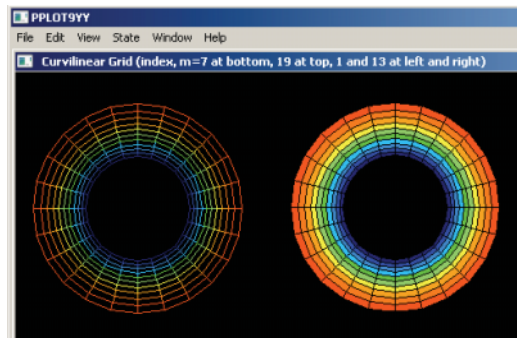
Figure 4-6-8. Concentric annulus re-definition.

We next explain the gridding system used. Axial z_i grid control is provided for in the central portion of the menu in Figure 4-6-1 (cross-sectional grid densities are hardcoded as suggested Figures 4-6-2 and 4-6-8). The main grid is indexed from $i = 1$ at the inlet to $i = 90$ at the outlet, again, with the flow moving from the left inlet to the right outlet. Initially, two fluids are permitted, the left with a concentration $C = 0$ and the right with $C = 1$. The initial (flat) interface is assumed at $i = i_{face}$ entered by the user. The finest z mesh length, or "Minimum DZ grid," is centered at this initial interface location and is defined by the user. The mesh amplification rate, or "DZ growth rate," is a number that equals or exceeds one. A geometrically varying mesh is generated internally and used together with our curvilinear cross-sectional grid to provide three-dimensional simulation capabilities. If we had chosen to modify the main annular geometry, the cross-sectional metrics would have been automatically changed internally. While the gridding and display options presented here are somewhat awkward, we note that users with more

computing resources have extended the algorithm and developed their own gridding and display capabilities. In one case, a fully three-dimensional grid was created which varied continuously in the z direction and which could be updated in real-time with borehole caliper measurements. Users interested in such capabilities should discuss their needs with the developers. Also note that, while we have discussed the initial condition for two phases, it is also straightforward to perform single-phase flow studies, i.e., if there is an interest in modeling single-phase flow in an annulus with internal cross-sectional changes as noted above. In this case, the left and right concentrations can be set entirely to 0 or to 1, and solutions to the concentration equations will be entirely 0 or 1 (thus suppressing any internal variations to fluid properties). The time step shown in Figure 4-6-1 is large. Generally speaking, it needs to be much smaller to provide the needed physical resolution. These steps are constant during the simulation. The total time simulated is simply the product of "time step" and "number of steps."
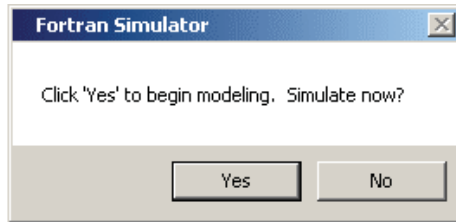
Figure 4-6-9. Simulation to commence.

Having made preliminary comments, we continue the simulation process. The final status box in Figure 4-6-9 appears. If interactive displays are desired, the box in "Interactive Display" should be checked. Because our fully three-dimensional simulators at the present time do not allow true three-dimensional color displays, we offer the limited options available in the option box. First, we can display fluid properties in any single azimuthal "m = constant" plane (click "Conventions" for definitions). And second, we can give cross-sectional plots at any single "i = constant" location. Users with special requirements can contact the developers for source code access or other support. If the interactive display box is not checked, a simple status box showing time and "percent complete" appears on screen. Upon run termination, all results are written to text output files and movie displays for the time evolution of axial velocity, and concentration-dependent viscosity and fluid density

are available. If interactive displays are required at periodic user-defined intervals, multiple screens appear, the first being that shown in Figure 4-6-10. All three diagrams have flow moving downward. The left diagram, here for "m = 19," gives the axial velocity. Blue represents low (zero) speeds at the pipe and annular surfaces, while the uniform red display indicates a high uniform velocity in the annular space. The middle and right diagrams show displacement of one fluid by a second, starting near "i = 10." These are accompanied by velocity plots in Figure 4-6-11. Closing these windows allows the simulation to continue.
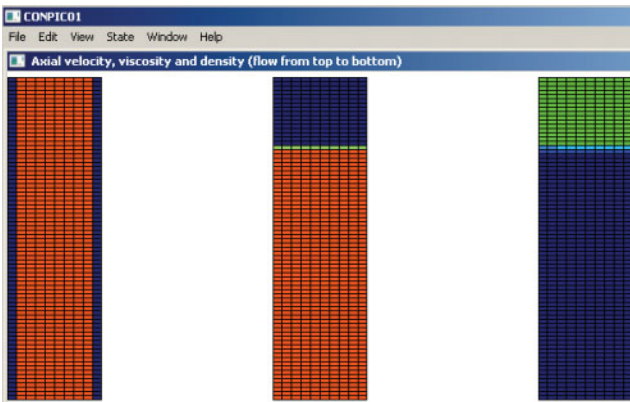
Figure 4-6-10. Axial velocity, viscosity and density at m = 19.
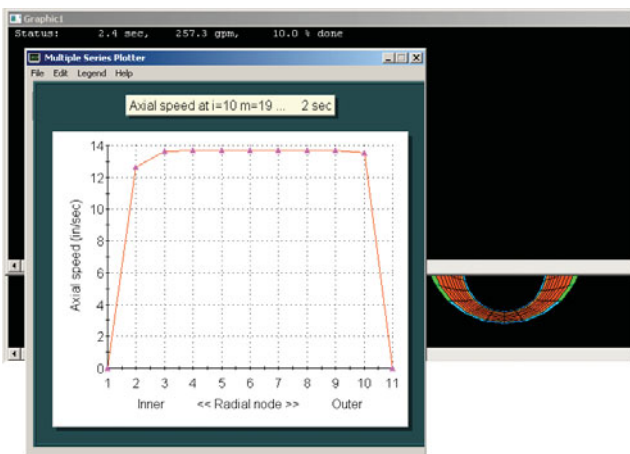
Figure 4-6-11. Velocity graph and cross-section plot in background.

Plots like those in Figure 4-6-10 are automatically generated internally (whether or not interactive displays are selected) and are assembled to create movies available for user access by clicking "Movie." Example frames are shown in Figure 4-6-12. The complete output menu is shown in Figure 4-6-13. The buttons labeled "Axial Velocity," "Azimuthal Velocity," "Concentration," "Viscosity," "Density" and "Reynolds Number" provide spreadsheet style numerical output for the respective quantities (Azimuthal velocities are identically zero for the present Newtonian flow simulator, but generally need not be.). Figure 4-6-14 shows numerical output in the case of concentrations, for azimuthal location m = 19, where the axial index "i" varies from 1 to 90 and the radial-like index varies from 1 at the pipe surface to 11 at the annular wall.
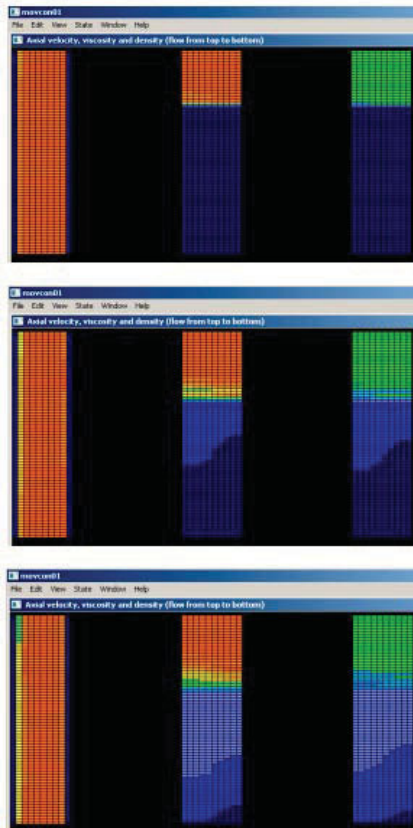
Figure 4-6-12. Movie frames at different times showing mixing.

Figure 4-6-13. Output menu.

Figure 4-6-14. Tabulated numerical output (for concentration shown).

4.7 Transient, 3D, eccentric multiphase analysis for general rotating non-Newtonian fluids – simulator description.

We give a brief description for the transient, three-dimensional, multiphase flow model in this book. General rheologies are permitted with highly eccentric annular cross-sections. Figure 4-7-1 illustrates the rotating flow problem considered, but for simplicity, displays only two contiguous non-Newtonian fluids. At the top, we have an initial condition in which a flat fluid interface is located arbitrarily in the flow. The situation shown at the bottom is a diffused interface, not necessarily planar nor uniform in thickness, encountered at a later instant in time. Our objective, of course, is to model the dynamics of this problem.
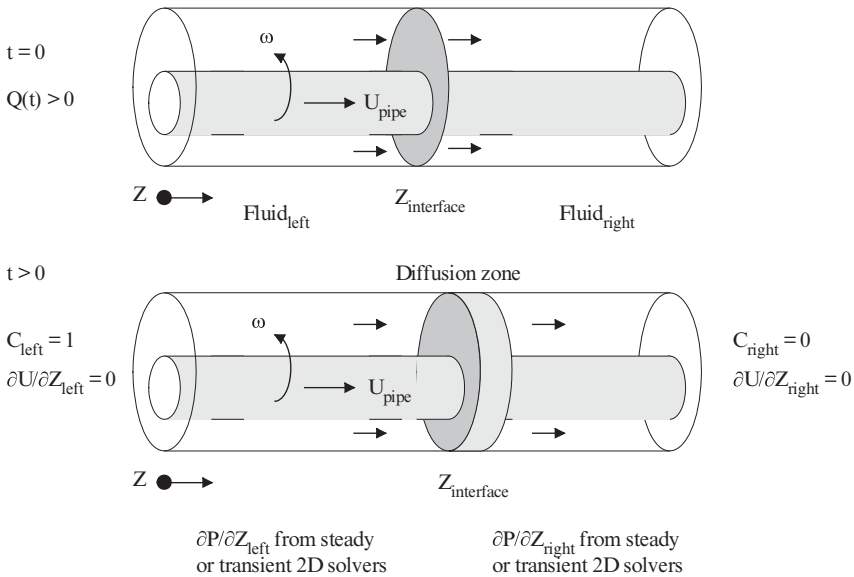
Figure 4-7-1. Mathematical problem formulation.

The work in the remainder of this chapter demonstrates how transient, three-dimensional, multiphase flow fields can be obtained computationally. Figures 4-7-2a,b illustrate, for instance, "movies" (with time increasing downward) in which a purely eccentric annulus which does not vary axially is considered followed by a mixed geometry having concentric and eccentric sections. These movies can be accessed from the "Start" menu for the "Transient 3D multiphase" solver shown in Figure 1-4b.
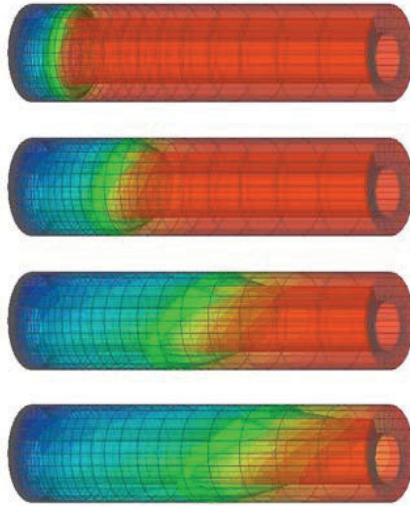
Figure 4-7-2a. Purely eccentric annulus.
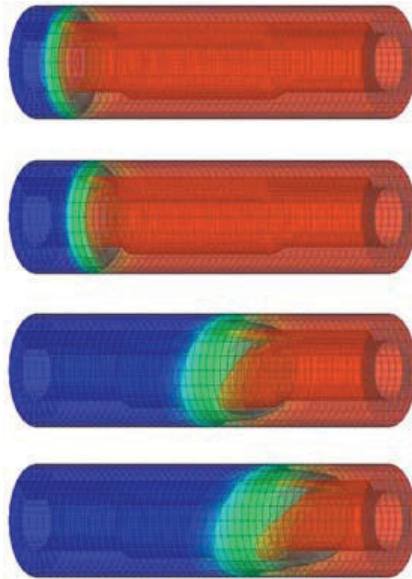
Figure 4-7-2b. Mixed concentric-eccentric flow.

Note: The above plots were created using Tecplot 360™ software described in the company website at www.tecplot.com.

4.8 Transient, 3D, eccentric, multiphase analysis for general rotating non-Newtonian fluids with axial pipe movement – Validation runs for completely stationary pipe.

Here, we will start with simple examples and graduate to more complicated ones, demonstrating first, that the three-dimensional algorithm is correct.
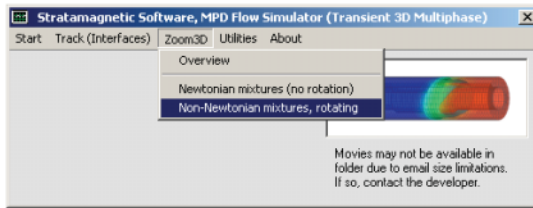
Figure 4-8-1a. General "Transient 3D Multiphase" menu.

Validation 1 – Concentric, single-phase Newtonian flow. In this example, we wish to demonstrate that our transient, three-dimensional simulator is correct in a limit where an exact solution is available. In particular, we refer to the concentric Newtonian flow solver in Figure 4-8-1d. For the parameters shown, the exact volumetric flow rate given in the bottom shaded box is 947.1 gpm. We ask,, "Can we solve a transient, three-dimensional problem for a long annulus with the same cross-section and obtain the above flow rate in the steady asymptotic limit?" To answer this question, we select the simulation option indicated in Figure 4-8-1a. This launches two screens, the main module in Figure 4-8-1b and the pump schedule and fluid properties menu in Figure 4-8-1c. In Figure 4-8-1c, we have populated both inlet and outlet boxes with Newtonian fluid parameters consistent with Figure 4-8-1d and assumed a pressure gradient of – 0.0001 psi/ft. everywhere. A low value of specific gravity is used to minimize mechanical inertia so that convergence to steady-state can be accelerated (Larger values will yield the same answers except that they require greater computing.). It is important next to click "Save." In the simulator of Figure 4-8-1b, we have entered the foregoing concentric geometry and assumed suitable computational parameters noting, in particular, a somewhat large time step size of 0.5 sec. Clicking "Simulate" leads to a picture of the assumed annulus and grid Figure 4-8-1e, provided for error checking, and the set-up menus in Figure 4-8-1f. Intermediate results (as requested in Figure 4-8-1b) are displayed in Figure 4-8-1g. Similar results appear

at periodic intervals in simulations and we will not duplicate them. On completion of the simulation, the volumetric flow rate versus time history is given as shown in Figure 4-8-1h, and a final value of 927.6 gpm is calculated. This is to be compared with the exact value of 947.1 gpm, and it is seen that the two simulators are consistent to within an acceptable 2 percent error. Of course, solving a steady, two-dimensional problem with an unsteady, three-dimensional solver is not an efficient use of computing resources. Our only purpose here is in validating the three-dimensional code logic which, as we have explained, involves a great deal of subtlety. The ultimate purpose is adaptation of the software platform to handle problems that are truly transient and three-dimensional, namely, those which involve convection and diffusive mixing.
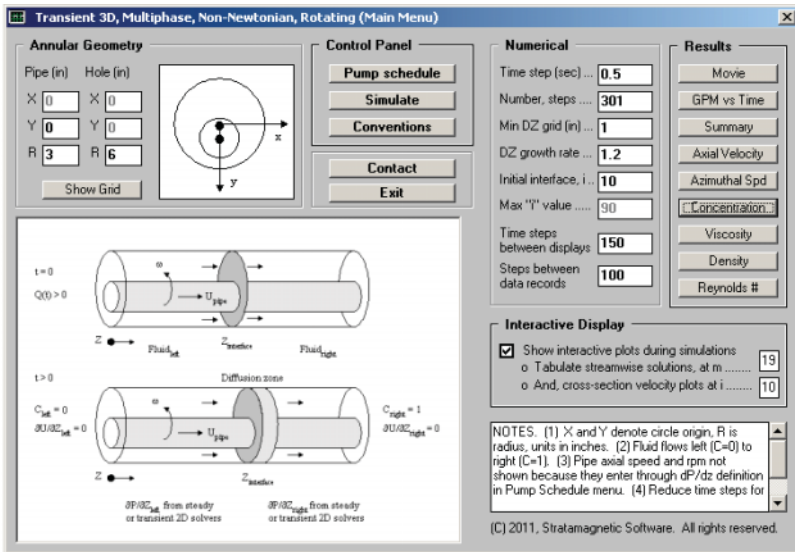
Figure 4-8-1b. Main simulation menu.
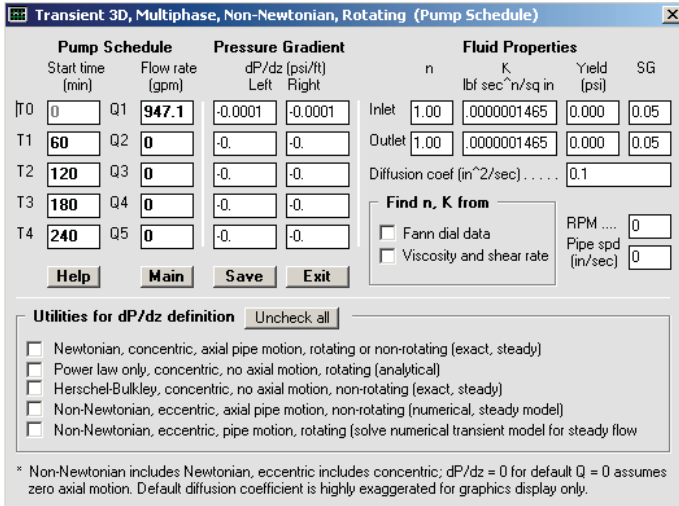
Figure 4-8-1c. Pump schedule and fluid properties definition.
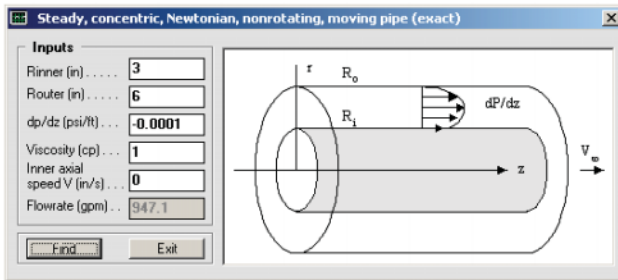
Figure 4-8-1d. Exact concentric Newtonian solution.
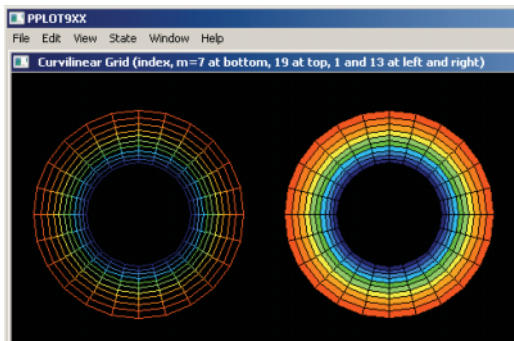
Figure 4-8-1e. Geometry displayed for error checking.
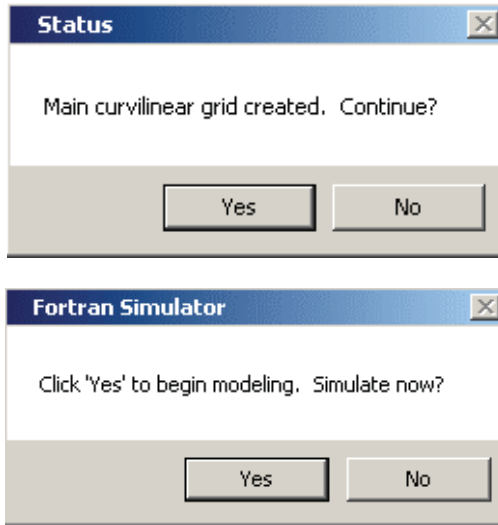
Figure 4-8-1f. Set-up menu status.
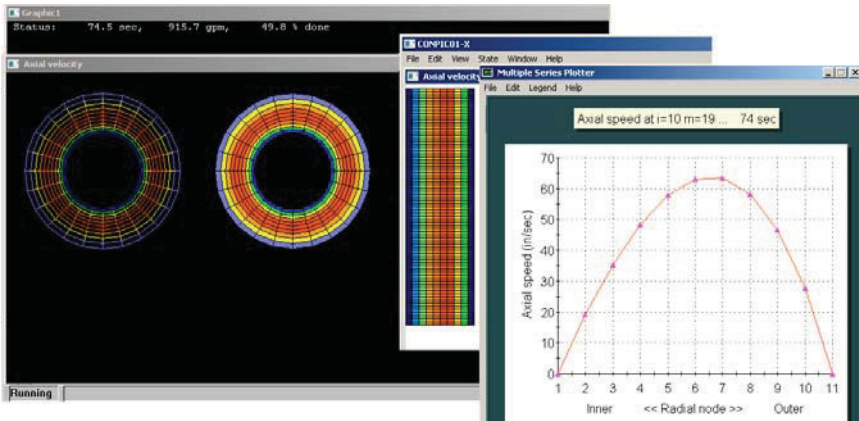
Figure 4-8-1g. Intermediate axial velocity displays requested by user, cross-section color plot and line plot at given azimuthal station.
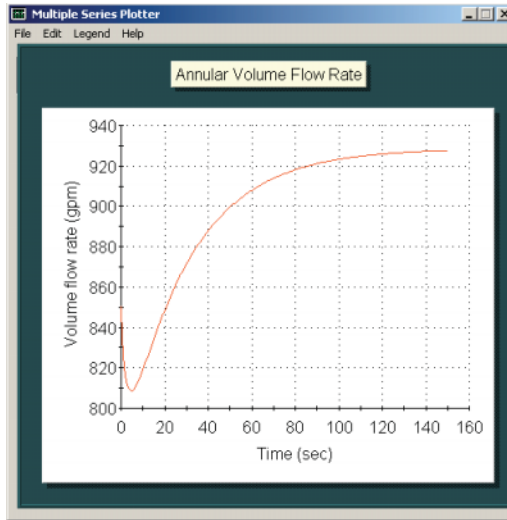
Figure 4-8-1h. Volumetric flow rate history at end of simulation.

Validation 2 – Concentric, two-phase Newtonian flow. In this example, we extend our discussion of Validation 1 and ask how the previous setup can be modified to handle the displacement of a thin fluid by a thicker one. For illustrative purposes, let us assume that the displaced (right) fluid is identical to the one treated in the earlier example, while the displacing fluid is ten times more viscous. While we can certainly use the calculator in Figure 4-8-1d, we need not do so. For Newtonian fluids, which satisfy linear pressure gradient and flow rate relationships, we need to simply enter the increased inlet viscosity and pressure gradient as indicated in Figure 4-8-2a. The corresponding simulation menu is shown in Figure 4-8-2b. Use of the 0.5 sec. time step in Validation 1 will lead to computational instabilities. Thus, a smaller 0.05 sec. is taken for this example; nonetheless, total computing time is just seconds. In Figure 4-8-2c, we importantly find that the specification of discontinuous pressure gradients within the field of flow (where the interface is moving) leads to stable computations and to the identical 927.6 gpm obtained earlier. However, the intermediate results are of greater interest. Figures 4-8-2d,e show results at time steps 150 and 300, while in Figure 4-8-2f we re-ran the simulation to 2,000 time steps (requiring about one minute of computing). These plots show the velocity and viscosity mixing thickness.
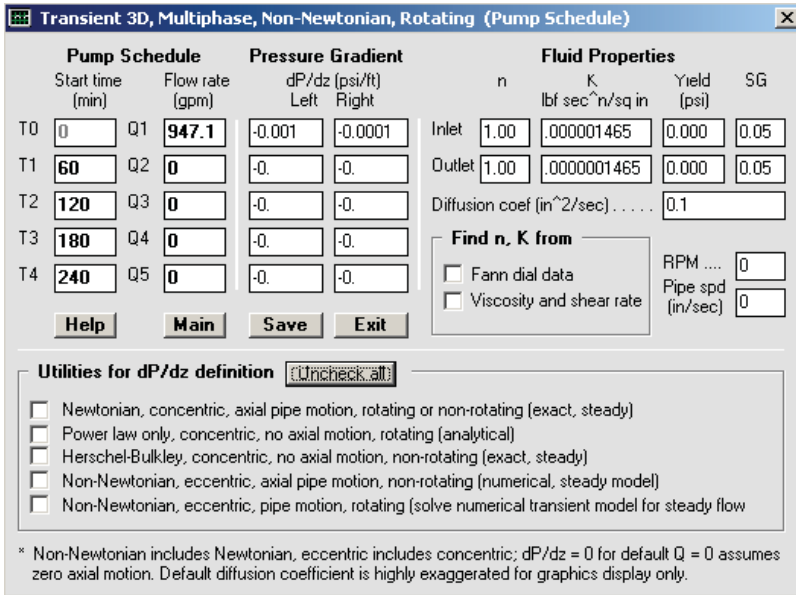
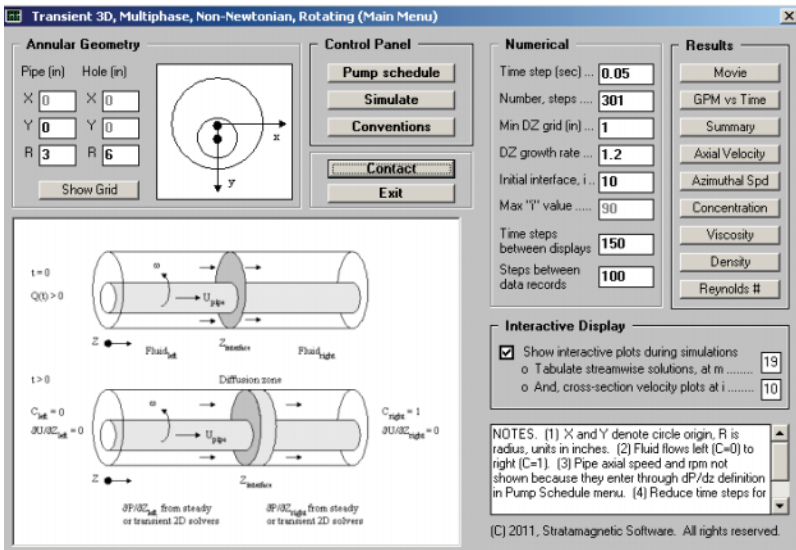**Figure 4-8-2a.** Viscosity and pressure gradient increased ten-fold.

Figure 4-8-2b. Simulation menu, with reduced time step, note
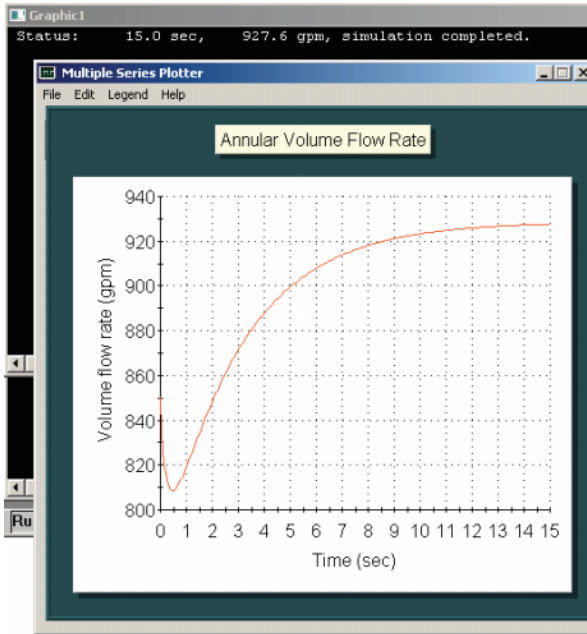displays selected at azimuthal station m = 19 and axial location i = 10.
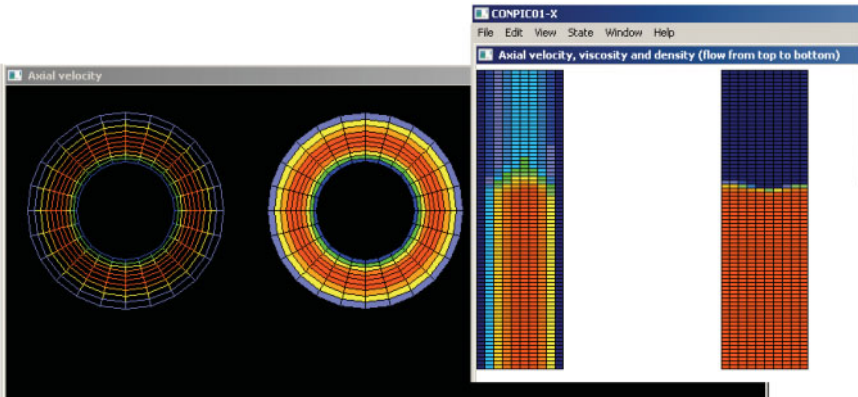
Figure 4-8-2c. Volumetric flow rate history.
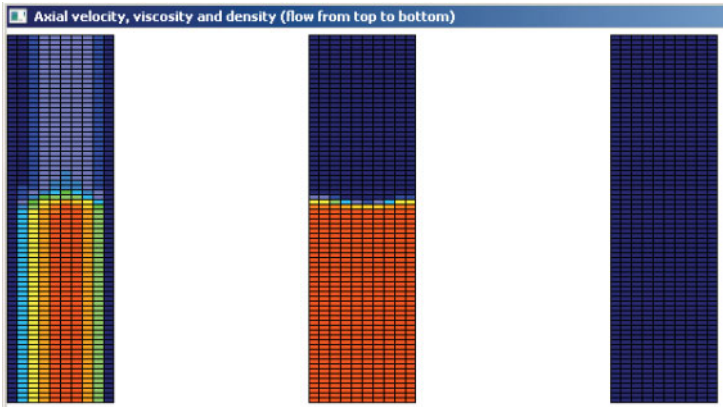

Figure 4-8-2d. Result at 150 time steps.

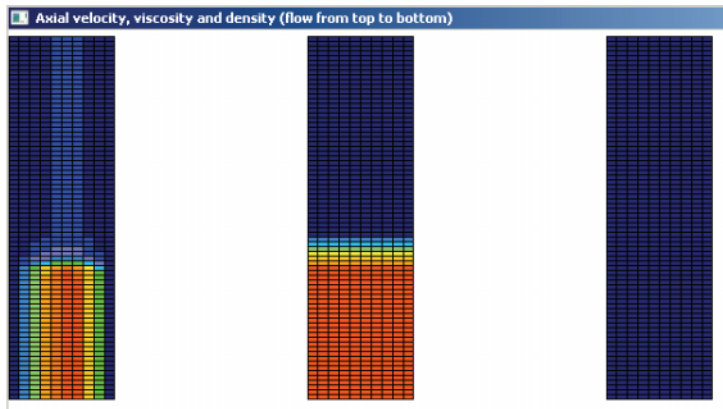**Figure 4-8-2e.** Result at 300 time steps.

Figure 4-8-2f. Result at 2,000 time steps (requiring one minute)

Validation 3 – Concentric, single-phase Herschel-Bulkley flow. Here, we repeat the example of Validation 1, except that instead of a Newtonian fluid, we consider a Herschel-Bulkley fluid with non-vanishing yield stress. Checking the "Herschel-Bulkley" box in the "Pump Schedule" menu automatically launches our exact solver for concentric, non-rotating, Herschel-Bulkley flow. In fact, we run this solver with the inputs and results shown in Figure 4-8-3a noting, in particular, the 471.9 gpm computed for this problem. The corresponding transient, three-dimensional calculation is performed in Figure 4-8-3b, in which a steady flow rate of about 487 gpm is shown, for a modest 3

percent error. Again, we have obtained an exact solution using our three-dimensional computational logic and demonstrated its correctness. We do emphasize that in all of our yield stress work, our "extended Herschel-Bulkley" model is *not* the same as the "conventional Herschel-Bulkley" offered in the literature since a smooth (but rapid) transition from sheared to plug flows is allowed. Thus, *agreement will not always be found and discrepancies can be significant for "small n" flows*. This, we emphasize, is to be expected.
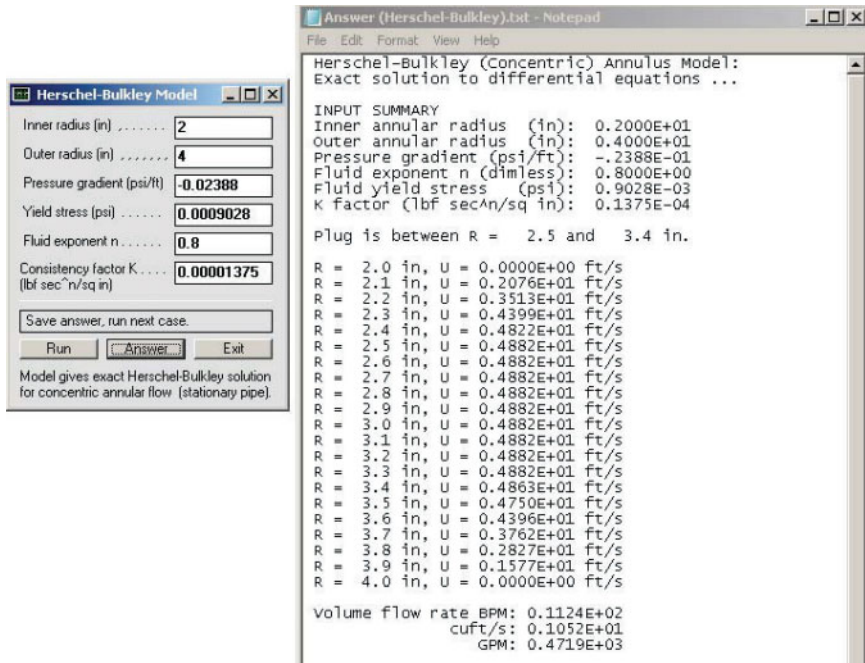

Figure 4-8-3a. Exact, steady, two-dimensional Herschel-Bulkley solution.
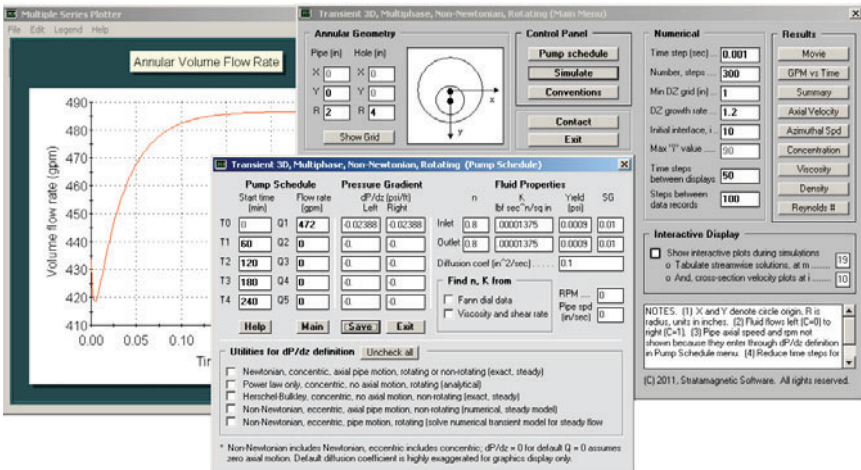
Figure 4-8-3b. Transient, three-dimensional flow.

Validation 4 – Concentric, two-phase Herschel-Bulkley flow. Here we repeat Validation 2 except that extended Herschel-Bulkley flow is considered. In fact, we will displace water with the Herschel-Bulkley fluid analyzed previously. In Figure 4-8-4a, we run our exact, two-dimensional, concentric model for Newtonian flow in the annulus shown to give a flow rate of 471.5 gpm. As evident from the line plot, the transient, three-dimensional solver leads to the same flow rate as required (actually, it is 462 gpm, for an error of less than 2 percent). In Figure 4-8-4b, we have set up the problem so that our thick Herschel-Bulkley fluid is displacing water at the 472 gpm flow rate (an actual rate of 486 gpm is successfully obtained, for an error of less than 3 percent, again noting that our extended Herschel-Bulkley model is not the conventional one). Of interest is the mixing result obtained at the end of the calculations, shown in Figure 4-8-4c. Computation times in both three-dimensional runs are less than one minute.
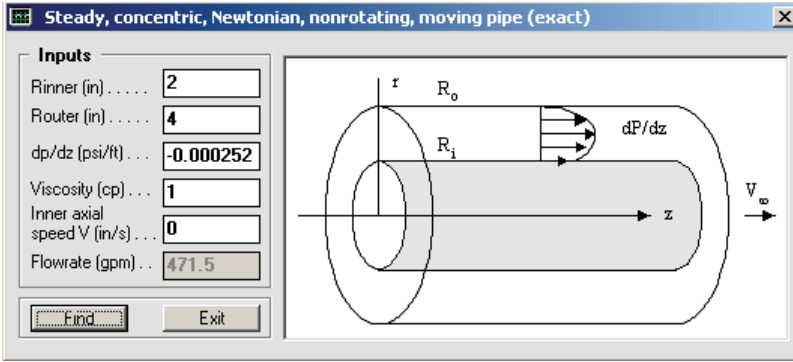
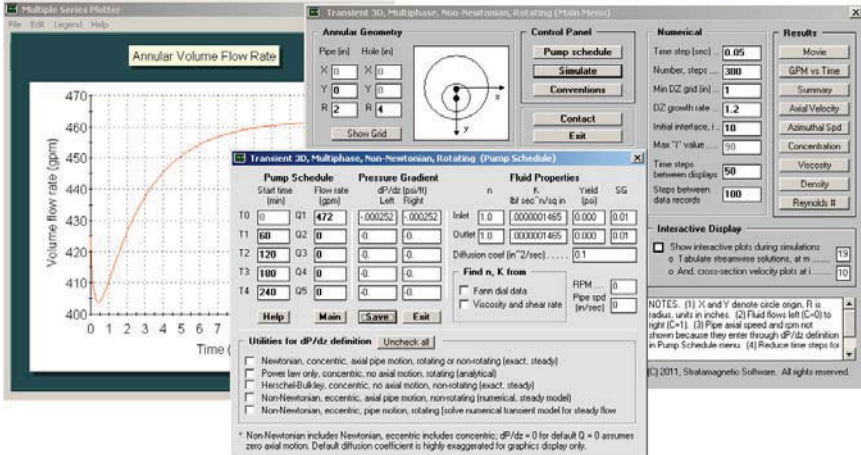**Figure 4-8-4a.** Newtonian flow validation (exact steady solution).

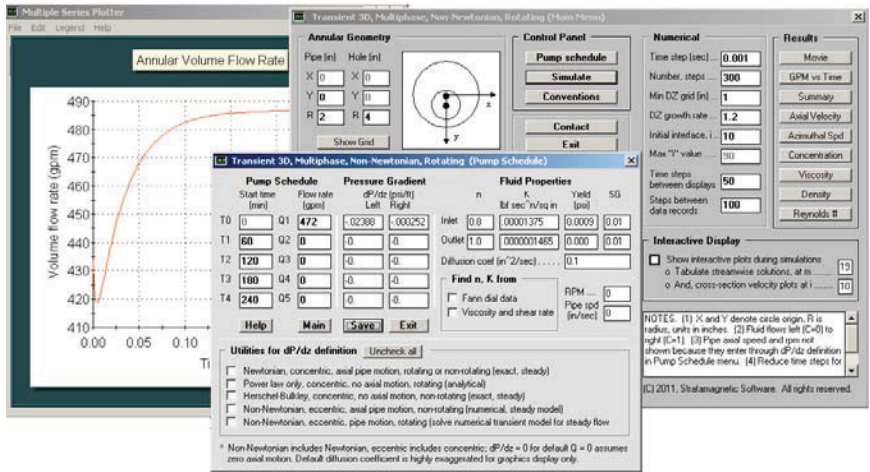**Figure 4-8-4a.** Newtonian flow validation, continued.

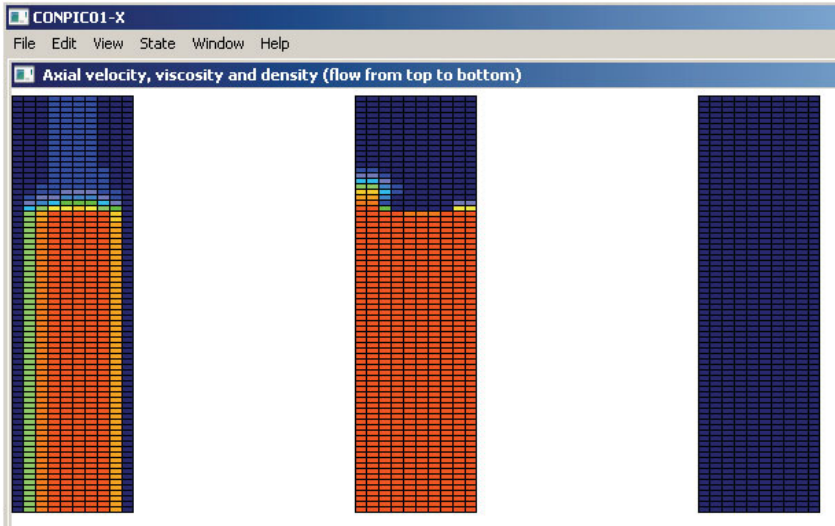**Figure 4-8-4b.** Displacement calculation setup.

Figure 4-8-4c. Mixing solutions for axial velocity, fluid viscosity and mass density.

Validation 5 – Eccentric, single and multiphase, non-Newtonian flow. Here we consider the challenging problem dealing with transient displacement and convective-diffusive mixing of Herschel-Bulkley fluids in highly eccentric three-dimensional annuli. We also address some subtleties of the formulations employed in this book and deal with practical simulation ideas. These discussions are given to promote well considered, and not blind, use of our simulation models. We will discuss the issues as they arise in the simulations. First we examine the eccentric annulus defined in Figure 4-8-5a. Here, the "Steady 2D" simulator is operated in "Volumetric flow rate specified" mode with a target flow rate of 500 gpm. The result of the iterative calculation gives a pressure gradient of – 0.002881 psi/ft. The computed velocity field and curvilinear grid used are shown in Figure 4-8-5b.
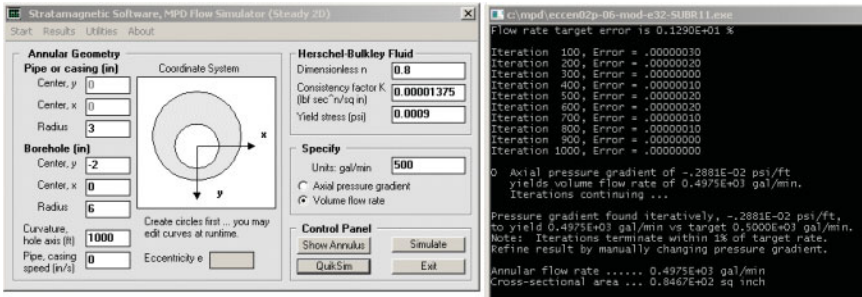

Figure 4-8-5a. "Steady 2D" calculation with target 500 gpm flow rate.
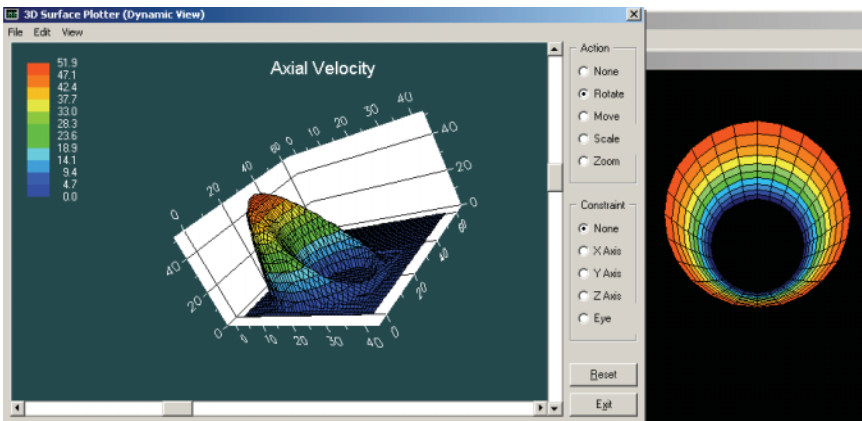

Figure 4-8-5b. Computed velocity field and curvilinear grid used.

Next, we run our transient, three-dimensional, non-Newtonian flow simulator with the – 0.002881 psi/ft. gradient specified throughout, as shown in Figure 4-8-5c below, in order to replicate results consistent with Figure 4-8-5b. However, the line graph shows an asymptotic flow rate of 430 gpm and not the 500 gpm assumed previously. What happened? What is the simulation doing? Are there errors in the formulation?
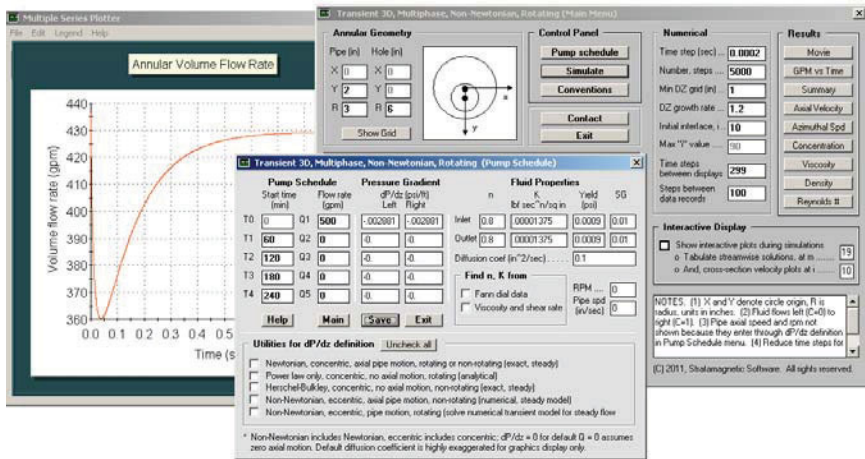
Figure 4-8-5c. The "wrong" answer (subject to explanation given).

Fortunately, the result is not incorrect – in order to understand the boxed entries, it is important to understand the underlying algorithm. The "500" in Figure 4-8-5c is not, in any sense, a boundary condition: it is only used to provide starting velocities to initialize the time integration – its effect dampens out with time and, in fact, one could have taken "1234" and the steady flow rate computed would be the same. The driving terms of dynamical significance insofar as the differential equations are concerned are the applied pressure gradients. Then, one might ask why the " – 0.002881 psi/ft" did not lead to 500 gpm. The reason lies in the formulations used. In "Steady 2D," the computations are exact in the sense that the variable apparent viscosity function N(x,y,x), and all of its spatial derivatives are included. In "Transient 3D" this is not the case. While N(x,y,z) itself is included, its derivatives are not; this approximation is consistent with the use of Landau's *ad hoc* concentration model. The approach is not unlike the use of significant digits in data interpretation, e.g., there is no reason to keep three decimal

place accuracy if some effects are only known to two places. The problem does not arise in Newtonian fluids, as we have shown by example earlier, since derivatives of the constant viscosity vanish identically.

All of this does not mean that simulations are not possible. Knowing now how the code is structured, we simply ignore the "500" in Figure 4-8-5d and, through trial and error, determine the pressure gradient that will yield "500" in the final line graph for flow rate. For the present example, the author obtained the "– 0.00335 psi/ft" shown after four tries, requiring about five minutes of desktop effort.
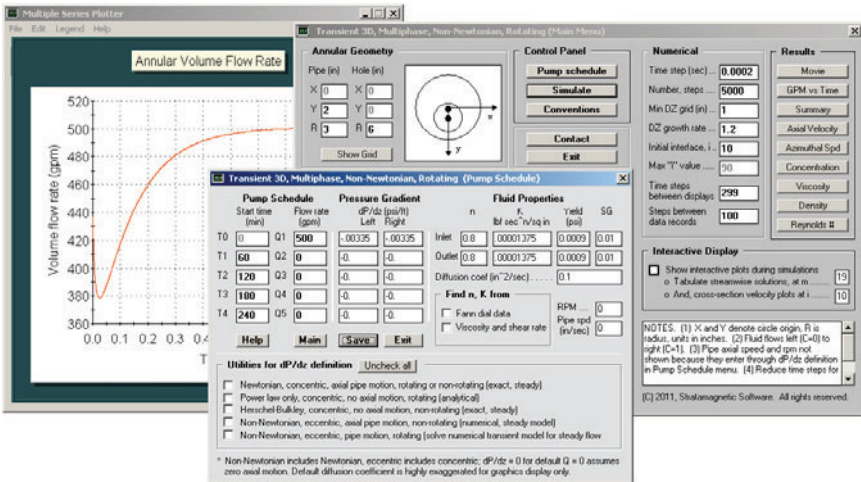
Figure 4-8-5d. Hand calculation result for target 500 gpm.

Now, let us turn to our second fluid, which we assume for simplicity as Newtonian. For the same eccentric annulus, running the exact "Steady 2D" solver in "Volumetric flow rate specified" mode with a target 500 gpm flow rate leads to a pressure gradient of – 0.00003281 psi/ft. as shown in Figure 4-8-5e.
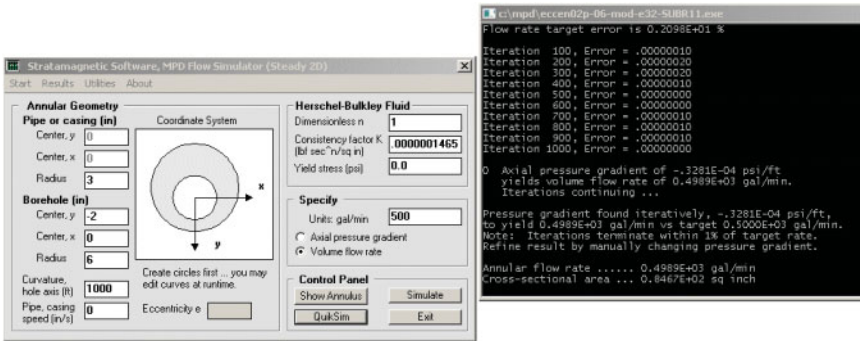
Figure 4-8-5e. "Steady 2D" menu calculation for second fluid.

As suggested earlier, there is no problem replicating the above result using the transient, three-dimensional solver for Newtonian fluids. As shown in Figure 4-8-5f below, a flow rate of 490 gpm is computed, which differs from 500 gpm by only 2 percent (The "minus" signs in the pressure gradient boxes do not appear because they have scrolled to the left, but they *are* entered.). In summary thus far, we have obtained the pressure gradients for two different fluids in the same eccentric annulus needed to achieve a flow rate of 500 gpm. In order to model the displacement of the second fluid by the first, plus the convection and diffusive mixing process, we combine the pressure gradients and fluid properties as shown in Figure 4-8-5g.
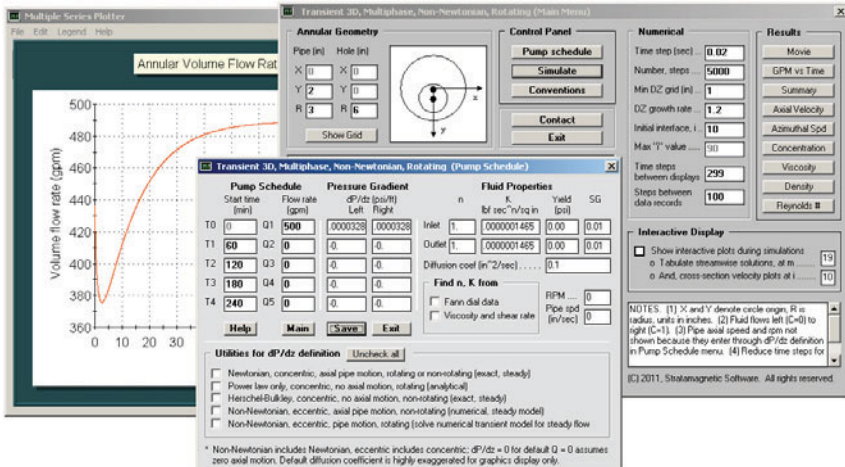
Figure 4-8-5f. Newtonian flow model set-up.
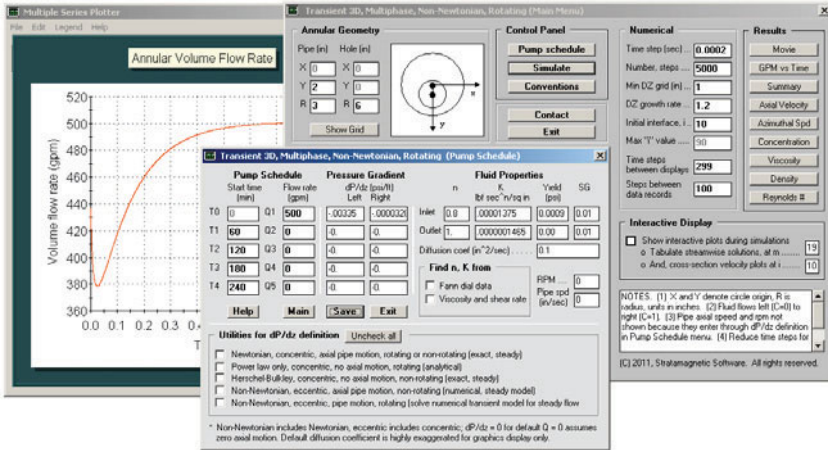
Figure 4-8-5g. Two-fluid displacement and mixing flow set-up.
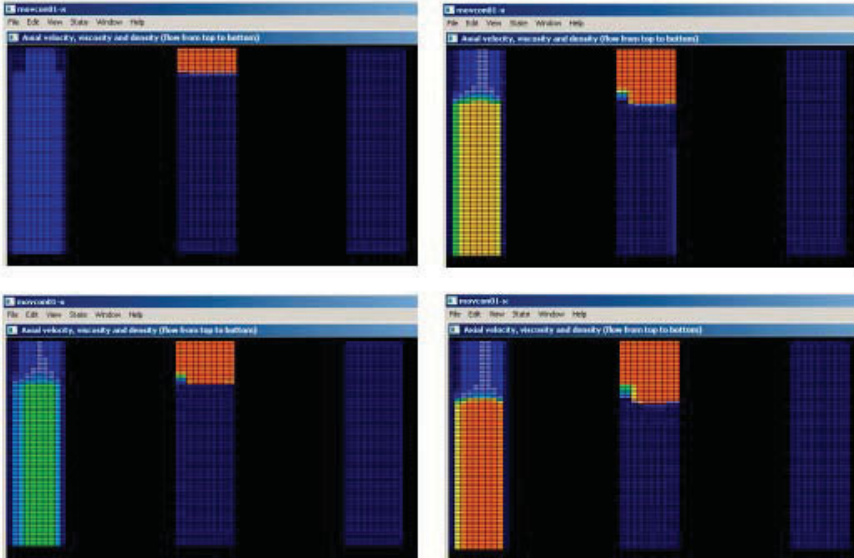
Figure 4-8-5h. "Wide side" axial velocity and fluid mixing.

For the two-fluid system assumed in Figure 4-8-5g, we have inputted strongly discontinuous axial pressure gradients that differ by two orders of magnitude. This difference is needed because the two fluids have contrasting rheological properties. Moreover, the discontinuous pressure gradients are applied to the fluid system while it

is moving and diffusing – the plots in Figure 4-8-5h give sectional properties at the azimuthal index "m = 19" (for the wide side of the annulus) with time increasing as the figures progress downward. The flow is moving from top to bottom. The left axial velocity plot correctly shows a uniformly lower "blue speed" for the non-Newtonian fluid while the displaced Newtonian fluid is more colorful, with blues, yellows, oranges and reds being indicative of the parabolic shape we expect. The viscosity plot, in fact, clearly shows how the mixing interface moves downward with time and widens.

4.9   Transient, 3D, concentric, multiphase analysis for rotating Power law fluids without axial pipe movement.

In the present calculation, we demonstrate how the foregoing procedures apply when the host pressure solver is the host model for Power law fluids in concentric annuli. Figures 4-9a and 4-9b show two calculations for pressure gradient with identical volumetric flow rates and rotational speeds. The differences between the two are fluid properties. The pressure gradients shown at the bottoms of the respective text output screens differ by a factor of ten.
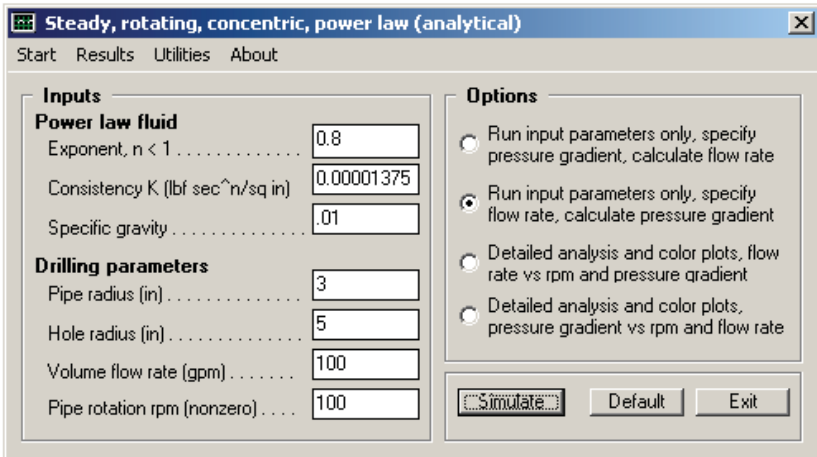
Figure 4-9a. Pressure gradient for "thin" Power law fluid.
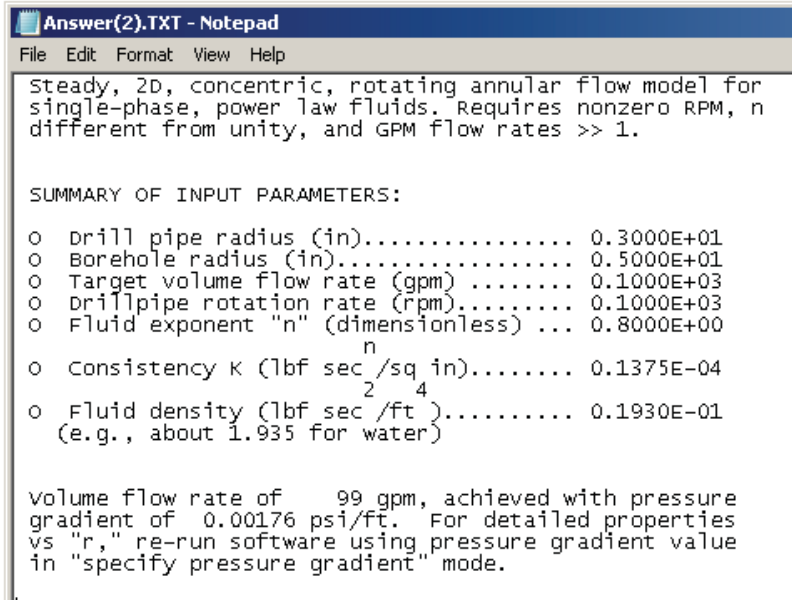
Figure 4-9a. Pressure gradient for "thin" Power law fluid (cont'd).
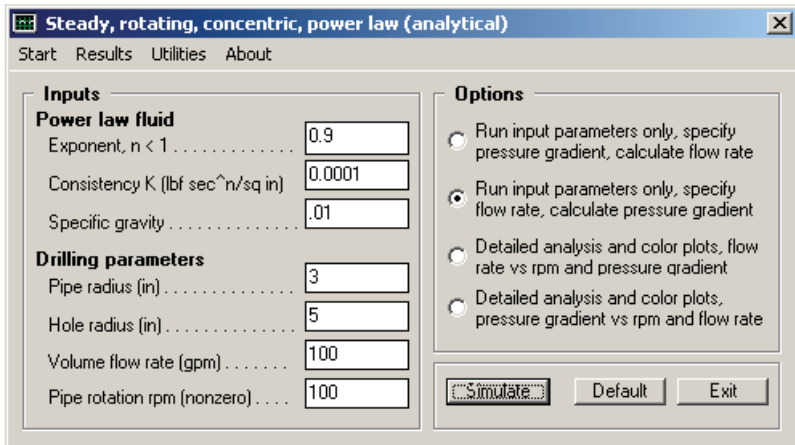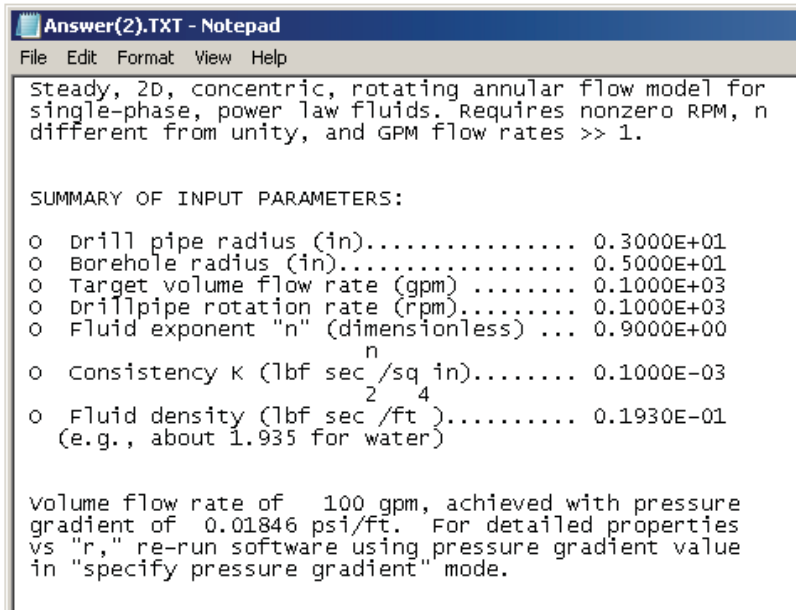
Figure 4-9b. Pressure gradient calculation for "thick" Power law fluid.

```
Answer(2).TXT - Notepad
File  Edit  Format  View  Help

Steady, 2D, concentric, rotating annular flow model for
single-phase, power law fluids. Requires nonzero RPM, n
different from unity, and GPM flow rates >> 1.


SUMMARY OF INPUT PARAMETERS:

o  Drill pipe radius (in)............... 0.3000E+01
o  Borehole radius (in)................. 0.5000E+01
o  Target volume flow rate (gpm) ....... 0.1000E+03
o  Drillpipe rotation rate (rpm)........ 0.1000E+03
o  Fluid exponent "n" (dimensionless) ... 0.9000E+00
                           n
o  Consistency K (lbf sec /sq in)....... 0.1000E-03
                       2    4
o  Fluid density (lbf sec /ft )......... 0.1930E-01
   (e.g., about 1.935 for water)


volume flow rate of   100 gpm, achieved with pressure
gradient of  0.01846 psi/ft.  For detailed properties
vs "r," re-run software using pressure gradient value
in "specify pressure gradient" mode.
```

Figure 4-9b. Pressure gradient calculation for "thick" Power law fluid (cont'd).

Calculated results are shown in Figures 4-9c and 4-9d.   Here it is important to note that the input 100 gpm in the software screens of Figures 4-9a and 4-9b are not replicated in the line graph shown although the "84" is not significantly different.   The reason for this discrepancy lies in the nature of the simulator in Figures 4-9a and 4-9b. Reference to the mathematics in Example 5-6 will show that simplifications to boundary condition implementation were made to enable closed form analytical solutions that can be rapidly evaluated by computer.
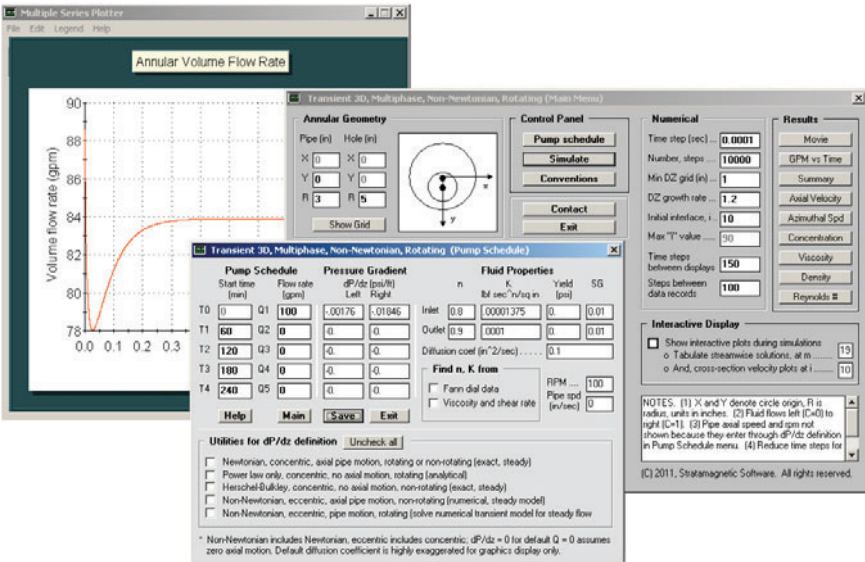
Figure 4-9c. Mixing calculation setup and results.
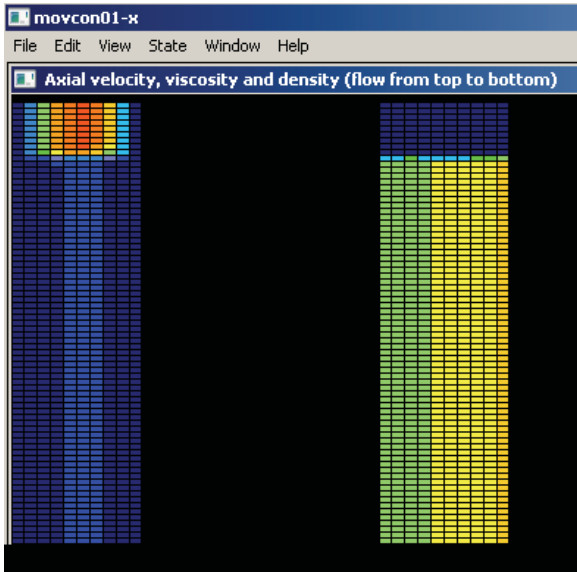
Figure 4-9d. Diffusion solutions in problem with 100 rpm rotation.

4.10   Transient, 3D, eccentric, multiphase analysis for general rotating non-Newtonian fluids with axial pipe movement – Validation runs for constant rate rotation and translation.

In this example, we consider a very complicated annular flow problem typical of those encountered in field operations. We study the highly eccentric annulus in Figure 4-10b. The pipe or casing is moving in the direction of flow at 10 in./sec. and simultaneously rotating at 100 rpm. The total volumetric flow rate is 100 gpm. A Herschel-Bulkley fluid, again, one with non-zero yield stress, is entering at the inlet and displacing a 10 cp Newtonian fluid that is partially present in the annulus. The fluid system is initially quiescent. We wish to calculate the time-dependent axial and azimuthal velocities and apparent viscosity fields along with the position and mixing zone history associated with the fluid interface undergoing transient movement. Following the strategy developed in this chapter, we first calculate the (very different) pressure gradients present near the inlet and outlet and which flow in single-phase manner. This is accomplished using our exact, transient, two-dimensional solvers, a process that requires only seconds. Then, both pressure gradients are used in the combined problem addressing convective and diffusive mixing to solve the questions posed in this paragraph. The two-dimensional solutions are fast, taking only seconds in computing time. We summarize our calculations.

Steady, rotating, non-Newtonian, single-phase, eccentric flow solution. Again, we remind the reader that solutions for rotating eccentric flow problems using purely steady flow formulations are presently numerically unstable for parameters of drilling and cementing interest. However, solutions are possible by solving the transient problem asymptotically for large times. This is possible using the "Transient 2D" simulator developed in this book. As noted in prior discussions, it is not possible to specify volumetric flow rate and obtain pressure gradient in a single pass for mathematical reasons. But because the two-dimensional solver is extremely fast, requiring only seconds or up to a minute per computation, we can determine pressure gradient by trial and error, entering various test values and "hand converging" the solutions for the targeted 100 gpm. For the problem at hand, the author was able to complete the complete example in about fifteen minutes of desk time. The input assumptions are shown in Figure 4-10a. For the targeted flow rate of 100 gpm, the required axial pressure gradient is –0.00016 psi/ft as indicated in Figures 4-10a and 4-10c.
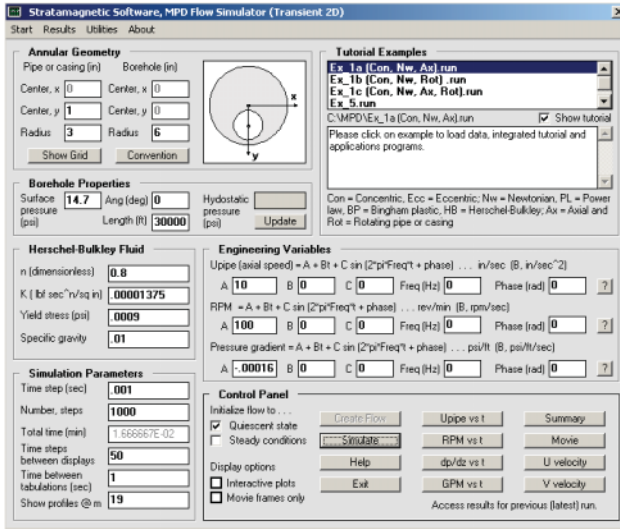
Figure 4-10a.   Non-Newtonian, single-phase flow set-up.
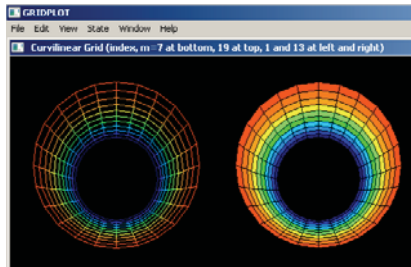
Figure 4-10b. Eccentric annulus.
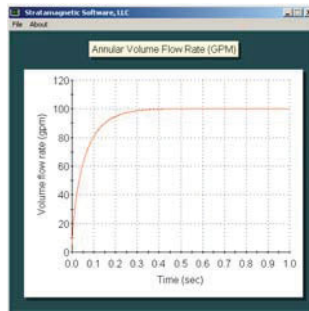
Figure 4-10c. Volumetric flow rate history for non-Newtonian fluid.

Steady, rotating, Newtonian, single-phase, eccentric flow solution. For our Newtonian (zero yield stress) fluid with a 10 cp viscosity, the unsteady formulation in Figure 4-10d leads to a pressure gradient of – 0.000026 psi/ft. for the 100 gpm target (The minus signed has scrolled to left.). Entries hidden by the graph are all zero as in Figure 4-10a. The axial velocity field is shown in Figure 4-10e, with high (red) velocities at the pipe because the pipe velocity exceeds those in the annulus. There is no symmetry about the vertical line passing through the center because rotation destroys the symmetry. The azimuthal picture is similar to this one because the rotational speeds are highest at the pipe and vanish at the annular wall.
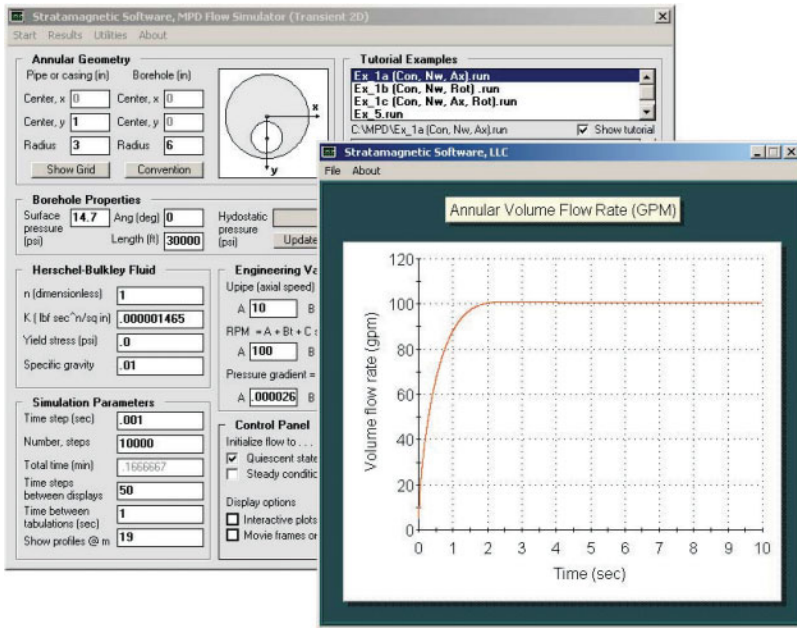
Figure 4-10d. Newtonian flow formulation and solution.
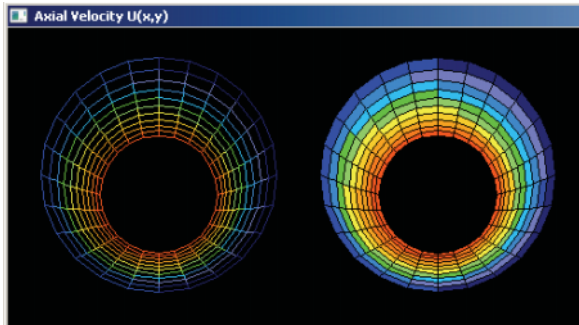
Figure 4-10e. Axial velocity profile in rotating flow.

Mixing problem.   Now, we solve the problem for the combined fluids using the "Zoom3D" solver shown at the top of Figure 4-10f. The target flow rate of 100 gpm is achieved with a 2 percent error.   For parameters indicated, about one minute of computing time is required. To create the color profiles shown in Figures 4-10g, the 10,000 step run selected requires about ten minutes.   In the screen captures given, time increases downward from frame to frame; each snapshot displays the "m = 19" azimuthal solution selected in Figure 4-10f shows axial velocity and apparent viscosity in the "streamwise-radial" plane.   The initial position index of the interface is 10 out of a maximum 90 grids in the direction of flow.   In these snapshots, the flow moves downward and the interface is seen progressing downward. As expected, diffusion causes this interface to widen with time.   Clicking the right-side buttons in Figure 4-10f leads to numerical output captured in text files, as shown in Figures 4-10h,i,j,k, that can be captured for external spreadsheet analysis.

Note that the very low Reynolds numbers in Figure 4-10k indicate fluid stability on a single-phase flow basis. The interface in Figure 4-10g is seen to widen gradually as it convects downward. Our analysis does not include computations for interfacial stability, an extremely difficult problem is formulated and solved rigorously.   Finally, in closing, we emphasize that large diffusion coefficients were assumed only for visualization purposes so that fluid movement could be seen using our somewhat crude twelve-color plotter. Also, very small specific gravities were taken in order for our transient results to approach steady conditions quickly. In general, smaller time steps will be required for higher fluid densities and rotational rates.

Figure 4-10f. Transient, 3D, two-phase mixture formulation.

Figure 4-10g. Axial velocity (left), apparent viscosity (right), flow moving downward in each frame, time increases downward from frame to frame.
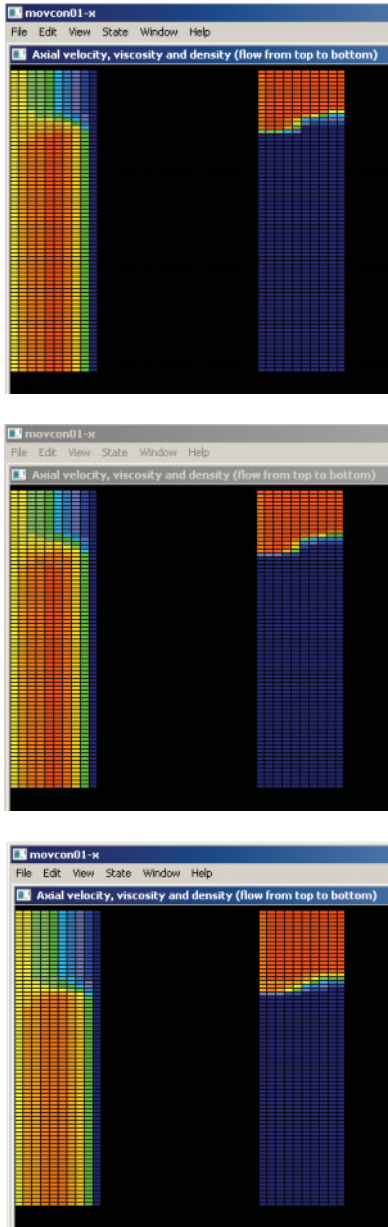
Figure 4-10g. Axial and apparent viscosity solutions (cont'd).

```
Ans-Vis-X.dat - Notepad
File  Edit  Format  View  Help

Time (sec):       9.0
I:        1          2          3          4          5          6          7
 1  0.997E+02  0.913E+02  0.913E+02  0.913E+02  0.913E+02  0.913E+02  0.913E+02
 2  0.101E+03  0.943E+02  0.943E+02  0.943E+02  0.943E+02  0.943E+02  0.943E+02
 3  0.101E+03  0.996E+02  0.996E+02  0.996E+02  0.996E+02  0.996E+02  0.996E+02
 4  0.101E+03  0.100E+03  0.100E+03  0.100E+03  0.100E+03  0.100E+03  0.100E+03
 5  0.101E+03  0.100E+03  0.100E+03  0.100E+03  0.100E+03  0.100E+03  0.100E+03
 6  0.101E+03  0.101E+03  0.101E+03  0.101E+03  0.101E+03  0.101E+03  0.101E+03
 7  0.101E+03  0.101E+03  0.101E+03  0.101E+03  0.101E+03  0.101E+03  0.101E+03
 8  0.101E+03  0.101E+03  0.101E+03  0.101E+03  0.101E+03  0.101E+03  0.101E+03
 9  0.101E+03  0.101E+03  0.101E+03  0.101E+03  0.101E+03  0.101E+03  0.101E+03
10  0.101E+03  0.101E+03  0.101E+03  0.101E+03  0.101E+03  0.101E+03  0.101E+03
11  0.101E+03  0.101E+03  0.101E+03  0.101E+03  0.101E+03  0.101E+03  0.101E+03
```

```
Ans-Vis-X.dat - Notepad
File  Edit  Format  View  Help

    87         88         89         90
0.100E+02  0.100E+02  0.100E+02  0.100E+02
0.100E+02  0.100E+02  0.100E+02  0.100E+02
0.100E+02  0.100E+02  0.100E+02  0.100E+02
0.100E+02  0.100E+02  0.100E+02  0.100E+02
0.100E+02  0.100E+02  0.100E+02  0.100E+02
0.100E+02  0.100E+02  0.100E+02  0.100E+02
0.100E+02  0.100E+02  0.100E+02  0.100E+02
0.100E+02  0.100E+02  0.100E+02  0.100E+02
0.100E+02  0.100E+02  0.100E+02  0.100E+02
0.100E+02  0.100E+02  0.100E+02  0.100E+02
0.100E+02  0.100E+02  0.100E+02  0.100E+02
```
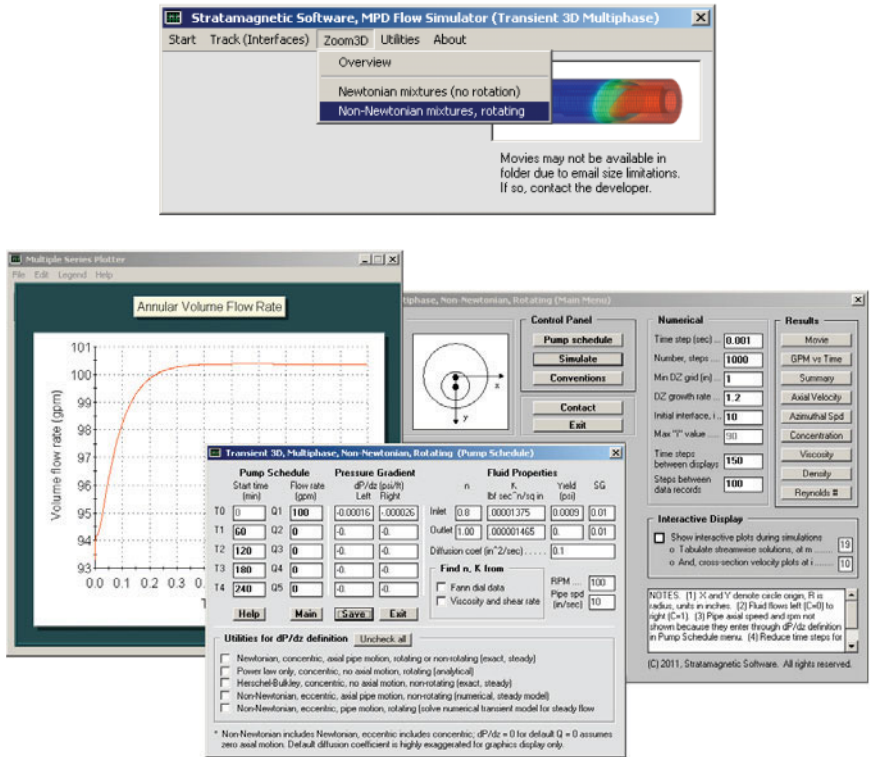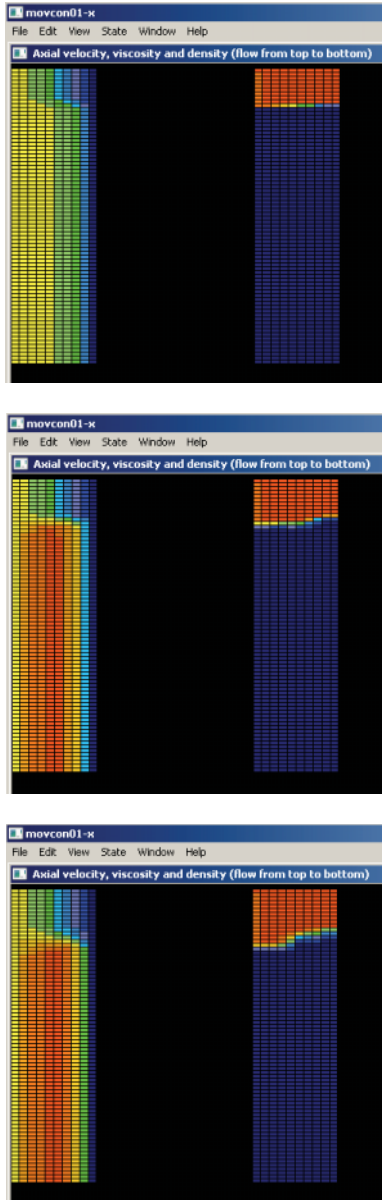
Figure 4-10h. Apparent viscosity for "constant m" or azimuthal angle.

```
Ans-Usp-X.dat - Notepad
File  Edit  Format  View  Help

Time (sec):       9.0
I:       1         2         3         4         5         6         7
 1  10.000    10.000    10.000    10.000    10.000    10.000    10.000
 2   9.464     9.464     9.464     9.464     9.464     9.464     9.464
 3   8.865     8.865     8.865     8.865     8.865     8.865     8.865
 4   8.198     8.198     8.198     8.198     8.198     8.198     8.198
 5   7.454     7.454     7.454     7.454     7.454     7.454     7.454
 6   6.616     6.616     6.616     6.616     6.616     6.616     6.616
 7   5.663     5.663     5.663     5.663     5.663     5.663     5.663
 8   4.567     4.567     4.567     4.567     4.567     4.567     4.567
 9   3.291     3.291     3.291     3.291     3.291     3.291     3.291
10   1.788     1.788     1.788     1.788     1.788     1.788     1.788
11   0.000     0.000     0.000     0.000     0.000     0.000     0.000
```

```
Ans-Usp-X.dat - Notepad
File  Edit  Format  View  Help

    84        85        86        87        88        89        90
10.000    10.000    10.000    10.000    10.000    10.000    10.000
11.700    11.700    11.700    11.700    11.700    11.700    11.700
12.930    12.930    12.930    12.930    12.930    12.930    12.930
13.756    13.756    13.756    13.756    13.756    13.756    13.756
14.222    14.222    14.222    14.222    14.222    14.222    14.222
14.327    14.327    14.327    14.327    14.327    14.327    14.327
13.973    13.973    13.973    13.973    13.973    13.973    13.973
12.930    12.930    12.930    12.930    12.930    12.930    12.930
10.755    10.755    10.755    10.755    10.755    10.755    10.755
 6.743     6.743     6.743     6.743     6.743     6.743     6.743
 0.000     0.000     0.000     0.000     0.000     0.000     0.000
```

Figure 4-10i. Axial velocity solution.

```
Ans-Vth-X.dat - Notepad
File  Edit  Format  View  Help

Time (sec):      9.0
I:       1           2           3           4           5           6           7
 1  0.314E+02  0.314E+02  0.314E+02  0.314E+02  0.314E+02  0.314E+02  0.314E+02
 2  0.277E+02  0.277E+02  0.277E+02  0.277E+02  0.277E+02  0.277E+02  0.277E+02
 3  0.242E+02  0.242E+02  0.242E+02  0.242E+02  0.242E+02  0.242E+02  0.242E+02
 4  0.208E+02  0.208E+02  0.208E+02  0.208E+02  0.208E+02  0.208E+02  0.208E+02
 5  0.176E+02  0.176E+02  0.176E+02  0.176E+02  0.176E+02  0.176E+02  0.176E+02
 6  0.145E+02  0.145E+02  0.145E+02  0.145E+02  0.145E+02  0.145E+02  0.145E+02
 7  0.114E+02  0.114E+02  0.114E+02  0.114E+02  0.114E+02  0.114E+02  0.114E+02
 8  0.851E+01  0.851E+01  0.851E+01  0.851E+01  0.851E+01  0.851E+01  0.851E+01
 9  0.564E+01  0.564E+01  0.564E+01  0.564E+01  0.564E+01  0.564E+01  0.564E+01
10  0.281E+01  0.281E+01  0.281E+01  0.281E+01  0.281E+01  0.281E+01  0.281E+01
11  0.000E+00  0.000E+00  0.000E+00  0.000E+00  0.000E+00  0.000E+00  0.000E+00
```
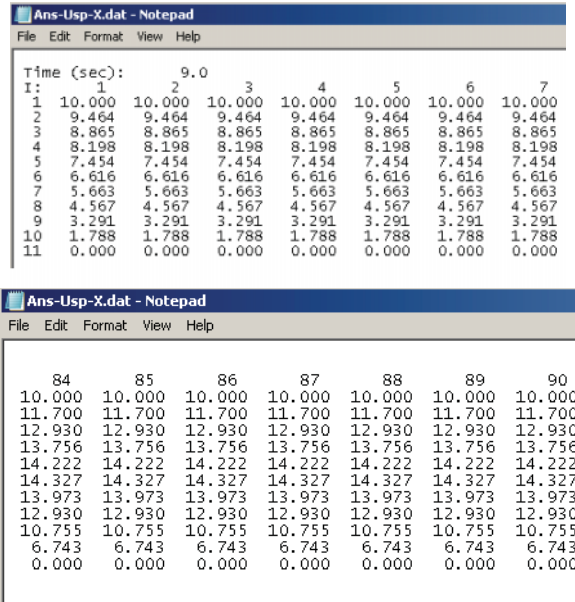
Figure 4-10j. Azimuthal velocity solution.

```
Ans-Rey-X.dat - Notepad
File  Edit  Format  View  Help

Time (sec):      9.0
I:       1           2           3           4           5           6           7
 1  0.192E+01  0.209E+01  0.209E+01  0.209E+01  0.209E+01  0.209E+01  0.209E+01
 2  0.180E+01  0.192E+01  0.192E+01  0.192E+01  0.192E+01  0.192E+01  0.192E+01
 3  0.168E+01  0.170E+01  0.170E+01  0.170E+01  0.170E+01  0.170E+01  0.170E+01
 4  0.156E+01  0.156E+01  0.156E+01  0.156E+01  0.156E+01  0.156E+01  0.156E+01
 5  0.141E+01  0.142E+01  0.142E+01  0.142E+01  0.142E+01  0.142E+01  0.142E+01
 6  0.125E+01  0.126E+01  0.126E+01  0.126E+01  0.126E+01  0.126E+01  0.126E+01
 7  0.107E+01  0.107E+01  0.107E+01  0.107E+01  0.107E+01  0.107E+01  0.107E+01
 8  0.866E+00  0.864E+00  0.864E+00  0.864E+00  0.864E+00  0.864E+00  0.864E+00
 9  0.624E+00  0.622E+00  0.622E+00  0.622E+00  0.622E+00  0.622E+00  0.622E+00
10  0.339E+00  0.338E+00  0.338E+00  0.338E+00  0.338E+00  0.338E+00  0.338E+00
11  0.000E+00  0.000E+00  0.000E+00  0.000E+00  0.000E+00  0.000E+00  0.000E+00
```

Figure 4-10k. Reynolds number solution.

4.11 References.

- Chin, W.C., *Borehole Flow Modeling in Horizontal, Deviated and Vertical Wells*, Gulf Publishing, Houston, 1992.

- Chin, W.C., *Computational Rheology for Pipeline and Annular Flow*, Elsevier Science, London, 2001.

- Chin, W.C., "Modeling and Simulation of Managed Pressure Drilling for Improved Design, Risk Assessment, Training and Operations," *RPSEA Ultra-Deepwater Technology Conference*, Houston, Tx, June 22-23, 2010.

- Chin, W.C., "Flow Simulation Methods for Managed Pressure Drilling and Cementing," *Drilling and Completing Trouble Zones Conference*, Galveston, Tx, Oct. 19-21, 2010.

- Chin, W.C., *Managed Pressure Drilling: Modeling, Strategy and Planning*, Elsevier, Amsterdam, 2012.

- Chin, W.C., *Managed Pressure Drilling: Modeling, Strategy and Planning*, Chinese Edition, Elsevier, Singapore, 2017.

- Chin, W.C., and Zhuang, X., "Exact Non-Newtonian Flow Analysis of Yield Stress Fluids in Highly Eccentric Borehole Annuli with Pipe or Casing Translation and Rotation," Paper 131234-PP, *CPS/SPE International Oil & Gas Conference and Exhibition*, Beijing, China, June 8-10, 2010.

- Chin, W.C., and Zhuang, X., "Effect of Rotation on Flowrate and Pressure Gradient in Eccentric Holes," Paper AADE-11-NTCE-45, *AADE 2011 National Technical Conference and Exhibition*, Houston, TX, April 12-14, 2011 (a).

- Chin, W.C., and Zhuang, X., "Advances in Swab-Surge Modeling for Managed Pressure Drilling," Paper AADE-11-NTCE-46, *AADE 2011 National Technical Conference and Exhibition*, Houston, TX, April 12-14, 2011 (b).

- Chin, W.C., and Zhuang, X., "Transient, Multiphase, Three-Dimensional Pumping Models for Cementing and Drilling," Paper AADE-11-NTCE-72, *AADE 2011 National Technical Conference and Exhibition*, Houston, TX, April 12-14, 2011 (c).

- Chin, W.C., and Zhuang, X., "Comprehensive Annular Flow Models for Drilling and Completions," Paper AADE-11-NTCE-73, *AADE 2011 National Technical Conference and Exhibition*, Houston, TX, April 12-14, 2011 (d).

- Chin, W.C. and Zhuang, X., "Advances in Swab-Surge Modeling for Managed Pressure Drilling," Paper OTC-21115-PP, *2011 Offshore Technology Conference*, Houston, TX, May 2-5, 2011 (e).

- Deawwanich, T., Liew, J.C., Nguyen, Q.D., Savery, M., Tonmukayakul, N., and Chin, W.C., "Displacement of Viscoplastic Fluids in Eccentric Annuli: Numerical Simulation and Experimental Validation," *Chemeca 2008 Conference*, Newcastle, Australia, Sept. 28 - Oct. 1, 2008.

- Nguyen, Q.D., Deawwanich, T., Tonmukayakul, N., Savery, M.R., and Chin, W.C., "Flow Visualization and Numerical Simulation of Viscoplastic Fluid Displacements in Eccentric Annuli," *XVth*

International Congress on Rheology (ICR 2008), Society of Rheology 80th Annual Meeting, Monterey, CA, Aug. 3-8, 2008.

- Savery, M., Chin, W.C., and Babu Yerubandi, K., "Modeling Cement Placement Using a New Three-Dimensional Flow Simulator," Paper AADE-08-DF-HO-08, 2008 AADE Fluids Conference and Exhibition, American Association of Drilling Engineers, Houston, Texas, April 8-9, 2008.

- Savery, M., Darbe, R., and Chin, W.C., "Modeling Fluid Interfaces During Cementing Using a Three-Dimensional Mud Displacement Simulator," OTC Paper 18513, *2007 Offshore Technology Conference (OTC)*, Houston, TX, April 30 – May 3, 2007.

- Savery, M., Tonmukayakul, P., Chin, W.C., Deawwanich, T., Liew, J., and Q. D. Nguyen, "Laminar Displacement of Viscoplastic Fluids in Eccentric Annuli – Numerical Simulation and Experimental Validations," *XXII International Congress of Theoretical and Applied Mechanics (ICTAM 2008)*, Adelaide, Australia, Aug. 24-29, 2008.

5

Mudcake Formation in Single-Phase Flow

The annular flow models in Chapters 2, 3 and 4 are state-of-the-art. Our presentation focused on applications, and we emphasize that the underlying theories and algorithms were developed over a decades long period and have undergone extensive testing and physical validation. Nonetheless, they only approximate the real world because they assume that the borehole wall is perfectly sealed by mudcake – a presumption that is not necessarily true. Why is sealing important? It is for a number of reasons. A poorly sealed formation may allow explosive gases or high pressure liquids from the formation to enter the borehole – or by contrast, it may allow rapid influx of mud into the reservoir and result in loss of borehole pressure and wellbore instability. Without a thick cake, formation tester pads will not seal properly – clean in situ fluids will not be collected and real-time prediction of mobilities and pore pressures will not be possible. But too much mudcake may increase the risk for stuck pipe – definitely not desired. This quick survey highlights the important role mudcake plays in wellbore and reservoir integrity.

Over the years, the author has developed numerous models for mudcake growth and downhole filtration, many of which are discussed in detail in his book publications (see Chin (2014, 2015, 2017)). Suffice it to say, the subject is non-trivial and details depend on the environment. For example, on miscible or immiscible multiphase flow interactions (that is, oil mud penetrating oil or water mud penetrating oil) which are important to pumping clean in situ fluid in formation testing. Or on absolute permeability in the underlying rock, which is typically high (compared to that of the cake) in "conventional" applications but low in "unconventional." And, of course, on mud formulations themselves, on erosion due to dynamic filtration, and on differential pressure.

The complete range of static and dynamic filtration models is presented in the three cited books. For practical reasons, it is not possible to summarize the results here – however, in the present chapter, we will develop the subject of "mudcake formation in single-phase flows," and in Chapter 6, provide additional insights into mudcake development in multiphase environments that may reside in reservoirs ranging from highly permeable to almost impermeable. We do emphasize that the single-phase limit considered here is important and more than academic. For many practical applications, the mobility in the formation is several orders of magnitude lower than that of the cake – thus, cake development in time proceeds independently of the reservoir flow in the rock – basically, because mudcake controls the flow rate.

Having justified why we should study mudcakes formed by single-phase oil or water muds, we turn to a more technical focus. How do we model dynamic cake growth? How rapidly are equilibrium results achieved? How valid is "classic √t growth" in practice? What role does surface measurement of cake properties play in large diameter wells with thin cakes versus, say, thick cake formation in slimholes? To answer these questions, we introduce useful empirical tests which characterize fundamental properties for mudcakes, properties which are used in math models for cake formation in reservoirs with permeability ranges from high to low and well diameters that vary from large diameter to very small. Key to modeling are ideas from "moving boundary value problems" – the solution of partial differential equations with moving boundaries which, in petroleum engineering, are represented by mudcakes with growing thicknesses and internal invasion fronts that propagate with non-constant speeds.

5.1 Flows with moving boundaries – four basic problems.

The development of a general model for mudcake formation in an environment characterized by arbitrary fluids and formation rock begins with controlled experiments. These are described in Chin (2017) in detail. In this chapter, we will discuss linear flow results and show how, in the single-phase limit, they can be used more generally. The apparatus used in shown in Figures 5-1-1 and 5-1-2, where mud flows from top to bottom. A linear core sample is installed in a cylindrical vessel and provision is made so that fluid flows through the core only and not at its sides. The entire vessel is placed in a Catscan imaging device and differential pressure is applied lengthwise through the core.
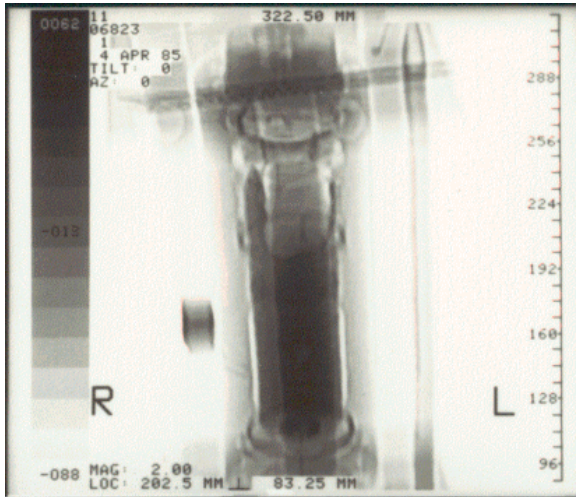
Figure 5-1-1. Linear flow filtration vessel (close-up).
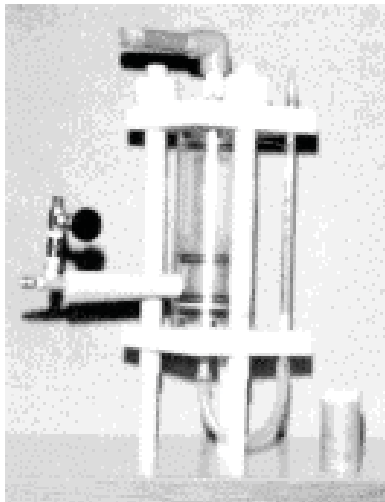

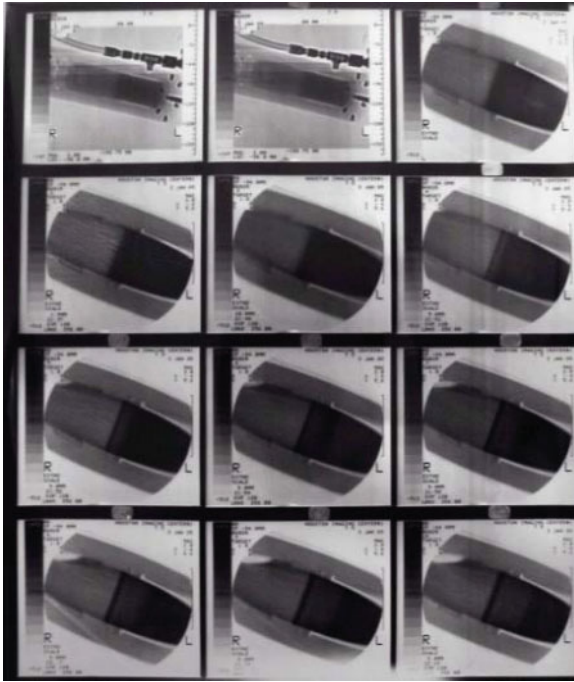**Figure 5-1-2.** Linear flow filtration vessel in Catscan device.

Figure 5-1-3. Time lapse photo of cake formation and filtration front.
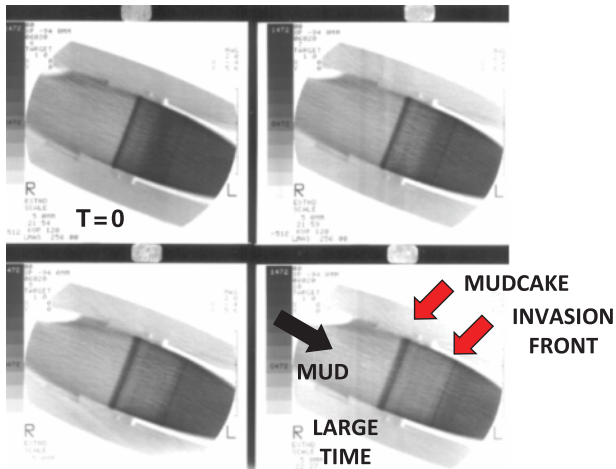

Figure 5-1-4. Close-up photo showing mudcake and invasion front.

Typical photographs recording the lineal flow invasion process showing mudcake formation and complementary fluid front invasion are obtained in time appear in Figures 5-1-3 and 5-1-4. The magnified photo in Figure 5-1-4 with good visual contrast clearly shows the distinctly formed mudcake along with the invasion front. We will now address different aspects of single-phase flow mudcake formation. We first consider lineal cake buildup on filter paper, and then we examine the plug flow of two dissimilar liquids in a linear core without mudcake. These two examples set the stage for problems where mudcake growth, formation properties and invasion front motion are dynamically couple.

5.1.1 Linear mudcake buildup on filter paper.

In order to understand the physics clearly, we study the problem of *isolated* mudcake growth, as would be obtained in the laboratory lineal flow test setup in Figure 5-1-5. We consider a one-dimensional experiment where mud, in essence a suspension of clay particles in water, is allowed to flow through filter paper. Initially, the flow rate is rapid. But as time progresses, solid particles (typically 6% to 40% by volume for light to heavy muds) such as barite are deposited onto the surface of the paper, forming a mudcake that, in turn, retards the passage of mud filtrate by virtue of the resistance to flow that the cake provides.
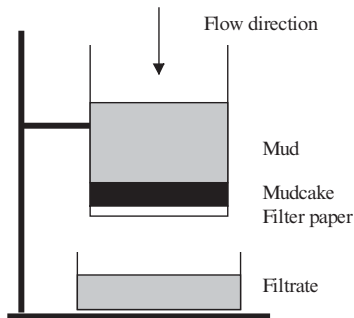
Figure 5-1-5. Simple laboratory mudcake buildup.

We therefore expect filtrate volume flow rate and cake growth rate to decrease with time, while filtrate volume and cake thickness continue to increase, but ever more slowly. These qualitative ideas can be formulated precisely, because the problem *is* based on well-defined physical processes. For one, the composition of the homogeneous mud during this filtration does not change: its solid fraction is always

constant. Second, the flow *within* the mudcake *is* a Darcy flow and is therefore governed by the equations used by reservoir engineers. The only problem is the presence of a moving boundary, namely, the position interface separating the mudcake from the mud that ultimately passes through it and that continually adds to its thickness. Thus the physical problem is a transient process that requires somewhat different mathematics than that taught in partial differential equations courses.

Mudcakes in reality may be compressible, that is, their mechanical properties may vary with applied pressure differential. It is possible to draw upon reservoir engineering methods for subsidence and formation compaction as discussed in Chin (2017). For now, a simple constitutive model for incompressible mudcake buildup, that is, the filtration of a fluid suspension of solid particles by a porous but rigid mudcake, can be constructed from first principles. First, let $x_c(t) > 0$ represent cake thickness as a function of the time, where $x_c = 0$ indicates zero initial thickness. Also, let V_s and V_l denote the volumes of solids and liquids in the mud suspension, and let f_s denote the solid fraction defined by $f_s = V_s/(V_s + V_l)$. Since this does not change throughout the filtration, its time derivative must vanish. If we set $df_s/dt = (V_s + V_l)^{-1} dV_s/dt - V_s (V_s + V_l)^{-2} (dV_s/dt + dV_l/dt) = 0$, we can show that $dV_s = (V_s/V_l) dV_l$. But since $V_s/V_l = f_s/(1- f_s)$, it follows that $dV_s = \{f_s/(1- f_s)\} dV_l$.

This is a conservation of species law for the solid particles making up the mud suspension and does not as yet embody any assumptions related to mudcake buildup. Frequently, we might note, the drilling fluid is thickened or thinned in the process of making hole; if so, the equations derived here should be reworked with $f_s = f_s(t)$ and its corresponding time-dependent pressure drop.

In order to introduce the mudcake dynamics, we observe that the total volume of solids dV_s deposited on an elemental area dA of filter paper during an infinitesimal time dt is $dV_s = (1 - \phi_c) dA\ dx_c$ where ϕ_c is the mudcake porosity. During this time, the volume of the filtrate flowing through our filter paper is $dV_l = |v_n|\ dA\ dt$ where $|v_n|$ is the Darcy velocity of the filtrate through the cake and past the paper. We now set our two expressions for dV_s equal to form $\{f_s/(1- f_s)\} dV_l = (1 - \phi_c) dA\ dx_c$, and replace dV_l with $|v_n|\ dA\ dt$, so that we obtain the

equality $\{f_s/(1- f_s)\}\ |v_n|$ dA dt = $(1 -\phi_c)$ dA dx_c. The dA's cancel, and we are led to a generic equation governing mudcake growth. In particular, the cake thickness $x_c(t)$ satisfies the ordinary differential equation

$$dx_c(t)/dt = \{f_s/\{(1- f_s)(1 -\phi_c)\}\}\ |v_n| \qquad (5\text{-}1\text{-}1a)$$

Now, as in the first example of the previous section, we assume a one-dimensional, constant density, single *liquid* flow. For such flows, the constant Darcy velocity is $(k/\mu)(\Delta p/L)$, where $\Delta p > 0$ is the usual delta p or pressure drop through the core of length L. The corresponding velocity for the present problem is $|v_n| = (k/\mu)(\Delta p/x_c)$ where k is the cake permeability, and μ is the filtrate viscosity. Substitution in Equation 5-1-1a leads to

$$dx_c(t)/dt = \{kf_s\Delta p/\{\mu(1- f_s)(1 -\phi_c)\}\}/x_c \qquad (5\text{-}1\text{-}1b)$$

If the mudcake thickness is infinitesimally thin at t = 0, with $x_c(0) = 0$, Equation 5-1-1b can be integrated, with the result that

$$x_c(t) = \sqrt{[\{2kf_s\Delta p/\{\mu(1- f_s)(1 -\phi_c)\}\}\ t]} > 0 \qquad (5\text{-}1\text{-}2)$$

This demonstrates that cake thickness in a lineal flow grows with time like $\sqrt{t}$. However, it grows ever more slowly, because increasing thickness means increasing resistance to filtrate throughflow, the source of the solid particulates required for mudcake buildup. Consequently, filtrate buildup also slows.

To obtain the filtrate production volume, we combine $dV_l = |v_n|$ dA dt and $|v_n| = (k/\mu)(\Delta p/x_c)$ to form $dV_l = (k\Delta pdA/\mu)\ x_c^{-1}dt$. Using Equation 5-1-2, $dV_l = (k\Delta pdA/\mu)\ [\{2kf_s\Delta p/\{\mu(1- f_s)(1 -\phi_c)\}\}]^{-1/2}(\ t)^{-1/2}$ dt. Direct integration, assuming zero filtrate initially, yields

$$V_l(t) = 2(k\Delta pdA/\mu)\ [\{2kf_s\Delta p/\{\mu(1- f_s)(1 -\phi_c)\}\}]^{-1/2}(\ t)^{1/2} \quad (5\text{-}1\text{-}3)$$
$$= \sqrt{\{2k\Delta p(1- f_s)(1 - \phi_c)/(\mu f_s)\}}\ \sqrt{t}\ \ dA$$

Chin *et al* (1986) and other industry papers required detailed, tedious laboratory measurement of the cake parameters f_s, ϕ_c, and k. This could pose operational difficulties. It turns out that this is unnecessary: their values can be inferred from the results of simple surface filtration experiments discussed in the next section.

So far, we have encountered two types of √t behavior, first for constant density, radial, single-liquid flows without mudcake, and then for lineal mudcake buildup and filtrate production without introducing any underlying rock, just the opposite problem. It turns out that there is still another type of √t behavior, obtained by considering the constant density flows of two sequential fluids through a lineal core without mudcake (treated next). Thus, there are at least three types of √t behavior each governed by different flow parameters or physical processes, and therefore, at least three different √t time scales! Log interpretation, therefore, can be challenging, to say the least.

5.1.2 Plug flow of two liquids in linear core without cake.

Let us consider the Darcy flow through a single lineal core in which one liquid displaces a second in a piston-like, plug, or slug-like manner, as in Figure 5-1-6. We assume that the permeability to each fluid is the same, so that a single permeability k suffices. Pressures P_l and P_r are fixed at the left and right sides, with $P_l > P_r$, so that the fluid system flows from left to right. No cake is present. For lineal liquid flows, $\partial^2 p(x,t)/\partial x^2 = (\phi\mu c/k) \, \partial p/\partial t$ describes transient, compressible liquids, with ϕ, μ, c, and k denoting rock porosity, fluid viscosity, fluid-rock compressibility, and permeability. We address the problem where an invading liquid displaces a pre-existing formation liquid, the respective viscosities being μ_1 and μ_2.
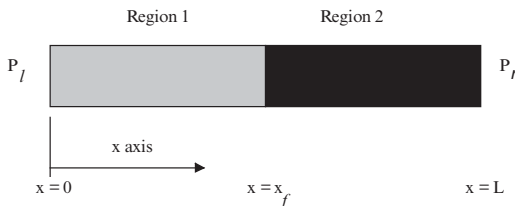
Figure 5-1-6. Simple linear flow of two dissimilar fluids.

A second objective of this exercise is the development of mathematical techniques that model internal moving interfaces, for example, the front $x = x_f(t)$ as indicated in Figure 5-1-6. For now, though, we may regard the pressure problem as a purely static one. For the incompressible fluids assumed here, the compressibility c vanishes, and the ordinary differential equations for pressure in Layers 1 and 2

become $d^2p_1(x)/dx^2 = 0$ and $d^2p_2(x)/dx^2 = 0$, which have the respective solutions $p_1(x) = Ax + B$ and $p_2(x) = Cx + D$, where A, B, C, and D are integration constants completely determined by the end pressure boundary conditions $p_1(0) = P_l$ and $p_2(L) = P_r$, *and* the interfacial matching conditions at $x = x_f$, $p_1(x_f) = p_2(x_f)$ and $q_1(x_f) = q_2(x_f)$. The pressure continuity equation assumes that interfacial tension effects are negligibly small. Velocity matching, on the other hand, is a kinematic statement stating that the local velocity is single-valued, that is, it takes on one and only one value – the moving interface is convected with this velocity as is physically clear.

Now, since the $k_1 = k_2 = k$, the Darcy velocities satisfy $q_1 = -(k_1/\mu_1) dp_1(x)/dx = -(k/\mu_1) A$ and $q_2 = -(k_2/\mu_2) dp_2(x)/dx = -(k/\mu_2) C$, so that $A/\mu_1 = C/\mu_2$. This leads to the pressure solution for $0 < x < x_f$,

$$p_1(x) = (\mu_1/\mu_2)(P_r - P_l) x /\{L + x_f(\mu_1/\mu_2 - 1)\} + P_l \qquad (5\text{-}1\text{-}4)$$

The pressure solution for $x_f < x < L$ is determined as

$$p_2(x) = (P_r - P_l)(x-L)/\{L + x_f(\mu_1/\mu_2 - 1)\} + P_r \qquad (5\text{-}1\text{-}5)$$

The invasion front can be determined, as in all of our preceding examples, by setting $dx_f/dt = q_1/\phi$ assuming that porosity is constant. We now use Equation 5-1-11 to obtain $dx_f/dt = -(k/(\phi\mu_1)) (\mu_1/\mu_2)(P_r - P_l)/\{L + x_f(\mu_1/\mu_2 - 1)\}$. If we follow the initial marked particle defined by the initial condition $x_f(0) = x_{f,o}$, we obtain the exact integral

$$(\mu_1/\mu_2 - 1)x_f + L = +\{\{(\mu_1/\mu_2 - 1)x_{f,o} + L\}^2$$
$$+ \{2k (P_l - P_r)/(\phi\mu_2)\}(\mu_1/\mu_2 - 1) t\}^{1/2} \quad (5\text{-}1\text{-}6)$$

Depending on the relative values of the μ_1 and μ_2, the displacement front may accelerate or decelerate. The foregoing analysis is easily reworked to handle time-dependencies in the total differential pressure applied across the core. If $(P_l - P_r)$ is a prescribed function of t, the differential equation should be integrated accordingly, for example, taking $\int (P_r - P_l) dt = P_r t - \int P_l (t)dt$. Similar comments apply to situations where $\phi = \phi(x)$. These changes lead to obvious analytical complications, which again motivate the need for numerical models.

5.1.3 Simultaneous mudcake buildup and filtrate invasion in a linear core (liquid flows).

Here we derive exact, closed-form, analytical solutions for lineal and radial flows where the growth of the mudcake and the progress of the invasion front are strongly coupled. The first solution was given in Chin *et al* (1986), but the radial solution at the time did not model spurt; the full solution is presented in Section 5.1.4.

We consider a realistic example where liquid mud filtrate displaces a preexisting formation liquid having a different viscosity. And while this process is ongoing, mudcake thickness is ever-increasing, so that filtrate influx rate is consequently decreasing. All the time, the filtrate-to-formation fluid displacement front moves to the right. In this problem, the dynamics of the mudcake growth are closely coupled to the invasion front motion. In our derivation, there is no assumption that the mudcake is significantly less permeable than the formation, an assumption usually taken to simplify the analysis. The work is exact in this regard, since the relative mobilities between cake, invaded zone, and virgin formation are left as completely free parameters for subsequent evaluation. This formulation, its solution procedure, and the exact, closed-form, analytical solution for lineal liquid flow were presented in Chin *et al* (1986). In the following, we will reconstruct the steps using the authors' published recipe and reproduce the earlier exact solution.
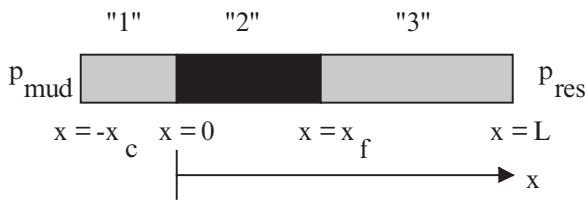

Figure 5-1-7. Three-layer lineal flow.

In Figure 5-1-7, let Layer 1 denote the mudcake, and Layers 2 and 3, the filtrate-invaded and virgin oil-bearing formations, respectively. The origin $x = 0$ is the fixed cake-to-rock interface; also, $x_c > 0$ represents the cake thickness, while $x_f > 0$ is the displacement front separating invaded from uninvaded rock zones. The transient compressible flow equation assuming constant liquid and rock properties is the classic parabolic partial differential equation, for example, $\partial^2 p_1(x,t)/\partial x^2 = (\phi_1\mu_1 c_1/k_1)\ \partial p_1/\partial t$, for Layer 1. If we ignore all

compressibilities, in effect considering incompressible liquids with $c = 0$, our layered equations reduce to the equations $d^2p_i(x)/dx^2 = 0$, where $i = 1, 2, 3$. These are solved together with the pressure boundary conditions $p_1(-x_c) = p_m$ and $p_3(L) = p_r$, where p_m and p_r represent mud and reservoir pressures. We also invoke interfacial matching conditions for pressure, that is, $p_1(0) = p_2(0)$ and $p_2(x_f) = p_3(x_f)$, plus interfacial matching conditions for velocity, that is, $k_1/\mu_1 \, dp_1(0)/dx = k_2/\mu_2 \, dp_2(0)/dx$ and $k_2/\mu_2 \, dp_2(x_f)/dx = k_3/\mu_3 \, dp_3(x_f)/dx$.

Note that we have retained three separate permeabilities, k_1, k_2, and k_3 in these equations, as explained in Chapter 16. The k_1 represents, of course, the mudcake permeability. However, while we have but a single rock core, characterized by a single permeability, we will derive our results with *two* values k_2 and k_3. This flexibility allows us to set $k_2 = k_3 = k_{rock}$ if desired, or allow them to differ, in order to represent separate permeabilities to filtrate (with residual oil) and oil (in the presence of immobile connate water). This *ad hoc* modeling permits us to mimic two-phase flow relative permeability effects within the framework of a simpler slug displacement approach. We also note that while three viscosities μ_1, μ_2, and μ_3 were explicitly shown for completeness, we in fact assume that $\mu_1 = \mu_2 = \mu_f$ for the mud filtrate, since the liquid filtrates present in Layers 1 and 2 are identical. Also, we will later denote $\mu_3 = \mu_o$ to represent oil viscosity, that is, the viscosity of the displaced formation fluid. Now, the solutions to our ordinary differential equations are $p_i(x) = \alpha_i x + \beta_i$, $i = 1, 2, 3$ with the constants

$$\alpha_1 = (p_m\text{-}p_r)/\{(\mu_3 k_1/\mu_2 k_3 - k_1/k_2)x_f - \mu_3 k_1 L/\mu_2 k_3 - x_c\} \qquad \text{(5-1-7a)}$$

$$\beta_1 = p_m + (p_m\text{-}p_r)x_c/\{(\mu_3 k_1/\mu_2 k_3 - k_1/k_2)x_f - \mu_3 k_1 L/\mu_2 k_3 - x_c\} \quad \text{(5-1-7b)}$$

$$\alpha_2 = (k_1/k_2)(p_m\text{-}p_r)/\{(\mu_3 k_1/\mu_2 k_3 - k_1/k_2)x_f - \mu_3 k_1 L/\mu_2 k_3 - x_c\} \quad \text{(5-1-7c)}$$

$$\beta_2 = p_m + (p_m\text{-}p_r)x_c/\{(\mu_3 k_1/\mu_2 k_3 - k_1/k_2)x_f - \mu_3 k_1 L/\mu_2 k_3 - x_c\} \quad \text{(5-1-7d)}$$

$$\alpha_3 = (\mu_3 k_1/\mu_2 k_3)(p_m - p_r)/$$
$$\{(\mu_3 k_1/\mu_2 k_3 - k_1/k_2)x_f - \mu_3 k_1 L/\mu_2 k_3 - x_c\} \qquad \text{(5-1-7e)}$$

$$\beta_3 = p_m + (p_m\text{-}p_r)x_c/\{(\mu_3 k_1/\mu_2 k_3 - k_1/k_2)x_f - \mu_3 k_1 L/\mu_2 k_3 - x_c\}$$
$$+ x_f\{k_1/k_2 - \mu_3 k_1/\mu_2 k_3\}(p_m - p_r)/$$
$$\{(\mu_3 k_1/\mu_2 k_3 - k_1/k_2)x_f - \mu_3 k_1 L/\mu_2 k_3 - x_c\} \qquad \text{(5-1-7f)}$$

Equations 5-1-7a to 5-1-7f completely define the spatial pressure distributions within Layers 1, 2, and 3. However, the solutions to the invasion problem are as yet incomplete because the positions x_c and x_f are unknown time-dependent functions that satisfy other constraints.

Consider the mudcake first. Our previous differential equation for cake growth can be evaluated as

$$dx_c/dt = \{f_s/\{(1-\phi_c)(1-f_s)\}\} |v_n| \qquad (5\text{-}1\text{-}8)$$

$$= - [f_s/\{(1-\phi_c)(1-f_s)\}](k_1/\mu_1)(p_m\text{-}p_r) /\{(\mu_3 k_1/\mu_2 k_3 - k_1/k_2)x_f - \mu_3 k_1 L/\mu_2 k_3 - x_c\}$$

But this cannot be integrated since it depends on the front displacement $x_f(t)$, which satisfies its own dynamic equation. To obtain it, we evaluate the interfacial kinematic condition using the now known Darcy velocity as

$$dx_f/dt = - \phi_{eff}^{-1} (k_2/\mu_2) dp_2(x)/dx \qquad (5\text{-}1\text{-}9)$$

$$= - (k_1/\mu_2 \phi_{eff}) (p_m\text{-}p_r)/\{(\mu_3 k_1/\mu_2 k_3 - k_1/k_2)x_f - \mu_3 k_1 L/\mu_2 k_3 - x_c\}$$

Here ϕ_{eff} denotes the effective porosity that Layer 2 offers if immobile fluids are left behind once the filtrate front passes. This usage provides some degree of flexibility in modeling two-phase flow relative permeability effects within the framework of single-phase flow theory. Still, Equations 5-1-8 and 5-1-9 are coupled; at first, recourse to numerical analysis appears necessary, but this is fortunately not the case. It turns out that exact analytical solutions can be obtained. If we assume the initial condition $x_f(t = 0) = x_{f,o} > 0$ for the mud spurt, and $x_c = 0$, until $x_f = x_{f,o} > 0$ with $x_c(t) > 0$, for $x_f > x_{f,o}$, we obtain the solution of Chin et al (1986),

$$x_f(t) = - H + \sqrt{\{H^2 + 2(Hx_{f,o} + \tfrac{1}{2}x_{f,o}^2 + Gt)\}} \qquad (5\text{-}1\text{-}10)$$

where

$$G = - \{k_1(p_m\text{-}p_r)/(\mu_f \phi_{eff})\}/ \qquad (5\text{-}1\text{-}11)$$

$$\{\mu_o k_1/\mu_f k_3 - k_1/k_2 - \phi_{eff} f_s/\{(1-\phi_c)(1-f_s)\}\}$$

$$H = [x_{f,o}\phi_{eff} f_s/\{(1-\phi_c)(1-f_s)\} - \mu_o k_1 L/\mu_f k_3] \qquad (5\text{-}1\text{-}12)$$

$$/\{\mu_o k_1/\mu_f k_3 - k_1/k_2 - \phi_{eff} f_s/\{(1-\phi_c)(1-f_s)\}\}$$

Equations 5-1-10 to 5-1-12 completely describe the progress of the invasion front, as it is affected by filtrate and reservoir liquid viscosities,

and mudcake properties and growth. The corresponding equation for mudcake growth is

$$x_c(t) = [\phi_{eff} f_s/\{(1-\phi_c)(1-f_s)\}] (x_f - x_{f,o}) \qquad (5\text{-}1\text{-}13)$$

for which $dx_c/dx_f = \phi_{eff} f_s/\{(1-\phi_c)(1-f_s)\} > 0$. This states that x_f increases if x_c increases; it is interesting that the proportionality factor depends on geometrical parameters only, and not on transport variables like viscosity and permeability. We emphasize that, in general, pure $\sqrt{t}$ behavior is not always obtained, although it does appear in the limit of very large t. The reader, following our earlier Taylor series exercise, should determine the exact dimensionless meaning of large time when pure $\sqrt{t}$ behavior is found. Finally, note that

$$x_f(t) - x_{f,o} = \phi_{eff}^{-1}\sqrt{\{2k_1(1-\phi_c)(1-f_s)(p_m-p_r)t/(\mu_f f_s)\}} \qquad (5\text{-}1\text{-}14)$$

is obtained in the limit when the mobility in the rock core greatly exceeds that of the mudcake. This is the restrictive limit typically considered in the literature; again, our solutions do not invoke any limiting assumptions about relative cake-to-formation mobilities. Finally, we emphasize that these results require us to characterize the mudcake by three independent parameters, namely, the solid fraction f_s, the porosity ϕ_c, and the cake permeability k. The work in Chin *et al* (1986) and in recent industry studies requires such empirical inputs and elaborate laboratory. It turns out that all of this is unnecessary, and that a simple lumped parameter defined by convenient lineal filtrate tests on standard filter paper is all that is required. These ideas are pursued in the following Section 5.2.

5.1.4 Simultaneous mudcake buildup and filtrate invasion in a radial geometry (liquid flows).

Here, we will reconsider the simultaneous mudcake buildup and filtrate invasion problem just discussed, but we will use realistic radial coordinates. Note that the exact *linear* flow solution in Chin *et al* (1986) includes the all-important effect of mud spurt. But while that paper alluded to progress towards a radial solution, the work at that time could not account for any spurt at all because of mathematical complexities and, furthermore, turned to numerical solution as a last resort. Thus, a useful solution was not available, and any applications to time lapse analysis would await further progress. Since then, the result of some significant efforts have led to a closed-form solution. The resulting

solution and derivation are described in detail here. This availability, together with the simple recipe for mudcake properties alluded to, brings time lapse analysis closer to reality.
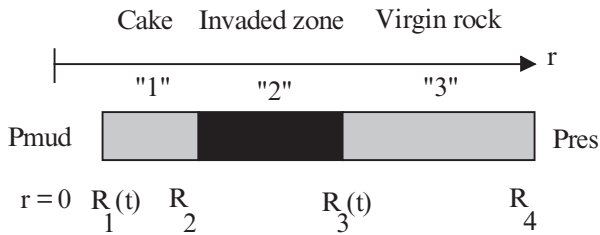
Cake   Invaded zone   Virgin rock

"1"   "2"   "3"

Pmud   Pres

$r = 0$ $R_1(t)$ R_2 $R_3(t)$ R_4

Figure 5-1-8. Three-layer radial flow.

We consider a realistic example where an incompressible liquid mud filtrate displaces a preexisting incompressible formation *liquid* having a different viscosity (gas displacement is discussed in Chapter 20).   Such fluids, flowing in homogeneous, isotropic media, satisfy Laplace's equation for pressure.   And while this process is ongoing, mud-cake thickness is ever-increasing, so that filtrate influx rate is consequently decreasing; all the time, the filtrate-to-formation fluid displacement front moves to the right. In this problem, as in our lineal one, the dynamics of the mudcake growth are closely coupled to the invasion front motion. In our derivation, there is *no* assumption that the mudcake is significantly less permeable than the formation, an assumption usually taken to simplify the analysis. Also, $\sqrt{t}$ behavior is not presumed at the outset; doing so would be wrong. The work is exact in this regard, since the relative mobilities between cake, invaded zone, and virgin formation are left as completely free parameters for subsequent evaluation.

In Figure 5-1-8, let Layer 1 denote the mudcake, and Layers 2 and 3, the filtrate-invaded and virgin oil-bearing formations, respectively. In this axisymmetric problem, the origin $r = 0$ is the borehole centerline. Here, $r = R_2$ represents the fixed cake-to-rock interface; R_2 is an absolute constant equal to the borehole radius.   Note that $r = R_1(t)$ represents the time-varying radial position of the mud-to-mudcake interface, while $R_3(t)$ denotes the time-dependent invasion front position. Finally, $r = R_4$ represents a fixed effective radius where the reservoir pore pressure P_r is specified. The driving pressure differential is just

$(p_m - p_r)$, where p_m is the pressure in the borehole. The transient compressible flow equations for constant liquid and rock properties are of standard parabolic form, for example, $\partial^2 p_1(r,t)/\partial r^2 + (1/r)\, \partial p_1/\partial r = (\phi_1 \mu_1 c_1/k_1)\, \partial p_1/\partial t$ for Layer 1. But since we are ignoring all fluid compressibilities, in effect considering constant density liquids with $c = 0$, our equations reduce to the differential equations $d^2 p_i(r)/dr^2 + (1/r)\, dp_i/dr = 0$, $i = 1, 2, 3$, which have the solutions $p_i(r) = \alpha_i \log r + \beta_i$, $i = 1, 2, 3$.

As in our earlier example, the integration constants can be determined from the end pressure boundary conditions $p_1(R_1) = p_m$ and $p_3(R_4) = p_r$. Also, we will require the interfacial matching conditions $p_1(R_2) = p_2(R_2)$ and $p_2(R_3) = p_3(R_3)$ for pressure, and $(k_1/\mu_1)\, dp_1(R_2)/dr = (k_2/\mu_2)\, dp_2(R_2)/dr$ and $(k_2/\mu_2)\, dp_2(R_3)/dr = (k_3/\mu_3)\, dp_3(R_3)/dr$ for velocity. Note that we have retained three separate permeabilities, namely, k_1, k_2, and k_3 in these equations. The k_1 represents, of course, the mudcake permeability. However, while we have but a single radial rock core, characterized by a single permeability, we will derive our results with *two* values k_2 and k_3. This flexibility allows us to set $k_2 = k_3 = k_{rock}$ if desired, or allow them to differ, in order to represent separate permeabilities to filtrate and oil. Note that we have also retained three viscosities μ_1, μ_2, and μ_3, even though the same liquid $\mu_1 = \mu_2$ flows through Layers 1 and 2 (in the previous example, we assumed that $\mu_1 = \mu_2$). This *ad hoc* modeling, consistent with our introduction of ϕ_{eff} earlier, permits us to *mimic* two-phase flow relative permeability effects within the framework of a simpler slug displacement approach. The six integration constants are easily found, using elementary algebra, as

$$\alpha_1 = \frac{(k_2/\mu_2)(p_r - p_m)}{\log[(R_2/R_1)^{k_2/\mu_2} (R_3/R_2)^{k_1/\mu_1} (R_4/R_3)^{k_1 k_2 \mu_3/\mu_1 \mu_2 k_3}]} \qquad \text{(5-1-15a)}$$

$$\beta_1 = p_m - \alpha_1 \log R_1 \qquad \text{(5-1-15b)}$$

$$\alpha_2 = (k_1 \mu_2/\mu_1 k_2)\, \alpha_1 \qquad \text{(5-1-15c)}$$

$$\beta_2 = p_m + \alpha_1 \log (R_2/R_1) - \alpha_2 \log R_2 \qquad \text{(5-1-15d)}$$

$$\alpha_3 = (\mu_3 k_1/\mu_1 k_3)\, \alpha_1 \qquad\qquad (5\text{-}1\text{-}15e)$$

$$\beta_3 = p_m + \alpha_1 \log(R_2/R_1) + \alpha_2 \log(R_3/R_2) - \alpha_3 \log R_3 \quad (5\text{-}1\text{-}15f)$$

where all logarithms are natural logarithms. It appears that we have defined the spatial pressure distributions within Layers 1, 2, and 3. However, the solutions to the invasion problem are incomplete because the position fronts $R_1(t)$ and $R_3(t)$ are unknown functions of t. As before, equations for cake growth and displacement front motion must be postulated. For mudcake growth, we have

$$- dR_1/dt = \{f_s/\{(1-\phi_c)(1-f_s)\}\}\, |v_n|$$

$$= [f_s/\{(1-\phi_c)(1-f_s)\}]\,(k_1/\mu_1)\, dp_1/dr$$

$$= [f_s/\{(1-\phi_c)(1-f_s)\}]\,(k_1/\mu_1)\, \alpha_1/r$$

$$= [f_s/\{(1-\phi_c)(1-f_s)\}]\,(k_1/\mu_1)\, \alpha_1(R_1,R_3)/R_1 \qquad (5\text{-}1\text{-}16)$$

The analogous equation for displacement front motion is obtained from

$$dR_3/dt = - \{k_2/(\mu_2\phi_{eff})\}\, dp_2/dr$$

$$= - \{k_2/(\mu_2\phi_{eff})\}\, \alpha_2/r$$

$$= - \{k_2/(\mu_2\phi_{eff})\}\, \alpha_2(R_1,R_3)/R_3 \qquad (5\text{-}1\text{-}17)$$

These nonlinear ordinary differential equations, as in the lineal case, are coupled. But again, it is possible to integrate them in closed, analytical form for general initial conditions. If we assume that $R_3 = R_{spurt} \geq R_2$, when $R_1 = R_2$ (i.e., no cake) at $t = 0$, we find that the displacement front history $R_3(t)$ satisfies

$$(k_1 R_2{}^2/\mu_1)[\; \tfrac{1}{2}(R_3/R_2)^2 \log(R_3/R_2) - \tfrac{1}{4}(R_3/R_2)^2$$
$$- \tfrac{1}{2}(R_{spurt}/R_2)^2 \log(R_{spurt}/R_2) + \tfrac{1}{4}(R_{spurt}/R_2)^2\;]$$
$$+ (k_1 k_2 \mu_3 R_4{}^2/\mu_1 \mu_2 k_3)[\; \tfrac{1}{2}(R_{spurt}/R_4)^2 \log(R_{spurt}/R_4) - \tfrac{1}{4}(R_{spurt}/R_4)^2$$
$$- \tfrac{1}{2}(R_3/R_4)^2 \log(R_3/R_4) + \tfrac{1}{4}(R_3/R_4)^2\;]$$
$$+ (k_2 R_2{}^2/4\mu_2\phi_{eff})\{(1-\phi_c)(1-f_s)/f_s\}\times$$
$$[\; \log\{1 + f_s\phi_{eff}\{(R_{spurt}/R_2)^2 - (R_3/R_2)^2\}/\{(1-\phi_c)(1-f_s)\}\}$$
$$- f_s\phi_{eff}\{(R_{spurt}/R_2)^2 - (R_3/R_2)^2\}/\{(1-\phi_c)(1-f_s)\}$$
$$+ f_s\phi_{eff}\{(R_{spurt}/R_2)^2 - (R_3/R_2)^2\}/\{(1-\phi_c)(1-f_s)\}\times$$
$$\log\{1 + f_s\phi_{eff}\{(R_{spurt}/R_2)^2 - (R_3/R_2)^2\}/\{(1-\phi_c)(1-f_s)\}\}\;] =$$
$$= \{k_1 k_2(p_m - p_r)/(\mu_1\mu_2\phi_{eff})\}\, t \qquad (5\text{-}1\text{-}18)$$

which does *not*, we emphasize, in general follow √t behavior (e.g., see Outmans, 1963). This exact formula is particularly useful in MWD logging applications where the extent of formation invasion needs to be estimated prior to taking measurements. Equation 5-1-18 can be solved by assuming values for R_3 and calculating the corresponding times. The associated cake radius function $R_1(t)$ is then obtained from

$$R_1^2 = R_2^2 + (R_{spurt}^2 - R_3^2)(f_s \phi_{eff})/\{(1-\phi_c)(1-f_s)\} \qquad (5\text{-}1\text{-}19)$$

It is also possible to show that

$$dR_1^2/dR_3^2 = -[f_s/\{(1-\phi_c)(1-f_s)\}] \phi_{eff} < 0 \qquad (5\text{-}1\text{-}20)$$

This equation indicates that as our filtration front advances, with R_3^2 increasing, the radius (squared) R_1^2 decreases. This decrease, following the schematic shown in Figure 5-1-8, indicates that mudcake thickness is consistently growing. Equation 5-1-20 is a Lagrangian mass conservation law that is independent of transport parameters such as permeability and viscosity.

   Unlike the lineal cake problem studied earlier where, in principle, the mudcake can increase indefinitely in thickness over time, the maximum radial thickness that can be achieved in this radial example is defined by $R_1(t_{max}) = 0$, and occurs at $t = t_{max}$. At this time, all fluid motions cease, at least within the framework of the piston-like displacements studied in this chapter, and molecular diffusion then becomes the dominant physical player. In order to determine the maximal radial displacement $R_{3,max}$ and its corresponding time scale t_{max}, we set $R_1(t)$ to zero in Equation 5-1-19, to obtain

$$R_{3,max} = \sqrt{[R_{spurt}^2 + \{(1-\phi_c)(1-f_s)/(f_s \phi_{eff})\}R_2^2]} \qquad (5\text{-}1\text{-}21)$$

Then t_{max} is obtained by substituting $R_{3,max}$ into Equation 5-1-18, that is,

$$(k_1 R_2^2/\mu_1)[\ \tfrac{1}{2}(R_{3,max}/R_2)^2 \log (R_{3,max}/R_2) - \tfrac{1}{4}(R_{3,max}/R_2)^2$$
$$- \tfrac{1}{2}(R_{spurt}/R_2)^2 \log (R_{spurt}/R_2) + \tfrac{1}{4}(R_{spurt}/R_2)^2\ ]$$
$$+(k_1 k_2 \mu_3 R_4^2/\mu_1 \mu_2 k_3)[\ \tfrac{1}{2}(R_{spurt}/R_4)^2 \log (R_{spurt}/R_4) - \tfrac{1}{4}(R_{spurt}/R_4)^2$$
$$- \tfrac{1}{2}(R_{3,max}/R_4)^2 \log (R_{3,max}/R_4) + \tfrac{1}{4}(R_{3,max}/R_4)^2\ ]$$
$$+(k_2 R_2^2/4\mu_2 \phi_{eff})\{(1-\phi_c)(1-f_s)/f_s\} \times$$
$$[\ \log \{1 + f_s \phi_{eff}\{(R_{spurt}/R_2)^2 - (R_{3,max}/R_2)^2\}/\{(1-\phi_c)(1-f_s)\}\}$$
$$- f_s \phi_{eff}\{(R_{spurt}/R_2)^2 - (R_{3,max}/R_2)^2\}/\{(1-\phi_c)(1-f_s)\}$$

$$+f_s\phi_{eff}\{(R_{spurt}/R_2)^2 - (R_{3,max}/R_2)^2\}/\{(1-\phi_c)(1-f_s)\} \times$$
$$\log\{1 + f_s\phi_{eff}\{(R_{spurt}/R_2)^2 - (R_{3,max}/R_2)^2\}/\{(1-\phi_c)(1-f_s)\}] =$$
$$= \{k_1 k_2 (p_m - p_r)/(\mu_1\mu_2\phi_{eff})\}\, t_{max} \quad (5\text{-}1\text{-}22)$$

In reality, hole plugging may be limited by borehole flow erosion, an essential element of the dynamic filtration process, a process that is considered in Chin (2017). We also indicate that radial experiments complementary to our linear flow results were also performed and described in Chin et al (1986). Figures 5-1-9 and 5-1-10 show the radial test vessel used and a sample Catscan with radial mudcake and fluid invasion. Figure 5-1-11 provides an example of compaction gradients inferred from Catscan measurements.
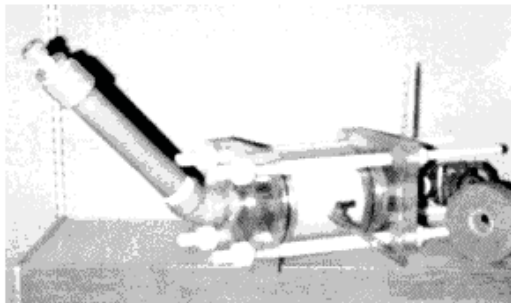

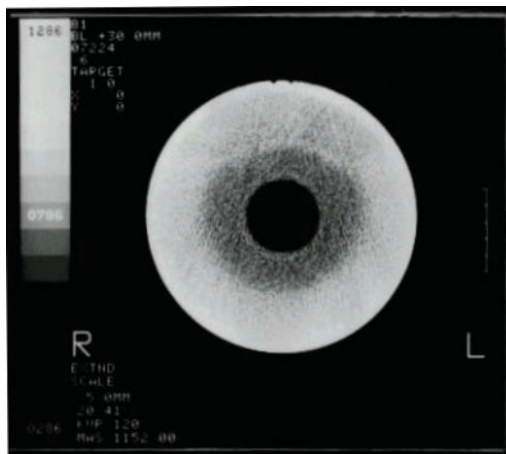**Figure 5-1-9.** Three-layer radial flow test vessel.

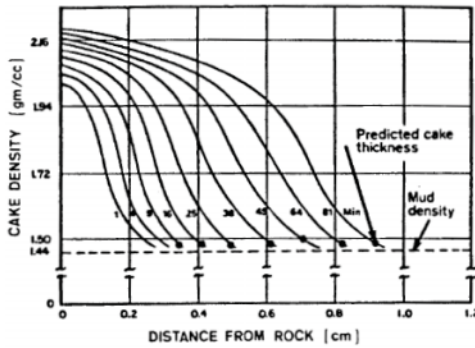**Figure 5-1-10.** Three-layer radial flow Catscan.

Figure 5-1-11. Experimental mudcake density and compaction.

5.2 Characterizing mud and mudcake properties.

The mudcake model used in early models required independent lab measurements for permeability, porosity and solid fraction. This implied tedious, time-consuming tasks involving weighing, drying, sorting, and so on, procedures similar to those reported later by other authors (e.g., Holditch and Dewan, 1991 and Dewan and Chenevert, 1993). The inaccuracies in such tests pose hurdles to practical field implementation, since any formation predictions obtained would only be as accurate as the mudcake properties. The early effort addressed sensitivities of predicted results as they depended on cake measurements. At the time, no solution to this problem was found, but it turns out that dynamically equivalent information *can* be obtained by a single measurement for filtrate volume and cake thickness at a single large time.

The foregoing modeling results required us to characterize the mudcake by three independent parameters, namely, the solid fraction f_s, the porosity ϕ_c, and the cake permeability k. The theoretical work in Chin *et al* (1986) and Collins (1961) required such empirical inputs, and elaborate laboratory procedures were developed to support the volume and Darcy flow resistance measurements needed. It turns out that all of this is unnecessary. The key idea lies in the fact that the foregoing parameters, for incompressible cakes anyway, only affect filtration by way of the two *lumped parameters* μ/k and $f_s/\{(1-f_s)(1-\phi_c)\}$, where μ is the filtrate viscosity. Thus, simple lineal filtrate tests performed at the surface – that is, building mudcake on filter paper (without underlying rock) and measuring cake thickness and filtrate volume are all that is necessary.

5.2.1 Simple extrapolation of mudcake properties.

In our study of *lineal* cake buildup on filter paper, we found that the cake thickness can be written as $x_C(t) = \sqrt{\{2kf_S\Delta p/\{\mu(1- f_S)(1 - \phi_C)\}\}}$ $\sqrt{t}$. For simplicity, consider a collection vessel having the same area dA as the cross-section of the core sample. (For lineal flows, the complete area A can be substituted in place of dA.) Then, the *filtrate height* h(t) = $V_f(t)$/dA of the liquid column is simply h(t) = $V_f(t)$/dA = $\sqrt{\{2k\Delta p(1- f_S)(1}$ $- \phi_C)/(\mu f_S)\}$ $\sqrt{t}$. Dividing the first equation by the second,

$$f_S/\{(1- f_S)(1 - \phi_C)\} = x_C(t)/h(t) \tag{5-2-1}$$

while the square of the equation for h(t) yields

$$\mu/k = 2\Delta p\{t/h^2(t)\} \bullet (1- f_S)(1 - \phi_C)/f_S \tag{5-2-2}$$

Thus, if $x_C(t)$ and h(t) are both known at some time t, the lumped quantities $f_S/\{(1- f_S)(1 - \phi_C)\}$ and μ/k are completely determined (our definition of the filtrate height h(t) excludes mud spurt contributions).

We emphasize that k and $f_S/\{(1- f_S)(1 - \phi_C)\}$ are material or constitutive *constants* intrinsic to the particular mudcake. The latter is a dimensionless number that depends only upon the packing arrangement of the solid particles making up the mudcake, which in turn depends on the instantaneous pressure gradient and the shearing effects of dynamic filtration, if present. These constants are not unlike others used in engineering analysis, for example, the viscosity of a lubricant or the yield stress of a steel test sample. This being so, their values can be obtained from the simple lineal buildup test just described, and are applied to more general cylindrical radial or spherical flow formulas derived for problems where mudcake and formation interaction are not weak.

The question of mudcake permeability often arises in assessing formation damage, which, for example, manifests itself through reduced production in reservoir engineering or by way of skin effects during transient well tests. Many researchers address this problem by forcing clean water through isolated mudcake (retrieved from filtration vessels) under pressure, thus ensuring a controlled test where the mudcake no longer grows; permeability is calculated by knowing the differential pressure, the cross-sectional area, the filtrate volume, and the water viscosity. This is the standard laboratory procedure used to determine rock core permeability, but its application to mudcake analysis is

inconvenient, since it is laborious, and more often than not results in cake damage and tearing. This procedure can be circumvented if we observe that Equations 5-2-1 and 5-2-2 imply that the cake permeability k takes the value

$$k = \mu \, h(t) x_c(t)/(2t\Delta p) \qquad\qquad (5\text{-}2\text{-}3)$$

which is completely determined using data from the foregoing test. Therefore, it is clear that separate flow tests for mudcake permeability prediction are unnecessary, since the test just described provides the needed information. In order to reduce the experimental error associated with mudcake characterization, the sample time t should be sufficiently large that errors due to initially nonuniform mudcake definition are minimized. This implies a wait of 30 to 60 minutes; in fact, a sequence of measurements corresponding to larger and larger wait times might be useful, to be terminated only when calculated results for mudcake properties converge to stable values. It is assumed, of course, that appropriate high temperature and pressure filtration vessels are used whenever necessary to model mudcake growth in deep holes. Experimentally, it has been observed that the mud-to-mudcake interface may be unclear and gel-like at times, thus introducing error into time lapse analysis. It may well be that special muds with easy-to-determine cake thicknesses will need to be formulated if inverse applications are to be successful.

5.2.2 Radial mudcake growth on cylindrical filter paper.

Many authors presume the universality of $\sqrt{t}$ mudcake-filtration behavior at large times; this may sometimes be valid in lineal flows. However, as we have seen from our general radial mudcake flow results, this assumption can be wrought with danger. The exact nature of mudcake growth is not only important to interpretation: cake thickness is a useful indicator for both formation damage and probability of differential sticking. While $\sqrt{t}$ behavior provides a "back of the envelope" guess, problems can arise when cake buildup is obviously radial, for example, when mudcake thickness is a substantial fraction of the hole radius, and in slimholes, where the buildup process may be uncertain. In this example, we will investigate the growth of mudcake in a radial flow vessel formed by thin cylindrically formed filter paper, as shown in Figure 5-2-1. Although it is possible to study this problem as a formal limit of our three-layer solution, it is instructive to reconsider its formulation from first principles. As shown earlier, the governing

ordinary differential equation for an incompressible, isotropic, homogeneous, cylindrical radial Darcy flow is $d^2p(r)/dr^2 + (1/r) \, dp/dr = 0$. Then, the general solution to this equation takes the form $p(r) = A \log r + B$.
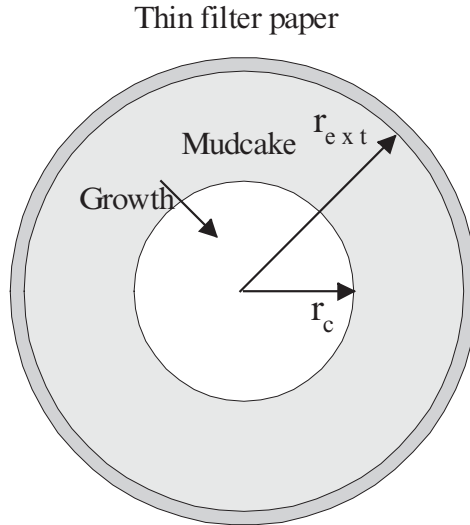
Thin filter paper

Figure 5-2-1. Radial mudcake growth on filter paper.

For this radial flow, we impose the mud pressure P_m at the edge of the growing cake interface and the external pressure P_{ext} at the circularly wrapped filter paper. Thus, the differential pressure acting on the cake ring is $P_m - P_{ext}$. Our boundary conditions are $p(r_c) = P_m$ and $p(r_{ext}) = P_{ext}$. If we now substitute these into the general solution, we find that the integration constant A satisfies $A = (P_m - P_{ext})/(\log r_c/r_{ext})$. The differential equation derived earlier for mudcake buildup, for the coordinates used, takes the form

$$dr_c(t)/dt \ = - \{f_s/\{(1- f_s)(1 - \phi_c)\}\} \, |v_n|$$
$$= + \{f_s/\{(1- f_s)(1 - \phi_c)\}\} \, (k/\mu) \, dp(r_c)/dr$$
$$= + \{f_s/\{(1- f_s)(1 - \phi_c)\}\} \, (k/\mu) \, A/r_c \qquad (5\text{-}2\text{-}4)$$

where A is again a function of $\log r_c$. This nonlinear ordinary differential equation can be integrated in exact closed form. To fix the

constant of integration, we assume that no mudcake exists at t = 0; that is, the cake radius is the same as that shown in Figure 5-2-2, with $r_c(t = 0) = r_{ext}$. Then, we obtain the following exact implicit solution for radial cake growth as a function of time,

$$\tfrac{1}{2}\,(r_c/r_{ext})^2 \log\,(r_c/r_{ext}) - \tfrac{1}{4}\,(r_c/r_{ext})^2\ + 1/4$$
$$= \{kf_s(P_m - P_{ext})/\{\mu(1 - f_s)(1 - \phi_c)r_{ext}^2\}\}\ t \qquad\qquad (5\text{-}2\text{-}5)$$

In deriving Equation 5-2-5, we assumed that P_m is constant. If it is instead a function of time, the integral $\int P_m(t)\ dt$ will simply appear in place of $P_m t$.

Now consider the conditions under which this general result reduces to the lineal $\sqrt{t}$ law. This is accomplished by introducing $r_c = r_{ext} - \Delta r$, with $\Delta r > 0$; that is, $r_c/r_{ext} = 1 - \Delta r/r_{ext} = 1 - \delta$ and $\delta > 0$. Then, we expand the above left-hand side *LHS* in Taylor series for small δ, so that *LHS* = $\tfrac{1}{2}\,(1 - \delta)^2\log\,(1 - \delta) - \tfrac{1}{4}\,(1 - \delta)^2\ + \tfrac{1}{4} \approx \tfrac{1}{2}\,\delta^2 = \ \tfrac{1}{2}\,(\Delta r/r_{ext})^2$. Substitution into Equation 5-2-5 and cancellation of common terms yield the cake thickness

$$\Delta r \approx \sqrt{[\{2kf_s(P_m - P_{ext})/\{\mu(1 - f_s)(1 - \phi_c)\}\}\ t]}\ > 0 \qquad\qquad (5\text{-}2\text{-}6)$$

in agreement with lineal theory. Some indication of the extent to which $\tfrac{1}{2}\,(1\text{-}\delta)^2 \log\,(1\text{-}\delta) - \tfrac{1}{4}\,(1\text{-}\delta)^2 + \tfrac{1}{4}$ can be approximated by $\tfrac{1}{2}\,\delta^2$ is found by tabulating these functions versus δ , noting that $\delta = \Delta r/r_{ext}$. This is done in Figure 5-2-3. The results show that the $\sqrt{t}$ law is satisfactory for $\Delta r/r_{ext} < 0.20$. This applies to radial and lineal mudcake buildup on resistance-free filter paper only and does *not* apply to cake buildup on formations having comparable mobilities.

$\Delta r/r_{ext}$	LHS (exact)	Lineal
.0500	.0012	.0013
.1000	.0048	.0050
.1500	.0107	.0113
.2000	.0186	.0200
.2500	.0285	.0313
.3000	.0401	.0450
.3500	.0534	.0613
.4000	.0681	.0800
.4500	.0840	.1013
.5000	.1009	.1250
.5500	.1185	.1513
.6000	.1367	.1800
.6500	.1551	.2113
.7000	.1733	.2450
.7500	.1911	.2813
.8000	.2078	.3200
.8500	.2230	.3613
.9000	.2360	.4050
.9500	.2456	.4513

Figure 5-2-3. Radial versus lineal mudcake theory.

Finally, note that a time scale of interest in drilling is the time required for cake to completely plug the well, under the assumption of static filtration. The required formula is useful in evaluating experimental muds drilled in slimholes. When the hole is plugged, we obtain $r_c = 0$. Then, substitution in Equation 5-2-5 yields the simple relationship $1/4 = \{kf_s(P_m - P_{ext})/\{\mu(1- f_s)(1 - \phi_c)r_{ext}^2\}\}$ t. The time to plug is

$$t_{plug} = \mu(1- f_s)(1 - \phi_c)\, r_{ext}^2/\{4kf_s(P_m - P_{ext})\} \qquad (5\text{-}2\text{-}7)$$

This provides an estimate of the time scale over which plugging may become important, and may be useful operationally in stuck pipe considerations. Again, Equations 5-2-5 and 5-2-7 appear as a result of exact radial flow theory.

5.3 Complex invasion problems – numerical modeling.

Here we introduce finite difference numerical methods for the solution of complicated invasion and mudcake buildup problems. We develop the basic ideas from first principles, initially for steady-state problems and then for problems with moving boundaries.   Our discussions, mathematical, numerical, and physical, are self-contained and presented in an easy-to-read manner.   Numerical analogies corresponding to the constant density flow analytical models given earlier are derived, coded in Fortran, explained and executed.   Then, computed results are given to illustrate the simulations and to demonstrate their physical correctness. These models include linear and radial incompressible flows, with and without mudcake. Prerequisites include course work in elementary calculus and undergraduate petroleum reservoir flow analysis.

5.3.1 Finite difference modeling.

Exact analytical solutions to practical engineering problems are rare, and recourse to numerical solutions is often necessary. Finite element, boundary integral (a.k.a., panel), and finite difference methods have been successfully used to solve complicated engineering problems. Recently, new finite difference technologies have been introduced to the petroleum industry. The author has applied these methods to annular borehole flow and pipeline modeling, to difficult problems in reservoir engineering, and to wave propagation problems in drillstring vibrations, MWD telemetry and swab-surge.   In this section, we extend standard finite difference techniques to problems related to cake growth and invasion – namely, physical problems involving moving boundaries.

Basic formulas.   Let us consider a differentiable function f(x) at three consecutive equidistant locations x_{i-1}, x_i, and x_{i+1}, where i-1, i, and i+1 are indexing parameters. Here, we will assume that all grids are uniformly separated by the constant grid block distance Δx. Now, it is clear from Figure 5-3-1 that the first derivative at an intermediate point A between x_{i-1} and x_i is

$$df(x_A)/dx = (x_i - x_{i-1})/\Delta x \qquad\qquad (5\text{-}3\text{-}1)$$

while the first derivative at an intermediate point B between x_i and x_{i+1} is

$$df(x_B)/dx = (x_{i+1} - x_i)/\Delta x \qquad\qquad (5\text{-}3\text{-}2)$$

Hence, the second derivative of f(x) at x_i satisfies

$$d^2f(x_i)/dx^2 = \{df(x_B)/dx - df(x_A)/dx\}/\Delta x \qquad (5\text{-}3\text{-}3)$$

or

$$d^2f(x_i)/dx^2 = \{f_{i-1} - 2f_i + f_{i+1}\}/(\Delta x)^2 + O(\Delta x)^2 \qquad (5\text{-}3\text{-}4)$$

Taylor series analysis shows that Equation 5-3-4 is second-order accurate in Δx. The $O(\Delta x)^2$ notation describes the order of the truncation error. If Δx is *small*, then $O(\Delta x)^2$ may be regarded as *very small*. Likewise, it is known that

$$df(x_i)/dx = \{f_{i+1} - f_{i-1}\}/(2\Delta x) + O(\Delta x)^2 \qquad (5\text{-}3\text{-}5)$$

is second-order accurate. Equations 5-3-4 and 5-3-5 are central difference representations for the respective quantities at x_i because they involve left and right quantities at x_{i-1} and x_{i+1}. Note that the backward difference formula

$$d^2f(x_i)/dx^2 = \{f_i - 2f_{i-1} + f_{i-2}\}/(\Delta x)^2 + O(\Delta x) \qquad (5\text{-}3\text{-}6)$$

for the second derivative is *not* incorrect. But it is not as accurate as the central difference formula, since it turns out to be first-order accurate, the error being only *somewhat small*. Similar comments apply to the forward differencing

$$d^2f(x_i)/dx^2 = \{f_i - 2f_{i+1} + f_{i+2}\}/(\Delta x)^2 + O(\Delta x) \qquad (5\text{-}3\text{-}7)$$

Alternative representations for the first derivative are the first-order accurate backward and forward difference formulas

$$df(x_i)/dx = \{f_i - f_{i-1}\}/\Delta x + O(\Delta x) \qquad (5\text{-}3\text{-}8)$$

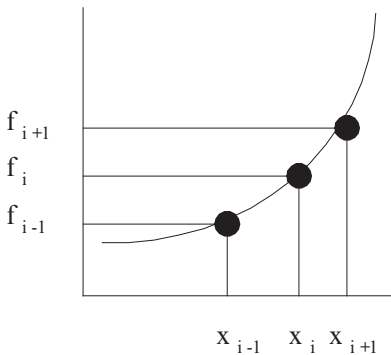$$df(x_i)/dx = \{f_{i+1} - f_i\}/\Delta x + O(\Delta x) \qquad (5\text{-}3\text{-}9)$$

Figure 5-3-1. Finite difference discretizations.

Despite their lesser accuracy, backward and forward difference formulas are often used for practical reasons. For example, they are applied at the boundaries of computational domains. At such boundaries, central difference formulas (e.g., Equations 5-3-4 and 5-3-5) require values of i that are outside the domain, and hence, undefined. Although high-order accurate backward and forward difference formulas are available, their use often forces simple matrix structures into numerical forms that are not suitable for efficient inversion.

Model constant density flow analysis. The more comprehensive treatment of filtration in Chin (2017) deals with compressibility (in addition to incompressible) effects. Here, the basic ideas behind constant density flows are modeled by numerical solutions of differential equations of the form

$$d^2p(x)/dx^2 = 0 \qquad\qquad (5\text{-}3\text{-}10)$$

whose solution $p(x) = Ax + B$ is determined by two side constraints. Suppose we supplement Equation 5-3-10 with the left and right boundary conditions

$$p(0) = P_l \qquad\qquad (5\text{-}3\text{-}11)$$

$$p(x = L) = P_r \qquad\qquad (5\text{-}3\text{-}12)$$

The steady-state pressure solution, applicable to constant density, lineal, liquid flows in a homogeneous core, is

$$p(x) = (P_r - P_l)\, x/L + P_l \qquad\qquad (5\text{-}3\text{-}13)$$

Suppose that we wish to solve Equation 5-3-10 numerically. We introduce along the x-axis the indexes $i = 1, 2, 3, ..., i_{max}\text{-}1, i_{max}$, where $i = 1$ and i_{max} correspond to the left- and right-side core ends $x = 0$ and $x = L$ (e.g., see Figure 5-3-1). With this convention, the constant width grid block size Δx used takes the value $\Delta x = L/(i_{max} - 1)$. Now, at any position x_i (or simply i), the second derivative in Equation 5-3-10 can be approximated using Equation 5-3-4, that is,

$$d^2p(x_i)/dx^2 = \{p_{i\text{-}1} - 2p_i + p_{i+1}\}/(\Delta x)^2 + O(\Delta x)^2 = 0 \quad (5\text{-}3\text{-}14)$$

so that the finite difference model for our differential equation becomes

$$p_{i\text{-}1} - 2p_i + p_{i+1} = 0 \qquad\qquad (5\text{-}3\text{-}15)$$

The pressures p_1, p_2, ..., and p_{imax} at the nodes $i = 1, 2, ...,$ and i_{max} are determined by writing Equation 5-3-15 for each internal node $i = 2, 3, ...,$ and $i_{max\text{-}1}$. This yields $i_{max} - 2$ linear algebraic equations, two

short of the number of unknowns i_{max}. The two additional required equations are obtained from boundary conditions, in this case, Equations 5-3-11 and 5-3-12; in particular, we write $p(0) = P_l$ and $p(L) = P_r$ in the form $p_1 = P_l$ and $p_{imax} = P_r$. To illustrate this, consider the simple case of five nodes (that is, four grid blocks), taking $i_{max} = 5$ and with the grid size $\Delta x = L/(i_{max} - 1) = L/4$. We therefore have

$$
\begin{array}{llll}
 & p_1 & = P_l & \text{(5-3-16a,b,c,d,e)} \\
i = 2: & p_1 - 2p_2 + p_3 & = 0 & \\
i = 3: & p_2 - 2p_3 + p_4 & = 0 & \\
i = 4: & p_3 - 2p_4 + p_5 & = 0 & \\
 & p_5 & = P_r & \\
\end{array}
$$

Equations 5-3-16a,b,c,d,e constitute five equations in five unknowns and easily yield to solution, using standard (but tedious) determinant or Gaussian elimination methods from elementary algebra. We could stop here, but we take the solution of Equation 5-3-16 one step further in order to develop efficient solution techniques. The simplicity seen here suggests that we can rewrite the system shown in Equations 5-3-16a,b,c,d,e in the matrix or linear algebra form

$$
\begin{vmatrix}
1 & 0 & & & \\
1 & -2 & 1 & & \\
 & 1 & -2 & 1 & \\
 & & 1 & -2 & 1 \\
 & & & 0 & 1 \\
\end{vmatrix}
\begin{vmatrix}
p_1 \\ p_2 \\ p_3 \\ p_4 \\ p_5
\end{vmatrix}
=
\begin{vmatrix}
P_l \\ 0 \\ 0 \\ 0 \\ P_r
\end{vmatrix}
\qquad \text{(5-3-17)}
$$

The left-side coefficient matrix multiplying the unknown vector **p** is said to be banded because its elements fall within diagonal bands. The product shown equals the nonzero right side in Equation 5-3-17, which contains the "delta-p" pressure drop $(P_l - P_r)$ that drives the Darcy flow. This delta-p, applied across the entire core, mathematically manifests itself by controlling the top and bottom rows of the governing tridiagonal matrix equation.

It is also interesting to note that our use of central differences physically implies that the pressure at each and every point depends on its left and right neighbors, so that coupled equations necessarily appear. This is not true in certain supersonic flow problems in high-speed

aerodynamics, governed by hyberbolic PDEs, where the time-like properties of some space variables may in fact require the use of backward differences! Also observe that the coefficient matrix in Equation 5-3-17 is sparse (or empty), with each equation containing at most three unknowns. If each equation had approached i_{max} number of unknowns, the coefficient matrix would have been said to be full. Furthermore, note that our banded matrix possesses a simple tridiagonal (or three-diagonal) structure that is amenable to rapid solution. We will not review tridiagonal solvers here. They are standard in linear algebra, and we simply note that Equation 5-3-17 represents a special instance of

$$
\begin{vmatrix}
B_1 & C_1 & & & \\
A_2 & B_2 & C_2 & & \\
& A_3 & B_3 & C_3 & \\
& & .... & & \\
& & & & \\
& A_{imax-1} & B_{imax-1} & C_{imax-1} & \\
& & A_{imax} & B_{imax} &
\end{vmatrix}
\begin{vmatrix}
V_1 \\
V_2 \\
V_3 \\
.. \\
\\
V_{imax-1} \\
V_{imax}
\end{vmatrix}
=
\begin{vmatrix}
W_1 \\
W_2 \\
W_3 \\
... \\
\\
W_{imax-1} \\
W_{imax}
\end{vmatrix}
\qquad (5\text{-}3\text{-}18)
$$

for the unknown vector $\mathbf{V}$ which, when programmed in the Fortran language, is easily solved by a call to the subroutine TRIDI in Figure 5-3-2.

```
      SUBROUTINE TRIDI(A,B,C,V,W,N)
      DIMENSION A(1000), B(1000), C(1000), V(1000), W(1000)
      A(N) = A(N)/B(N)
      W(N) = W(N)/B(N)
      DO 100  I = 2,N
      II = -I+N+2
      BN = 1./(B(II-1)-A(II)*C(II-1))
      A(II-1) = A(II-1)*BN
      W(II-1) = (W(II-1)-C(II-1)*W(II))*BN
100   CONTINUE
      V(1) = W(1)
      DO 200  I = 2,N
      V(I) = W(I)-A(I)*V(I-1)
200   CONTINUE
      RETURN
      END
```

Figure 5-3-2. Tridiagonal equation solver.

Thus, once the coefficient matrixes $\mathbf{A}$, $\mathbf{B}$, $\mathbf{C}$, and $\mathbf{W}$ are defined in the main body of the computer program, with $B_1 = 1$, $C_1 = 0$, $W_1 = P_l$; $A_2 = A_3 = A_4 = 1$, $B_2 = B_3 = B_4 = -2$, $C_2 = C_3 = C_4 = 1$, $W_2 = W_3 = W_4 = 0$; and, finally, $A_5 = 0$, $B_5 = 1$, $W_5 = P_r$, the statement CALL TRIDI(A,B,C,P,W,5) will solve and store the pressure solution in the

elements of **P**.   For machine purposes, we will typically initialize
memory using the dummies A(1) = 99 and C(IMAX) = 99, noting that
these values do not affect the solution.   In general, the internal
coefficients are easily defined using the code fragment,

```
     DO 200   I=2,IMAXM1
     A(I)  =   1.
     B(I)  =  -2.
     C(I)  =   1.
     W(I)  =   0.
200  CONTINUE
```

which is followed by the subroutine call to the tridiagonal matrix solver
(in our Fortran, IMAXM1 denotes IMAX-1).   In this chapter, we will
study how the engine in the above Fortran will change from problem to
problem.   For $d^2p(x)/dx^2 = 0$, the exact linear pressure variation will
always be obtained for any choice of grid number; unfortunately, this is
not so with more complicated equations and formulations.   The reader
who is not familiar with Fortran should program, execute, and
understand this simple example.

5.3.2 Invasion and mudcake growth examples.

5.3.2.1 Lineal liquid displacement *without* mudcake.

We have shown how $d^2p(x)/dx^2 = 0$ is easily solved.   We now
return to an early example for the piston-like Darcy displacement of two
constant density *liquids* with different viscosities in a homogeneous
lineal core of given permeability k.   The transient displacement depends
on the relative proportions of fluid initially present and on which
portions of the core (i.e., upstream or downstream) they occupy.   Now
$d^2p(x)/dx^2 = 0$ applies to constant density liquids, but parametric time
dependence in the solution is permissible.   In this problem, since two
liquids are present, two such equations are needed,

$$d^2p_i(x)/dx^2 = 0, \, i = 1, 2 \qquad\qquad (5\text{-}3\text{-}19)$$

for the first (left) and second (right) sections.   For numerical purposes, it
is convenient to define an unknown, upper-case solution vector P(x) by

$$P(x) = p_1(x), \, \, 0 < x < x_f \qquad\qquad (5\text{-}3\text{-}20)$$
$$= p_2(x), \, \, x_f < x < L$$

where $x = x_f(t)$ represents the position of the unsteady moving front. The boundary value problem for $d^2P(x)/dx^2 = 0$ satisfies the left- and right-side pressure boundary conditions

$$p_1(0) = P_l \tag{5-3-21a}$$

$$p_2(L) = P_r \tag{5-3-21b}$$

which are easily programmed as demonstrated earlier. Now, the difference equation corresponding to $d^2P(x)/dx^2 = 0$ at $x = x_f$ does not apply, since the differential equation description of motion breaks down at the boundary separating two distinct fluids where pressure gradients need not be continuous. We therefore replace that equation with an alternative statement that encompasses the requirements posed by the interfacial matching conditions

$$p_1(x_f) = p_2(x_f) \tag{5-3-22a}$$

$$q_1(x_f) = q_2(x_f) \tag{5-3-22b}$$

This can be done in any number of ways, but the best choice is a technique that can be carried over to transient compressible flows without modification and that allows us to retain the diagonally dominant features of the time-marching scheme derived earlier. The final result is easily derived.

First, Equation 5-3-22b requires $-(k_1/\mu_1)\, dp_1(x_f)/dx = -(k_2/\mu_2)\, dp_2(x_f)/dx$ as a consequence of Darcy's law $q = -(k/\mu)\, dp(x)/dx$. But since $k_1 = k_2$, this statement simplifies to $(1/\mu_1)\, dp_1(x_f)/dx = (1/\mu_2)\, dp_2(x_f)/dx$. Now, we will denote by $if\text{-}$ and $if\text{+}$ the spatial locations infinitesimally close to the left and to the right of the front $x = x_f$, which is itself indexed by $i = if$. (Note that this index satisfies $if = x_f/\Delta x + 1$ in our nodal convention.) Then, in Section 1, we can approximate the pressure gradient $dp_1(x_f)/dx$ using backward differences, while in Section 2, we can apply forward differences (again, differentiation through the interface itself is forbidden since the pressure gradient changes suddenly). This leads to $(1/\mu_1)(p_{if\text{-}} - p_{if\text{-}1})/\Delta x = (1/\mu_2)(p_{if+1} - p_{if+})/\Delta x$, but since Δx cancels, $(1/\mu_1)(p_{if\text{-}} - p_{if\text{-}1}) = (1/\mu_2)(p_{if+1} - p_{if+})$. Assuming that surface tension is unimportant, Equation 5-3-28a,

which calls for pressure continuity, requires that $p_{if-} = p_{if+}$ or simply p_{if}. Thus, at the interface,

$$(1/\mu_1) \, p_{if-1} - (1/\mu_1 + 1/\mu_2)p_{if} + (1/\mu_2) \, p_{if+1} = 0 \qquad (5\text{-}3\text{-}23)$$

applies. However, unlike the difference approximation to the differential equation, which is second-order accurate, our use of backward and forward differences in deriving Equation 5-3-23 renders it only $O(\Delta x)$ accurate. In deriving Equation 5-3-23, we emphasize that we have used the same mesh size to the left and to the right of the front. This is physically permissible if the two viscosities are comparable, but clearly incorrect if they are not; later, in modeling mudcake flows, we will find that significant mobility contrasts existing in the problem demand dual mesh systems.

It is interesting, however, to observe that we can rewrite Equation 5-3-29 as $p_{if-1} - (1 + \mu_1/\mu_2)p_{if} + (\mu_1/\mu_2) \, p_{if+1} = 0$. In the single-fluid problem where $\mu_1 = \mu_2$, this matching condition reduces to $p_{if-1} - 2p_{if} + p_{if+1} = 0$, which is identical to Equation 5-3-15 for the exact differential equation. This fortuitous situation does not apply to compressible transient flows or radial flows. This completes our discussion for the solution of Equations 5-3-19 to 5-3-22 for the spatial pressure distribution, which assumes that the front location x_f is prescribed. But the front *does* move with time, and our formulation needs to accommodate this fact. The physical problem is an initial value problem, a transient formulation in which an interface, initially located at $x = x_{f,o}$ moves with time – even though Equation 5-3-19 governing time-dependent pressure does not contain time derivatives!

We can solve this unsteady problem by first producing the pressure distribution as just outlined, then updating the front location $x = x_f$, and subsequently, repeating this process recursively, as required. The update formula is obtained from the kinematic requirement that

$$dx_f/dt = u/\phi = - (k/\mu_1 \phi) \, dp_1/dx$$
$$= - (k/\mu_1 \phi)(p_{if} - p_{if-1})/\Delta x \qquad (5\text{-}3\text{-}24)$$

in Section 1. This kinematic statement, formally derived previously, was used in the analytical invasion modeling leading to our closed form solution. If we evaluate the right side of Equation 5-3-24 with the

pressure solution just obtained, denoting existing solutions for p and x_f as *old*, then the *new* x_f is obtained by approximating Equation 5-3-24 as

$$(x_{f,new} - x_{f,old})/\Delta t = - (k/\mu_1\phi)(p_{if} - p_{if-1})_{old}/\Delta x \qquad (5\text{-}3\text{-}25)$$

or

$$x_{f,new} = x_{f,old} - \{k\Delta t/(\mu_1\phi\Delta x)\}(p_{if} - p_{if-1})_{old} \qquad (5\text{-}3\text{-}26)$$

With this new front position available, we again solve for the pressure, followed by a front update, and so on. In Figure 5-3-3a, the Fortran listing showing the structural components of the recursive algorithm is given. The front matching conditions and position updating logic are shown in bold print. Details related to dimension statements, interactive input queries, print statements, and so on, are omitted for brevity. Only those salient features that relate to the algorithm are replicated. Note that the Fortran statement IFRONT = XFRONT/DX +1, because IFRONT is a Fortran *integer* variable, will discard the fractional part of the right-side division. This means that the algorithm will not move IFRONT from one time step to the next unless it has advanced sufficiently. In this sense, the scheme is not truly boundary conforming; however, it is easily modified at the expense of programming complexity. Small meshes, in general, should be used in modeling invasion front motions.

```
.
C      INITIAL SETUP
       IMAX = XCORE/DX +1
       IMAXM1 = IMAX-1
       IFRONT = XFRONT/DX +1
       .
       N = 0
       T = 0.
       NSTOP = 0
       MINDEX = 1
       TIME(1) = 0.
       XPLOT(1) = XFRONT
C
C      START TIME INTEGRATION
       DO 300  N=1,NMAX
       T = T+DT
       DO 200  I=2,IMAXM1
       A(I)  =   1.
       B(I)  =  -2.
       C(I)  =   1.
       W(I)  =   0.
 200   CONTINUE
       A(1)  = 99.
       B(1)  = 1.
       C(1)  = 0.
       W(1)  = PLEFT
```

Figure 5-3-3a. Fortran source code (5.3.2.1).

```
     A(IMAX) = 0.
     B(IMAX) = 1.
     C(IMAX) = 99.
     W(IMAX) = PRIGHT
     IF(VISCIN.EQ.VISCDP) GO TO 240
     A(IFRONT) =  1./VISCL
     B(IFRONT) = -1./VISCL -1./VISCR
     C(IFRONT) =  1./VISCR
     W(IFRONT) =  0.
240  CALL TRIDI(A,B,C,VECTOR,W,IMAX)
     DO 250  I=1,IMAX
     P(I) = VECTOR(I)
250  CONTINUE
     PGRAD = (P(IFRONT)-P(IFRONT-1))/DX
     XFRONT = XFRONT - (K*DT/(PHI*VISCL))*PGRAD
     IFRONT = XFRONT/DX +1
     IF(XFRONT.GE.XMAX.OR.XFRONT.LE.XMIN) NSTOP=1
     .
     .
     WRITE(*,280) N,T,XFRONT,IFRONT
280  FORMAT(1X,'T(',I4,')= ',E8.3,' sec, Xf= ',E8.3,' ft, I= ',I3)
     MINDEX = MINDEX+1
     TIME(MINDEX) = T
     XPLOT(MINDEX) = XFRONT
300  CONTINUE
400  WRITE(*,10)
     CALL GRFIX(XPLOT,TIME,MINDEX)
     STOP
     END
```

Figure 5-3-3a. Continued.

```
INPUT PARAMETER SUMMARY:
Rock core permeability (darcies): .100E+00
Rock core porosity (decimal nbr): .200E+00
Viscosity of invading fluid (cp): .100E+02
Viscosity, displaced  fluid (cp): .100E+01
Pressure at left boundary  (psi): .100E+03
Pressure at right boundary (psi): .000E+00
Length of rock core sample  (ft): .100E+01
Initial "xfront" position (feet): .500E+00
Integration space step size (ft): .200E-02
Integration time step size (sec): .100E+01
Maximum allowed  number of steps: .200E+04
```

```
Time (sec)  Position (ft)
 .000E+00    .500E+00          |              *
 .600E+02    .539E+00          |               *
 .120E+03    .576E+00          |                *
 .180E+03    .611E+00          |                 *
 .240E+03    .644E+00          |                  *
 .300E+03    .676E+00          |                   *
 .360E+03    .706E+00          |                   *
 .420E+03    .736E+00          |                    *
 .480E+03    .764E+00          |                     *
 .540E+03    .792E+00          |                     *
 .600E+03    .818E+00          |                      *
 .660E+03    .844E+00          |                       *
 .720E+03    .870E+00          |                       *
 .780E+03    .895E+00          |                        *
 .840E+03    .919E+00          |                        *
 .900E+03    .942E+00          |                         *
 .960E+03    .965E+00          |                          *
 .102E+04    .988E+00          |                           *
```

Figure 5-3-3b. Numerical results (5.3.2.1).

```
     INPUT PARAMETER SUMMARY:
     Rock core permeability (darcies): .100E+00
     Rock core porosity (decimal nbr): .200E+00
     Viscosity of invading fluid (cp): .100E+01
     Viscosity, displaced  fluid (cp): .100E+02
     Pressure at left boundary  (psi): .100E+03
     Pressure at right boundary (psi): .000E+00
     Length of rock core sample  (ft): .100E+01
     Initial "xfront" position (feet): .500E+00
     Integration space step size (ft): .200E-02
     Integration time step size (sec): .100E+01
     Maximum allowed  number of steps: .200E+04

  Time (sec)  Position (ft)
                               _____
   .000E+00    .500E+00     |                      *
   .600E+02    .542E+00     |                        *
   .120E+03    .586E+00     |                          *
   .180E+03    .635E+00     |                            *
   .240E+03    .690E+00     |                              *
   .300E+03    .753E+00     |                                 *
   .360E+03    .830E+00     |                                    *
   .420E+03    .938E+00     |                                        *
```

Figure 5-3-3c. Numerical results (5.3.2.1).

We will consider *two* computational limits that demonstrate the physics of piston-like fluid displacement, as well as the correctness of the program.   For the first example, consider the simulation input and solution in Figure 5-3-3b. Note the high viscosity of the invading fluid relative to that of the displaced fluid. The plot and tabulated results correctly show that the front *decelerates* with time. This is so because fluid of increased viscosity displaces and replaces fluid having lower viscosity, with the relative proportion of the former increasing with time, as the low viscosity fluid is forced out the right side of the core. Hence, continual slowdown is anticipated and is indeed obtained. In our second example, we reverse the role of the two fluids and allow a less viscous fluid to displace one having much higher viscosity. As the latter is forced through the core and emptied, fluid having lower viscosity replaces it, so that it naturally *accelerates* through the core. Again, our computed results are physically correct; also note the differences in the time scales of the two problems.

It is clear that our calculations produce results that make physical sense. Of course, in the present problem where an analytical solution is available, there is no need to resort to numerical methods.   But the solution is useful because it allows us to study the effects of grid selection, that is, the role of Δx and Δt in affecting computed solutions. We emphasize that the above calculations provide the *time scales* characteristic of the displacement flows. Both fronts start at the midpoint of the core, and both simulations terminate near the end of the core.

Their total transit times are obviously different. These time scales, as our earlier closed-form solution

$$(\mu_1/\mu_2 - 1)x_f + L = +\{\{(\mu_1/\mu_2 - 1)x_{f,o} + L\}^2$$
$$+ \{2k\,(P_l - P_r)/(\phi\mu_2)\}(\mu_1/\mu_2 - 1)\,t\}^{1/2} \qquad (5\text{-}1\text{-}6)$$

shows, depend on numerous parameters, combined in well-defined groups. For example, both $(\mu_1/\mu_2 - 1)$ and $2k\,(P_l - P_r)t/(\phi\mu_2)$ are individually important.

The power of well-formulated numerical models lies, of course, in their potential for simple extension. For example, if the left- and right-side boundary pressures PLEFT and PRIGHT are to be prescribed functions of time, these constants are easily replaced by Fortran function statements. Likewise, time dependences in the left side invading fluid viscosity VISCL are readily incorporated. These generalizations are not unusual to actual drilling situations. Changes in mud weight, which alter borehole pressure, are used for formation control; these changes are effected by varying both solids and viscosifier content. Finally, some notes on the computational efficiency of the scheme are in order. Using standard Windows computers, 1,000 time steps requires approximately two seconds for a 500 grid block problem, all the time printing intermediate solutions to the screen. (This is the slowest part of the process and can be omitted for increased speed). The compiled code, dimensioned for a maximum of 1,000 grid blocks, requires 40,000 bytes of RAM memory.   By contrast, canned finite element simulators designed to solve general 3D problems, by contrast, can require orders-of-magnitude more computing times for the same number of steps.

5.3.2.2 Cylindrical radial liquid displacement *without* cake.

We now rework the preceding problem and alter the formulation so that it handles cylindrical radial flows. Thus, we replace Equation 5-3-10 (that is, $d^2p(x)/dx^2 = 0$) by Laplace's equation in cylindrical radial flows,

$$d^2p(r)/dr^2 + (1/r)\,dp(r)/dr = 0 \qquad (5\text{-}3\text{-}27)$$

The required changes are minor. Using Equation 5-3-14, we find that a simple change of notation gives $d^2p(r_i)/dr^2 = \{p_{i-1} - 2p_i + p_{i+1}\}/(\Delta r)^2 + O(\Delta r)^2$. Similarly, from Equation 5-3-5, $dp(r_i)/dr = \{p_{i+1} - p_{i-1}\}/(2\Delta r) + O(\Delta r)^2$. We will define the radial variable r by $r = R_{well} + (i-1)\Delta r$ so that $i = 1$ corresponds to the left boundary of the computational

grid. Then, substitution in Equation 5-3-27 and minor rearrangement lead to

$$[1 - \tfrac{1}{2}\Delta r/\{R_{well} + (i\text{-}1)\Delta r\}] \; p_{i\text{-}1} - 2 \; p_i$$
$$+ \; [1 + \tfrac{1}{2}\Delta r/\{R_{well} + (i\text{-}1)\Delta r\}] \; p_{i+1} = 0 \qquad (5\text{-}3\text{-}28)$$

Recall that the matrix coefficients **A**, **B**, **C**, and **W** of the finite difference equation for the lineal flow model $d^2p(x)/dx^2 = 0$, extracted from the simple formula [1] $p_{i\text{-}1}$ - 2 p_i + [1] $p_{i+1} = 0$, were defined by the code fragment

```
    DO 200  I=2,IMAXM1
    A(I) =  1.
    B(I) = -2.
    C(I) =  1.
    W(I) =  0.
200 CONTINUE
```

Comparison with Equation 5-3-28 shows that the only required change needed to model fully radial flow effects is a correction $\pm\tfrac{1}{2}\Delta r/\{R_{well} + (i\text{-}1)\Delta r\}$ to the **C** and **A** matrix coefficients. That is, we replace the preceding code with

```
    DO 200  I=2,IMAXM1
    CORRECT = 0.5*DX/(WELRAD + (I-1)*DX)
    A(I) =  1. - CORRECT
    B(I) = -2.
    C(I) =  1. + CORRECT
    W(I) =  0.
200 CONTINUE
```

Of course, there will be additional input and output nomenclature changes, calling for wellbore and farfield radii, starting front radii, and so on. For readability, we have retained DX to represent the radial mesh length Δr, in order to limit the number of typographical changes; WELRAD represents the wellbore radius. The Fortran source code for this example, appearing in Figure 5-3-4a, uses the same front matching logic as does lineal flows.

We will consider *two* computational limits that demonstrate the physics of radial displacement flows, as well as the correctness of the computer program. For the first example, we assume simulation input parameters that are identical to those of the first run in 5.3.2.1, plus wellbore and farfield radii of 100 ft and 101 ft, so that the net radial extent of 1 ft equals the core length of the previous example. This large radius allows the program to mimic purely lineal flows; we will compare the computed results with those obtained for exact lineal flow. For such

large radii, the effect of the radial terms should be insignificant. If so, then the computed radial front positions should be identical to those in Figure 5-3-3c. The two-decimal-place bold numbers in Figure 5-3-4b, when compared to their three-decimal place counterparts in Figure 5-3-3c, demonstrate that exactly the same water-to-oil displacement results are obtained as we expected. This provides a useful computing and programming check.

```
C     INITIAL SETUP
      IMAX = (XCORE-WELRAD)/DX +1
      IMAXM1 = IMAX-1
      IFRONT = (XFRONT-WELRAD)/DX +1
      .
      N = 0
      T = 0.
      NSTOP = 0
      MINDEX=1
      TIME(1) = 0.
      XPLOT(1) = XFRONT
C
C     START TIME INTEGRATION
      DO 300  N=1,NMAX
      T = T+DT
      DO 200  I=2,IMAXM1
      CORRECT = 0.5*DX/(WELRAD + (I-1)*DX)
      A(I) =  1. - CORRECT
      B(I) = -2.
      C(I) =  1. + CORRECT
      W(I) =  0.
 200  CONTINUE
      A(1) = 99.
      B(1) = 1.
      C(1) = 0.
      W(1) = PLEFT
```

Figure 5-3-4a. Fortran source code (5.3.2.2).

```
      A(IMAX) = 0.
      B(IMAX) = 1.
      C(IMAX) = 99.
      W(IMAX) = PRIGHT
      IF(VISCIN.EQ.VISCDP) GO TO 240
      A(IFRONT) =  1./VISCL
      B(IFRONT) = -1./VISCL -1./VISCR
      C(IFRONT) =  1./VISCR
      W(IFRONT) =  0.
240   CALL TRIDI(A,B,C,VECTOR,W,IMAX)
      DO 250  I=1,IMAX
      P(I) = VECTOR(I)
250   CONTINUE
      PGRAD = (P(IFRONT)-P(IFRONT-1))/DX
      XFRONT = XFRONT - (K*DT/(PHI*VISCL))*PGRAD
      IFRONT = (XFRONT-WELRAD)/DX +1
      .
      WRITE(*,280) N,T,XFRONT,IFRONT
280   FORMAT(1X,'T(',I4,')= ',E8.3,' sec, Rf= ',E10.5,' ft,I= ',I3)
      MINDEX = MINDEX+1
      TIME(MINDEX) = T
      XPLOT(MINDEX) = XFRONT
300   CONTINUE
400   WRITE(*,10)
      CALL GRFIX(XPLOT,TIME,MINDEX)
      STOP
      END
```

Figure 5-3-4a. Continued.

```
INPUT PARAMETER SUMMARY:
Rock core permeability (darcies): .100E+00
Rock core porosity (decimal nbr): .200E+00
Viscosity of invading fluid (cp): .100E+01
Viscosity, displaced  fluid (cp): .100E+02
Pressure at well boundary  (psi): .100E+03
Pressure, effective radius  (psi): .000E+00
Radius of  the  bore  hole  (ft): .100E+03
Reservoir effective radius  (ft): .101E+03
Initial "Rfront" position (feet): .101E+03 (i.e., 100.5)
Integration space step size (ft): .200E-02
Integration time step size (sec): .100E+01
Maximum allowed  number of steps: .200E+04
Number spatial DR grids selected: .500E+03

COMPUTED RESULTS:
T(  0)= .000E+00 sec, Rf= .10050E+03 ft, I= 250
T( 60)= .600E+02 sec, Rf= .10054E+03 ft, I= 271
T(120)= .120E+03 sec, Rf= .10059E+03 ft, I= 294
T(180)= .180E+03 sec, Rf= .10064E+03 ft, I= 318
T(240)= .240E+03 sec, Rf= .10069E+03 ft, I= 346
T(300)= .300E+03 sec, Rf= .10075E+03 ft, I= 377
T(360)= .360E+03 sec, Rf= .10083E+03 ft, I= 416
T(420)= .420E+03 sec, Rf= .10094E+03 ft, I= 470
```

Figure 5-3-4b. Numerical results (5.3.2.2).

```
    INPUT PARAMETER SUMMARY:
    Rock core permeability (darcies): .100E+00
    Rock core porosity (decimal nbr): .200E+00
    Viscosity of invading fluid (cp): .100E+01
    Viscosity, displaced  fluid (cp): .100E+02
    Pressure at well boundary  (psi): .100E+03
    Pressure, effective radius (psi): .000E+00
    Radius  of  the  bore  hole (ft): .100E+00
    Reservoir effective radius  (ft): .110E+01
    Initial "Rfront" position (feet): .600E+00
    Integration space step size (ft): .200E-02
    Integration time step size (sec): .100E+01
    Maximum allowed  number of steps: .200E+04
    Number spatial DR grids selected: .500E+03


 Time (sec)  Position (ft)

                              _____
   .000E+00    .600E+00    |                    *
   .600E+02    .647E+00    |                   *
   .120E+03    .695E+00    |                      *
   .180E+03    .745E+00    |                       *
   .240E+03    .796E+00    |                         *
   .300E+03    .849E+00    |                          *
   .360E+03    .906E+00    |                            *
   .420E+03    .967E+00    |                              *
   .480E+03    .104E+01    |                                *
```

Figure 5-3-4c. Numerical results (5.3.2.2).

Next, we consider a physical situation where the geometric effects of radial spreading must be important, and accordingly we select a small slimhole radius of 0.1 ft and a farfield radius of 1.1 ft. These choices therefore fix the length of the core to one foot. Again, we initialize our front position to the center of the core sample. Computed results demonstrate important geometric effects. From t = 360 to 420 sec, the radial front has advanced from r = 0.906 ft to 0.967 ft, for a total extent of 0.061 ft. If we refer to Figure 5-3-3c for the lineal result, in the same time period, the front has advanced from x = 0.830 ft to 0.938 ft, for a total of 0.108 ft. The decrease in distance obtained in the radial case is clearly the result of geometric spreading, and the twofold change indicates that such effects can be significant for small-diameter holes. These changes are all-important to resistivity interpretation and modeling.

5.3.2.3 Spherical radial liquid displacement *without* cake.

Now let us rework the preceding cylindrical radial problem, and alter the analytical and numerical formulations so that they handle spherical radial flows. Such formulations model invasion at the drillbit and also point fluid influx into formation testers at small times. We will replace the governing equation for cylindrical radial flows, namely,

$d^2p(r)/dr^2 + (1/r) \, dp(r)/dr = 0$ in Equation 5-3-27, by the spherical flow equation

$$d^2p(r)/dr^2 + (2/r) \, dp(r)/dr = 0 \qquad (5\text{-}3\text{-}29)$$

Again, we are restricted to constant density flows in homogeneous rocks. The required changes are minor, since we have merely substituted a "2/r" variable coefficient in favor of 1/r. Instead of Equation 5-3-28, we have

$$[1 - \Delta r/\{R_{well} + (i\text{-}1)\Delta r\}] \, p_{i\text{-}1} - 2 \, p_i$$

$$+ \, [1 + \Delta r/\{R_{well} + (i\text{-}1)\Delta r\}] \, p_{i+1} = 0 \qquad (5\text{-}3\text{-}30)$$

The code fragment

```
      DO 200  I=2,IMAXM1
      CORRECT = 0.5*DX/(WELRAD + (I-1)*DX)
      A(I) =  1. - CORRECT
      B(I) = -2.
      C(I) =  1. + CORRECT
      W(I) =  0.
200   CONTINUE
```

appearing in the cylindrical radial program requires only a one-line change in order to implement Equation 5-3-30, so that instead we have

```
      DO 200  I=2,IMAXM1
      CORRECT = DX/(WELRAD + (I-1)*DX)
      A(I) =  1. - CORRECT
      B(I) = -2.
      C(I) =  1. + CORRECT
      W(I) =  0.
200   CONTINUE
```

As before, there are obvious input and output nomenclature changes, calling for bit and farfield radii, starting front radii and so on. (Again, for readability, we have retained DX to represent the radial mesh length Δr.) The source code is similar to that in Figure 5-3-4a, except for the single line change just described.   In order to demonstrate the differences between cylindrical and spherical radial flows, we have assumed parameters identical to those in the second run of 5.3.2.2. At t = 480 sec, the *cylindrical* radial position is 1.04 ft, whereas at the same instant, the spherical radial position is 0.852 ft, which is significantly less. As the calculated results in Figures 5-3-5a and 5-3-5b show, the spherical front requires more time to reach the farfield boundary defined by the effective radius r = 1.1 ft. Its acceleration is less than that in the previous example as a result of increased geometric spreading.

```
INPUT PARAMETER SUMMARY:
Rock core permeability (darcies): .100E+00
Rock core porosity (decimal nbr): .200E+00
Viscosity of invading fluid (cp): .100E+01
Viscosity, displaced  fluid (cp): .100E+02
Pressure at "bit" boundary (psi): .100E+03
Pressure, effective radius (psi): .000E+00
Radius  at  the  drill  bit (ft): .100E+00
Reservoir effective radius  (ft): .110E+01
Initial "Rfront" position (feet): .600E+00
Integration space step size (ft): .200E-02
Integration time step size (sec): .100E+01
Maximum allowed  number of steps: .200E+04
Number spatial DR grids selected: .500E+03
```

Figure 5-3-5a. Numerical results (5.3.2.3).

```
Time (sec)   Position (ft)

.000E+00    .600E+00    |                     *
.600E+02    .637E+00    |                      *
.120E+03    .673E+00    |                       *
.180E+03    .706E+00    |                        *
.240E+03    .738E+00    |                         *
.300E+03    .768E+00    |                          *
.360E+03    .797E+00    |                           *
.420E+03    .825E+00    |                            *
.480E+03    .852E+00    |                             *
.540E+03    .878E+00    |                              *
.600E+03    .904E+00    |                               *
.660E+03    .928E+00    |                                *
.720E+03    .952E+00    |                                 *
.780E+03    .975E+00    |                                  *
.840E+03    .998E+00    |                                   *
.900E+03    .102E+01    |                                    *
.960E+03    .104E+01    |                                     *
.102E+04    .106E+01    |                                      *
.108E+04    .108E+01    |                                       *
```
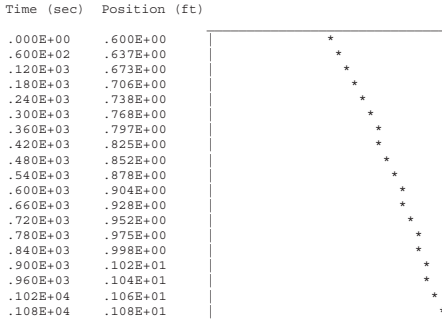
Figure 5-3-5b. Numerical results (5.3.2.3).

5.3.2.4 Simultaneous mudcake buildup and displacement front motion for incompressible liquid flows.

In this last exercise, we reconsider the problem of dynamically coupled invasion front motion and mudcake growth in lineal flow; this was studied analytically earlier when it was solved in closed form, but we will approach its solution numerically. This is pursued for several reasons. First, we wish to demonstrate how problems with moving boundaries and disparate space *scales* (characterizing mudcake and rock) are formulated and solved with finite differences. Second, computational methods are ultimately needed because they are more convenient when cake compaction, time-dependent applied pressures, and formation heterogeneities are required. Because the present problem can be described analytically, we at least possess a tool with which to evaluate the quality of more approximate solution methods. In the foregoing examples, we emphasized how the effects of transients due to fluid compressibility, and the nonlinear effects of gas displacement by liquids, can be numerically modeled. For the present, we return to simple

incompressible flows of liquids to illustrate the main ideas, so that we need not address the complicating, but nonetheless straightforward, effects. Here, we have instead two moving boundaries: the displacement front within the rock and the surface of the mudcake, which moves in such a way as to increase cake thickness with time. Thus, analytical and computational changes to our schemes are required. In addition, as we have noted, disparate space scales enter the numerical formulation in a subtle way: mudcakes are thin relative to the distance that the filtrate penetrates the formation. The problem domain appears in Figure 5-3-6a.
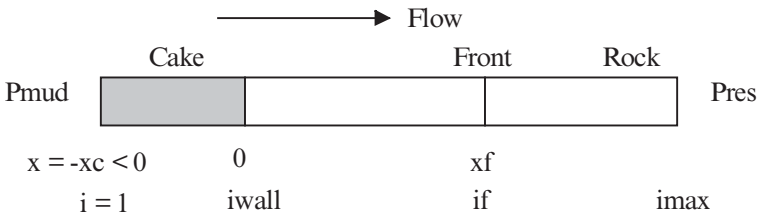
Figure 5-3-6a. Three-layer lineal flow problem.

For simplicity, we assume that in the cake and rock, the permeabilities k_c and k_r are constant, although they can be different constants. Therefore, whether we start with $d(k_c \, dp/dx)/dx = 0$ or $d(k_r \, dp/dx)/dx = 0$, the permeabilities factor out, leaving

$$d^2p(x)/dx^2 = 0 \qquad\qquad (5\text{-}3\text{-}10)$$

in either case. Now, we can approximate Equation 5-3-10 with the central difference formula used earlier, namely,

$$d^2p(x_i)/dx^2 = \{p_{i-1} - 2p_i + p_{i+1}\}/(\Delta x)^2 + O(\Delta x)^2 = 0 \quad (5\text{-}3\text{-}14)$$

Our combined mudcake-growth and displacement-front-movement problem, with its clearly disparate length scales, is not unlike boundary layer or shock layer type flows in classical fluid mechanics. That is, the cake is extremely thin, while the scale of the front motion is orders of magnitude larger: any attempt to characterize both flows using the same physical measures of length is likely to result in inaccuracy. Therefore, we would like to select Δx, as usual, for the rock, but Δx_c for the mudcake, with $\Delta x_c \ll \Delta x$. Fortunately, this does not lead to numerical complexity, since the grid length completely drops out when applying Equation 5-3-14 to Equation 5-3-10. (This is not the case with radial flows, or transient compressible flows, where minor changes are needed.)

Thus, Equation 5-3-15, which we have reproduced as follows, applies throughout the entire domain of flow in the general case where we have both different permeabilities and grid sizes.

$$p_{i-1} - 2p_i + p_{i+1} = 0 \qquad\qquad (5\text{-}3\text{-}15)$$

This does not mean that changes won't be needed; they are needed, and they will be discussed shortly. But for now, the pressures p_1, p_2, ..., and p_{imax} at the nodes $i = 1, 2, ...,$ and i_{max} are determined as in our earlier examples by writing Equation 5-3-15 for each of the *internal nodes* $i = 2$, 3, ..., and i_{max-1} (with two notable exceptions, to be discussed). This yields $i_{max} -2$ number of linear equations, two short of the number of unknowns i_{max}. The two additional required equations are obtained from boundary conditions; in this case,

$$p(-x_c) = P_{mud}, \; x_c > 0 \qquad\qquad (5\text{-}3\text{-}31)$$

$$p(L) = P_{res} \qquad\qquad (5\text{-}3\text{-}32)$$

for the mud and the farfield reservoir. That is, we assume that $p_1 = P_{mud}$ and $p_{imax} = P_{res}$ where L is the core length. This leads to the coupled equations

$$
\begin{array}{lll}
 & p_1 & = P_{mud} \\
i = 2: & p_1 - 2p_2 + p_3 & = 0 \\
i = 3: & p_2 - 2p_3 + p_4 & = 0 \\
i = 4: & p_3 - 2p_4 + p_5 & = 0 \\
\;\;\;\cdot & & \\
i = i\textit{wall}: & & \qquad\qquad (5\text{-}3\text{-}33) \\
\;\;\;\cdot & & \\
i = i\textit{front or } i_f: & & \\
\;\;\;\cdot & & \\
i = imax\text{-}2: & p_{imax\text{-}3} - 2p_{imax\text{-}2} + p_{imax\text{-}1} & = 0 \\
i = imax\text{-}1: & p_{imax\text{-}2} - 2p_{imax\text{-}1} + p_{imax} & = 0 \\
 & p_{imax} & = P_{res}
\end{array}
$$

or

$$
\begin{vmatrix}
1 & 0 & & & & & \\
1 & -2 & 1 & & & & \\
 & 1 & -2 & 1 & & & \\
 & \cdots & & & & & \\
 & \cdots & & & & & \\
 & \cdots & & & & & \\
 & \cdots & & & & & \\
 & & 1 & -2 & 1 & & \\
 & & & 1 & -2 & 1 & \\
 & & & & 0 & 1 & \\
\end{vmatrix}
\begin{vmatrix}
p_1 \\
p_2 \\
p_3 \\
. \\
. \\
. \\
. \\
p_{imax-2} \\
p_{imax-1} \\
p_{imax} \\
\end{vmatrix}
=
\begin{vmatrix}
P_{mud} \\
0 \\
0 \\
.. \\
.. \\
.. \\
.. \\
0 \\
0 \\
P_{res} \\
\end{vmatrix}
\qquad (5\text{-}3\text{-}34)
$$

just as we had obtained for simple liquid flows. The crucial differences, however, arise from the matching conditions that need to be enforced at the mud-to-mudcake and displacement front interfaces. Let the subscripts c and r denote cake and rock properties, while mf and o denote mud filtrate and formation oil or displaced fluid. At the front interface separating invading from displaced fluids, velocity continuity requires that $-(k_r/\mu_{mf})\, dp_r(x_f-)/dx$ to the left of the front equal the velocity $-(k_r/\mu_o)\, dp_r(x_f+)/dx$ just to the right.

Matching conditions at displacement front. Since rock permeability cancels, we have $(1/\mu_{mf})\, dp(x_f-)/dx = (1/\mu_o)\, dp(x_f+)/dx$. Now we will denote by if- and if+ the spatial locations infinitesimally close to the left and right of the front $x = x_f$, which is itself indexed by $i = i\,f$. Then, we can approximate the pressure gradient $dp(x_f-)/dx$ using backward differences, whereas the gradient $dp(x_f+)/dx$ can be modeled using forward differences. (Again, differentiation through the interface itself is forbidden since the pressure gradient in general changes suddenly.) This process leads to $(1/\mu_{mf})\, (p_{if-} - p_{if-1})/\Delta x = (1/\mu_o)\, (p_{if+1} - p_{if+})/\Delta x$, or $(1/\mu_{mf})\, (p_{if-} - p_{if-1}) = (1/\mu_o)\, (p_{if+1} - p_{if+})$. Now, since surface tension is unimportant, pressure continuity requires that $p_{if-} = p_{if+}$ or simply p_{if}. Thus, at the interface, the matching condition

$$(1/\mu_{mf})\, p_{if-1} - (1/\mu_{mf} + 1/\mu_o)p_{if} + (1/\mu_o)\, p_{if+1} = 0 \qquad (5\text{-}3\text{-}35)$$

applies, and straightforward changes are made to Equations 5-3-33 and 5-3-34 corresponding to the row defined by $i = ifront$. Unlike the central difference approximation, which is second-order accurate, our use of backward and forward differences in deriving Equation 5-3-35 renders it only $O(\Delta x)$ accurate.

Matching conditions at the cake-to-rock interface. It is tempting to invoke similar arguments at the index $i = i_{wall}$ representing the cake-to-rock interface, modifying Equation 5-3-35 in the obvious manner to account for differences between mudcake and rock permeabilities. This would lead to

$$k_c \, p_{iwall-1} - (k_c + k_r) \, p_{iwall} + k_r \, p_{iwall+1} = 0 \qquad (5\text{-}3\text{-}36)$$

In Equation 5-3-36, viscosity drops out identically, since the same filtrate flows through the mudcake as through the flushed zone in the rock. However, any attempt to use Equation 5-3-36 would produce gross numerical error and poor physical resolution in the mudcake, since identical grid sizes Δx are implicit in its derivation. Also, the fact that Equation 5-3-36 is not as numerically stable as $p_{i-1} - 2p_i + p_{i+1} = 0$, say, would lead to inaccuracies if our algorithm were extended to transient compressible flows. Thus, we need to return to basics and consider the more general statement

$$- (k_c/\mu_{mf}) \, dp(x_{wall} \, \text{-})/dx = - (k_r/\mu_{mf}) \, dp(x_{wall}\text{+})/dx \qquad (5\text{-}3\text{-}37)$$

Since physical length scales in the mudcake are much smaller than those characterizing the rock, we wish to use the mesh Δx_s in the cake, and the usual Δx in the rock, such that $\Delta x_s \ll \Delta x$, in constructing our backward and forward differences. This leads to the matching condition

$$(k_c/\Delta x_s) \, p_{iwall-1} - (k_c/\Delta x_s + k_r/\Delta x) \, p_{iwall} + (k_r/\Delta x) \, p_{iwall+1} = 0 \qquad (5\text{-}3\text{-}38)$$

since $p_{iwall-} = p_{iwall+}$. This difference equation, if we choose $k_c \propto \Delta x_s$ and $k_r \propto \Delta x_s$, leads directly to our desired $p_{iwall-1} - 2 \, p_{iwall} + p_{iwall+1} = 0$! Thus, we use Equation 5-3-38 in Equations 5-3-33 and 5-3-34 to separate the finite difference equation blocks for the cake and flushed zone flows; this matching condition applies at the matrix row corresponding to $i = iwall$.

Coding modifications.   Equations 5-3-35 and 5-3-38 represent, theoretically, the most significant modifications, but other equally important details must be addressed. At the end of each time step, we advance the displacement front using Equations 5-3-24 to 5-3-26, as in 5.3.2.1. In the notation of the present example, we have

$$x_{f,new} = x_{f,old} - \{k_r \Delta t/(\mu_{mf}\phi\Delta x)\}(p_{if} - p_{if-1})_{old} \qquad (5\text{-}3\text{-}39)$$

where the p refers to the pressure in the flushed zone. The mud-to-mudcake boundary $x = x_c(t)$ is updated using our earlier mudcake growth

formula, modified to accommodate the sign convention of Figure 5-3-6a, that is,

$$dx_c/dt = - \{f_s/\{(1-f_s)(1-\phi_c)\}\}|v_n| < 0 \qquad\qquad (5\text{-}3\text{-}40)$$

where $|v_n|$ is proportional to the Darcy velocity $(k_c/\mu_{mf})\, dp(x_c)/dx$ at the cake surface. The mudcake counterpart to Equation 5-3-39 is therefore

$$x_{c,new} = x_{c,old} + \{f_s/\{(1-f_s)(1-\phi_c)\}\}\{k_c\Delta t/(\mu_{mf}\Delta x)\}(p_2 - p_1)_{old} \qquad (5\text{-}3\text{-}41)$$

Numerically, as Equation 5-3-33 suggests, three separate matrix regimes (separated by two matching conditions) are required. Initially, the i_{wall} index shown in Figure 5-3-6a must at least equal three; in this minimal setup, $i = 1$ handles the left mud pressure boundary condition, $i = 3$ handles Equation 5-3-38, while $i = 2$ would correspond to a single finite difference equation $p_{i-1} - 2p_i + p_{i+1} = 0$ written for the index $i = 2$. More initial mudcake grids, of course, would lead to inaccuracy, since mudcake thickness is vanishingly small at initial times (unless, of course, mesh sizes were significantly decreased). The suggested value of three allows us to grow our cake outward as time advances. Finally, observe that we will dynamically adjust our meshes at each time step. The leading index $i = 1$ is always assigned to the moving mud-to-mudcake boundary. Then we take the mudcake-to-rock interface at $i_{wall} = |x_c|/\Delta x + 3$ (so that $i_{wall} = 3$ if $x_c = 0$), and additionally, $i_f = x_f/\Delta x + i_{wall}$. Also, while Equation 5-3-63 explicitly requires that the mudcake properties f_s, ϕ_c, and k_c be available, we understand from a prior discussion that they can equivalently be replaced by lumped parameters obtained from the surface filtration test developed there. Relevant portions of the Fortran source code that we designed to implement the foregoing changes are shown in Figure 5-3-6b, where we have added descriptive comment statements as needed. Key notes corresponding to ideas we have emphasized so far are shown in bold type for emphasis. Finally, typical computed results are displayed in Figure 5-3-6c.

```
        .
C     Mudcake properties can be entered as shown, but lumped data
C     from the  filtration  test  in Chapter 4 is more convenient.
      WRITE(*,36)
 36   FORMAT(' Mud cake  permeability (darcies): ',$)
      READ(*,32) KCAKE
      WRITE(*,37)
 37   FORMAT(' Mud cake porosity  (decimal nbr): ',$)
      READ(*,32) PHIMUD
      WRITE(*,38)
 38   FORMAT(' Mud solid fraction (decimal nbr): ',$)
      READ(*,32) FS
        .
C     INITIAL SETUP
      IWALL = 3
      IMAX  = XCORE/DX + IWALL
      IMAXM1 = IMAX-1
      IFRONT = XFRONT/DX + IWALL
        .
      N = 0
      T = 0.
      XCAKE = 0.
        .
C     START TIME INTEGRATION
      DO 300  N=1,NMAX
      T = T+DT
      DO 200  I=2,IMAXM1
      A(I) =  1.
      B(I) = -2.
      C(I) =  1.
      W(I) =  0.
 200  CONTINUE
      A(1) = 99.
      B(1) = 1.
      C(1) = 0.
      W(1) = PLEFT
      A(IMAX) = 0.
      B(IMAX) = 1.
      C(IMAX) = 99.
      W(IMAX) = PRIGHT
      IF(VISCIN.EQ.VISCDP) GO TO 240
      A(IFRONT) =  1./VISCL
      B(IFRONT) = -1./VISCL -1./VISCR
      C(IFRONT) =  1./VISCR
      W(IFRONT) =  0.
 240  A(IWALL) =  KC/DXCAKE
      B(IWALL) = -KC/DXCAKE -K/DX
      C(IWALL) =  K/DX
      W(IWALL) =  0.
      CALL TRIDI(A,B,C,VECTOR,W,IMAX)
      DO 250  I=1,IMAX
      P(I) = VECTOR(I)
 250  CONTINUE
      PGRAD  = (P(IFRONT)-P(IFRONT-1))/DX
      XFRONT = XFRONT - (K*DT/(PHI*VISCL))*PGRAD
      PGRADC = (P(2)-P(1))/DXCAKE
      XCAKE  = XCAKE+(FS/((1.-PHIMUD)
     1          *(1.-FS)))*(KC/VISCL)*PGRADC*DT
```

Figure 5-3-6b. Fortran source code (5.3.2.4).

```
      IWALL  = -XCAKE/DXCAKE + 3
      IFRONT = XFRONT/DX + IWALL
      IMAX   = XCORE/DX + IWALL
      .
      WRITE(*,280) N,T,XFRONT,IFRONT,XCAKE,IWALL
      MINDEX = MINDEX+1
      TIME(MINDEX) = T
      XPLOT(MINDEX) = XFRONT
      XC(MINDEX) = -XCAKE
300   CONTINUE
      .
```

Figure 5-3-6b. Continued.

```
INPUT PARAMETER SUMMARY:
Rock core permeability (darcies): .100E+01
Rock core porosity (decimal nbr): .100E+00
Mud cake permeability  (darcies): .100E-02
Mud cake porosity  (decimal nbr): .100E+00
Mud solid fraction (decimal nbr): .100E+00
Viscosity of invading fluid (cp): .100E+01
Viscosity, displaced  fluid (cp): .100E+01
Pressure at left boundary  (psi): .100E+03
Pressure at right boundary (psi): .000E+00
Length of rock core sample  (ft): .100E+01
Initial "xfront" position (feet): .100E+00
DX grid size in rock sample (ft): .200E-02
DX grid size in the mudcake (ft): .200E-03
Integration time step size (sec): .100E+00
Maximum allowed  number of steps: .100E+04


 INVASION FRONT POSITION VERSUS TIME:
 Time (sec)  Position (ft)
                           _____
  .000E+00    .100E+00    | *
  .600E+01    .283E+00    |     *
  .120E+02    .388E+00    |         *
  .180E+02    .470E+00    |            *
  .240E+02    .540E+00    |               *
  .300E+02    .602E+00    |                 *
  .360E+02    .659E+00    |                   *
  .420E+02    .710E+00    |                     *
  .480E+02    .759E+00    |                      *
  .540E+02    .804E+00    |                        *
  .600E+02    .847E+00    |                         *
  .660E+02    .888E+00    |                           *
  .720E+02    .927E+00    |                            *
  .780E+02    .965E+00    |                              *

 MUD CAKE THICKNESS VERSUS TIME:
 Time (sec)  Position (ft)
                           _____
  .000E+00    .000E+00    |
  .600E+01    .226E-02    |   *
  .120E+02    .356E-02    |      *
  .180E+02    .457E-02    |         *
  .240E+02    .544E-02    |            *
  .300E+02    .620E-02    |              *
  .360E+02    .690E-02    |                *
  .420E+02    .753E-02    |                  *
  .480E+02    .813E-02    |                    *
  .540E+02    .869E-02    |                      *
  .600E+02    .922E-02    |                        *
  .660E+02    .973E-02    |                          *
  .720E+02    .102E-01    |                           *
  .780E+02    .107E-01    |                             *
```
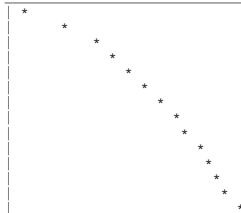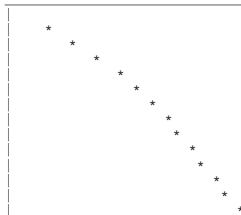
Figure 5-3-6c. Numerical results (5.3.2.4).

Modeling formation heterogeneities.   Rock heterogeneities such as internal filter cake, or damaged zones, are easily modeled by allowing k_r to vary with x.   If so, the differential equation $d^2p(x)/dx^2 = 0$ no longer applies, as it is derived for constant permeabilities only.   Instead, we must consider

$$d(k_r \, dp/dx)/dx = 0 \qquad\qquad (5\text{-}3\text{-}42)$$

$$k_r(x) \, d^2p(x)/dx^2 + (dk_r/dx) \, dp/dx \; = 0 \qquad\qquad (5\text{-}3\text{-}43)$$

Then, the central difference approximation

$$k_r(x_i) \, \{p_{i\text{-}1} - 2p_i + p_{i+1}\}/(\Delta x)^2$$

$$+ \, \{(k_{r,i+1} - k_{r,i\text{-}1})/(2\Delta x)\}\{(p_{i+1} - p_{i\text{-}1})/(2\Delta x)\} = 0 \qquad (5\text{-}3\text{-}44)$$

leads to

$$\{p_{i\text{-}1} - 2p_i + p_{i+1}\} + \{(k_{r,i+1} - k_{r,i\text{-}1})/(4k_r(x_i))\}(p_{i+1} - p_{i\text{-}1}) = 0$$
$$(5\text{-}3\text{-}45)$$

or

$$[1 - \{(k_{r,i+1} - k_{r,i\text{-}1})/(4k_r(x_i))\}] \; p_{i\text{-}1} - 2p_i$$
$$+ [1 + \{(k_{r,i+1} - k_{r,i\text{-}1})/(4k_r(x_i))\}] \; p_{i+1} = 0 \qquad (5\text{-}3\text{-}46)$$

Thus, the only required change when $k_r(x)$ is an explicitly prescribed function of x is the replacement of $p_{i\text{-}1} - 2p_i + p_{i+1} = 0$ by Equation 5-3-46. When k_r (p) is a function of p, which additionally depends on x, the physics changes, and the algorithm modifications discussed next are required.

Mudcake compaction and compressibility.   Mudcake compaction, meaning pressure-dependent permeability and porosity, is easily handled. For example, if $k_c = k_c(p)$, the governing pressure equation in the mudcake

$$d(k_c \, dp/dx)/dx = 0 \qquad\qquad (5\text{-}3\text{-}47)$$

becomes

$$k_c(p) \, d^2p(x)/dx^2 + (dk_c/dp) \, (dp/dx)^2 \; = 0 \qquad\qquad (5\text{-}3\text{-}48)$$

Following the lead of earlier examples, Equation 5-3-48 can be linearized about pressure values obtained from one earlier time step, so that we can write

$$k_c(p_{old}) \, d^2p(x)/dx^2 + \{(dk_c/dp)(dp/dx)\}_{old} \, (dp/dx) \; = 0 \; (5\text{-}3\text{-}49)$$

This is exactly Equation 5-3-43, with $k_r(x)$ replaced by $k_c(p_{old})$ and (dk_r /dx) replaced by $\{(dk_c/dp)(dp/dx)\}_{old}$. Thus, an equation analogous

to Equation 5-3-46 is easily obtained.   The function $k_c(p)$ and the function $\phi_c(p)$ in Equation 5-3-41 could be hard-coded into the main program, or declared as subroutines or statement functions, as desired. Finally, mudcake compressibility transients are easily modeled using the ideas developed in Chin (2017) – the interested reader is referred to the comprehensive discussions presented therein.

Modeling borehole activity.   We have developed the foregoing example in detail assuming lineal flows, but as we have shown, the extension to cylindrical radial flows requires but two lines of Fortran changes.   These are specifically redefinitions for the **A** and **C** matrix coefficients as indicated in 5.3.2.2.   We also observe that mud weight is often increased or decreased during drilling and that this weight change is accomplished by adding or removing solid particulates (e.g., *barite*), and modifying viscosifiers (e.g., *bentonite*).   The mud pressure PLEFT and the invading filtrate viscosity VISCIN can be redefined as general time-dependent Fortran statement functions.   This allows modeling flexibility that cannot be achieved with exact analytical solutions. Finally, note that the erosive effects of dynamic filtration can be used to limit radial mudcake growth to an equilibrium value, by introducing if-then programming logic (e.g., do *not* update x_c if $x_c > x_{c,equil}$).

We have selected a cross-section of examples, ranging from constant density, two-fluid flows without mudcake to flows with transients due to compressibility to problems with mudcake thickening with time.   Naturally, other combinations of problems with lineal, radial, and spherical geometries, single or multiple fluids in formations, compressible mudcake, general transient effects, and so on, can be modeled by combining appropriate pieces of theory and source code. Finally, this author warns prospective users of canned computational fluid mechanics software of likely formulation errors.   In an environment driven by high-resolution graphics and user-friendly screen interfaces, it is important to understand precisely which equations are solved and the methodology employed.   The highly specialized problems typical of formation invasion applications are unlikely to be pre-programmed in commercial solvers; users should carefully direct technical questions to research and development staff.

5.4 References.

- Chin, W.C., *Formation Invasion, with Applications to Measurement-While-Drilling, Time Lapse Analysis, and Formation Damage*, Gulf Publishing, Houston, 1995.

- Chin, W.C., *Quantitative Methods in Reservoir Engineering*, Elsevier Science, Amsterdam, 2002.

- Chin, W.C., *Quantitative Methods in Reservoir Engineering*, Second Edition, Elsevier Science, Amsterdam, 2017.

6
Mudcake Growth for Multiphase Flow

In Chapters 2, 3 and 4, we demonstrated rapid and accurate methods for calculating annular flows under numerous scenarios. All of our "perfectly sealing" methods assumed that fluid did not flow into or from the formation, that is, that mudcakes provided perfect seals at the sandface. Mudcake dynamics is of central focus to both well logging and drilling. In formation testing, for example, thick mudcakes are desired so that pads extending from tools perfectly seal the formation to reduce mud penetration through surface gaps. Thick cakes are also necessary so that mud minimally invades the formation and not contaminate the in situ fluid being extracted – further, mudcake would isolate high mud pressures in the wellbore so that formation pore pressure measurements were meaningful. Thus, thick cakes are "good."

On the other hand, thick mudcakes are not desirable because prolonged contact with formation testers could result in sticking and lost tools. In slimholes, rapid mudcake growth and thick mudcakes could plug the well and lead to additional operational problems. Whatever the mudcake objective, it is important to understand the physical principles behind mudcake growth, so that sound mathematical procedures to model cake thickness and filtration volume as functions of time can be developed. Cake and fluid transients are also coupled with pressure fields that evolve with time. For example, when a formation tester probe measures transient pressure, what is the contribution from the well and how is this removed to correct pore pressure measurements?

In Chapter 5, we noted that, when the formation mobility (that is, the ratio of permeability divided by viscosity) is relatively high compared to that of the mudcake, its role in cake formation can be ignored. Our derived "cake growth on filter paper" suffices for all practical purposes, using the differential pressure obtained from mud and equilibrated reservoir values (the latter, obtained from immediate formation tester readings). However, when the formation mobility is very low or "tight," two questions arise. What is the pore pressure? And what is the "equivalent distance" in the rock over which pressure drop is measured – more to the point, is this concept even necessary?

In this chapter, we revisit the "three layer" radial model considered in Chapter 5. In the prior discussion, we had postulated three different viscosities in three separate layers to *mimic* two-phase flow effects. And so, while the mathematics allowed an "exact" closed form analytical solution (that was strictly correct only in the limit of a single-phase fluid), the physical model was only approximate. In the work below, we consider realistic multiphase mixing, that is, oil-based mud invading an oil reservoir, but in general, do not place any restrictions on the values of formation mobilities. Thus, the formation may be higher in mobility as in "conventional" applications or extremely low as may be the case "unconventional" problems. The work in this chapter is rigorous and assumes that the constant pore pressure far from the well is known – the subject of pore pressure estimation is addressed in Chapters 7 and 8.

6.1 Physical problem description.

To facilitate our discussion of mudcakes and their physical consequences, it is useful to introduce "formation testers," which are well logging instruments designed to extract in situ reservoir fluid samples for surface evaluation (e.g., see Figure 6.1a for CNOOC/COSL tools). Typically, a "source probe" is pressed against the sandface and a retracting piston withdraws fluid into collection chambers. Answers to two questions are sought. First, because mudcake *is* permeable, near-well pumped samples *are* generally contaminated by mud filtrate – what pumping rates and times are required to obtain a clean sample? Second, measurements of flowline transients can be interpreted to deduce formation permeability and steady-state pore pressure – but flowline volume effects (that is, the "cushioning" due to pre-existing fluid in the tubing) and high local pressures exerted by drilling mud must be accurately accounted for. How are these objectives accomplished?

These questions are addressed in the author's books on formation testing (see Chin (2014,2015)) and are not considered here. We only present related calculation results insofar as they illustrate mudcake presence and their physical consequences. The math models developed are numerically intensive and details are found in the references. They solve the full reservoir engineering equations for multiphase fluids in the formation without a priori assumptions on rock and cake permeability, subject to a constant pore pressure in the farfield (that is equal to the initial pressure of the quiescent reservoir) and a known pressure in the well. Between the wellbore mud and the rock matrix resides a mudcake that wraps radially around the well, whose thickness is allowed to change in time. The boundary conditions and cake growth models used in the finite difference simulator are identical to those derived in Chapter 5. Note that the time required to pump a clean sample differs from that required to perform a buildup analysis. Results of computations are "exact" in this sense: the physical formulation is general, although its solutions are numerical.

We consider the axisymmetric problem in Figure 6.1b for a three-layer formation. Initially, high pressure mud from the newly drilled borehole invades the formation and forms a mudcake that grows with time. In a homogeneous medium, the flow would be cylindrical; however, when multiple layers are present with different properties, significant vertical cross-flow can occur after pumping begins when permeability contrasts are moderate or high (this cross-flow is permitted in our general formulation). At some point in time, a single-probe formation tester begins to withdraw fluid from the formation and terminates after a given period, while "supercharging" invasion from the well continues at a slower rate. This withdrawal is associated with a pressure drawdown and buildup – importantly, the fluid initially withdrawn will be contaminated by mud filtrate while later time, the net fluid is more representative of the formation fluid. The pressure measured by the probe is not the true formation pressure, but a combined pressure partly characteristic of the high pressure in the borehole. How the detected pressure is allocated between borehole and formation effects will affect pore pressure and permeability interpretation. For example, without understanding that invasion is continually present, an unrealistically high pore pressure may be predicted.

Figure 6.1a. Example CNOOC/COSL single and dual probe tools.
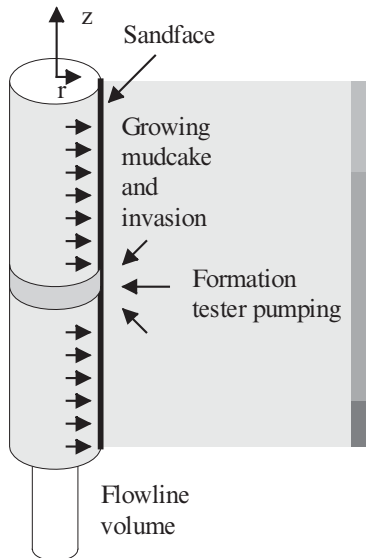
Figure 6.1b.   Single-probe supercharging and pumping model.

The pumping process is sketched in Figures 6.1c, 6.1d and 6.1e, where flow processes in a r-z plane of fixed azimuthal angle are shown. A left sketch describes pressure variations while a right sketch describes variations in saturation or concentration.
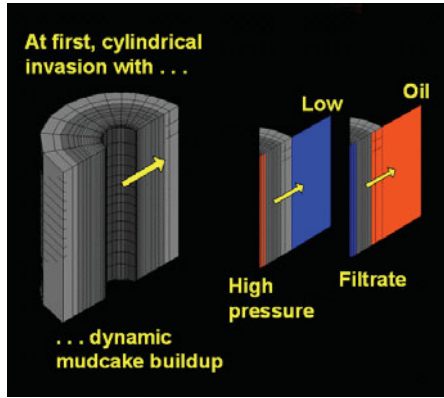
Figure 6.1c. General problem – initial cylindrical invasion.
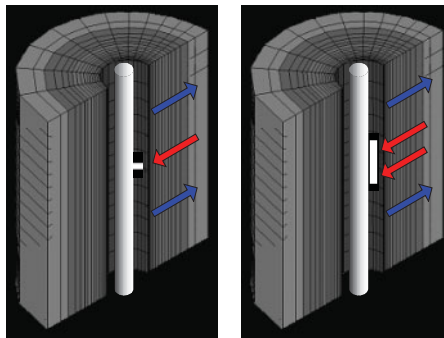
Figure 6.1d. Pumping begins (single-probe, left, elongated pad, right).
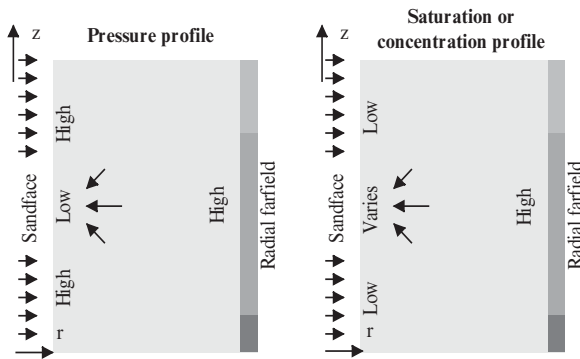
Figure 6.1e. Pressure and contamination profiles in r-z plane.

6.2 Overview physics and simulation capabilities.

Because there are dozens of input parameters, and because the governing equations are complicated, general conclusions cannot be drawn from the limited number of simulations presented below. However, the results are representative of typical results and are physically expected.   We will focus on the qualitative effects of mudcakes obtained.   Because the mudcakes are physically thin by comparison to the r-z planes displayed, it is not possible to display them on the printed page.   However, text outputs do tabulate "thickness versus time" for applications where cake properties are required. We will focus on general capabilities and applications results next.

6.2.1 Example 1, Single probe, infinite anisotropic media.

For this first simulation, we describe our graphical output results and explain potential uses and implications. Once all input quantities are saved and the "Simulate" button is clicked, interactive field displays of pressure and oil saturation (or formation fluid concentration) are given periodically in time. Consider Figure 6.2.1a, which contains two field plots, with pressure at the left and concentration at the right for a miscible run (for immiscible runs, concentration plots are replaced by oil saturations). For each of the diagrams in Figure 6.2.1a, the left vertical side corresponds to the sandface at the borehole wall – the right side corresponds to the radial farfield. The top and bottom horizontal lines coincide with the reservoir top and bottom. These cross-sections display computed solutions in the r-z plane for our axisymmetric formulation. The left pressure plot is uniform vertically, indicating identical pressure profiles at all z stations. The red at the left represents high mud pressure, relative to the lower blue formation pressure at the right. The right concentration plot again indicates a purely radial flow without z variations.   Invading blue mud is displacing red formation fluid. The multicolored zones between blue and red in either case represent events in the diffusive mixing zone. Cylindrical radial invasion occurs while drilling. Sometimes the invasion time is short – at other times, it can exceed a day. For long invasion times, it is not necessary to simulate extraordinarily long – we equivalently model the invasion associated with a higher permeability mud for a shorter time. Equivalence formulas are given in Chin (1995, 2002). The relatively short times in Figures 6.2.1a and 6.2.1b mimic twenty-four hour invasion.

Note how the effects of mud pressure and filtrate invasion are deeper at "1 min" than at "0.33 sec," as expected physically. At some point in time designated by the user, the formation tester starts pumping – it can extract fluid from or inject fluid into the reservoir according to a multi-rate schedule. The left pressure plot in Figure 6.2.1c shows the effects of fluid withdrawal, that is, typical fluid sampling performed, in this case, by a single centered nozzle (in general, single, dual and straddle packer probes are permitted, which can be located arbitrarily along the sandface). The left side of the pressure plot in Figure 6.2.1c shows a blue-green area associated with the low pressure at the nozzle. Above and below this zone are red colored pressures which indicate higher pressures associated with supercharging – that is, as the nozzle withdraws fluid, high pressure mud invades the formation through the mudcake. Not shown in the pressure plot are reverse flow streamlines that would indicate filtrate pumping by the formation tester nozzle.

The right plot in Figure 6.2.1c displays the corresponding concentration profile. The blue zone represents the mud filtrate that has penetrated the formation – it is now deeper than that shown in Figure 6.2.1b. Figures 6.2.1d and 6.2.1e illustrate similar phenomena at later times. Again, note the high supercharge pressures above and below the nozzle, indicating continuing filtrate invasion while the tester nozzle attempts to extract a clean sample. Whether or not this is possible for the input parameters assumed is one question the simulation addresses. There are several related objectives. Is a clean sample possible? If so, how long must the formation be pumped? If not, how might mud properties and weight to changed? The time scale for adequate clean-up is different from that for pressure transient interpretation. How long must be tool stay in place to ensure good pressure data for permeability and anisotropy prediction – without risking a stuck tool? Good pressure data for permeability prediction, of course, can be obtained even when mud filtrate has not been flushed. Thus, for tools that do not collect samples (e.g., formation-testing-while-drilling tools), the job planning simulator can be used to study pressure transients – while, for wireline formation testers, the simulator serves dual clean-up and pressure transient objectives.
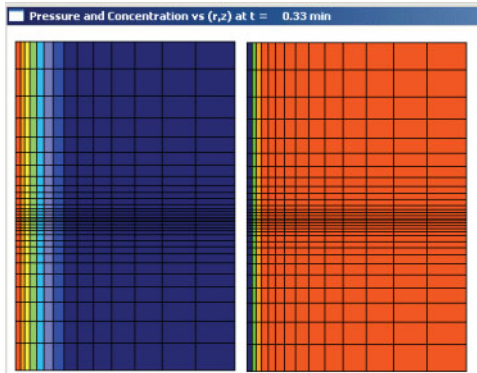
Figure 6.2.1a. Pressure-concentration profiles, 0.33 sec.
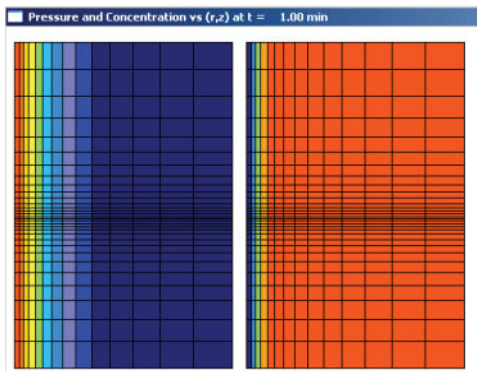
Figure 6.2.1b. Pressure-concentration profiles, 1.00 min.
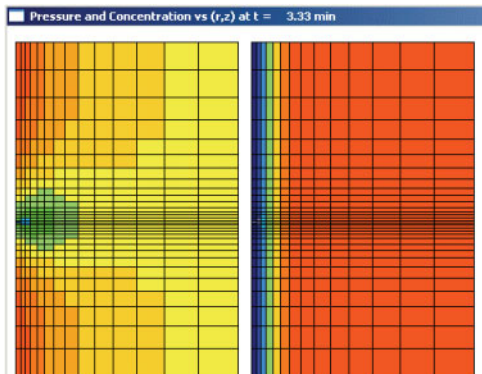
Figure 6.2.1c. Pressure-concentration profiles, 3.33 min.
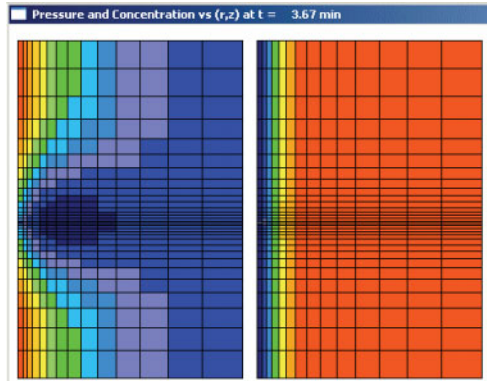
Figure 6.2.1d. Pressure-concentration profiles, 3.67 min.
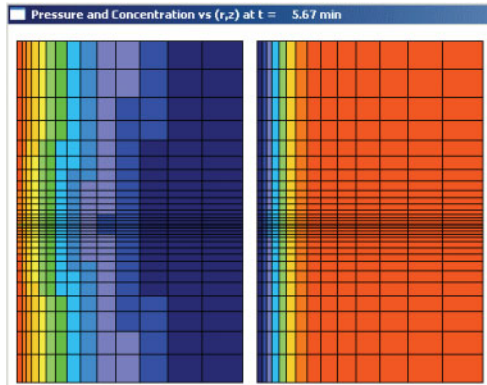
Figure 6.2.1e. Pressure-concentration profiles, 5.67 min.

The left plot of Figure 6.2.1c indicates probe presence because its low (blue-green) pressures contrast strongly with the high (red) ones due to supercharging. At the right, a small green zone associated with the probe is embedded in the blue filtrate – this small zone is not red because the fluid is still contaminated. The variable meshes used allow high resolution simulations near the probe. At the end of the simulation – a point in time defined by the user, the pressure-concentration screens shown above may be played back in the software's "movie mode." This playback feature enhances the field engineer's physical intuition about the formation under consideration.

6.2.2 Example 2, Single probe, three layer medium.

In this second simulation, we describe a situation without the upper-lower symmetries obtained earlier. Here the formation consists of three layers, with the lowest porosity layer at the top. Before pumping, there is strong cylindrical radial filtrate invasion into the formation, as is evident from the right-side plot of Figure 6.2.2a. The left-side pressure plot shows a small blue zone marking the lower pressures realized at the nozzle. That the entire plot is a single color indicates relatively little pressure variation otherwise, characteristic of the low permeabilities assumed.

Figure 6.2.2b gives pressure-concentration plots at a later point in time. The concentration plot shows continuing strong invasion in the low porosity layer. The pressure plot, with the high color contrast and the strong red zones above and below the probe along the sandface (left vertical boundary) indicates strong supercharging. The formation tester probe will measure high pressures, but the high values characterize more the high pressure in the mud than the pore pressure in the rock.

The pressure-concentration behavior noted for Figure 6.2.2b continues with increased intensity in Figure 6.2.2c. In all the runs shown thus far, note our use of variable spatial grids in the radial and vertical directions. Internal software logic also activates variable time gridding, enabling large time steps when flow gradients are small and smaller time steps when they are large. For example, smaller time steps are selected whenever a change in flow rate is imposed; higher grid densities are always selected near nozzles.
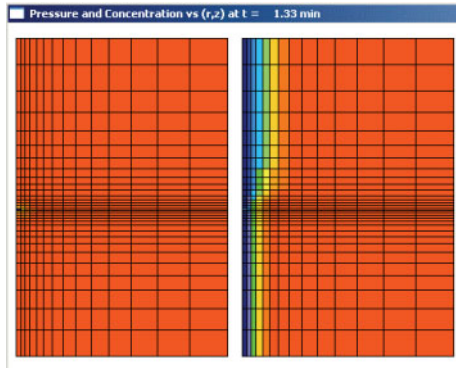
Figure 6.2.2a. Initial pumping, highly invaded upper zone.
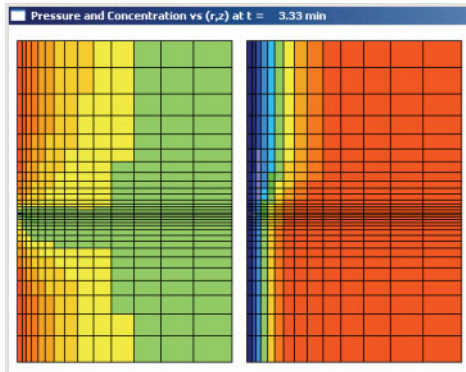
Figure 6.2.2b. Supercharging seen in left pressure plot.
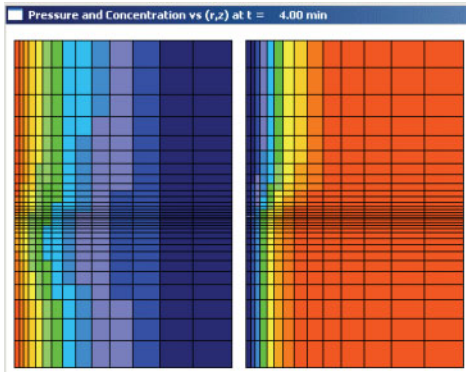
Figure 6.2.2c. Continued supercharging and invasion.

6.2.3 Example 3, Dual probe pumping, three layer medium.

We consider a three layer medium again – the higher permeabilities here allow stronger pressure penetration as seen in the left pressure plot of Figure 6.2.3a. Pumping has initiated in Figure 6.2.3b. The two small blue areas in the left pressure plot mark the low pressure zones associated with two pumping nozzles. The two small red areas in the right concentration plot mark the high formation fluid concentrations associated with continued pumping. From Figure 6.2.3c, at large times pumping has ceased and supercharging at the sandface is evident from the left red pressure zones.
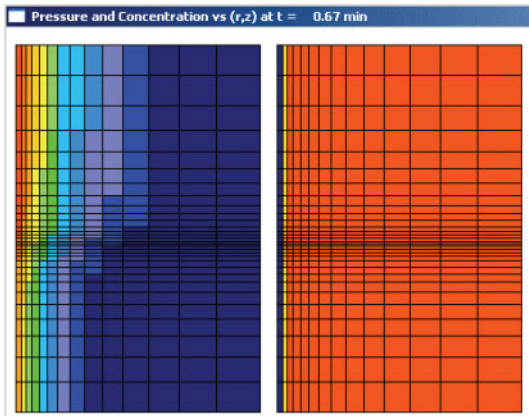
Figure 6.2.3a. Initial cylindrical invasion before pumping.
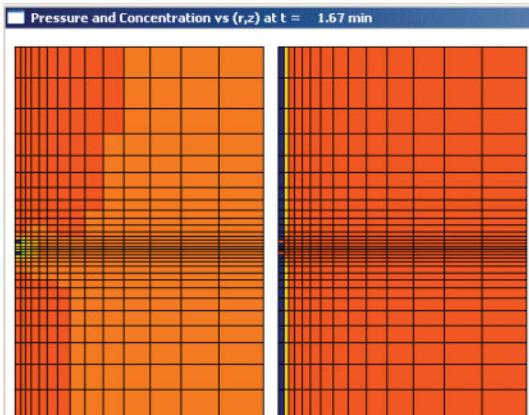
Figure 6.2.3b. Dual probe pumping initiated.
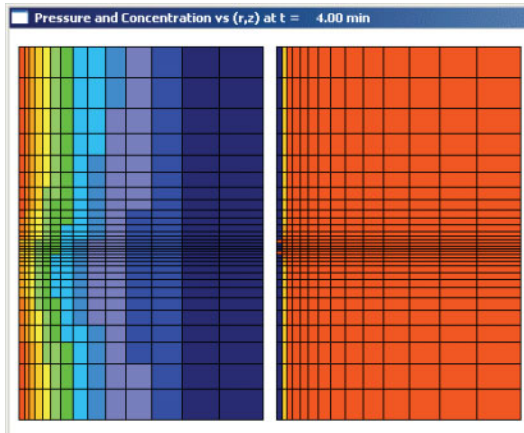
Figure 6.2.3c. Supercharging evident at large times.

6.2.4 Example 4, Straddle packer pumping.

So far we have demonstrated how pumpouts using single probe and dual probe nozzles can be realistically simulated. In many field situations, particularly in unconsolidated sands and naturally fractured formations, pad nozzles may not be effective in reliably contacting producing zones. In such applications, straddle packer nozzles are employed. Whereas pad nozzles "see" a single point along the borehole wall, packer nozzles see axial extents that may be several feet in length and then pump from all azimuthal directions. Because they are associated with pump rates that may reach 1 gpm, they offer good depth of investigation and strong signal propagation – thus they are extremely useful in so-called "mini-DST" applications that seek to determine permeability over larger spatial scales than those normally possible with pad-type tools.

Again, we consider a layered region that is initially invaded by mud filtrate. The left pressure plot in Figure 6.2.4a shows an elongated low pressure zone associated with the length of the straddle packer. The nonuniform vertical pressure variations indicate that the radial flux into the tool is not uniform – computational evidence that "uniform flux" pumping models are not correct even the packer resides entirely within a uniform layer. The formation fluid concentration plot in Figure 6.2.4b highlights the continuing invasion of mud filtrate into the near-sandface rock.

The pressure plots in Figures 6.2.4c and 6.2.4d highlight the strong impact on local flow exerted by the straddle packer nozzle. Its long vertical extent allows it to withdraw large amounts of fluid into the tool. The low pressures at the bottom and bottom-right of the formation unfortunately encourage stronger invasion at the top, an effect clearly seen in the concentration plot of Figure 6.2.4d. Not shown are computed pressure plots along various tool stations. As noted earlier, while our algorithm allows nonuniform radial flux along the length of the tool, pressures along it do not vary although they do vary with time. Pressures fields away from the packer are deeper than they are for pad type nozzles because of the higher pump rates utilized.
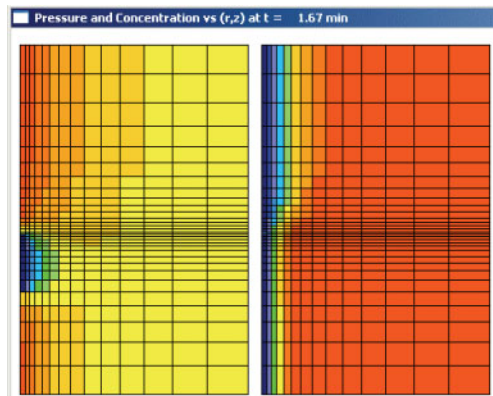
Figure 6.2.4a. Initial pumping of cylindrical invaded region.
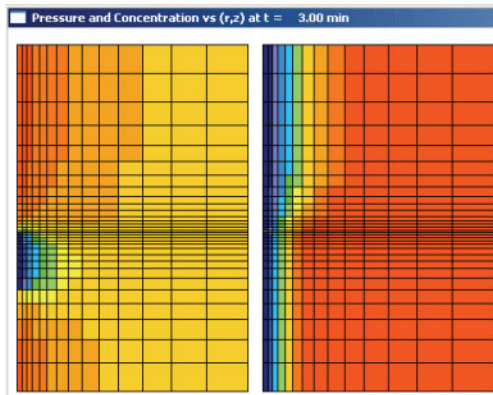
Figure 6.2.4b. Continued straddle packer pumping.
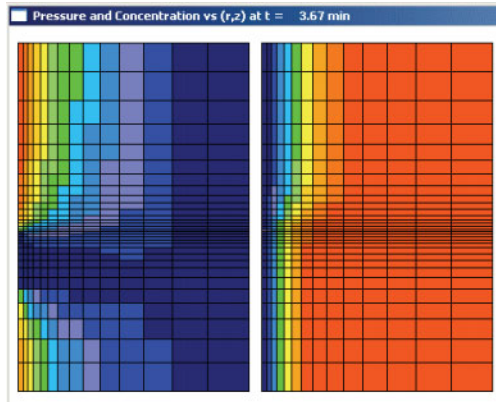
Figure 6.2.4c. Strong lateral pumping.
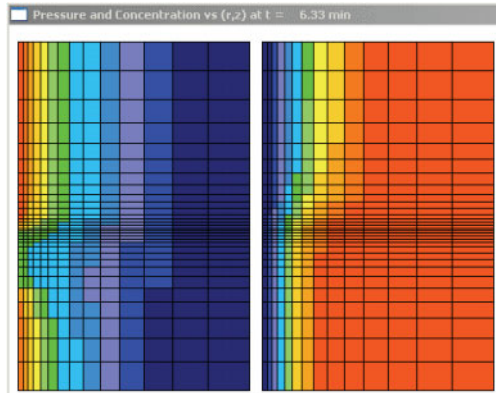
Figure 6.2.4d. Lower formation strongly affected.

6.3 Model and user interface notes.

The original multiphase math model in Chin and Proett (2005) differs substantially from that of Chin (2015), in particular, with respect to inclusion of Forchheimer effects to account for rapid pumping speeds. These extensions required key modifications to the numerical integration scheme. Here we discuss user interface changes. Originally, all input boxes were placed on a single screen as in Figure 6.3.1. Users were required to enter vast amounts of data, comprising of physical properties, boundary conditions and grid generation variables. As one would expect, few combinations actually led to usable solutions, so that the simulation experience was less than ideal. Major rework has led to the modular menu system in Figures 6.3.2a and 6.3.2b.

In particular, the high-level control menu in Figure 6.3.2a opens any number of lower-level submenus, as shown in Figure 6.3.2b, each focusing on a particular function.   Typical menus include "formation fluid properties," "layer properties," "mudcake parameters," "source probe type," "boundary conditions," "pumping schedules" and numerical gridding parameters.   When a user has developed a meaningful simulation, he is provided the option to save that run and re-run the model at any time – or run changes to that simulation defined by editing one or more of the input screens in Figure 6.3.2b. This allows him to build a useful library of simulations for future use, accessible through database calls under "File Open."   Compressed data files can now be shared by users working from different locations and color graphics plots and movies are always recreated "on the fly" to conserve disk storage space and to reduce file transmit times.

Figure 6.3.1. Original user interface.
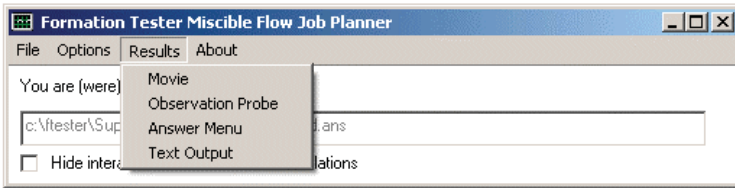
Figure 6.3.2a. New program structure (high level).
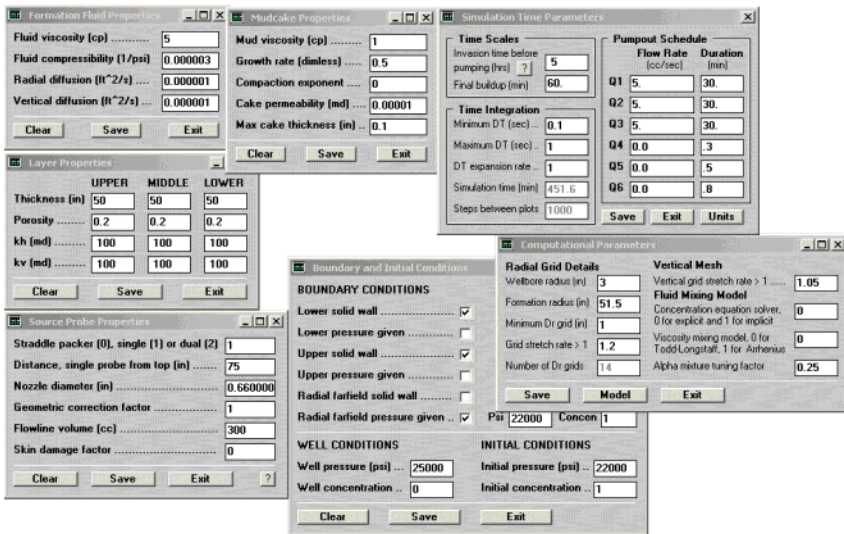
Figure 6.3.2b. Modularized submenus (low level).
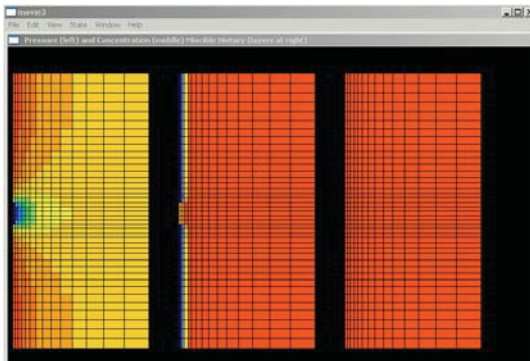
Figure 6.3.4. Color display frame (pressure left,
concentration middle, lithology screen added right).

6.4 Detailed applications.

In this section, we present results of several detailed simulations illustrating the effects of different controlling variables. More examples can be found in Chin et al (2015).

6.4.1   Run No. 1, Clean-up, single-probe, uniform medium.

We consider formation clean-up about a single-probe tool in a uniform medium. The seven sub-menu inputs defining the run appear in Figure 6.4.1.
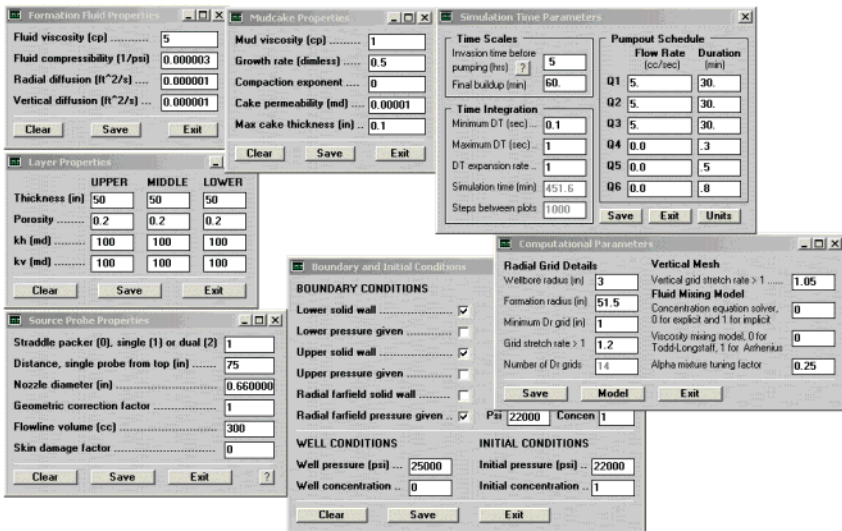
Figure 6.4.1. Seven submenus for input parameter definition.

We first summarize the physical assumptions behind the above simulation. The problem is shown schematically in Figure 6.4.2. At first, the borehole undergoes pure cylindrical radial invasion with dynamic mudcake buildup as indicated at the left – an actual wellbore with nonzero radius is assumed, and as will be demonstrated later, the (vertical) borehole can traverse up to three horizontal layers each having different thicknesses and formation properties. The color diagrams to the right of Figure 6.4.2 display complementary pressure P(r,z,t) and "contamination" or "concentration" C(r,z,t) profiles frozen at a time t, where r is the radial coordinate, z is the vertical coordinate.
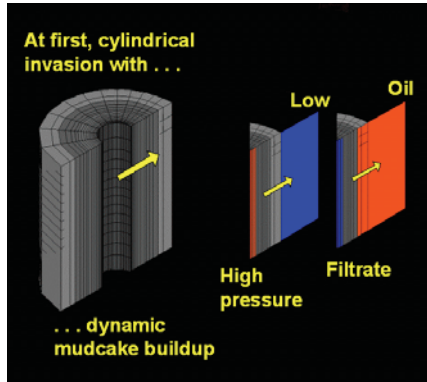
Figure 6.4.2. General problem definition – initial cylindrical invasion.
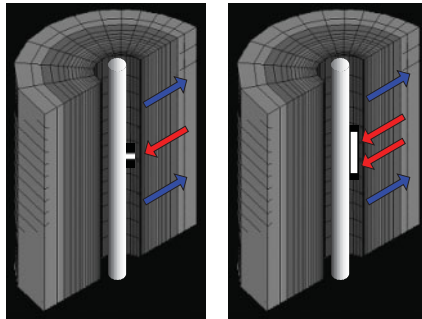
Figure 6.4.3. Pumping (single-probe, left, elongated pad, right).

The complete physical picture requires both P and C descriptors since these are coupled, and both are, in turn, dynamically coupled to mudcake growth. For pressure plots, red indicates high pressure while blue indicates low; for concentration plots, blue indicates "dirty" (filtrate) while red indicates "clean" (formation fluid). These twin pictures are displayed periodically during the simulations. Prior to pumping by the formation tester, of course, we expect purely cylindrical radial behavior. At a time prescribed by the user, the formation tester will commence pumping. In Figure 6.4.3, a single-probe tool is shown at the left – the red arrows indicate fluid withdrawal by the tool while the blue arrows indicate continual invasion into the formation (an elongated probe is shown at the right for comparison, whose properties will be considered in later runs). The pressure-concentration profiles show

Low pressure will be evident at the pumping probes while high pressure will be evident along the borehole walls adjacent to the probes due to continuing invasion – this effect is known as "supercharging." The pressure calculated at the probes (and measured in reality by the tool) is a combination of wellbore mud pressure and formation pore pressure.   One purpose of this present simulator is to explore the complicated relationship between measured probe pressure, borehole mud pressure and distant pore pressure.   How much of the measured pressure is the pore pressure?   Using incorrect pressure inputs in our inverse permeability methods will, of course, lead to errors in formation evaluation results.
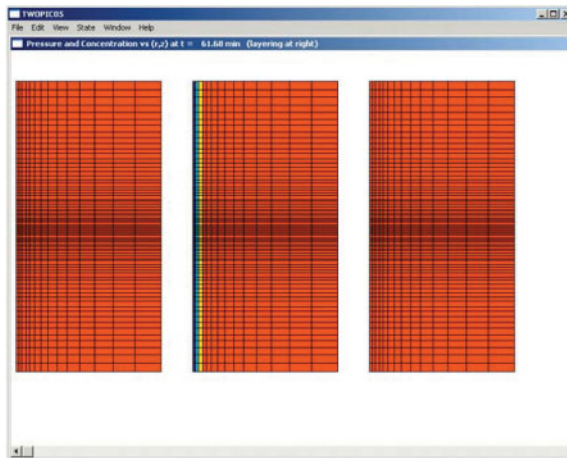
Figure 6.4.4a. Pressure-concentration-lithology display (61 min).

We now describe the sequence of events observed on screen. During simulations, a status screen appears that indicates that cylindrical invasion is proceeding – the physical time and the percentage of the simulation completed are displayed. A series of r-z color screen displays appears periodically at pre-set time intervals. Consider, for example, Figure 6.4.4a, which displays cross-sectional results at time t = 61.68 min. The left-most pressure plot is uniform in color indicating that the pressure is almost constant throughout since a very low permeability mudcake has been assumed – in later examples, greater color variations showing the effects of supercharging will be evident. The left side of each color diagram represents the borehole sandface while the right side represents farfield radial infinity as suggested in Figure 6.4.2.

The top and bottom of each box correspond to the top and bottom of the reservoir. The center concentration plot indicates invasion, with blue filtrate at the left (borehole sidewall) and red reservoir fluid at the right. The right-most plot will, in simulations involving more than one layer, display lithology and layer thicknesses; for simulations in uniform media, it can be ignored.
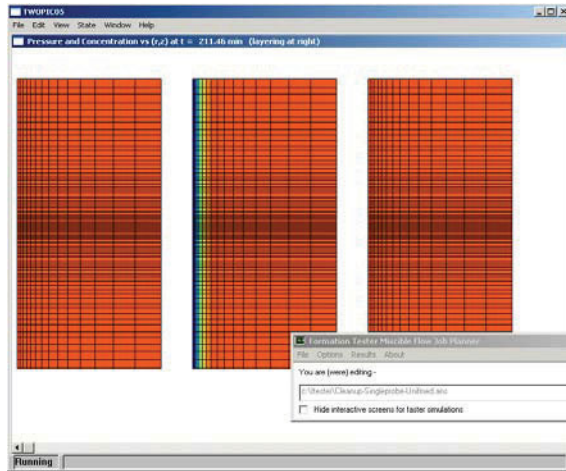
Figure 6.4.4b. Later time cylindrical radial invasion (211 min).

At 211 minutes, Figure 6.4.4b indicates that invasion has proceeded beyond that shown in Figure 6.4.4a, although from the history of color displays (not shown) the rate of radial invasion has slowed. This occurs because mudcake is dynamically building and slows the invasion rate – geometric spreading also contributes to the slower radial penetration. Once formation tester pumping starts, the computer status screen reflects that fact by indicating "pumping started," together with the elapsed physical time and percentage done.
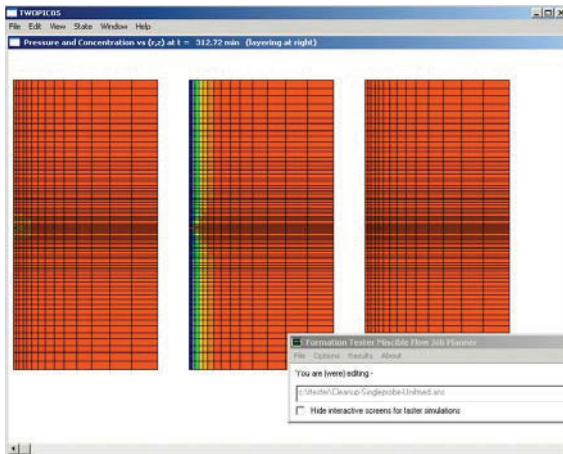
Figure 6.4.4c. Single-probe pumping (312 min).
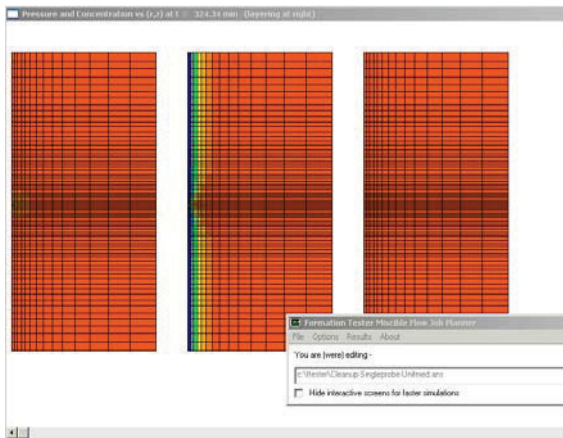
Figure 6.4.4d. Middle-time pumping result (324 min).

Figure 6.4.4c shows the onset of pumping for the single-probe tool assumed. The left-most pressure plots shows a small blue low-pressure zone associated with the probe nozzle, while the center concentration plot shows an orange zone of contaminated fluid being withdrawn into the probe (this orange is a mixture of blue filtrate and red formation fluid). Note that, even at 312 minutes, the pressure field is uniformly red – there is minimal supercharging because the mudcake permeability is very low at 0.00001 md. With time, the orange zone will – hopefully – turn into a completely red zone. There is, however, no guarantee that

this will occur; for example, this is physically not possible if the mudcake is too permeable or if excessive diffusion is present in the formation fluid. Figures 6.4.4d and 6.4.4e display two additional screen dumps at later instants in time for comparison.
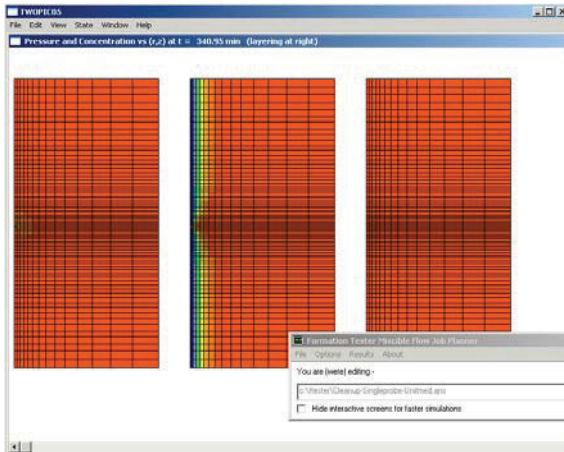
Figure 6.4.4e. Later time pumping result (340 min).
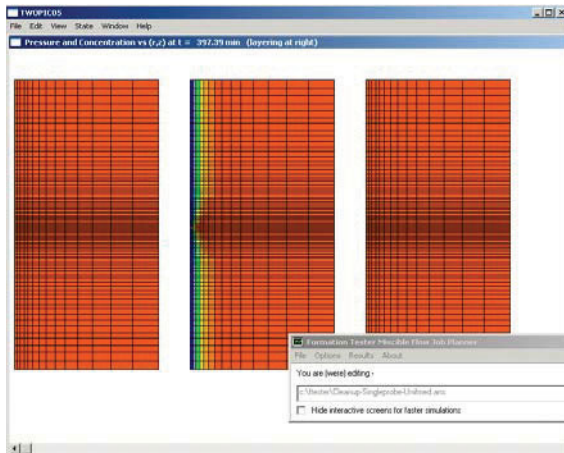
Figure 6.4.4f. Pumping ceases, but invasion continues (397 min).

In Figure 6.4.4f, the blue low-pressure zone at the nozzle has disappeared because the probe has stopped pumping (refer to the "Simulation Time Parameters" pump schedule in Figure 6.4.1). Again, the pressure plot is a single color because the reservoir pressure is almost uniform on account of low mudcake permeabilities – actually, a slight pressure variation exists but it cannot be resolved by the coarse color palette used to paint the screen – palette refinement is planned for software upgrades. Although pumping has stopped, invasion continues through the mudcake – eventually, the "dent" seen in the central figure would equalize and tend toward a pure cylindrical radial pattern.

6.4.2 Run No. 2, A low-permeability "supercharging" example.

We now modify the above example by decreasing all formation permeability values from 100 md to 1 md. Also, we increase the mudcake permeability from 0.00001 md to 0.001 md. This example demonstrates the effects of invasion in low permeability reservoirs – in other words, we wish to observe "supercharging" as it evolves dynamically. The assumed menus are shown in Figure 6.4.5a.
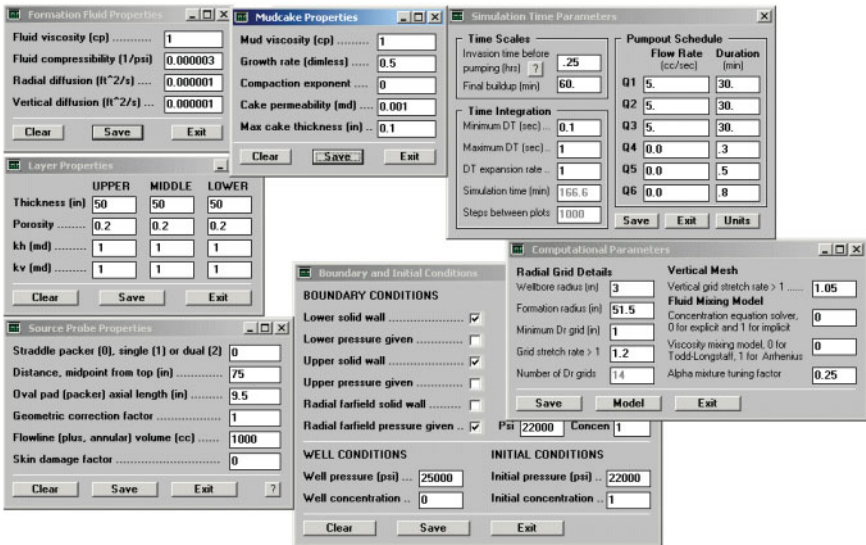
Figure 6.4.5a. A low permeability "supercharging" example.

This is a rather interesting run. Unlike the previous simulations in which our color pressure plots possessed more or less uniform red pressures, with only a small blue zone near the source probe, the pressure

plots obtained here are much more colorful. Figure 6.4.5b displays the initial pressure and concentration fields associated with purely cylindrical radial invasion before pumping commences. Figures 6.4.5c and 6.4.5d display solutions obtained at two later instants in time.

The pressure plots are especially significant. While the probe is naturally associated with a low-pressure blue zone, it is of interest to observe the higher red pressures obtained adjacent to the probe along the sidewall of the well. This high pressure is indicative of "supercharging," that is, the high pressure resident in the borehole mud. The pressure measured by the tool in practice, and that calculated by the present simulator, is a combination of the pressure based on the mud pressure and the formation pore pressure.

The probe does *not* read formation pore pressure – the present simulator can be used to assist in proper extrapolation of pore pressure from measured readings. These figures also demonstrate that pressure variations and actual fluid invasion occur on different time scales. Pressure equilibrates much more rapidly while invasion is ongoing. In a way, this is expected for two reasons. First, the steady-state pressure distribution in an all-oil formation is identical to that in an all-water formation, and is independent of viscosity – and second, invasion will occur even in a "water-water" situation even without fluid changes. At the end of the simulation, the line plots discussed earlier appear automatically, but for brevity they are not reproduced here.
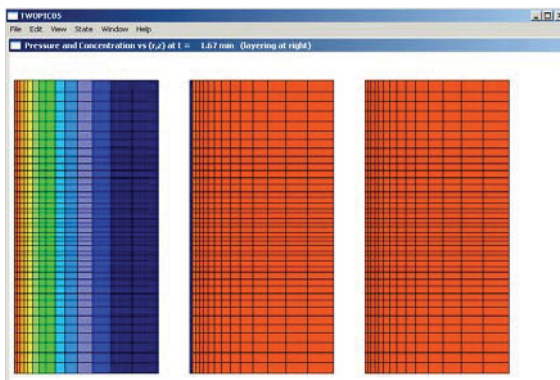
Figure 6.4.5b. A low permeability "supercharging" example (1.67 min).
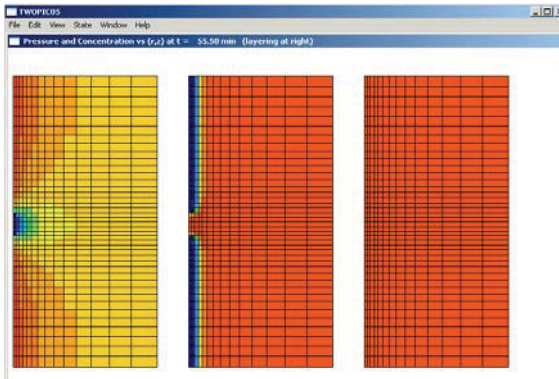
Figure 6.4.5c. A low permeability "supercharging" example (55 min).
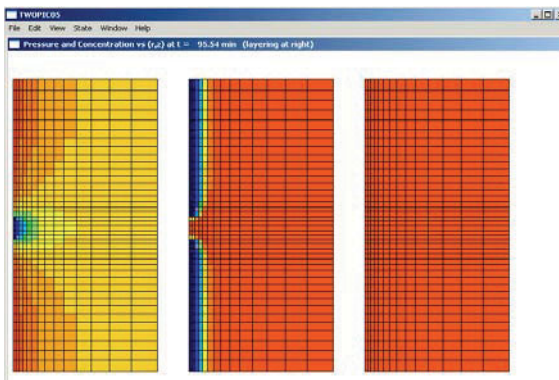
Figure 6.4.5d. A low permeability "supercharging" example (95 min).

6.4.3 Run No. 3, A three-layer simulation.

We now reduce all formation permeabilities to 0.1 md; also, instead of the porosity taking the value of 0.2 in all three layers, we assume 0.1 in the middle layer. Our simulation assumptions are given in Figure 6.4.6a. Notice that we have changed our original permeabilities by several orders of magnitude. Also, the elongated pad is not centered in the grid. This decreased porosity implies more rapid invasion in the middle layer relative to the upper and lower layers. Together with the pumping that is occurring in this layer, a number of rapidly varying flow events are simultaneously evolving. Nonetheless, the simulator performs the required calculations with a high degree of numerical stability.

This, together with the rapid middle layer invasion, is clearly seen in the time sequence of snapshots shown in Figures 6.4.6b,c,d,e. The

diagrams at the far right of these figures indicate the relative heights associated with various layers. The present simulator, as is evident from the "Layer Properties" menu, permits arbitrary layer heights and formation properties. This concludes our discussion of mudcake modeling and effects in diffusive miscible flow simulations.
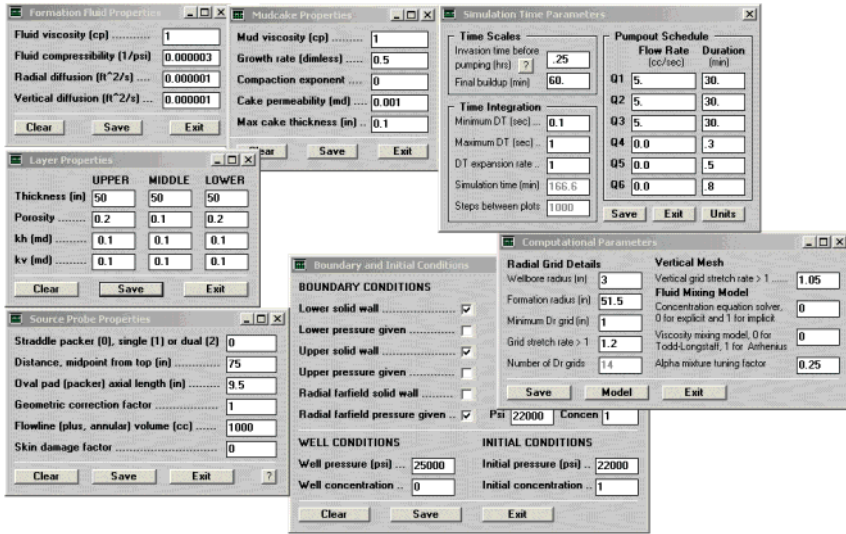
Figure 6.4.6a. Three layer run.
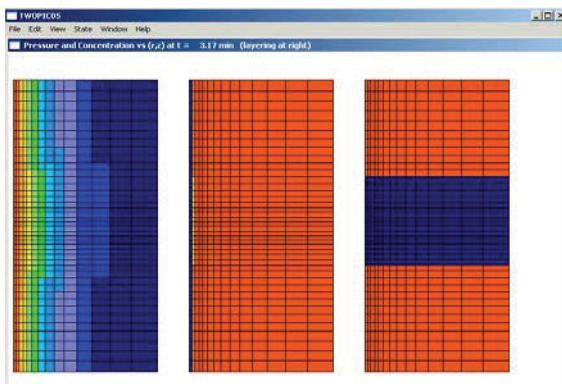
Figure 6.4.6b. Three layer cylindrical invasion before pumping (3 min).
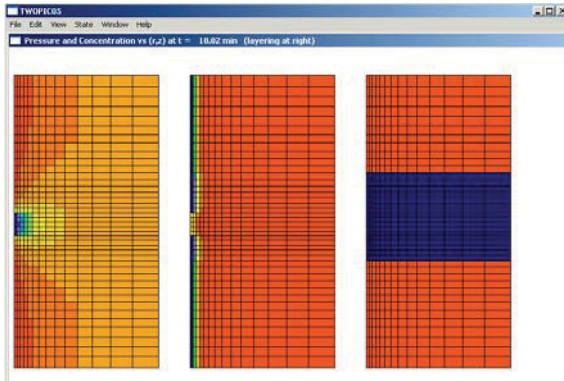
Figure 6.4.6c. Pumping in three-layer formation (18 min).
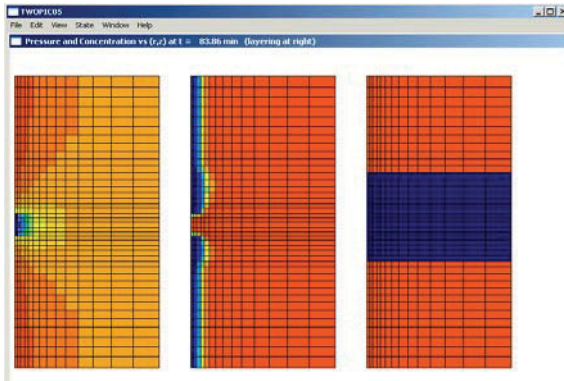
Figure 6.4.6d. Pumping in three-layer formation (83 min).
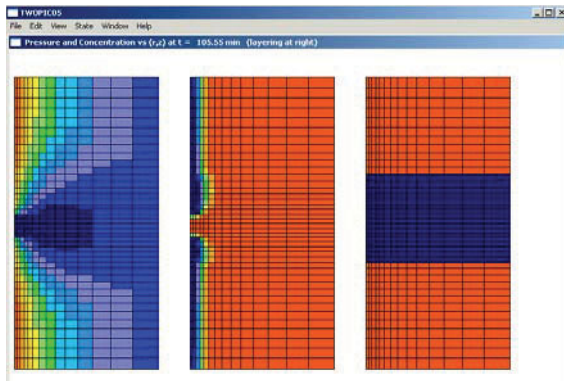
Figure 6.4.6e. Pumping in three-layer formation (105 min).

6.5 References.

- Chin, W.C., Zhou, Y., Feng, Y., Yu, Q. and Zhao, L., *Formation Testing: Pressure Transient and Contamination Analysis*, John Wiley & Sons, Hoboken, New Jersey, 2014.

- Chin, W.C., Zhou, Y., Feng, Y. and Yu, Q., *Formation Testing: Low Mobility Pressure Transient Analysis*, John Wiley & Sons, Hoboken, New Jersey, 2015.

- Chin, W.C. and Proett, M.A., "Formation Tester Immiscible and Miscible Flow Modeling for Job Planning Applications," *SPWLA 46th Annual Logging Symposium*, New Orleans, Louisiana, June 26-29, 2005.

7

Pore Pressure in Higher Mobility Formations

In Chapters 2, 3 and 4, we focused on rapid and accurate annular flow modeling assuming that mudcake provided perfect sealing at the sandface, so that fluid neither flowed into or from the formation. Chapters 5 and 6 conceded that flows were indeed possible and depended on mudcake growth and thickness. Models were developed for linear and radial flow in terms of fundamental mud characteristics. We noted that when the formation mobility greatly exceeded that of the mudcake, the cake controls the invasion rate into the formation – for the purposes of modeling cake growth, the dynamics of flow within the reservoir are not important. On the other hand, when cake and reservoir mobilities are comparable (or, say, within two orders of magnitude), flow in the formation cannot be ignored, and a coupled "three layer" problem with moving boundaries must be considered.

But how can we estimate the mobility of the reservoir? In the simplest isotropic problems, we need numerical values for the permeability "k." And in more mature applications, values for the horizontal and vertical permeabilities k_h and k_v are required. Suppose that permeabilities are found to be high. Then, of course, the formation itself is not required in mudcake modeling; the pressure drop through the mudcake is simply the difference between mud pressure and the rapidly equilibrated pressure obtained in formation testing.

On the other hand, if permeabilities are found to be extremely low, then the rock itself is important and the methods in Chapter 6 (where the radial extent of the formation is important) must be used. But then, what is the pore pressure? And in low mobility applications, where formation tester values may require hours to equilibrate, how are steady-state values found?   We emphasize that, while important in different exploration scenarios, we do not focus on empirical geographical or geological pressure correlations here – only quantitative measurements and predictive methods utilizing formation testing data are used.

7.1 Forward and inverse modeling approaches.

The author's formation testing research in formation tester pressure response simulation and inversion is described in two recent books, namely, Chin et al (2014) and Chin et al (2015). Two types of formulations exist. "Forward models" forecast pressure responses when fluid, formation properties, pumping rates and time durations, and mechanical tool properties are specified. "Inverse methods" predict properties like permeability or mobility when pressure responses to tools are known. The foregoing references provide comprehensive treatments for both types of methods – mathematical formulations are given, rapid and accurate algorithms are developed, and extensive validations between forward and inverse methods are documented.

Central to our work is the development of FT-00, so named because this very first forward modeling algorithm provides the rigorous foundation underlying all subsequent inverse methods. We will not review its underlying details, except note that exact, closed form analytical solutions are obtained for linear liquid flows, allowing flowlines of arbitrary length, with and without the effects of skin damage, for a wide range of flow rate pumping schedules. The model, whose user interface is shown in Figure 7.1, automatically plots pressure responses at source and observation probes on completion of a simulation, with typical simulations requiring at most five seconds. The host solution is obtained using advanced methods in differential equations. A key objective is the simulation of pressure responses in low permeability formations where tool volumes are typically "not small" in value. These applications are the most critical in petroleum engineering. Measured pressure buildups almost never equilibrate quickly to give the required steady-state pore pressure values – rapid inverse methods are required that predict permeability and pore pressure from transient data.
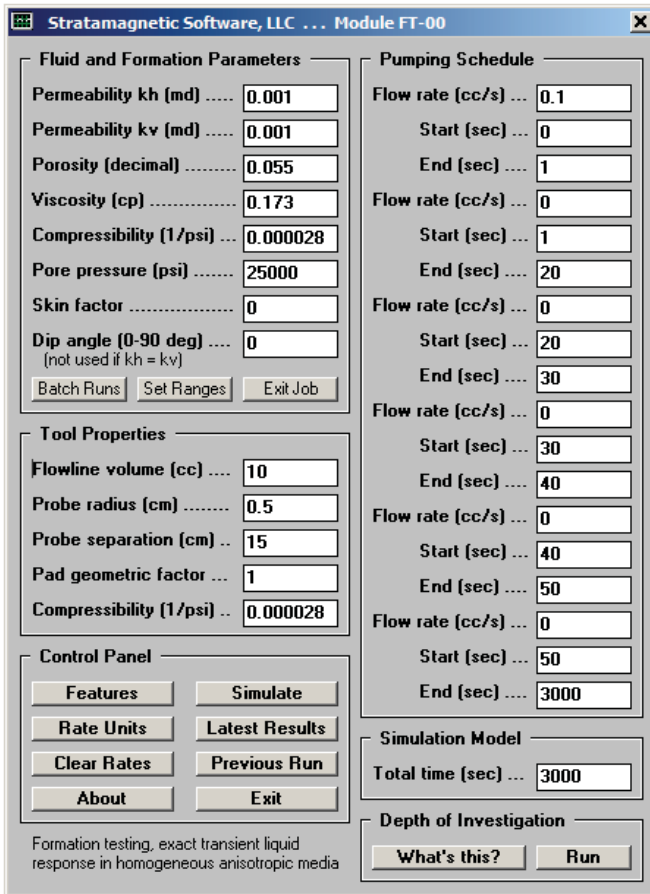
Figure 7.1. FT-00 forward model interface.

7.2 Preliminary ideas.

7.2.1 Qualitative effects of storage and skin.

Numerous fluid and rock properties affect the shape of the pressure transient drawdown and buildup curve – and the magnitude of the pressure drop – among them, vertical and horizontal permeability levels, anisotropy, dip angle, flowline volume and compressibility, skin factor and so on. We can use our exact FT-00 source model – which omits the supercharging handled in Chapter 6 – to illustrate some effects qualitatively (this model solves the forward problem exactly in

homogeneous anisotropic media for all dip angles). For the present, we will consider a simple isotropic medium in which constant rate withdrawal terminates after a short pumping period. Our Figures 7.2a,b,c,d consider various permutations for small and large flowline volume and for flows with and without skin. The source probe pressure response is shown in each case – this is the response obtained at the pumping probe – or at the only probe in the case of many formation-testing-while-drilling tools. The four pressure transient responses shown are very different qualitatively and quantitatively. It is clear that without a comprehensive and stable model to interpret measured pressures, almost any value for permeability, say, can be inferred!

7.2.2 The simplest inverse model – steady pressure drop for arbitrary dip angles.

More than fifty years ago, petrophysicists developed the simplest known method for permeability prediction utilizing formation testing pressure data. Liquid flow from single-probe tools was extracted at constant volume flow rates Q until steady-state pressure drops ΔP_s were obtained. Then, the solution for a simple source, for which transient flowline storage effects associated with fluid compressibility disappeared, applied. Let k_h denote the horizontal permeability in the x and y directions, k_v the vertical permeability in the z direction, μ the fluid viscosity, R_w the effective spherical radius of the tester nozzle, and P_0 the background hydrostatic pressure. If Q denotes an assumed constant volume flow rate, which may be positive or negative, then the pressure $P_{source}(t_\infty)$ at the source (pumping) probe at large times t satisfies

$$\Delta P_s \equiv P_{source}(t_\infty) - P_0 = - Q(t_\infty)\mu \,/\, (4\pi \, k_h^{2/3} \, k_v^{1/3} \, R_w) \qquad (7.1)$$

while the pressure $P(x,y,z,t_\infty)$ at any other location (x,y,z) in the flow domain away from the source satisfies

$$\Delta P_d \equiv P(x,y,z,t_\infty) - P_0$$
$$= - \{Q(t_\infty)\mu \,/\, (4\pi \, k_v^{1/2} \, k_h)\}/\sqrt{\{(x^2 + y^2)/k_h + z^2/k_v \}} \qquad (7.2)$$
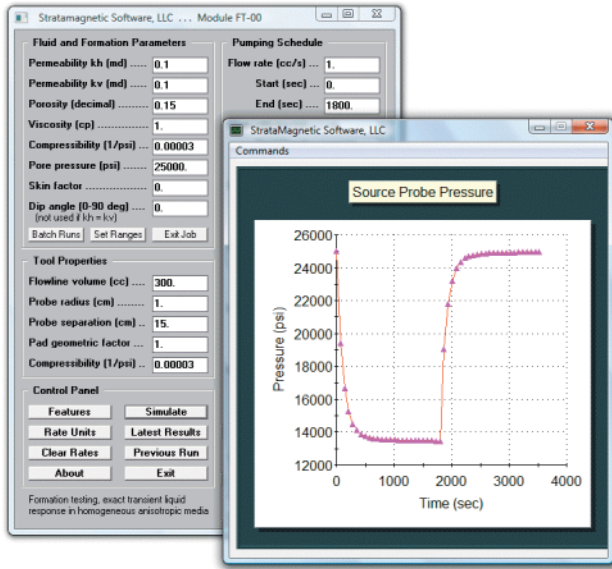
Figure 7.2a. Isotropic, low permeability –
small flowline volume, no skin.
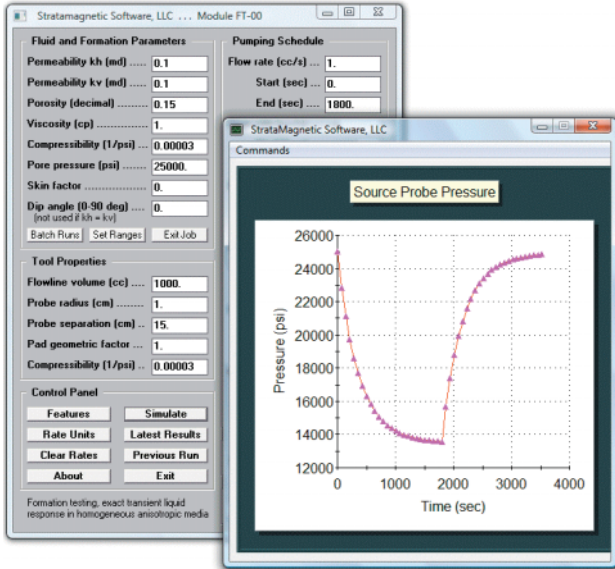
Figure 7.2b. Isotropic, low permeability –
large flowline volume, no skin.
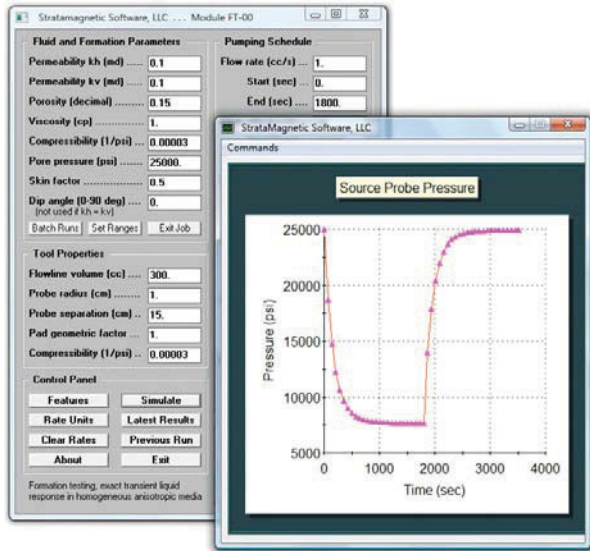
Figure 7.2c. Isotropic, low permeability –
small flowline volume, with skin.
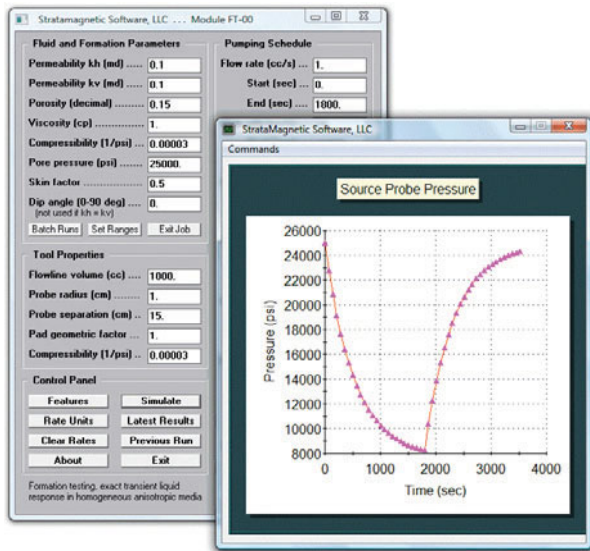
Figure 7.2d. Isotropic, low permeability –
large flowline volume, with skin.

Consider this scenario. A single formation tester probe with nozzle radius R_w withdraws fluid at a constant volume flow rate Q until steady-state is achieved.   Then the pressure drop $\Delta P_s \equiv P_{source}(t_\infty) - P_0$ is measured.   The combination $k_h^{2/3} k_v^{1/3}$ in Equation 7.1 is the "spherical permeability," usually denoted by k_s. When Q > 0, the tool operates in a fluid withdrawal mode; when Q < 0, it is operating in an injection mode. Therefore, k_s can be obtained using $\Delta P_s = - Q\mu / (4\pi k_s R_w)$ or straightforwardly, $k_s = - Q\mu / (4\pi R_w \Delta P_s)$. Simple? No. The ∞ subscript emphasizes that these results apply at steady-state only – at the rigsite this may mean long wait times for low permeability formations that exceed hours and days. Second, even if wait times were small, only the lumped quantity $k_h^{2/3} k_v^{1/3}$ is available and not k_h and k_v individually. Both are needed in hydraulic fracturing, wellbore instability and infill drilling applications, in addition to mudcake formation analysis. Thus, this well known procedure is limited in usefulness.

In this chapter, we will focus on applications where steady-state pressures *can* be achieved. This assumption means that transient effects associated with formation tester flowline compression effects have disappeared so that the "flowline volume" term in the complete mathematical pressure transient formulation no longer exists (note, formation fluid entering or leaving the flowline first encounter "cushioning" effects due to compressibility, effects which disappear at steady-state).   When this is so, major simplifications for the analytic solution are possible and exact solutions are possible.

7.2.3 FT-00 and FT-01.

Forward model "FT-00" is an exact, closed form analytical solution for liquid flow problems for all horizontal and vertical permeabilities, viscosities, porosities and compressibilities, for a wide range of tool parameters and flow rate functions. It is derived in Chin et al (2014) and accessible through the user interface in Figure 7.1. On the other hand, inverse model "FT-01" is exact, applying to all dip angles, but only when the volume flow rate is a constant Q for all time. This model is also derived from the complete formulation, but its algebraic structure does not resemble that of FT-00 at all. In our research, we created numerical solutions for pressure response using FT-00 for sets of horizontal and vertical permeabilities at given dip angles – using this pressure response together with FT-01, we reproduce the k_h and k_v values originally assumed. We now discuss FT-01 in detail.

Chin et al (2014) provides detailed mathematical models for permeability prediction – remember, again, that the pore pressure is assumed to be known (and immediately measurable) in this chapter. It is shown that k_h, k_v and the anisotropy k_h/k_v satisfy nonlinear cubic algebraic equations of the form $k_h^3 + (\ ) \ k_h + (\ ) = 0$, $k_v^{3/2} + (\ ) \ k_v + (\ ) = 0$ and $(k_h/k_v) + (\ ) \ (k_h/k_v)^{1/3} + (\ ) = 0$ are obtained where ( ) represents various lumped parameters depending on pressure drops, fluid and formation properties. The quantities in parentheses are explicitly stated in the foregoing reference.

7. 3 Inverse examples – dip angle, multivalued solutions and skin.

We introduce new permeability prediction methods by way of examples. We begin by presenting the capabilities of the single-phase-flow forward simulator FT-00 for liquids.

7.3.1   Forward model FT-00.

We will straightforwardly summarize the required input parameters by reproducing the software screen shown in Figure 7.3.1a. Several blocks are apparent, namely, "Fluid and Formation Parameters," "Tool Properties," and "Pumping Schedule." A basic understanding of these input variables is assumed and we will not explain their physical significance here.   Figure 7.3.1a summarizes input parameters for a multi-rate pump schedule with mixed production and injection with both long and short time durations. Simulations are extremely fast and require at most seconds in typical applications. The pump schedule constructed above is plotted in program output in Figure 7.3.1b.

Source and observation probe transient pressure responses are given in Figures 7.3.1c and 7.3.1d. Observe the rapid equilibration in source pressure and close correlation between it and flow rate (this is, compare Figures 7.3.1b and 7.3.1c). At the observation probe, as is evident from Figure 7.3.1d, slower equilibration and smearing due to diffusion are found. In general, the lower the formation permeability, the greater the diffusion. This diffusion is both bad and good. It is "bad" when steady pressure drops are required for input into steady flow models for permeability prediction. However, it is "good" when rapid transient interpretation approaches (for low permeability formations) are used.
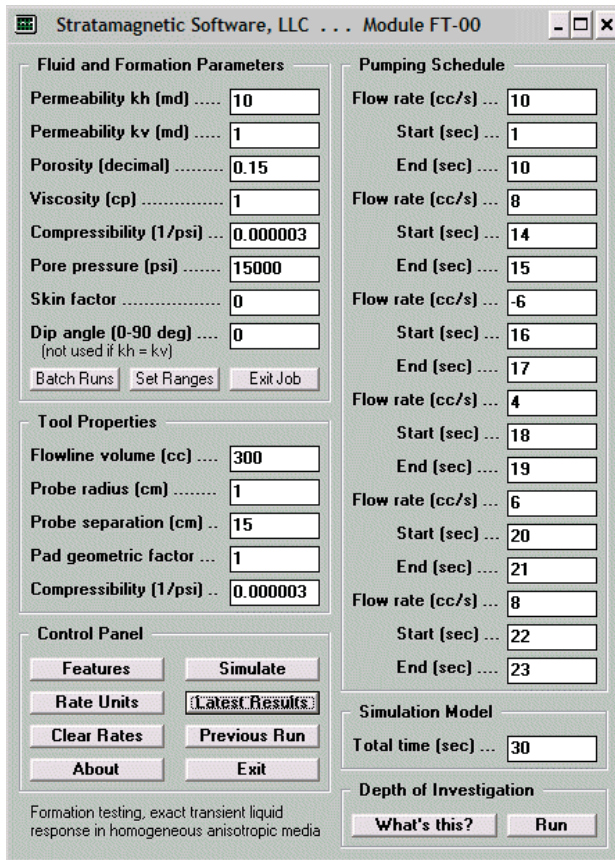
Figure 3.1a. Forward simulation assumptions.
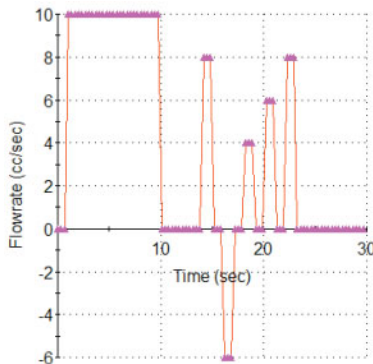
Figure 7.3.1b. Pumpout schedule, volume flow rate.
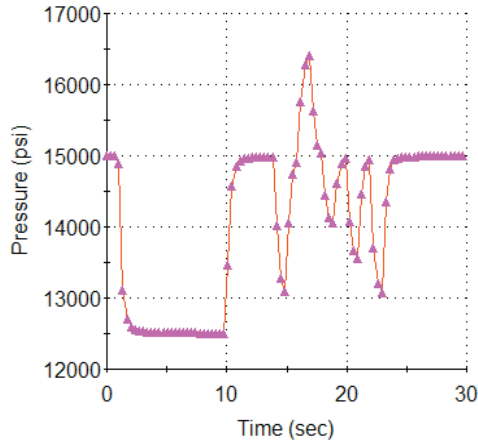
Figure 7.3.1c. Source probe pressure.
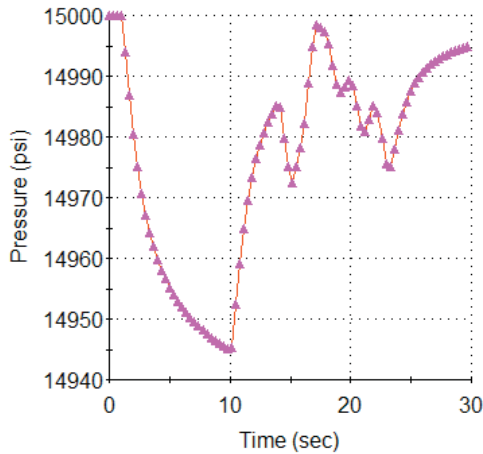
Figure 7.3.1d. Observation probe pressure (used for dual probe tools).

7.3.2 Inverse model FT-01 – multivalued solutions.

We will describe new inverse capabilities by way of calculation. In the following run, the fluid, formation and tool parameters of Figure 7.3.1a are retained, except that the dip angle is changed from 0 to 45 deg and a constant 10 cc/s pump rate is assumed for all time. Source (left) and observation probe (right) pressure transient responses are shown in Figure 7.3.2a – again, observe how diffusion slows the equilibration to steady-state at a location just 15 cm away from the source.
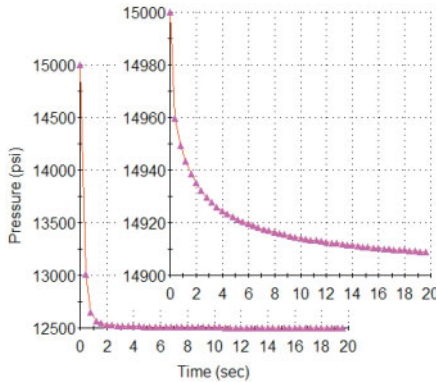
Figure 7.3.2a. Source (bottom) and observation probe (top)
pressure responses.

The computed Δp's (probe *minus* a dynamically unimportant pore
pressure) from FT-00 are

Time (s)	Δp_{source} (psi)	Δp_{observ} (psi)
0.100E+02	-0.24948E+04	-0.85789E+02
0.200E+02	-0.25001E+04	-0.91263E+02
0.500E+02	-0.25045E+04	-0.96208E+02
0.100E+05	-0.25116E+04	-0.10421E+03

We now consider the inverse problem and assume that pressure pair
data (above table) are obtained from a dual probe tool. The input screen
in Figure 7.3.1a assumes that the skin coefficient is S = 0; thus, the
assumptions in the software input screen for FT-01 in Figure 7.3.2b
consistently assume zero skin. First examine our 10,000 sec (three hour)
data. Exact calculation shows three possible solutions, namely,

Tentative permeabilities (md) ...

```
Complex KH root # 1:   -10.97 +    0.00 i, KV:    0.83
Complex KH root # 2:    10.07 +    0.00 i, KV:    0.99
Complex KH root # 3:     0.91 +    0.00 i, KV: 121.96
```
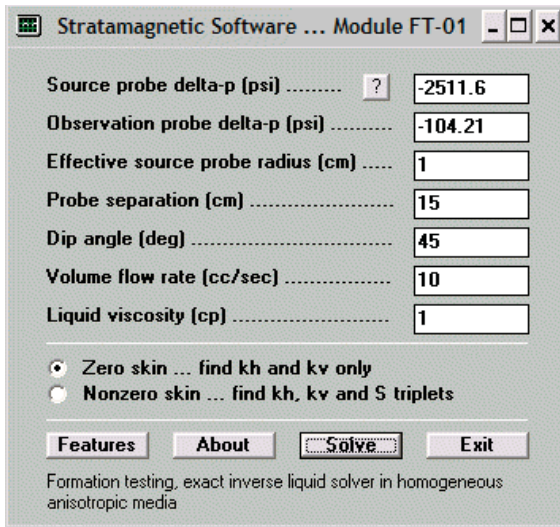
Figure 7.3.2b. Inverse steady-state solver FT-01.

In this case, two of the roots are easily ruled out; the first k_h is negative, while the third k_h is substantially less than k_v. The remaining k_h and k_v results, at 10.07 md and 0.99 md, are almost identical to the assumed 10 md and 1 md in the forward simulation creating the data. The method reproduces assumed permeability data exactly in this calculation with non-vanishing dip.

We emphasize that this success is a nontrivial event. FT-00 solves a fully transient model (via a complex complementary error function with flowline storage and dip angle) while FT-01 solves an analytically derived polynomial equation valid only at steady-state. Agreement and consistency between the two approaches ensures correct mathematics and software logic. This large time validation case thus provides a demanding test of both models.

In field applications, one might use unsteady data that is not consistent with the math model due to cost considerations and risks of tool sticking. Using ten-second pressure data in this case gives k_h = 12.49 md and $k_v = 0.65$ md. Twenty-second data yields 11.68 and 0.74, while fifty-second data leads to 11.02 and 0.83 – all acceptable, relative to the 10 md and 1 md assumed in FT-00. This accuracy is possible because the formation is relatively permeable.

If in the screen of Figure 7.3.2b we had checked "nonzero skin," or "S," a different less restrictive mathematical model with increased degrees of freedom is used. In the present calculation, the algorithm would return a list of possible solutions, that is, (k_h, k_v, S) triplets, together with the corresponding spherical permeability k_s listed at the far right of the table below (the zero skin solution obtained above is highlighted in bold red).

```
kh(md)  kv(md)  S   ks(md)

 7.00    8.00  0.62  7.32
 7.00    9.00  0.63  7.61
 7.00   10.00  0.64  7.88
 8.00    5.00  0.52  6.84
 8.00    6.00  0.56  7.27
 8.00    7.00  0.59  7.65
 9.00    3.00  0.36  6.24
 9.00    4.00  0.44  6.87
10.00    1.00  0.01  4.64 (red)
10.00    2.00  0.21  5.85
```

7.3.3 Effects of dip angle – detailed calculations.

The effects of dip angle are well known physically. For example, at zero dip, the tester "sees" k_h from all directions, while at 90 deg, it "sees" k_h from left and right, but k_v from top and bottom (actually, a complicated function of both applies at each azimuthal angle). Since typically $k_h > k_v$, the measured pressure drop in a vertical well is less than that for one that is horizontal or deviated. As an example, first consider the forward simulation analysis in Figure 7.3.3a with zero dip angle and a pump rate fixed at 10 cc/s for all time.

We will vary the dip angle from 0 to 90 deg with all other parameters unchanged. Source pressure responses for all runs will be identical since they depend on spherical permeability k_s only, in particular, as shown in Figure 7.3.3b. But, as expected, transient responses at the observation probe (numbered by dip angle) vary significantly in both magnitude and shape as seen from Figure 7.3.3c. For the $k_h = 10$ md, $k_v = 1$ md example here, pressure drops vary over a 200 psi range as dip angles increase. These forward simulation results are exact consequences of the analytical source model.
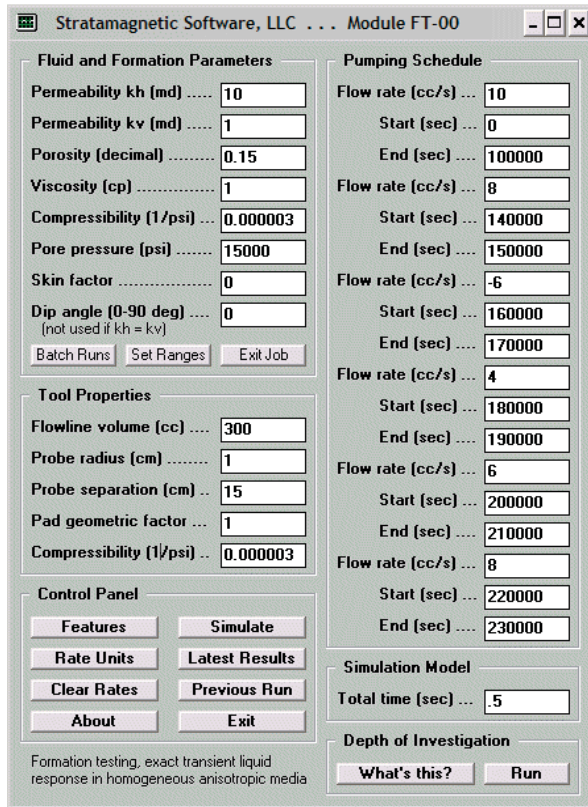
Figure 7.3.3a. Constant rate pumping example.
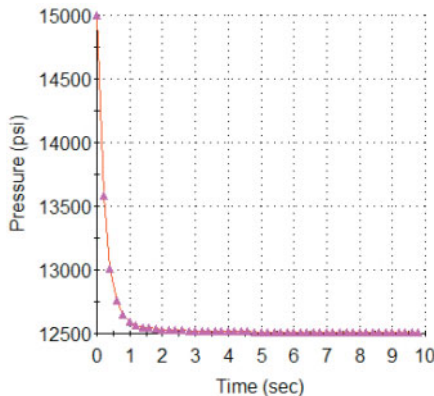
Figure 7.3.3b. Source probe response.
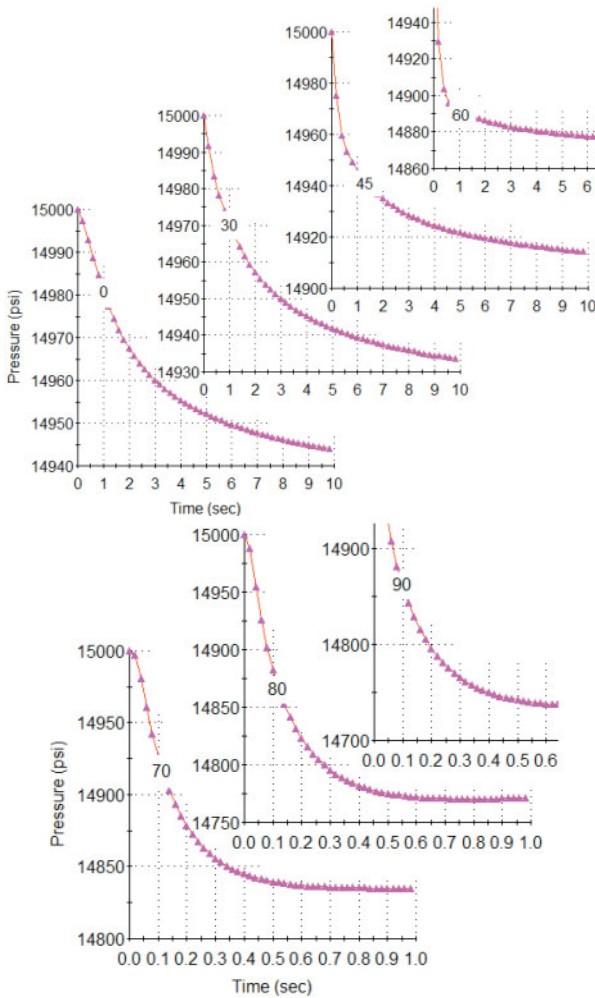
Figure 7.3.3c. Observation probe responses versus dip angle.

We can view the foregoing conclusions from the inverse perspective. Suppose a deviated well were drilled at 45 degrees dip. The 45 degree dip, zero skin forward simulation gives large time (100,000 sec) pressure drops of 2,512 psi at the source and 104.6 psi at the distant probe; the corresponding inverse calculation gives a consistently accurate k_h = 10.02 md and k_v = 1.00 md (in agreement with permeabilities assumed in the forward FT-00 simulation).

But what if, for this measured pressure pair, the exact FT-01 inverse solver were not available? If the industry-standard formula (implicitly assuming zero dip) were used, one would instead calculate $k_h = 7.43$ md and $k_v = 1.81$ md with a k_v/k_h of 0.244 versus an exact value of 0.1. Such large errors imply grave production and economic planning consequences. In the table below, inverse calculations for permeability using FT-01 are performed with the above pressures through a range of dip angles to show the significance of hole deviation.

```
Dip   kh    kv   kv/kh
0     7.43  1.81  0.244
30    8.35  1.44  0.172
45   10.02  1.00  0.100
60   14.13  0.50  0.035
70   20.88  0.23  0.011
80   41.89  0.06  0.001
90  424.89  0.00  0.000
```

Comprehensive discussions for inverse methods at "higher," that is, "not low" permeabilities or mobilities are offered in Chin et al (2014) and Chin et al (2015) and readers are referred to these references for additional details.

7.3.4 Pulse interaction method – an introduction.

In the next and final chapter, we highlight inverse methods for pore pressure and mobility in tight zones which, using early time data, say from the first five minutes of logging, provide usable predictions. The "Formation Testing While Drilling" (or, FTWD) method will operate with a single source probe and give predictions for pore pressure and spherical permeability or mobility. On the other hand, the "pulse interaction" method for dual probe tools will provide k_h and k_v individually – when used together with the FTWD approach, pore pressure can also be extrapolated from unequilibrated pressure readings. This approach works best for low permeability environments, but applies to those that are not especially low – tus, a short introduction is given below. A new "phase delay" approach is also described in Chin et al (2015), however, because hardware is not available at the present time to obtain data, we will omit discussion of the method here.

The above FT-01 inverse approach requires fully equilibrated steady pressure drop data at source and observation probes. In a higher permeability environment, this is not severe; as seen earlier, 20 sec data may well suffice under certain conditions if data integrity problems are not an issue. In low permeability "tight" formations, however, steady observation probe responses may not be achievable for hours or days. Even if rig costs were not a concern, the risks of tool sticking are – thus, one is motivated to design permeability prediction methods that take advantage of the physics and respond to earlier time dynamic data.

We emphasize that the application of steady formulas to permeability interpretation is an artificial limitation used only to render the mathematics tractable. As noted, steady conditions are usually achievable in higher permeability formations so that such models are sometimes useful. In low permeability zones, field experience and exact calculations (using FT-00) show that source probe responses equilibrate very rapidly. Since they depend only on the spherical permeability k_s (and not k_h or k_v individually), the value of k_s inferred from the source probe pressure drop is an accurate one for interpretation purposes. The conventional steady flow permeability formula $k_s = Q\mu / \{4\pi R_w (P_0 - P_s)\}$ can be used which, again, only constrains the relationship between k_h and k_v (here, Q is volume flow rate, μ is viscosity, R_w is effective probe radius, and "$P_0 - P_s$" is the source probe pressure drop). In order to quantify k_h and k_v, additional information is required. Unlike FT-01, we will not draw upon steady pressure data at the observation probe.

In the example below, a k_s of 4.642 md (corresponding to a $k_h = 10$ md, $k_v = 1$ md and "zero skin" S = 0 case) is *fixed* throughout and simulations are performed with different combinations of k_h and k_v. We can think of k_s as being available from a single source probe drawdown measurement and that k_h and k_v are to be found. Again, source probe results for the three runs are identical, but observation probe pressure transients are discernible from each other. Figures 7.3.4a and 7.3.4b are clearly different – the former is highly smeared while the pulses in the latter remain distinct; peak pressure drops (from printed FT-00 output not shown) are 19 psi for Figure 7.3.4a and 159 psi for Figure 7.3.4b. Again, these differences are seen from early time transient behavior. Observation probe pressure transient waveform shapes in Figures 7.3.4b and 7.3.4c are similar, at least on a normalized basis. However, they are very different in magnitude. From printed FT-00 output, peak pressure drops are 159 psi and 787 psi, respectively.

Clear differences in observation probe characteristics suggest that permeability contrasts can be effectively examined using short duration pulse interference rather than long time steady-state drawdown.   The dynamical interactions are strongly dependent on anisotropy so that conclusions on k_h and k_v can be found from enough trial and error runs.
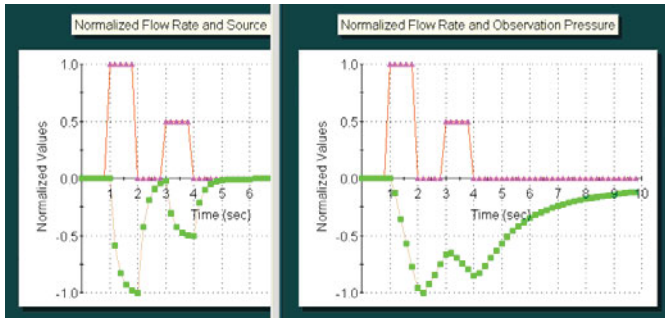

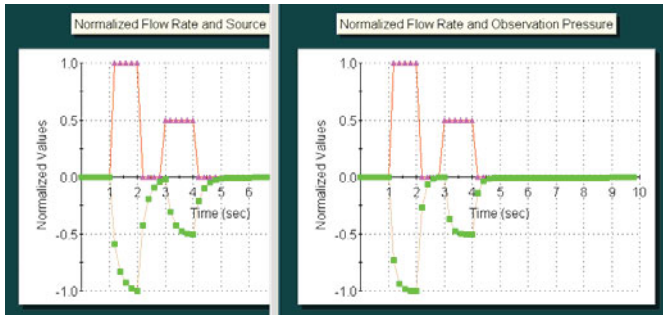**Figure 7.3.4a.** $k_h = 10$ md, $k_v = 1$ md (that is, $k_h > k_v$).
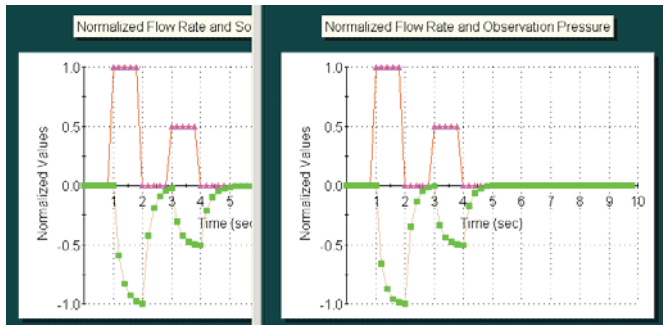

Figure 7.3.4b. $k_h = k_v = 4.642$ md (that is, isotropic).

Figure 7.3.4c. $k_h = 1$ md, $k_v = 100.0$ md (that is, $k_h < k_v$).

Under what circumstances is our "pulse interaction method" expected to perform optimally? Interestingly, the lower the permeability, the better the accuracy – a somewhat counter-intuitive situation that runs at odds to our experiences with steady-state methods. The explanation is simple: at low permeabilities, diffusion predominates, so that dynamical interactions between short pulses with high frequency content are strongest. This means that high signal-to-noise ratios are achieved for the purposes of history matching for permeability.

Again, interference effects are most pronounced at low permeabilities when diffusion is dominant – precisely the field condition associated with long wait times, high rig costs and increased risk of tool sticking. In contrast, large-time pressure responses associated with constant rate drawdown methods only produce small pressure drops which may not be accurately measured. We do emphasize that, at earlier times, the effects of porosity, fluid compressibility and flowline volume do appear in the data, so that repeated calculation using different pulse types with varied durations, amplitudes and time separations is advisable.

It is important to emphasize that no new hardware is required for pulse interaction analysis. We offer a word of caution in the forward history matching procedure, however. Because we are evaluating flow differences associated with the diffusion process itself, it is important that the host mathematical model does not itself introduce additional numerical diffusion effects related to round-off and truncation errors. These effects, commonly referred to as "artificial viscosity," are most prominent with finite difference and finite element simulators, even when second, up to fourth-order, schemes are used. For this reason, exact analytical models such as that underlying FT-00 should be used to interpret pulse interactions.

7.4 References.

- Chin, W.C., Zhou, Y., Feng, Y., Yu, Q. and Zhao, L., *Formation Testing: Pressure Transient and Contamination Analysis*, John Wiley & Sons, Hoboken, New Jersey, 2014.

- Chin, W.C., Zhou, Y., Feng, Y. and Yu, Q., *Formation Testing: Low Mobility Pressure Transient Analysis*, John Wiley & Sons, Hoboken, New Jersey, 2015.

8
Pore Pressure Prediction
in Low Mobility or Tight Formations

In Chapter 7, we assumed that formation permeabilities or mobilities were high enough that pore pressures could be obtained from almost immediate formation tester readings. Pore pressures are required for mudcake growth analysis and a simple measurement from a single-probe formation tester provides the needed value. When single-probe tools are used in such formations, the spherical permeability $k_h^{2/3}k_v^{1/3}$ is also available as noted. Although this does not give k_h or k_v individually, so long as the net value of spherical permeability is large, say 10 md or higher, formation effects are unlikely to contribute to mudcake growth. Thus, no further analysis is required. On the other hand, if k_s is extremely small, it may be necessary to determine "worst small case" values for k_h and k_v to ascertain if fluid in the direction of mud flow is impacted - thus, the dual probe methods described earlier are necessary.

Previously we also introduced a "pulse interaction" method. We noted that while k_s is uniquely determined from the rapidly equilibrating flow at the source probe, the values of k_h and k_v are not. To determine these, we consider multiple sets of (k_h, k_v) values and simulate the interaction of rectangular pulse trains at the observation probe. Interactions are highly dependent on anisotropy. The correct solution is the one that matches observed empirical results. We will explore pulse interaction methods here in greater detail. Finally, we return to the problem of obtaining pore pressure and k_s from single-probe measurements in low mobility formations, ideally using methods specially designed to take advantage of environmental properties so that solutions are possible from data obtained during the first minute of logging. Our last subject in this regard will be "formation testing while drilling" (or, "FTWD") methods that this author had designed for commercial Halliburton and CNOOC/COSL applications.

8.1 Low permeability pulse interference testing – nonzero skin.

Again, pulse interaction methods are useful in low mobility formations because closely-spaced pulses interact strongly as they propagate toward the observation probe.   The interaction is strongly dependent on anisotropy, making pulse interaction approaches attractive in determining horizontal and vertical permeabilities. Test times are also shortened.   Moreover, signal-to-noise ratios are strongest in low permeability formations, for which diffusion-based interactions are be strongest. In this section, we present some examples with and without skin effects and demonstrate the versatility of the new approach.

To   demonstrate   this   new   capability,   we   summarize   some simulations from Chapter 5 of Chin et al (2014). In that reference, Run 4 considered   a   conventional   drawdown-only   test   on   an   anisotropic formation with the FT-00 forward simulation assuming $k_h = 10$ md, $k_v = 1$ md and $S = 3$. The prediction of these same values is the objective of any inverse model.   Using our FT-01 inverse model and the FT-00 calculated pressure drop data in the "with skin" mode, we had obtained the following possible inverse triplet solutions from steady-state inputs.

```
kh(md) kv(md)  S    ks(md)
 11.00   1.00  3.26   4.95
 11.00   2.00  4.36   6.23
 11.00   3.00  5.14   7.13
 11.00   4.00  5.76   7.85
 11.00   5.00  6.28   8.46
 11.00   6.00  6.74   8.99
 11.00   7.00  7.14   9.46
 11.00   8.00  7.51   9.89
 11.00   9.00  7.85  10.29
 12.00  10.00  8.17  10.66
```

A unique determination for k_h, k_v and S usually cannot be made because only two pressure drop data sets are available.   Within the framework of steady-state flow, the above solution sets are the best that can be done. There is no way to determine which triplet represents the physical solution. A transient pulse interaction test provides useful clues. To illustrate the proposed method, consider the first red dataset from the top line with $k_h = 11$ md, $k_v = 1$ md and $S = 3.26$, assuming the pulse train in the input screen below, which lasts about four seconds (other assumed parameters are given in the input screen). We also consider the last red dataset at the bottom line with $k_h = 12$ md, $k_v = 11$ md and $S = 8.17$. Pulse interaction results are displayed under Run A and Run B.

Run A, Pulse interaction, k_h >> k_v, moderate skin.

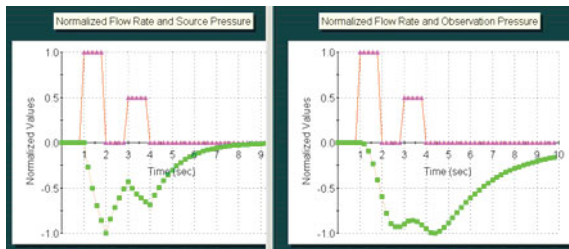**Figure 8.1.** Run 7 inputs and outputs.

```
FORMATION TESTER PRESSURE TRANSIENT ANALYSIS

Exact analytical solution for Darcy ellipsoidal flow
(homogeneous anisotropic media with flowline storage
and skin) using complex complementary error function.

Specific limit considered -
....... Anisotropic flow model with storage and skin

FLUID AND FORMATION PARAMETERS
Formation kh permeability ....... (md):   0.1100E+02
Formation kv permeability ....... (md):   0.1000E+01
Porosity ................... (decimal):   0.1500E+00
Viscosity ...................... (cp):   0.1000E+01
Pore fluid compressibility ... (1/psi):   0.3000E-05
Pore pressure .................. (psi):   0.1500E+05
Skin factor ......... (dimensionless):   0.3260E+01
Dip angle ................ (0-90 deg):   0.0000E+00

TOOL PROPERTIES
Flowline volume ................ (cc):   0.4000E+03
Probe radius ................... (cm):   0.1000E+01
Probe separation ............... (cm):   0.1500E+02
Pad geometric factor . (dimensionless):   0.1000E+01
Flowline fluid compressibility (1/psi):   0.3000E-05

PUMPING SCHEDULE AND SIMULATION PARAMETERS
Drawdown #1, Flow rate ........ (cc/s):   0.1000E+02
            Beginning time .... (sec):   0.1000E+01
            Ending time ....... (sec):   0.2000E+01
Drawdown #2, Flow rate ....... (cc/s):   0.5000E+01
            Beginning time .... (sec):   0.3000E+01
            Ending time ....... (sec):   0.4000E+01
Total simulation time ......... (sec):   0.1000E+02

DEFINITIONS
Time ... Elapsed time (sec)
Rate ... Drawdown flow rate (cc/s)
Ps* .... Source pressure with hydrostatic (psi)
Pr* .... Observation pressure with hydrostatic (psi)
Ps** ... Source pressure, no hydrostatic (psi)
Pr** ... Observation pressure, no hydrostatic (psi)

 Time (s)  Rate (cc/s)  Ps* (psi)   Pr* (psi)   Ps**(psi)    Pr**(psi)    Pr**/Ps**
0.120E+01  0.10000E+02  0.13468E+05  0.15000E+05 -0.15325E+04 -0.17012E+00  0.11101E-03
0.200E+01  0.00000E+00  0.93599E+04  0.14991E+05 -0.56401E+04 -0.93821E+01  0.16635E-02
0.300E+01  0.50000E+01  0.12543E+05  0.14986E+05 -0.24571E+04 -0.14148E+02  0.57580E-02
0.400E+01  0.00000E+00  0.11105E+05  0.14985E+05 -0.38953E+04 -0.14915E+02  0.38289E-02
0.500E+01  0.00000E+00  0.13299E+05  0.14986E+05 -0.17010E+04 -0.13845E+02  0.81393E-02
0.600E+01  0.00000E+00  0.14254E+05  0.14990E+05 -0.74637E+03 -0.96114E+01  0.12877E-01
0.700E+01  0.00000E+00  0.14671E+05  0.14994E+05 -0.32923E+03 -0.64756E+01  0.19669E-01
0.800E+01  0.00000E+00  0.14854E+05  0.14996E+05 -0.14636E+03 -0.44665E+01  0.30517E-01
0.900E+01  0.00000E+00  0.14934E+05  0.14997E+05 -0.65891E+02 -0.32082E+01  0.48689E-01
0.980E+01  0.00000E+00  0.14965E+05  0.14997E+05 -0.35309E+02 -0.25414E+01  0.71976E-01
```

Run B, Pulse interaction, $k_h \approx k_v$, high skin.

Next consider the last nearly isotropic triplet with $k_h = 12$ md, $k_v = 10$ md and $S = 8.17$, representing a significant contrast to that of Run A.
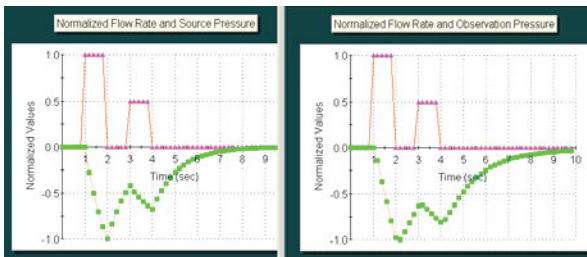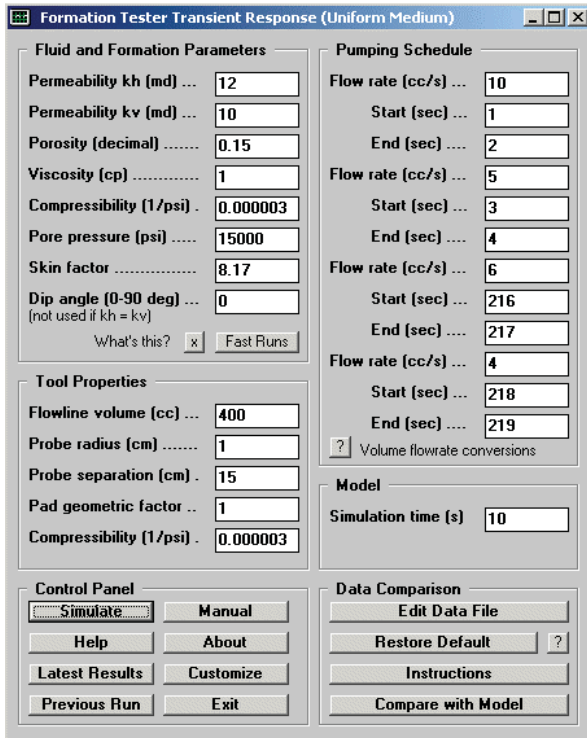

Figure 8.2. Run 8 inputs and outputs.

```
FORMATION TESTER PRESSURE TRANSIENT ANALYSIS

Exact analytical solution for Darcy ellipsoidal flow
(homogeneous anisotropic media with flowline storage
and skin) using complex complementary error function.

Specific limit considered -
....... Anisotropic flow model with storage and skin

FLUID AND FORMATION PARAMETERS
Formation kh permeability ....... (md):   0.1200E+02
Formation kv permeability ....... (md):   0.1000E+02
Porosity .................. (decimal):   0.1500E+00
Viscosity ...................... (cp):   0.1000E+01
Pore fluid compressibility ... (1/psi):   0.3000E-05
Pore pressure ................. (psi):   0.1500E+05
Skin factor ......... (dimensionless):   0.8170E+01
Dip angle ................ (0-90 deg):   0.0000E+00

TOOL PROPERTIES
Flowline volume ................ (cc):   0.4000E+03
Probe radius ................... (cm):   0.1000E+01
Probe separation ............... (cm):   0.1500E+02
Pad geometric factor . (dimensionless):   0.1000E+01
Flowline fluid compressibility (1/psi):   0.3000E-05

PUMPING SCHEDULE AND SIMULATION PARAMETERS
Drawdown #1, Flow rate ........ (cc/s):   0.1000E+02
            Beginning time .... (sec):   0.1000E+01
            Ending time ....... (sec):   0.2000E+01
Drawdown #2, Flow rate ........ (cc/s):   0.5000E+01
            Beginning time .... (sec):   0.3000E+01
            Ending time ....... (sec):   0.4000E+01
Total simulation time ......... (sec):   0.1000E+02

DEFINITIONS
Time ... Elapsed time (sec)
Rate ... Drawdown flow rate (cc/s)
Ps* .... Source pressure with hydrostatic (psi)
Pr* .... Observation pressure with hydrostatic (psi)
Ps** ... Source pressure, no hydrostatic (psi)
Pr** ... Observation pressure, no hydrostatic (psi)

 Time (s)   Rate (cc/s)   Ps* (psi)    Pr* (psi)     Ps**(psi)     Pr**(psi)     Pr**/Ps**
0.120E+01  0.10000E+02  0.13473E+05  0.14996E+05  -0.15272E+04  -0.36738E+01  0.24056E-02
0.200E+01  0.00000E+00  0.94656E+04  0.14975E+05  -0.55344E+04  -0.25413E+02  0.45919E-02
0.300E+01  0.50000E+01  0.12705E+05  0.14984E+05  -0.22947E+04  -0.16436E+02  0.71627E-02
0.400E+01  0.00000E+00  0.11280E+05  0.14979E+05  -0.37201E+04  -0.20984E+02  0.56407E-02
0.500E+01  0.00000E+00  0.13456E+05  0.14988E+05  -0.15437E+04  -0.12433E+02  0.80541E-02
0.600E+01  0.00000E+00  0.14358E+05  0.14994E+05  -0.64165E+03  -0.63941E+01  0.99651E-02
0.700E+01  0.00000E+00  0.14733E+05  0.14997E+05  -0.26726E+03  -0.34062E+01  0.12745E-01
0.800E+01  0.00000E+00  0.14888E+05  0.14998E+05  -0.11168E+03  -0.19431E+01  0.17399E-01
0.900E+01  0.00000E+00  0.14953E+05  0.14999E+05  -0.46928E+02  -0.12074E+01  0.25728E-01
0.980E+01  0.00000E+00  0.14976E+05  0.14999E+05  -0.23619E+02  -0.87933E+00  0.37230E-01
```

In Runs A and B, the pressure waveforms at the observation probes clearly differ in shape. Also, differences in their magnitudes are clearly discernible, e.g., peak pressure drawdowns of 14.9 psi versus 21.0 psi, values easily resolved by typical pressure transducers. *It is clear that by generating and measuring pulse interactions – and comparing their effects with exact forward simulation results – a unique determination of k_h, k_v and S can be made without using acoustic or resistivity or other measurements.*

8.2 Low permeability pulse interference testing – zero skin.

Dual probe methods offer some improvement over those for single-probe tools. With traditional constant rate drawdown methods, large wait times are still required in low permeability formations, but only because interpretation formulas for shorter times are not available. Multipulse interaction methods are different. Pressure waveform differences between different test runs at the observation probe are clearly discernible because diffusion allows pulses to strongly interfere – and can be analyzed by "history matching" methods. What are typical pulse widths and separations in practice? The answer depends on waveform sampling times. For example, one often-used tool samples pressure measurements at 0.25 sec – therefore, operational time scales would be taken on the order of 2-5 seconds.

In Runs C, D and E, a spherical permeability k_s of 4.642 md is fixed and simulations are performed with different combinations of k_h and k_v (again, spherical permeability can be determined from source probe data alone). Source probe results for the three runs are identical, but observation probe pressure transients are discernible from each other. For example, those in Runs C and D are clearly different – the former is highly smeared while the pulses in the latter remain distinct. These shape contrasts are evident from Figures 8.3 and 8.4; peak pressure drops are 19 psi in Run C and 159 psi in Run D. Again, these differences are seen from early time transient behavior. Observation probe pressure transient waveform shapes in Runs D and E are similar, as indicated in Figures 8.4 and 8.5. However, they are very different in magnitude, e.g., peak pressure drops are 159 psi and 787 psi, respectively. Clear differences in observation probe characteristics importantly suggest that permeability contrasts can be effectively examined using short duration pulse interference rather than long time steady-state drawdown. In summary, k_s is determined from a single source probe continuous drawdown measurement, and k_h and k_v are individually obtained by trial and error using computations with exact solvers like FT-00. The correct values are those whose waveforms match those at the observation probe. Again, pulse interactions are used to determine horizontal and vertical permeability, while pore pressure and spherical permeability (from single probe tools) require the FTWD method to be discussed next.

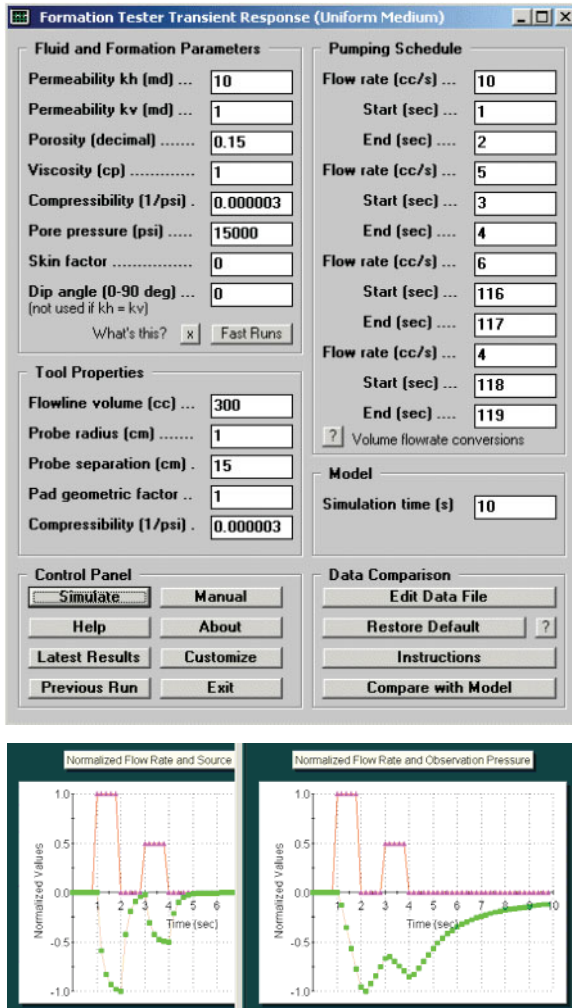**Run C, k_s = 4.642 md, with k_h = 10 md and k_v = 1 md.**

Figure 8.3. Run C inputs and outputs.

```
FORMATION TESTER PRESSURE TRANSIENT ANALYSIS

Exact analytical solution for Darcy ellipsoidal flow
(homogeneous anisotropic media with flowline storage
and skin) using complex complementary error function.

Specific limit considered -
.... Anisotropic flow model with storage and no skin

FLUID AND FORMATION PARAMETERS
Formation kh permeability ....... (md):  0.1000E+02
Formation kv permeability ....... (md):  0.1000E+01
Formation spherical permeability  (md):  0.4642E+01
Porosity ................... (decimal):  0.1500E+00
Viscosity ....................... (cp):  0.1000E+01
Pore fluid compressibility ... (1/psi):  0.3000E-05
Pore pressure ................. (psi):  0.1500E+05
Skin factor .......... (dimensionless):  0.0000E+00
Dip angle ................ (0-90 deg):  0.0000E+00

TOOL PROPERTIES
Flowline volume ................ (cc):  0.3000E+03
Probe radius ................... (cm):  0.1000E+01
Probe separation ............... (cm):  0.1500E+02
Pad geometric factor . (dimensionless):  0.1000E+01
Flowline fluid compressibility (1/psi):  0.3000E-05

PUMPING SCHEDULE AND SIMULATION PARAMETERS
Drawdown #1, Flow rate ....... (cc/s):  0.1000E+02
            Beginning time .... (sec):  0.1000E+01
            Ending time ....... (sec):  0.2000E+01
Drawdown #2, Flow rate ....... (cc/s):  0.5000E+01
            Beginning time .... (sec):  0.3000E+01
            Ending time ....... (sec):  0.4000E+01
Total simulation time ......... (sec):  0.1000E+02

 Time (s)  Rate (cc/s)  Ps* (psi)   Pr* (psi)   Ps**(psi)   Pr**(psi)    Pr**/Ps**
0.100E+01  0.10000E+02  0.15000E+05  0.15000E+05 -0.74470E-03  0.00000E+00  0.00000E+00
0.200E+01  0.00000E+00  0.12591E+05  0.14981E+05 -0.24089E+04 -0.19185E+02  0.79640E-02
0.300E+01  0.50000E+01  0.14941E+05  0.14987E+05 -0.58947E+02 -0.13339E+02  0.22629E+00
0.400E+01  0.00000E+00  0.13785E+05  0.14983E+05 -0.12150E+04 -0.16961E+02  0.13959E-01
0.500E+01  0.00000E+00  0.14965E+05  0.14989E+05 -0.34729E+02 -0.11348E+02  0.32675E+00
0.600E+01  0.00000E+00  0.14991E+05  0.14993E+05 -0.86384E+01 -0.69764E+01  0.80760E+00
0.700E+01  0.00000E+00  0.14995E+05  0.14995E+05 -0.50172E+01 -0.48148E+01  0.95966E+00
0.800E+01  0.00000E+00  0.14997E+05  0.14996E+05 -0.34922E+01 -0.35945E+01  0.10293E+01
0.900E+01  0.00000E+00  0.14997E+05  0.14997E+05 -0.26323E+01 -0.28226E+01  0.10723E+01
0.980E+01  0.00000E+00  0.14998E+05  0.14998E+05 -0.21761E+01 -0.23871E+01  0.10970E+01
```

Run D, k$_s$ = 4.642 md, with k$_h$ = 4.642 md and k$_v$ = 4.642 md.

Figure 8.4. Run D inputs and outputs.

FORMATION TESTER PRESSURE TRANSIENT ANALYSIS

Exact analytical solution for Darcy ellipsoidal flow (homogeneous anisotropic media with flowline storage and skin) using complex complementary error function.

Specific limit considered -
...... Isotropic flow model with storage and no skin

FLUID AND FORMATION PARAMETERS
```
Formation kh permeability ....... (md):   0.4642E+01
Formation kv permeability ....... (md):   0.4642E+01
Formation spherical permeability (md):    0.4642E+01
Porosity ................... (decimal):   0.15000E+00
Viscosity ....................... (cp):   0.1000E+01
Pore fluid compressibility ... (1/psi):   0.3000E-05
Pore pressure ................. (psi):    0.1500E+05
Skin factor .......... (dimensionless):   0.0000E+00
Dip angle ................ (0-90 deg):     0.0000E+00
```

TOOL PROPERTIES
```
Flowline volume ................. (cc):   0.3000E+03
Probe radius ................... (cm):    0.1000E+01
Probe separation ............... (cm):    0.1500E+02
Pad geometric factor . (dimensionless):   0.1000E+01
Flowline fluid compressibility (1/psi):   0.3000E-05
```

PUMPING SCHEDULE AND SIMULATION PARAMETERS
```
Drawdown #1, Flow rate ........ (cc/s):   0.1000E+02
            Beginning time .... (sec):    0.1000E+01
            Ending time ....... (sec):    0.2000E+01
Drawdown #2, Flow rate ........ (cc/s):   0.5000E+01
            Beginning time .... (sec):    0.3000E+01
            Ending time ....... (sec):    0.4000E+01
Total simulation time ......... (sec):    0.1000E+02
```

Time (s)	Rate (cc/s)	Ps* (psi)	Pr* (psi)	Ps**(psi)	Pr**(psi)	Pr**/Ps**
0.100E+01	0.00000E+00	0.15000E+05	0.15000E+05	0.00000E+00	0.00000E+00	-----------
0.120E+01	0.10000E+02	0.13585E+05	0.14884E+05	-0.14147E+04	-0.11614E+03	0.82098E-01
0.200E+01	0.10000E+02	0.12591E+05	0.14841E+05	-0.24087E+04	-0.15868E+03	0.65879E-01
0.300E+01	0.50000E+01	0.14941E+05	0.15000E+05	-0.58929E+02	-0.30115E+00	0.51103E-02
0.400E+01	0.50000E+01	0.13785E+05	0.14920E+05	-0.12149E+04	-0.80226E+02	0.66034E-01
0.500E+01	0.00000E+00	0.14965E+05	0.14999E+05	-0.34719E+02	-0.90049E+00	0.25936E-01
0.600E+01	0.00000E+00	0.14991E+05	0.14999E+05	-0.86369E+01	-0.10268E+01	0.11889E+00
0.700E+01	0.00000E+00	0.14995E+05	0.14999E+05	-0.50165E+01	-0.83866E+00	0.16718E+00
0.800E+01	0.00000E+00	0.14997E+05	0.14999E+05	-0.34917E+01	-0.66929E+00	0.19168E+00
0.900E+01	0.00000E+00	0.14997E+05	0.14999E+05	-0.26319E+01	-0.54492E+00	0.20704E+00
0.980E+01	0.00000E+00	0.14998E+05	0.15000E+05	-0.21758E+01	-0.46971E+00	0.21588E+00

Run E, k_s = 4.642 md, with k_h = 1 md and k_v = 100.027 md.

Figure 8.5. Run E inputs and outputs.

```
FORMATION TESTER PRESSURE TRANSIENT ANALYSIS

Exact analytical solution for Darcy ellipsoidal flow
(homogeneous anisotropic media with flowline storage
and skin) using complex complementary error function.

Specific limit considered -
.... Anisotropic flow model with storage and no skin

FLUID AND FORMATION PARAMETERS
Formation kh permeability ....... (md):   0.1000E+01
Formation kv permeability ....... (md):   0.1000E+03
Formation spherical permeability  (md):   0.4642E+01
Porosity .................. (decimal):   0.1500E+00
Viscosity ....................... (cp):   0.1000E+01
Pore fluid compressibility ... (1/psi):   0.3000E-05
Pore pressure ................. (psi):   0.1500E+05
Skin factor .......... (dimensionless):   0.0000E+00
Dip angle ................ (0-90 deg):   0.0000E+00

TOOL PROPERTIES
Flowline volume ................ (cc):   0.3000E+03
Probe radius ................... (cm):   0.1000E+01
Probe separation ............... (cm):   0.1500E+02
Pad geometric factor . (dimensionless):   0.1000E+01
Flowline fluid compressibility (1/psi):   0.3000E-05

PUMPING SCHEDULE AND SIMULATION PARAMETERS
Drawdown #1, Flow rate ....... (cc/s):   0.1000E+02
            Beginning time .... (sec):   0.1000E+01
            Ending time ...... (sec):   0.2000E+01
Drawdown #2, Flow rate ....... (cc/s):   0.5000E+01
            Beginning time .... (sec):   0.3000E+01
            Ending time ...... (sec):   0.4000E+01
Total simulation time ......... (sec):   0.1000E+02

 Time (s)  Rate (cc/s)   Ps* (psi)   Pr* (psi)    Ps**(psi)    Pr**(psi)    Pr**/Ps**
0.120E+01  0.10000E+02  0.13585E+05  0.14481E+05 -0.14147E+04 -0.51926E+03  0.36704E+00
0.200E+01  0.00000E+00  0.12591E+05  0.14213E+05 -0.24087E+04 -0.78710E+03  0.32677E+00
0.300E+01  0.50000E+01  0.14941E+05  0.14997E+05 -0.58928E+02 -0.33926E+01  0.57571E-01
0.400E+01  0.00000E+00  0.13785E+05  0.14606E+05 -0.12149E+04 -0.39355E+03  0.32393E+00
0.500E+01  0.00000E+00  0.14965E+05  0.14998E+05 -0.34719E+02 -0.16963E+01  0.48857E-01
0.600E+01  0.00000E+00  0.14991E+05  0.15000E+05 -0.86368E+01  0.00000E+00  0.00000E+00
0.700E+01  0.00000E+00  0.14995E+05  0.15000E+05 -0.50164E+01  0.00000E+00  0.00000E+00
0.800E+01  0.00000E+00  0.14997E+05  0.15000E+05 -0.34917E+01  0.00000E+00  0.00000E+00
0.900E+01  0.00000E+00  0.14997E+05  0.15000E+05 -0.26319E+01  0.00000E+00  0.00000E+00
0.980E+01  0.00000E+00  0.14998E+05  0.15000E+05 -0.21758E+01  0.00000E+00  0.00000E+00
```

8.3 Formation Testing While Drilling (FTWD).

"Formation testing while drilling" (or, FTWD) aims at providing real-time pore pressure and mobility information to drillers and reservoir engineers. Accurate and timely pore pressure measurements are important to drilling safety and mud program planning as well as production, while mobility information is essential to geosteering and economic analysis. Meeting the challenges posed by FTWD is difficult. For example, tools will operate in high shock and vibration environments that degrade mechanical integrity, while high temperatures and pressures will limit microprocessor computing power and memory storage capabilities. Present FTWD tools are therefore single-pad devices which host both pumping and pressure measurement functions. Economic drivers also require quick data acquisition, which allow higher density information, while at the same time reducing the risks of stuck pipe incurred by steady-state methods. Toward these ends, a robust FT-PTA-DDBU approach was developed for FTWD applications, although the methodology applies to wireline, dual-probe and also packer tools without change.

8.3.1   Pressure transient drawdown-buildup approach.

The FTWD model was designed to accommodate several logging scenarios. Specific code implementations, using the "rational polynomial" in Chin et al (2014) discussed previously, include four options: (1) drawdown only, steady-state pressures available, (2) drawdown only, using general transient data, (3) drawdown-buildup, steady-state source pressures available, and (4) drawdown-buildup, general transient data. For practical reasons explained in the foregoing reference, "Best practices – data acquisition and processing," we will not focus on "drawdown only" approaches. Option (3) is actually doable in FTWD – steady-states are easier to achieve at source positions as opposed to other locations (as would be required in steady dual probe methods). However, for generality and brevity, we discuss only the validation of the Option (4) model.

8.3.2   Interpretation in low mobility, high flowline storage environments.

We will use the forward pressure data computed by FT-00 as shown in Figure 8.6a, noting a permeability of 0.1 md and a relatively large flowline storage volume of 400 cc, to evaluate Option (4) above. The

source probe response shows highly transient pressures that are far from equilibrium – pressures at a second observation location are provided for informational purposes only. In fact, the prospects of pore pressure and mobility prediction from the source response at first do not appear optimistic. From Figure 8.6a, the pore pressure and mobility should be 10,000 psi and 0.1 md/cp. For the inverse calculation, hosted by the screen in Figure 8.6b, we have used FT-00 source probe pressure data from 10.0, 14.8 and 19.6 seconds in FT-PTA-DDBU to find, with high accuracy, predictions of 9,951 and 0.11 md/cp. While the pressure curve is highly distorted, at least visually, math filters easily remove non-geological effects due to flowline volume and extrapolate pressures accurately to large times. FT-PTA-DDBU represents the interpretation algorithm to be used in downhole processors. It is fast, stable and accurate. Detailed FT-00 calculated results are shown in Figure 8.6c, where **red bold font** is used to highlight values assumed in Figure 8.6b.
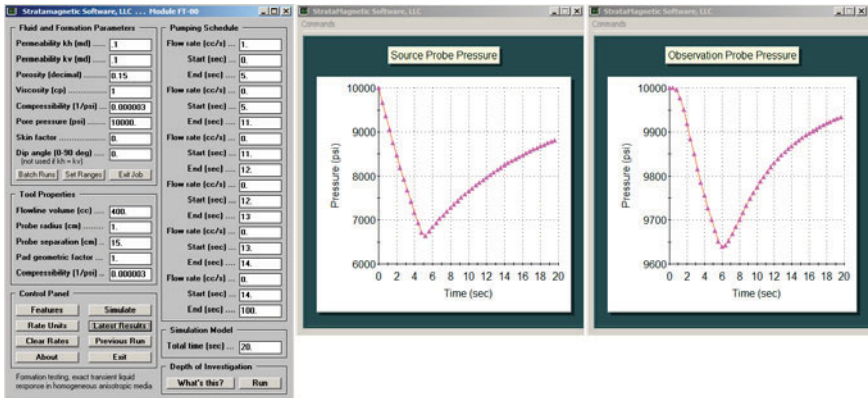

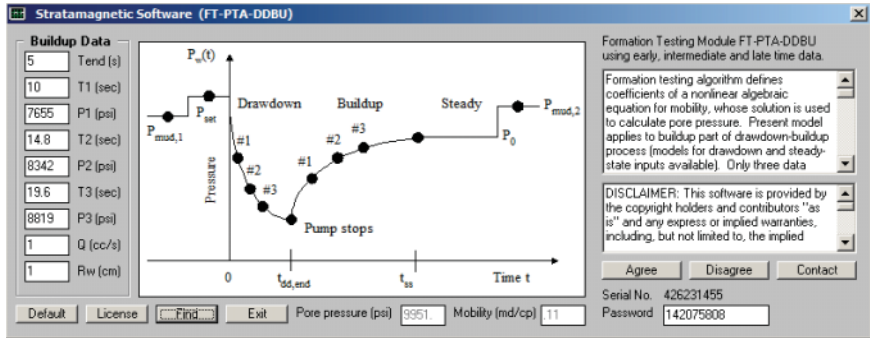**Figure 8.6a**. Low mobility, no skin, storage (forward simulation).

Figure 8.6b. Pore pressure and mobility from buildup data.

Time (s)	Rate (cc/s)	Ps* (psi)	Pr* (psi)	Ps**(psi)	Pr**(psi)	Pr**/Ps**
0.000E+00	0.10000E+01	0.10000E+05	0.10000E+05	0.00000E+00	0.00000E+00	-----------
0.400E+00	0.10000E+01	0.96742E+04	0.99999E+04	-0.32579E+03	-0.60676E-01	0.18624E-03
0.800E+00	0.10000E+01	0.93598E+04	0.99952E+04	-0.64019E+03	-0.47898E+01	0.74819E-02
0.120E+01	0.10000E+01	0.90556E+04	0.99778E+04	-0.94438E+03	-0.22208E+02	0.23516E-01
0.160E+01	0.10000E+01	0.87610E+04	0.99504E+04	-0.12390E+04	-0.49571E+02	0.40009E-01
0.200E+01	0.10000E+01	0.84755E+04	0.99181E+04	-0.15245E+04	-0.81907E+02	0.53728E-01
0.240E+01	0.10000E+01	0.81988E+04	0.98840E+04	-0.18012E+04	-0.11596E+03	0.64379E-01
0.280E+01	0.10000E+01	0.79304E+04	0.98500E+04	-0.20696E+04	-0.14996E+03	0.72456E-01
0.320E+01	0.10000E+01	0.76701E+04	0.98170E+04	-0.23299E+04	-0.18298E+03	0.78534E-01
0.360E+01	0.10000E+01	0.74175E+04	0.97854E+04	-0.25825E+04	-0.21459E+03	0.83097E-01
0.400E+01	0.10000E+01	0.71725E+04	0.97554E+04	-0.28275E+04	-0.24462E+03	0.86515E-01
0.440E+01	0.10000E+01	0.69347E+04	0.97270E+04	-0.30653E+04	-0.27302E+03	0.89067E-01
0.480E+01	0.10000E+01	0.67039E+04	0.97002E+04	-0.32961E+04	-0.29981E+03	0.90958E-01
0.520E+01	0.00000E+00	0.66443E+04	0.96749E+04	-0.33557E+04	-0.32506E+03	0.96869E-01
0.560E+01	0.00000E+00	0.67467E+04	0.96522E+04	-0.32533E+04	-0.34777E+03	0.10690E+00
0.600E+01	0.00000E+00	0.68447E+04	0.96406E+04	-0.31553E+04	-0.35936E+03	0.11389E+00
0.640E+01	0.00000E+00	0.69390E+04	0.96426E+04	-0.30610E+04	-0.35743E+03	0.11677E+00
0.680E+01	0.00000E+00	0.70299E+04	0.96530E+04	-0.29701E+04	-0.34700E+03	0.11683E+00
0.720E+01	0.00000E+00	0.71176E+04	0.96677E+04	-0.28824E+04	-0.33234E+03	0.11530E+00
0.760E+01	0.00000E+00	0.72024E+04	0.96841E+04	-0.27976E+04	-0.31594E+03	0.11293E+00
0.800E+01	0.00000E+00	0.72843E+04	0.97008E+04	-0.27157E+04	-0.29917E+03	0.11016E+00
0.840E+01	0.00000E+00	0.73636E+04	0.97173E+04	-0.26364E+04	-0.28272E+03	0.10723E+00
0.880E+01	0.00000E+00	0.74402E+04	0.97331E+04	-0.25598E+04	-0.26694E+03	0.10428E+00
0.920E+01	0.00000E+00	0.75145E+04	0.97480E+04	-0.24855E+04	-0.25199E+03	0.10138E+00
0.960E+01	0.00000E+00	0.75863E+04	0.97621E+04	-0.24137E+04	-0.23792E+03	0.98571E-01
0.100E+02	0.00000E+00	0.76559E+04	0.97753E+04	-0.23441E+04	-0.22473E+03	0.95871E-01
0.104E+02	0.00000E+00	0.77234E+04	0.97876E+04	-0.22766E+04	-0.21238E+03	0.93288E-01
0.108E+02	0.00000E+00	0.77887E+04	0.97992E+04	-0.22113E+04	-0.20084E+03	0.90824E-01
0.112E+02	0.00000E+00	0.78520E+04	0.98100E+04	-0.21480E+04	-0.19004E+03	0.88475E-01
0.116E+02	0.00000E+00	0.79134E+04	0.98201E+04	-0.20866E+04	-0.17994E+03	0.86236E-01
0.120E+02	0.00000E+00	0.79729E+04	0.98295E+04	-0.20271E+04	-0.17048E+03	0.84101E-01
0.124E+02	0.00000E+00	0.80306E+04	0.98384E+04	-0.19694E+04	-0.16162E+03	0.82064E-01
0.128E+02	0.00000E+00	0.80866E+04	0.98467E+04	-0.19134E+04	-0.15330E+03	0.80119E-01
0.132E+02	0.00000E+00	0.81408E+04	0.98545E+04	-0.18592E+04	-0.14549E+03	0.78258E-01
0.136E+02	0.00000E+00	0.81935E+04	0.98618E+04	-0.18065E+04	-0.13816E+03	0.76476E-01
0.140E+02	0.00000E+00	0.82445E+04	0.98687E+04	-0.17555E+04	-0.13125E+03	0.74768E-01
0.144E+02	0.00000E+00	0.82941E+04	0.98752E+04	-0.17059E+04	-0.12475E+03	0.73128E-01
0.148E+02	0.00000E+00	0.83421E+04	0.98814E+04	-0.16579E+04	-0.11862E+03	0.71551E-01
0.152E+02	0.00000E+00	0.83888E+04	0.98872E+04	-0.16112E+04	-0.11284E+03	0.70032E-01
0.156E+02	0.00000E+00	0.84340E+04	0.98926E+04	-0.15660E+04	-0.10738E+03	0.68569E-01
0.160E+02	0.00000E+00	0.84779E+04	0.98978E+04	-0.15221E+04	-0.10222E+03	0.67156E-01
0.164E+02	0.00000E+00	0.85205E+04	0.99027E+04	-0.14795E+04	-0.97335E+02	0.65791E-01
0.168E+02	0.00000E+00	0.85619E+04	0.99073E+04	-0.14381E+04	-0.92714E+02	0.64469E-01
0.172E+02	0.00000E+00	0.86020E+04	0.99117E+04	-0.13980E+04	-0.88336E+02	0.63190E-01
0.176E+02	0.00000E+00	0.86410E+04	0.99158E+04	-0.13590E+04	-0.84186E+02	0.61948E-01
0.180E+02	0.00000E+00	0.86789E+04	0.99198E+04	-0.13211E+04	-0.80250E+02	0.60743E-01
0.184E+02	0.00000E+00	0.87156E+04	0.99235E+04	-0.12844E+04	-0.76514E+02	0.59571E-01
0.188E+02	0.00000E+00	0.87512E+04	0.99270E+04	-0.12488E+04	-0.72966E+02	0.58431E-01
0.192E+02	0.00000E+00	0.87859E+04	0.99304E+04	-0.12141E+04	-0.69595E+02	0.57321E-01
0.196E+02	0.00000E+00	0.88195E+04	0.99336E+04	-0.11805E+04	-0.66390E+02	0.56238E-01

Figure 8.6c. Detailed FT-00 forward calculation results.

8.3.3 Multiple pretests, modeling and interpretation.

So-called "pre-tests" are often used to test for data repeatability, to ensure good pad contact and sealing with the formation, sand-free flowlines and nozzles, and so on. Here we consider a conventional pretest sequence and demonstrate how FT-00 and FT-PTA-DDBU are used. The first test withdraws fluid at 0.5 cc/sec for five seconds; the second, starting at 100 seconds, withdraws fluid at 1 cc/sec, also for five seconds. The total simulation time is set at 200 sec. From Figure 8.7a, the pore pressure and mobility are 10,000 psi and 0.1 md/cp. In Figure 8.7b, we use time data at 10, 15 and 20 sec for the first pre-test, entering a 0.5 cc/sec flow rate; the predictions are 9,988 psi and 0.11 md/cp. In order to analyze the second pretest, FT-PTA-DDBU requires that the time origin reset to zero. Thus, source pressures at 110, 115 and 120 seconds are relabeled to correspond to 10, 15 and 20 seconds; the time at which drawdown terminates, 105 seconds, is similarly relabeled at 5 sec. The flow rate for this second pretest is 1 cc/sec. Figure 8.7c shows accurate predictions of 9,960 psi and 0.11 md/cp. Key portions of the FT-00 output are given in Figure 8.7d. Note that FT-00 is exact while FT-PTA-DDBU is approximate. This is required to keep downhole calculations simple, fast and not memory-intensive.
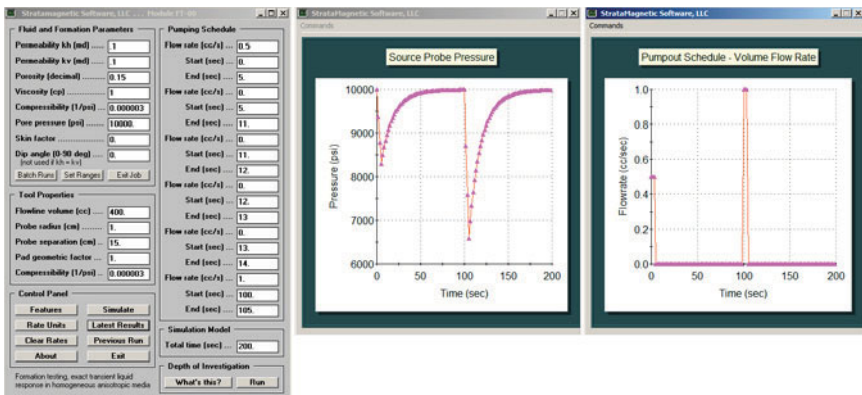

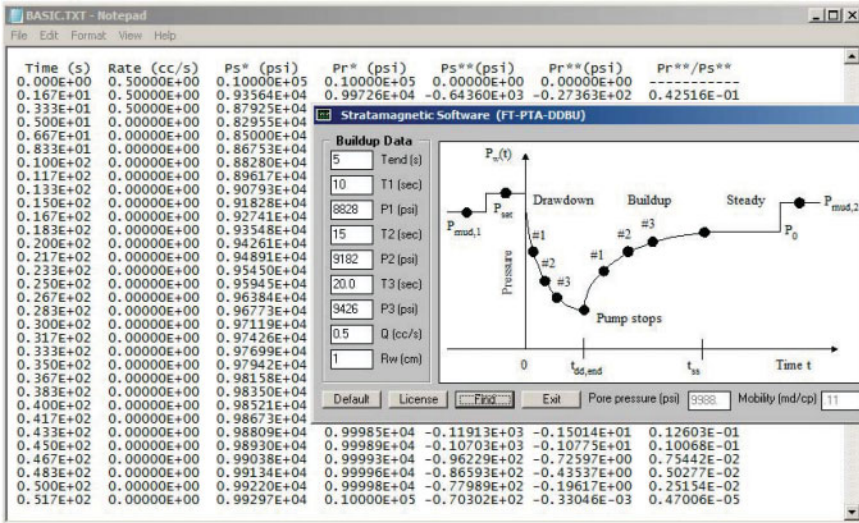**Figure 8.7a**. Two pretests, source pressure and pumpout schedule.

BASIC.TXT - Notepad
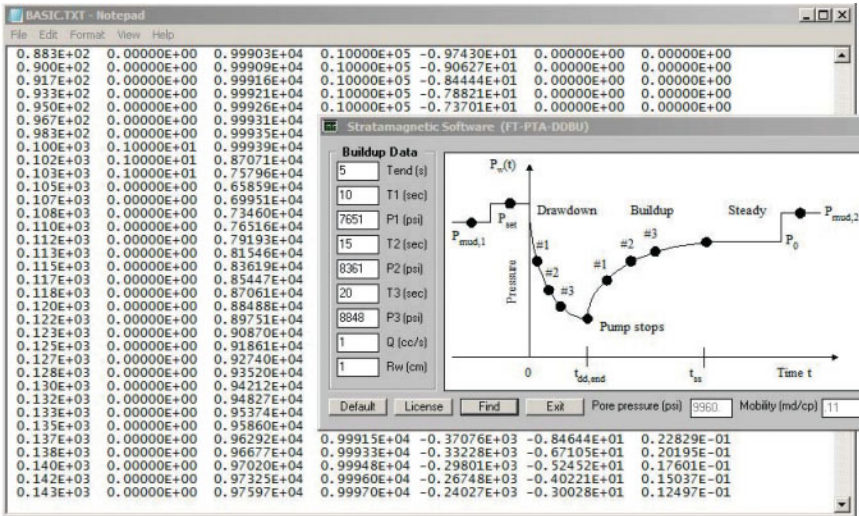File Edit Format View Help

Time (s)	Rate (cc/s)	Ps* (psi)	Pr* (psi)	Ps**(psi)	Pr**(psi)	Pr**/Ps**
0.000E+00	0.50000E+00	0.10000E+05	0.10000E+05	0.00000E+00	0.00000E+00	----------
0.167E+01	0.50000E+00	0.93564E+04	0.99726E+04	-0.64360E+03	-0.27363E+02	0.42516E-01
0.333E+01	0.50000E+00	0.87925E+04				
0.500E+01	0.00000E+00	0.82955E+04				
0.667E+01	0.00000E+00	0.85000E+04				
0.833E+01	0.00000E+00	0.86753E+04				
0.100E+02	0.00000E+00	0.88280E+04				
0.117E+02	0.00000E+00	0.89617E+04				
0.133E+02	0.00000E+00	0.90793E+04				
0.150E+02	0.00000E+00	0.91828E+04				
0.167E+02	0.00000E+00	0.92741E+04				
0.183E+02	0.00000E+00	0.93548E+04				
0.200E+02	0.00000E+00	0.94261E+04				
0.217E+02	0.00000E+00	0.94891E+04				
0.233E+02	0.00000E+00	0.95450E+04				
0.250E+02	0.00000E+00	0.95945E+04				
0.267E+02	0.00000E+00	0.96384E+04				
0.283E+02	0.00000E+00	0.96773E+04				
0.300E+02	0.00000E+00	0.97119E+04				
0.317E+02	0.00000E+00	0.97426E+04				
0.333E+02	0.00000E+00	0.97699E+04				
0.350E+02	0.00000E+00	0.97942E+04				
0.367E+02	0.00000E+00	0.98158E+04				
0.383E+02	0.00000E+00	0.98350E+04				
0.400E+02	0.00000E+00	0.98521E+04				
0.417E+02	0.00000E+00	0.98673E+04				
0.433E+02	0.00000E+00	0.98809E+04	0.99985E+04	-0.11913E+03	-0.15014E+01	0.12603E-01
0.450E+02	0.00000E+00	0.98930E+04	0.99989E+04	-0.10703E+03	-0.10775E+01	0.10068E-01
0.467E+02	0.00000E+00	0.99038E+04	0.99993E+04	-0.96229E+02	-0.72597E+00	0.75442E-02
0.483E+02	0.00000E+00	0.99134E+04	0.99996E+04	-0.86593E+02	-0.43537E+00	0.50277E-02
0.500E+02	0.00000E+00	0.99220E+04	0.99998E+04	-0.77989E+02	-0.19617E+00	0.25154E-02
0.517E+02	0.00000E+00	0.99297E+04	0.10000E+05	-0.70302E+02	-0.33046E-03	0.47006E-05

Stratamagnetic Software (FT-PTA-DDBU)

Buildup Data
5 Tend (s)
10 T1 (sec)
8828 P1 (psi)
15 T2 (sec)
9182 P2 (psi)
20.0 T3 (sec)
9426 P3 (psi)
0.5 Q (cc/s)
1 Rw (cm)

$P_w(t)$ — Drawdown / Buildup / Steady; P_{set}; $P_{mud,1}$; $P_{mud,2}$; P_0; #1 #2 #3; Pump stops; Pressure vs Time t; $t_{dd,end}$; t_{ss}

Default License Find Exit Pore pressure (psi) 9988 Mobility (md/cp) 11

Figure 8.7b. Analysis of first pre-test.

BASIC.TXT - Notepad
File Edit Format View Help

0.883E+02	0.00000E+00	0.99903E+04	0.10000E+05	-0.97430E+01	0.00000E+00	0.00000E+00
0.900E+02	0.00000E+00	0.99909E+04	0.10000E+05	-0.90627E+01	0.00000E+00	0.00000E+00
0.917E+02	0.00000E+00	0.99916E+04	0.10000E+05	-0.84444E+01	0.00000E+00	0.00000E+00
0.933E+02	0.00000E+00	0.99921E+04	0.10000E+05	-0.78821E+01	0.00000E+00	0.00000E+00
0.950E+02	0.00000E+00	0.99926E+04	0.10000E+05	-0.73701E+01	0.00000E+00	0.00000E+00
0.967E+02	0.00000E+00	0.99931E+04				
0.983E+02	0.00000E+00	0.99935E+04				
0.100E+03	0.10000E+01	0.99939E+04				
0.102E+03	0.10000E+01	0.87071E+04				
0.103E+03	0.10000E+01	0.75796E+04				
0.105E+03	0.00000E+00	0.65859E+04				
0.107E+03	0.00000E+00	0.69951E+04				
0.108E+03	0.00000E+00	0.73460E+04				
0.110E+03	0.00000E+00	0.76516E+04				
0.112E+03	0.00000E+00	0.79193E+04				
0.113E+03	0.00000E+00	0.81546E+04				
0.115E+03	0.00000E+00	0.83619E+04				
0.117E+03	0.00000E+00	0.85447E+04				
0.118E+03	0.00000E+00	0.87061E+04				
0.120E+03	0.00000E+00	0.88488E+04				
0.122E+03	0.00000E+00	0.89751E+04				
0.123E+03	0.00000E+00	0.90870E+04				
0.125E+03	0.00000E+00	0.91861E+04				
0.127E+03	0.00000E+00	0.92740E+04				
0.128E+03	0.00000E+00	0.93520E+04				
0.130E+03	0.00000E+00	0.94212E+04				
0.132E+03	0.00000E+00	0.94827E+04				
0.133E+03	0.00000E+00	0.95374E+04				
0.135E+03	0.00000E+00	0.95860E+04				
0.137E+03	0.00000E+00	0.96292E+04	0.99915E+04	-0.37076E+03	-0.84644E+01	0.22829E-01
0.138E+03	0.00000E+00	0.96677E+04	0.99933E+04	-0.33228E+03	-0.67105E+01	0.20195E-01
0.140E+03	0.00000E+00	0.97020E+04	0.99948E+04	-0.29801E+03	-0.52452E+01	0.17601E-01
0.142E+03	0.00000E+00	0.97325E+04	0.99960E+04	-0.26748E+03	-0.40221E+01	0.15037E-01
0.143E+03	0.00000E+00	0.97597E+04	0.99970E+04	-0.24027E+03	-0.30028E+01	0.12497E-01

Stratamagnetic Software (FT-PTA-DDBU)

Buildup Data
5 Tend (s)
10 T1 (sec)
7651 P1 (psi)
15 T2 (sec)
8361 P2 (psi)
20 T3 (sec)
8848 P3 (psi)
1 Q (cc/s)
1 Rw (cm)

$P_w(t)$ — Drawdown / Buildup / Steady; P_{set}; $P_{mud,1}$; $P_{mud,2}$; P_0; #1 #2 #3; Pump stops; Pressure vs Time t; $t_{dd,end}$; t_{ss}

Default License Find Exit Pore pressure (psi) 9960 Mobility (md/cp) 11

Figure 8.7c. Inverse analysis of second pre-test.

FORMATION TESTER PRESSURE TRANSIENT ANALYSIS

```
Exact analytical solution for Darcy ellipsoidal flow
(homogeneous anisotropic media with flowline storage
and skin) using complex complementary error function.

Specific limit considered -
...... Isotropic flow model with storage and no skin

Developer, Wilson C. Chin, Ph.D., MIT.
Copyright (C) 2004-2007, StrataMagnetic Software, LLC.
All rights reserved.   Email, wilsonchin@aol.com.

FLUID AND FORMATION PARAMETERS
Formation kh permeability ....... (md):  0.1000E+00
Formation kv permeability ....... (md):  0.1000E+00
Formation spherical permeability  (md):  0.1000E+00
Porosity .................. (decimal):  0.1500E+00
Viscosity ....................... (cp):  0.1000E+01
Pore fluid compressibility ... (1/psi):  0.3000E-05
Pore pressure ................. (psi):  0.1000E+05
Skin factor ......... (dimensionless):  0.0000E+00
Dip angle ................ (0-90 deg):  0.0000E+00

TOOL PROPERTIES
Flowline volume ................. (cc):  0.4000E+03
Probe radius .................... (cm):  0.1000E+01
Probe separation ............... (cm):  0.1500E+02
Pad geometric factor . (dimensionless):  0.1000E+01
Flowline fluid compressibility (1/psi):  0.3000E-05

PUMPING SCHEDULE AND SIMULATION PARAMETERS
Schedule #1, Flow rate ........ (cc/s):  0.5000E+00
            Beginning time .... (sec):  0.0000E+00
            Ending time ....... (sec):  0.5000E+01
Schedule #2, Flow rate ........ (cc/s):  0.0000E+00
            Beginning time .... (sec):  0.5000E+01
            Ending time ....... (sec):  0.1100E+02
Schedule #3, Flow rate ........ (cc/s):  0.0000E+00
            Beginning time .... (sec):  0.1100E+02
            Ending time ....... (sec):  0.1200E+02
Schedule #4, Flow rate ........ (cc/s):  0.0000E+00
            Beginning time .... (sec):  0.1200E+02
            Ending time ....... (sec):  0.1300E+02
Schedule #5, Flow rate ........ (cc/s):  0.0000E+00
            Beginning time .... (sec):  0.1300E+02
            Ending time ....... (sec):  0.1400E+02
Schedule #6, Flow rate ........ (cc/s):  0.1000E+01
            Beginning time .... (sec):  0.1000E+03
            Ending time ....... (sec):  0.1050E+03
Total simulation time ......... (sec):  0.2000E+03

DEFINITIONS
Time ... Elapsed time (sec)
Rate ... Drawdown flow rate (cc/s)
Ps* .... Source pressure with hydrostatic (psi)
Pr* .... Observation pressure with hydrostatic (psi)
Ps** ... Source pressure, no hydrostatic (psi)
Pr** ... Observation pressure, no hydrostatic (psi)

        NOTE: Ps* or Pr* < 0 means volume flow
        rate cannot be achieved in practice
```

Time (s)	Rate (cc/s)	Ps* (psi)	Pr* (psi)	Ps** (psi)	Pr** (psi)	Pr**/Ps**
0.000E+00	0.50000E+00	0.10000E+05	0.10000E+05	0.00000E+00	0.00000E+00	----------
0.167E+01	0.50000E+00	0.93564E+04	0.99726E+04	-0.64360E+03	-0.27363E+02	0.42516E-01
0.333E+01	0.50000E+00	0.87925E+04	0.99032E+04	-0.12075E+04	-0.96843E+02	0.80203E-01
0.500E+01	0.00000E+00	0.82955E+04	0.98437E+04	-0.17045E+04	-0.15631E+03	0.91706E-01
0.667E+01	0.00000E+00	0.85000E+04	0.98244E+04	-0.15000E+04	-0.17556E+03	0.11704E+00
0.833E+01	0.00000E+00	0.86753E+04	0.98573E+04	-0.13247E+04	-0.14271E+03	0.10773E+00
0.100E+02	0.00000E+00	0.88280E+04	0.98876E+04	-0.11720E+04	-0.11236E+03	0.95871E-01
0.117E+02	0.00000E+00	0.89617E+04	0.99108E+04	-0.10383E+04	-0.89159E+02	0.85873E-01
0.133E+02	0.00000E+00	0.90793E+04	0.99285E+04	-0.92071E+03	-0.71499E+02	0.77656E-01
0.150E+02	0.00000E+00	0.91828E+04	0.99422E+04	-0.81719E+03	-0.57844E+02	0.70784E-01
0.167E+02	0.00000E+00	0.92741E+04	0.99529E+04	-0.72588E+03	-0.47113E+02	0.64905E-01
0.183E+02	0.00000E+00	0.93548E+04	0.99614E+04	-0.64523E+03	-0.38562E+02	0.59764E-01
0.200E+02	0.00000E+00	0.94261E+04	0.99683E+04	-0.57394E+03	-0.31671E+02	0.55182E-01
0.217E+02	0.00000E+00	0.94891E+04	0.99739E+04	-0.51086E+03	-0.26069E+02	0.51030E-01
0.233E+02	0.00000E+00	0.95450E+04	0.99785E+04	-0.45499E+03	-0.21482E+02	0.47215E-01
0.250E+02	0.00000E+00	0.95945E+04	0.99823E+04	-0.40549E+03	-0.17706E+02	0.43666E-01
0.267E+02	0.00000E+00	0.96384E+04	0.99854E+04	-0.36160E+03	-0.14583E+02	0.40330E-01
0.283E+02	0.00000E+00	0.96773E+04	0.99880E+04	-0.32266E+03	-0.11992E+02	0.37166E-01
0.300E+02	0.00000E+00	0.97119E+04	0.99902E+04	-0.28808E+03	-0.98352E+01	0.34140E-01
.						
.						
.						
0.883E+02	0.00000E+00	0.99903E+04	0.10000E+05	-0.97430E+01	0.00000E+00	0.00000E+00
0.900E+02	0.00000E+00	0.99909E+04	0.10000E+05	-0.90627E+01	0.00000E+00	0.00000E+00
0.917E+02	0.00000E+00	0.99916E+04	0.10000E+05	-0.84444E+01	0.00000E+00	0.00000E+00
0.933E+02	0.00000E+00	0.99921E+04	0.10000E+05	-0.78821E+01	0.00000E+00	0.00000E+00
0.950E+02	0.00000E+00	0.99926E+04	0.10000E+05	-0.73701E+01	0.00000E+00	0.00000E+00
0.967E+02	0.00000E+00	0.99931E+04	0.10000E+05	-0.69034E+01	0.00000E+00	0.00000E+00
0.983E+02	0.00000E+00	0.99935E+04	0.10000E+05	-0.64775E+01	0.00000E+00	0.00000E+00
0.100E+03	0.10000E+01	0.99939E+04	0.10000E+05	-0.60883E+01	0.00000E+00	0.00000E+00
0.102E+03	0.10000E+01	0.87071E+04	0.99453E+04	-0.12929E+04	-0.54726E+02	0.42327E-01
0.103E+03	0.10000E+01	0.75796E+04	0.98063E+04	-0.24204E+04	-0.19369E+03	0.80024E-01
0.105E+03	0.00000E+00	0.65859E+04	0.96874E+04	-0.34141E+04	-0.31262E+03	0.91569E-01
0.107E+03	0.00000E+00	0.69951E+04	0.96489E+04	-0.30049E+04	-0.35112E+03	0.11685E+00
0.108E+03	0.00000E+00	0.73460E+04	0.97146E+04	-0.26540E+04	-0.28542E+03	0.10754E+00
0.110E+03	0.00000E+00	0.76516E+04	0.97753E+04	-0.23484E+04	-0.22473E+03	0.95694E-01
0.112E+03	0.00000E+00	0.79193E+04	0.98217E+04	-0.20807E+04	-0.17832E+03	0.85702E-01
0.113E+03	0.00000E+00	0.81546E+04	0.98570E+04	-0.18454E+04	-0.14300E+03	0.77490E-01
0.115E+03	0.00000E+00	0.83619E+04	0.98843E+04	-0.16381E+04	-0.11569E+03	0.70622E-01
0.117E+03	0.00000E+00	0.85447E+04	0.99058E+04	-0.14553E+04	-0.94226E+02	0.64745E-01
0.118E+03	0.00000E+00	0.87061E+04	0.99229E+04	-0.12939E+04	-0.77123E+02	0.59606E-01
0.120E+03	0.00000E+00	0.88488E+04	0.99367E+04	-0.11512E+04	-0.63342E+02	0.55024E-01
0.122E+03	0.00000E+00	0.89751E+04	0.99479E+04	-0.10249E+04	-0.52138E+02	0.50873E-01
0.123E+03	0.00000E+00	0.90870E+04	0.99570E+04	-0.91301E+03	-0.42965E+02	0.47059E-01
0.125E+03	0.00000E+00	0.91861E+04	0.99646E+04	-0.81389E+03	-0.35412E+02	0.43510E-01
0.127E+03	0.00000E+00	0.92740E+04	0.99708E+04	-0.72599E+03	-0.29167E+02	0.40175E-01
0.128E+03	0.00000E+00	0.93520E+04	0.99760E+04	-0.64800E+03	-0.23983E+02	0.37011E-01
0.130E+03	0.00000E+00	0.94212E+04	0.99803E+04	-0.57877E+03	-0.19670E+02	0.33987E-01

Figure 8.7d. Detailed FT-00 forward simulation data for two pre-tests.

8.3.4   Reverse flow injection processes.

The prior FT-PTA-DDBU validation, focusing on draw-*then*-buildup (arising from fluid withdrawal-*then*-stoppage), showed how pore pressure and spherical mobility can be accurately recovered from time-pressure data.   For injection processes, the opposite occurs, namely, injection-*then*-stoppage.   It is clear that the DDBU algorithm for drawdown-buildup also applies unchanged to buildup-drawdown with only a sign modification to flowrate inputs.   In this section, we demonstrate this using our software for tutorial purposes.

8.3.4.1   Conventional fluid withdrawal, drawdown-*then*-buildup.

Here, we create a conventional drawdown-*then*-buildup data set using the exact FT-00 simulator shown in Figure 8.8a. This produces transient pressure histories at both source and observation probes, e.g., see Figures 8.8b and 8.8c. In this discussion, we focus on single-probe applications and do not need observation probe results; thus, they are not shown. Answers are obtained within seconds. The output file is shown below with important items highlighted in red.
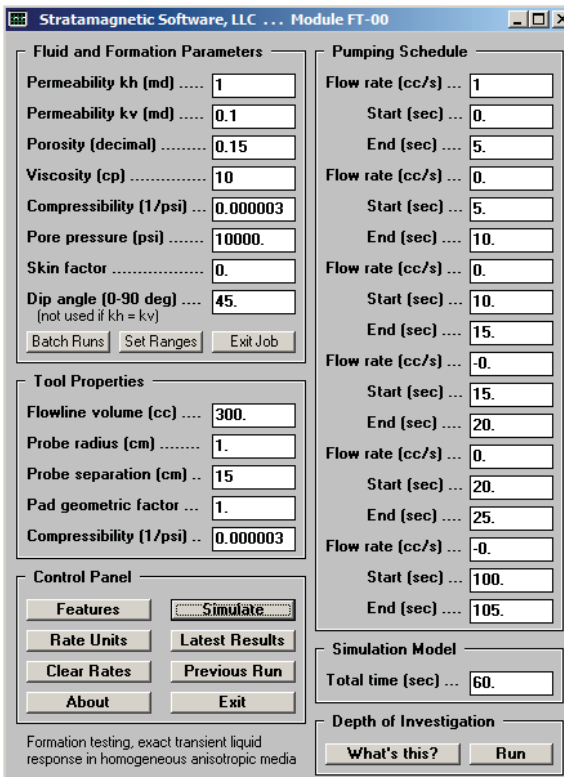
Figure 8.8a. FT-00, exact forward transient analysis.
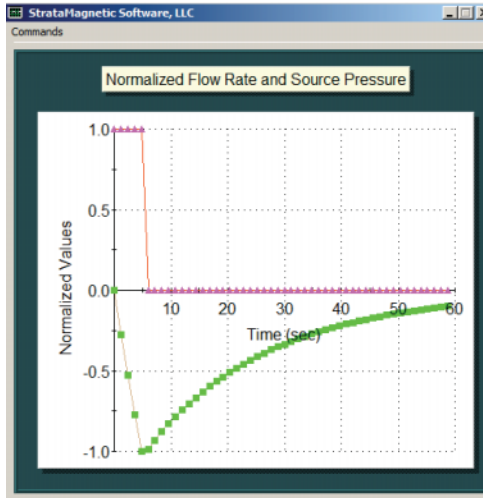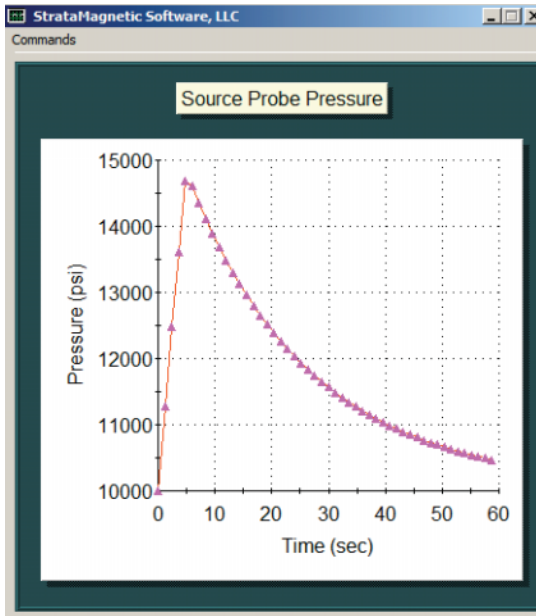
Figure 8.8b. FT-00, exact dimensionless flowrate and source pressure.
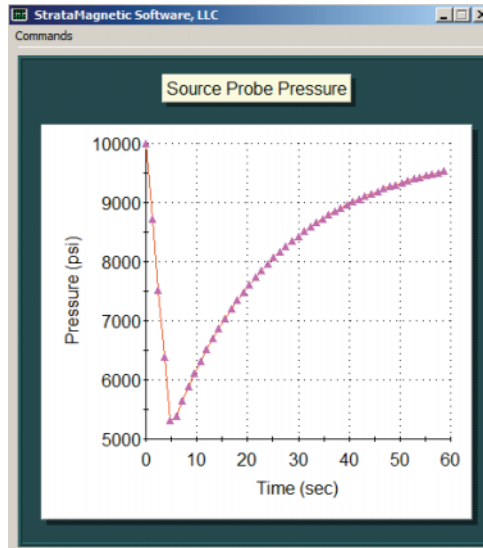
Figure 8.8c. FT-00, exact source pressure.

```
FORMATION TESTER PRESSURE TRANSIENT ANALYSIS
Exact analytical solution for Darcy ellipsoidal flow
(homogeneous anisotropic media with flowline storage
and skin) using complex complementary error function.

Specific limit considered -
.... Anisotropic flow model with storage and no skin

Developer, Wilson C. Chin, Ph.D., MIT.
Copyright (C) 2004-2007, StrataMagnetic Software, LLC.
All rights reserved.   Email, wilsonchin@aol.com.

FLUID AND FORMATION PARAMETERS
Formation kh permeability ....... (md):   0.1000E+01
Formation kv permeability ....... (md):   0.1000E+00
Formation spherical permeability  (md):   0.4642E+00
Porosity .................. (decimal):   0.1500E+00
Viscosity ..................... (cp):   0.1000E+02
Pore fluid compressibility ... (1/psi):   0.3000E-05
Pore pressure ................. (psi):   0.1000E+05
Skin factor .......... (dimensionless):   0.0000E+00
Dip angle ................ (0-90 deg):   0.4500E+02

TOOL PROPERTIES
Flowline volume ................. (cc):   0.3000E+03
Probe radius ................... (cm):   0.1000E+01
Probe separation ............... (cm):   0.1500E+02
Pad geometric factor . (dimensionless):   0.1000E+01
Flowline fluid compressibility (1/psi):   0.3000E-05

PUMPING SCHEDULE AND SIMULATION PARAMETERS
Schedule #1, Flow rate ........ (cc/s):   0.1000E+01 (Drawdown +1 cc/s
                                                     at t=0 and ends t=5)
            Beginning time .... (sec):   0.0000E+00
            Ending time ....... (sec):   0.5000E+01
Schedule #2, Flow rate ........ (cc/s):   0.0000E+00 (Piston stops, rate 0
                                                     cc/s, buildup starts)
            Beginning time .... (sec):   0.5000E+01
            Ending time ....... (sec):   0.1000E+02
Schedule #3, Flow rate ........ (cc/s):   0.0000E+00
            Beginning time .... (sec):   0.1000E+02
            Ending time ....... (sec):   0.1500E+02
Schedule #4, Flow rate ........ (cc/s):   0.0000E+00
            Beginning time .... (sec):   0.1500E+02
            Ending time ....... (sec):   0.2000E+02
Schedule #5, Flow rate ........ (cc/s):   0.0000E+00
            Beginning time .... (sec):   0.2000E+02
            Ending time ....... (sec):   0.2500E+02
Schedule #6, Flow rate ........ (cc/s):   0.0000E+00
            Beginning time .... (sec):   0.1000E+03
            Ending time ....... (sec):   0.1050E+03
Total simulation time ......... (sec):   0.6000E+02

DEFINITIONS
Time ... Elapsed time (sec)
Rate ... Drawdown flow rate (cc/s)
Ps* .... Source pressure with hydrostatic (psi)
Pr* .... Observation pressure with hydrostatic (psi)
Ps** ... Source pressure, no hydrostatic (psi)
Pr** ... Observation pressure, no hydrostatic (psi)

        NOTE: Ps* or Pr* < 0 means volume flow
        rate cannot be achieved in practice
```

```
 Time (s)   Rate (cc/s)   Ps* (psi)    Pr* (psi)    Ps**(psi)    Pr**(psi)    Pr**/Ps**
0.000E+00  0.10000E+01  0.10000E+05  0.10000E+05  0.00000E+00  0.00000E+00  ----------
0.120E+01  0.10000E+01  0.87188E+04  0.10000E+05 -0.12812E+04 -0.42301E-04  0.33016E-07
0.240E+01  0.10000E+01  0.75168E+04  0.99999E+04 -0.24832E+04 -0.14086E+00  0.56724E-04
0.360E+01  0.10000E+01  0.63844E+04  0.99978E+04 -0.36156E+04 -0.22378E+01  0.61892E-03
0.480E+01  0.10000E+01  0.53157E+04  0.99909E+04 -0.46843E+04 -0.91429E+01  0.19518E-02
0.600E+01  0.00000E+00  0.53799E+04  0.99785E+04 -0.46201E+04 -0.21528E+02  0.46597E-02
0.720E+01  0.00000E+00  0.56401E+04  0.99617E+04 -0.43599E+04 -0.38273E+02  0.87785E-02
0.840E+01  0.00000E+00  0.58813E+04  0.99435E+04 -0.41187E+04 -0.56483E+02  0.13714E-01
0.960E+01  0.00000E+00  0.61064E+04  0.99281E+04 -0.38936E+04 -0.71882E+02  0.18462E-01
0.108E+02  0.00000E+00  0.63173E+04  0.99176E+04 -0.36827E+04 -0.82394E+02  0.22373E-01
0.120E+02  0.00000E+00  0.65152E+04  0.99118E+04 -0.34848E+04 -0.88200E+02  0.25310E-01
0.132E+02  0.00000E+00  0.67013E+04  0.99097E+04 -0.32987E+04 -0.90315E+02  0.27379E-01
0.144E+02  0.00000E+00  0.68765E+04  0.99102E+04 -0.31235E+04 -0.89812E+02  0.28753E-01
0.156E+02  0.00000E+00  0.70415E+04  0.99124E+04 -0.29585E+04 -0.87565E+02  0.29598E-01
0.168E+02  0.00000E+00  0.71971E+04  0.99158E+04 -0.28029E+04 -0.84225E+02  0.30049E-01
0.180E+02  0.00000E+00  0.73439E+04  0.99197E+04 -0.26561E+04 -0.80252E+02  0.30214E-01
0.192E+02  0.00000E+00  0.74824E+04  0.99240E+04 -0.25176E+04 -0.75962E+02  0.30173E-01
0.204E+02  0.00000E+00  0.76133E+04  0.99284E+04 -0.23867E+04 -0.71570E+02  0.29986E-01
0.216E+02  0.00000E+00  0.77369E+04  0.99328E+04 -0.22631E+04 -0.67215E+02  0.29700E-01
0.228E+02  0.00000E+00  0.78537E+04  0.99370E+04 -0.21463E+04 -0.62988E+02  0.29347E-01
0.240E+02  0.00000E+00  0.79641E+04  0.99411E+04 -0.20359E+04 -0.58945E+02  0.28953E-01
 .
 .
 .
0.480E+02  0.00000E+00  0.92694E+04  0.99820E+04 -0.73062E+03 -0.18002E+02  0.24639E-01
0.492E+02  0.00000E+00  0.93048E+04  0.99828E+04 -0.69515E+03 -0.17225E+02  0.24779E-01
0.504E+02  0.00000E+00  0.93385E+04  0.99835E+04 -0.66150E+03 -0.16510E+02  0.24958E-01
0.516E+02  0.00000E+00  0.93704E+04  0.99841E+04 -0.62957E+03 -0.15851E+02  0.25177E-01
0.528E+02  0.00000E+00  0.94007E+04  0.99848E+04 -0.59927E+03 -0.15243E+02  0.25435E-01
```

Figure 8.8d. FT-00, detailed flow rate, source and observation probe pressure versus time.

```
FLUID AND FORMATION PARAMETERS
Formation kh permeability ....... (md):   0.1000E+01
Formation kv permeability ....... (md):   0.1000E+00
Formation spherical permeability  (md):   0.4642E+00
Porosity .................. (decimal):    0.1500E+00
Viscosity ..................... (cp):     0.1000E+02
```

Note from the output file that the spherical permeability assumed in the forward simulation is 0.4642 md (this is calculated from given k_h and k_v values) and the viscosity is taken as 10 cp. Thus, the assumed spherical mobility is 0.04642 md/cp. Also note that the pore pressure was assumed as 10,000 psi. The tabulated results from FT-00 in Figure 8.8d are <u>exact</u> mathematical solutions for single-phase liquid flows.

Now we demonstrate how buildup data from t = 6, 19.2 and 50.4 sec can be used to recover spherical mobility and pore pressure, using the approximate FT-PTA-DDBU.EXE model which is an approximate theory for low mobilities and high flowline storage. Simplifications were made to allow fast real-time solutions in downhole microprocessors while using minimal computer memory.
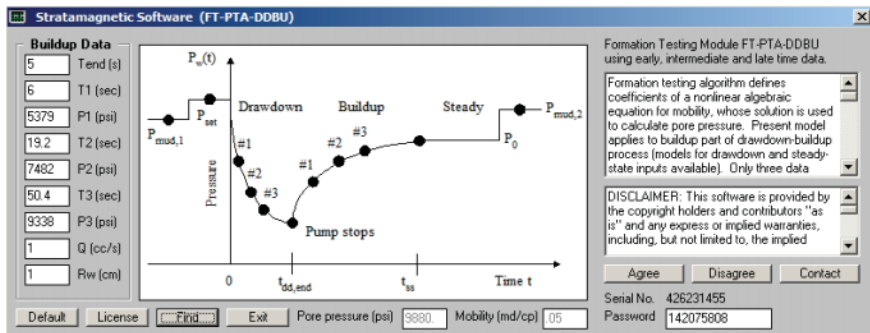
Figure 8.8e. FT-PTA-DDBU, approximate predictions for spherical mobility and pore pressure.

In the inverse calculation using FT-PTA-DDBU, we find 0.05 md/cp (agreeing with 0.04642 md/cp) and 9,880 psi (very close to 10,000 psi). In practice, different choices for (time, pressure) will give slightly different results; several runs should be performed and averages taken to provide final solutions. Now, we repeat the foregoing calculation but assuming buildup-*then*-drawdown.

8.3.4.2   Reverse flow injection process, buildup-*then*-drawdown.

In the above exercise, we *withdrew* fluid from the formation by retracting the piston (the flow rate is positive, by convention) and then stopped the piston (the flow rate is zero) at t = 5 sec. Correspondingly, the pressure decreases (drawdown) and then increases (buildup). Thus, we have *drawdown-buildup*.

Now we will demonstrate how FT-00 and FT-PTA-DDBU can be used in a "reverse pumping" or "flow injection" mode. Thus, we inject fluid into the formation by *pushing* the piston into the sandface (the flow rate is now negative, by convention) and then the piston is stopped (the flow rate is zero) at t = 5 sec. We expect the pressure to increase at first (buildup) and then decrease (drawdown), that is, exactly in opposite sequence to the previous example. Thus, we have *buildup-drawdown*.

Both software modules were designed with "standard withdrawal, drawdown-buildup" and "flow injection, buildup-drawdown" applications in mind. To show how we perform forward and inverse calculations, we repeat the above example, making only minor changes to the text input boxes. To create pressure transient data, we again use forward model FT-00, and in Figure 8.8a, change the +1 cc/s value at the

top right to – 1 cc/s (this is the only change). We obtain the results on the next page. Here we are concerned with single-probe inverse analysis only, and thus, do not focus on observation probe pressures. Calculated FT-00 results are shown after Figures 8.9a,b,c,d.

We demonstrate how the inverse solver FT-PTA-DDBU can be used to predict spherical mobility and pore pressure from the transient pressure data in Figure 8.9d for reverse injection. We will use data from the times t = 6, 19.2 and 50.4 sec again. Of course, since we are now *injecting* fluid into the formation, the pressures will be higher than the assumed pore pressure of 10,000 psi. The input data are displayed in Figure 8.9d. Note that the flow rate Q (cc/s) now has a "minus" sign. From Figure 8.9e, the predicted spherical mobility is 0.05 md/cp, agreeing with 0.04642 md/cp, while the pore pressure is 10,121 which agrees with the assumed 10,000 psi.
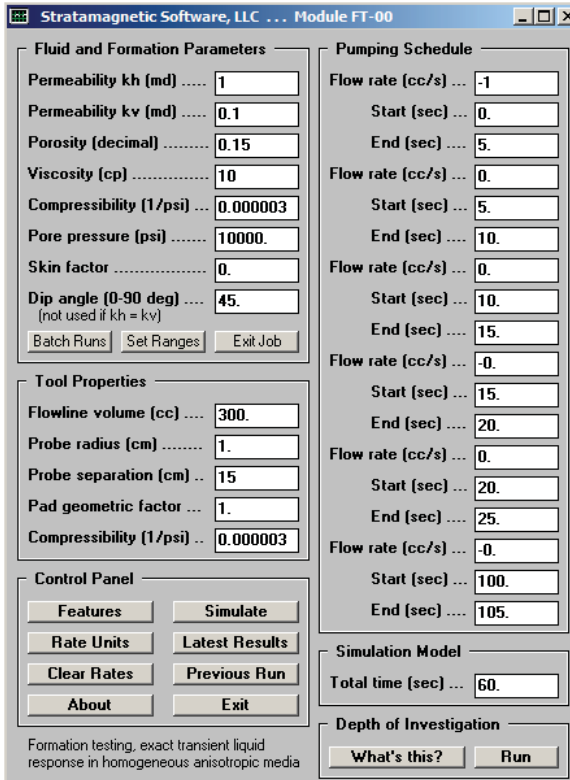
Figure 8.9a. FT-00, exact forward transient analysis.
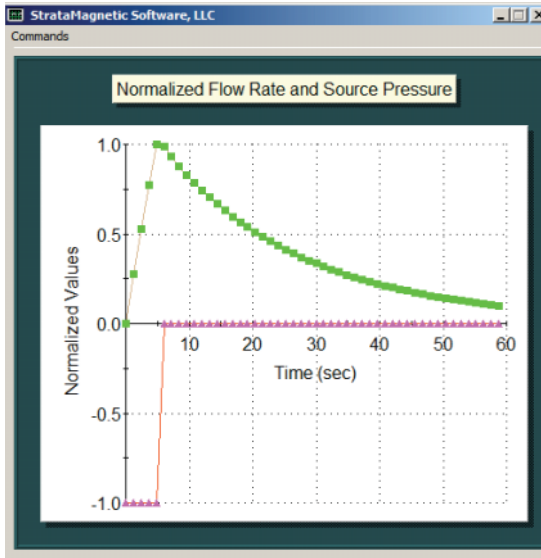
Figure 8.9b. FT-00, exact flowrate and source pressure.

Figure 8.9c. FT-00, exact source pressure.

```
FORMATION TESTER PRESSURE TRANSIENT ANALYSIS

Exact analytical solution for Darcy ellipsoidal flow
(homogeneous anisotropic media with flowline storage
and skin) using complex complementary error function.

Specific limit considered -
.... Anisotropic flow model with storage and no skin

Developer, Wilson C. Chin, Ph.D., MIT.
Copyright (C) 2004-2007, StrataMagnetic Software, LLC.
All rights reserved.   Email, wilsonchin@aol.com.

FLUID AND FORMATION PARAMETERS
Formation kh permeability ....... (md):   0.1000E+01
Formation kv permeability ....... (md):   0.1000E+00
Formation spherical permeability  (md):   0.4642E+00
Porosity .................. (decimal):     0.1500E+00
Viscosity ....................... (cp):   0.1000E+02   (spherical mobility
                                                        again 0.04642 md/cp)
Pore fluid compressibility ... (1/psi):   0.3000E-05
Pore pressure ................... (psi):   0.1000E+05
Skin factor .......... (dimensionless):   0.0000E+00
Dip angle ................ (0-90 deg):    0.4500E+02

TOOL PROPERTIES
Flowline volume ................. (cc):   0.3000E+03
Probe radius .................... (cm):   0.1000E+01
Probe separation ............... (cm):    0.1500E+02
Pad geometric factor . (dimensionless):   0.1000E+01
Flowline fluid compressibility (1/psi):   0.3000E-05

PUMPING SCHEDULE AND SIMULATION PARAMETERS
Schedule #1, Flow rate ........ (cc/s): -0.1000E+01
             Beginning time .... (sec):   0.0000E+00
             Ending time ....... (sec):   0.5000E+01
Schedule #2, Flow rate ........ (cc/s):   0.0000E+00
             Beginning time .... (sec):   0.5000E+01
             Ending time ....... (sec):   0.1000E+02
Schedule #3, Flow rate ........ (cc/s):   0.0000E+00
             Beginning time .... (sec):   0.1000E+02
             Ending time ....... (sec):   0.1500E+02
Schedule #4, Flow rate ........ (cc/s):   0.0000E+00
             Beginning time .... (sec):   0.1500E+02
             Ending time ....... (sec):   0.2000E+02
Schedule #5, Flow rate ........ (cc/s):   0.0000E+00
             Beginning time .... (sec):   0.2000E+02
             Ending time ....... (sec):   0.2500E+02
Schedule #6, Flow rate ........ (cc/s):   0.0000E+00
             Beginning time .... (sec):   0.1000E+03
             Ending time ....... (sec):   0.1050E+03
Total simulation time ......... (sec):    0.6000E+02

DEFINITIONS
Time ... Elapsed time (sec)
Rate ... Drawdown flow rate (cc/s)
Ps* .... Source pressure with hydrostatic (psi)
Pr* .... Observation pressure with hydrostatic (psi)
Ps** ... Source pressure, no hydrostatic (psi)
Pr** ... Observation pressure, no hydrostatic (psi)

       NOTE: Ps* or Pr* < 0 means volume flow
       rate cannot be achieved in practice
```

```
Time (s)  Rate (cc/s)   Ps* (psi)    Pr* (psi)   Ps**(psi)   Pr**(psi)   Pr**/Ps**
0.000E+00 -0.10000E+01 0.10000E+05 0.10000E+05 0.00000E+00 0.00000E+00 -----------
0.120E+01 -0.10000E+01 0.11281E+05 0.10000E+05 0.12812E+04 0.42301E-04 0.33016E-07
0.240E+01 -0.10000E+01 0.12483E+05 0.10000E+05 0.24832E+04 0.14086E+00 0.56724E-04
0.360E+01 -0.10000E+01 0.13616E+05 0.10002E+05 0.36156E+04 0.22378E+01 0.61892E-03
0.480E+01 -0.10000E+01 0.14684E+05 0.10009E+05 0.46843E+04 0.91429E+01 0.19518E-02
0.600E+01  0.00000E+00 0.14620E+05 0.10022E+05 0.46201E+04 0.21528E+02 0.46597E-02
0.720E+01  0.00000E+00 0.14360E+05 0.10038E+05 0.43599E+04 0.38273E+02 0.87785E-02
0.840E+01  0.00000E+00 0.14119E+05 0.10056E+05 0.41187E+04 0.56483E+02 0.13714E-01
0.960E+01  0.00000E+00 0.13894E+05 0.10072E+05 0.38936E+04 0.71882E+02 0.18462E-01
0.108E+02  0.00000E+00 0.13683E+05 0.10082E+05 0.36827E+04 0.82394E+02 0.22373E-01
0.120E+02  0.00000E+00 0.13485E+05 0.10088E+05 0.34848E+04 0.88200E+02 0.25310E-01
0.132E+02  0.00000E+00 0.13299E+05 0.10090E+05 0.32987E+04 0.90315E+02 0.27379E-01
0.144E+02  0.00000E+00 0.13124E+05 0.10090E+05 0.31235E+04 0.89812E+02 0.28753E-01
0.156E+02  0.00000E+00 0.12959E+05 0.10088E+05 0.29585E+04 0.87565E+02 0.29598E-01
0.168E+02  0.00000E+00 0.12803E+05 0.10084E+05 0.28029E+04 0.84225E+02 0.30049E-01
0.180E+02  0.00000E+00 0.12656E+05 0.10080E+05 0.26561E+04 0.80252E+02 0.30214E-01
0.192E+02  0.00000E+00 0.12518E+05 0.10076E+05 0.25176E+04 0.75962E+02 0.30173E-01
0.204E+02  0.00000E+00 0.12387E+05 0.10072E+05 0.23867E+04 0.71570E+02 0.29986E-01
0.216E+02  0.00000E+00 0.12263E+05 0.10067E+05 0.22631E+04 0.67215E+02 0.29700E-01
0.228E+02  0.00000E+00 0.12146E+05 0.10063E+05 0.21463E+04 0.62988E+02 0.29347E-01
.
.
.
0.480E+02  0.00000E+00 0.10731E+05 0.10018E+05 0.73062E+03 0.18002E+02 0.24639E-01
0.492E+02  0.00000E+00 0.10695E+05 0.10017E+05 0.69515E+03 0.17225E+02 0.24779E-01
0.504E+02  0.00000E+00 0.10662E+05 0.10017E+05 0.66150E+03 0.16510E+02 0.24958E-01
0.516E+02  0.00000E+00 0.10630E+05 0.10016E+05 0.62957E+03 0.15851E+02 0.25177E-01
0.528E+02  0.00000E+00 0.10599E+05 0.10015E+05 0.59927E+03 0.15243E+02 0.25435E-01
0.540E+02  0.00000E+00 0.10571E+05 0.10015E+05 0.57050E+03 0.14682E+02 0.25735E-01
```

Figure 8.9d. Computed presssure transient history for reverse flow.
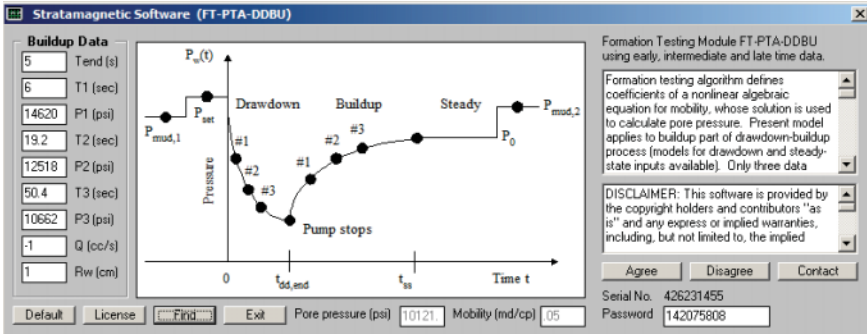
Figure 8.9e. FT-PTA-DDBU, approximate predictions for
spherical mobility and pore pressure.

In closing, we note that we have addressed pore pressure and permeability prediction at higher mobilities in Chapter 7, and at very low values here in Chapter 8. While these are typically used in well logging and reservoir engineering, the quantities are also important in dictating mudcake growth as explained in Chapters 5 and 6 – and consequently, are influential on affecting wellbore stability and drilling safety.

8.4 References.

- Chin, W.C., Zhou, Y., Feng, Y., Yu, Q. and Zhao, L., *Formation Testing: Pressure Transient and Contamination Analysis*, John Wiley & Sons, Hoboken, New Jersey, 2014.

- Chin, W.C., Zhou, Y., Feng, Y. and Yu, Q., *Formation Testing: Low Mobility Pressure Transient Analysis*, John Wiley & Sons, Hoboken, New Jersey, 2015.

Cumulative References

(i) Drilling, Cementing and Annular Flow.

- Anderson, A.G., "Sedimentation," *Handbook of Fluid Mechanics*, Streeter, V.L., Editor, McGraw-Hill, New York, 1961.

- Batchelor, G.K., *Fluid Dynamics*, Cambridge University Press, Cambridge, 1970.

- Becker, T.E., Azar, J.J., and Okrajni, S.S., "Correlations of Mud Rheological Properties with Cuttings Transport Performance in Directional Drilling," SPE Paper No. 19535, 64th Annual Technical Conference and Exhibition, Society of Petroleum Engineers, San Antonio, October 1989.

- Becker, T.E., Morgan, R.G., Chin, W.C., and Griffith, J.E., "Improved Rheology Model and Hydraulics Analysis for Tomorrow's Wellbore Fluid Applications," Paper 82415*, SPE Production and Operations Symposium*, Oklahoma City, OK, March 2003.

- Bird, R.B., Armstrong, R.C., and Hassager, O., *Dynamics of Polymeric Liquids, Volume 1: Fluid Mechanics*, John Wiley & Sons, New York, 1987.

- Bird, R.B., Stewart, W.E., and Lightfoot, E.N., *Transport Phenomena*, Second Edition, John Wiley & Sons, New York, 2002.

- Chhabra, R.P., and Richardson, J.F., *Non-Newtonian Flow in the Process Industries*, Butterworth-Heinemann, Oxford, 1999.
- Chin, W.C., *Borehole Flow Modeling in Horizontal, Deviated and Vertical Wells*, Gulf Publishing, Houston, 1992.
- Chin, W.C., *Computational Rheology for Pipeline and Annular Flow*, Elsevier Science, London, 2001.
- Chin, W.C., "Modeling and Simulation of Managed Pressure Drilling for Improved Design, Risk Assessment, Training and Operations," *RPSEA Ultra-Deepwater Technology Conference*, Houston, Tx, June 22-23, 2010.
- Chin, W.C., "Flow Simulation Methods for Managed Pressure Drilling and Cementing," *Drilling and Completing Trouble Zones Conference*, Galveston, Tx, Oct. 19-21, 2010.
- Chin, W.C., *Managed Pressure Drilling: Modeling, Strategy and Planning*, Elsevier, Amsterdam, 2012.
- Chin, W.C., *Managed Pressure Drilling: Modeling, Strategy and Planning*, Chinese Edition, Elsevier, Singapore, 2016.
- Chin, W.C., and Zhuang, X., "Exact Non-Newtonian Flow Analysis of Yield Stress Fluids in Highly Eccentric Borehole Annuli with Pipe or Casing Translation and Rotation," Paper 131234-PP, *CPS/SPE International Oil & Gas Conference and Exhibition*, Beijing, China, June 8-10, 2010.
- Chin, W.C., and Zhuang, X., "Effect of Rotation on Flowrate and Pressure Gradient in Eccentric Holes," Paper AADE-11-NTCE-45, *AADE 2011 National Technical Conference and Exhibition*, Houston, TX, April 12-14, 2011 (a).
- Chin, W.C., and Zhuang, X., "Advances in Swab-Surge Modeling for Managed Pressure Drilling," Paper AADE-11-NTCE-46, *AADE 2011 National Technical Conference and Exhibition*, Houston, TX, April 12-14, 2011 (b).
- Chin, W.C., and Zhuang, X., "Transient, Multiphase, Three-Dimensional Pumping Models for Cementing and Drilling," Paper AADE-11-NTCE-72, *AADE 2011 National Technical Conference and Exhibition*, Houston, TX, April 12-14, 2011 (c).

- Chin, W.C., and Zhuang, X., "Comprehensive Annular Flow Models for Drilling and Completions," Paper AADE-11-NTCE-73, *AADE 2011 National Technical Conference and Exhibition*, Houston, TX, April 12-14, 2011 (d).

- Chin, W.C. and Zhuang, X., "Advances in Swab-Surge Modeling for Managed Pressure Drilling," Paper OTC-21115-PP, *2011 Offshore Technology Conference*, Houston, TX, May 2-5, 2011 (e).

- Deawwanich, T., Liew, J.C., Nguyen, Q.D., Savery, M., Tonmukayakul, N., and Chin, W.C., "Displacement of Viscoplastic Fluids in Eccentric Annuli: Numerical Simulation and Experimental Validation," *Chemeca 2008 Conference*, Newcastle, Australia, Sept. 28 - Oct. 1, 2008.

- Dodge, D.W., and Metzner, A.B., "Turbulent Flow of Non-Newtonian Systems," American Institute of Chemical Engineering Journal, June 1959, Vol. 5, No. 2, pp. 189-204.

- Escudier, M.P., Gouldson, I.W., Oliveira, P.J., and Pinho, F.T., "Effects of Inner Cylinder Rotation on Laminar Flow of a Newtonian Fluid Through an Eccentric Annulus," International Journal of Heat and Fluid Flow, 2000, Vol. 21, pp. 92-103.

- Fang, P., and Manglik, R.M., "The Influence of Inner Cylinder Rotation on Laminar Axial Flows in Eccentric Annuli of Drilling Bore Wells," I.J. Trans. Phenomena, Old City Publishing, 2002, Vol. 4, pp. 257-274.

- Fraser, L.J., "Field Application of the All-Oil Drilling Fluid Concept," IADC/SPE Paper No. 19955, 1990 IADC/SPE Drilling Conference, Houston, February 27-March 2, 1990.

- Fraser, L.J., "Green Canyon Drilling Benefits from All OilMud," *Oil and Gas Journal*, March 19, 1990, pp. 33-39.

- Fraser, L.J., "Effective Ways to Clean and Stabilize High-Angle Hole," *Petroleum Engineer International*, November 1990, pp.30-35.

- Fredrickson, A.G., and Bird, R.B., "Non-Newtonian Flow in Annuli," *Ind. Eng. Chem.*, Vol. 50, 1958, p. 347.

- Halliday, W.S., and Clapper, D.K., "Toxicity and Performance Testing of Non-Oil Spotting Fluid for Differentially Stuck Pipe," Paper No. 18684, SPE/IADC Drilling Conference, New Orleans, February 28-March 3, 1989.

- Hussain, Q.E., and Sharif, M.A.R., "Numerical Modeling of Helical Flow of Viscoplastic Fluids in Eccentric Annuli," AIChE Journal, Oct. 2000, Vol. 46, No. 10, pp. 1937-1946.

- Ibraheem, S.O., Adewumi, M.A., and Savidge, J.L., "Numerical Simulation of Hydrate Transport in Natural Gas Pipeline," *Journal of Energy Resources Technology*, Transactions of the ASME, Vol. 120, March 1998, pp. 20-26.

- Kapfer, W.H., "Flow of Sludges and Slurries," *Piping Handbook*, King, R., Editor, McGraw-Hill, New York, 1973.

- Landau, L.D., and Lifschitz, E.M., *Fluid Mechanics*, Pergamon Press, London, 1959.

- Milne-Thomson, L.M., *Theoretical Hydrodynamics*, Fifth Edition, McMillan Company, New York, 1968.

- Morrison, F.A., *Understanding Rheology*, Oxford University Press, Oxford, 2001.

- Nguyen, Q.D., Deawwanich, T., Tonmukayakul, N., Savery, M.R., and Chin, W.C., "Flow Visualization and Numerical Simulation of Viscoplastic Fluid Displacements in Eccentric Annuli," *XVth International Congress on Rheology (ICR 2008)*, Society of Rheology 80th Annual Meeting, Monterey, CA, Aug. 3-8, 2008.

- Outmans, H.D., "Mechanics of Differential Pressure Sticking of Drill Collars," *Petroleum Transactions*, AIME, Vol. 213, 1958, pp. 265-274.

- Quigley, M.S., Dzialowski, A.K., and Zamora, M., "A Full-Scale Wellbore Friction Simulator," IADC/SPE Paper No. 19958, 1990 IADC/SPE Drilling Conference, Houston, February 27-March 2, 1990.

- Savery, M., Chin, W.C., and Babu Yerubandi, K., "Modeling Cement Placement Using a New Three-Dimensional Flow Simulator," Paper AADE-08-DF-HO-08, 2008 AADE Fluids Conference and Exhibition, American Association of Drilling Engineers, Houston, Texas, April 8-9, 2008.

- Savery, M., Darbe, R., and Chin, W.C., "Modeling Fluid Interfaces During Cementing Using a Three-Dimensional Mud Displacement Simulator," OTC Paper 18513, *2007 Offshore Technology Conference (OTC)*, Houston, TX, April 30 – May 3, 2007.

- Savery, M., Tonmukayakul, P., Chin, W.C., Deawwanich, T., Liew, J., and Q. D. Nguyen, "Laminar Displacement of Viscoplastic Fluids in Eccentric Annuli – Numerical Simulation and Experimental Validations," *XXII International Congress of Theoretical and Applied Mechanics (ICTAM 2008)*, Adelaide, Australia, Aug. 24-29, 2008.

- Savins, J.G., "Generalized Newtonian (Pseudoplastic) Flow in Stationary Pipes and Annuli," *Petroleum Transactions*, AIME, Vol. 213, 1958, pp. 325-332.

- Savins, J.G., and Wallick, G.C., "Viscosity Profiles, Discharge Rates, Pressures, and Torques for a Rheologically Complex Fluid in a Helical Flow," *A.I.Ch.E. Journal*, Vol. 12, No. 2, March 1966, pp. 357-363.

- Schlichting, H., *Boundary Layer Theory*, McGraw Hill, New York, 1968.

- Seeberger, M.H., Matlock, R.W., and Hanson, P.M., "Oil Muds in Large Diameter, Highly Deviated Wells: Solving the Cuttings Removal Problem," SPE/IADC Paper No. 18635, 1989 SPE/IADC Drilling Conference, New Orleans, February 28-March 3, 1989.

- Skelland, A.H.P., *Non-Newtonian Flow and Heat Transfer*, John Wiley & Sons, New York, 1967.

- Slattery, J.C., *Momentum, Energy, and Mass Transfer in Continua*, Robert E. Krieger Publishing Company, New York, 1981.

- Souza Mendes, P.R., Braga, A.M.B., Azevedo, L.F.A., and Correa, K.S., "Resistive Force of Wax Deposits During Pigging Operations," *Journal of Energy Resources Technology*, Transactions of the ASME, Vol. 121, September 1999, pp. 167-171.

- Souza Mendes, P.R., and Dutra, E.S.S., "A Viscosity Function for Viscoplastic Liquids," Annual Transactions of the Nordic Rheology Society, Vol. 12, 2004.

- Streeter, V.L., *Handbook of Fluid Dynamics*, McGraw-Hill, New York, 1961.

- Tamamidis, P., and Assanis, D.N., "Generation of Orthogonal Grids with Control of Spacing," *Journal of Computational Physics*, Vol. 94, 1991, pp. 437-453.

- Thompson, J.F., "Grid Generation Techniques in Computational Fluid Dynamics," *AIAA Journal*, November 1984, pp. 1505-1523.

- Thompson, J.F., Warsi, Z.U.A., and Mastin, C.W., *Numerical Grid Generation*, Elsevier Science Publishing, New York, 1985.

- Turner, J.S., *Buoyancy Effects in Fluids*, Cambridge University Press, London, 1973.

- Walton, I.C., and Bittleston, S.H., "The Axial Flow of a Bingham Plastic in a Narrow Eccentric Annulus," Journal of Fluid Mechanics, 1991, Vol. 222, pp. 39-60.

- Yih, C.S., "Exact Solutions for Steady Two-Dimensional Flow of a Stratified Fluid," Journal of Fluid Mechanics, 1960, Volume 9, pp. 161-174.

- Yih, C.S., Fluid Mechanics, McGraw-Hill, New York, 1969.

- Yih, C.S., *Stratified Flows*, Academic Press, New York, 1980.

(ii)   Formation Testing Pressure and Contamination Analysis.

- Adeyemi, O.S. and Edwards, M.D., "Matrix Selection for Conventional and Nonconventional Testing and Sampling in Gas Reservoirs," SPE Paper No. 96972, *2005 SPE Annual Technical Conference and Exhibition*, Dallas, Texas, Oct. 9-12, 2005.

- Akkurt, R., Bowcock, M., Davies, J., Del Campo, C., Hill, B., Joshi, S., Kundu, D., Kumar, S., O'Keefe, M., Samir, M., Tarvin, J., Weinheber, P., Williams, S., Zeybek, M., "Focusing on Downhole Fluid Sampling and Analysis," *Oilfield Review*, Winter 2006/2007.

- Al-Mohsin, A., Tariq, S. and Haq, S.A., "Application of Wireline Formation Tester (Openhole and Cased-Hole) Sampling Techniques for Estimation of Nonhydrocarbon Gas Content of Khuff Reservoir Fluids in the North Field, Qatar," IPTC Paper No. 10622, *International Petroleum Technology Conference*, Doha, Qatar, Nov. 21-23, 2005.

- Andrews, R.J., Beck, G., Castelijns, K., Chen, A., Cribbs, M.E., Fadnes, F.H., Irvine-Fortescue, J., Williams, S., Hashem, M., Jamaluddin, A., Kurkjian, A., Sass, B., Mullins, O.C., Rylander, E., and van Dusen, A., "Quantifying Contamination Using Color of Crude and Condensate," *Oilfield Review*, Autumn 2001.

- Angeles, R., Torres-Verdin, C., Lee, H.J., Alpak, F.O. and Sheng, J., "Estimation of Permeability and Permeability Anisotropy from Straddle Packer Formation Tester Measurements Based on the Physics of Two-Phase Immiscible Flow and Invasion," *SPE Journal*, Sept. 2007, pp. 339-354.

- Ayan, C., Hafez, H., Hurst, S., Kuchuk, F., O'Callaghan, A., Peffer, J., Pop, J., and Zeybek, M., "Characterizing Permeability with Formation Testers," *Oilfield Review*, Autumn 2001.

- Aziz, K. and Settari, A., *Petroleum Reservoir Simulation*, Applied Science Publishers, London, 1979.

- Bassiouni, Z. and Yildiz, T., "Interpretation of Wireline Formation Tester (WFT) Data in Tight Gas Sands," *Journal of Canadian Petroleum Technology*, June 1999, Vol. 38, No. 6, pp. 29-36.

- Bowles, D., "Bridging the Gap Between Wireline Formation, Drill Stem Testing," *Offshore Magazine*, June 1, 2004.

- Brigham, W.E., Peden, J.M., Ng, K.F., and O'Neill, N., "The Analysis of Spherical Flow with Wellbore Storage," SPE Paper No. 9294, *55th Annual Fall Technical Conference and Exhibition of the Society of Petroleum Engineers of AIME*, Dallas, Texas, Sept. 21-24, 1980.

- Chin, W.C., *Modern Reservoir Flow and Well Transient Analysis*, Gulf Publishing, Houston, 1993.

- Chin, W.C., *Formation Invasion, with Applications to Measurement-While-Drilling, Time Lapse Analysis, and Formation Damage*, Gulf Publishing, Houston, 1995.

- Chin, W.C., *Quantitative Methods in Reservoir Engineering*, Elsevier Science, Amsterdam, 2002.

- Chin, W.C., *Quantitative Methods in Reservoir Engineering*, Second Edition, Elsevier Science, Amsterdam, 2017.

- Chin, W.C., "FTWD-Processing-Algorithms-V56a," *Stratamagnetic Software Internal Report*, July 2012.

- Chin, W.C., "Formation Tester Flow Analysis in Anisotropic Media With Flowline Storage and Skin at Arbitrary Dip," *Well Logging Technology Journal*, Xi'an, China, Feb. 2013.

- Chin, W.C. and Proett, M.A., "Formation Evaluation Using Phase Shift Periodic Pressure Pulse Testing," United States Patent No. 5,672,819 issued Sept. 30, 1997.

- Chin, W.C. and Proett, M.A., "Formation Tester Immiscible and Miscible Flow Modeling for Job Planning Applications," *SPWLA 46th Annual Logging Symposium*, New Orleans, Louisiana, June 26-29, 2005.

- Chin, W.C., Suresh, A., Holbrook, P., Affleck, L. and Robertson, H., "Formation Evaluation Using Repeated MWD Logging Measurements," *SPWLA 27th Annual Logging Symposium*, Houston, Texas, June 9-13, 1986.

- Chin, W.C., Zhou, Y., Feng, Y., Yu, Q. and Zhao, L., *Formation Testing: Pressure Transient and Contamination Analysis*, John Wiley & Sons, Hoboken, New Jersey, 2014.

- Chin, W.C. and Zhuang, X., "Formation Tester Inverse Permeability Interpretation for Liquids in Anisotropic Media with Flowline

Storage and Skin at Arbitrary Dip," *SPWLA 48th Annual Logging Symposium*, Austin, Texas, June 3-6, 2007.

- Chow, W.K., Ho, C.M., and Fong, N.K., "Evaluation of the Finite Control Volume Method in Simulating Thermal Fire Resistance of Building Elements," *Building Simulation, Fifth International IBPSA Conference*, Sept. 8-10, 1997, Prague, Czech Republic, Vol. 1, p. 273.

- Crombie, A., Halford, F., Hashem, M., McNeil, R., Thomas, E.C., Melbourne, G. and Mullins, O.C., "Innovations in Wireline Fluid Sampling," *Oilfield Review*, Autumn 1998.

- Doll, Henri-Georges, "Methods and Apparatus for Determining Hydraulic Characteristics of Formations Traversed by a Borehole," U. S. Patent No. 2,747,401, issued May 29, 1956.

- Dussan, E.B., Auzerais, F.M. and Kenyon, W.E., "Apparatus for Determining Horizontal and/or Vertical Permeability of an Earth Formation," United States Patent No. 5,279,153 awarded Jan. 18, 1994.

- Fan, L., Harris, B.W., Jamaluddin, A., Kamath, J., Mott, R., Pope, G.A., Shandrygin, A., Whitson, C.H., "Understanding Gas-Condensate Reservoirs," *Oilfield Review*, Winter 2005/2006.

- Goode, P.A. and Thambynayagam, R.K.M., "Analytic Models for a Multiple Probe Formation Tester," SPE Paper No. 20737, *65th Annual Technical Conference and Exhibition of the Society of Petroleum Engineers*, New Orleans, Louisiana, Sept. 23-26, 1990.

- Goode, P.A., and Thambynayagam, R.K.M., "Permeability Determination With a Multiprobe Formation Tester," *SPE Formation Evaluation Journal*, Dec. 1992, pp. 297-303.

- Ireland, T., Joseph, J., Colley, N., Reignier, P., Richardson, S. and Zimmerman, T., "The MDT Tool: A Wireline Testing Breakthrough," *Oilfield Review*, April 1992.

- Jones, C., Alta, W., Singh, J., Engelman, B., Proett, M. and Pedigo, B., "Collecting Single-Phase Retrograde Gas Samples at Near-Dewpoint Reservoir Pressure in Carbonates Using a Pump-Out Formation Tester with an Oval Pad," SPE Paper No. 110831, *2007 SPE Annual Technical Conference and Exhibition*, Anaheim, Ca., Nov. 11-14, 2007.

- Joseph, J.A., and Koederitz, L.F., "Unsteady-State Spherical Flow with Storage and Skin," *Society of Petroleum Engineers Journal*, Dec. 1985, pp. 804-822.

- Kasap, E., Huang, K., Shwe, T. and Georgi, D., "Formation-Rate-Analysis Technique: Combined Drawdown and Buildup Analysis for Wireline Formation Test Data," SPE Reservoir Evaluation and Engineering Journal, June 1999 (this is a revision of SPE Paper No. 36525, *Society of Petroleum Engineers Annual Technical Conference and Exhibition*, Denver, Colorado, Oct. 6-9, 1996).

- Kool, H., Azari, M., Soliman, M.Y., Proett, M.A., Irani, C.A., Dybdahl, B., "Testing of Gas Condensate Reservoirs - Sampling, Test Design and Analysis," SPE Paper No. 68668, *SPE Asia Pacific Oil and Gas Conference and Exhibition*, Jakarta, Indonesia, April 17-19, 2001.

- Liu, W, Hildebrand, M.A., Lee, J. and Sheng, J., "High-Resolution Near-Wellbore Modeling and Its Applications in Formation Testing," SPE Paper 90767, *SPE Annual Technical Conference and Exhibition*, Houston, Texas, Sept. 26-29, 2004.

- Moran, J. H. and Finklea, E.E., "Theoretical Analysis of Pressure Phenomena Associated with the Wireline Formation Tester," *Journal of Petroleum Technology*, August 1962, pp. 899-908.

- Peaceman, D.W., *Fundamentals of Numerical Reservoir Simulation*, Elsevier Scientific Publishing, Amsterdam, 1977.

- Peaceman, D.W. and Rachford, H.H., "Numerical Calculation of Multidimensional Miscible Displacement," *Society of Petroleum Engineers Journal*, Dec., 1962, pp. 327-339.

- Proett, M.A. and Chin, W.C., "Supercharge Pressure Compensation with New Wireline Formation Testing Method," *Annual Meeting of the Society of Professional Well Log Analysts*, New Orleans, Louisiana, June 1996.

- Proett, M.A. and Chin, W.C., "Supercharge Pressure Compensation Using a New Wireline Testing Method and Newly Developed Early Time Spherical Flow Model," SPE Paper No. 36524, *Annual Technical Conference and Exhibition of the Society of Petroleum Engineers*, Denver, Colorado, Oct. 1996.

- Proett, M.A. and Chin, W.C., "Multi-Probe Pressure Transient Analysis for Determination of Horizontal Permeability, Anisotropy

and Skin in an Earth Formation," United States Patent No. 7,059,179 issued June 13, 2006.

- Proett, M.A., Chin, W.C., Beique, J.M., Hardin, J.R., Fogal, J.M., Welshans, D., and Gray, G.C., "Methods for Measuring a Formation Supercharge Pressure," United States Patent No. 7,243,537, issued July 17, 2007.

- Proett, M.A., Chin, W.C. and Mandal, B., "Advanced Permeability and Anisotropy Measurements While Testing and Sampling in Real-Time Using a Dual Probe Formation Tester," SPE Paper No. 64650, *Seventh International Oil & Gas Conference and Exhibition*, Beijing, China, Nov. 2000.

- Proett, M.A., Chin, W.C., Manohar, M., Gilbert, G.N., and Monroe, M.L., "New Dual Probe Wireline Formation Testing and Sampling Tool Enables Real-Time Permeability and Anisotropy Measurements," SPE Paper No. 59701, *2000 SPE Permian Basin Oil and Gas Recovery Conference*, Midland, Texas, Mar. 21-23, 2000.

- Proett, M.A., Seifert, D., Chin, W.C., Lysen, S., and Sands, P., "Formation Testing in the Dynamic Drilling Environment," *SPWLA 45th Annual Logging Symposium*, Noordwijk, The Netherlands, June 6–9, 2004.

- Proett, M.A. and Waid, M.C., "Wireline Formation Testing for Low Permeability Formations Utilizing Pressure Transients," United States Patent No. 5,602,334, awarded February 11, 1997.

- Proett, M.A., Weintraub, P.N., Golla, C.A., and Simeonov, S.D., "Formation Testing While Drilling Data Compression," United States Patent 6,932,167 B2, awarded August 23, 2005.

- Raghavan, R., *Well Test Analysis*, Prentice Hall, Englewood Cliffs, New Jersey, 1993.

- Schlumberger Staff, *Fundamentals of Formation Testing*, Schlumberger Marketing Communications, Sugar Land, Texas, 2006.

- Sheng, J.J., Georgi, D.T. and Burge, J., "Concept of Geometric Factor and Its Practical Application to Estimate Horizontal and Vertical Permeabilities," SPE Reservoir Evaluation and Engineering Journal, December 2006, pp. 698-707.

- SPWLA Staff, *SPWLA Wireline Formation Testing Technology Workshop*, 38th SPWLA Annual Symposium, Society of Professional Well Log Analysts, Houston, Texas, June 15-18, 1997.

- SPWLA Staff, *SPWLA Formation Testing: Applications and Practices*, Spring Topical Conference, Society of Petrophysicists and Well Log Analysts, Taos, New Mexico, Mar. 28 – April 1, 2004.

- Staff, *Log Interpretation Principles/Applications*, Schlumberger Wireline and Testing, Sugar Land, 1989.

- Stewart, G. and Wittmann, M., "Interpretation of the Pressure Response of the Repeat Formation Tester," SPE Paper No. 8362, *54th Annual Fall Technical Conference and Exhibition of the Society of Petroleum Engineers of AIME*, held in Las Vegas, Nevada, Sept. 23-26, 1979.

- Todd, M.R. and Longstaff, W.J., "The Development, Testing and Application of a Numerical Simulator for Predicting Miscible Flood Performance," *Journal of Petroleum Technology*, July 1972, pp. 874-882.

- Villareal, S.G., Ciglenec, R., Stucker, M.J., and Duong, K., "Formation Evaluation While Drilling," United States Patent No. 7,367,394 issued May 6, 2008.

- Wang, X. and Economides, M., "Aggressive Fracturing Slashes Turbulence in High-Permeability Gas Wells," *World Oil*, July 2004, pp. 73-79.

- Xu, H., Bassiouni, Z., and Desbrandes, R., "Three-Dimensional Finite Difference Modeling of Wireline Formation Tests in Tight Gas Sands," SPE Paper No. 24886, *67th Annual Technical Conference and Exhibition of the Society of Petroleum Engineers*, Washington, DC, Oct. 4-7, 1992.

- Zhou, Y., Hao, Z., Feng, Y., Yu, Q. and Chin, W.C., "Formation Testing: New Methods for Rapid Mobility and Pore Pressure Prediction," Paper OTC-24890-MS, 2014 Offshore Technology Conference Asia (OTC Asia), Kuala Lumpur, Malaysia, Mar. 25-28, 2014.

- Zhou, Y., Zhao, L., Feng, Y., Yu, Q., and Chin, W.C., "Formation Testing: New Methods for Rapid Mobility and Pore Pressure Prediction," Paper 17214, 7th International Petroleum Technology Conference (IPTC), Doha, Qatar, Jan. 19-22, 2014.

(iii) Reservoir Engineering and Simulation.

- Aguilera, R., *Naturally Fractured Reservoirs*, PennWell Publishing Company, Tulsa, 1980.

- Aguilera, R., Artindale, J.S., Cordell, G.M., Ng, M.C., Nicholl, G.W. and Runions, G.A., *Horizontal Wells – Formation Evaluation, Drilling, and Production*, Gulf Publishing, Houston, 1991.

- Allen, D., Auzerais, F., Dussan, E., Goode, P., Ramakrishnan, T.S., Schwartz, L., Wilkinson, D., Fordham, E., Hammond, P., and Williams, R., "Invasion Revisited," *Schlumberger Oilfield Review*, July 1991, pp. 10-23.

- Allen, D.F., and Jacobsen, S.J., "Resistivity Profiling with a Multi-Frequency Induction Sonde," *SPWLA 28th Annual Logging Symposium*, London, June 29-July 2, 1987.

- Allen, M.B., and Pinder, G.F., "The Convergence of Upstream Collocation in the Buckley-Leverett Problem," SPE Paper No. 10978, *57th Annual Fall Technical Conference and Exhibition of the Society of Petroleum Engineers*, New Orleans, La., Sept. 26-29, 1982.

- Aziz, K., and Settari, A., *Petroleum Reservoir Simulation*, Applied Science Publishers, London, 1979.

- Batchelor, G.K., *An Introduction to Fluid Dynamics*, Cambridge University Press, London, 1970.

- Bear, J., *Dynamics of Fluids in Porous Media*, American Elsevier Publishing, Inc., New York, 1972.

- Broussard, S., "The Annulus Effect," *Schlumberger Technical Review*, Vol. 37, No. 1, 1989, pp. 41-47.

- Cardwell, W.T., "The Meaning of the Triple Value in Noncapillary Buckley-Leverett Theory," *Petroleum Transactions, AIME*, Vol. 216, 1959, pp. 271-276.

- Chappelear, J.E., and Williamson, A.S., "Representing Wells in Numerical Reservoir Simulation: Part 2–Implementation," *Society of Petroleum Engineers Journal*, June 1981, pp. 339-344.

- Chen-Charpentier, B., and Kojouharov, H.V., "Modeling of Subsurface Biobarrier Formation," *Proceedings of the 2000 Conference on Hazardous Waste Research* (Larry E. Erickson, Editor), Great Plains/Rocky Mountain Hazardous Substance Research Center, Manhattan, KS, 2001, pp. 228-237.

- Cherry, J.A., and Freeze, R.A., *Groundwater*, Prentice-Hall, Englewood Cliffs, NJ, 1979.

- Chin, W.C., "Simulating Horizontal Well Fracture Flow," *Offshore*, Aug. 1988, pp. 49-52.

- Chin, W.C., *Borehole Flow Modeling in Horizontal, Deviated and Vertical Wells*, Gulf Publishing, Houston, 1992.

- Chin, W.C., *Petrocalc 14: Horizontal and Vertical Annular Flow Modeling, Petroleum Engineering Software for the IBM PC and Compatibles*, Gulf Publishing, Houston, 1992.

- Chin, W.C., *Modern Reservoir Flow and Well Transient Analysis*, Gulf Publishing, Houston, 1993.

- Chin, W.C., *3D/SIM: 3D Petroleum Reservoir Simulation for Vertical, Horizontal, and Deviated Wells, Petroleum Engineering Software for the IBM PC and Compatibles*, Gulf Publishing, Houston, 1993.

- Chin, W.C., *Wave Propagation in Petroleum Engineering, with Applications to Drillstring Vibrations, Measurement-While-Drilling, Swab-Surge and Geophysics*, Gulf Publishing, Houston, 1994.

- Chin, W.C., *Formation Invasion, with Applications to Measurement-While-Drilling, Time Lapse Analysis and Formation Damage*, Gulf Publishing, Houston, 1995.

- Chin, W.C., *Quantitative Methods in Reservoir Engineering, First Edition*, Elsevier Science, Woburn, MA, 2002.

- Chin, W.C., "FTWD-Processing-Algorithms-V56a," Stratamagnetic Software Internal Report, July 2012.

- Chin, W.C., "Formation Tester Flow Analysis in Anisotropic Media With Flowline Storage and Skin at Arbitrary Dip," *Well Logging Technology Journal*, Xi'an, China, Feb. 2013.

- Chin, W.C., "Formation Evaluation Using Phase Shift Periodic Pressure Pulse Testing in Anisotropic Media," United States Provisional Patent Application No. 62172120, June 7, 2015.

- Chin, W.C., *Quantitative Methods in Reservoir Engineering, Second Edition – with New Topics in Formation Testing and Multilateral Well Flow Analysis*, Elsevier Science, Woburn, MA, 2016.

- Chin, W.C., *Reservoir Engineering in Modern Oilfields: Vertical, Deviated, Horizontal and Multilateral Well Systems*, John Wiley & Sons, Hoboken, New Jersey, 2016 (a).

- Chin, W.C., *Resistivity Modeling: Propagation, Laterolog and Micro-Pad Analysis*, John Wiley & Sons, Hoboken, New Jersey, 2016 (b).

- Chin, W.C. and Proett, M.A., "Formation Evaluation Using Phase Shift Periodic Pressure Pulse Testing," United States Patent No. 5,672,819 issued Sept. 30, 1997.

- Chin, W.C. and Proett, M.A., "Formation Tester Immiscible and Miscible Flow Modeling for Job Planning Applications," *SPWLA 46th Annual Logging Symposium*, New Orleans, Louisiana, June 26-29, 2005.

- Chin, W.C., Suresh, A., Holbrook, P., Affleck, L., and Robertson, H., "Formation Evaluation Using Repeated MWD Logging Measurements," Paper No. U, *SPWLA 27th Annual Logging Symposium*, Houston, TX, June 9-13, 1986.

- Chin, W.C., Zhou, Y., Feng, Y. and Yu, Q., *Formation Testing: Low Mobility Pressure Transient Analysis*, John Wiley & Sons, Hoboken, New Jersey, 2015.

- Chin, W.C., Zhou, Y., Feng, Y., Yu, Q. and Zhao, L., *Formation Testing Pressure Transient and Contamination Analysis*, John Wiley & Sons, Hoboken, New Jersey, 2014 (b).

- Chin, W.C. and Zhuang, X., "Formation Tester Inverse Permeability Interpretation for Liquids in Anisotropic Media with Flowline Storage and Skin at Arbitrary Dip," *SPWLA 48th Annual Logging Symposium*, Austin, Texas, June 3-6, 2007.

- Cobern, M.E., and Nuckols, E.B., "Application of MWD Resistivity Relogs to Evaluation of Formation Invasion," *SPWLA 26th Annual Logging Symposium*, June 17-20, 1985.

- Collins, R.E., *Flow of Fluids Through Porous Materials*, Reinhold Publishing, New York, 1961.

- Craig, F.F., *The Reservoir Engineering Aspects of Waterflooding, SPE Monograph Series*, Society of Petroleum Engineers, Dallas, 1971.

- Dake, L.P., *Fundamentals of Reservoir Engineering*, Elsevier Scientific Publishing, Amsterdam, 1978.

- Dewan, J.T., and Chenevert, M.E., "Mudcake Buildup and Invasion in Low Permeability Formations: Application to Permeability Determination by Measurement While Drilling," Paper NN, SPWLA 34th Annual Logging Symposium, June 13-16, 1993.

- Dewan, J.T., and Holditch, S.A., "Radial Response Functions for Borehole Logging Tools," Topical Report, Contract No. 5089-260-1861, Gas Research Institute, Jan. 1992.

- Ding, D.Y., Wu, Y.S., Farah, N., Wang, C., and Bourbiaus, B., "Numerical Simulation of Low Permeabiliity Unconventional Gas Reservoirs," SPE Paper 167711, SPE/EAGE European Unconventional Conference and Exhibition, Vienna, Austria, Feb. 25-27, 2014.

- Doll, H.G., "Filtrate Invasion in Highly Permeable Sands," *The Petroleum Engineer*, Jan. 1955, pp. B-53 to B-66.

- Douglas, J., Blair, P.M., and Wagner, R.J., "Calculation of Linear Waterflood Behavior Including the Effects of Capillary Pressure," *Petroleum Transactions, AIME*, Vol. 213, 1958, pp. 96-102.

- Douglas, J., Peaceman, D.W., and Rachford, H.H., "A Method for Calculating Multi-Dimensional Immiscible Displacement," *Petroleum Transactions, AIME*, Vol. 216, 1959, pp. 297-306.

- Durlofsky, L.J. and Aziz, K., "Advanced Techniques for Reservoir Simulation and Modeling of Nonconventional Wells," Final Report, DOE Award DE-AC26-99BC15213, Department of Petroleum Engineering, Stanford University, Aug. 20, 2004.

- Durst, D.G. and Vento, M.C., "Unconventional Shale Play Selective Fracturing Using Multilateral Technology," SPE Paper 151989-MS, SPE/EAGE European Unconventional Resources Conference and Exhibition, Vienna, Austria, March 20-22, 2012.

- Economides, M.J., and Nolte, K.G., *Reservoir Stimulation*, Schlumberger Educational Services, Houston, 1987.

- Estrada, R., and Kanwal, R.P., "The Carleman Type Singular Integral Equations," *SIAM Review*, Vol. 29, No. 2, June 1987, pp. 263-290.

- Fayers, F.J., and Sheldon, J.W., "The Effect of Capillary Pressure and Gravity on Two-Phase Fluid Flow in a Porous Medium," *Petroleum Transactions, AIME*, Vol. 216, 1959, pp. 147-155.

- Fordham, E.J., Allen, D.F., Ladva, H.K.J., and Alderman, N.J., "The Principle of a Critical Invasion Rate and Its Implications for Log Interpretation," SPE Paper No. 22539, 66th Annual Technical Conference and Exhibition of the Society of Petroleum Engineers, Dallas, TX, Oct. 6-9, 1991.

- Fraser, L., Williamson, D., and Haydel, S., "MMH Fluids Reduce Formation Damage in Horizontal Wells," *Petroleum Engineer International*, Feb. 1994, pp. 44-49.

- Fredrickson, A.G., and Bird, R.B., "Non-Newtonian Flow in Annuli," *Ind. Eng. Chem.*, Vol. 50, 1958, p. 347.

- Gondouin, M., and Heim, A., "Experimentally Determined Resistivity Profiles in Invaded Water and Oil Sands for Linear Flows," *Journal of Petroleum Technology*, March 1964, pp. 337-348.

- Heckman, T., Olsen, G., Scott, K., Seiller, B., Simpson, M., and Blasingame, T., "Best Practices for Reserves Estimation in Conventional Reservoirs - Present and Future Considerations," SPE Unconventional Resources Converence, The Woodlands, Texas, April 10-12, 2013.

- Holditch, S.A., and Dewan, J.T., "The Evaluation of Formation Permeability Using Time Lapse Logging Measurements During and After Drilling," Annual Report, Contract No. 5089-260-1861, Gas Research Institute, December 1991.

- Hovanessian, S.A., and Fayers, F.J., "Linear Water Flood with Gravity and Capillary Effects," *Society of Petroleum Engineers Journal*, Mar. 1961, pp. 32-36.

- Lamb, H., *Hydrodynamics*, Dover Press, New York, 1945.

- Landau, L.D., and Lifshitz, E.M., *Fluid Mechanics*, Pergamon Press, London, 1959.

- Lane, H.S., "Numerical Simulation of Mud Filtrate Invasion and Dissipation," Paper D, *SPWLA 34th Annual Logging Symposium*, June 13-16, 1993.

- Lantz, R.B., "Quantitative Evaluation of Numerical Diffusion (Truncation Error)," *Society of Petroleum Engineers Journal*, Sept. 1971, pp. 315-320.

- Lapidus, L., and Pinder, G.F., *Numerical Solution of Partial Differential Equations in Science and Engineering*, John Wiley & Sons, New York, 1982.

- Latil, M., *Enhanced Oil Recovery*, Gulf Publishing, Houston, 1980.

- Lee, E.H., and Fayers, F.J., "The Use of the Method of Characteristics in Determining Boundary Conditions for Problems in Reservoir Analysis," *Petroleum Transactions, AIME*, Vol. 216, 1959, pp. 284-289.

- Lee, S.H. and Milliken, W.J., "The Productivity Index of an Inclined Well in Finite Difference Reservoir Simulation," Paper No. SPE-25247-MS, *SPE Symposium on Reservoir Simulation*, New Orleans, LA, Feb. 28 – Mar. 3, 1993.

- Marle, C.M., *Multiphase Flow in Porous Media*, Gulf Publishing, Houston, 1981.

- Matthews, C.S., and Russell, D.G., *Pressure Buildup and Flow Tests in Wells, SPE Monograph Series*, Society of Petroleum Engineers, Dallas, 1967.

- McEwen, C.R., "A Numerical Solution of the Linear Displacement Equation with Capillary Pressure," *Petroleum Transactions, AIME*, Vol. 216, 1959, pp. 412-415.

- Messenger, J.U., *Lost Circulation*, PennWell Books, Tulsa, OK, 1981.

- Mikhlin, S.G., *Multidimensional Singular Integrals and Integral Equations*, Pergamon Press, London, 1965.

- Milne-Thomson, L.M., *Proc. Camb. Phil. Soc.*, Vol. 36, 1940.

- Milne-Thomson, L.M., *Theoretical Aerodynamics*, Macmillan & Co., London, 1958.

- Milne-Thomson, L.M., *Theoretical Hydrodynamics*, Macmillan Co., New York, 1968.

- Moretti, G., and Salas, M.D., "Numerical Analysis of Viscous One-Dimensional Flows," in *Numerical Methods in Fluid Dynamics: AGARD Lecture Series No. 48*, Advisory Group for Aerospace Research and Development, North Atlantic Treaty Organization, von Karman Institute, Rhode-Saint-Genese, Belgium, May 1972.

- Muskat, M., *Flow of Homogeneous Fluids Through Porous Media*, McGraw-Hill, New York, 1937.

- Muskat, M., *Physical Principles of Oil Production*, McGraw-Hill, New York, 1949.

- Outmans, H.D., "Mechanics of Static and Dynamic Filtration in the Borehole," Society of Petroleum Engineers Journal, Sept. 1963, pp. 236-244.

- Peaceman, D.W., *Fundamentals of Numerical Reservoir Simulation*, Elsevier Scientific Publishing, Amsterdam, 1977.

- Peaceman, D.W., "Interpretation of Well-Block Pressures in Numerical Reservoir Simulation," *Society of Petroleum Engineers Journal*, June 1978, pp. 183-194.

- Peaceman, D.W., "Interpretation of Well-Block Pressures in Numerical Reservoir Simulation with Nonsquare Grid Blocks and Anisotropic Permeability," *Society of Petroleum Engineers Journal*, June 1983, pp. 531-543.

- Peaceman, D.W., and Rachford, H.H., "Numerical Calculation of Multidimensional Miscible Displacement," *Society of Petroleum Engineers Journal*, Dec. 1962, pp. 327-339.

- Phelps, G.D., Stewart, G., and Peden, J.M., "The Analysis of the Invaded Zone Characteristics and Their Influence on Wireline Log and Well-Test Interpretation," SPE Paper No. 13287, *59th Annual Technical Conference and Exhibition*, Houston, TX, Sept. 16-19, 1984.

- Proett, M.A., Belanger, D., Manohar, M., and Chin, W.C., "Sample Quality Prediction with Integrated Oil and Water-Based Mud Invasion Modeling," *SPE Paper No. 77964, SPE Asia Pacific Oil & Gas Conference and Exhibition (APOGCE)*, Oct. 2002, Melbourne, Australia.

- Proett, M.A. and Chin, W.C., "Supercharge Pressure Compensation with New Wireline Formation Testing Method," *37th Annual SPWLA Symposium*, New Orleans, Louisiana, June 16-19, 1996.

- Proett, M.A., and Chin, W.C., "Exact Spherical Flow Solution with Storage for Early-Time Test Interpretation," *SPE Journal of Petroleum Technology*, Nov. 1998.

- Proett, M.A., and Chin, W.C., "Advanced Permeability and Anisotropy Measurements While Testing and Sampling in Real-Time Using a Dual Probe Formation Tester," *SPE Paper No. 64650, Seventh International Oil & Gas Conference and Exhibition*, Nov. 2000, Beijing, China.

- Proett, M.A., Chin, W.C., Manohar, M., Sigal, R., and Wu, J., "Multiple Factors That Influence Wireline Formation Tester Pressure Measurements and Fluid Contact Estimates," SPE Paper No. 71566, *2001 SPE Annual Technical Conference and Exhibition*, New Orleans, LA, Sept. 30 – Oct. 3, 2001.

- Richtmyer, R.D., and Morton, K.W., *Difference Methods for Initial Value Problems*, Interscience Publishers, New York, 1957.

- Roache, P.J., *Computational Fluid Dynamics*, Hermosa Publishers, Albuquerque, NM, 1972.

- Saad, M.A., *Thermodynamics for Engineers*, Prentice-Hall, Englewood Cliffs, NJ, 1966.

- Sabet, M.A., *Well Test Analysis*, Gulf Publishing, Houston, 1991.

- Scheidegger, A.E., *The Physics of Flow Through Porous Media*, University of Toronto Press, Toronto, 1957.

- Schlichting, H., *Boundary Layer Theory*, McGraw-Hill, New York, 1968.

- Scholz, N., *Aerodynamics of Cascades*, Neuilly sur Seine, France: Advisory Group for Aerospace Research and Development (AGARD), North Atlantic Treaty Organization (NATO), 1977.

- Semmelbeck, M.E., and Holditch, S.A., "The Effects of Mud-Filtrate Invasion on the Interpretation of Induction Logs," *SPE Formation Evaluation Journal*, June 1988, pp. 386-392.

- Sharpe, H.N., and Anderson, D.A., "Orthogonal Curvilinear Grid Generation with Preset Internal Boundaries for Reservoir Simulation," *Paper No. 21235, Eleventh SPE Symposium on Reservoir Simulation*, Anaheim, CA, Feb. 17-20, 1991.

- Sheldon, J.W., Zondek, B., and Cardwell, W.T., "One-Dimensional, Incompressible, Noncapillary, Two-Phase Fluid Flow in a Porous Medium," *Petroleum Transactions, AIME*, Vol. 216, 1959, pp. 290-296.

- Sichel, M., "The Effect of Longitudinal Viscosity on the Flow at a Nozzle Throat," *Journal of Fluid Mechanics*, 1966, pp. 769-786.

- Slattery, J.C., *Momentum, Energy, and Mass Transfer in Continua*, Robert E. Krieger Publishing Company, New York, 1981.

- Streeter, V.L., *Handbook of Fluid Dynamics*, McGraw-Hill, New York, 1961.

- Streltsova, T.D., *Well Testing in Heterogeneous Formations*, John Wiley & Sons, New York, 1988.

- Tamamidis, P., and Assanis, D.N., "Generation of Orthogonal Grids with Control of Spacing," *J. Computational Physics*, Vol. 94, 1991, pp. 437-453.

- Thomas, G.B., *Calculus and Analytic Geometry*, Addison-Wesley, Reading, MA, 1960.

- Thomas, G.W., *Principles of Hydrocarbon Reservoir Simulation*, International Human Resources Development Corporation, Boston, 1982.

- Thomas, P.D., "Composite Three-Dimensional Grids Generated by Elliptic Systems," *AIAA J.*, Sept. 1982, pp. 1195-1202.

- Thomas, P.D., and Middlecoff, J.F., "Direct Control of the Grid Point Distribution in Meshes Generated by Elliptic Equations," *AIAA J.*, June 1980, pp. 652-656.

- Thompson, J.F., "Numerical Solution of Flow Problems Using Body-Fitted Coordinate Systems," *Lecture Series 1978-4, von Karman Institute for Fluid Dynamics*, Brussels, Belgium, Mar. 1978.

- Thompson, J.F., "Grid Generation Techniques in Computational Fluid Dynamics," *AIAA J.*, Nov. 1984, pp. 1505-1523.

- Thompson, J.F., Warsi, Z.U.A., and Mastin, C.W., *Numerical Grid Generation*, Elsevier Science Publishing, New York, 1985.

- Thwaites, B., *Incompressible Aerodynamics*, Oxford Press, Oxford, 1960.

- Tobola, D.P., and Holditch, S.A., "Determination of Reservoir Permeability from Repeated Induction Logging," SPE Paper No. 19606, 64*th* Annual Technical Conference and Exhibition of the Society of Petroleum Engineers, San Antonio, Texas, October 8-11, 1989.

- van Everdingen, A.F., and Hurst, W., "The Application of the Laplace Transformation to Flow Problems in Reservoirs," *Transactions of the A.I.M.E.*, Vol. 186, 1949, pp. 305-324.

- van Golf-Racht, T.D., *Fundamentals of Fractured Reservoir Engineering*, Elsevier Scientific Publishing, Amsterdam, 1982.

- van Poollen, H.K., Breitenbach, E.A., and Thurnau, D.H., "Treatment of Individual Wells and Grids in Reservoir Modeling," *Society of Petroleum Engineers Journal*, Dec. 1968, pp. 341-346.

- Weinig, F.S., "Theory of Two-Dimensional Flow Through Cascades," in *High Speed Aerodynamics and Jet Propulsion, Vol. X: Aerodynamics of Turbines and Compressors*, edited by W.R. Hawthorne, Princeton University Press, Princeton, NJ, 1964.

- Wesseling, P., *An Introduction to Multigrid Methods*, John Wiley & Sons, Chichester, 1992.

- Williamson, A.S., and Chappelear, J.E., "Representing Wells in Numerical Reservoir Simulation: Part 1–Theory," *Society of Petroleum Engineers Journal*, June 1981, pp. 323-338.

- Wolfsteiner, C., Durlofsky, L.J. and Aziz, K., "Calculation of Well Index for Nonconventional Wells on Arbitrary Grids," *Computational Geosciences* 7: 61–82, Kluwer Academic Publishers, The Netherlands, 2003.

- Yih, C.S., *Fluid Mechanics*, McGraw-Hill, New York, 1969.

- Zarnowski, R., and Hoff, D., "A Finite Difference Scheme for the Navier-Stokes Equations of One-Dimensional, Isentropic, Compressible Flow," *SIAM Journal of Numerical Analysis*, Feb. 1991, 78-112.

- Zhou, Y., Hao, Z., Feng, Y., Yu, Q. and Chin, W.C., "Formation Testing: New Methods for Rapid Mobility and Pore Pressure Prediction," Paper No. OTC 24890-MS, *Offshore Technology Conference Asia*, Kuala Lumpur, Malaysia, Mar. 25-28, 2014.

- Zhou, Y., Zhao, L., Feng, Y., Yu, Q. and Chin, W.C., "Formation Testing: New Methods for Rapid Mobility and Pore Pressure Prediction," Paper No. IPTC 17214-MS, *International Petroleum Technology Conference*, Doha, Qatar, Jan. 20-22, 2014.

Index

About the Author

Wilson C. Chin earned his Ph.D. from the Massachusetts Institute of Technology and his M.Sc. from the California Institute of Technology.

He has authored more than one hundred papers, over four dozen patents, and almost twenty books in petroleum engineering with Gulf Publishing, Elsevier Scientific and John Wiley & Sons. His interests include formation testing, reservoir engineering, acoustic and resistivity logging, MWD design and telemetry, and managed pressure drilling.

SCIENTIFIC BOOK PUBLICATIONS

Eighteen original books, describing personal research in reservoir engineering, electromagnetics, formation evaluation, Measurement-While-Drilling, sensor design, and drilling and cementing rheology, namely,

- *Measurement While Drilling Signal Analysis, Optimization and Design, Second Edition* (Wiley-Scrivener, 2018)
- *Modern Borehole Analytics for Annular Flow, Hole Cleaning and Pressure Control* (Wiley-Scrivener, 2017)
- *Quantitative Methods in Reservoir Engineering, Second Edition – with New Topics in Formation Testing and Multilateral Well Flow Analysis* (Elsevier, 2017)
- *Managed Pressure Drilling: Modeling, Strategy and Planning, Chinese Edition* (Elsevier, 2016)
- *Resistivity Modeling: Propagation, Laterolog and Micro-Pad Analysis* (Wiley-Scrivener, 2016)
- *Reservoir Engineering in Modern Oilfields: Vertical, Deviated, Horizontal and Multilateral Well Systems* (Wiley-Scrivener, 2016)
- *Formation Testing: Low Mobility Pressure Transient Analysis* (*with CNOOC*, Wiley-Scrivener, 2015)
- *Wave Propagation in Drilling, Well Logging and Reservoir Applications* (Wiley-Scrivener, 2014)
- *Measurement While Drilling Signal Analysis, Optimization and Design* (*with CNPC*, Wiley-Scrivener, 2014)
- *Electromagnetic Well Logging: Models for MWD/LWD Interpretation and Tool Design* (Wiley-Scrivener, 2014)
- *Formation Testing Pressure Transient and Contamination Analysis* (*with CNOOC*, Wiley-Scrivener, 2014)
- *Managed Pressure Drilling: Modeling, Strategy and Planning* (Elsevier, 2012)
- *Quantitative Methods in Reservoir Engineering* (Elsevier, 2002)
- *Computational Rheology for Pipeline and Annular Flow* (Elsevier, 2001)
- *Formation Invasion, with Applications to Measurement-While-Drilling, Time Lapse Analysis and Formation Damage* (Gulf Publishing, 1995)
- *Wave Propagation in Petroleum Engineering, with Applications to Drillstring Vibrations, Measurement-While-Drilling, Swab-Surge and Geophysics* (Gulf Publishing, 1994)
- *Modern Reservoir Flow and Well Transient Analysis* (Gulf Publishing, 1993)
- *Borehole Flow Modeling in Horizontal, Deviated and Vertical Wells* (Gulf Publishing, 1992)

UNITED STATES PATENTS

- U.S. Patent No. 7,243,537 Methods for Measuring a Formation Supercharge Pressure, with M. Proett, J. Beique, J. Hardin, J. Fogal, D. Welshans, and G. Gray, July 17, 2007

- U.S. Patent No. 7,224,162 System and Methods for Upscaling Petrophysical Data, with M. Proett, J. Fogal, and P. Aadireddy, May 29, 2007

- U.S. Patent No. 7,082,078. Magneto-Rheological Fluid Controlled Mud Pulser, with M. Fripp and N. Skinner, July 25, 2006

- U.S. Patent No. 7,059,179. Multi-Probe Pressure Transient Analysis for Determination of Horizontal Permeability, Anisotropy and Skin in an Earth Formation, with M. Proett, June 13, 2006

- U.S. Patent No. 6,327,538. Method and Apparatus for Evaluating Stoneley Waves, and for Determining Formation Parameters in Response Thereto, Dec. 4, 2001

- U.S. Patent No. 5,969,638. Multiple Transducer MWD Surface Signal Processing, Oct. 19, 1999

- U.S. Patent No. 5,831,177. Fluid Driven Siren Flowmeter, with J. Anders, M. Proett, and M. Waid, Nov. 3, 1998

- U.S. Patent No. 5,787,052. Snap Action Rotary Pulser, with W. Gardner, July 28, 1998

- U.S. Patent No. 5,740,126. Turbosiren Signal Generator for Measurement While Drilling Systems, with T. Ritter, April 14, 1998

- U.S. Patent No. 5,703,286. Method of Formation Testing, with M. Proett and C. Chen, Dec. 30, 1997

- U.S. Patent No. 5,672,819. Formation Evaluation Using Phase Shift Periodic Pressure Pulse Testing, with M. Proett, Sept. 30, 1997

- U.S. Patent No. 5,644,076. Wireline Formation Tester Supercharge Correction Method, with M. Proett and M. Waid, July 1, 1997

- U.S. Patent No. 5,586,083. Turbosiren Signal Generator for Measurement While Drilling Systems, with T. Ritter, Dec. 17, 1996

- U.S. Patent No. 5,583,827. Measurement-While-Drilling System and Method, Dec. 10, 1996

- U.S. Patent No. 5,535,177. MWD Surface Signal Detector Having Enhanced Acoustic Detection Means, with K. Hamlin, July 9, 1996

- U. S. Patent No. 5,515,336. MWD Surface Signal Detector Having Bypass Loop Acoustic Detection Means, with W. Gardner and M. Waid, May 7, 1996

- U. S. Patent No. 5,459,697. MWD Surface Signal Detector Having Enhanced Acoustic Detection Means, with K. Hamlin, Oct. 17, 1995
- U. S. Patent No. 4,785,300. Pressure Pulse Generator, with J. Trevino, Nov. 15, 1988

INTERNATIONAL AND DOMESTIC PATENTS

- CA2556937, 9/21/2010, Methods for measuring a formation supercharge pressure
- BRPI0508357, 7/24/2007, Método para determinar a pressão de supercarga em uma formação interceptada por um furo de sondagem
- US7243537, 7/17/2007, Methods for measuring a formation supercharge pressure
- US7224162, 5/29/2007, System and methods for upscaling petrophysical data
- CA2156224, 10/17/2006, MWD surface signal detector having bypass loop acoustic detection means
- CA2156223, 8/1/2006, MWD surface signal detector having bypass loop acoustic detection means
- US7082078, 7/25/2006,   Magneto-rheological fluid controlled mud pulser
- US7059179, 6/13/2006, Multi-probe pressure transient analysis for determination of horizontal permeability, anisotropy and skin in an earth formation
- WO2005084332, 9/15/2005, Methods for measuring a formation supercharge pressure
- WO2005036338, 4/21/2005, System and methods for upscaling petrophysical data
- WO2005017301, 2/24/2005, Electroactive fluid controlled mud pulser
- US06327538 , 12/04/2001, Method and apparatus for evaluating Stoneley waves, and for determining formation parameters in response thereto
- EP00936477A3, 12/13/2000, Evaluating Stoneley waves and formation parameters
- EP1053488, 11/22/2000, Multiple transducer MWD surface signal processing
- NO20003826A, 09/26/2000, Behandling av signal fra multippel MWD-transducer p overflaten
- NO20003826A0, 07/26/2000, Behandling av signal fra multippel MWD-transducer p overflaten
- EP00747571B1, 02/02/2000, Downhole pressure pulse generator

- EP0950795, 10/20/1999, Tool for and method of geological formation evaluation testing
- US5969638, 10/19/1999, Multiple transducer MWD surface signal processing
- NO00990872A, 10/18/1999, Verktoey og fremgangsmte for geologisk formasjonsevaluering og testing
- EP936477A2, 8/18/1999, Evaluating Stoneley waves and formation parameters
- NO00990615A, 8/18/1999, Evaluering av Stoneley-boelger og formasjonsparametre
- WO09938032, 7/29/1999, Multiple transducer MWD surface signal processing
- NO00990872A0, 02/24/1999, Verkt y og fremgangsmte for geologisk formasjonsevaluering og testing
- NO00990615A0, 02/09/1999, Evaluering av Stoneley-boelger og formasjonsparametre
- US05831177, 11/03/1998, Fluid driven siren flowmeter
- US05787052, 07/28/1998, Snap action rotary pulser
- US05740126, 04/14/1998, Turbo-siren signal generator for measurement while drilling systems
- US05703286, 12/30/1997, Method of formation testing
- EP0747571, 12/11/1996, Downhole pressure pulse generator
- US05672819, 09/30/1997, Formation evaluation using phase shift periodic pressure pulse testing
- EP00697499A3, 07/30/1997, Apparatus for detecting an acoustic signal in drilling mud
- US05644076, 07/01/1997, Wireline formation tester supercharge correction method
- US05586083, 12/17/1996 Turbo siren signal generator for measurement while drilling systems
- EP00747571A2, 12/11/1996, Downhole pressure pulse generator
- US05583827, 12/10/1996, Measurement-while-drilling system and method
- US05535177, 07/09/1996, MWD surface signal detector having enhanced acoustic detection means
- US05515336, 05/07/1996, MWD surface signal detector having bypass loop acoustic detection means

- EP00697498, 02/21/1996, Apparatus for detecting pressure pulses in a drilling fluid supply
- EP00697499A2, 02/21/1996, Apparatus for detecting an acoustic signal in drilling mud
- EP00697498A2, 02/21/1996, Apparatus for detecting pressure pulses in a drilling fluid supply
- NO00953224A, 02/19/1996, Anordning til paavisning av trykkpulser i en ledning for tilfoersel av borevaeske
- NO00953223A, 02/19/1996, Overflate-signaldetektor for maaling I loepet av boringen med forsterket akustisk detektorinnretning
- CA02156224AA, 02/18/1996, MWD surface signal detector having bypass loop acoustic detection means
- CA02156223AA, 02/18/1996, MWD surface signal detector having enhanced acoustic detection means
- US05459697, 10/17/1995, MWD surface signal detector having enhanced acoustic detection means
- NO00953224A0, 08/16/1995, Anordning for aa detektere trykkpulser I en borefluid
- NO00953223A0, 08/16/1995, Overflate-signaldetektor for maaling I loepet av boringen med forsterket akustisk detektorinnretning
- US4785300, 11/15/1988, Pressure pulse generator
- CA1228909, 11/03/1987, Pressure pulse generator
- BRPI8405278, 8/27/1985, Gerador de pulsos de pressao
- EP0140788, 5/8/1985, Pressure pulse generator
- NO00844026A, 04/25/1985, Trykkpulsgenerator

About one dozen domestic and international patent applications filed or in preparation for filing, covering aapplications in MWD telemetry and hardware design, advanced gas lift, turbine power generation, and formation testing.

JOURNAL ARTICLES AND CONFERENCE PUBLICATIONS

Single-authored unless noted otherwise.

- Exact Three-Dimensional Electromagnetic Model: MWD/LWD Anisotropic Prediction for R_h and R_v, *Journal of Sustainable Energy Engineering*, 2015

- High-Data-Rate Measurement-While-Drilling System for Very Deep Wells, with Y. Su, L. Sheng, L. Li, H. Bian and R. Shi, *Well Logging Technology Journal*, Xi'an, China, Dec. 2014

- Strategies in High-Speed MWD Mud Pulse Telemetry, with Y. Su, L. Sheng, L. Li, H. Bian, R. Shi and X. Zhuang, *Journal of Sustainable Energy Engineering*, Dec. 2014

- Formation Testing: New Methods for Rapid Mobility and Pore Pressure Prediction, with Y. Zhou, Z. Hao, Y. Feng and Q. Yu, Paper OTC-24890-MS, *2014 Offshore Technology Conference Asia (OTC Asia)*, Kuala Lumpur, Malaysia, Mar. 25-28, 2014

- Formation Testing: New Methods for Rapid Mobility and Pore Pressure Prediction, with Y. Zhou, L. Zhao, Y. Feng and Q. Yu, Paper 17214, *7th International Petroleum Technology Conference (IPTC)*, Doha, Qatar, Jan. 19-22, 2014

- Formation Tester Flow Analysis in Anisotropic Media With Flowline Storage and Skin at Arbitrary Dip, *Well Logging Technology Journal*, Xi'an, China, Feb. 2013

- Advances in Swab-Surge Modeling for Managed Pressure Drilling, with X. Zhuang, Paper OTC-21115-PP, *2011 Offshore Technology Conference*, Houston, TX, May 2-5, 2011

- Effect of Rotation on Flowrate and Pressure Gradient in Eccentric Holes, with X. Zhuang, Paper AADE-11-NTCE-45, *AADE 2011 National Technical Conference and Exhibition*, Houston, TX, April 12-14, 2011

- Advances in Swab-Surge Modeling for Managed Pressure Drilling, with X. Zhuang, Paper AADE-11-NTCE-46, *AADE 2011 National Technical Conference and Exhibition*, Houston, TX, April 12-14, 2011

- Transient, Multiphase, Three-Dimensional Pumping Models for Cementing and Drilling, with X. Zhuang, Paper AADE-11-NTCE-72, *AADE 2011 National Technical Conference and Exhibition*, Houston, TX, April 12-14, 2011

- Comprehensive Annular Flow Models for Drilling and Completions, with X. Zhuang, Paper AADE-11-NTCE-73, *AADE 2011 National Technical Conference and Exhibition*, Houston, TX, April 12-14, 2011

- High-Data-Rate Measurement-While-Drilling System for Very Deep Wells, with Y. Su, L. Sheng, L. Li, H. Bian and R. Shi, Paper AADE-11-NTCE-74, *AADE 2011 National Technical Conference and Exhibition*, Houston, TX, April 12-14, 2011

- Flow Simulation Methods for Managed Pressure Drilling and Cementing, *Drilling and Completing Trouble Zones Conference*, Galveston, TX, Oct. 19-21, 2010

- Modeling and Simulation of Managed Pressure Drilling for Improved Design, Risk Assessment, Training and Operations, *RPSEA Ultra-Deepwater Technology Conference*, Houston, TX, June 22-23, 2010

- Exact Non-Newtonian Flow Analysis of Yield Stress Fluids in Highly Eccentric Borehole Annuli with Pipe or Casing Translation and Rotation, with X. Zhuang, SPE Paper 131234-PP, *CPS/SPE International Oil & Gas Conference and Exhibition*, Beijing, China, June 8-10, 2010

- Displacement of Viscoplastic Fluids in Eccentric Annuli: Numerical Simulation and Experimental Validation, with T. Deawwanich, J.C. Liew, Q.D. Nguyen, M. Savery and N. Tonmukayakul, *Chemeca 2008 Conference*, Newcastle, Australia, Sept. 28 - Oct. 1, 2008

- Laminar Displacement of Viscoplastic Fluids in Eccentric Annuli – Numerical Simulation and Experimental Validations, with M. Savery, P. Tonmukayakul, T. Deawwanich, J. Liew and Q. Dzuy Nguyen, *XXII International Congress of Theoretical and Applied Mechanics (ICTAM 2008)*, Adelaide, Australia, Aug. 24-29, 2008

- Flow Visualization and Numerical Simulation of Viscoplastic Fluid Displacements in Eccentric Annuli, with Q.D. Nguyen, T. Deawwanich, N. Tonmukayakul and M.R. Savery, *XVth International Congress on Rheology (ICR 2008)*, Society of Rheology 80th Annual Meeting, Monterey, CA, Aug. 3-8, 2008

- Modeling Cement Placement Using a New Three-Dimensional Flow Simulator, with M. Savery, *AADE 2008 Fluids Technology Conference*, Houston, April 8-9, 2008

- Formation Tester Inverse Permeability Interpretation for Liquids in Anisotropic Media with Flowline Storage and Skin at Arbitrary Dip, with X. Zhuang, *48th Annual SPWLA Meeting*, Austin, TX, June 3-6, 2007

- Modeling Fluid Interfaces During Cementing Using a Three-Dimensional Mud Displacement Simulator, with M. Savery and R. Darbe, OTC Paper 18513, *2007 Offshore Technology Conference (OTC)*, Houston, TX, April 30 – May 3, 2007

- Formation Tester Immiscible and Miscible Flow Modeling for Job Planning Applications, with M. Proett, *46th Annual SPWLA Meeting*, New Orleans, LA, June 26-29, 2005

- MWD Siren Pulser Fluid Mechanics, *Petrophysics*, Journal of the Society of Petrophysicists and Well Log Analysts (SPWLA), Vol. 45, No. 4, July – August 2004, pp. 363-379

- Formation Testing in the Dynamic Drilling Environment, with M. Proett, D. Seifert, S. Lysen, and P. Sands, *SPWLA 45th Annual Logging Symposium*, Noordwijk, The Netherlands, June 6-9, 2004

- Job Planning Simulators for Immiscible and Miscible Flow, *SPWLA Spring Topical Conference, Formation Testing: Applications and Practices*, Taos, NM, Mar. 28 – Apr. 1, 2004

- Mudcake Growth, Invasion, and Dynamic Coupling with Reservoir Flow: Experiment and Theory, *SPWLA Spring Topical Conference, Formation Testing: Applications and Practices*, Taos, NM, Mar. 28 – Apr. 1, 2004

- Sample Quality Prediction with Integrated Oil and Water-based Mud Invasion Modeling, with M. Proett, D. Belanger, M. Manohar, and J. Wu, *PetroMin Magazine,* Sept. 2003

- Improved Rheology Model and Hydraulics Analysis for Tomorrow's Wellbore Fluid Applications, with R. Morgan, T. Becker, and J. Griffith, SPE Paper 82415*, SPE Production and Operations Symposium*, Oklahoma City, OK, Mar. 2003

- Sample Quality Prediction with Integrated Oil and Water-based Mud Invasion Modeling, with M. Proett, D. Belanger, M. Manohar, and J. Wu, SPE Paper 77964*, SPE Asia Pacific Oil & Gas Conference and Exhibition (APOGCE)*, Melbourne, Australia, Oct. 2002

- Multiple Factors That Influence Wireline Formation Tester Pressure Measurements and Fluid Contacts Estimates, with M. Proett, M. Manohar, R. Sigal, and J. Wu, SPE Paper 71566*, SPE Annual Technical Conference and Exhibition*, New Orleans, LA, Oct. 2001

- Comprehensive Look at Factors Influencing Wireline Formation Tester Pressure Measurements and Fluid Contacts, with M. Proett, M. Manohar, and R. Sigal*, 42nd SPWLA Annual Symposium, Society of Professional Well Log Analysts*, Houston, TX, June 2001

- New Wireline Formation Testing Tool With Advanced Sampling Technology, with M. Proett, G. Gilbert, and M. Monroe*, SPE Reservoir Evaluation and Engineering*, April 2001

- Advanced Permeability and Anisotropy Measurements While Testing and Sampling in Real-Time Using a Dual Probe Formation Tester, with M. Proett, SPE Paper 64650, *Seventh International Oil & Gas Conference and Exhibition*, Beijing, China, Nov. 2000

- Modern Flow Assurance Methods, Part III: Coupled Velocity and Temperature Fields in Bundled Pipelines, *Offshore*, Nov. 2000

- Modern Flow Assurance Methods, Part II: Detailed Physical Properties and Engineering Application, *Offshore*, Oct. 2000

- Modern Flow Assurance Methods, Part I: Clogged Pipelines, Wax Deposition, and Hydrate Plugs, *Offshore*, Sept. 2000

- Advanced Permeability and Anisotropy Measurements While Testing and Sampling in Real Time Using a Dual Probe Formation Tester, with M. Proett, SPE Paper 62919, *2000 SPE Annual Technical Conference and Exhibition*, Dallas, TX, Oct. 2000

- General Three-Dimensional Electromagnetic Model for Nondipolar Transmitters in Layered Anisotropic Media With Dip, *Well Logging Technology Journal*, Xi'an, China, Aug. 2000

- New Dual Probe Wireline Formation Testing and Sampling Tool Enables Real-Time Permeability and Anisotropy Measurements, with M. Proett, *41st SPWLA Annual Symposium, Society of Professional Well Log Analysts*, Dallas, TX, June 2000

- Clogged Pipe, Non-Newtonian Fluid, and Coupled Solids Deposition Flow Modeling, Final Technical Report, Brown & Root Energy Services, Houston, TX, May 2000

- Irregular Grid Generation and Rapid 3D Color Display Algorithm, Final Technical Report, DOE Grant No. DE-FG03-99ER82895, United States Department of Energy, May 2000

- New Dual-Probe Wireline Formation Testing and Sampling Tool Enables Real-Time Permeability and Anisotropy Measurements, with M. Proett, M. Manohar, G. Gilbert, and M. Monroe, SPE Paper 59701, *SPE Permian Basin Oil & Gas Recovery Conference*, Midland, TX, March 2000. Also presented at *SPE Rocky Mountain Regional Low Permeability Reservoirs Symposium and Exhibition*, Denver, CO, March 2000

- New Wireline Formation Testing Tool with Advanced Sampling Technology, with M. Proett, G. Gilbert, and M. Monroe, SPE Paper 56711, *1999 SPE Annual Technical Conference and Exhibition*, Houston, TX

- Exact Spherical Flow Solution with Storage for Early-Time Test Interpretation, with M. Proett, *SPE Journal of Petroleum Technology*, Nov. 1998

- New Exact Spherical Flow Solution with Storage *and Skin* for Early-Time Interpretation, with Applications to Wireline Formation and Early-Evaluation Drillstem Testing, with M. Proett, SPE Paper 49140, *1998 SPE Annual Technical Conference and Exhibition*, New Orleans, LA, Sept. 1998

- New Exact Spherical Flow Solution for Early-Time Well Test Interpretation with Applications to Wireline Formation Testing and Early-Evaluation Drillstem Testing, with M. Proett, SPE Paper 39915, *SPE Rocky Mountain Regional Meeting/Low Permeability Reservoirs Symposium*, April 1998

- New Exact Spherical Flow Solution for Early-Time Well Test Interpretation with Applications to Wireline Formation Testing and Early-Evaluation Drillstem Testing, with M. Proett, SPE Paper 39768*, SPE Permian Basin Oil and Gas Recovery Conference*, Midland, TX, March 1998

- Pressure Test Validity Shown by Comparing Field Tests and Simulations, Part II: Formation Pressure Test Tools, with N. Skinner, M. Proett, P. Ringgenberg, and R. Aadireddy, *Oil & Gas Journal*, Jan. 12, 1998

- Testing System Combines Advantages of Wireline and Drillstem Testers, Part I: Formation Pressure Test Tools, with N. Skinner, M. Proett, P. Ringgenberg, and R. Aadireddy, *Oil & Gas Journal*, Jan. 5, 1998

- New Early Formation Pressure System Field Test Results and Advances in Early Time Pressure Buildup Analysis, with N. Skinner, M. Proett, P. Ringgenberg, K. Manke, H. Smith, and R. Aadireddy, SPE Paper 38648, *1997 SPE Annual Technical Conference and Exhibition*, San Antonio, TX, Oct. 1997

- Permeability Prediction from Formation Tester "Phase Delay" and "Sonic Pulse" Analysis, with M. Proett, *GRI – SPWLA Research Forum on Permeability Logging*, Houston, TX, Feb. 1997

- Permeability Prediction from Stoneley Waveform Data, *GRI – SPWLA Research Forum on Permeability Logging*, Houston, TX, Feb. 1997

- Supercharge Pressure Compensation Using a New Wireline Testing Method and Newly Developed Early Time Spherical Flow Model, with M. Proett, SPE Paper 36524*, 1996 Annual Technical Conference and Exhibition of the Society of Petroleum Engineers*, Denver, CO, Oct. 1996

- Supercharge Pressure Compensation with New Wireline Formation Testing Method, with M. Proett, *1996 Annual Meeting of the Society of Professional Well Log Analysts*, New Orleans, LA, June 1996

- Supercharge Pressure Compensation with New Wireline Formation Testing Method, with M. Proett, *SPE Paper 35178, Permian Basin Oil and Gas Recovery Conference*, Midland, TX, March 1996

- Modeling Complex Horizontal Wells in Heterogeneous Formations, *Offshore*, Oct. 1993
- Eccentric Annular Flow Modeling for Highly Deviated Boreholes, *Offshore*, Aug. 1993
- Model Offers Insight Into Spotting Fluid Performance, *Offshore*, Feb. 1991
- Annular Flow Model Explains Conoco's Borehole Cleaning Success, *Offshore*, Oct. 1990
- Exact Cuttings Transport Correlations Developed for High Angle Wells, *Offshore*, May 1990
- Advances in Annular Borehole Flow Modeling, *Offshore*, Feb. 1990
- Comparative Studies in Dual Porosity Reservoir Simulation, *BP Exploration Reservoir Technology Report No. H090.0005*, Houston, TX, Jan. 1990
- Automating the Acquisition Planning Process at the Johnson Space Center (using Artificial Intelligence Methods), with J. Golej, MITRE Corporation Report MTR-88D00065, NASA/JSC Contract No. NAS9-18057, Sept. 1988
- Simulating Horizontal Well Fracture Flow, *Offshore*, Aug. 1988
- Why Drill Strings Fail at the Neutral Point, *Petroleum Engineer International*, May 1988
- Fatal Tubular Bending Motions Difficult to Detect Uphole, *Offshore*, April 1988
- Formation Evaluation Using Repeated MWD Logging Measurements, with A. Suresh, P. Holbrook, L. Affleck, and H. Robertson, *SPWLA 27th Annual Logging Symposium*, Houston, TX, June 9-13, 1986

More than thirty aerospace engineering, computational fluid dynamics and mathematics papers in *ASME Journal of Applied Mechanics*, *AIAA Journal*, *Journal of Aircraft* and *Journal of Hydronautics* omitted for brevity. Complimentary copies of all articles available upon request.